

An Inverted Hydride-fueled Pressurized Water Reactor Concept

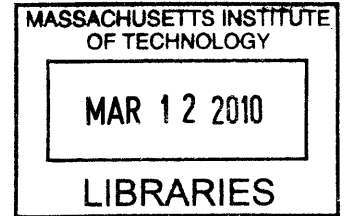
by

Paolo Ferroni

M.S. Nuclear Engineering
Torino Polytechnic, Italy (2004)

M.S Nuclear Science and Engineering
Massachusetts Institute of Technology (2006)

ARCHIVES



Submitted to the Department of Nuclear Science and Engineering
in partial fulfillment of the requirements for the degree of

DOCTOR OF PHILOSOPHY

at the

MASSACHUSETTS INSTITUTE OF TECHNOLOGY

February 2010

Copyright © 2010 Massachusetts Institute of Technology
All rights reserved

Signature of Author _____

Department of Nuclear Science and Engineering
January 07, 2010

Certified by _____

Neil E. Todreas (thesis supervisor)
Professor Emeritus of Nuclear Engineering

Dr. Pavel Hejzlar (thesis reader)
Reactor Core Design Lead at TerraPower LLC

Accepted by _____

Jacquelyn C. Yanch
Chair, Department Committee on Graduate Students

An Inverted Hydride-fueled Pressurized Water Reactor Concept

by

Paolo Ferroni

Submitted to the Department of Nuclear Science and Engineering on January 7, 2010
in partial fulfillment of the requirements for the degree of
Doctor of Philosophy in Nuclear Science and Engineering
at the Massachusetts Institute of Technology

Abstract

Previous studies conducted at MIT showed that power performance of typical pin geometry PWRs are limited by three main constraints: core pressure drop, critical heat flux (CHF) and fretting phenomena of the fuel rods against grid spacers. The present work investigates the possibility to reduce the limiting effect exerted by these constraints by radically changing the core geometry, rather than by only taking measures to address specific constraints. The geometry modification consists of inverting the relative position of fuel and coolant, thus generating the so-called inverted geometry. An inverted assembly consists of a fuel prism perforated with cylindrical, vertically oriented, cooling channels, arranged in a triangular lattice. A pin vs inverted comparison, performed at cell level, shows that an inverted geometry can attain the same fuel volume fraction of the pin geometry but with a much lower pressure drop and fuel temperature. Also, CHF performance can be enhanced, relative to the pin geometry, by inserting multiple short-length twisted tapes (MSLTTs) inside the cooling channels, and fretting concerns do not apply since spacer grids are not needed.

When the pin vs inverted comparison is performed at whole-core level, the same conclusion on pressure drop and fuel temperature apply to reactor types in which, thanks to low operating pressure and/or fuel-coolant chemical compatibility, the inverted core can be designed as to closely resemble a modular repetition of the inverted unit cell, i.e. the so-called continuous inverted geometry. However, the high operating pressure characterizing a PWR, together with the need of avoiding fuel-water interaction, require the inverted PWR (IPWR) to be provided with particularly thick ducts enclosing the fuel prisms. These ducts, together with the wide inter-assembly water gaps needed for control rod insertion, cause the inverted geometry to become discontinuous, and to lose part of the pressure drop and fuel temperature advantages characterizing a continuous inverted geometry.

A U-Th-Zr-hydride fuel was selected for the IPWR. The main reasons that led to its choice were the negligible fission gas release which is compatible with the need to enclose the fuel in a large duct, and the pre-hydrating metal structure of the fuel which allows an effective drilling.

A detailed study was performed to maximize the performance of a hydride-fueled IPWR, accounting for structural mechanics, thermal hydraulics, neutronics and manufacturing-related constraints. The analysis was performed over a wide spectrum of lattice geometries, each characterized by specific values of the cooling channel diameter and pitch. Three cooling channel designs were examined: MSLTT-provided channels, channels provided with a long twisted tape inserted in the top half of the core, and empty channels. Two duct designs were

examined: collapsible and non-collapsible. The former, about 210 mm wide and with ~9 mm thick walls, is designed to collapse onto the fuel prism upon primary system pressurization. The latter, about 100 mm wide and with ~6 mm thick walls, is internally pressurized: its small size together with the reduced differential pressure across its walls, allow preventing duct-fuel contact, but significantly penalize the reactor power performance due to the reduced volume available for fuel and coolant. As a consequence of these design options, a total of six IPWR designs were examined.

Because of the scarcity of pressure drop data referred to MSLTT designs, pressure drop tests were performed and results entered in the IPWR computational analysis model. Besides usefulness for the IPWR study, the wide range of MSLTT designs that were tested allowed supplementing the literature with valuable experimental data.

It was found that pressure drop is the most limiting IPWR design constraint, followed by CHF and, only marginally, fuel temperature. The fuel web thickness, i.e. the minimum thickness of fuel meat between adjacent cooling channels, was also found to significantly affect the attainable power. Specifically, the smaller this thickness, the higher is the power. To allow fuel prism manufacturability, fuel web thicknesses as low as 2 mm were examined.

The IPWR provided with collapsible ducts and empty cooling channels was verified to outperform all the other IPWR designs examined. Conclusions on the competitiveness, from the attainable power viewpoint, of this IPWR design against typical pin geometry PWRs depend on the IPWR considered (maximum powered, but provided with a very small web thickness, or a “selected design”, having lower power but larger fuel web thickness) and on the PWR relative to which the comparison is performed (maximum powered, but with thin 6.5 mm OD fuel rods, or reference geometry 9.5 mm OD rods). If the maximum powered IPWR is considered, maximum power gains are of 13% and 48% with respect to the maximum powered PWR and to the reference PWR respectively. If the selected IPWR design is considered, no power gain is possible relative to the maximum powered PWR, while a power gain of 19% is achievable relative to the reference PWR.

A comprehensive analysis, including LBLOCA modeling and neutronics, was performed on the selected IPWR design. This reactor was demonstrated to be able to deliver a thermal power of 4078 MW, corresponding to a 19% gain with respect to the reference PWR analyzed with the same pressure drop limit. Power density and specific power are 119 MW/m³ and 73.6 kW/kg_{HM} respectively. Required fuel enrichment to achieve a 17.2 month fuel cycle is 15%.

Although a net power gain was demonstrated, the economic competitiveness of the IPWR concept is penalized by the higher enrichment required and, eventually, by higher manufacture costs of the inverted assemblies relative to pin assemblies. A complete economic analysis, not performed in this work, would be needed to assess the benefits of the IPWR design.

Thesis Supervisor: Neil. E. Todreas
Title: Professor Emeritus of Nuclear Engineering

Thesis Reader: Pavel Hejzlar
Title: Reactor Core Design Lead at TerraPower LLC

Acknowledgements

I would like to express my sincere gratitude to my supervisor, Professor Todreas, for his continuous guidance and help during my five years at MIT. Our collaboration has been fruitful and this thesis is the tangible proof. Less tangible proof also exists: work planning and multi-tasking are precious things I learned from him. Learning to write concisely, or at least more concisely than when we first met, is another personal achievement. I wish him and his wife Carol happiness and joy, and hope to stay in touch in the future.

I am also grateful to Professor Buongiorno, for being available to me throughout the years, and for the academic and personal advice he gave me.

Together with the above mentioned, Professor Lester and Professor Golay made important contributions to my financial support. Being a TA for their courses has been a pleasure, as well as a source of learning.

My gratitude goes to Dr. Hejzlar, for the countless pieces of advice he gave me to improve my work. His knowledge, spanning all the fields in nuclear reactor design, was valuable to improve the technical content of this work.

Special thanks to Dr. McKrell, for his help and supervision in setting up and running the pressure drop experiments. Their positive outcomes were due also to another valuable contributor: Professor Bergles. It was a privilege to meet with him, and to be given the opportunity to take advantage of his tremendous experience in heat transfer enhancement. I also want to thank Robert Block, for helping me to complete the experiments, and Peter Stahle for sharing his hand-on experience.

Several other people provided great assistance to my work. The availability demonstrated by Dr. Shwageraus was precious, and thanks to him I finally succeeded in benchmarking CASMO against MCODE. I wish him best of luck in his career and personal life. Valuable input to my work also came from University of California at Berkeley: Kurt Terrani, Dr.

Francesco Ganda, Professor Greenspan and Professor Olander have been of great help whenever I needed to gain insights on hydride fuel. An important input also came from Michael Anness, Larry Conway and Dave Kitch from Westinghouse. A special thanks to Rachel for helping me in getting codes and solving PC-related problems. I also want to thank Dr. T. S. Ramakrishnan of Schlumberger-Doll Research Center in Cambridge, MA, for providing me access to the confocal microscope.

Gratitude goes also to all those with whom I talked less about my nuclear research, and more about life. I give my thanks to Luisa, for the gifts of friendship and support she has always given to me and my family. I wish for her what I know she cares about most: a happy life. Thanks to Taeshin, who recently became Dr. Kwak: I enjoyed the periodical lunch we had together. Thanks too to Fausto and Ale, for their friendship which can only grow now that we will be together in Pittsburgh. And finally thanks to my long-time office mates: Edo and Anna. I didn't talk much at work but you see: you are in my thesis!

I want to thank my parents, Fabio and Gina, who have always encouraged and supported me. They don't know what an inverted PWR is, but they are the roots of this thesis.

I dedicate this work to my wife Francesca. I thank her for the boundless love and for the sacrifices she has made throughout these years. A final note is for somebody who cannot read it yet: my little son Davide. Your daily smiles have been an important boost in the last 10 months. I hope to spend more time with you in the future: I will teach you soccer, and you will teach me English!

Table of contents

Abstract.....	3
Acknowledgements	5
Table of contents.....	7
Acronyms	14

VOLUME 1: IPWR design

Chapter I: Introduction

I.1 Introduction, motivations and objective	18
I.1.1 Motivations of the study	19
I.1.2 Objective of the study and competitor PWR designs	23
I.2 Volume and chapter organization.....	24
I.3 IPWR design: an overview	25
I.4 Inverted vs pin geometry in nuclear reactors.....	29
I.4.1 Comparison continuous inverted vs pin geometry: pressure drop and fuel temperature.....	33
I.4.2 Inverted geometry performance degradation due to discontinuities	37
I.5 Reactor designs adopting inverted fuel geometry.....	39
Appendix I-A: Analytical methods for inverted-pin comparison.....	41

Chapter II: Materials

II.1 Fuel	47
II.1.1 Historical remarks on hydride fuels	48
II.1.2 Motivations for the choice of $UTh_{0.5}Zr_{2.25}H_{5.625}$	49
II.1.3 Composition and structure	50
II.1.4 Swelling	51
II.1.5 Fission gas release.....	55
II.1.6 Hydrogen release	59
II.1.6.1 <i>Hydrogen release limitation</i>	62

II.1.6.2 Limitation of consequences of hydrogen release.....	64
II.1.7 Thermal conductivity and specific heat	65
II.1.8 Summary of thermophysical properties	67
II.2 Cladding and duct material	68
II.3 Liquid metal bond.....	71
Appendix II-A: Relation between FIMA% and MWD/kg_{HM}	74

Chapter III: Analysis methodology and design constraints

III.1 Analysis methodology and code used	75
III.1.1 Analysis methodology	75
III.1.2 Code used.....	77
III.2 Design constraints	79
III.2.1 Structural/material constraints.....	82
III.2.1.1 Cladding thickness and fuel-clad gap width	82
III.2.1.2 Fuel-duct gap width	83
III.2.1.3 Stress intensity on the duct and duct lateral deformation	85
III.2.1.4 Fission gas release	87
III.2.1.5 Hydrogen pickup protection.....	88
III.2.1.6 Selection of gap filling material	89
III.2.1.7 Inter-assembly water gap width	89
III.2.2 Thermalhydraulic constraints	89
III.2.2.1 Core pressure drop	89
III.2.2.2 Steady-state MCHFR	90
III.2.2.3 Steady-state peak fuel temperature	91
III.2.2.4 Steady-state peak inside cladding temperature	91
III.2.2.5 Core inlet temperature and coolant enthalpy rise	92
III.2.2.6 Peak cladding temperature and oxidation thickness during LOCA	92
III.2.3 Neutronic/economic constraints	96
III.2.3.1 Void reactivity coefficient	96
III.2.3.2 Fuel temperature reactivity coefficient.....	97
III.2.3.3 Soluble boron concentration and IFBA loading.....	98

III.2.3.4 Enrichment and cycle length	102
III.2.3.5 Number of assemblies	103
III.2.3.6 Hot Full Power to Cold Zero Power reactivity insertion	103
III.2.4 Manufacturing constraints.....	104
Appendix III-A: Steady-state analysis of the reference PWR	106
Appendix III-B: History of 2200F PCT and 17% oxidation safety criteria for LOCA.....	112
Appendix III-C: Fuel swelling calculation.....	120

Chapter IV: Duct design and assembly/core construction methods

IV.1 Assembly duct design	122
IV.1.1 Duct material	124
IV.1.2 Duct height.....	124
IV.1.3 Duct flat-to-flat distance and wall thickness	126
IV.1.3.1 Design rationale and design limits.....	126
IV.1.3.2 Stress and deformation analysis	131
IV.1.4 Conclusions on assembly duct design.....	144
IV.2 Number of fuel cells per assembly.....	144
IV.2.1 Fuel cell geometry.....	145
IV.2.2 Computation of the number of fuel cells per assembly	148
IV.3 Number of assemblies in the core	149

Chapter V: Core pressure drop

V.1 Gravity pressure drop.....	154
V.2 Acceleration pressure drop.....	155
V.3 Friction pressure drop	156
V.3.1 Isothermal liquid-only friction factor calculation	158
V.3.1.1 TT-free axial zones with purely axial flow.....	158
V.3.1.2 Axial zones provided with a long TT	159
V.3.1.3 MSLTT-provided channels.....	160
V.3.2 Two-phase multiplier	161

V.4 Form losses	164
Appendix V-A: Benchmark of pressure drop correlations against experimental data	165

Chapter VI: Critical Heat Flux

VI.1 CHF in pure axial flow.....	190
VI.2 CHF in swirl flow.....	193
VI.2.1 Phenomenology of the influence of swirl flow on CHF	195
VI.2.1.1 <i>Subcooled boiling and low-quality saturated boiling</i>	195
VI.2.1.2 <i>Medium and high-quality saturated boiling</i>	197
VI.2.2 Experimental evidence of swirl flow effect on CHF at high pressure	200
VI.2.2.1 <i>FLTT geometries</i>	200
VI.2.2.2 <i>SLTT geometries</i>	204
VI.2.3 CHF calculation method in presence of long TTs.....	210
VI.2.3 CHF calculation method in decaying swirl flow	211
Appendix VI-A: Benchmark of CHF predictions against experimental data	216
Appendix VI-B: Swirl decay analysis.....	233

Chapter VII: Fuel temperature and heat transfer coefficient calculation methods

VII.1 Maximum fuel temperature: the corrected equivalent annulus approximation	244
VII.2 Coolant-cladding heat transfer coefficient.....	248
VII.2.1 Axial flow htc correlations	248
VII.2.2 Swirl flow htc correlations	251
VII.3 Temperature drop across clad and clad-fuel gap	253

Chapter VIII: LBLOCA analysis

VIII.1 Analysis methodology	255
VIII.1.1 RELAP plant nodalization and pre-accident power distribution.....	256
VIII.1.2 Plant response model	257
VIII.2 Peak cladding temperature and quenching time for pin and inverted core geometries	261

VIII.2.1 Stored energy comparison between pin and inverted cell having same volume	262
VIII.2.2 Quenching time comparison between pin and inverted cores	266

Chapter IX: Neutronics

IX.1 Determination of VRC sign.....	271
IX.1.1 Calculation of H/HM	272
IX.1.2 Effect of soluble boron concentration on maximum allowed H/HM	278
IX.2 FTFC sign	283
IX.3 Cycle length and enrichment	286
IX.3.1 Formula for the cycle length calculation	287
IX.3.2 Method of application of cycle length and enrichment constraints	287
IX.3.3 Depletion analysis of an inverted cell	288
IX.3.4 Critical boron concentration at BOC	290
IX.4 Considerations on shutdown margin	293
Appendix IX-A: Benchmark CASMO-MCODE	295

Chapter X: Inverted assembly manufacture

X.1 Manufacture phases and concerns	313
X.1.1 Manufacture of the fuel prism.....	313
<i>X.1.1.1 Base metal ingot fabrication.....</i>	<i>314</i>
<i>X.1.1.2 Base metal ingot cleaning prior to hydriding.....</i>	<i>325</i>
<i>X.1.1.3 Base metal ingot hydriding</i>	<i>327</i>
<i>X.1.1.4 Fuel prism shaping/sizing</i>	<i>342</i>
<i>X.1.1.5 Fuel prism superficial oxidation</i>	<i>343</i>
X.1.2 Securing of the short-length twisted tapes (for S-IPWR design only)	345
X.1.3 Final assembling	347
X.2 Conclusions on inverted assembly manufacture	348

Chapter XI: IPWR design selection

XI.1 IPWR core geometry characterization.....	351
--	------------

XI.2 Power maps.....	356
XI.2.1 E-IPWR power maps.....	357
XI.2.2 H-IPWR power maps.....	358
XI.2.3 S-IPWR power maps.....	360
XI.2.4 Power map comparison	362
<i>XI.2.4.1 Maximum powered IPWR designs</i>	<i>362</i>
<i>XI.2.4.2 Selected E-IPWR design.....</i>	<i>366</i>
XI.3 LBLOCA analysis of selected E-IPWR geometry	369
XI.4 Neutronic analysis of selected E-IPWR geometry	371
XI.4.1 E-IPWR neutronic characterization	371
XI.4.2 Shutdown margin.....	376
XI.5 Complete characterization of selected IPWR	377

Chapter XII: Conclusions and future work

XII.1 Conclusions	379
XII.2 Future work.....	381
References for Volume 1	384

VOLUME 2: Pressure drop tests

Table of contents.....	404
Introduction to Volume 2	406
1. Twisted tapes: an introduction	407
2. Motivation for the test and existing literature on the subject.....	410
2.1 Available literature on SLTTs	411
3 Objectives of the tests and definition of SLTT module	417
4. Test planning	418
4.1 Choice of the geometric variables	419
5. Experimental apparatus.....	421

5.1 Test sections.....	422
5.1.1 Test section geometry	422
5.1.2 Test section manufacture	426
5.1.3 Pressure tap geometry and manufacture.....	429
5.2 Pump	430
5.3 Differential pressure transducer	431
5.4 Flow meter	431
5.5 Pressurizer.....	432
5.6 Heat exchanger	432
5.7 Data acquisition system	432
5.8 Other components	432
6. Test methodology description	433
7. Data scatter and error propagation analysis	434
7.1 Data scatter at constant pump speed.....	434
7.1 Error propagation analysis	436
8. Tube roughness determination and pressure drop measurement accuracy	442
8.1 Determination of test section inner surface roughness	443
8.1 Determination of pressure drop measurement accuracy	444
9. Data elaboration method: definition of friction factor and directions for using friction factor correlations	446
9.1 Friction factor: definition	446
9.2 Method for using friction factor correlations to predict pressure drops	447
10. Results	447
10.1 Result elaboration and interpretation	452
Appendix A: Calculation of the pressure drop penalty due to the use of a FLTT	456
Appendix B: Criteria for the selection of N_{rev}	464
Appendix C: Investigation of swirl flow development.....	473
Appendix D: Effect of water deaeration on pressure drop	487
References for Volume 2	489

Acronyms

ANL: Argonne National Laboratory

ARO: All Rods Out

BOC: Beginning Of Cycle

BOL: Beginning Of Life

BWR: Boling Water Reactor

CANDU: CANadian Deuterium Uranium reactor

CHF: Critical Heat Flux

CZP: Cold Zero Power

E-IPWR: IPWR provided with TT-free cooling channels

EOC: End Of Cycle

EOL: End Of Life

FGR: Fission Gas Release

FLTT: Full-length TT

FTRC: Fuel Temperature Reactivity Coefficient

GCFR and GFR: Gas Cooled Fast Reactor

GT-MHR: Gas Turbine Modular Helium Reactor

HFP: Hot Full Power

H-IPWR: IPWR in which a 1.6 m long TT occupies the uppermost portion (almost half) of each cooling channel

HTGR: High Temperature Gas Reactor

HZP: Hot Zero Power

IFBA: Integral Fuel Burnable Absorber

IPWR: Inverted Pressurized Water Reactor

LEU: Low Enriched Uranium

LBLOCA: Large Break Loss-Of-Coolant Accident

LM: Liquid Metal

LMBFR: Liquid Metal Fast Breeder Reactor

LOCA: Loss-Of-Coolant Accident

LS-VHTR: Liquid Salt Very High Temperature Reactor

LWR: Light Water Reactor

MA: Minor Actinides

MCHFR: Minimum Critical Heat Flux Ratio

MDNBR: Minimum Departure from Nucleate Boiling Ratio

MOX: Mixed OXide fuel

MIT: Massachusetts Institute of Technology

MSLTT: Multiple Short-length TTs

NA: Not Applicable

OD: Outer Diameter

PCT: Peak Cladding Temperature

PPF: Power Peaking Factor

PWR: Pressurized Water Reactor

RCP: Reactor Coolant Pump

SFR; Sodium-cooled Fast Reactor

S-IPWR: IPWR in which each cooling channel is provided with MSLTTs

SLTT: Short-length TT

TT: Twisted Tape

UCB: University of California at Berkeley

USAR: Ultimate safety Analysis Report

VHTR: Very High Temperature Reactor

VRC: Void Reactivity Coefficient

VOLUME 1
IPWR design

Chapter I

Introduction

This chapter introduces the design work performed on the Inverted Pressurized Water Reactor (IPWR). The chapter is organized as follows:

- Introduction, motivations and objective of the study: Section I. 1;
- Volume and chapter organization: Section I. 2;
- Overview of the IPWR design: Section I. 3;
- Inverted vs pin geometry in nuclear reactors: Section I. 4;
- Reactor designs adopting inverted geometry: Section I. 5.

I. 1 Introduction, motivations and objective

The Inverted Pressurized Water Reactor (IPWR) is an innovative reactor concept initially explored by Malen et al. (2009), as part of a project on the feasibility of recycling plutonium and Minor Actinides (MA) in Light Water Reactors (LWRs) using hydride fuel (Greenspan et al., 2009). The project, a collaboration between University of California at Berkeley (UCB), Massachusetts Institute of Technology (MIT) and Argonne National Laboratory (ANL), investigated the possibility of replacing UO_2 fuel with hydride fuel, either in the form of $\text{UZr}_{3.13}\text{H}_{5.01}$, often referred to as $\text{U}(45\% \text{ w/o})\text{ZrH}_{1.6}$, or U-Th-Zr-hydride¹. While, for all the other studies performed as part of the hydride fuel project, the innovative aspect concerned the fuel type only, i.e. hydride in place of oxide, Malen's IPWR design was also innovative in the core

¹ Throughout this work, fuel compositions are written using stoichiometric indexes when reference to a specific fuel composition is required. In these cases, stoichiometry indexes are normalized with respect to the uranium atom density and, as a consequence, uranium stoichiometric index is always 1. Whenever the context does not require referring to a specific fuel, but rather to a family of fuels, hyphens (-) are instead used. For example, the nomenclature $\text{U-ZrH}_{1.6}$ is used to refer to uranium-zirconium hydride fuels in general, with no distinction based on the amount of uranium actually present in the fuel. Likewise, the nomenclature "U-Th-Zr-hydride" is used to refer to all the hydride fuels containing U, Th and Zr.

geometry. This geometry, referred to in this work as “inverted”, has the fuel as the continuous medium, as opposed to the coolant like in typical LWRs. This is since instead of having fuel rods surrounded by coolant, i.e. the so-called pin-geometry, the inverted geometry has cooling channels surrounded by fuel. This is shown in Figure I- 1, which compares inverted and pin geometries. The inversion in relative position between coolant and fuel motivated the choice of the term “inverted geometry”.

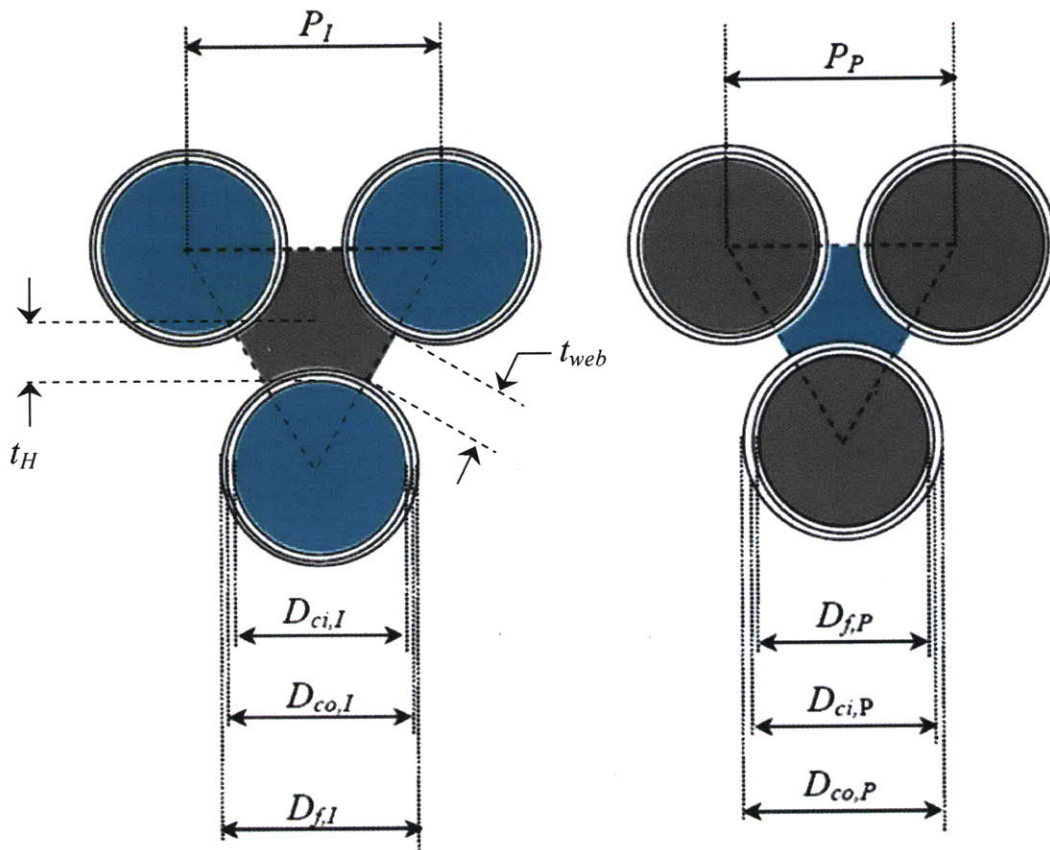


Figure I- 1: Inverted geometry (left) vs pin geometry (right). Light blue indicates coolant; grey indicates fuel

I.1. 1 Motivation of the study

Interest in the IPWR concept was raised during the first hydride fuel project, which was carried out by UCB, MIT and Westinghouse Electric Company LLC to investigate the performance of U(45% w/o)ZrH_{1.6}-fueled LWRs and to compare them with those of typical UO₂-fueled LWRs

(Greenspan et al., 2006). In that project hydride-fueled PWRs were found to perform the same as UO_2 -fueled PWRs, in terms of maximum achievable power (Shuffler et al., 2009). Particularly, it was found that the parameters limiting core power were mainly pressure drop, Minimum Departure from Nucleate Boiling Ratio (MDNBR) and fretting phenomena of the fuel rods against grid spacers, as shown in Figure I- 2 and Figure I- 3. These figures, which only differ in the imposed pressure drop limit, are composed of a power map, on the left, and a constraint map, on the right. The former shows the maximum attainable power, accounting for thermal hydraulic and structural constraints, while the latter shows the constraints limiting such power. Both maps have the fuel rod pitch-to-diameter ratio on the x-axis and the fuel rod outer diameter on the y-axis. It can be seen that the core geometries characterized by the highest power levels are located at the bottom right hand corner of the power maps, where the power is limited by:

- pressure drop and MDNBR when the pressure drop limit is fixed at the reference core value (Figure I- 2);
- pressure drop and fretting wear when the pressure drop limit is equal to two times the reference core value (Figure I- 3).

In a companion study (Ferroni et al., 2009), the same constraints were found to also limit the power of hydride-fueled BWRs.

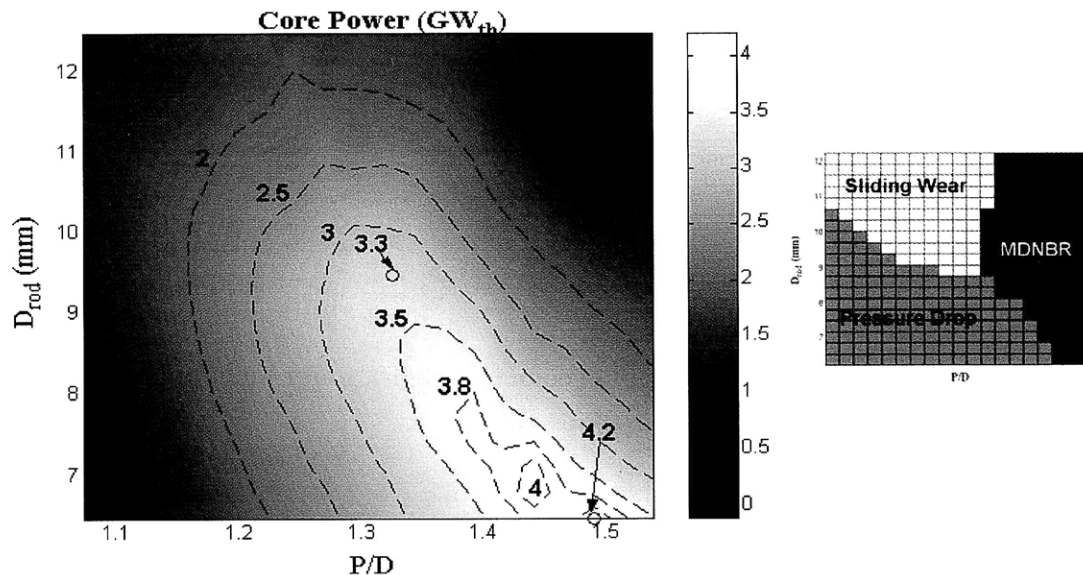


Figure I- 2: Maximum power attainable by U(45% w/o)ZrH_{1.6}-fueled pin geometry PWRs (left) and parameters limiting core power (right). Pressure drop limit = reference core pressure drop. (from Shuffler et al., 2009)

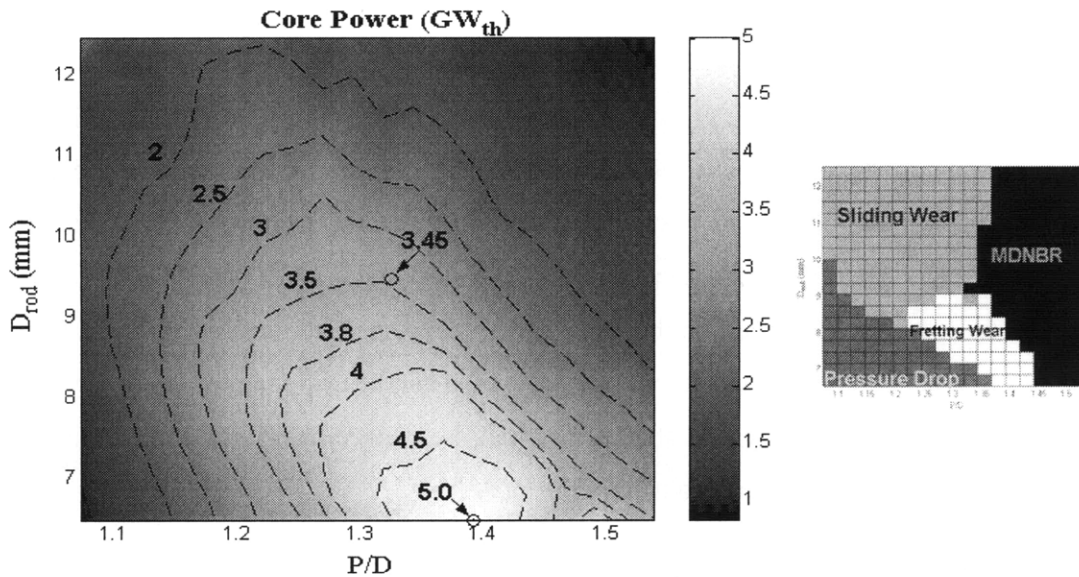


Figure I- 3: Maximum power attainable by U(45% w/o)ZrH_{1.6}-fueled pin geometry PWRs (left) and parameters limiting core power (right). Pressure drop limit = 2×reference core pressure drop. (from Shuffler et al., 2009)

The limiting effect exerted on power by the mentioned constraints induced MIT researchers to investigate the possibility to achieve higher powers by means of a core geometry that was not so limited by those constraints. The inverted geometry was selected for this purpose since:

- at high fuel volume fractions it has a smaller pressure drop relative to a pin geometry having the same fuel volume fraction (see Section I.4. 1);
- its Critical Heat Flux (CHF) performance can be easily enhanced by inserting turbulence promoters inside the cooling channels²;
- it does not have supporting grids and thin pins, which are susceptible to vibration and fretting concerns.

The choice of hydride as the candidate for inverted geometry implementation was a direct consequence of two characteristics that a fuel for inverted geometry must have: low fission gas release (FGR) and manufacturability potential. As explained in Section I. 3, inverted geometry requires cladding and an outer boundary duct to enclose the fuel, which would be internally

² In pin geometries, CHF enhancement is already achieved using mixing-vane provided grid spacers which, as known, penalize pressure drop and are susceptible to fuel rod fretting.

pressurized by fission gases if FGR was significant. Such pressurization would endanger the duct structural stability during scenarios, like Loss-Of-Coolant Accident (LOCA) and refueling, characterized by low pressure of the primary system. Also, as shown in Figure I- 1, the inverted geometry requires cooling channels to be made inside the fuel matrix and drilling the fuel is clearly the easiest way to obtain such channels. UO_2 does not meet either of these requisites since it has a not-negligible FGR and, because of its physical state, i.e. sintered powder, cannot be effectively drilled³. Hydride fuel, on the other hand, is expected⁴ to have a negligible FGR at the maximum IPWR operating temperature and burnup and can be drilled before being hydrided. Prior to hydriding, in fact, the physical state of the fuel, i.e. a pure metal made of uranium and zirconium, makes drilling particularly easy to perform.

The work performed by Malen et al. (2009) was a preliminary investigation of the IPWR concept, aimed at estimating the maximum power attainable by this reactor. The analysis, performed at cell-level, searched for the inverted cell geometry that, upon application of some design constraints, resulted in the maximum achievable core power. This power was calculated to be in excess of 4500 MW_t, with an optimistic scenario reaching about 6800 MW_t. The power uprates associated with these values, and calculated with respect to a typical, pin geometry, PWR of the same size, are of 32% and 100% respectively. These promising results, together with the possibility, demonstrated in a companion study (Ganda and Greenspan, 2009), of hydride fuel to be used for plutonium and MA recycling more effectively than Mixed Oxide fuel (MOX), motivated the decision to investigate the IPWR concept more in detail.

Also, it is important to mention that even though this study is focused on a thermal reactor, inverted geometry offers significant advantages over pin geometry in fast reactors as well. This is qualitatively discussed in Section I. 4.

³ Even though a sintered powder cannot be drilled, other methods can be envisioned to generate an inverted configuration with such material. For example, petal-shaped UO_2 fuel pellets, obtained through typical sintering, can be arranged so that circular holes are left between them. This method, more involved than drilling, has the disadvantage of reducing (1) the average fuel density in an inverted assembly and (2) the average fuel thermal conductivity. The latter aspect, coupled with the already low thermal conductivity characterizing oxide fuel, would lead to higher temperatures and therefore higher fission gas release.

⁴ Some uncertainty however exists about the exact magnitude of FGR for the hydride fuel proposed for the IPWR, i.e. $\text{UTh}_{0.5}\text{Zr}_{2.25}\text{H}_{5.625}$. No experimental data are available on FGR of this fuel, whereas data are available for the most well-known member of the hydride fuel family, i.e. $\text{U-ZrH}_{1.6}$. These data (Baldwin et al., 1980) show that for $\text{U-ZrH}_{1.6}$ the FGR fraction is less than 10^{-3} at burnup values up to 200 MWD/kg_U and temperatures of 650°C, which is the maximum fuel temperature limit established for the IPWR. The mentioned uncertainty is mainly due to the larger heavy metal density characterizing $\text{UTh}_{0.5}\text{Zr}_{2.25}\text{H}_{5.625}$ relative to $\text{U-ZrH}_{1.6}$, which typically tends to favor FGR.

I.1. 2 Objective of the study and competitor PWR designs

The work presented here is aimed at estimating the maximum power attainable by an IPWR, accounting for a comprehensive set of design constraints, most of which were not considered in the original work by Malen et al. (2009). The design constraints used in that work were only four: maximum fuel temperature and maximum inside cladding temperature during steady-state operation, and Minimum Critical Heat Flux Ratio (MCHFR) and Peak Cladding Temperature (PCT) during LOCA. Two additional constraints, on cladding thickness and fuel-clad gap width, were also considered, but applied to a single inverted cell geometry. This work presented here accounts instead for more than 20 design constraints, described in Chapter III, covering most of the study areas typically assessed in reactor design: structural mechanics, thermalhydraulics, neutronics and manufacture. Fuel performance was only marginally investigated due to the lack of experimental data on irradiated $U_{0.5}Zr_{2.25}H_{5.625}$. Factors affecting a sixth key area, economics, are considered, but an economic analysis was not performed. The completeness deriving from considering all these constraints makes the analysis approach more realistic, thus allowing calculation of a maximum achievable core power closer to that actually “achievable”.

The maximum attainable power resulting from the analysis will be then compared to that of competitor PWR designs, as shown in Table I- 1, and particularly to that of typical pin geometry PWRs, to assess the IPWR competitiveness. Table I- 1 summarizes the main characteristics of some PWR designs, recently investigated mainly at MIT and UCB. In particular, the table shows the power uprate characterizing each design, relative to that of the PWR core used as reference in this study, i.e. the Seabrook Power Station core (Seabrook USAR, 2002), and to the maximum powered design found by Shuffler et al. (2009). It can be noticed that:

- with its 50% uprate, annular fuel has the best power performance;
- the optimization of the pin lattice, performed by Shuffler et al. (2009), resulted in the same power uprate regardless of the type of fuel;

Also, it is important to note that the maximum powered pin geometry PWRs resulting from Shuffler study have very thin fuel rods (OD~6.5 mm), which are challenging to manufacture and susceptible to vibrations. Hence, IPWR power performance will be compared not only with the maximum powered pin geometry PWRs, but also with the reference pin geometry PWR (fuel rod OD= 9.5 mm). Using, as the only base of comparison, the maximum powered PWRs would in

fact overestimate the power performance actually attainable by pin geometry PWRs, thus unjustly penalizing the IPWR design competitiveness.

Table I- 1: PWR competitor designs					
Geometry →	OXIDE			HYDRIDE	
	Pin		Annular	Pin	IPWR
	Reference	Maximum powered geometry		Maximum powered geometry	
Power uprate relative to reference pin oxide (%)	0	+32%	+50%	+32%	
Power uprate relative to max powered pin (%)	-24%	0	~14%	0	
Cladding outside diameter (mm)	9.5	6.5	8.63(i); 15.37(o)	6.5	
P/D	1.33	1.4-1.5	1.07	1.4-1.5	
Core pressure drop	Ref	2×ref	1.8×ref	2×ref	
Cycle length (months)	18	~14	18	~14	
Enrichment	5%	5%	8-9%	12.5%	
Reference	Seabrook USAR (2002)	Shuffler et al. (2009)	Kazimi and Hejzlar (2006)	Shuffler et al. (2009)	This study

I. 2 Volume and chapter organization

The work performed for the design of the IPWR is presented in two volumes: the main volume, i.e. Volume 1, contains the actual design of the core, while Volume 2 describes the experimental work performed to support the IPWR design. Specifically, the latter volume describes the experimental tests performed to predict the pressure drop across multiple short-length twisted tapes (MSLTTs) which, as discussed in Section I. 3, are turbulence promoters used to increase CHF in one of the examined IPWR designs. Table I- 2 shows the work layout.

Table I- 2: Volume and chapter organization	
VOLUME 1: IPWR design	
<i>Chapter</i>	<i>Content</i>
I	Introduction
II	Materials
III	Analysis methodology and design constraints
IV	Duct design and assembly/core construction methods
V	Core pressure drop
VI	Critical heat flux
VII	Fuel temperature and heat transfer coefficient calculation methods
VIII	LBLOCA analysis
IX	Neutronic analyses
X	Inverted assembly manufacture
XI	IPWR design selection
XII	Conclusions and recommended future work
VOLUME 2: Pressure drop tests	

I. 3 IPWR design: an overview

The IPWR is a Pressurized Water Reactor. It operates at typical PWR conditions of coolant temperature and pressure, but significantly differs in core geometry. An IPWR assembly consists of a hexagonal hydride fuel prism perforated with vertically-oriented cooling channels arranged in a triangular lattice. A cylindrical Zr-2.5Nb clad forms the walls of each coolant channel, and a gap separates the outer clad surface from the inner surface of the fuel. An hexagonal duct, also made of Zr-2.5Nb, provided with a perforated top and a bottom lid, encloses each fuel prism and a gap separates the inner surface of the duct from the outer surface of the fuel. Two duct designs were examined: a collapsible and a non-collapsible duct. A collapsible duct is a large, relatively thin walled duct, designed to be only slightly pressurized internally, so that it can collapse onto the fuel prism soon after the primary system is brought to nominal pressure. A non-collapsible duct is instead a small and relatively⁵ thick-walled duct, internally pressurized to about 7.8 MPa, designed to sustain the pressure differential across its walls without collapsing onto the fuel. For this design, the fuel-clad and fuel-duct gaps are filled with a liquid metal which, thanks to its high thermal conductivity, prevents high temperature to be reached in the fuel. The negligible gap thermal resistance resulting from the contact between duct/clad and fuel does not require, in the collapsible duct design, use of any liquid metal bonding. As discussed in Chapter IV, the

⁵ “Relatively” is used to indicate that the wall is quite thick relative to the duct flat-to-flat distance. If compared, the wall thickness of the non-collapsible duct is smaller than that of the collapsible duct. The latter is, however, larger in size.

collapsible duct design allows reducing the volume occupied by structural materials, thus increasing that available for fuel and coolant. However, hard contact of the duct with the fuel makes the latter more susceptible to hydrogen pickup and consequent embrittlement. The non-collapsible ducts, on the other hand, are better protected against hydrogen pickup, but (1) occupy a significant fraction of the core volume, thus penalizing power performance and (2) are more challenging to assembly (see Chapter X). Figure I- 4 and Figure I- 5 are qualitative representations of the IPWR assembly design concept. Particularly, Figure I- 5 refers to an assembly with non-collapsible duct design.

Y-shaped control rods are inserted in the water gaps separating adjacent assemblies, as shown in Figure I- 6. Since not all the water gaps contain water rods, space is available for placement of Linear Power Range Monitors (LPRMs), which are needed for neutron flux measurement.

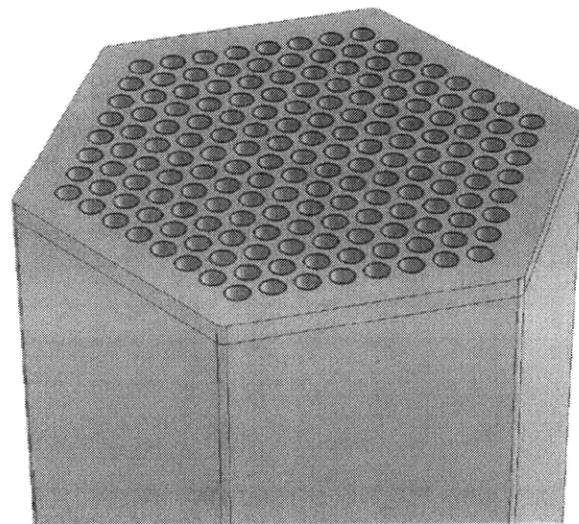


Figure I- 4: 3D view of top of IPWR assembly. Qualitative representation.

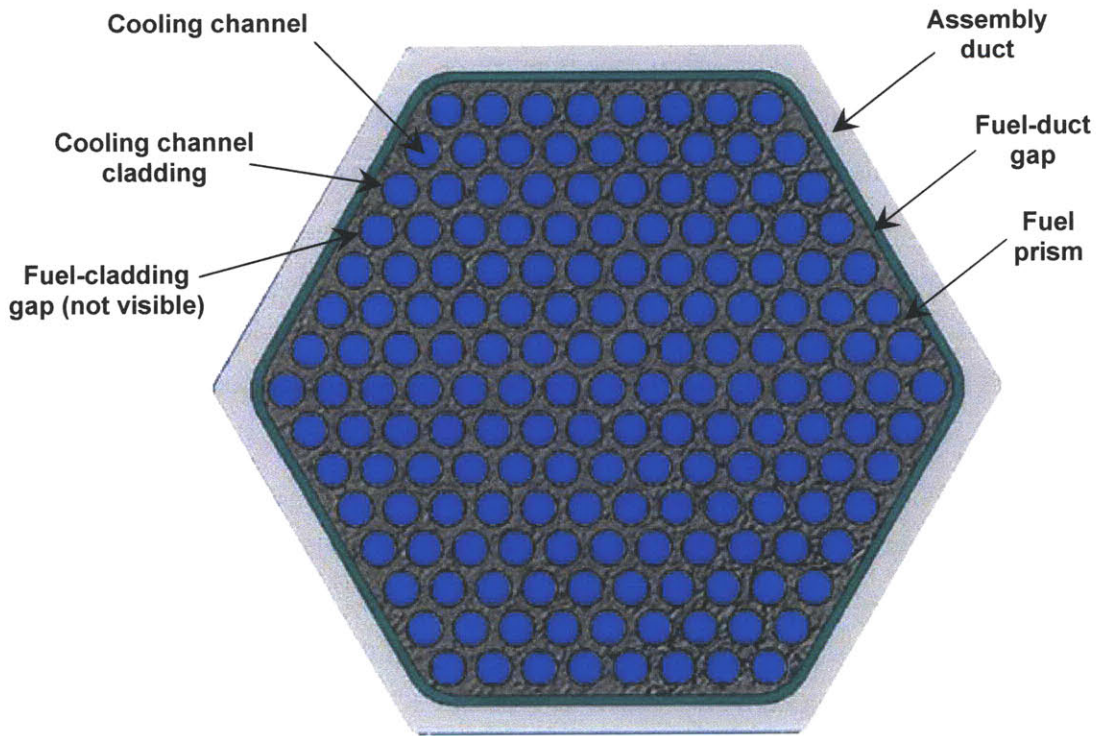


Figure I- 5: Top view of inverted assembly, with upper lid removed. Qualitative representation.

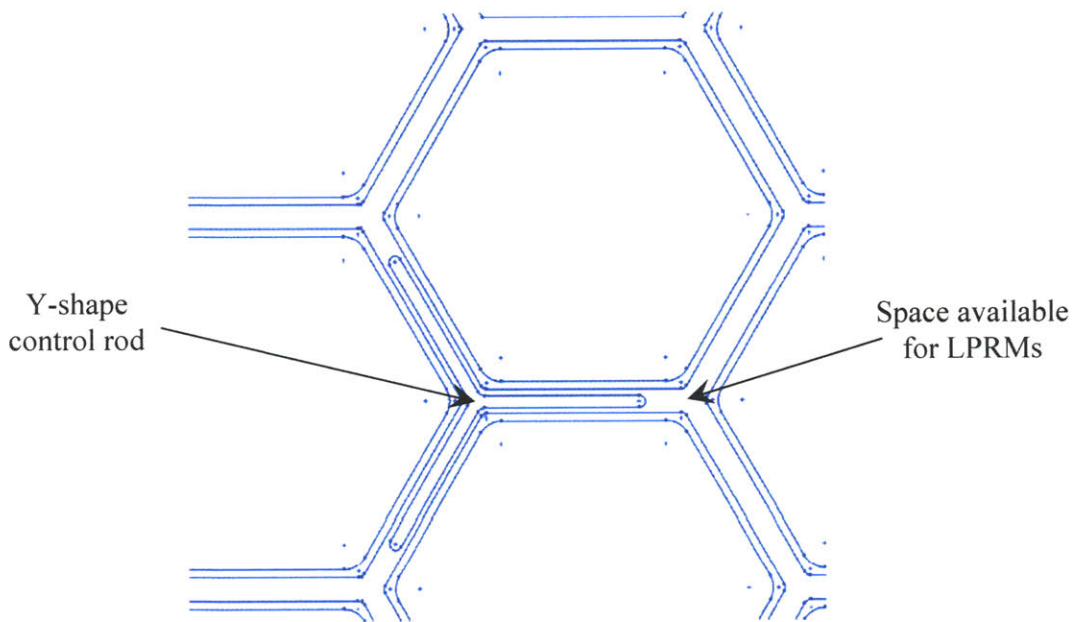


Figure I- 6: Sketch showing control rod arrangement. Qualitative representation.

Six IPWR designs were analyzed, which differ in the type of duct (collapsible and non-collapsible), in whether or not CHF performance is enhanced with twisted tapes (TTs) and, if it is enhanced, in what type of TTs are used. The fact that IPWR cooling channels are not communicating makes them more susceptible to CHF than typical PWR bundle subchannels operating in the same mass flux and equilibrium quality conditions. To compensate for this, IPWR designs featuring TT-provided cooling channels are examined. Two types of TTs are considered: half-length⁶ twisted tapes (HLTTs) and multiple short-length twisted tapes (MSLTTs). HLTTs are 1.66 m long TTs occupying the top region of each cooling channel: they are easy to install since they can be welded at the exit, but result in a significant pressure drop penalty. MSLTTs are short TTs (<10 cm long) inserted into the top half of each cooling channel and spaced 50 diameters from each other. A sketch of a SLTT is shown in Figure I- 7. They provide the same, or nearly the same CHF enhancement as HLTTs, but with a much lower pressure drop. The reactor designs resulting from the adoption of these TT designs are referred to as H-IPWR and S-IPWR respectively. The IPWR design with empty cooling channels, i.e. without TTs, is referred to as E-IPWR. The combination of these three cooling channel configurations with the two duct types results in the six IPWR designs mentioned above.

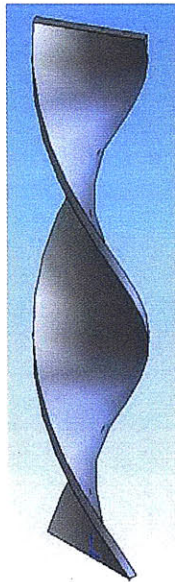


Figure I- 7: Sketch of a short-length twisted tape

⁶ Half-length TTs are termed in this way even though they actually occupy less than half of the core heated length, i.e. 1.6 vs 1.84 m.

I. 4 Inverted vs pin geometry in nuclear reactors

The comparison between inverted and pin geometries, aimed at identifying which one yields best performance, depends on the operating conditions and generally on the characteristics of the reactor of interest. On this regard it is important to make a distinction between continuous and discontinuous inverted geometries. A continuous inverted geometry is a modular repetition, throughout the core, of the elementary fuel cell shown in Figure I- 1, either without discontinuities (ideal case) or with small discontinuities due, for example, to the need of separating fuel prisms with narrow gaps, to allow for assembly removal and to accommodate for thermal expansion, or due to the presence of very thin ducts enclosing the fuel prisms. A discontinuous inverted geometry is instead an inverted geometry in which the mentioned discontinuities are large in size: e.g. they can be large water gap for control rod insertion and/or thick ducts to guarantee structural stability of the assemblies. The main effects of adding large “discontinuities” are to reduce the core active⁷ flow area, with consequent increase in coolant velocity and thus pressure drop, and to reduce the amount of fuel that can be loaded into the core, with consequent shortening of the cycle length. These effects can drastically change the comparison between inverted and pin geometries, causing a worsening of the inverted geometry performance. For pin geometries the classification in continuous and discontinuous is not made, not because “discontinuous pin geometries” do not exist (BWRs are an example), but because pin geometries are more flexible than inverted geometries and the implementation of a continuous pin geometry is generally feasible. Existing PWRs are examples of continuous pin geometries⁸.

When the characteristics of a reactor allow implementation of a continuous inverted geometry, a lower pressure drop and a lower fuel temperature, relative to a pin geometry having the same fuel volume fraction, can be attained. This concept, quantitatively discussed in Section I.4. 1, can be reworded saying that a continuous inverted geometry has a larger fuel volume fraction than a pin geometry having the same pressure drop and maximum fuel temperature. Even though increasing the fuel volume fraction is beneficial for any reactor, due to the consequent increase in

⁷ “Active” is the term used to refer to the flow area of the inverted cooling channels in an inverted geometry, and to the flow area of the subchannels in a pin geometry. This term allows distinction from the total core flow area, which includes areas through which coolant flows without however removing much heat, e.g. water gaps between adjacent assemblies.

⁸ The distance between the axes of two fuel rods belonging to the outermost rings of adjacent assemblies is less than 1 mm larger than the fuel rod pitch (Seabrook USAR, 2002). This justifies referencing to PWRs as continuous pin geometries.

fuel cycle length, this characteristic of continuous inverted geometries is particularly useful in fast reactors, due to their need of minimizing the coolant volume fraction, v_c . In fact, from the neutronic viewpoint, fast reactors are somewhat penalized by the existence of a lower limit on v_c , needed to guarantee adequate heat transfer removal, since a reduction in v_c would be beneficial to:

- reduce the coolant void reactivity coefficient: the lower the coolant volume fraction the lower is the core power increase resulting from the neutron spectrum hardening that the core experiences upon coolant voiding;
- achieve higher fuel volume fraction to improve uranium utilization without the need of blankets, which pose concerns from the proliferation viewpoint.

Designers of water-cooled reactor concepts do not strive for such coolant minimization, even though the need to increase the operating cycle length applies as well. Rather, they tend to increase the coolant fraction to provide, in addition to sufficient core cooling, a reasonable core reactivity lifetime since an increase in coolant volume fraction moves the design away from the low-reactivity epithermal region (see Figure I- 8). On the other hand, the coolant fraction increase is limited by the existence of an upper bound which arises from the need to keep the moderator temperature coefficient negative. For PWRs this last consideration dictates a limit on the hydrogen-to-heavy-metal ratio, H/HM, sufficient to prevent an overmoderated steady-state configuration: this limit is, in Figure I- 8, the H/HM ratio corresponding to the maximum of the curve.

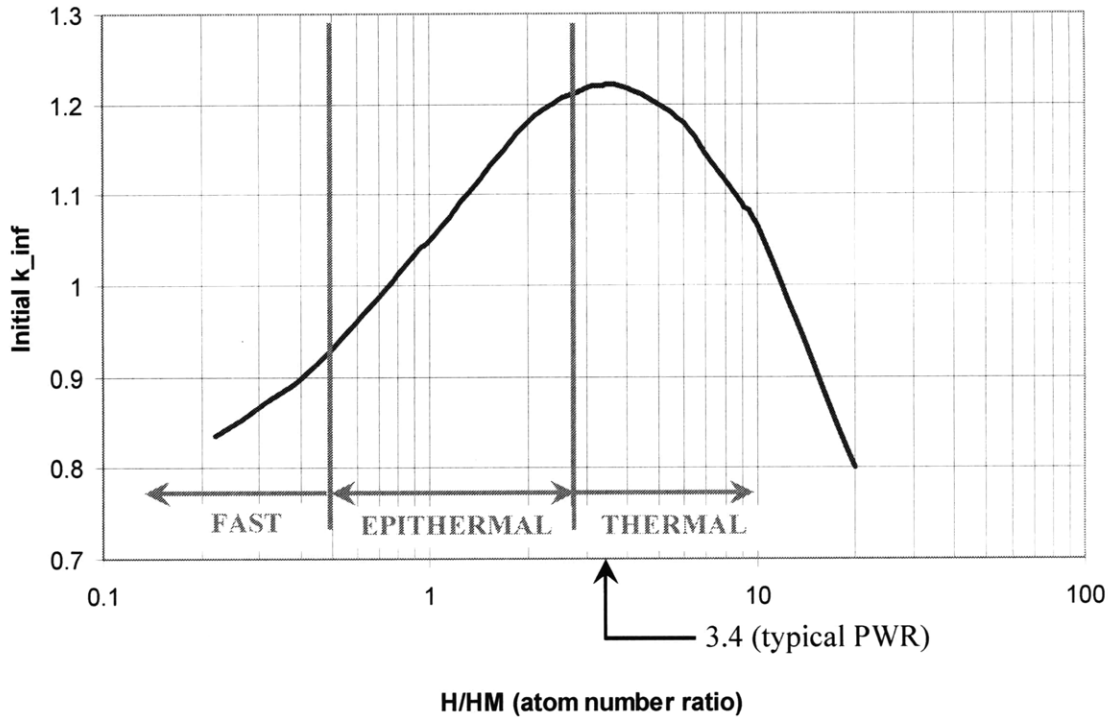


**Figure I- 8: Infinite multiplication factor vs H/HM (2000 ppm Boron, 4.5% Enriched UO₂).
(Adapted from Xu, 2003)**

It is important to note that fast reactors, and in general reactors that do not use water as coolant, are more likely able to attain a reduced coolant volume fraction through implementation of an inverted geometry since the inverted geometry can be continuous. This is because the assembly ducts, typically needed to enclose the fuel prisms and to avoid their contact with the coolant, can be either very thin, thanks to the low pressure at which some fast reactors operate, or can even be absent, due to the possibility of having an inert coolant, like helium, in contact with a fuel matrix⁹. However, the low pressure at which liquid metal- or liquid salt-cooled reactors operate is not a sufficient criterion to allow adoption of thin assembly ducts, and thus to implement a continuous inverted geometry. In fact, the pressure gradient across the duct walls is also function of the pressure inside the duct, which mainly¹⁰ depends on the degree of fission gas release

⁹ This is the case of the GT-MHR design, where TRISO-type fuel particles are incorporated into graphite-matrix fuel compacts which, in turn, are loaded into helium-cooled graphite matrix fuel assemblies.

¹⁰ Another phenomenon responsible for duct internal pressurization is He generation in case Integral Fuel Burnable Absorber (IFBA) is chosen as burnable poison. As discussed in Chapter IV, in spite of its good performance as

(FGR) characterizing the fuel used. From this viewpoint, pin geometries are easier to implement since they can withstand high pressure differentials without requiring thick wall cladding. This is because a pin geometry cladding is very small in radius and, as well known, the stresses on any container subjected to a pressure gradient increase as the container size, in the direction normal to the walls, increases. An inverted assembly, on the other hand, does not contain a single fuel cell, but a modular repetition of multiple cells, as shown in Figure I- 5. Therefore, if a duct is needed to contain the fuel, its size will be much larger than that of a pin geometry cladding. If a pressure differential exists between inside and outside the duct, thick walls, of the order of several mm, will be needed to withstand the same pressure differentials that a half mm thick clad can withstand in a pin geometry. These walls clearly penalize neutron economy and reduce the space available for fuel and coolant, thus degrading core performance. For this reason it is desirable to avoid, or reduce as much as possible, any pressure differential that can be generated during the life of the assembly. FGR is one of the major causes of pressurization, and adequate fission gas engineering strategies must be employed to allow use of the inverted geometry:

- retain the fission gases in microspheres within the fuel region;
- vent the fission gases to an offgas system;
- limit the release of fission gases from the fuel.

The first strategy is adopted in the HTGR, where the fuel is in the form of TRISO-type particles inside graphite-based compacts. The solution of venting the fission gases was “*specified in the design of the General Atomics pin-type GFR of the 1970’s (Capana et al., 1974)*”. Also, the vented fuel was “*evaluated favorably for LMFBR service (O’Neill et al., 1965) and was used successfully on the Peach Bottom HTGR (de Hoffmann et al., 1965)*” (Pope et al., 2005). More recently, a vented inverted assembly, for Gas Cooled Fast Reactor applications, was proposed by Pope et al. (2005). In this assembly fission gases diffusing through the fuel “*encounter an absorber region which increases the holdup of fission products. A small plenum at the top of the assembly allows the fuel volume to communicate with fission gas conduits. These conduits lead fission gases to a debris trap and then to a “flower-holder” type lower plate, the center plenum of which leads to the offgas system*” (Pope et al., 2005). The third strategy, i.e. limiting fission

burnable poison, e.g. negligible reactivity penalty at End Of Life, IFBA was discarded in the design of the IPWR just because of the need to avoid He generation and thus duct pressurization.

gas release, can be performed by either choosing a fuel with low fission gas release, or by limiting the operating fuel temperature. These actions are both adopted in the design of the IPWR.

The main advantages of an inverted geometry relative to a pin geometry, i.e. a lower pressure drop and maximum fuel temperature, have been only qualitatively discussed so far. The following sections quantitatively examine these advantages. In particular, Section I.4. 1 presents a comparison between a continuous inverted geometry and a pin geometry, while Section I.4. 2 discusses how such comparison changes if large discontinuities are assumed to characterize the inverted geometry. Appendix I-A of this chapter discusses the analytical procedure used to obtain the results shown in these sections.

I.4. 1 Comparison continuous inverted vs pin geometry: pressure drop and fuel temperature

A continuous inverted geometry has lower pressure drop and lower maximum fuel temperature than a pin geometry having the same fuel volume fraction, v_f . This is presented in Figure I- 9 which shows the variation of the maximum heat path length ratio (pin/inv) and of the pressure drop ratio (pin/inv) as a function of the fuel volume fraction. The maximum heat path length, t_H , is the maximum distance between any point in the fuel and the closest cooled surface. The larger this length the larger the fuel temperature. For a pin geometry t_H is clearly equal to the cladding outside radius, while for an inverted geometry it is the distance shown in Figure I- 1. Therefore, by using the subscript P to indicate variables referred to the pin geometry, and I to indicate those referred to the inverted geometry, the maximum heat path lengths are:

$$(t_H)_P = \frac{(D_{co})_P}{2} \quad (I-1)$$

$$(t_H)_I = \frac{P_I}{\sqrt{3}} - \frac{(D_{ci})_I}{2} \quad (I-2)$$

and their ratio is:

$$R_H = \frac{(t_H)_P}{(t_H)_I} = \frac{(D_{co})_P}{(D_{ci})_I \left[\frac{2}{\sqrt{3}} \left(\frac{P}{D_{ci}} \right)_I - 1 \right]} \quad (I-3)$$

From Figure I- 9 it can be seen that the heat path length ratio is larger than one for the fuel volume fraction range of practical interest ($0.3 \leq v_f \leq 0.6$), while the pressure drop ratio is lower than one up to $v_f \sim 0.37$ and increases dramatically past 0.37. Such a dramatic increase is more evident in Figure I- 10, which reproduces the pressure drop ratio of Figure I- 9 but using linear scale. For example, for a continuous inverted geometry having a fuel volume fraction of a VVER-440 reactor¹¹, i.e. 0.35 (AER, 1999), the maximum heat path length would be 1.7 times smaller than that of a pin geometry with the same fuel volume fraction, while the pressure drop would be about 1.3 times higher. However, as the fuel volume fraction increases, and reaches that of a typical IPWR design, i.e. 0.4, the pressure drop ratio becomes larger than one while the heat path length ratio is still significantly above unity, and equal to 1.63 and 1.54 respectively. Thus, from the pressure drop viewpoint, inverted configurations are advantaged over pin geometries at high fuel volume fractions. It is important to note that, as discussed in Appendix I-A of this chapter, which describes the calculations used to obtain Figure I- 9, the comparison shown in this figure is between geometries having same heat transfer surface area, i.e. $(D_{co})_P = (D_{ci})_I$.

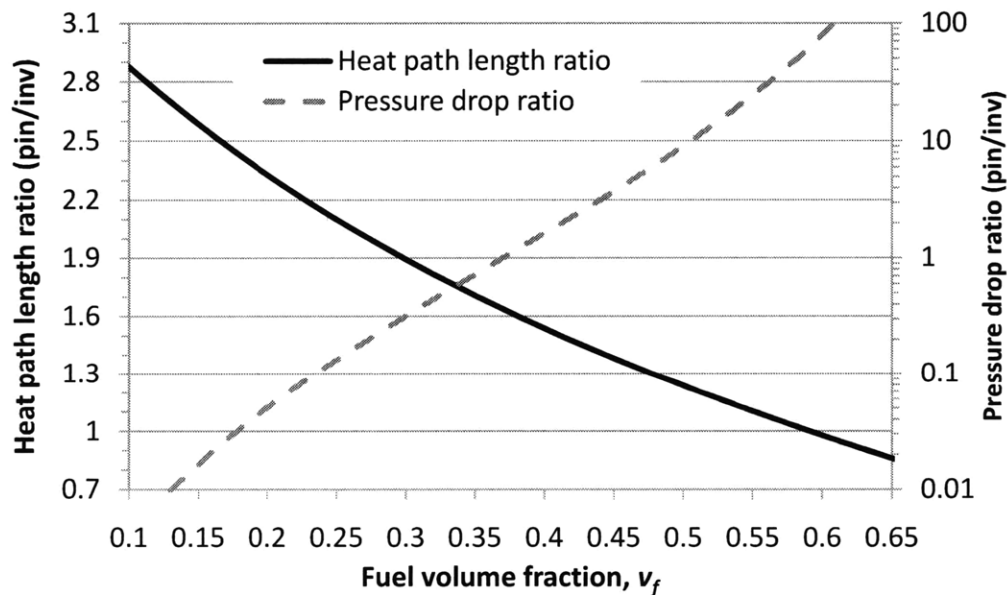


Figure I- 9: Comparison continuous inverted-pin geometry for same flow rate and heat transfer area per cell

¹¹ The VVER reactor is chosen here as example of existing hexagonal lattice pin geometry. Lattice parameters for a VVER-440 reactor are: $D_f = 7.6$ mm, $D_{co} = 9.1$ mm, $P = 12.2$ mm (AER, 1990). The fuel volume fraction of the reference core is very similar, i.e. 0.33 (Seabrook USAR, 2002).

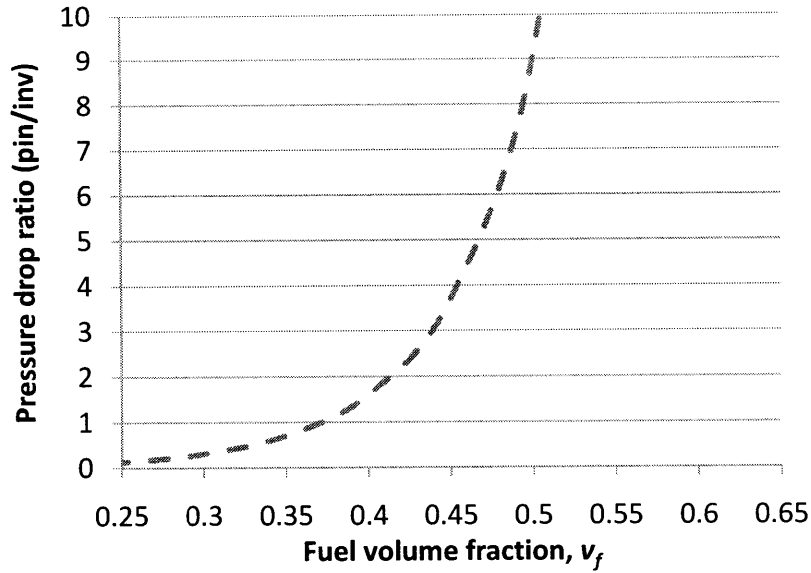


Figure I-10: Reproduction of pressure drop ratio of Figure I-9 using linear scale

The reason for the significantly better pressure drop performance of a continuous inverted geometry with respect to a pin geometry, for $v_f \geq 0.37$, lays in the fundamental difference between the two geometries, i.e. the inversion of fuel and coolant. In fact, as demonstrated in Appendix I-A of this chapter, for geometries having same heat transfer area, the pressure drop ratio between pin and inverted geometries only depends on a parameter, the pitch-to-diameter ratio of the pin geometry, which causes this ratio to be larger and larger as the fuel volume fraction increases:

$$\frac{(\Delta p)_p}{(\Delta p)_i} = \left(\frac{8}{\pi}\right)^{-1.8} \left[\frac{\pi(0.86)^2}{8(v_f)_p} - \frac{\pi}{8} \right]^{-1.8} \left[\frac{(0.86)^2}{(v_f)_p} - 1 \right]^{-1.2} \quad (I-4)$$

where $(v_f)_p$, pin geometry fuel volume fraction, is a function of the pitch-to-diameter ratio only:

$$(v_f)_p = \frac{\text{Fuel volume}}{\text{Cell volume}} = \frac{\left(\frac{\pi}{8} D_f^2\right)_p}{\frac{\sqrt{3}}{4} P_p^2} = \frac{\pi}{2\sqrt{3}} \frac{1}{\left(\frac{P}{D_f}\right)_p^2} \quad (I-5)$$

The analogous relation to Eq. I-5 for an inverted geometry is:

$$(v_f)_l = \frac{\text{Fuel volume}}{\text{Cell volume}} = \frac{\frac{\sqrt{3}}{4} P_l^2 - \left(\frac{\pi}{8} D_f^2\right)_l}{\frac{\sqrt{3}}{4} P_l^2} = 1 - \frac{\pi}{2\sqrt{3}} \frac{1}{\left(\frac{P}{D_f}\right)_l^2} \quad (\text{I-6})$$

As it can be seen from Figure I- 11, for pin geometries increasing the fuel volume fraction requires decreasing the pitch-to-diameter ratio which, per Eq. I-4 and Eq. I-5, clearly penalizes pressure drop thus preventing the attainment of high fuel volume fractions.

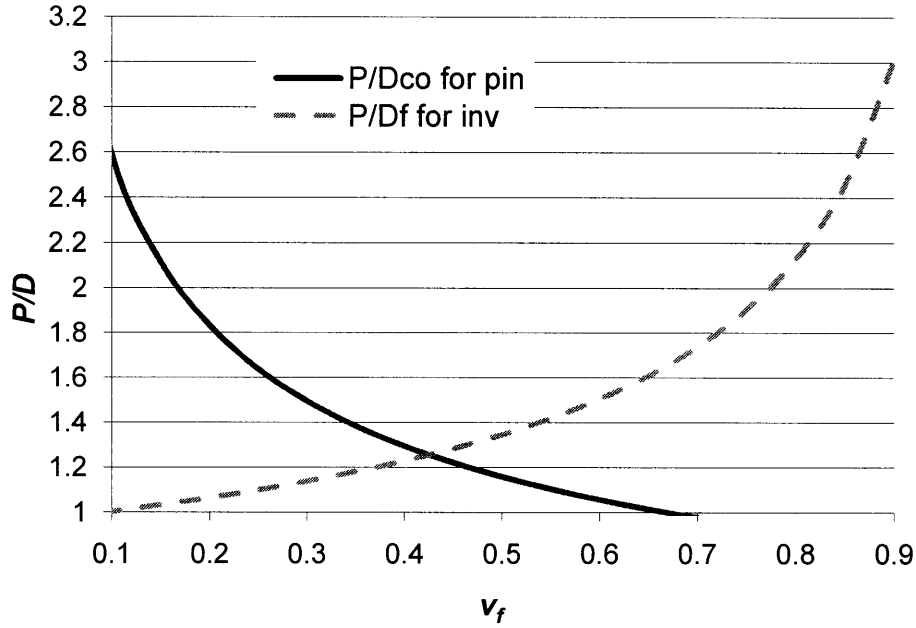


Figure I- 11: Variation of pitch-to-diameter ratio with fuel volume fraction¹²

Also for an inverted geometry the increase in v_f is accompanied by a variation in the pitch-to-diameter ratio, but the latter does not affect the pressure drop ratio between the two geometries, as shown in Eq. I-4. It instead affects the fuel temperature, which therefore plays the constraining role on v_f that is played by pressure drop in pin geometries. This constraining effect does not, however, prevent a continuous inverted geometry from performing better than a pin geometry from the fuel temperature viewpoint since, as shown in Figure I- 9, up to $v_f \sim 0.58$ the maximum

¹² Unlike in Eq. I-5 this figure shows, for the pin geometry, the variation of the pitch-to-cladding outside diameter ratio and not the variation of the pitch-to-fuel pellet diameter ratio. This was done for two reasons: (1) P/D_{co} is more frequently used than P/D_f for pin lattices, and (2) using P/D_{co} allows avoiding an error that can be easily made, i.e. showing apparently correct geometries having P/D_f values slightly larger than 1, which however correspond to unphysical situations characterized by P/D_{co} less than 1. The variation of P/D_{co} with v_f for the pin geometry was obtained assuming that the ratio between the fuel pellet diameter and the cladding outside diameter is constant, and equal to the value of the reference core, i.e. 0.86 (Seabrook USAR, 2002).

heat path length of an inverted geometry is smaller than that of a pin geometry. Beyond this value, for an inverted geometry the increase in maximum heat path length required to increase the fuel volume fraction by a fixed amount becomes too large, and the inverted geometry starts to perform worse than the pin geometry. This is evident from Figure I- 12, which shows the derivative of the heat path length in the fuel¹³, t_{Hf} , with respect to v_f , for the two geometries and for different values of the pin geometry pitch and inverted geometry fuel hole diameter, which are the only geometric parameters, additionally to v_f , which the derivatives depend on. It can be seen that pin and inverted geometry have opposite behavior: as fuel volume fraction increases, the derivative decreases for the pin geometry, while it increases for the inverted geometry.

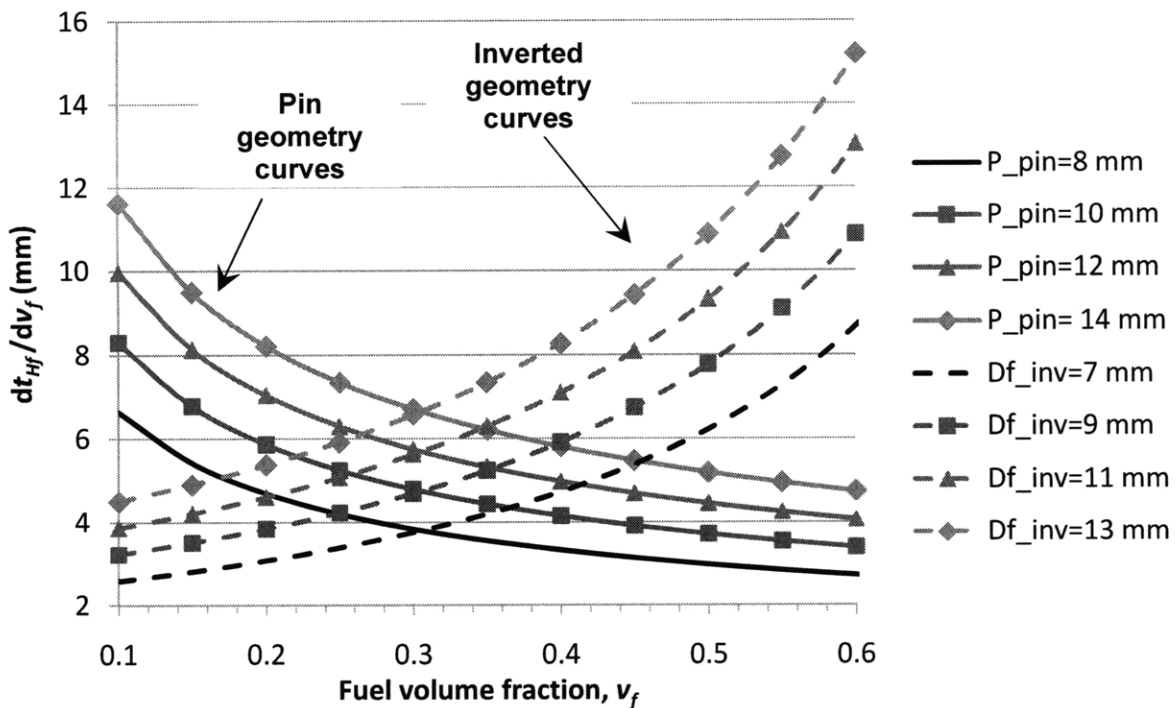


Figure I- 12: Derivative of the maximum heat path length in the fuel, t_{Hf} , with respect to v_f

I.4. 2 Inverted geometry performance degradation due to discontinuities

When large discontinuities are present, e.g. wide water gap for control blade insertion and/or thick ducts for assembly structural stability, the performance of the inverted geometry degrades, with respect to a continuous inverted geometry. A systematic evaluation of such degradation

¹³ As discussed in Appendix I-A of this chapter, while the maximum heat path length t_H represents the maximum distance that heat has to travel to reach the coolant, t_{Hf} is the part of this length travelled in the fuel. For generating Figure I- 12 t_{Hf} was preferred over t_H since it allowed simplifying the calculations.

would need to be performed on a case-by-case basis, since geometry-specific factors come into play, and a generalized yet precise treatment is not possible. For this reason, in this section the effect of discontinuities is analyzed in a simplified way, by assuming that they only cause the active flow area to decrease by a factor K_D ($K_D < 1$), with consequent increase of the active mass flux by a factor $1/K_D$, and by then verifying how this reduction affects the pressure drop results shown in Figure I- 9. This is shown in Figure I- 13, which reproduces the pressure drop ratio curve of Figure I- 9, over a narrower v_f range and using linear scale instead of the logarithmic one to improve readability. Different pressure drop curves are shown, each referred to an assumed value for the discontinuity factor K_D . It can be seen that, at the fuel volume fraction previously used as example, i.e. 0.35 of a VVER-440 reactor, a reduction in K_D by 30%, i.e. from 1 to 0.7, would cause the pressure drop ratio to decrease from 0.7 to 0.38, i.e. a 180% reduction. For the IPWR the discontinuities causing the inverted geometry to deviate from the continuous configuration are the assembly ducts and the inter-assembly water gaps. As it can be seen¹⁴ from Figure I- 5, the ducts alone are responsible for a reduction, in active flow area, of about 30%. The water gaps cause a reduction in active flow area approximately of the same amount but, unlike the flow area “stolen” by the ducts, that taken by the water gaps is not entirely lost since some coolant flows through them¹⁵. A reasonable value for the overall discontinuity factor for the IPWR geometry of Figure I- 5 is about 0.6. From Figure I- 13 it can be noticed that this degree of discontinuities causes the inverted geometry to lose any pressure drop advantage with respect to a pin geometry, since the pressure drop ratio decreases from 1.53 (for $K_D=1$) to 0.65 (for $K_D=0.6$).

¹⁴ For the inverted assembly shown in Figure I- 5, the removal of the duct and its replacement with fuel cells would allow, approximately, 30% more fuel cells.

¹⁵ Given a reduction in active flow area equal to 30%, the corresponding discontinuity factor will be 0.7 if the cause of the reduction is the addition of the ducts, while it will be slightly larger than 0.7 if the cause of the reduction is the addition of water gaps. This is because, in the method presented here, the role of the discontinuity factor is to represent, through its inverse ($1/K_D$), the increase in active mass flux resulting from the reduction in active flow area. The addition of water gaps causes most, not all, the coolant to flow through the remaining active flow area, since a small percentage of total flow, typically around 10%, still flows through them.

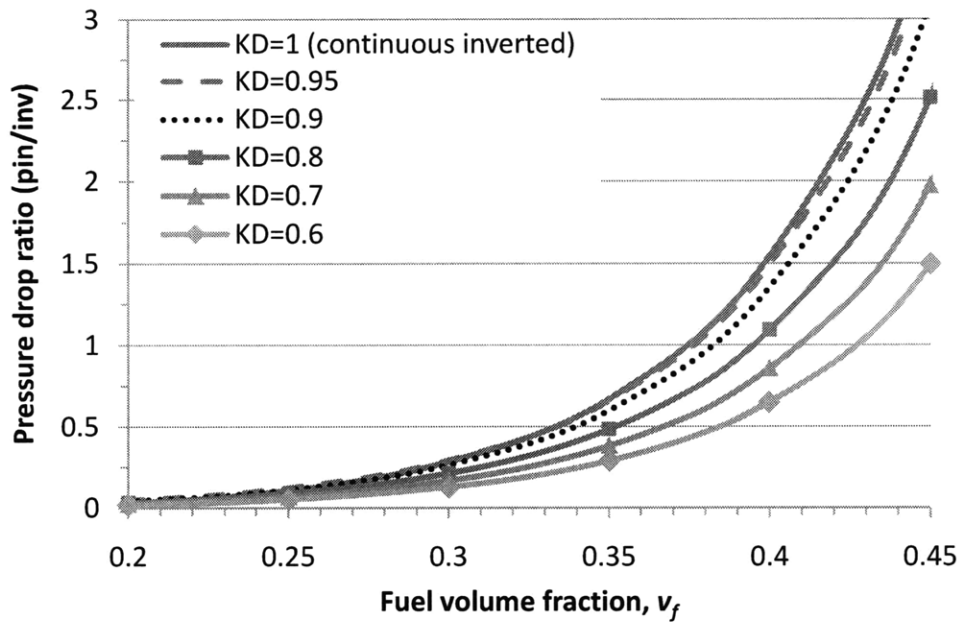


Figure I- 13: Variation of pressure drop ratio with discontinuity factor K_D

I. 5 Reactor designs adopting inverted fuel geometry

Inverted fuel geometries, even though less popular than pin geometries, have been investigated, built or even operated¹⁶ in the past. Eight reactor designs using inverted geometry are listed below. Of them, five are thermal reactor designs, while three are fast reactors. They are:

- Thermal reactors:
 - High Temperature Particle Fuel Designs:
 - GT-MHR (He-cooled) (Shenoy, 1996);
 - VHTR (He-cooled) (Schultz, 2005);
 - LS-VHTR (liquid salt-cooled) (Ingersoll et al, 2004);
 - Solid solution fuel designs:
 - Tube-in-shell CANDU (water-cooled) (Groeneveld, 2008)
 - IPWR (this work);
- Fast reactors:
 - the GFR in two designs: solid solution-fueled, CO₂-cooled (Pope et al., 2009) and dispersion-fueled, He-cooled (Weaver et al., 2004);

¹⁶ The Fort St Vrain High Temperature Gas Reactor (HTGR) operated for 10 years, from 1979 to 1989.

- the SFR NOVEX fuel design using U-Zr metal (Driscoll, 2009)

A description of these designs, except for the tube-in-shell CANDU design, can be found in Todreas and Ferroni (2009).

Appendix I-A: Analytical methods for inverted-pin comparison

This Appendix presents the analytical procedure used to compare the performance of pin and inverted geometries and, specifically, to obtain the pressure drop- and heat path length-related results shown in Sections I.4. 1 and I.4. 2. The fuel cells to which the method refers are those shown in Figure I- 1.

I-A. 1 Calculation of pin-inverted pressure drop ratio

The friction pressure drop through a channel can be calculated using the well known expression:

$$\Delta p = f \frac{L}{D_e} \frac{G^2}{2\rho} \quad (I-7)$$

where f is the Darcy friction factor, L and D_e are the length and equivalent diameter of the channel, G is the mass flux and ρ is the coolant density. For the comparison presented in this section, the friction factor is computed using the McAdams relation (Todreas and Kazimi, 1993):

$$f = 0.184 \text{Re}^{-0.2} = 0.184 \left(\frac{GD_e}{\mu} \right)^{-0.2} \quad (I-8)$$

By introducing Eq. I-8 into Eq. I-7 we get the following proportionality:

$$\Delta p = 0.184 \left(\frac{GD_e}{\mu} \right)^{-0.2} \frac{L}{D_e} \frac{G^2}{2\rho} \propto \frac{G^{1.8}}{D_e^{1.2}} = \left(\frac{\dot{m}}{A_{flow}} \right)^{1.8} \frac{1}{D_e^{1.2}} \quad (I-9)$$

which, assuming the mass flow rate per cell to be the same for both pin and inverted geometry, becomes:

$$\Delta p \propto \frac{1}{A_{flow}^{1.8} D_e^{1.2}} \quad (I-10)$$

The equivalent diameter of pin and inverted cells can be expressed as (see Figure I- 1 for the meaning of the geometric parameters):

$$(D_e)_p = \frac{4(A_{flow})_p}{(P_w)_p} = \frac{4 \left(\frac{\sqrt{3}}{4} P^2 - \frac{\pi}{8} D_{co}^2 \right)_p}{\left(\frac{\pi}{2} D_{co} \right)_p} = \frac{2\sqrt{3}}{\pi} \left(\frac{P}{D_{co}} \right)_p^2 D_{co} - D_{co} \quad (I-11)$$

$$(D_e)_I = \frac{4(A_{flow})_I}{(P_w)_I} = \frac{4\left(\frac{\pi}{8}D_{ci}^2\right)_I}{\left(\frac{\pi}{2}D_{ci}\right)_I} = (D_{ci})_I \quad (I-12)$$

By introducing Eq. I-11, Eq. I-12 and the expressions for the flow areas into Eq. I-10, the friction pressure drop ratio between inverted and pin geometry, assumed to have the same mass flow rate, is:

$$\frac{(\Delta p)_I}{(\Delta p)_P} = \left[\frac{(D_{co})_P}{(D_{ci})_I} \right]^{4.8} \left(\frac{8}{\pi} \right)^{1.8} \left[\frac{\sqrt{3}}{4} \left(\frac{P}{D_{co}} \right)_P^2 - \frac{\pi}{8} \right]^{1.8} \left[\frac{2\sqrt{3}}{\pi} \left(\frac{P}{D_{co}} \right)_P^2 - 1 \right]^{1.2} \quad (I-13)$$

In obtaining this friction pressure drop ratio, no constraint on fuel or coolant volume fraction has been set. It is desirable to convert Eq. I-13 into an equivalent expression in which the fuel volume fraction, set to be the same for the two geometries, appears. This can be done by first expressing the fuel volume fraction, v_f , for the two geometries:

$$(v_f)_P = \frac{\text{Fuel volume}}{\text{Cell volume}} = \frac{\left(\frac{\pi}{8}D_f^2\right)_P}{\frac{\sqrt{3}}{4}P_P^2} = \frac{\pi}{2\sqrt{3}} \left(\frac{D_f}{P} \right)_P^2 \quad (I-5)$$

$$(v_f)_I = \frac{\text{Fuel volume}}{\text{Cell volume}} = \frac{\frac{\sqrt{3}}{4}P_I^2 - \left(\frac{\pi}{8}D_f^2\right)_I}{\frac{\sqrt{3}}{4}P_I^2} = 1 - \frac{\pi}{2\sqrt{3}} \left(\frac{D_f}{P} \right)_I^2 \quad (I-6)$$

Since, in Eq. I-13, the cladding outside diameter for the pin geometry appears, and not the pellet diameter (as in Eq. I-5), it is convenient to express $(D_f)_P$ as a function of $(D_{co})_P$ by assuming that the ratio between these parameters is constant and equal to the value of a typical PWR pin geometry rod, i.e. 0.86 (Seabrook USAR, 2002). Therefore:

$$(D_f)_P = 0.86(D_{co})_P \quad (I-14)$$

By introducing Eq. I-14 into Eq. I-5, the ratio $(P/D_{co})_P$ can be expressed as function of the pin geometry fuel volume fraction:

$$\left(\frac{P}{D_{co}} \right)_P^2 = 0.86^2 \frac{\pi}{2\sqrt{3}(v_f)_P} \quad (I-15)$$

which can be inserted into Eq. I-13 to get:

$$\frac{(\Delta p)_I}{(\Delta p)_P} = \left[\frac{(D_{co})_P}{(D_{ci})_I} \right]^{4.8} \left(\frac{8}{\pi} \right)^{1.8} \left[\frac{\pi(0.86)^2}{8(v_f)_P} - \frac{\pi}{8} \right]^{1.8} \left[\frac{(0.86)^2}{(v_f)_P} - 1 \right]^{1.2} \quad (I-16)$$

The diameter ratio on the right hand side of Eq. I-16 is equal to the heat transfer area ratio between the two geometries, and it is therefore equal (assuming same linear power per cell) to the reciprocal of the heat flux ratio:

$$\frac{(D_{co})_P}{(D_{ci})_I} = \frac{(q'')_I}{(q'')_P} \quad (I-17)$$

If the margin from Critical Heat Flux (CHF) is required to be the same in both geometries, the ratio of Eq. I-17 can be set to unity. Therefore, the pressure drop ratio between a continuous inverted and a pin geometry both having the same mass flow rate and heat flux can be expressed as:

$$\frac{(\Delta p)_I}{(\Delta p)_P} = \left(\frac{8}{\pi} \right)^{1.8} \left[\frac{\pi(0.86)^2}{8(v_f)_P} - \frac{\pi}{8} \right]^{1.8} \left[\frac{(0.86)^2}{(v_f)_P} - 1 \right]^{1.2} \quad (I-4)$$

The reciprocal of this pressure drop ratio is plotted as a function of the pin geometry fuel volume fraction in Figure I- 9.

I-A. 2 Calculation of pin-inverted maximum heat path length ratio

The maximum temperature reached by the fuel, either in a pin or in an inverted geometry, is a function of several parameters. Among them, a key role is played by the maximum heat path length, t_H , which is the maximum distance between any point in the fuel and the closest cooled surface. The larger this length the larger the fuel temperature. For a pin geometry, t_H is clearly equal to the cladding outside radius, while for an inverted geometry it is the distance shown in Figure I- 1. Therefore:

$$(t_H)_P = \frac{(D_{co})_P}{2} \quad (I-1)$$

$$(t_H)_I = \frac{P_I}{\sqrt{3}} - \frac{(D_{ci})_I}{2} \quad (I-2)$$

The ratio between the two can be expressed as:

$$R_H = \frac{(t_H)_P}{(t_H)_I} = \frac{(D_{co})_P}{(D_{ci})_I \left[\frac{2}{\sqrt{3}} \left(\frac{P}{D_{ci}} \right)_I - 1 \right]} \quad (I-3)$$

The coolant volume fractions of the two geometries are:

$$(v_c)_P = \frac{\text{Coolant volume}}{\text{Cell volume}} = 1 - \frac{\pi}{2\sqrt{3}} \left(\frac{D_{co}}{P} \right)_P^2 \quad (I-18)$$

$$(v_c)_I = \frac{\text{Coolant volume}}{\text{Cell volume}} = \frac{\pi}{2\sqrt{3}} \left(\frac{D_{ci}}{P} \right)_I^2 \quad (I-19)$$

$(P/D_{ci})_I$ can be expressed, using Eq. I-19, as a function of $(v_c)_I$ and introduced into Eq. I-3 to obtain:

$$R_H = \frac{(D_{co})_P}{(D_{ci})_I} \frac{1}{\sqrt{\frac{2\pi}{3\sqrt{3}(v_c)_I} - 1}} \quad (I-20)$$

Again, as done for the comparison described in Section I-A. 1, the diameter ratio can be set to unity to keep the margin from CHF the same in both geometries. As a consequence, Eq. I-20 reduces to the simple form:

$$R_H = \frac{1}{\sqrt{\frac{2\pi}{3\sqrt{3}(v_c)_I} - 1}} \quad (I-21)$$

To be consistent with the comparison in Section I-A. 1, R_H needs to be expressed as a function of the fuel volume fraction. It is therefore needed to express $(v_c)_I$ as a function of $(v_f)_I$, which is possible after assuming a relation between $(D_{ci})_I$ and $(D_f)_I$. Analogously with the assumption made for the pin geometry (see Eq. I-14), it is reasonable to use the following relation:

$$(D_{ci})_I = 0.86(D_f)_I \quad (I-22)$$

By introducing Eq. I-22 into Eq. I-19, and the resulting expression into Eq. I-6, a relation between fuel and coolant volume fractions in a continuous inverted geometry can be found. By substituting this relation into Eq. I-21 we obtain:

$$R_H = \frac{1}{\sqrt{\frac{2\pi}{3\sqrt{3}(0.86)^2[1-(v_f)_I]} - 1}} \quad (I-23)$$

which is plotted in Figure I-9.

I-A. 3 Calculation of the increase in heat path length required to increase fuel volume fraction

Additionally to the comparison of the maximum heat path lengths of the two geometries, it is instructive to compare pin and inverted geometries on the basis of the increase in maximum heat path length required to increase, by a fixed amount, the fuel volume fraction. To simplify the calculations, it is convenient to use the maximum heat path length in the fuel, t_{Hf} , instead of the overall maximum heat path length, t_H . This parameter, slightly smaller than t_H , represents the maximum distance that the heat has to travel in the fuel, before being transferred through the fuel-clad gap and finally removed by the coolant. Analogously to the expressions for t_H , t_{Hf} is given by:

$$(t_{Hf})_P = \frac{(D_f)_P}{2} \quad (I-24)$$

$$(t_{Hf})_I = \frac{P_I}{\sqrt{3}} - \frac{(D_f)_I}{2} \quad (I-25)$$

By introducing these equations into the expressions for the fuel volume fraction, i.e. Eq. I-5 and Eq. I-6, the following relations can be obtained:

$$(t_{Hf})_P = P_P \sqrt{\frac{\sqrt{3}}{2\pi} (v_f)_P} \quad (I-26)$$

$$(t_{Hf})_I = (D_f)_I \left[\sqrt{\frac{\pi}{6\sqrt{3}} \frac{1}{1-(v_f)_I}} - \frac{1}{2} \right] \quad (I-27)$$

The derivation of these expressions with respect to v_f provides a measure of the fuel temperature penalty resulting from an increase in fuel volume fraction:

$$\left(\frac{dt_{Hf}}{dv_f} \right)_P = P_P \sqrt{\frac{\sqrt{3}}{8\pi}} \frac{1}{[(v_f)_P]^{\frac{3}{2}}} \quad (I-28)$$

$$\left(\frac{dt_{Hf}}{dv_f}\right)_l = (D_f)_l \sqrt{\frac{\pi}{24\sqrt{3}}} \frac{1}{[1 - (v_f)_l]^{\frac{3}{2}}} \quad (I-29)$$

The variation of these derivatives with v_f is shown in Figure I- 12.

Chapter II

Materials

This chapter describes the materials selected for the IPWR, in the following order:

- Section II.1: fuel
- Section II.2: Zr-2.5Nb (cladding and duct);
- Section II.3: Sn-Pb-Bi liquid metal.

Properties are discussed within the sections, and summarized in tables at the end of each.

II. 1 Fuel

The fuel selected for the IPWR is $UTh_{0.5}Zr_{2.25}H_{5.625}$ ¹. Although experimental studies on this fuel are currently undergoing at University of California at Berkeley (Terrani et al., 2009A), its characterization in terms of thermophysical and nuclear-related properties is not complete yet. For this reason, whenever the value of a certain property is not available or cannot be estimated, the analysis refers to the most well-known hydride fuel, i.e. U-ZrH_{1.6}, and adopts the corresponding value for that property.

After a brief discussion of the history of hydride fuels (Section II.1.1), of the motivations leading to the choice of $UTh_{0.5}Zr_{2.25}H_{5.625}$ (Section II.1.2) and of its composition and structure (Section II.1.3), key fuel properties for inverted design, i.e. fuel swelling, fission

¹ The literature is not consistent in the way the hydride fuel stoichiometric formulae have to be written. Throughout this work, stoichiometric indexes are calculated as ratios between the atom number density of the element to which they refer, and the uranium atom density. However, whenever the context does not require referring to a specific fuel, but rather to a family of fuels, hyphens (-) are used in place of stoichiometric indexes. For example, the nomenclature U-ZrH_{1.6} is used to refer to uranium-zirconium hydride fuels in general, with no distinction based on the amount of uranium actually present in the fuel. Likewise, the nomenclature “U-Th-Zr-hydride” is used to refer to all the hydride fuels containing U, Th and Zr.

gas release and hydrogen release, are discussed in detail. The last section, i.e. Section II.1.8, lists the numerical values of the fuel thermophysical properties that do not require particular discussion, e.g. density, and combine them with the numerical findings about swelling, fission gas release and hydrogen release.

II.1. 1 Historical remarks on hydride fuels

The fuel selected for the IPWR belongs to the family of the U-Th-Zr hydride fuels, and has stoichiometric composition $UTh_{0.5}Zr_{2.25}H_{5.625}$. Historically, the first experimental studies on U-Th-Zr hydrides were performed in the '90s in Japan, followed by the more recent investigations carried out in US, by researchers at University of California at Berkeley. The latter experiments, currently undergoing, are the continuation of a broader research project that investigated the feasibility of replacing UO_2 with hydride fuel, in pin-geometry LWRs (Greenspan et al., 2009). Besides electricity generation, U-Th-Zr hydride-fueled LWRs can be employed for Pu/Minor Actinides burning since they can achieve TRU (transuranic elements) destruction fractions as high as twice those obtainable with mixed-oxide fuels (MOX). Also, unlike MOX fuel, they allow infinite cycles of partitioning and transmutation without resulting in large positive reactivity coefficients (Ganda and Greenspan, 2008).

Ternary hydrides, i.e. compounds containing, besides hydrogen, three other elements, were not the first hydride fuels to be investigated. The most well know hydride fuel is in fact a binary hydride, i.e. $U-ZrH_{1.6}$, which received attention starting in the late '50s. From 1956 to 1973, a series of small $U-ZrH_{1.6}$ -fueled reactors (0.5 kW_e to about 50 kW_e) were developed, for space applications, under the System for Nuclear Auxiliary Power (SNAP) program, led by Atomic International. $U-ZrH_{1.6}$ fuel was chosen "*based on minimum reactor weight, achievable and practical operating temperatures, ease of control, and reasonable extrapolation of reactor and materials technology*" (Stadnik and Page, 1988). One of these reactors, the SNAP-10A, was flight tested in April 1965, and operated in space for over 40 days.

The current most well known application of U-ZrH_{1.6} fuel is however in TRIGA (Training, Research, Isotopes, General Atomics) reactors: low power density², pool-type reactors used primarily for research and educational purposes, that General Atomics has developed and sold around the world since late '50s.

Table II- 1 compares key characteristics of reactors using hydride fuels with a typical UO₂-fueled PWR.

	SNAP S8DR (Lillie and Rooney, 1971) (Lillie et al., 1973)	Romanian TRIGA (Iorgulis et al., 1998) Toma et al., 2002) (Olander, 2006)	Typical PWR (Seabrook USAR, 2002)	IPWR (“selected design” in Chapter XI)
Fuel stoichiometry	UZr _{21.6} H _{34.5}	UZr _{3.1} H ₅	UO ₂	UTh _{0.5} Zr _{2.25} H _{5.625}
Fuel density, kg/m ³	6090	8256	10400	9096
U weight % in the fuel	10.5	45	88	42
U density in the fuel, kg/m ³	639	3715	9152	3829
Enrichment in ²³⁵ U, %	93	19.7	4.5	15
Cladding material	Hastelloy N	Incoloy 800	Zircaloy-4	Zr-2.5Nb
Fuel pellet diameter, mm	13.44	12.94	8.19	12.74 (fuel hole diameter)
Fuel rod outer diameter, mm	14.27	13.77	9.5	12.12 (cladding OD)
Pitch, mm	14.61	16.3	12.6	15.64
Reactor power, MW _t	0.6	14	3400	4078
Average LHGR, kW/m	6.7	34	18.2	35.3
Peak LHGR, kW/m	12.1	81	45	88
Coolant	NaK	H ₂ O	H ₂ O	H ₂ O
Nominal coolant inlet temp., °C	593	Not found	293	293
Nominal coolant outlet temp., °C	704	~70	325	325
Typical maximum fuel temperature, °C	830	550	1400	590
Discharge BU, MWD/kg	~50	121	~60	91
Average power density, MW/m ³	37	Not found	104	142

II.1. 2 Motivations for the choice of UTh_{0.5}Zr_{2.25}H_{5.625}

The motivations that led to the choice of a hydride fuel for the IPWR were mainly related to the suitability of this fuel category to be implemented in an inverted configuration, due to their low fission gas release and possibility to be drilled (before being hydrided) to

² An exception to the low-power density characteristics of TRIGA reactors is the Romanian TRIGA, which has been calculated to have operated at a maximum LHGR of about 81 kW/m (using an hot rod power of 35 kW from Toma et al., 2002, and axial peaking factor of 1.3 from Iorgulis et al., 1998).

create fuel channels. Also, regardless of whether the configuration is inverted or not, the presence of hydrogen inside the fuel allows obtaining the same degree of moderation using less coolant, thus creating the potential for higher fuel volume fractions. Specifically, $UTh_{0.5}Zr_{2.25}H_{5.625}$ was chosen, among all the hydride fuels documented in the literature, because:

- it has the highest heavy metal loading³;
- it has a superior hydrogen retention capability with respect to binary hydrides (see Section II.1.6);
- it has the potential to be used for Pu/Minor Actinides burning (Ganda and Greenspan, 2008).

The IPWR concept was originally investigated using U(45% w/o)ZrH_{1.6}, i.e. $UZr_{3.13}H_{5.01}$, but considerations on its low heavy metal loading, which negatively impacts cycle length and/or enrichment, and void reactivity coefficient, required the fuel to be changed.

II.1.3 Composition and structure

$UTh_{0.5}Zr_{2.25}H_{5.625}$ is a multi-phase mixture of δ -Zr hydride ($ZrH_{1.6+x}$), Th-Zr hydride ($ThZr_2H_{7-x}$) and U-metal. Figure II- 1 shows a backscattered electron image of the fuel structure (Terrani et al., 2009A). Unlike Th and Zr, U is not present in hydrided form since UH_3 is the least stable of the hydrides that can potentially form. The increasing order of thermodynamic stability of these hydrides is in fact: UH_3 , ThH_2 , δ -ZrH_{1.6+x}, $ThZr_2H_{7-x}$ (Terrani et al., 2009A).

³ It is important to note that even higher heavy metal loadings are, in principle, obtainable. In fact, unlike for oxide fuels, the stoichiometry of hydride fuels can be designed, and the obtainable concentrations of their components span broad ranges. As a proof of this, most of the papers on U-Zr-Th-hydrides do not deal with a single fuel, but investigate the properties of fuels having the same components but in different concentrations (e.g. Yamawaki et al., 1999). Even though it is possible to speculate on the possibility to obtain even higher heavy metal loadings, it was decided to use for the IPWR a fuel whose manufacture has been experimentally proven.

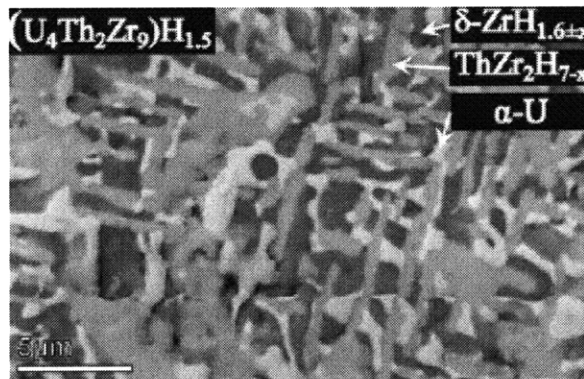


Figure II- 1: Backscattered electron image of $UTh_{0.5}Zr_{2.25}H_{5.625}$ fuel (from Terrani et al., 2009A)

II.1. 4 Irradiation-induced fuel swelling

Experimental data on fuel swelling are not available for Th-containing hydride fuels. Therefore, for the IPWR project it is assumed that the swelling behavior of $UTh_{0.5}Zr_{2.25}H_{5.625}$ is the same as that of the only hydride fuel for which experimental swelling data are available, i.e. $U(10\% \text{ w/o})ZrH_{1.6}$. This assumption requires experimental verification since, although reasonable based on the phase composition similarity of the two fuels, it may not be conservative because of the 9 times larger heavy metal atom density of $UTh_{0.5}Zr_{2.25}H_{5.625}$ relative to $U(10\% \text{ w/o})ZrH_{1.6}$. As known, fission products, which are responsible for swelling, accumulate as interstitials in the fuel matrix, and the space available for such accumulation to occur without resulting in an excessive volume growth decreases as the heavy metal atom density increases.

For $U-ZrH_{1.6}$, irradiation-induced swelling is a phenomenon that has to be considered carefully, and accommodated by appropriately designing the gaps separating the fuel from structural components. It has a key role in the core design since it sets the limit on fuel temperature: it is in fact more temperature-limiting than fission gas release and hydrogen release.

Swelling of $U-ZrH_{1.6}$ fuels depends on temperature, burnup and power density. This phenomenon received significant attention during the development of the SNAP program. In 1969, after almost a year of operation, the 600 kW_t, NaK cooled S8DR reactor, operating at high vacuum and inlet/outlet coolant temperatures of 593 and 704°C

respectively, was prematurely shut down because cladding ruptures were observed in 72 of the 211 fuel pins composing the core. Each fuel pin consisted of a U(10.5% w/o, 93% enriched)ZrH_{1.55-1.85} fuel slug inside a Hastelloy N cladding, with dimensions (Lillie and Rooney, 1971):

$$D_f = 13.44 \text{ mm}$$

$$D_{ci} = 13.61 \text{ mm}$$

$$D_{co} = 14.27 \text{ mm}$$

$$t_{gap} = 0.089 \text{ mm (width of the gap between fuel slug and cladding inside surface)}$$

The ruptures were the result of excessive cladding strain caused by fuel swelling resulting from localized operation at temperatures above the design value (up to 820°C vs the design value of 760°C). Swelling was found to be almost isotropic and was observed to consist of two phases (Lillie et al., 1973):

- a rapid early-life, offset, growth, due to vacancy-condensation, whose extent depends on fuel temperature and burnup rate. In particular, swelling increases as temperature increases and as burnup rate, i.e. power, decreases⁴.
- a much slower long-term growth, resulting from fission product accumulation in the fuel matrix, whose extent depends on the cumulative burnup.

These two phases are clearly visible in Figure II- 2 and Figure II- 3. Figure II- 2 shows the swelling percentage as a function of burnup and fuel temperature, at constant burnup rate, i.e. power. In Figure II- 3 the temperature is held constant, while the power is varied. With respect to their original form presented in Lillie et al. (1973), both figures have been supplemented with the inclusion of burnup in MWD/kg_{HM} and with fuel composition. Lillie et al. (1973) correlated the experimental data⁵ in the following way:

⁴ The counterintuitive dependence of the early-life growth on the burnup rate is due to the fact that interstitial-vacancy recombination, which increases with neutron flux, tends to offset the mechanism responsible for early-life growth, i.e. vacancy recombination (Lillie et al., 1973).

⁵ Of the 150 U(10.5% w/o)ZrH_{1.55-1.85} fuel samples examined, 83 were actually used to develop the correlation. The distribution of the samples based on their BU was the following:

- 0 ≤ BU ≤ 50 MWD/kg_U: 63 samples;
- 50 < BU ≤ 80 MWD/kg_U: 10 samples;
- BU > 80 MWD/kg_U: 11 samples.

$$\left(\frac{\Delta V}{V}\right)\% = \underbrace{5.5e^A}_{\substack{\text{Rapid, early-life, offset growth} \\ \text{(vacancy-condensation-induced)}}} + \underbrace{3 \times FIMA\%}_{\substack{\text{Linear growth (fission product} \\ \text{accumulation-induced swelling)}}} \quad (\text{II-1})$$

where:

FIMA% = burnup expressed in Fraction of Initial Metal Atom percentage (for the conversion to/from MWD/kg_{HM} see Appendix II-A);

$$A = - \left[2.3 \times \dot{F} \times e^{10.75 \left(\frac{1033.3}{T} - 1 \right)} + 21.5 \left(\frac{1033.3}{T} - 1 \right) \right] \quad (\text{II-2})$$

\dot{F} = burnup rate, expressed as FIMA% per 10000 hours of operation⁶;

T = fuel temperature (K);

with an average BU of 48 MWD/kg_U and a maximum of 200 MWD/kg_U.

⁶ The burnup rate is dimensionally equivalent to a power per unit mass of heavy metal. Once the core thermal power, \dot{Q}_{core} (MW), and the heavy metal mass in the core, $M_{HM,core}$ (kg), are known, or alternatively the average linear power, q' (kW/m), and the heavy metal density in the fuel, ρ_{HM} (kg/m³), are known, the value of \dot{F} to plug into Eq. II-2 can be calculated as:

$$\dot{F} = 416.7 \frac{\dot{Q}_{core}}{M_{HM,core}} \frac{\left(M_U + \frac{t}{u} M_{Th} \right)}{2.23316 \left(1 + \frac{t}{u} + \frac{z}{u} \right)} = 416.7 \frac{q'}{10^3 \left(\frac{\sqrt{3}}{2} P^2 - \frac{\pi}{4} D_f^2 \right) \rho_{HM}} \frac{\left(M_U + \frac{t}{u} M_{Th} \right)}{2.23316 \left(1 + \frac{t}{u} + \frac{z}{u} \right)}$$

where M_U and M_{Th} are the uranium and thorium atomic masses (kg/mol); t , u and z are the stoichiometric coefficients in the fuel formula $U_uTh_tZr_zH_h$ (see Appendix II-A for details); P and D_f are the cooling channel pitch and the diameter of the holes in the fuel (m).

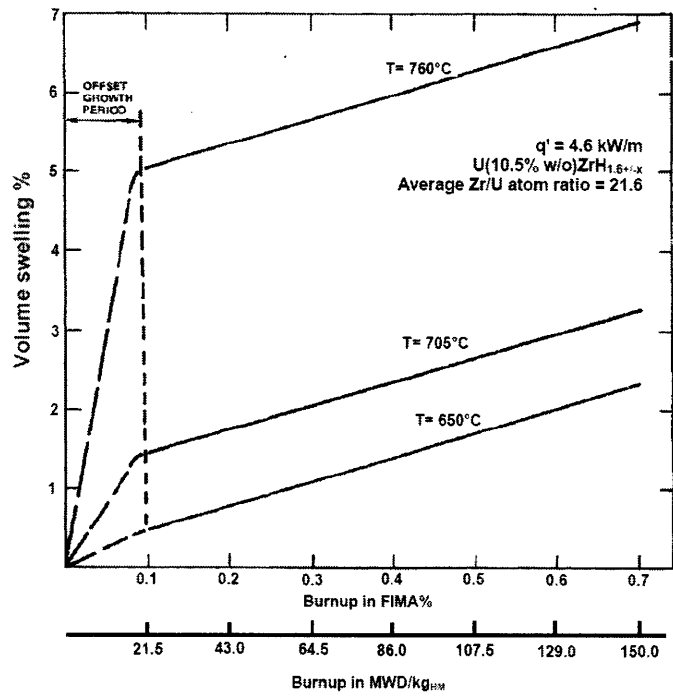


Figure II- 2: Effect of fuel operating temperature and burnup on fuel swelling, at constant linear power (modified from Lillie et al., 1973)

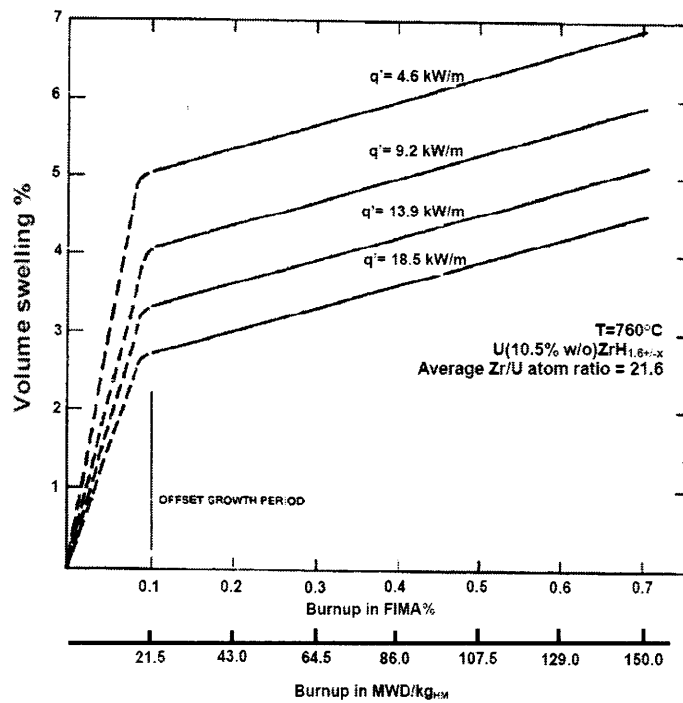


Figure II- 3: Effect of linear power and burnup on fuel swelling, at constant fuel temperature (modified from Lillie et al., 1973)

The broad burnup range characterizing the samples used to develop the correlation would allow its application to the IPWR if the fuel was the same. However, as mentioned earlier, the heavy metal density of $UTh_{0.5}Zr_{2.25}H_{5.625}$ is, relative to that of $U(10\% \text{ w/o})ZrH_{1.6}$, about 9 times higher. This will probably cause the swelling of $UTh_{0.5}Zr_{2.25}H_{5.625}$ to be larger than that of $U(10\% \text{ w/o})ZrH_{1.6}$ at the same burnup. However, since no irradiation data are available for the IPWR fuel, data for $U(10\% \text{ w/o})ZrH_{1.6}$ are used.

None of the samples tested by Lillie et al. (1973) experienced irradiation at temperatures below $\sim 650^{\circ}C$, and therefore it is not possible to know whether the curves shown in Figure II- 2 would keep lowering as the temperature is reduced. However, from this figure it can be seen that swelling increases significantly as the fuel temperature increases above $650^{\circ}C$. This is the reason why the maximum fuel temperature for the IPWR was fixed to $650^{\circ}C$.

II.1. 5 Fission gas release

Fission gas release (FGR) is a key property for fuels employed in inverted configurations. This is because the extent of FGR affects the level of pressurization of the assembly duct, which is ill-suited geometrically to contain fission gas released from the fuel with burnup. A high internal pressurization, while beneficial during normal operation since it reduces the differential pressure across the duct walls, is clearly not acceptable during LOCA and after the assembly has been removed from the core. Design solutions to overcome this limitation are discussed in Section I.4 of Chapter I.

Unlike for $U-ZrH_{1.6}$, no experimental data are available on FGR for U-Th-Zr-hydrides, and only two papers have been found that mention, or speculate, about FGR for these fuels: Yamamoto et al. (1998) and Konashi and Yamawaki (2004). Yamamoto et al. (1998) hydrided $5 \times 5 \times 6$ mm U-Th-Zr samples, obtaining samples of composition $UThZr_4H_{7.2}$, $UTh_2Zr_6H_{11.4}$ and $UTH_4Zr_{10}H_{19.4}$ respectively, which were then irradiated. Note that neither the burnup, temperature or degree of fission gas release were reported⁷.

⁷ Sample irradiation was performed using a neutron flux spectrum of 5.3×10^{16} n/m² s ($E > 1$ MeV) and 8.6×10^{17} n/m² s (thermal flux). Yamamoto et al. (1998) do not mention the burnup reached, but mention the thermal fluence obtained: 7.4×10^{23} n/m². Assuming they used natural uranium, and accounting only for

However while discussing the structural changes resulted from hydriding (before performing irradiation), they state: “*The low crack formation illustrated by this result is one of the most attractive properties of the alloys from the viewpoint of fabrication, thermal conductivity and fission gas retention if they are used as fuels*”. Konashi and Yamawaki (2004) irradiated $UTh_4Zr_{10}H_{20}$ specimens, at a maximum temperature of $554^{\circ}C$, up to 1.1 FIMA% (equivalent to about 31 MWD/kg_{HM}), and state that: “*Released fission gas was not observed because of low burnup of peller*”.

Because of the absence of FGR experimental data for Th-containing hydrides, it is assumed for the IPWR analysis that U-Th-Zr-hydrides behave like $U-ZrH_{1.6}$. This assumption is reasonable would be reasonable if only based on the microstructure similarity between $U-ZrH_{1.6}$ and Th-containing hydride fuels, i.e. the fact that uranium, segregated as a separate phase from the hydrides, acts as fission gas well (Baldwin et al., 1980). However, the larger heavy metal density of the IPWR fuel relative to that of $U-ZrH_{1.6}$ may cause FGR to be larger. Experimental verification is needed in this regard. For $U-ZrH_{1.6}$ fuel, experimental tests on FGR have been performed in the past, mainly within the TRIGA and SNAP programs. Simnad (1981), in his complete overview on $U-ZrH_{1.6}$, states: “*many experiments have been performed to determine the extent to which fission products are retained by U-ZrH fuel. Experiments of fuel with 8.5 wt% U were conducted for 11 years under a variety of conditions. Results prove that only a small fraction of the fission products are released, even in completely unclad U-ZrH fuel. The release fraction varies from 1.5×10^{-5} for an irradiation temperature of $350^{\circ}C$ to $\sim 10^{-2}$ at $800^{\circ}C$* ”. This conclusion was then found to also apply to fuels containing a higher U weight percentage, i.e. 45% (Baldwin et al., 1980). These release fractions are much lower than that of typical UO_2 -fueled PWRs which, as shown by Massih (2006), is of about 4×10^{-2} at a burnup of 60 MWD/kg_{HM}. Figure II- 4 is the collection of experimental data upon which Simnad based his quantitative conclusion on fractional FGR. In addition to the data, indicated with markers, Figure II- 4 shows a curve derived from an analytical FGR model, discussed in Langer and Baldwin (1971), having expression:

fissions from ^{235}U , for $UThZr_4H_{7.2}$ this fluence is equivalent to about 0.1 MWD/kg_{HM} (using a density of 8080 kg/m³ for $UThZr_4H_{7.2}$, and a microscopic fission cross section for ^{235}U of 560 barns).

$$FGR = 1.5 \times 10^{-5} + 3600 \exp\left(\frac{-1.34 \times 10^4}{T + 273}\right) \quad (\text{II.3})$$

where FGR is the fractional fission gas release and T is the irradiation temperature in °C. The figure lacks information on burnup, and the curve itself is not associated to any burnup level. However, West et al. (1986) irradiated other TRIGA fuel samples, in the Oak Ridge Research Reactor (ORR), up to about 180 MWD/kg_{HM}, and concluded that the FGR from highly-burned TRIGA fuel is not “*significantly different from the well documented and very low values for unirradiated and slightly burned up fuel, at least over the temperature range experienced during the ORR irradiation (25°C to 650°C)*”. This means that Figure II- 4 can be considered valid for any burnup level up to, at least, 180 MWD/kg_{HM}. This conclusion is supported by the fact that the figure contains data derived from the SNAP program, for which it is known that burnup levels up to 200 MWD/kg_{HM} had been reached (Birney, 1967).

Eq. II.3 is a conservative estimate of the fractional FGR from U-ZrH_{1.6} fuels. Simnad (1981) states in fact that: the figure “*shows that the measured values of fractional releases fall well below the curve. Therefore, for safety considerations, this curve gives very conservative values for the high-temperature release from TRIGA fuel*”. Also, he says that at temperatures below 750°C there is a safety factor of approximately four between the FGR fraction predicted with Eq. II.3 and the experimental values.

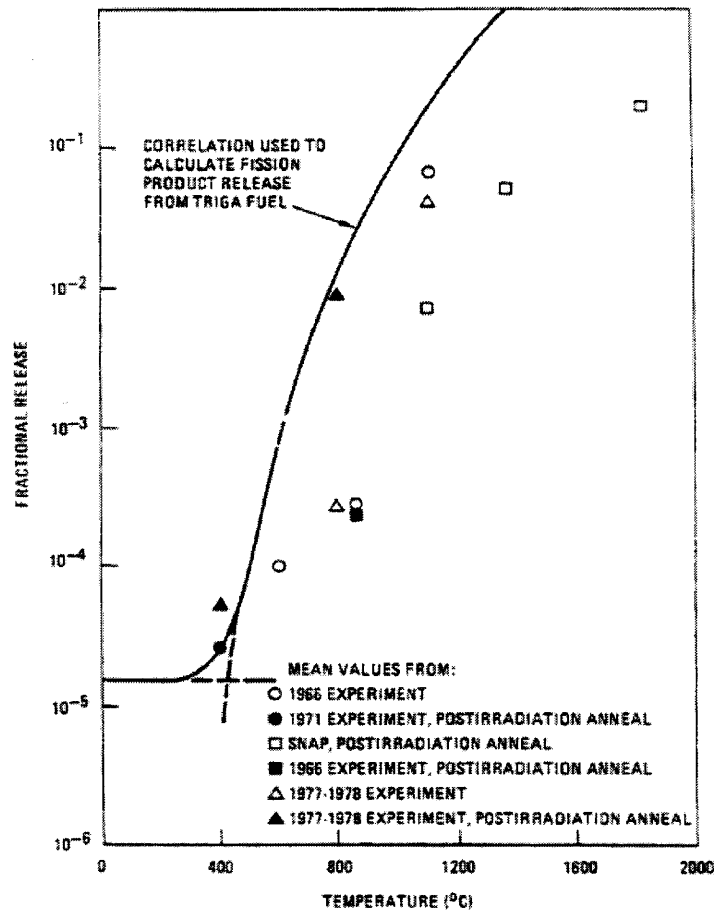


Figure II- 4: Fractional FGR for infinite irradiation⁸, as a function of irradiation temperature (from Baldwin et al., 1980)

⁸ The concept of “infinite irradiation”, reported in the caption of this figure in almost all the literature sources that show it, is misleading. In fact, it could be interpreted as if the curve, as well as the experimental points, referred to a situation of complete fissioning of all the available fissile materials. However, the concept of infinite irradiation time has to be interpreted as solely time-related, with no extrapolation relative to the burnup. Baldwin et al. (1980) state that the FGR from U-ZrH_{1.6} fuels consist of a rapid-release component, suggesting diffusion of individual atoms, followed by a slow-release component that may be associated with the diffusion of clustered atoms, i.e. bubbles. This latter FGR component is a function of time, and since the fractional FGRs for the samples of Figure II- 4 were not measured as a function of time, but after relatively short irradiation times, the experimental data have been corrected assuming that the samples are allowed to rest, at the irradiation temperature, but without being further irradiated. Simnad (1981), who refers to the solid line as “theoretical maximum”, gives the following explanation to the curve: the curve “applies to a TRIGA fuel element which has been irradiated for a time sufficiently long that all fission product activity is at equilibrium and the release fraction is at its theoretical maximum”.

According to Simnad (1981), there are two mechanisms involved in the release of fission products from U-ZrH_{1.6} fuels, each of which predominates over a different temperature range: below 400°C the dominant mechanism is fission fragment recoil, which is dependent on the fuel-to-volume ratio but is independent on fuel temperature. Above 400°C a diffusion-like process dominates, and the rate of release depends on fuel-to-volume ratio, temperature and irradiation time.

According to Baldwin et al. (1980), the high fission gas retention capacity of U-ZrH_{1.6} is due to the structure of the fuel itself: uranium is separated from the zirconium hydride matrix and thus not only acts as fission gas generator, but also as a fission gas well, and the more segregated is uranium from the hydride matrix, the higher is the retention extent. U-ZrH_{1.6} samples with high U loading (45%) were found to retain fission gases more than samples having 8-10% U loading: for the latter loading, in fact, uranium is finely dispersed and a fission fragment born in the uranium has a high probability of recoiling out of the uranium phase into the hydride matrix through which it will then easily diffuse. As the U particles increase in size, i.e. with higher U loadings, the probability of recoiling out of the uranium phase decreases and fewer fragments are deposited in the ZrH.

II.1. 6 Hydrogen release

Temperature has a strong effect on the hydrogen content of hydride fuels. Variations in temperature, both those time-dependent characterizing transient scenarios and those, spatial-dependent, during steady-state, cause hydrogen to redistribute. The consequences of such redistribution, i.e. phase changes and hydrogen release, are discussed next.

Phases changes occur since each phase can only exist as long as the hydrogen concentration is within certain limits, and when such limits are exceeded the material can no longer exist in that phase and transits to another phase. Different phases have different densities, and the transition from one to another is often accompanied by swelling/shrinking phenomena, which results in additional stresses not only on the fuel itself but also, in case the fuel comes in contact with the cladding, on the cladding. Fuel cracking can also result from these additional stresses, thus creating preferential paths for fission gas release. Figure II- 5 and Figure II- 6 show two examples of phase changes

resulting from temperature variations: the former indicates the trajectories that U(45% w/o)ZrH_{1.6} would experience upon hydrogen loss, for He- and liquid metal-bonded fuel rods⁹. As shown, for the liquid-metal bonded rod the trajectory enters the $\delta+\epsilon$ phase which, relative to the original δ -phase, is characterized by larger fission product swelling (Huang et al., 2000). Figure II- 6 shows instead the effect that temperature variations had on the operating ranges of some of the SNAP reactors which, as evident and with the exception of the SNAP-ORC reactor, did not always operate in the same Zr-hydride phase.

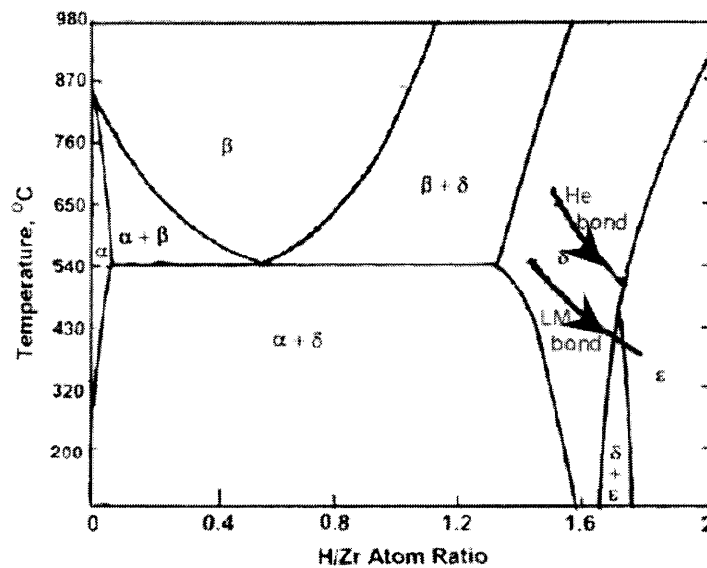


Figure II- 5: Hydrogen redistribution trajectories superimposed on the Zr-H phase diagram, for He- and liquid metal-bonded gap designs (Olander and Ng, 2005)

⁹ The thermal conductivity of the gap separating fuel from cladding affects the temperature profile across the fuel, and therefore the extent of hydrogen redistribution which, in turns, results in phase changes.

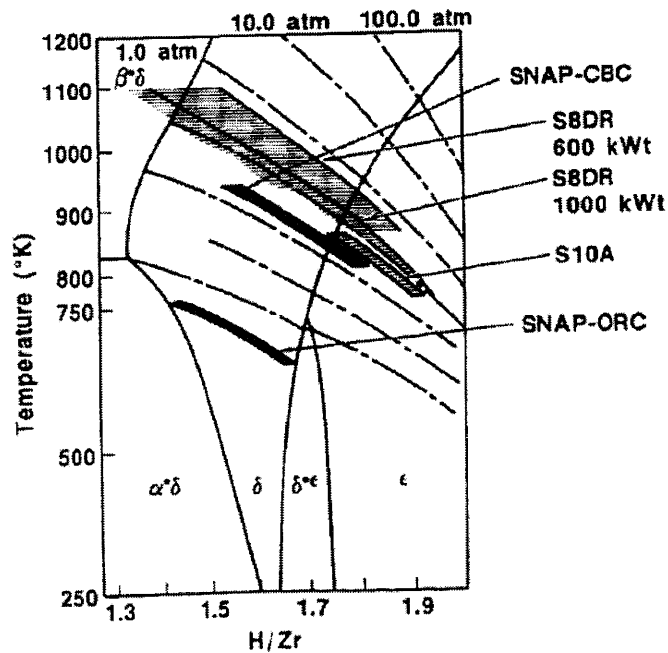


Figure II- 6: Operating ranges of the SNAP reactors in the Zr-H diagram (Stadnik and Page, 1988)

Hydrogen release has negative structural and positive neutronic consequences:

- hydrogen, no longer bonded to the metal composing the fuel, migrates to low-temperature regions in the fuel (Huang et al., 2000), i.e. to the surface, where the higher hydrogen concentration facilitates its release into the fuel-cladding (and fuel-duct) gaps. This increases the pressurization level of the structural components designed to retain fission products but, especially, making them more susceptible to hydriding and therefore embrittlement. An example of hydrogen redistribution is shown in Figure II- 7, which refers to a δ -ZrH_{1.6} pellet: hydrogen diffusion results in a H/Zr atom ratio of about 1.65-1.7 at the pellet surface, and of about 1.5-1.55 at the centerline. Since the hydride density increases as the hydrogen content decreases, it is evident that the pellet centerline will be subjected to tensile stresses, while the periphery experiences compression stresses.
- hydrogen release results in loss of moderation by the fuel, and thus in a negative reactivity insertion. This is the delayed feedback mechanism, beneficial from the

safety viewpoint, that characterizes hydride-fueled reactors and that is not present in typical UO_2 cores. The term “delayed” is used to differentiate this feedback from the so-called “prompt” feedback that kicks in as soon as temperature is increased, regardless of whether hydrogen is still bonded to the hydride structure or is diffusing in the fuel. In fact, temperature increase also enhances the vibrational motion of the hydrogen atoms in the fuel, resulting in neutron upscattering and therefore loss of moderation.

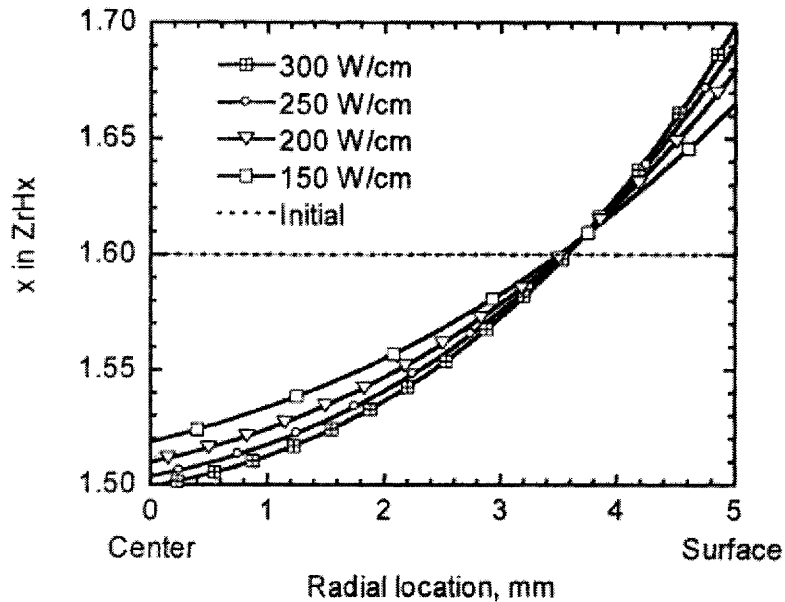


Figure II- 7: Hydrogen redistribution in a δ -ZrH_{1.6} fuel pellet (from Huang, 2000)

The hazard of structural material embrittlement, which can result in failure and consequent release of radioactivity, forces the IPWR design to be performed with the aim of preventing/limiting hydrogen release thereby protecting the structural materials from hydrogen-induced embrittlement. These strategies are discussed in the following sections.

II.1.6. 1 Hydrogen release limitation

Hydrogen release can be limited by design, by choosing a stable hydride fuel form and by simultaneously limiting its maximum operating temperature. These design strategies are linked since the stability of an hydride against hydrogen release is typically measured through its hydrogen equilibrium pressure, which is a function of temperature.

Specifically, the higher the temperature, the higher the hydrogen equilibrium pressure, and thus the more hydrogen is released. For U(45% w/o)ZrH_{1.6} the equilibrium pressure corresponding to the steady-state temperature limit of 750°C (Simnad, 1981) is about 0.3 atm, as shown in Figure II- 8. This figure also shows that Th-Zr-hydrides have a lower hydrogen equilibrium pressure than ZrH_{1.6}, which is consistent with the statement by Yamamoto et al. (1995): “*the ternary alloy can hold more hydrogen than U-Zr alloy at the same temperature. In other words, it can hold a certain amount of hydrogen at a higher temperature than the U-Zr alloy. This fact gives an attractive advantage if it is used as a nuclear fuel* “. From this observation it follows that the selection of thorium-containing fuels, i.e. UTh_tZr_zH_h, in place of binary hydrides, i.e. UZr_zH_h, which was mainly motivated by neutronic reasons (see Chapter IX), simultaneously allows for better hydrogen retention performance.

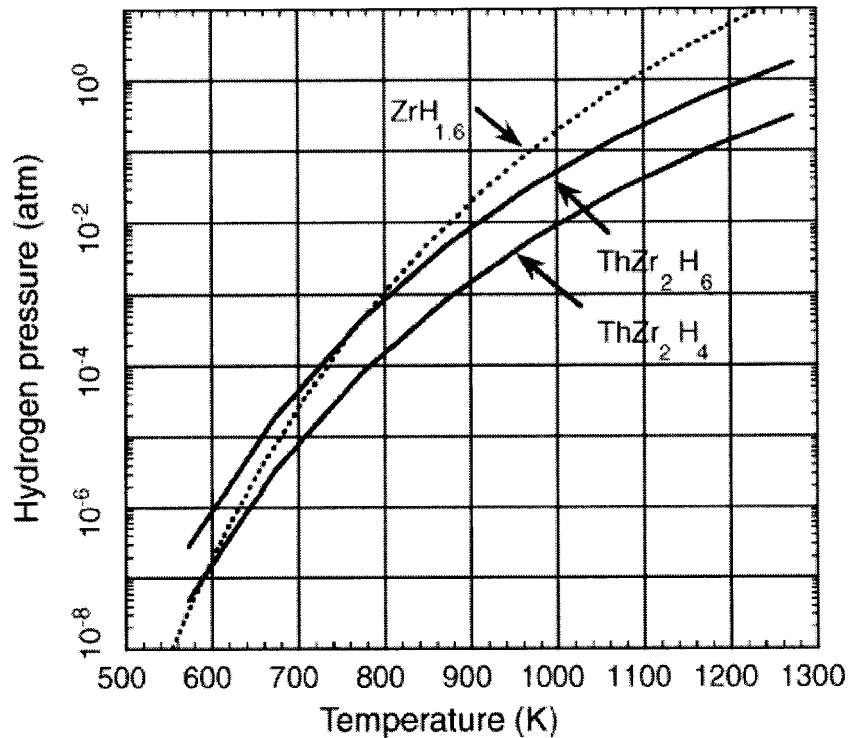


Figure II- 8: Hydrogen equilibrium pressure for Th-Zr-hydrides compared to ZrH_{1.6} (from Konashi et al., 2005)

II.1.6. 2 Limitation of consequences of hydrogen release

The main hazard resulting from hydrogen release, but also from the simple chemical interaction between the fuel and the clad/duct, is hydrogen-induced embrittlement of the latter. The replacement, in the fuel-clad and fuel-duct gaps, of helium with liquid metal, in which hydrogen is insoluble, hinders movement of hydrogen to the cladding, as long as the gap is open. When closure of the gap occurs, however, “*hard contact between the two solids may provide a mechanism to overcome the sluggishness of the solid-solid reaction*” (Olander et al., 2009). This implies that, if other preventive measures against hydrogen diffusion into the clad/duct are not taken, the gaps must be designed to be wide enough to avoid closure throughout the entire fuel life. However, since other preventive measures against hydrogen permeation into the clad/duct are documented in the literature, some of which are proposed for the IPWR, both non-closing and closing gap designs were examined for this reactor. In the past, the measures investigated were in the form of adding hydrogen permeation barriers to either the cladding inner surface or the fuel outer surface, such as:

- *Zirconium cladding oxidation*: this solution is based on the low solubility that hydrogen has in ZrO_2 , and it is applicable to Zr-based claddings which have therefore to be oxidized on the side facing the fuel.
- *Cladding coating with ceramic layer*: this coating, between 0.051 and 0.076 mm thick and made of a mixture of Si-, Ba-, Ti- and Al-oxide, was successfully applied to the inner surface of the Hastelloy cladding of SNAP reactors (Stadnik and Page, 1988). The liner was proven to be “*a remarkably tough and durable fuel element component*” since its effectiveness in preventing hydrogen diffusion into the cladding was found to not be susceptible to irradiation-induced damage and short-term loadings producing stresses in the cladding less than the yield stress (Lillie et al., 1973).
- *Fuel outer oxidation*: this method, demonstrated and patented by Eggers (1978) for U-Zr-hydride, consists of oxidizing the outer surface of the fuel, so that a ZrO_2 oxide layer forms. The hydrogen equilibrium pressure of the resulting oxidized U-

Zr-hydride was found to be 10 times lower than that of the original, non-oxidized, fuel, allowing operation without appreciable hydrogen release even above 800°C.

- *Cladding stainless steel liner*: this solution consists of adopting duplex cladding, consisting of a thin interior liner of stainless steel, and the rest made of Zr alloy. Hydrogen has a very low solubility in stainless steel, which causes hydrogen eventually released from the fuel to be “rejected” by the stainless steel liner. However, the addition of the SS liner creates extra stresses resulting from differential thermal expansion between the two layers, which may cause debonding of the two (Olander et al, 2009).
- *Cladding coating with silicon carbide*: this carbide, which is very resistant to hydrogen permeation, was successfully used in HTGR fuel as a tritium permeation barrier (Olander et al., 2009).

Of these measures, fuel superficial oxidation and either clad/duct oxidation or coating with ceramic liner are proposed for the IPWR.

II.1. 7 Thermal conductivity and specific heat

Thermal conductivity and specific heat of $UTh_{0.5}Zr_{2.25}H_{5.625}$ have never been measured. However, conductivities of other hydride fuels, of similar composition, have been measured and an estimate of that of the IPWR fuel can be obtained from them. Those conductivities have been collected by Terrani et al. (2009B), and plotted together as a function of temperature, as shown Figure II-9. For the IPWR design, it is assumed that $UTh_{0.5}Zr_{2.25}H_{5.625}$ thermal conductivity is the same as that of $U(45\% \text{ w/o})ZrH_{1.6}$ in the range 0-600°C and that, above 600°C, remains constant. This assumption is conservative since $UTh_{0.5}Zr_{2.25}H_{5.625}$ (1) has a higher metal density than $U(45\% \text{ w/o})ZrH_{1.6}$ (9007 kg/m³ vs 8117 kg/m³) and (2) contains Th, which has a thermal conductivity about twice that of U. The temperature dependence relation used for the IPWR analysis derives from Figure II-9 and can be expressed as:

if $T \leq 600$ °C

$$k_{fuel} = -1.5722 \times 10^{-10} T^4 + 2.4557 \times 10^{-7} T^3 - 1.3714 \times 10^{-4} T^2 + 3.8068 \times 10^{-2} T + 13.75$$

otherwise

$$k_{fuel} = 19.9 \text{ W/m K} \quad (\text{II.4})$$

where k_{fuel} is in W/m K and the temperature is expressed in °C.

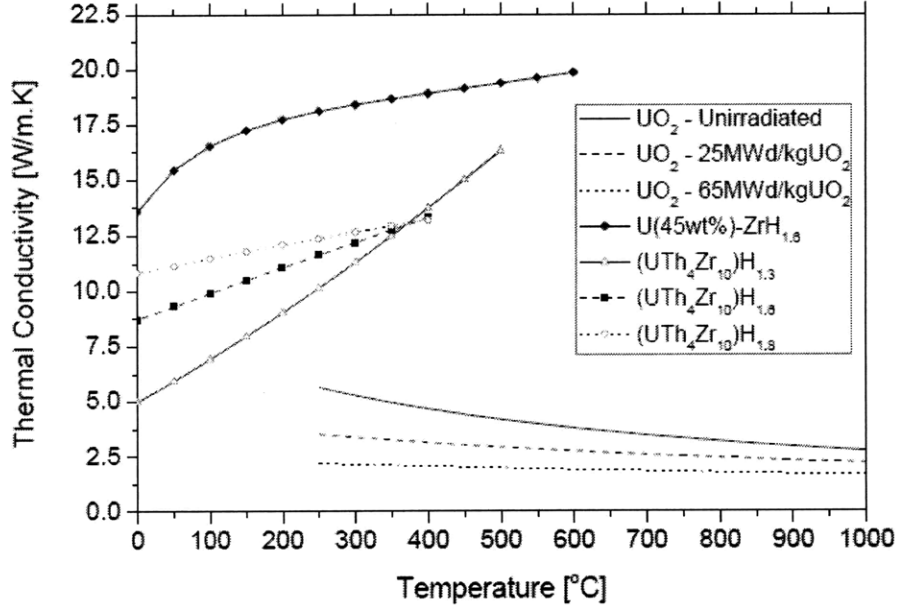


Figure II- 9: Thermal conductivity vs temperature for UO_2 and some hydride fuels (Terrani et al., 2009B)

Specific heat of $\text{UTh}_{0.5}\text{Zr}_{2.25}\text{H}_{5.625}$ is calculated as a weighted average of the specific heat values of the single components, i.e. U, $\text{ZrH}_{1.6+x}$ and $\text{ThZr}_2\text{H}_{7-x}$:

$$C_{p,fuel} = W_U C_{p,U} + W_{ZrH} C_{p,ZrH} + W_{ThZrH} C_{p,ThZrH} \quad (\text{II.5})$$

where W_U (=0.42), W_{ZrH} (=0.20) and W_{ThZrH} (=0.38) are the weight fractions of U, $\text{ZrH}_{1.6+x}$ and $\text{ThZr}_2\text{H}_{7-x}$ respectively. The specific heat of these components is expressed by means of the following relations (C_p in J/kg K, T in Kelvin):

For uranium (NUREG/CR-6150, 1993):

$$C_{p,U} = \begin{cases} 104.82 + 5.3686 \times 10^{-3} T + 10.1823 \times 10^{-5} T^2 & \text{if } T < 938 \text{ K} \\ 176.41 & \text{if } 938 \leq T < 1049 \text{ K} \\ 156.81 & \text{if } T \geq 1049 \text{ K} \end{cases} \quad (\text{II.6})$$

For $ZrH_{1.6+x}$ the expression for $ZrH_{1.6}$ is used (IAEA-TECDOC-643, 1992):

$$C_{p,ZrH} = \frac{69.76(T - 273) + 33706}{92.83} \quad (II.7)$$

For $ThZr_2H_{7-x}$ the method proposed by Tsuchiya et al. (2000) is used:

$$C_{p,ThZrH} = W'_{ThH_2} C_{p,ThH_2} + W'_{ZrH} C_{p,ZrH} \quad (II.8)$$

where W'_{ThH_2} (=0.55) W' and W'_{ZrH} (=0.45) are the weight fractions of ThH_2 and $ZrH_{1.6-x}$ in $ThZr_2H_{7-x}$. The specific heat of $ZrH_{1.6-x}$ is from Eq. II.7 while that for ThH_2 is (Rand et al., 2008):

$$C_{p,ThH_2} = 35.44 + 0.5366T + 2.159 \times 10^{-4} T^2 - \frac{4.0410 \times 10^5}{0.2341 \times T^2} \quad (II.9)$$

II.1. 8 Summary of thermophysical properties

Table II- 2 lists the properties of the IPWR fuel. As mentioned at the beginning of Section II.1, whenever the value of a property is not available in the literature, data referred to similar hydrides, mainly U(45% w/o)ZrH_{1.6} are used.

Table II- 2– Properties adopted for $UTh_{0.5}Zr_{2.25}H_{5.625}$				
Property	Units	Value	Notes	Reference
Stoichiometric formula	-	$UTh_{0.5}Zr_{2.25}H_{5.625}$		Terrani et al. (2009A)
Fuel density	kg/m ³	9096		
U density in the fuel	kg/m ³	3829	Calculated from stoichiometry	
Th density in the fuel	kg/m ³	1870		
Zr density in the fuel	kg/m ³	3308		
H density in the fuel	kg/m ³	89		
Thermal conductivity	W/m K	Eq. II.4	Assumed same as that of U(45%)ZrH _{1.6}	
Specific heat	J/kg K	Eq. II-5		See Section II.1.7
Elastic modulus	GPa	172		Terrani et al. (2009A)
Irradiation-induced volume swelling	%	Eq. II-1	Assumed same as that of U-ZrH _{1.6}	Lillie et al. (1973)
Fission gas release fraction	-	Eq. II.3	Assumed same as that of U-ZrH _{1.6}	Langer and Baldwin (1971)
Volume expansion upon hydriding	%	17.7		Terrani et al. (2009A)

II. 2 Cladding and duct material

The material chosen for the cladding and for the hexagonal duct is Zr-2.5Nb. This material, originally studied by the Soviets in the late '50s, has been successfully used for the pressure tubes in CANDU reactors for many decades. These pressure tubes, which have an inside diameter of 104 mm and wall thickness of 4.3 mm, are subjected to a differential pressure, compressive, of about 10 MPa (Kim et al., 2003). The key characteristic that makes Zr-2.5Nb more suited than Zircaloy to be the structural material for the IPWR is the resistance to hydrogen pickup, as shown in Figure II- 10. In fact, quoting AECL (1997): *“the choice”* of using Zr-2.5Nb for CANDU pressure tubes, rather than Zircaloy, *“was based on superior tensile strength and creep resistance. Twenty five years later we still feel that the choice was correct, even if made for the wrong reasons. We know now that the difference in in-reactor creep between cold-worked Zircaloy-2 and cold-worked Zr-2.5Nb is quite small, whereas the great advantage of Zr-2.5Nb is now recognized to be its very low deuterium pickup”*.

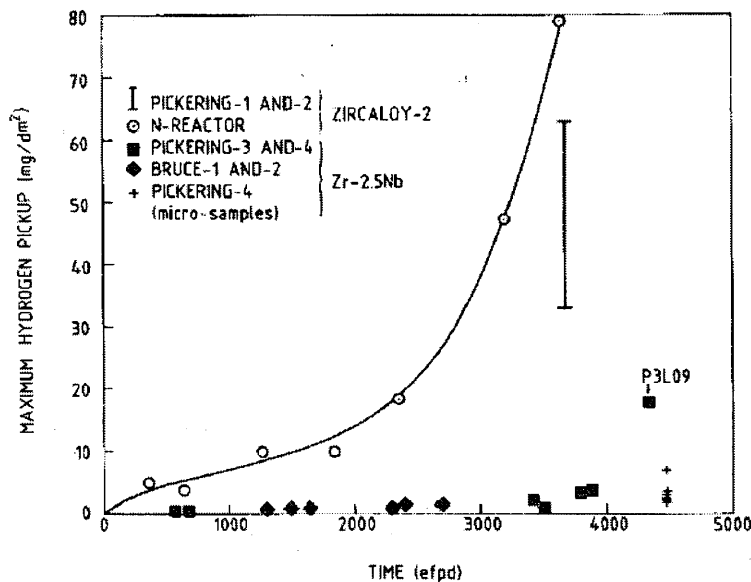


Figure II- 10: Hydrogen pickup of cold-worked Zr-2.5Nb and Zircaloy-2 pressure tubes (Urbanic et al., 1989)

Having a low-hydrogen pickup material is particularly important for the IPWR since not only the coolant but also the fuel contains hydrogen. This choice, coupled to the

constraint on maximum fuel temperature to limit hydrogen release and the oxidation of the fuel outer surface as well as the oxidation, or coating, of the cladding/duct inner surfaces, renders the cladding and ducts of the IPWR well protected against hydrogen-induced embrittlement.

Thermophysical properties of Zr-2.5Nb are summarized in Table II- 3. It has to be stressed that mechanical properties such as yield strength, ultimate strength and fracture strength are strongly dependent upon fabrication procedures, composition and extent of irradiation and hydriding. Because of these sources of variability, inconsistent data have been found in the literature, and those reported in Table II- 3 are representative of most of the consulted literature sources. For temperature-dependent properties of which such dependence was found in the literature, the table refers to equations that are presented next.

Table II- 3– Properties of Zr-2.5Nb				
Property	Units	Value	Notes	Reference
Density	kg/m ³	6550	Assumed same as Zircaloy	NUREG/CR-6150, 1993
Melting point	°C	1850		ATI Wah Chang, 2003
Specific heat	J/kg K	Eq. II-10	Unirradiated and unhydrided	INSC, 1998
Thermal conductivity	W/m K	Eq. II-11		
Yield strength	MPa	Eq. II-12 through Eq. II-15		Shi and Puls (1994 and 1999) and Hunt and Foote (1977)
Ultimate tensile strength	MPa	500	Unirradiated and unhydrided, at 350°C	IAEA-TECDOC-1410, 2004
Fracture strength	MPa	Eq. II-16	Hydrided and unirradiated	Shi and Puls, 1999
Elastic modulus	MPa	Eq. II-17	Unhydrided and unirradiated	Shi and Puls, 1994
Shear modulus	MPa	33800	Unirradiated at 25°C	Cheong et al., 2000
Poisson ratio	-	Eq. II-18	Unirradiated but hydrided	Shi and Puls, 1994
Coefficient of thermal expansion	K ⁻¹	4.44×10^{-6}	For $T \leq 1050$ K	NUREG/CR-6150, 1993
		9.7×10^{-6}	For $T \geq 1200$ K	
		Interpolation	For $1050 < T < 1200$ K	

The following equations express the temperature dependence of some of the thermophysical properties listed in Table II- 3. In all the expressions, temperature is in Kelvin.

Zr-2.5Nb specific heat (J/kg K) (from INSC, 1998)

$$C_p = \begin{cases} 252.5 + 9.486 \times 10^{-2} T & \text{for } 298 \leq T \leq 1100 \text{ K} \\ 281.3 + 6.625 \times 10^{-2} T & \text{for } 1250 \leq T \leq 2000 \text{ K} \end{cases} \quad (\text{II-10})$$

For $1100 < T < 1250 \text{ K}$, C_p can be obtained from interpolation between the value at 1100 K and that at 1250 K.

Zr-2.5Nb thermal conductivity (W/m K) (from INSC, 1998)

$$k = \begin{cases} 16.85 - 2.186 \times 10^{-3} T + 8.899 \times 10^{-6} T^2 & \text{for } 298 \leq T \leq 1100 \text{ K} \\ 5 + 0.02T & \text{for } 1130 \leq T \leq 1600 \text{ K} \end{cases} \quad (\text{II-11})$$

For $1100 < T < 1130 \text{ K}$, k can be obtained from interpolation between the value at 1100 K and that at 1130 K.

Zr-2.5Nb yield strength, at 0.2% offset (MPa)

For $T < 623 \text{ K}$:

$$\sigma_y = 1088 - 1.02T \quad (\text{unhydrided and unirradiated, Shi and Puls, 1994}) \quad (\text{II-12})$$

$$= 1388 - 1.02T \quad (\text{unhydrided and irradiated, Shi and Puls, 1994}) \quad (\text{II-13})$$

$$= 782.69 - 1.0254(T - 273.1) \quad (\text{hydr. and unirradiated, Shi and Puls, 1999}) \quad (\text{II-14})$$

For $623 \leq T \leq 900 \text{ K}$:

$$\sigma_y = 1106 - 1.17T \quad (\text{unhydrided and unirradiated, Hunt and Foote, 1977}) \quad (\text{II-15})$$

Zr-2.5Nb fracture strength (hydrided and unirradiated) (MPa) (Shi and Puls, 1999)

$$\sigma_f = 650.84 - 0.09096(T - 273.1) \quad \text{for } 293 \leq T \leq 573 \text{ K} \quad (\text{II-16})$$

Zr-2.5Nb Young modulus (unhydrided and unirradiated) (MPa) (Shi and Puls, 1994)

$$E = 95900 - 57.4(T - 273) \quad (\text{II-17})$$

Zr-2.5Nb Poisson ratio (from Shi and Puls, 1994)

$$\nu = 0.436 - 4.8 \times 10^{-4}(T - 300) \quad (\text{II-18})$$

II. 3 Liquid metal bond

In the inverted assembly design adopting non-collapsible duct, a low-melting liquid metal (LM) composed of Sn, Pb and Bi, each 33.3% w/o, fills the gaps between the cladding and the fuel block, and the gap between the hexagonal duct and the fuel block. The choice of LM bonded rods in place of He-bonded rods has been a common practice in the design of pin-geometry hydride-fueled reactors recently carried out at University of California at Berkeley and MIT (Greenspan et al., 2009), and it is adopted for the non collapsible duct IPWR design as well. There are three main reasons for this choice:

- to more easily meet the fuel temperature limit: the peak temperature limit adopted for the IPWR fuel, i.e. 650°C, is much lower than the temperature limits typically adopted for UO₂-fueled LWRs, which are 1400°C for the average temperature, to limit fission gas release below 5% (Todreas and Kazimi, 1993), and 2800°C for the peak temperature, to avoid fuel melting. LM has a thermal conductivity about 100 times larger than He (Olander et al., 2009), allowing for a smaller temperature drop across the gap separating the cladding from the fuel. This is evident from Table II- 4, which shows the reduction in fuel peak temperature and temperature drop across the gap resulting from the replacement of He with LM, for a typical PWR rod geometry.
- to have wide enough gaps so that, in the so-called non-collapsible duct design (see Chapter IV), gap closure can be prevented: even though hydrogen diffusion (towards the cladding and duct) and permeation (through the cladding and duct) barriers are implemented in the IPWR design (see Section II.1.6), contact between the fuel and the structural materials has to be minimized, to reduce hydrogen pickup and therefore hydrogen-induced embrittlement. If He was used in place of LM, a too wide gap would result in a large temperature drop across the gap, thus penalizing the fuel temperature.
- to limit hydrogen diffusion from the fuel towards the cladding and the duct: as discussed in Section II.1.6, LM creates a barrier against hydrogen diffusion since

hydrogen is insoluble in it. The barrier role is also against those fission products, i.e. iodine and cadmium, which assist inside diameter crack propagation in the event of contact between fuel and cladding (Wongsawaeng and Olander, 2007).

A secondary advantage of using LM in place of He is the high accuracy with which thermal calculations across fuel, gap and claddings can be performed. As stated by Wongsawaeng and Olander (2007): “*whereas estimation of the gap conductance for*” He-bonded rods “*has been a persistent source of uncertainty in fuel performance calculations, thermal analysis of an LM-bonded gap is assured of greater accuracy because the gap resistance is several orders of magnitude smaller than the thermal resistance of the fuel (i.e. $\Delta T_{fuel} \gg \Delta T_{gap}$)*”.

As for material compatibility, the proposed LM lacks chemical reactivity with water (Wongsawaeng and Olander, 2003) and was demonstrated to react with Zircaloy-4 cladding forming a thin $ZrSn_2$ that passivates the cladding from further attack (Wright et al., 1996).

Table II- 4– Operating temperatures of PWR fuel rods with hydride or oxide fuel and He or LM bonds (from Olander et al., 2009)

Temperature, °C	$U_{0.31}ZrH_{1.6}$ (He)	$U_{0.31}ZrH_{1.6}$ (LM)	UO_2 (He)
Fuel centerline	680	555	1450 ^a
ΔT_{fuel}	170	170	665
ΔT_{gap}	125 ^b	1 ⁺	125 ^b
ΔT_{clad}	46	46	46
T_{fluid}	39	39	39

^a UO_2 thermal conductivity = $(22.7 + 7 \times 10^{-3}T(K))^{-1}$.

^b For a gap thickness of 35 μm .

However, using LM in place of He has also disadvantages, mainly related to assembly fabrication, clad failure scenarios and technology inexperience. These aspects are discussed as follows:

- assembly fabrication: fabricating an He-bonded assembly is much simpler than a LM-bonded one, both because of the ease with which He can be handled, and because of the uniformity with which He tends to fill the gaps. As discussed in Chapter X, for the manufacture of an IPWR assembly, solid Sn-Pb-Bi powder

has to be poured inside the duct, under vacuum conditions¹⁰ and before fuel insertion, so that a successive heating above about 120°C causes it to melt. The sliding of the fuel hexagonal slices inside the duct, using the tubes as guides, would then allow the LM to fill the gaps.

- clad failure scenarios: in the event of clad/duct failure, LM would tend to leak from the assembly into the primary coolant, causing its contamination. Because of its liquid state, its removal would be much more difficult than for helium which, being a gas can be easily vented.
- technology inexperience: little experience exists in the fabrication of LM-bonded rods, while no experience exists in the fabrication of LM-bonded inverted assemblies. Wongsawaeng and Olander (2007) successfully developed a methodology to fabricate UO₂-fueled, LM-bonded rods, saying that: *“Replacement of helium in the fuel-cladding gap with a low-melting Pb-Sn-Bi alloy has been as thoroughly investigated on a laboratory scale as possible. A fabrication technique that should fit well with existing manufacturing lines was developed and shown to work on a full-size fuel element. All in all, the improvements in performance over helium-bonded fuel elements appear to outweigh any disadvantages and the (probably) higher fabrication cost.”*

Key properties of the proposed LM are summarized in Table II- 5.

Table II- 5– Properties of Sn-Pb-Bi liquid metal				
Property	Units	Value	Notes	Reference
Composition	wt %	Sn (33.3), Pb (33.3), Bi (33.3)	-	Wright et al., 1996
Density	kg/m ³	9049	At 25°C	Garkisch and Petrovic, 2003
Specific heat	J/kg K	173.4		
Thermal conductivity	W/m K	35		
Melting point	°C	~120	-	Wongsawaeng and Olander, 2007

¹⁰ Vacuum conditions are needed to prevent gases to remain trapped in the fuel-clad gaps. This would in fact result in a non-uniform distribution of the LM and therefore in the formation of local hot spots due to the lower thermal conductivity of gases with respect to the LM (Wongsawaeng and Olander, 2007).

Appendix II.A: Relation between FIMA% and MWD/kg_{HM}

This Appendix explains how to convert an irradiation level expressed as Fraction of Initial Metal Atom percentage (FIMA%) into MWD/kg_{HM}. The discussion considers a generic fuel having stoichiometry U_uTh_tZr_zH_h and density ρ (kg/m³).

From the definition of FIMA%:

$$FIMA\% = 100 \left(\frac{U^{235} \text{ atoms consumed}}{\text{metal atoms initially present}} \right)_{\text{per } m^3}$$

the number of fissions per unit volume can be calculated as:

$$\begin{aligned} N_{f,m^3} &= (U^{235} \text{ atoms consumed})_{\text{per } m^3} = \frac{FIMA\%}{100} (\text{metal atoms initially present})_{\text{per } m^3} = \\ &= \frac{FIMA\%}{100} \left[\frac{\rho}{uM_U + tM_{Th} + zM_{Zr} + hM_H} N_{AV} (u + t + z) \right] \end{aligned}$$

where M_x is the atomic weight of element x , expressed in kg/mol, while N_{AV} is the Avogadro's number ($6.022 \times 10^{23} \text{ mol}^{-1}$). The number of fissions per unit of mass of heavy metal (U+Th) is therefore equal to:

$$N_{f,HM} = \frac{N_{f,m^3}}{\rho \frac{uM_U + tM_{Th}}{uM_U + tM_{Th} + zM_{Zr} + hM_H}} = \frac{N_{AV} (u + t + z) FIMA\%}{(uM_U + tM_{Th}) 100}$$

Since a fission generates about 200 MeV ($=3.204 \times 10^{-11} \text{ J} = 3.7083 \times 10^{-22} \text{ MWD}$), the energy generated, in MWD per unit of mass of heavy metal is:

$$\begin{aligned} BU(MWD/kg_{HM}) &= N_{f,HM} \times 3.7083 \times 10^{-22} = \frac{3.7083 \times 10^{-22} N_{AV} (u + t + z) FIMA\%}{(uM_U + tM_{Th}) 100} = \\ &= \frac{2.23316 \left(1 + \frac{t}{u} + \frac{z}{u} \right)}{\left(M_U + \frac{t}{u} M_{Th} \right)} FIMA\% \end{aligned}$$

Chapter III

Analysis methodology and design constraints

This chapter presents design methodology and design constraints. In particular, Section III.1 describes the methodology used to analyze the IPWR power performance, while Section III.2 describes the design constraints which play a key role in the identification of the optimum IPWR design. For some constraints the study performed went beyond the sole scope of assigning them a limit value, and included thorough investigations on how they need to be calculated in the design of the IPWR. Other chapters are aimed at presenting these calculation methods and more general discussion of specific constraints. References to these chapters are given in Section III.2.

III. 1 Analysis methodology and codes used

III.1.1 Analysis methodology

The search for the optimum IPWR design is performed by setting design constraints and by searching, among the IPWR geometries that meet these constraints, that attaining the maximum thermal power. This procedure is performed in four phases, each characterized by the application of certain constraints:

- Phase 1: application of structural constraints;
- Phase 2: application of steady-state thermal hydraulic constraints;
- Phase 3: LBLOCA analysis of a promising design/geometry meeting the constraints examined in Phases 1 and 2, and determination of the maximum power satisfying LBLOCA constraints;

- Phase 4: application of neutronic constraints to the selected IPWR design/geometry, using the power level determined in Phase 3.

The analyses in Phase 1 and 2 were performed on a spectrum of core geometries, defined as (D_{ci} is the cooling channel inner diameter, t_{web} is the fuel web thickness):

$$7 \leq D_{ci} \leq 15 \text{ mm} \quad \text{and} \quad 2 \leq t_{web} \leq 6 \text{ mm} \quad (\text{III-1})$$

while Phases 3 and 4 were focused on one geometry only. Figure III- 1 shows the flowchart of the methodology, which is also described next.

The first phase of the analysis allows defining the core geometry. In particular, for each D_{ci} - t_{web} combination, the fuel-clad gap width, clad thickness, number of fuel cells per assembly, fuel-duct gap width, duct wall thickness, duct size and number of assemblies in the core are computed. In the second phase, for each geometry the core thermal power is increased starting from a low value. For each power level, a steady-state thermal-hydraulic analysis of the hot channel is performed, and its results are compared to the steady-state thermal hydraulic constraints. If they are not exceeded, the power is further increased until one of them reaches a value between 99.9% and 100.0% of the corresponding limit value (between 100.0% and 100.1% for the MCHFR). The core power which leads to this situation is recorded as the maximum steady-state power that could be attained if LOCA and neutronic constraints did not apply. The whole procedure is repeated for all the core geometries within the analysis range defined in Eq. III-1, resulting in the construction of geometry vs power maps. Multiple maps will be generated since different pressure drop limits, as well as different cooling channel designs, will be analyzed. In Phase 3, a promising geometry selected by screening the power maps is subjected to a LBLOCA analysis, and its performance is compared against the design constraints associated with this accident scenario. The corresponding power is reduced as necessary until the LBLOCA constraints are met. In Phase 4 the selected IPWR geometry is subjected to enrichment and burnable poison characterization. As for the latter, the analysis examines Integral Fuel Burnable Absorber (IFBA) and Er_2O_3 , and searches for the minimum loading needed to control reactivity and to guarantee a negative void reactivity coefficient. Cycle length calculation and considerations on shutdown margin conclude Phase 4.

III.1.2 Codes used

Different analyses throughout the project required different codes to be used:

- a MATLAB program was developed to perform core construction and core steady-state thermal hydraulic analysis (i.e. Phases 1 and 2 described in Section III.1.1);
- RELAP 3D[®] (RELAP, 2003) was used for the LBLOCA analysis (i.e. Phase 3 of the analysis);
- MCNP4C (LANL, 2000) and CASMO-4 (Edenius et al., 1995) were used for the neutronic analyses performed in Phase 4. Specifically, MCNP was used for void reactivity coefficient calculations, while CASMO for cycle length calculations.

Three other codes were used, even though less extensively than those mentioned above: COSMOSWorks (SolidWorks, 2007), VIPRE (Cuta et al., 1985) and MCODE (Xu and Hejzlar, 2008). COSMOSWorks is a design analysis software, embedded in the well known 3D design software SolidWorks, that allows testing of the thermal and mechanical stress performance of components. It was used for stress/deformation analyses of the hexagonal duct, and provided the thickness of the duct to be entered in the MATLAB program. The thermal hydraulic code VIPRE was used to benchmark the MATLAB program and to determine the MCHFR constraint. MCODE (Xu and Hejzlar, 2008), a linkage program developed at MIT that couples MCNP4C and ORIGEN22, was used to demonstrate that CASMO, after appropriate modifications of the input file, can be used to study the depletion of an inverted fuel configuration by modeling a neutronicly equivalent pin configuration.

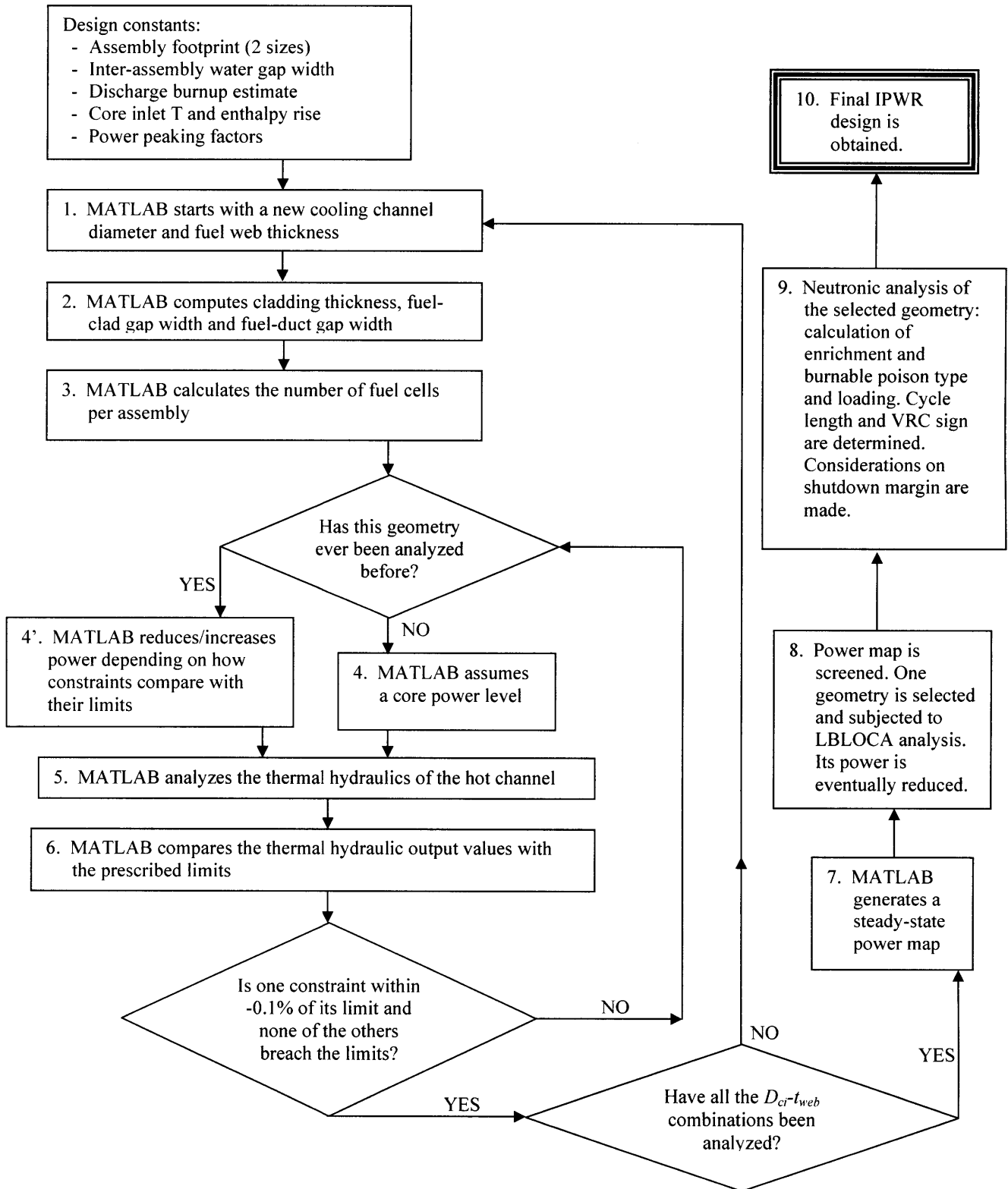


Figure III- 1: Flowchart of the methodology used to determine the final IPWR design

III. 2 Design constraints

The constraints used for the design of the IPWR are summarized in Table III- 1, and briefly described thereafter. Two types of design constraints are considered: quantitative and qualitative. A quantitative constraint is a parameter, or it is related to a parameter that, if exceeded, may either induce a failure mechanism or negatively impact the economics of the electricity generation: two situations that must obviously be avoided. Examples of quantitative constraints are the maximum fuel temperature or the core pressure drop. A qualitative constraint is instead a required but qualitative measure not directly associated with a limit value. The need to choose a particular material for the structural components, in order to protect them from hydrogen-induced embrittlement, is an example of qualitative constraint. No distinction between quantitative and qualitative constraints is made in Table III- 1, but rather a distinction in structural/material, thermal hydraulic, neutronic/economic and manufacturing constraints is made.

The purposes of this Section are to describe the constraints used, giving emphasis to the way they affect the IPWR design and discussing the limit values eventually selected. Constraint calculation methods that required thorough literature reviews and benchmarks are presented in constraint-specific chapters, which are referenced in Table III- 1.

Table III- 1: Constraints used for the design of the IPWR			
Constraint	Motivation for the constraint	Limit value (if applicable)	Section (and chapter number if elaborated further)
Structural/material constraints			
Clad thickness	To guarantee clad strength and avoid its contact with the fuel	Geometry-dependent	III.2.1.1
Fuel-clad gap width	To avoid fuel-clad contact (for non-collapsible duct only)		
Fuel-duct gap width	To avoid fuel-duct contact (for non-collapsible duct only)		
Maximum stress intensity on the duct ¹	To prevent mechanical failure of the duct during normal operation	< 167 MPa (primary stresses) < 501 MPa (primary+sec. str.)	III.2.1.3 (and Chapter IV)
	To prevent mechanical failure of the duct during LBLOCA	< 84 MPa (primary stresses)	
Maximum duct lateral deformation	To prevent fuel-duct contact and duct-control blade interference during normal operating conditions and LBLOCA	Inward: < fuel-duct gap thickness ² . Outward: < 1.4 mm	
Fission gas release	To prevent excessive duct internal pressurization	Limit is on fuel temperature	
Cladding and duct material selection and implementation of H ₂ protection techniques	To protect structural material from hydrogen pickup	-	III.2.1.5
Fuel-clad and fuel-duct gap filling material	To guarantee high gap conductance in spite of its large width (non-collapsible duct only)	-	III.2.1.6
Inter-assembly water gap width	To allow for control blade insertion	= 12.24 mm	III.2.1.7
Core shroud diameter	To allow IPWR core to be loaded into a vessel of the same size of that of the reference plant	=3.66 m	-
Thermohydraulic constraints			
Core pressure drop	To comply with performance of existing reactor coolant pumps (lower limit) and with performance achievable in the near future (higher limits)	150, 225 and 300 kPa	III.2.2.1 (and Chapter V)
Steady-state MCHFR	To avoid reaching critical heat transfer conditions	≥ 1.79	III.2.2.2 (and Chapter VI)
Steady-state peak fuel temperature	To limit irradiation-induced fuel swelling, hydrogen release and fission gas release ³	< 650°C	III.2.2.3
Steady-state peak inside cladding temperature	To limit cladding oxidation so that a sufficient margin is maintained, from the 17% limit, in case of LOCA	< 370°C	III.2.2.4
Core inlet temperature and coolant enthalpy rise	To avoid exceeding the reference core outlet temperature, which would cause unacceptable corrosion rate in the steam generator tubes	= 296.3°C and = 195.2 kJ/kg	III.2.2.5
Peak cladding temperature during LBLOCA	To guarantee cladding ductility during LOCA scenarios	< 1204°C	III.2.2.6 (and Chapter VIII)
Oxide thickness as % of original clad thickness during LBLOCA		< 17%	

¹ The numerical values indicated for the stresses, both for normal operation and LBLOCA, are material-specific, and refer to Zr-2.5Nb alloy.

² The limit on inward deformation is only applied to the non-collapsible duct design.

³ Of these three phenomena, irradiation-induced fuel swelling is that limiting fuel temperature. A temperature limit of about 750°C would in fact limit hydrogen and fission gas release to acceptable values (see Chapter II).

Table III-1 (cont'd): Constraints used for the design of the IPWR			
Constraint	Motivation for the constraint	Limit value (if applicable)	Section (and chapter number if elaborated further)
Neutronic/economic constraints			
Void reactivity coefficient	To avoid power increase upon coolant voiding	<0	III.2.3.1 (and Chapter IX)
Fuel temperature reactivity coefficient	To avoid power increase upon fuel temperature increase	<0	III.2.3.2
Soluble boron concentration	To avoid challenging the Chemical Volume Cooling System capabilities and to limit B-induced corrosion	<2000 ppm B	III.2.3.3 and Chapter IX
	To avoid positive void reactivity coefficient	Geometry-dependent	
Burnable poison selection and loading	For IFBA: loading constrained to limit duct pressurization due to He-production (via n- α reaction from ^{10}B)	Geometry-dependent	III.2.3.3 and IV.1.2.2.4
	For IFBA: loading constrained to avoid IFBA layer detachment in case of excessively thick layer	^{10}B loading ⁴ < $0.168 \times D_f$ mg/cm	III.2.3.3
Enrichment	To comply with the Low Enriched Uranium requirement	< 20%	III.2.3.4 (and Chapter IX)
Cycle length	To limit reactor downtime	About 18 months	
Number of assemblies in the core	To limit refueling time	<1132	III.2.3.5
Hot Full Power to Cold Zero Power reactivity insertion	To guarantee sufficient shutdown margin	~ same as reference PWR	III.2.3.6 (and Chapter IX)
Manufacturing constraints			
Assembly manufacturability	To assess the manufacturability of an hydride-fueled inverted assembly	-	III.2.4 (and Chapter X)

Maximum fuel temperature during LBLOCA was not used as constraint, due to the lack of data on hydrogen release for the fuel under examination. Discussion on the expected limiting effect exerted by this parameter, as well as limit values applied to fuels of similar composition, are discussed in Section III.2.2.6.

⁴ In this formula, D_f is the fuel hole diameter expressed in mm.

III.2. 1 Structural/material constraints

Structural constraints are imposed to guarantee that the structural components, i.e. cooling channel cladding and hexagonal ducts:

- are protected against hydrogen pickup, which would result in hydrogen-induced embrittlement;
- can withstand mechanical stresses that originate during normal operation and accident scenarios.

Also, the constraint on core shroud diameter allows the IPWR core to be designed so that it can fit into vessels of the same size of the reference PWR vessel (Seabrook USAR, 2002).

III.2.1. 1 Clad thickness and fuel-clad gap width

Clad thickness and fuel-clad gap width are sized using correlations developed by Westinghouse for U(45% w/o)ZrH_{1,6}-fueled, liquid-metal bonded PWR rods (Garkisch and Petrovic, 2003), adapted to the inverted geometry⁵. The purpose of Garkisch and Petrovic work was to develop correlations for clad thickness and fuel-clad gap width that would allow the clad to withstand the differential pressure-induced mechanical stresses and to prevent pellet-clad interaction to avoid clad hydriding. After adaptation to the inverted configuration, the correlations for clad thickness and fuel-clad gap width have the following form (geometric parameters expressed in mm):

$$t_{clad} = \begin{cases} 0.508 & \text{if } D_{ci} < 6.731 \\ 0.24532 + 0.039025 D_{ci} & \text{otherwise} \end{cases} \quad (\text{III-2})$$

$$t_{gap} = \frac{11.548 \times 10^{-3} (FIMA\%) D_{ci}}{2 + 0.023096 (FIMA\%)} \quad (\text{III-3})$$

⁵ The nine times higher heavy metal atom density of the fuel used for the IPWR, i.e. UTh_{0.5}Zr_{2.25}H_{5.625}, relative to that used for the correlation development, i.e. U(45% w/o)ZrH_{1,6}, may cause the correlations to underpredict the gap width needed to accommodate fuel swelling. As known, fission products, which are responsible for swelling, accumulate as interstitials in the fuel matrix, and the space available for such accumulation to occur without resulting in an excessive volume growth decreases as the heavy metal atom density increase. This issue should be addressed in future work.

where FIMA% is the discharge burnup expressed in Fissile Initial Metal Atom percentage. Appendix II-A in Chapter II discusses the meaning of this unit and explains how MWD/kg_{HM} can be converted into FIMA%.

III.2.1. 2 Fuel-duct gap width

The width of the gap separating the fuel prism from the duct, $t_{gap,out}$, is fixed to 2 mm for all the IPWR geometries adopting a non-collapsible duct design. A much narrower gap, about 0.2 mm wide, characterizes instead the IPWR geometries adopting a collapsible duct design. A quantitative gap sizing was only performed for the non-collapsible duct designs, since for them it is required that no fuel-duct contact occurs during the life of the assembly. The 2 mm value was chosen to accommodate fuel swelling and duct creepdown. Fuel swelling is primarily caused by irradiation, while thermal expansion, in comparison, is negligible. The extent of swelling is estimated using the correlation developed by Atomics International (Lillie et al., 1973) discussed in Section II.1.4:

$$\left(\frac{\Delta V}{V}\right)\% = 5.5e^A + 3 \times FIMA\% \quad (II-1)$$

$$A = - \left[2.3 \times \dot{F} \times e^{10.75 \left(\frac{1033.3}{T} - 1 \right)} + 21.5 \left(\frac{1033.3}{T} - 1 \right) \right] \quad (II-2)$$

where FIMA% is the discharge burnup expressed in Fissile Initial Metal Atom percentage (see Appendix II-A in Chapter II for the conversion FIMA% - MWD/kg_{HM}), \dot{F} is the burnup rate expressed as FIMA% per 10000 hours of operation, T is the fuel temperature expressed in K. For the sizing of the fuel-duct gap, a discharge burnup of 5.3% FIMA% (which corresponds to 125 MWD/kg_{HM} for U₄Th₂Zr₉H_{22.5}) and a temperature of 873 K (600°C) were assumed. Concerning the burnup rate, a value for \dot{F} equal to 0.4 is assumed⁶. Using Eq. II-1, the fuel volume swelling percentage derived from these

⁶ Eq. II-1 expresses the swelling percentage as sum of two terms: an early-life, rapid, offset growth ($5.5e^A$), occurring during the first 0.1 FIMA% burnup period and due to vacancy condensation, and a linear growth ($3 \times FIMA\%$) due to fission product accumulation. While the second term shows the typical trend of increasing swelling as burnup increases, in the first term the higher is the burnup rate, which is dimensionally equivalent to a power per unit mass of heavy metal, the lower is the volume swelling percentage. The reason for this counterintuitive behavior lays in the swelling mechanism characterizing the early phase of fuel burnup: vacancy condensation. According to Lillie et al. (1973), the higher is the neutron flux the more significant is the recombination between vacancies and interstitials, with consequent

choices is about 16%. If the swelling is assumed to be isotropic, i.e. if the relative variation of the fuel prism side-to-side distance P_{prism} , of the diameter of the holes in the fuel prism D_f and of the prism height H_{prism} are assumed to be equal:

$$\frac{(P_{prism})_f - (P_{prism})_i}{(P_{prism})_i} = -\frac{(D_f)_f - (D_f)_i}{(D_f)_i} = \frac{(H_{prism})_f - (H_{prism})_i}{(H_{prism})_i} = K \quad (\text{III-4})$$

it can be easily demonstrated that (see Appendix III-C):

$$\left(\frac{\Delta V}{V}\right)\% = 100 \left\{ \frac{\left[\frac{\sqrt{3}}{2} (P_{prism})_i^2 (1+K)^2 - N_{cells/A} \frac{\pi}{4} (D_f)_i^2 (1-K)^2 \right] (1+K)}{\frac{\sqrt{3}}{2} (P_{prism})_i^2 - N_{cells/A} \frac{\pi}{4} (D_f)_i^2} - 1 \right\} \quad (\text{III-5})$$

where $N_{cells/A}$ is the number of fuel cells per assembly, while the subscripts i and f were used to denote the initial and the post-swelling values respectively. In principle, Eq. III-5 could be used to calculate the coefficient K for any fuel prism geometry, if the volume swelling percentage is input. However, this calculation is complicated by the fact that $N_{cells/A}$ is a function⁷ of K , and by the fact that the width of the fuel-duct gap, and therefore $N_{cells/A}$, depends also on the duct creepdown, which cannot be simultaneously accounted for in this calculation and is estimated separately (see Section III.2.1.3). Therefore, a simplified approach was adopted: a single geometry ($P_{prism}=92$ mm, $D_f=8.44$ mm, $t_{web}=3$ mm and $N_{cells/A}=61$) was initially used to estimate K , and considerations on how the choice of a different geometry would have affected K were successively made. It can be easily verified that, with this geometry and the volume swelling of 16%

reduction in swelling. The experimental data that led to the development of Eq. II-1 covered a burnup rate ranging from 0.1 to 0.4 FIMA% per 10000 hours of operation. As shown in Section II.1.4 of Chapter II, this range corresponded to a linear power between 4.6 and 18.5 kW/m (for the fuel type investigated). For a typical inverted geometry having $P=14.6$ mm and $D_f=11.848$ mm, and an heavy metal density of 5600 kg/m³, a burnup rate of 0.4 FIMA%/10000 hours (i.e. $\dot{F}=0.4$) corresponds to a cell linear power of about 10 kW/m, which is about one third the average linear power expected for the IPWR. This makes, from the early-life fuel swelling viewpoint, $\dot{F}=0.4$ a conservative assumption.

⁷ $N_{cells/A}$ is a weak function of K since the selection of the fuel-duct gap width is performed after the target value for the duct flat-to-flat distance has been fixed. The fuel swelling, which is expressed through K , affects the fuel-duct gap sizing which, in turn, affects the space available for the fuel prism and therefore the number of fuel cells.

previously calculated, Eq. III-5 is satisfied for $K=0.02409$. Therefore, the minimum fuel-duct gap thickness to accommodate fuel swelling is:

$$t_{gap,out}^{MIN} = \frac{(P_{prism})_f - (P_{prism})_i}{2} = \frac{(1+K)(P_{prism})_i - (P_{prism})_i}{2} = \frac{K(P_{prism})_i}{2} = 1.11 \text{ mm}$$

The same procedure was repeated keeping P_{prism} approximately constant⁸ and increasing D_f up to 15.3 mm ($N_{cells/A}$ decreased from 61 to 19): it was verified that these new geometries required smaller values of $t_{gap,out}^{MIN}$, with a minimum equal to 0.8 mm for $D_f = 15.3$ mm. Therefore, the choice of the initial geometry was conservative, and a gap width of 1.11 mm was therefore selected as the minimum fuel-duct gap width that would be needed if fuel swelling was the only phenomenon to cause gap shrinking. As noted above, however, while the fuel swells outward, the duct moves inward due to the high pressure in the primary system. The width of the fuel-duct gap needs to be increased by an amount equivalent to the duct radial displacement which, as discussed in Section III.2.1.3, is determined by the stress intensity limit and amounts to about 0.2 mm. The minimum gap width accommodating fuel swelling and duct creepdown, without causing fuel-duct interaction, is therefore $1.11+0.2=1.31$ mm. Due to the uncertainties involved, particularly the fact that the higher heavy metal density of the IPWR fuel with respect to that of the fuel used for the development of Eq. II-1 may cause this equation to underpredict fuel swelling, a 1.5 safety factor is applied, and the value selected for the fuel-duct gap width, for all the IPWR non-collapsible duct geometries analyzed, is $t_{gap,out} = 1.5 \times 1.11 \sim 2$ mm.

III.2.1. 3 Stress intensity on the duct and duct lateral deformation

The assembly duct design is performed using the material-specific (Zr-2.5Nb alloy) stress- and deformation-related constraints summarized below.

Stress limits for normal operation:

⁸ The fuel prism side-to-side distance, P_{prism} , ranged from 79 to 94 mm. It was not possible to keep this parameter fixed since the variation of the fuel hole diameter, performed while keeping the web thickness constant, leads to fuel prisms having different side-to-side distances.

$$S_{\max} < \begin{cases} \min\left(\frac{2}{3}\sigma_y; \frac{1}{3}\sigma_u\right) = 167 \text{ MPa} & \text{for primary gen. membrane stresses} \\ 3 \times \min\left(\frac{2}{3}\sigma_y; \frac{1}{3}\sigma_u\right) = 501 \text{ MPa} & \text{for prim. gen. mem. + secondary str.} \end{cases} \quad (\text{III-6})$$

Stress limit for LOCA conditions:

$$S_{\max} < 84 \text{ MPa} \quad \text{for primary gen. membrane stresses} \quad (\text{III-7})$$

Duct deformation limits for both normal operating conditions and LOCA:

$$\frac{\Delta P_{duct}}{2} < \begin{cases} t_{gap,out} - \frac{\Delta P_{prism}}{2} & \text{for inward deformation (for non collapsible duct only)} \\ \frac{1}{2} \times \frac{(t_{inter} - t_{CB})}{2} = 1.4 \text{ mm} & \text{for outward deformation} \end{cases} \quad (\text{III-8})$$

In the relations above S_{max} is the maximum value of the through-wall averaged stress intensity in the duct walls, ΔP_{duct} is the (diametral) variation of the duct flat-to-flat distance due to pressure and thermal gradients across the walls, $t_{gap,out}$ is the (as-designed) width of the gap separating the fuel prism from the duct, ΔP_{prism} is the (diametral) variation of the fuel prism flat-to-flat distance due to irradiation-induced swelling, t_{inter} is the (as-designed) width of the water gap separating adjacent assemblies, t_{CB} is the thickness of the control blades. The values assigned to the last two parameters are 12.24 and 6.60 mm respectively (see Section III.2.1.7). These criteria, which are discussed in detail in Chapter IV together with the description of the structural analysis performed on the duct, were established to prevent:

- duct failure during normal operation and LOCA scenarios: the pressure gradient across the duct walls, together with the thermal gradient, originate stresses on the duct that, if not limited, can result in duct failure and consequent fission product release into the primary system. The ASME criteria against failure (ASME, 1969), i.e. Eq. III-6, and the criterion against yielding, i.e. Eq. III-7, were used in the IPWR design.

- fuel-duct contact during normal operation: because of hydriding hazard, the design of the non-collapsible duct is performed so that the duct creepdown resulting from the pressure gradient between the primary system and the duct inside does not lead to fuel-duct gap closure. This was done considering the gap thinning caused by irradiation-induced fuel swelling, with a 1.5 safety factor to account for uncertainties. No limit on inward deformation was set for the collapsible duct since, by design, the fuel-duct gap is expected to close once the primary system is brought to nominal pressure. Fuel prism superficial oxidation as well as duct internal oxidation/coating are measures taken to avoid duct hydriding, for both duct designs.
- avoid duct-control blade interference during LOCA: because of the pressure gradient reversal characterizing a LOCA scenario, the duct design is performed so that the duct lateral expansion due to the tensile stresses is much smaller than the clearance existing between the duct outer surfaces and the control blades. Because of the safety-related role of control rods, a safety factor of 2 was used, as shown in the criterion of Eq. III-8 referred to outward deformation.

III.2.1. 4 Fission gas release

Fission gas release (FGR) is a primary concern in the design of fuel assemblies having inverted configuration. In fact, if FGR is large and the reactor is neither provided with a fission gas venting system (option suggested in Pope et al., 2005) nor with a fuel in the form of TRISO particles, fission gases accumulate inside the assembly, causing duct pressurization. While this phenomenon is beneficial during normal operating conditions, since it reduces the pressure differential existing between inside and outside the duct, and therefore the stresses on the duct itself, it is a safety hazard during scenarios in which the pressure outside the duct is low, like LOCA or refueling. In these conditions the inside pressure would not be balanced by the outside pressure, and duct failure can occur. Conceptually, the same pressurization occurs in pin geometry designs; however, the diameter of a fuel pin is much smaller than the flat-to-flat distance of an inverted

assembly duct, and the same differential pressure results in much smaller stresses⁹. For pin designs, therefore, the fuel rod internal pressurization can be handled more easily.

The fuel selected for the IPWR, i.e. $\text{UTh}_{0.5}\text{Zr}_{2.25}\text{H}_{5.625}$, is expected to have a very low FGR (see Chapter II), which is further reduced by constraining the maximum fuel temperature. The 650°C limit imposed on this temperature, which was chosen to avoid excessive irradiation-induced fuel swelling, limits FGR to less than 0.1% (see Figure II-4 in Chapter II).

III.2.1. 5 Hydrogen pickup protection

In the IPWR hydrogen can, in principle, come in contact and diffuse into structural components, i.e. ducts and cladding. Unlike in UO_2 -fueled PWR, where hydrogen is only contained in the coolant, in the IPWR it is also contained in the fuel: this makes structural components susceptible to hydrogen uptake on both the internal and the external surfaces. This fact required:

- an ad-hoc selection of the structural materials: because of its enhanced resistance to hydrogen pickup, Zr-2.5Nb alloy was selected in place of the more common Zircaloy;
- designing the fuel-clad and fuel-duct gap to be wide enough to avoid gap closure: see Section III.2.1.1 and III.2.1.2;
- adopting strategies aimed at cladding and duct protection from hydrogen accidentally released from the fuel: the surfaces of ducts and cladding facing the fuel were designed to be oxidized during assembly manufacture. In this way, the thin ZrO_2 layer formed at the surface would act as a barrier to hydrogen diffusion. A detailed discussion on material selection and hydrogen protection is presented in Chapter II.

⁹ For a cylinder subjected to a pressure differential across its walls, the maximum stress, i.e. the tangential (hoop) stress, is proportional to the cylinder radius, according to the formula: $\sigma_t = \frac{\Delta p \times \bar{R}}{t_{wall}}$, where Δp is

the pressure differential, \bar{R} is the average radius and t_{wall} is the wall thickness. Even though this formula cannot be applied to an hexagonal cross section duct, the proportionality of the stress to the duct size holds.

III.2.1. 6 Selection of gap filling material

For the IPWR designs adopting a non-collapsible duct, the need for wide gaps between the fuel prism and the clad/duct does not allow using helium as gap filling material, because of its low thermal conductivity. These gaps are therefore designed to be filled with a low-melting, highly conductive liquid metal (Sn-Bi-Pb eutectic). The main reason was the need to reduce fuel temperature, and consequently phenomena that are worsened by temperature increase, such as irradiation-induced fuel swelling, fission gas release and hydrogen release (see Chapter II). The liquid metal bond also allows alleviating one other concern related to the use of hydride fuel: since hydrogen is insoluble in it, liquid metal acts as barrier against its migration from the fuel to the structural components. Key properties of the liquid metal bond are discussed in Chapter II.

III.2.1. 7 Inter-assembly water gap width

The width of the gap separating adjacent assemblies has to be as small as possible to maximize the number of assemblies in the core, but large enough to allow for control rod insertion. The gap width selected for the IPWR¹⁰ coincides with the distance between fuel channels of a modern BWR-5, i.e. 12.24 mm (Ferroni et al., 2009). Duct thickness design was performed to guarantee that the differential pressure existing between the inside of the duct and the primary system does not yield duct deformations in excess of the available duct-control blade clearance, but rather abundantly smaller than it.

III.2. 2 Thermohydraulic constraints

III.2.2. 1 Core pressure drop

Core pressure drop is constrained by reactor coolant pump (RCP) performance since an excessive core pressure drop would prevent RCPs from delivering the required flow. In the analysis of the IPWR three core pressure drop limits were used: the reference core pressure drop (150 kPa), 1.5 times this value (225 kPa) and 2 times this value (300 kPa). Adopting the reference core pressure drop as limit allows the IPWR core performance to

¹⁰ IPWR control blade thickness was also assumed to be the same as that of BWR-5 control blades.

be attained using current RCP technology. Adopting the other two limits implies the need of providing the IPWR with higher performance RCPs. The development of these pumps, which are not currently available, is expected to require a relatively short time of the order of 2-3 years, during which R&D work would be needed to address the major design issues implied by the higher pump head and flow (Anness, 2010):

- RCP motor power: a RCP pump able to develop twice the head and about 1.3 times the flow¹¹ of a typical 4-loop PWR RCP would require a $\sim 2 \times 1.3 = 2.6$ higher motor power. Since RCPs of existing 4-loop PWRs have 6 MW (8000 HP) motors, the power required to achieve twice the head and 30% more flow would be about 15.6 MW. The largest Westinghouse RCP, now produced by Curtiss-Wright's Electro Mechanical Corporation, is the Model 100 RCP, to be employed for the South Texas Project plant, which is rated at about 7.5 MW. Combustion Engineering RCPs for the System 80+ plants have ~ 10.4 MW motors. There also exist boiler feed pumps in the 15+ MW range.
- Number of stages and speed: such large pumps would probably require at least two stages, versus current RCPs which are single-stage. Also, a 4-pole motor rotating at 1800 rpm would be needed in place of current 6-pole motors rotating at 1200 rpm.
- Large flywheel: achievement of the same coastdown characteristics as current RCPs would require a much larger flywheel.

III.2.2. 2 Steady-state MCHFR

A limit on the Minimum Critical Heat Flux Ratio (MCHFR) is set to prevent critical heat transfer conditions in the hot channel, and therefore at any location in the core, during steady-state operation. The value chosen for this limit, i.e. 1.79, derives from a reverse engineering steady-state analysis of the reference core, mostly performed with the VIPRE code, and described in detail in Appendix III-A. This analysis was not entirely performed with the VIPRE code since the CHF calculation method selected, in Chapter VI, for axial

¹¹ These values are indicative of the RCP head and flow requirements for the IPWR, as shown in Chapter XI.

flow, i.e. the most recent version of the Groeneveld look-up tables (Groeneveld et al., 2007), is not among the CHF correlations available in VIPRE. This inconsistency was solved by simply applying the Groeneveld look-up tables to the reference core hot channel, whose thermal hydraulics characteristics were provided by the VIPRE code. Figure III-A. 3 in Appendix III-A shows the resulting CHF axial profile, and compares it with those calculated by VIPRE using the Babcock and Wilcox (Gellerstedt et al., 1969), W3-S (Tong, 1972), Combustion Engineering (Combustion Engineering, 1977), Bowring (Bowring, 1979) and EPRI-1 (EPRI, 1982) correlations.

III.2.2. 3 Steady-state peak fuel temperature

The maximum fuel temperature for the IPWR is limited to 650°C to avoid excessive irradiation-induced fuel swelling. Other phenomena, i.e. fission gas release and hydrogen release, also limit fuel temperature, but fuel swelling is more limiting and sets the maximum fuel temperature to the selected value. Higher fuel temperatures, however not in excess of 750°C, would be acceptable if larger fuel-clad and fuel-duct gaps were to be designed, to accommodate fuel swelling. Both temperature limits are mentioned in the literature: Stadnik and Page (1988) state that the fuel temperature limit for the SNAP-DYN reactor was of about 677°C “*due to hydrogen leakage and fuel growth concerns*”. Simnad (1981) states that, for TRIGA reactors, “*there is a steady-state operational fuel temperature design limit of 750°C based on consideration of irradiation- and fission-product-induced fuel growth and deformation*”. Olander (2006A) recommends using a 650°C limit rather than 750°C. The effect that temperature has on irradiation-induced fuel swelling, fission gas and hydrogen release is discussed in detail in the sections referred to the fuel in Chapter II.

III.2.2. 4 Steady-state peak inside clad temperature

The limit on the maximum steady-state inside cladding temperature was set to 370°C to limit steady-state oxidation. Specifically, this limit avoids leaving too little margin, in terms of oxide thickness, between the oxide thickness formed during normal operation and the 17% limit accepted during LOCA scenarios (and discussed in Section III.2.2.6). Using the Baker-Just correlation (Baker and Just, 1962) introduced in Section III.2.2.6 it

can be easily demonstrated that a steady-state operation at temperatures below 400°C for 18×3 months results in an oxide thickness much smaller than 1% of the as-fabricated clad thickness.

It is important to mention that, even if a limit on cladding temperature was not imposed, the other considerations establishing the steady-state thermal conditions would prevent the cladding inside temperature from increasing above about $T_{sat}+5^{\circ}\text{C}$, i.e. above 350°C, because of the wall temperature constancy characterizing subcooled and saturated boiling heat transfer regimes.

III.2.2. 5 Core inlet temperature and coolant enthalpy rise

Core inlet temperature and enthalpy rise are fixed to 296.3°C and 195.2 kJ/kg respectively. The core inlet temperature is the value used in the safety analyses of the reference PWR, i.e. Seabrook Power Station (Seabrook USAR, 2002), which corresponds to the nominal core inlet temperature (293.1°C) conservatively incremented by 5.8 F (3.2°C). The enthalpy rise coincides with the enthalpy rise of the same plant, which can be easily obtained by dividing its thermal power (3411 MW) by its effective¹² core flow rate (~17476 kg/s). The purpose of holding these parameters constant was to constrain the temperature of the primary coolant in the steam generators, to maintain steam generator tube corrosion rate the same as that of typical PWRs.

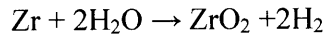
III.2.2. 6 Peak cladding temperature and oxide thickness during LOCA

To comply with US 10CFR50.46 (1974), peak cladding temperature and thickness of oxidized cladding, during LOCA, are limited to 1204°C (2200 F) and 17% respectively¹³. These limits are imposed to prevent excessive cladding embrittlement and therefore to avoid the stresses that originate during a LOCA from causing clad failure and fission product release into the primary system. It is important to note that cladding temperature and oxide thickness affect the degree of embrittlement in different ways. As the

¹² The effective coolant flow rate is the fraction of RCS flow rate, about 95%, which actually removes heat from the core. The remaining 5% comprises flow through control rod guide thimbles, flow for control rod mechanism and vessel head cooling, and flow between core baffle and core barrel.

¹³ The oxide thickness percentage is defined with respect to the original, i.e. as-fabricated, cladding thickness.

temperature increases, oxygen solubility in zirconium increases and, at about 1200°C, it reaches a value that jeopardizes the ductility of the metal, regardless of whether superficial oxidation has occurred (see Appendix III-B). The explanation of the role that oxide thickness plays on embrittlement is instead more intuitive: the thicker is the oxide layer, which forms upon the reaction:



the smaller is the amount of the remaining ductile material that can prevent brittle failure. Appendix III-B presents the history of these embrittlement criteria and, most importantly, the reasons why the numerical values 2200 F and 17% were historically selected. Even though these criteria were historically developed for Zircalloys, they are also applicable to the clad material used in the IPWR, i.e. Zr-2.5Nb. The similarity in corrosion behavior of these materials was in fact experimentally verified by Urbanic (1977) who concluded that: *“there is no significant difference between the oxidation rate of Zr-2.5Nb and the Zircalloys in steam at temperatures greater than 1000°C”*.

Appendix III-B also discusses that, while the 1204°C limit is not associated with any specific temperature calculation method, the 17% oxide thickness limit is strongly tied to the use the correlation that was used to fix this limit, i.e. the Baker-Just correlation (Baker and Just, 1962), which was later demonstrated to be conservative by Urbanic (1977). If another correlation, better in terms of accuracy, was used, the predicted oxide thickness would be closer to the actual value, but much smaller than that obtainable using the Baker-Just correlation. Therefore, the comparison of the value found with the 17% limit would not lead to an accurate estimate of the margin, and may even predict a margin when the margin actually does not exist. The Baker-Just correlation has the following form (Baker and Just, 1962):

$$K_R = 3330 \times e^{\frac{-22896}{T}} \quad (\text{III-9})$$

where K_R is the reaction constant ($\text{kg}^2/\text{m}^4 \text{ s}$) and T is the cladding temperature (K). At a generic time t during the oxidation process, the mass of metal (zirconium) converted to oxide, per unit of area, can be expressed as (Kim et al., 2007):

$$(M_{\text{reacted}})_t = \sqrt{K_R t} \quad (\text{III-10})$$

This mass per unit of area can be expressed as a function of the thickness of cladding that, at time t , has been converted to oxide, δ_t , and of the cladding density ρ_c :

$$(M_{reacted})_t = \rho_c \delta_t \quad (III-11)$$

By introducing Eq. III-11 into Eq. III-10, and differentiating with respect to time we obtain:

$$\frac{d\delta_t}{dt} = \frac{K_R}{2\rho_c^2 \delta_t} \quad (III-12)$$

which, integrated, expresses the thickness of cladding consumed as a function of time and cladding temperature (Kim et al., 2007):

$$\delta_t = \sqrt{\delta_{t-\Delta t}^2 + \Delta t \frac{K_R}{\rho_c^2}} = \sqrt{\delta_{t-\Delta t}^2 + \Delta t \frac{3330 \times e^{\frac{-22896}{T}}}{\rho_c^2}} \quad (III-13)$$

The percentage of original cladding thickness that, at time t , has been oxidized can be therefore computed as:

$$(P_{OX})_t = 100 \frac{\delta_t}{t_{clad}} \quad (III-14)$$

This function is plotted in Figure III- 2, for an as-fabricated cladding thickness of 0.63 mm (which is the thickness corresponding to a cladding inside diameter of 10 mm, by virtue of Eq. III-2). This figure, eventually redrawn for the cladding thickness under consideration, is used in LBLOCA analysis to verify whether the 17% limit is met. As discussed in Chapter VIII, the main output of the LBLOCA analysis is the variation, in time, of the cladding temperature for the hot channel. It is evident that Eqs. III-10 and III-14 can be used to convert this output into percentage of oxidized cladding as a function of time.

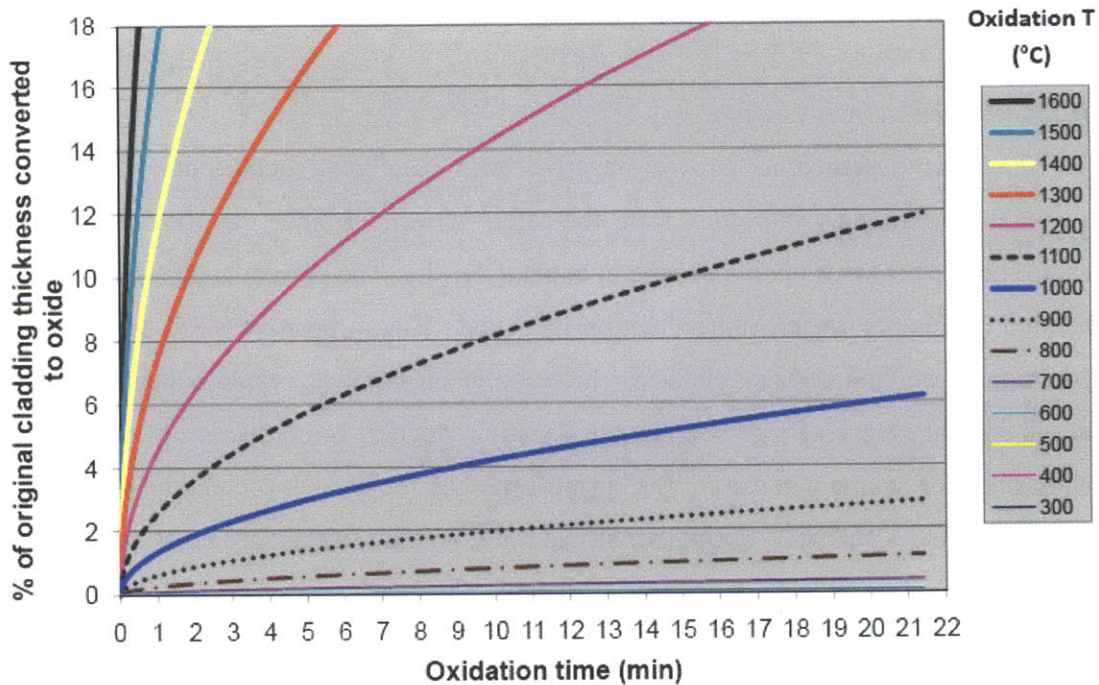


Figure III- 2: Percentage of oxidized cladding (relative to as-fabricated cladding thickness) as a function of oxidation time and cladding temperature, using Baker-Just correlation

A third limit often considered in LOCA analyses, i.e. the maximum fuel temperature, was not used as constraint in this work. For hydride fuels, this limit is typically imposed to avoid excessive hydrogen release during the accidental scenario, which would result in the pressurization of the structural component enclosing the fuel, i.e. the fuel cladding in pin geometries, the assembly duct for the IPWR. For stainless steel clad pin geometries employing U-ZrH_{1.6} fuel, “a fuel temperature safety limit of 1150°C (...) is used as a design value to preclude the loss of clad integrity when the clad temperature is below 500°C. When clad temperatures can equal the fuel temperature, the fuel temperature limit is 950°C” (Simnad, 1981). The lack of data on hydrogen release for UTh_{0.5}Zr_{2.25}H_{5.625} did not allow establishment of a limit on fuel temperature for the IPWR geometry undergoing a LBLOCA. Based on the superior hydrogen retention capability of ternary hydrides, like UTh_{0.5}Zr_{2.25}H_{5.625}, with respect to the binary hydride U-ZrH_{1.6} (see Chapter II), and on the relatively low maximum fuel temperature during LBLOCA (<900°C, see Chapter XI), it is reasonable to exclude that fuel temperature can limit the IPWR power performance.

III.2. 3 Neutronic/economic constraints

III.2.3.1 Void reactivity coefficient

The IPWR is designed to have a negative void reactivity coefficient (VRC). This constraint is extremely important from the safety viewpoint since the VRC defines the reactor power behavior upon a change in coolant density. The present analysis focuses on the sign of this parameter, rather than on its actual value: a positive VRC means that a reduction in coolant density yields an increase in core power, while a negative VRC means that the core response to a coolant density reduction is a reduction in power. The requirement of having a negative VRC is motivated by the need to protect the plant in the event of a LOCA scenario, during which the rapid voiding of the core must not result in an increase in power, but rather in its reduction. The prediction of the VRC sign is not performed by analyzing how the core power or, equivalently, the neutron multiplication factor vary with coolant void fraction but by using, in place of this latter parameter, the hydrogen-to-heavy metal ratio (H/HM) computed at cell level¹⁴. This, other than being practical for design purposes, avoids the inconsistency that would arise if void fraction had to be calculated in a reactor, a PWR, in which the coolant is subcooled, and the void fraction is zero during the early phases of any transient scenario. Monitoring the H/HM ratio is clearly equivalent to monitoring coolant temperature or void fraction since any reduction in coolant density results in a reduction in H/HM. The verification of whether an IPWR geometry complies with the VRC constraint is performed by simply comparing the corresponding normal operating H/HM, which is geometry dependent, with a maximum H/HM value above which VRC would become positive. This H/HM limit value, which depends on the soluble boron concentration, is that corresponding to the maximum of the k_{∞} vs H/HM curve. An example of this curve is shown in Figure III- 3, which presents two k_{∞} vs H/HM curves obtained for the unit cell of the reference PWR (Seabrook USAR, 2002). The curve to be considered is the lower one, since it refers to

¹⁴ The term “cell level” is used to differentiate from calculations performed at “assembly level”. The H/HM at cell level is calculated by considering a single unit cell, while that at assembly level, which is larger, considers also the water gap surrounding the assembly. VRC calculation at cell-level gives conservative results since leakage effect is not accounted for.

the realistic scenario of soluble boron contained in the coolant¹⁵. It can be seen that the operating H/HM of a typical UO₂-fueled PWR, which is about 3.2, is located just to the left of the curve maximum: this implies that, in case of core voiding, the resulting H/HM reduction will cause the operating point to move along the curve, toward lower multiplication factors and therefore lower power.

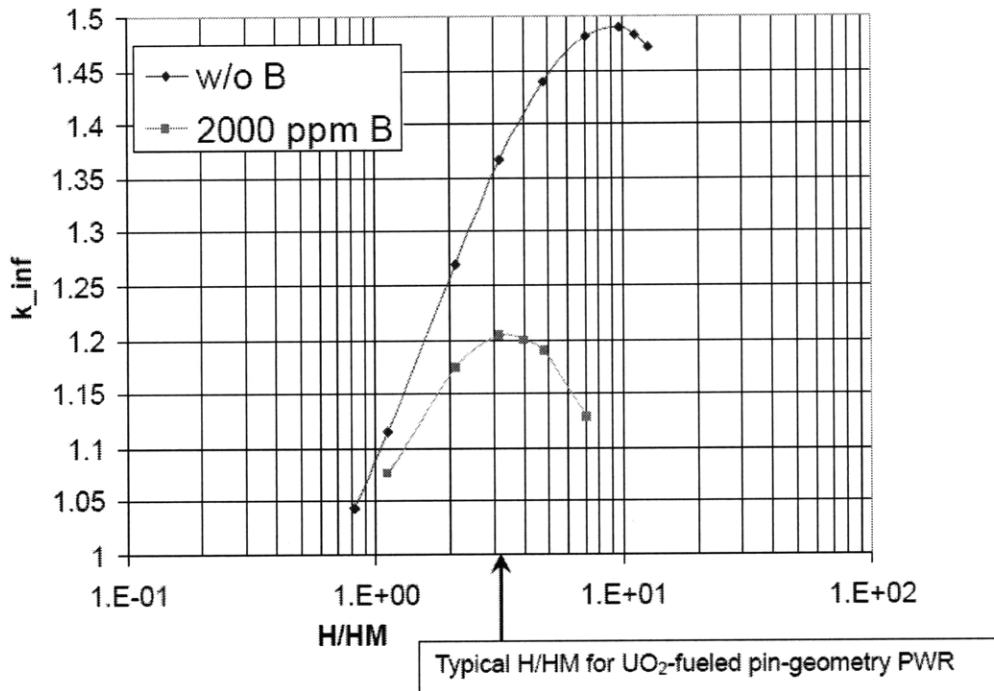


Figure III- 3: Initial infinite multiplication factor vs H/HM for the reference, UO₂-fueled, PWR (MCNP unit cell analysis, with no burnable poisons)

III.2.3.2 Fuel temperature reactivity coefficient

The IPWR is designed to have a negative fuel temperature reactivity coefficient (FTRC). This allows the reactor to respond, as the fuel temperature increases, with a reduction in power, which results in a reduction in temperature and consequent re-equilibrating effect. The FTRC is a property of the fuel, and for UTh_{0.5}Zr_{2.25}H_{5.625} at the IPWR operating burnups is negative. This conclusion was not obtained within the IPWR project, but is

¹⁵ As discussed in Chapter IX, soluble boron causes the maximum of the curve to shift toward lower H/HM values, thus reducing the range of allowed operating H/HM ratios.

contained in the work by Ganda and Greenspan (2010). A summary of their main findings and conclusions is presented in Chapter IX.

III.2.3.3 Soluble boron concentration and IFBA loading

Soluble boron, together with the burnable poisons examined for the IPWR, i.e. IFBA and Er_2O_3 , are needed to compensate for the reactivity excess characterizing the early phases of the fuel cycle. However, soluble boron concentration and IFBA loading have to be limited since:

- the higher the soluble boron concentration:
 - the more difficult is the design of a Chemical and Volume Control System (CVCS) able to handle it;
 - the more pronounced is corrosion of primary system components;
 - the less negative is the void reactivity coefficient: as shown in Figure III-3, addition of soluble boron causes the maximum of the k vs H/HM curve to move to the left making the VRC less and less negative as the boron concentration increases, for a geometry with a fixed H/HM.
- the higher the IFBA loading:
 - the higher the amount of helium generated upon the reaction:
$$^{10}\text{B} + \text{n} \rightarrow ^7\text{Li} + ^4\text{He}$$
which causes duct internal pressurization;
 - the more likely is the IFBA layer detachment from the fuel surface due to the reduction in layer cohesion with the fuel as the thickness of the layer increases (Lahoda, 2007).

The limits imposed on these two parameters are discussed as follow.

Limit on soluble boron concentration

The unrodded Hot Zero Power critical boron concentration for a typical PWR is of about 1750 ppm and the design basis for refueling conditions is of about 2000 ppm (Seabrook

USAR, 2002). Therefore, the maximum soluble boron concentration that a CVCS can handle can be reasonably assumed to be 2000 ppm.

The limit on soluble boron due to the void reactivity coefficient becoming less and less negative was found to only depend on the hydrogen to heavy metal ratio (H/HM) characterizing each inverted geometry. A map associating each inverted geometry with the corresponding maximum soluble boron concentration was generated (see Chapter IX).

Limit on IFBA loading

The limits to be imposed on IFBA loading should be based on the maximum allowed pressurization of the duct and on the maximum thickness of the IFBA layer that can be applied without falling off from the fuel surface. According to Xu (2003), Westinghouse limits the IFBA loading below 1.2 mg ¹⁰B/cm, but no information is provided on whether this limit is linked to the fuel rod internal pressurization or to the IFBA layer falling off from the pellets. It is known, however, that in order to have enough ¹⁰B without making the IFBA layer too thick, the boron contained in IFBA is enriched in the ¹⁰B isotope, typically around 1.25 times. From this observation it is possible to infer that the same ¹⁰B mass per unit length achieved, instead, with non-enriched IFBA, would require a layer too thick to remain adherent to the pellet surface. The IFBA layer thickness corresponding to this situation can be easily calculated¹⁶, and it is equal to 0.022 mm. This value, conservatively rounded down to 0.02 mm, is used as estimate of the maximum IFBA layer thickness, $t_{IFBA,max}$, that can be applied to the fuel surface without resulting in layer detachment. Since, however, input for neutronic calculations is not the IFBA layer thickness but the ¹⁰B loading, it is more useful to express this limit in terms of ¹⁰B loading:

$$\begin{aligned} \text{Max. ZrB}_2 \text{ mass per unit length} &= \pi \times D_f \times t_{IFBA,max} \times \rho_{IFBA} = \\ &= \pi \times D_f \times (0.02 \times 10^{-3}) \times 6090 = 0.383 D_f \text{ kg/m} \end{aligned}$$

¹⁶ This calculation consists of finding the thickness of the non-enriched IFBA layer that, on a pellet having diameter equal to 8.19 mm (Seabrook USAR, 2002) would yield a ¹⁰B loading of 1.2 mg/cm, knowing the IFBA density, i.e. 6090 kg/m³ (Morita, 1998) and the ¹⁰B mass fraction in natural boron, i.e. 0.183 (Xu, 2003).

from which it follows that:

$$\text{Max. boron mass per unit length} = 0.383D_f \times 0.192 = 0.0735D_f \text{ kg/m}$$

where 0.192 is the boron mass fraction in IFBA, i.e. in ZrB_2 . Finally, using the ^{10}B mass fraction (over total boron) in 1.25X enriched IFBA, i.e. 0.229, the maximum ^{10}B loading is:

$$\text{Max. } ^{10}\text{B mass per unit length} = 0.0735D_f \times 0.229 = 0.01684D_f \text{ kg/m}$$

or, equivalently:

$$\text{Max. } ^{10}\text{B mass per cm} = 0.01684D_f \times 10 = 0.168D_f \text{ mg/cm} \quad (\text{III-15})$$

with D_f expressed in mm. Eq. III-15 is used to express the limit on the amount of ^{10}B that can be applied to an inverted channel having fuel hole diameter D_f , due to IFBA layer adhesion concerns only.

The IFBA loading limit due to pressurization concerns derives from the fact that the duct must be protected against failure during scenarios, like LOCA and refueling, during which the primary system pressure is low. If no limits on IFBA loading was imposed, the amount of He generated upon neutron capture by ^{10}B may cause the pressure inside the duct to exceed the design value, leading to duct failure. The constraint on IFBA loading is different depending on the duct design. For non-collapsible ducts, the loading is constrained by requiring that the amount of He generated from ^{10}B is small compared to the amount of He initially introduced into the duct during assembly manufacture. This is because the duct internal pressure is a function of three parameters: amount of gas present, assembly plenum volume available for gas expansion, and plenum temperature. Of these, plenum volume is fixed by design, and its temperature can be reasonably assumed constant. Also, fission gas release from hydride fuels is negligible (see Chapter II), which implies that He is the only gas responsible for duct pressurization. Using the ideal gas law, the pressure dependence reduces to:

$$P = \frac{n_{\text{He}} RT}{V_{\text{plenum}}} \propto n_{\text{He}} = (n_{\text{He}})_{\text{initial}} + (n_{\text{He}})_{\text{from B}} \quad (\text{III-16})$$

The increase in pressure during fuel burning is small when the number of He moles generated from IFBA, $(n_{He})_{from B}$, is small compared to the number of moles initially present in the duct, $(n_{He})_{initial}$. This latter parameter is a function of the assembly design since the volume of the plenum, although of fixed height, varies in cross sectional area depending on the duct flat-to-flat distance and on the number and diameter of cooling channels. The number of moles of He to be introduced into the non-collapsible duct to reach a pressure of 7.8 MPa after reactor heat up, is shown in Figure III- 4¹⁷ as a function of the number of cooling channels in the assembly. The figure also shows the amount of He that would be generated by ¹⁰B if it was loaded on the fuel hole surfaces with an amount equal to the maximum permitted by IFBA layer detachment constraint, i.e. that established by Eq. III-15. It can be seen that, for each number of channels, the amount of helium generated from ¹⁰B is always larger than that needed for duct pressurization. This means that IFBA loading is not limited by layer detachment concerns, but by duct pressurization concerns. To estimate a reasonable limit for IFBA loading, that accounts for pressurization concerns, the calculations performed to generate Figure III- 4 were repeated, with reduced IFBA loadings relative to that specified in Eq. III-15. For each loading the pressure increase fraction due to He generation from ¹⁰B:

$$\text{Pressure increase fraction} = \frac{(n_{He})_{initial} + (n_{He})_{from B}}{(n_{He})_{initial}} \quad (\text{III-17})$$

was calculated. It was verified that an IFBA loading of about 1/10th of that of Eq. III-15 would result in a 10-15% pressure increase relative to HZP-BOL conditions, which is considered manageable. The limit set on IFBA loading for non-collapsible ducts, based on duct pressurization concerns, is therefore:

$$\text{Max. } ^{10}\text{B mass per cm} = 0.1 \times 0.168D_f = 0.0168D_f \text{ mg/cm} \quad (\text{III-18})$$

with D_f expressed in mm.

¹⁷ To perform this calculation, a constant fuel web thickness and temperature of, respectively, 2.5 mm and 370°C, are assumed, while the cooling channel inner diameter is varied from 7 to 15 mm. The fuel cells resulting from these geometric assumptions are then arranged to lead to a duct flat-to-flat distance close, but never equal to, 100 mm, as shown on the secondary axis of Figure III- 4.

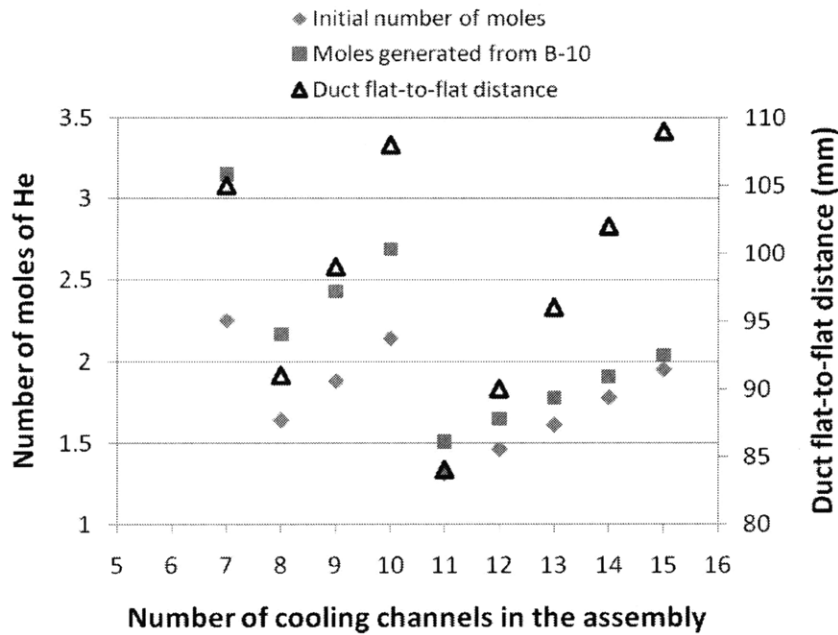


Figure III- 4: Comparison of number of moles of He to be introduced during assembly manufacture with number of moles generated through ^{10}B if IFBA loading is set to the maximum value allowed by layer detachment constraint)

Unlike non-collapsible ducts, collapsible ducts are not pressurized during manufacture. For them, the pressurization-related limit on IFBA loading results from requiring that the contribution to the duct internal pressure by the helium generated from ^{10}B must be smaller than 1.4 MPa. The reason for this limit is that, as explained in Section IV.1.2.2.4 of Chapter IV, when accounting for a fission gas release pressurization of about 0.7 MPa, the margin from duct yielding during LOCA scenario is 1.4 MPa. Section IV.1.2.2.4 of Chapter IV calculates the amount of IFBA corresponding to this pressure.

III.2.3.4 Enrichment and cycle length

The IPWR is designed to be fueled with Low Enriched Uranium (LEU), which is defined as “enriched uranium containing less than 20% of the isotope ^{235}U ” (IAEA, 2002). Uranium-based fuel with enrichment below this threshold “virtually eliminates the possibility that the material could be directly used for the construction of a nuclear explosive device. Specifically, LEU cannot be used in a simple gun-type device, both

because of its large critical mass and the corresponding neutron emission rate. Simultaneously and coincidentally, at an enrichment level between 15-20%, plutonium production is sufficiently suppressed to minimize the total strategic value of the material” (Glaser, 2005).

The cycle length was fixed at about 18 months to be consistent with existing US LWR plant refueling schedule.

III.2.3.5 Number of assemblies

The maximum allowed number of assemblies was fixed to 1132, to limit refueling time. The value chosen coincides with the number of assemblies of the ESBWR core (ESBWR DCD, 2006) which, being the largest found among reactor designs, is used as upper limit.

III.2.3.6 Hot Full Power to Cold Zero Power reactivity insertion

In any reactor, control rods must be designed as to be able to guarantee subcriticality, with some margin, at any time during the life of the reactor. This margin, referred to as shutdown margin, must be guaranteed in the worst case scenario of the most reactive control rod stuck in withdrawn position while the reactor experiences sudden transition from Hot Full Power (HFP) to Cold Zero Power (CZP). A precise control rod design would require a whole core analysis that, for the IPWR, was not performed. A partial indication of the control rod worth required to guarantee a certain shutdown margin can be obtained by comparing the reactivity variation resulting from Hot Full Power (HFP) to Cold Zero Power (CZP) transition to that characterizing a typical pin geometry PWR. Similarity of the reactivity insertion characterizing the IPWR to that of the reference PWR is adopted as indication of the need, by the IPWR, of a total control rod worth similar to that of existing PWRs.

III.2. 4 Manufacturing constraints

Manufacturing constraints play a key role in the design of any reactor. In fact, before analyzing power performance, manufacture feasibility of the reactor components must be assessed. For the IPWR, establishing manufacturing constraints consisted of assessing whether an inverted assembly, hydride-fueled, can be effectively fabricated, and of suggesting appropriate manufacture techniques. Assembly manufacture is discussed in detail in Chapter X, while here it is only briefly described.

Inverted assembly manufacture consists of the following phases:

- 1) Manufacture of the fuel prism
 - a) Fabrication of U-Th-Zr hexagonal prisms: U-Th-Zr alloy is casted into ~1 cm tall solid hexagonal prisms;
 - b) U-Th-Zr prisms are drilled;
 - c) U-Th-Zr prisms are cleaned and superficially abraded to remove hydrogen permeation barriers;
 - d) U-Th-Zr prisms are hydrided;
 - e) U-Th-Zr-hydride prisms are shaped and brought to design dimensions;
 - f) U-Th-Zr-hydride prisms are superficially oxidized to create a barrier against hydrogen release.
- 2) Insertion and fixing of twisted tapes (TTs) to cooling tubes (for H-IPWR and S-IPWR designs only).
- 3) Assembling phase, consisting of (for assemblies provided with collapsible duct):
 - a) welding of assembly lower cap to hexagonal duct;
 - b) insertion of cooling tubes into lower cap holes and welding of the tubes lower end to the cap;
 - c) stacking of multiple fuel prisms inside the duct, with the cooling tubes into the fuel prism holes;

- d) welding of the assembly upper cap to the duct and to the upper end of the cooling tubes.

For non-collapsible duct designs the assembling phase is complicated by the need to bond the fuel-clad and fuel-duct gaps with liquid metal. Chapter X discusses possible methods to do this.

Appendix III-A: Steady-state analysis of the reference PWR

A steady-state analysis of the reference core (Seabrook USAR, 2002) was performed in order to calculate its MCHFR and core pressure drop: two parameters that were then used to set the design limits for the IPWR. In particular, the limit value on MCHFR was set equal to the reference core steady-state MCHFR, while the limit value on core pressure drop was set equal to the reference core pressure drop multiplied by a certain factor. This approach, often termed as “reverse engineering approach”, allowed the design of an IPWR whose safety margin from critical heat transfer conditions was the same (or greater) than that of an existing reactor.

III-A.1 Reference core model

The analysis of the reference core was performed with the VIPRE thermal hydraulic code (Cuta et al., 1985). Geometry and operating conditions of the reference core are summarized in Table III-A. 1. Particularly, core power and core inlet temperature were conservatively increased relative to their nominal values in accordance with the common practice in safety analyses (Section 15 of Seabrook Power Station, 2002). Core power was increased by 2%, while core inlet temperature was increased by 5.8 F (3.2°C). Since no specific directions have been found for the coolant flow rate, the nominal value was used. This value, 17476 kg/s, does not include the coolant flowing between the barrel and the baffle and between the baffle and peripheral fuel assemblies, i.e. these flows are not modeled.

The power distribution in the core is accounted for by means of three Power Peaking Factors (PPFs):

- assembly radial peaking: 1.515;
- local pin peaking: 1.089;
- axial peaking: 1.515.

The total peaking factor, defined as the product of these three PPFs, is equal to 2.5, which is a conservative value typically encountered in PWR safety analyses. It is important to note that the conservatism is embedded in the assembly radial and axial PPFs, while the value chosen for the local pin peaking is that of a typical assembly at Beginning Of Life

(BOL) (Seabrook USAR, 2002). The pin-by-pin power distribution modeled with VIPRE is shown in Figure III-A. 1.

Table III-A. 1: Reference core key characteristics	
Operating Conditions	
Pressure (MPa)	15.51
Core inlet temperature (°C)	296.3 (293.1+3.2)
Average core outlet temperature (°C)	329.1
Power and flow rates	
Core thermal power (MW)	3479.2 (1.02×3411)
Hot assembly radial peaking factor	1.515
Axial peaking factor	1.515
Axial power profile	Chopped cosine
Hot pin radial peaking factor	1.089
Effective coolant flow rate through the core (kg/s)	17476
Percentage of coolant flowing through guide thimbles	2
Coolant enthalpy rise across the core (kJ/kg)	195
Geometry	
Number of assemblies	193
Assembly lattice	17×17
Number of fuel rods per assembly	264
Number of guide thimbles per assembly	24
Number of instrumentation tubes per assembly	1
Total assembly height (m)	4.063
Active assembly height (m)	3.658
Assembly pitch (mm)	215.04
Fuel rod pitch (mm)	12.6
Cladding outside diameter (mm)	9.5
Cladding inside diameter (mm)	8.3566
Fuel pellet diameter (mm)	8.1915
Guide thimble inner/outer diameter (mm)	11.430/12.243
Instrumentation tube inner/outer diameter (mm)	11.379/ 12.294
Number of grids per assembly (including Intermediate Flow Mixers, IFM)	8
Number of IFMs per assembly	3
Form loss coefficients	
Bottom fuel nozzle	1.6992
Bottom grid spacer	0.389
Intermediate grid spacers	0.4822
Upper grid spacer	0.3834
Intermediate Flow Mixers	0.4154
Top fuel nozzle	0.5519

0									
1.035	0.972								
0.992	1.012	0.978							
0	1.002	1.054	0						
0.999	1.018	0.986	1.064	1.008					*Hot Pin
1.050	0.985	1.022	1.018	*1.089	0				
0	1.059	1.008	0	1.012	1.034	0.940			
0.999	1.028	1.019	0.992	1.001	0.935	0.916	0.960		
1.003	1.007	1.003	0.995	0.987	0.971	0.962	0.960	0.918	

Figure III-A. 1: Hot assembly pin-by-pin power distribution used for the analysis of the reference core (Seabrook USAR, 2002)

As shown in Figure III-A. 2, the VIPRE input file did not model the whole core, but 1/8th of it. While the hot assembly was modeled at subchannel level, i.e. all its subchannels were individually modeled, other assemblies were lumped in groups, according to the scheme (see Figure III-A. 2):

- “a” is 1/8th of the hot assembly;
- “b” and “c” are half assemblies;
- “d” derives from the lumping of 2 equivalent¹⁸ assemblies;
- “e” derives from the lumping of 7 equivalent assemblies;
- “f” derives from the lumping of 14 equivalent assemblies.

The lumping approach is a common practice in core thermal hydraulic analysis, which allows accurate modeling both of the thermal hydraulics of the power-limiting channels and the pressure drop, set by the rest of the core, creating the boundary condition for the hot channel. Besides the numerical value given to the radial peaking factor of the hottest assembly, the other peaking factors assigned to the assemblies (and to the lumped assemblies) forming the 1/8th core analyzed are shown in Figure III-A. 2.

¹⁸ (d) is formed by 1 whole assembly and two halves of two separate assemblies. The term equivalent assembly is used to identify a combination of assembly fractions such that the resulting number of fuel rods is equivalent to that characterizing a single assembly.

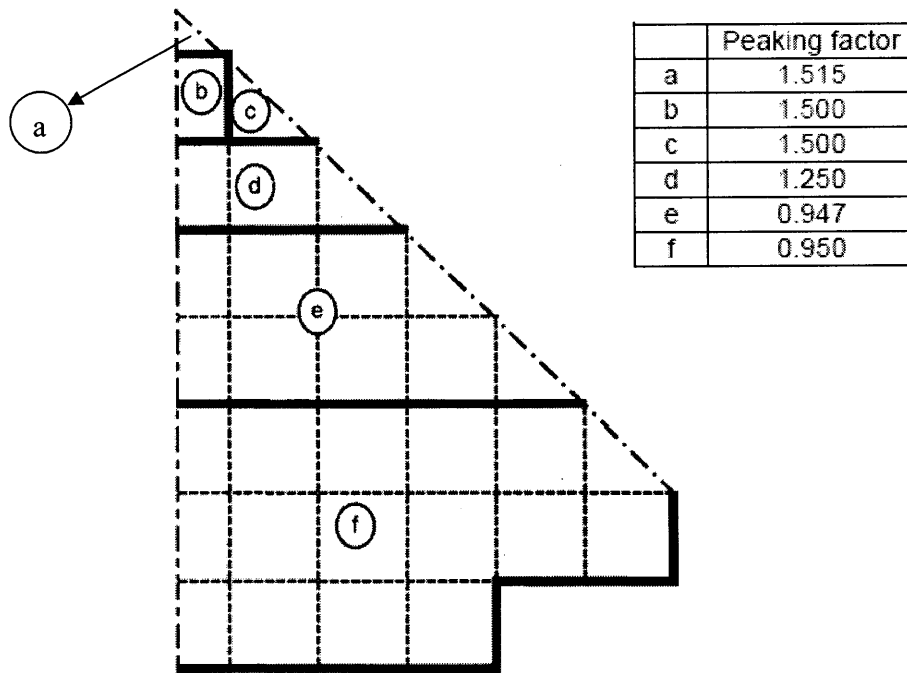


Figure III-A. 2: 1/8th core fraction modeled with VIPRE

The numerical values used for the peaking factors of assemblies “b” and “c” are a conservative estimate of the power disequilibrium existing in the neighborhood of the hot assembly. It has been separately verified that, in an UO₂ core at BOL, the neighboring assemblies are typically 6-8% colder than the hot assembly. In contrast, the SS analysis assumes they are only 1% colder. Because of the non-limiting effect exerted by the mild and cold assemblies on the thermal hydraulic limits, the peaking factors of “d”, “e” and “f” were chosen in a less rigorous way, simply trying to reproduce a reasonable and normalized power distribution.

III-A.2 Results

The results of the steady-state analysis of the reference core are summarized in Table III-A. 2. For the purposes of this analysis, the most important data are the core pressure drop, 150 kPa, and the MCHFR, 1.92. It is important to note that, while the pressure drop was directly extracted from the VIPRE output, the MCHFR was not. In fact, the CHF calculation method selected for the IPWR channels in axial flow, i.e. the newest version of the Groeneveld look-up tables (Groeneveld et al., 2007), is not among the CHF

correlations available in the VIPRE code. Therefore, it was decided to extract, from the VIPRE output file, the thermal hydraulic parameters required, as input, by the Groeneveld look-up tables¹⁹, and to enter them separately in those tables. In this way the consistency between the correlation used to set the MCHFR limit and that actually used to calculate the MCHFR, was preserved. The importance of this procedure is evident from Figure III-A. 3, which shows the CHF axial profile obtained with the Groeneveld look-up tables (Groeneveld, 2007) and with the following CHF correlations available in the VIPRE code:

- Babcock and Wilcox correlation (Gellerstedt et al., 1969);
- W3-S correlation (Tong, 1972);
- Combustion Engineering correlation (Combustion Engineering, 1977);
- Bowring correlation (Bowring, 1979);
- EPRI-1 correlation (EPRI, 1982).

From the figure it can be easily inferred that the use of a correlation for the CHF computation different from that used to set the MCHFR limit could lead to significant errors.

¹⁹ The Groeneveld look-up tables (Groeneveld, 2007) require, as main input, three parameters: equilibrium quality, mass flux and system pressure. These parameters had to be supplemented with other three parameters, i.e. channel equivalent diameter, steam flow quality and axial power distribution, which are needed to compute the correction factors required to convert the CHF for an 8 mm-tube under axial uniform power distribution (shown in the tables) to that for the fuel bundle under examination. Except for the diameter correction factor, which is from Groeneveld et al. (2007), the formulation for the axial power distribution correction factor, bundle correction factor and heated length correction factor are from an older version of the same look-up tables (Groeneveld et al., 1986), which was recommended to be applied to the 2006 version tables by Groeneveld (Groeneveld, 2009). It must be mentioned, however, that the computation of the axial flux distribution factor was performed after correcting two typos in Groeneveld et al. (1986): the correction factor is in fact the reciprocal of that shown, and the steam quality used to define the two ranges over which the factor is presented is the equilibrium quality, and not the flow quality (as indicated in the nomenclature table).

Table III-A. 2: Main results of reference core steady-state thermal hydraulic analysis		
Parameter	Units	Value
MCHFR (with 2006 Groeneveld look-up tables)	-	1.79
Core pressure drop	kPa	150
Maximum fuel temperature	°C	2069
Maximum average fuel temperature	°C	1321
Maximum pellet surface temperature	°C	685
Maximum cladding inside temperature	°C	402
Maximum average cladding temperature	°C	374
Maximum cladding outside temperature	°C	348
Maximum subchannel exit quality	%	0.3
Hot assembly exit quality (subch. averaged)	%	0.09
Maximum subchannel exit void fraction	%	1.88
Hot assembly exit void fraction (subch. averaged)	%	0.51

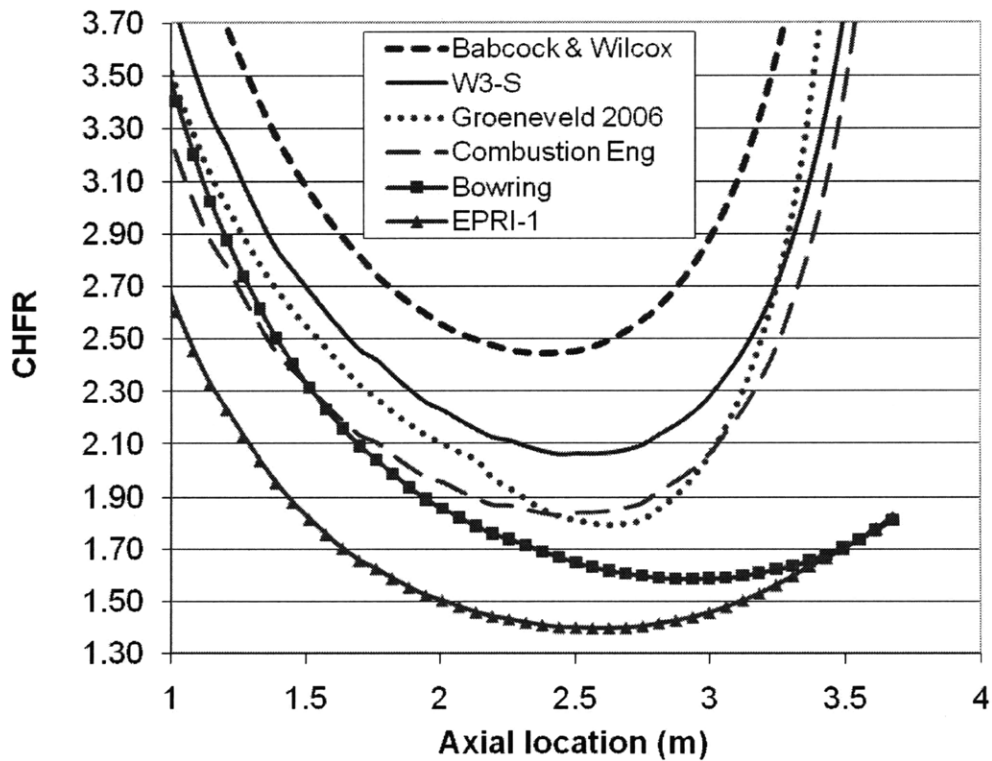


Figure III-A. 3: CHFR axial profiles for the reference core at steady-state conditions

Appendix III-B: History of 2200 F PCT and 17% oxidation safety criteria for LOCA

This Appendix, which is a summary of the more detailed report by Hache and Chung (2001), discusses the rationale behind the selection of the two most well known safety criteria used in LOCA analysis: the 2200 F (1204°C) peak cladding temperature (PCT) and 17% oxide thickness limits. Also, it explains how the oxide thickness has to be calculated, when the comparison with the 17% limit is to be performed. This was revealed to be a fundamental piece of information for the design of the IPWR

III-B.1 Safety criteria motivations

The 17% oxidation and the 2200 F (1204°C) peak cladding temperature (PCT) criteria in 10 CFR 50.46(b) were established to protect Zircaloy fuel rod cladding from an excessive embrittlement which, under the thermal and mechanical stresses that are generated during LOCA and post-LOCA scenarios, could cause cladding failure. The phenomena that cause cladding embrittlement, whose severity is therefore limited by the application of the mentioned criteria, are cladding oxidation and oxygen dissolution in the β -Zr phase.

An as-fabricated Zircaloy cladding is mainly composed of zirconium, in β -phase (Body Centered Cubic). During oxidation above the α - to β - transition temperature ($\sim 550^\circ\text{C}$), during a LOCA for example, the cladding loses composition homogeneousness and different layers become clearly distinguishable, as shown in Figure III-B. 1. In particular, the brittle phases zirconium oxide and oxygen-stabilized α -Zr phase form, causing a reduction in ductility for the whole cladding. The only load bearing layer is the β -Zr which, however, may also lose some ductility if the amount of oxygen dissolved in it is too large.

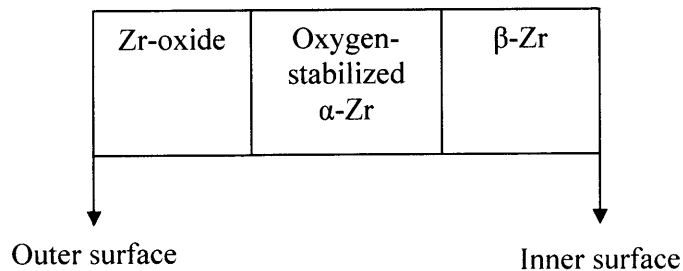


Figure III-B. 1: Layers forming the cladding wall upon oxidation (not to scale)

Both the 17% oxidation limit and the 1204°C PCT limit were established to limit the reduction in ductility that the cladding can experience during a LOCA. However, while the former is aimed at reducing such ductility loss by mainly limiting the fraction of cladding thickness that is not made of β -Zr, the latter aims at preventing an excessive ductility loss by limiting the amount of oxygen that can dissolve in β -Zr.

III-B.2 Rationale behind the choice of the safety criteria

Both the 17% oxidation and the 1204°C PCT criteria derive mainly from the results of post-quenching ductility tests conducted by Hobson and Rittenhouse (1972). They oxidized Zircaloy-4 tubes at various temperatures with steam, both internally and externally, and then quenched them in water. Short ring specimens were then cut from the oxidized tubes, and subjected to slow compression tests at temperatures ranging between 23 and 150°C. Depending on the appearance of the rings after these tests, they were categorized in increasing order of ductility as:

- zero ductility specimens;
- specimens with 4 fractures;
- specimens with one to three fractures;
- total ductility specimens;

These specimens were introduced in a diagram, as shown in Figure III-B. 2. The diagram has the compression test temperature on the y-axis, and the ratio between the thickness of the β -Zr layer (which is the load-bearing layer than preserves cladding ductility) and the

post-oxidation total thickness of the cladding on the x-axis. Each specimen in Figure III-B. 2 is indicated with an identification number, followed by:

- a symbol indicating the ductility category;
- the oxidation time in minutes;
- the oxidation temperature in F, and
- the first maximum load in pounds.

Based on the position of most of the “zero ductility specimens”, Hobson and Rittenhouse traced a “zero ductility line” for slow compression (dashed line on the left side of the diagram). This line identifies, for each temperature at which the specimen is required to withstand slowly applied mechanical stresses, the minimum β -Zr thickness fraction that allows the specimen to withstand those stresses. They were able to easily trace the “zero ductility line” because the “zero ductility specimens” they used for that purpose fall in a very distinct part of the diagram. This was not only due to the fact that, as expected, the thinner is the β -Zr layer the more brittle is the cladding, but also to the fact that “zero ductility specimens” oxidized at temperatures $\geq 2400^\circ\text{F}$ were not accounted for in tracing that line²⁰. In fact, “zero ductility specimens” are also located on the right of the line, but they are only those oxidized at temperatures $\geq 2400^\circ\text{F}$. For example, specimen 352 failed in spite of having a β -Zr thickness fraction of ~ 0.72 and of being oxidized for only 2 minutes. This was explained on the basis of the oxygen concentration in the β -Zr phase: for the retention of good mechanical properties near room temperature it is important that the oxygen concentration in the β -Zr phase remains below ~ 0.7 wt%. Above this value the solid-solution induced hardening effect causes the β -Zr phase to lose ductility. Since (1) the temperature at which the oxygen solubility in β -Zr is 0.7 wt% is 2200°F (1204°C) and (2) oxygen solubility increases with temperature, it was decided to limit the peak cladding temperature to 1204°C . It can be said, therefore, that the PCT limit of 1204°C prevents the β -Zr from losing ductility due to an excessive oxygen concentration in solution.

²⁰ This is why it has been said that that most of the “zero ductility specimens”, and not all, have been used to trace the “zero ductility-slow compression” line.

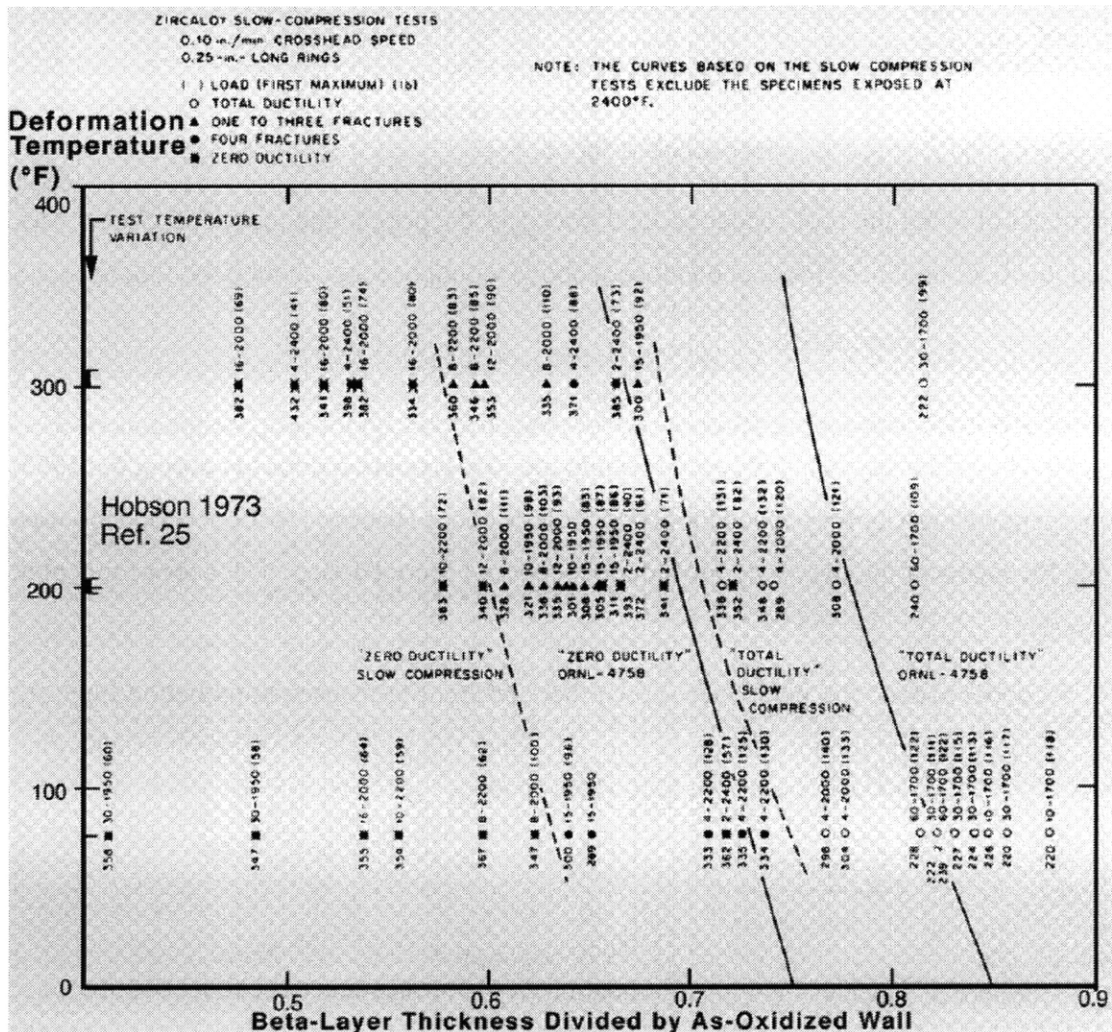


Figure III-B. 2: Ductility of two-side-oxidized Zircaloy rings as function of compression temperature and fraction of transformed- β -Zr-layer (Hobson and Rittenhouse, 1972)

Since the saturation temperature during reflood was estimated to be 135°C (275°F), this value was used as representative of the temperature at which oxidized claddings are required to withstand mechanical stresses that originate during a LOCA scenario. From Figure III-B. 2, the “zero-ductility” β -Zr layer thickness fraction corresponding to this temperature is about 0.58. Since, upon oxidation, the cladding wall is composed by the layers shown in Figure III-B. 1, a β -Zr layer thickness fraction of 0.58 corresponds to a

fraction of thickness occupied by zirconium oxide and oxygen-stabilized α -Zr of $1-0.58 = 0.42$, i.e.:

$$\frac{t_{Ox+\alpha Zr}}{t_{TOT_post-ox}} = \frac{t_{Ox+\alpha Zr}}{t_{Ox+\alpha Zr} + t_{\beta Zr}} = 0.42$$

If instead of using the post-oxidation total thickness the pre-oxidation total thickness was used, the 0.42 thickness fraction mentioned above would become about 0.44, that is:

$$X_{oa} \equiv \frac{t_{Ox+\alpha Zr}}{t_{TOT_pre-ox}} \approx 0.44$$

$X_{oa} = 0.44$ was the key number in establishing the 17% oxidation criterion during the 1973 Emergency Core Cooling System (ECCS) Rule-Making Hearing (AEC, 1973). This was done by means of the overlying procedure shown in Figure III-B. 3. The axes of this plot represent:

- upper x-axis: the parameter shown, here referred to as pseudo-oxidation time, A , allows adaptation of the plot to any cladding thickness and oxidation orientation, i.e. one-side or two-side oxidation. It is defined as:

$$A \equiv \frac{0.343N}{t_{clad_pre-ox}} \sqrt{t}$$

where N indicates the type of oxidation ($N=1$ for one-side oxidation, $N=2$ for two-side oxidation), t is the oxidation time expressed in seconds and t_{clad_pre-ox} is the pre-oxidation cladding thickness, in mm.

- lower x-axis: it shows the oxidation time, in minutes, for a 0.686 mm thick clad oxidized on both sides. It is obtained from the upper x-axis by introducing, in the expression for A , $N=2$ and $t_{clad_pre-ox} = 0.686$.
- y-axis: it shows the percentage of cladding thickness converted to oxide, using the Baker-Just correlation.

Figure III-B. 3 shows:

- black straight lines: predictions, obtained with the Baker-Just correlation (Baker and Just, 1962), of the variation of the oxide thickness percentage (y-axis) with the pseudo oxidation time (upper x-axis), for different oxidation temperatures;
- red dashed curves: four curves of constant X_{oa} , two referred to $X_{oa}=0.35$ and two to $X_{oa}=0.44$. For each value, one curve is the prediction with the Pawel correlation (Pawel, 1974), while the other is the prediction with the Hobson and Rittenhouse (1972) correlation;
- green continuous curves: they represent six thermal shock experiments performed by Hesson (1970), in which oxide thickness was monitored as a function of time. Of those, only two resulted in cladding failure, and such failures occurred at values of X_{oa} equal to about 19% and 30% respectively.
- empty squares: Combustion Engineering isothermal experiments terminated without cladding failure;
- black squares: Combustion Engineering isothermal experiments terminated with cladding failure;
- the horizontal line corresponding to an oxide thickness percentage of 17%.

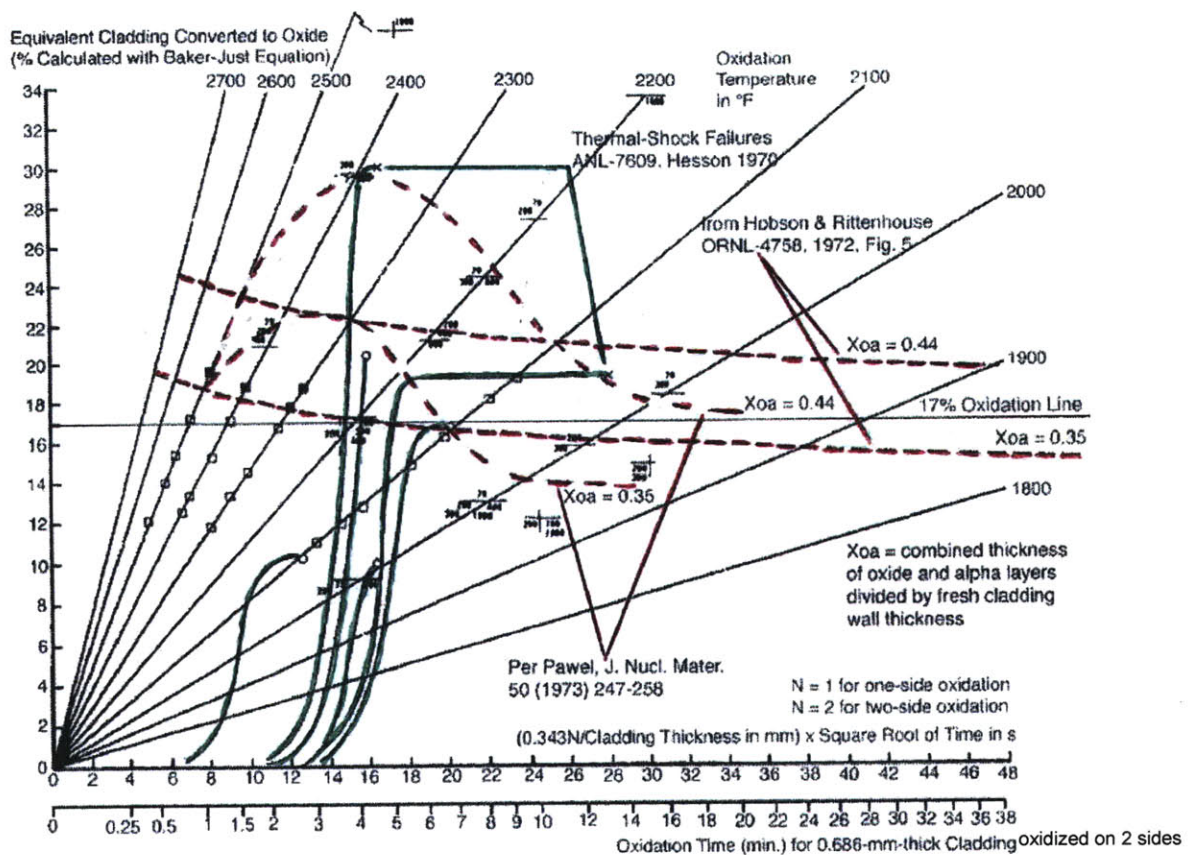


Figure III-B. 3: Summary of multistep procedure used to establish 17% oxidation criterion during 1973 Rule-Making Hearing (from AEC, 1973).

The establishment of the 17% oxide thickness limit was done through three observations:

- 1) $X_{oa} \leq 0.44$ is a reasonable embrittlement criterion (based on Figure III-B. 2);
- 2) the use of the 17% thickness limit, calculated with the Baker-Just correlation (Baker and Just, 1962) is conservative when compared to the limit $X_{oa} \leq 0.44$. This is because both correlations used for X_{oa} , i.e. Pawel correlation (Pawel, 1974) and Hobson and Rittenhouse (1972) correlation, predict an $X_{oa} = 0.44$ curve lying above the 17% oxide thickness line, i.e. it is reasonable to say that an oxide thickness percentage, calculated with the Baker-Just correlation, equal to 17% identifies an extent of oxidation lower than $X_{oa} = 0.44$.

- 3) no cladding failures, at temperatures above 135°C, were observed below an oxide thickness percentage of 17% (see Figure III-B. 3).

By means of these observations, the NRC concluded that 17% oxide thickness is a satisfactory criterion to prevent embrittlement-induced cladding failure. It must be pointed out, however, that such value is tied with the use of the Baker-Just (1962) correlation, and the use of another correlation, even if better in terms of accuracy, may not necessarily be conservative in evaluating post-quenching cladding ductility. The conservatism embedded in the Baker-Just correlation was in fact experimentally verified by Urbanic (1977). By measuring corrosion rates of Zr-2.5Nb alloy and comparing them with earlier results for Zircaloy-2 and Zircaloy-4, as well as with predictions made through the Baker-Just correlation, he concluded that: *“the oxidation rates of Zr-2.5Nb and the Zircalloys in steam are consistently less than those given by the Baker and Just correlation for zirconium oxidation in steam”*.

Appendix III-C: Fuel swelling calculation

This Appendix presents the method used to obtain Eq. III-5. This equation allows obtaining the fuel prism volume swelling percentage as a function of the initial fuel prism dimensions and of the coefficient K , which expresses the variation of the fuel prism flat-to-flat distance, P_{prism} , fuel prism height H_{prism} and fuel hole diameter D_f with respect to the as-designed dimensions, i.e.:

$$\frac{(P_{prism})_f - (P_{prism})_i}{(P_{prism})_i} = -\frac{(D_f)_f - (D_f)_i}{(D_f)_i} = \frac{(H_{prism})_f - (H_{prism})_i}{(H_{prism})_i} = K \quad (III-4)$$

where the subscript i indicates initial dimensions while the subscript f indicates post-swelling dimensions. The volume swelling percentage is defined as:

$$\left(\frac{\Delta V}{V}\right)\% = 100 \frac{(V_{prism})_f - (V_{prism})_i}{(V_{prism})_f} \quad (III-19)$$

where the volume of the fuel prism is given by:

$$V_{prism} = \left(\frac{\sqrt{3}}{2} P_{prism}^2 - N_{cells/A} \frac{\pi}{4} D_f^2 \right) H_{prism} \quad (III-20)$$

with $N_{cells/A}$ being the number of fuel cells, and therefore the number of holes, in the fuel prism. The post-swelling fuel prism flat-to-flat distance can be expressed as:

$$(P_{prism})_f = (P_{prism})_i + \Delta P = (P_{prism})_i + [(P_{prism})_f - (P_{prism})_i] = (P_{prism})_i + K(P_{prism})_i \quad (III-21)$$

and, analogously:

$$(D_f)_f = (D_f)_i - K(D_f)_i \quad (III-22)$$

$$(H_{prism})_f = (H_{prism})_i + K(H_{prism})_i \quad (III-23)$$

By introducing Eq. III-21 through Eq. III-23 into Eq. III-20, and the latter into Eq. III-19, the following expression for the fuel swelling percentage can be obtained:

$$\left(\frac{\Delta V}{V}\right)\% = 100 \left\{ \frac{\left[\frac{\sqrt{3}}{2} (P_{prism})_i^2 (1+K)^2 - N_{cells/A} \frac{\pi}{4} (D_f)_i^2 (1-K)^2 \right] (1+K)}{\frac{\sqrt{3}}{2} (P_{prism})_i^2 - N_{cells/A} \frac{\pi}{4} (D_f)_i^2} - 1 \right\} \quad (\text{III-5})$$

Chapter IV

Duct design and assembly/core construction methods

This chapter presents the methodology used to geometrically define the IPWR core, specifically the size of the assembly duct (Section IV. 1), the number of fuel cells per assembly (Section IV. 2) and the number of assemblies in the core (Section IV. 3). The values selected for these parameters result, directly or indirectly, from the application of design constraints, mainly structural, described in Chapter III. In fact, the size of the assembly duct, i.e. overall flat-to-flat distance and wall thickness, is determined by applying the stress and deformation constraints. The number of cells per assembly is a function of the duct size, fuel-duct gap width and fuel cell pitch. The number of assemblies in the core depends on the flat-to-flat distance selected for the ducts, on the inter-assembly spacing and on the core shroud radius.

IV. 1 Assembly duct design

The duct enclosing the fuel block, together with the cooling channel cladding, serves three main functions:

- it allows retaining fission products, hydrogen and fuel fragments generated during reactor operation;
- it prevents coolant interaction with the fuel;
- it increases the structural strength of the whole assembly, allowing the assembly to sustain mechanical stresses that are generated during operation, refueling and accident scenarios, e.g. assembly drop during refueling.

In order to perform these functions, the assembly duct must be sufficiently thick. However, duct thickening penalizes neutron economy, through extra absorptions, as well as fuel economy, through reduction of the volume available for the fuel. Both aspects penalize fuel cycle length and therefore the economics of the whole design. Because of this complex tradeoff, two duct designs have been examined:

- collapsible duct: it consists of a relatively large but thin-walled¹ duct, designed to be only slightly pressurized internally, so that the high pressure of the primary system causes it to collapse onto the fuel prism. Progressive outward duct deformation would then occur during fuel burnup, due to irradiation-induced fuel swelling. No liquid metal bonding is needed for the fuel-clad and fuel-duct gaps, since gap closure occurs immediately after the primary system has been pressurized.
- non-collapsible duct: it consists of a small, thick-walled duct that, due to a fuel swelling-induced pressurization, does not collapse onto the fuel prism. Liquid metal fills the fuel-clad and fuel-duct gaps which remain open throughout the life of the assembly². Upon fuel swelling the liquid metal is squeezed toward the assembly upper plenum, where helium, introduced during assembly manufacture, is compressed thus causing duct pressurization.

Because of the reduction in volume occupied by structural materials, the collapsible duct design has the advantage of a larger space available for fuel and cooling channels, thus allowing higher power densities to be attained. However, in spite of the measures taken, for both designs, to prevent duct hydriding (choice of a low hydrogen uptake material and duct superficial oxidation and coating, discussed in Chapter II), the contact between duct and fuel makes the collapsible duct susceptible to hydrogen uptake and consequent embrittlement. The non-collapsible duct is instead well protected from hydriding since (1) no hard contact with the fuel is expected throughout the life of the core and (2) the liquid metal bond acts as additional barrier to hydrogen migration toward the duct.

¹ "Thin-walled" has to be intended as compared to the duct overall size, not as absolute wall thickness.

² Use of helium is incompatible with open gaps: its low thermal conductivity would in fact lead to excessive fuel temperatures.

However, from the power performance viewpoint, the non-collapsible duct design is penalized by its own geometry: the small assembly size combined with the large wall thickness significantly reduce the space available for fuel and coolant, while the need for a tall upper plenum (to accommodate the liquid metal that is squeezed out from the gaps after fuel swelling) penalizes pressure drop.

The design of the collapsible and non-collapsible ducts differed in the choice of the duct flat-to-flat distance, P_{duct} , wall thickness, t_{wall} , and duct height L_{duct} , while the material was selected without making distinction between the two designs. Sections IV.1. 1 and IV.1.2 discuss duct material and duct height respectively, while Section IV.1.3 presents the analysis methodology used to select P_{duct} and t_{wall} .

IV.1. 1 Duct material

The material selected for IPWR assembly duct (and clad) is Zr-2.5Nb. This choice was motivated by three characteristics of this Zr-based alloy: low neutron absorption cross section, good mechanical properties and especially low hydrogen pickup. This last characteristic, very important in LWRs and even more so in a reactor like the IPWR which uses a hydrogen-containing fuel, is the main reason why in CANDU reactors, Zr-2.5Nb is currently preferred over Zircaloy for the manufacture of the pressure tubes (AECL, 1997). More details on this alloy, e.g. its thermophysical properties, are discussed in Chapter II.

IV.1. 2 Duct height

The duct height differs depending on the duct design. The collapsible duct does not contain liquid metal and does not need to be internally pressurized with helium. These features allow the duct to be relatively short, i.e. 3.8 m tall, of which 3.66 m are occupied by the fuel while the rest by a 10 cm tall plenum and by the two lids. The non-collapsible duct needs instead a much taller plenum, which serves to accommodate the liquid metal that is squeezed out from the fuel-clad and fuel-duct gaps, as well as the helium introduced to achieve the desired level of pressurization. The length of such plenum is

design-dependent³ and ranges between 0.5 and 1 m, as shown in Figure IV-1. Thus, non-collapsible ducts range between ~4.1 and ~4.7 m in height.

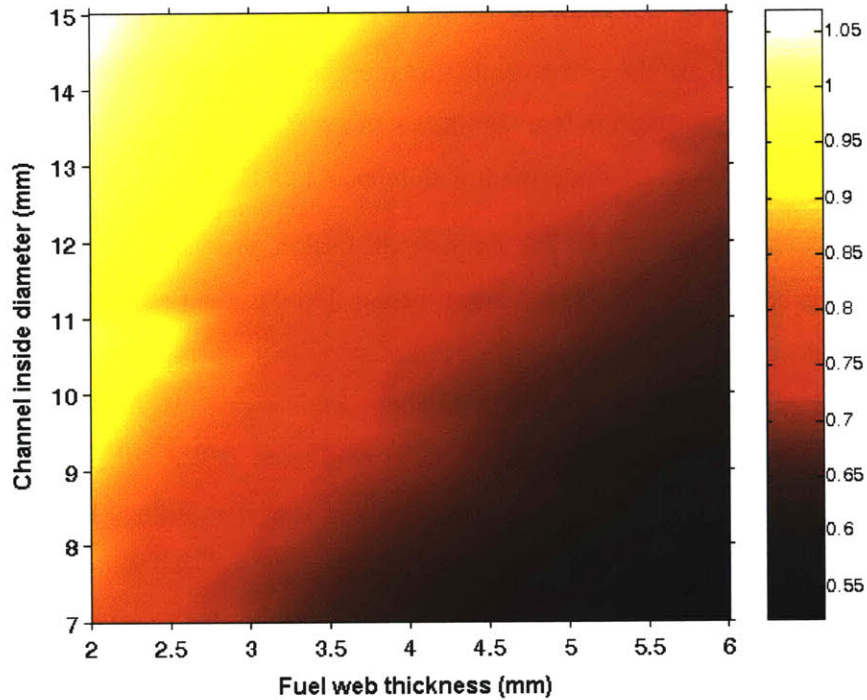


Figure IV- 1: Assembly plenum height (m) needed to accommodate liquid metal upon gap closure (non-collapsible duct design)

From the manufacturing viewpoint the lengths of both the collapsible and the non-collapsible ducts are attainable since the tubes for the cooling channels, as well as the hexagonal ducts, can be fabricated in any length. Instead, as discussed in Chapter X, the fuel prisms cannot be fabricated in lengths above about 50 cm and, consequently, multiple prisms need to be stacked one above the other to complete the assembly. Possible concerns of having long assemblies have been considered, but they are not considered sufficiently important to force the choice of shorter assemblies. Specifically, they are:

³ The amount of liquid metal contained in the assembly is a function of the number and size of the cooling channels.

- assembly bowing: fuel channel bowing and fuel assembly bowing have been experienced in existing BWRs and PWRs respectively (Karve, 2006 and Andersson et al., 2004), mainly because of neutron flux axial gradients. For the IPWR this is not expected to be of a concern since, relative to BWR fuel channels, which are the components that most resemble IPWR ducts, IPWR ducts are stiffer and subjected to less significant neutron flux axial gradients (because of the more uniform axial moderation with respect to a BWR).
- fission product inventory: the amount of fission products, especially gaseous fission products, contained in a duct is proportional to the fuel mass, and therefore to the duct size. In the event of duct failure, either during normal operation or because of assembly drop during refueling, fission gases would be released into the primary system. For a hypothetical UO₂-fueled IPWR this would probably constrain the assembly height. Instead, for the IPWR examined here the amount of “free” fission gases, i.e. available for release upon duct failure, is very small, due to the negligible fission gas release characterizing hydride fuels (see Chapter II).

If shorter assemblies had to be used, they would be stacked one on top of the other, with no plenum in between. This is to avoid the pressure drops associated with the contraction experienced by the coolant while flowing from the plenum into the assembly. The stacked assembly design would probably imply, relative to the design actually examined for the IPWR, a slight reduction in cycle length due the smaller amount of fuel loadable into the core.

IV.1. 3 Duct flat-to-flat distance and wall thickness

IV.1.3. 1 Design rationale and design limits

In principle, optimum duct dimensions could be obtained through a complex tradeoff analysis, which would maximize core power while satisfying constraints on mechanical stresses and radial deformation. However, when subjected to a certain pressure differential between inside and outside, hexagonal ducts, unlike cylindrical ducts,

experience stress concentrations at the corners. The stress level at these locations does not depend on the differential pressure, duct flat-to-flat distance and wall thickness only, but also on the shape of the corners, i.e. sharp vs rounded, and, if rounded, on the radii of the inner and outer fillets. As a consequence, the mentioned optimization procedure would have to include, in addition to the duct size optimization, a corner shape dimension optimization, which is outside of the scope of the IPWR project.

The selection of the duct dimensions was therefore made through a simplified procedure, consisting of examining the variation of the stress intensity and wall deformation with wall thickness for different duct sizes, temperature and pressure gradient. In particular, two temperature conditions were examined:

- a temperature gradient of 200°C (inside surface temperature = 500°C, outside surface temperature = 300°C) for normal operating conditions;
- an uniform temperature of 600°C for LOCA scenario.

The imposed pressure gradients ($p_{out} - p_{in}$) were equal to:

- +7.7 and -7.7 MPa for the non-collapsible duct design;
- +15.4 and -0.9 MPa for the collapsible duct design⁴.

The pressure gradients were selected as representative of typical steady-state operating conditions (positive values) and LOCA (negative values) respectively⁵. The numerical values of such gradients derive from the following considerations:

- as discussed in Chapter II, fission gas release for hydride fuels is almost negligible. Figure IV-2 shows⁶ that a fission gas release fraction of 10^{-3} , which is a conservative value for hydride fuels at the IPWR maximum allowed fuel temperature (650°C), yields a maximum internal pressurization of only 0.7 MPa.

⁴ In spite of not being expected during a LOCA, pressure gradients of -1.9 and -2.9 MPa were also analyzed. The purpose of this was to determine, using the margin from the duct internal pressure leading to failure, the maximum amount of IFBA (Integral Fuel Burnable Absorber) that can be loaded in each inverted assembly.

⁵ During normal operation and LOCA the primary system pressures are assumed to be 15.5 MPa and 0.1 MPa respectively.

⁶ Figure IV-2 was obtained by modeling the depletion of an inverted cell, using MCODE (Xu and Hejzlar, 2008). The amount of the major fission gases (Kr, I and Xe isotopes) was recorded as a function of burnup, and then used to determine the pressure evolution.

- the non-collapsible duct assembly is designed to be pressurized with helium during manufacture. Helium is added in an amount such that, upon assembly heating, an internal pressure of 7.8 MPa (=15.5-7.7) is reached. This pressure was chosen to limit the maximum pressure gradient that the duct can experience throughout its life, accounting for both normal operating conditions ($p_{out} = 15.5$ MPa) and LOCA scenario ($p_{out} = 0.1$ MPa).
- the collapsible duct assembly is not pressurized during manufacture, and the only pressure buildup during fuel burnup is that due to fission gas release. The pressure gradient chosen for LOCA scenario, i.e. 0.9 MPa, derives from assuming an internal pressurization of 1 MPa. The margin from the maximum pressurization shown in Figure IV-2, i.e. ~0.3 MPa, accounts for the higher temperature that may characterize the plenum gases during a LOCA scenario relative to the 370°C assumed in Figure IV-2.
- of the two burnable poisons examined for the IPWR, Er_2O_3 does not contribute to duct pressurization while IFBA, although responsible for He build up and therefore duct pressurization, is constrained in the amount that can be loaded in each assembly.

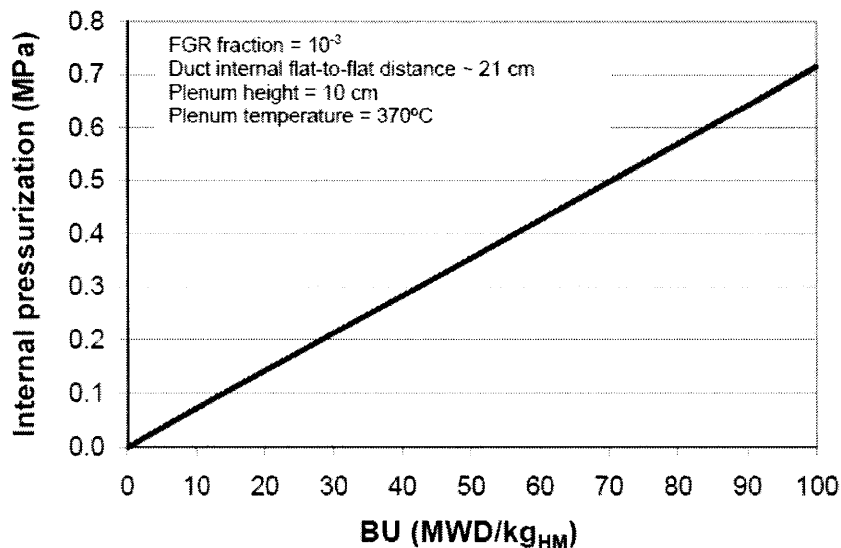


Figure IV- 2: Assembly internal pressurization due to fission gas release (collapsible duct design)

IV.1.3.1. 1 Stress intensity limit

The stress intensity at a particular location, S_{loc} , is defined as the maximum difference between two principal stresses, i.e.:

$$S_{loc} = \max(|\sigma_1 - \sigma_2|; |\sigma_1 - \sigma_3|; |\sigma_2 - \sigma_3|) \quad (IV.1)$$

where σ_1 , σ_2 and σ_3 are the principal stresses at the location of interest. The present analysis only considers the region of duct away from the bottom and top lids, since a comprehensive analysis of the stress discontinuities at the lid junctions would require optimization of the junction design/welding technique. In the region considered, pressure gradient- and temperature gradient-induced stresses are calculated using the COSMOSWorks code (SolidWorks, 2007), converted into wall average⁷ stress intensity, and compared with the prescribed limits. These limits differ depending on whether the analysis refers to normal operating conditions or LOCA, as discussed next.

Limits for normal operating conditions

For normal operating conditions the ASME limits (ASME, 1969) for primary general membrane stresses⁸ and for primary plus secondary stresses (the latter are inclusive of thermal gradient-induced stresses) are used. For primary general membrane stresses the following limit is imposed:

$$S_{max} = \max(\bar{S}_{loc}) \leq S_m = \min\left(\frac{2}{3}\sigma_y; \frac{1}{3}\sigma_u\right) \quad (IV.2)$$

⁷ According to the ASME code, the prescribed limits have to be compared with the maximum value of the average of the stress intensity across the wall of the duct, and not with the maximum local stress intensity (Rao, 2006, page 310).

⁸ According to Rao (2006, page 309): “Primary stresses are those developed by the imposed loadings and are necessary to satisfy the laws of equilibrium between external and internal forces. Such stresses (...) may cause distortion or collapse. Primary stresses are further divided into general membrane, local membrane, and bending. A general membrane stress extends over a large enough portion of the vessel shell so that an effective redistribution of load is not possible when the material yields. An example of such stress category is the membrane stress due to pressure. (...) A local primary stress is that produced by pressure or mechanical loading and is associated with a discontinuity effect. (...) A primary bending stress is the through thickness bending at a point caused by external loading.” Since the present analysis considers the region of the duct away from the bottom and top lids, local and bending stresses can be neglected. In particular, the extra stresses characterizing the duct corners, relative to those on the flat faces, should not be considered local primary stresses since they extend circumferentially over a short distance but axially over the whole duct length.

where S_{max} is the maximum value of the average stress intensity across the wall (Rao, 2006, page 310), S_m is the so-called allowable stress, σ_y and σ_u are the yield and the ultimate stresses of the material under consideration. For primary plus secondary stresses the criterion to be met is (ASME, 1969):

$$S_{max} = \max(\bar{S}_{loc}) \leq 3S_m = 3 \times \min\left(\frac{2}{3}\sigma_y; \frac{1}{3}\sigma_u\right) \quad (IV.3)$$

Since extensive hydrogen protection measures have been taken (limit on fuel temperature, oxidation of duct and cladding surfaces facing the fuel and, for the non-collapsible design, thick liquid metal gap between fuel and duct/claddings), for normal operation the values selected for σ_y and σ_u are those of the unhydrided and unirradiated⁹ Zr-2.5Nb at 350°C: $\sigma_y = 452$ MPa and $\sigma_u = 500$ MPa (see Table II-3 in Chapter II). By introducing these values in Eq.IV.2 and IV.3, the design criteria to satisfy become:

$$S_{max} \leq 167 \text{ MPa} \quad \text{for primary general membrane only} \quad (IV.4)$$

$$S_{max} \leq 501 \text{ MPa} \quad \text{for primary general membrane + secondary} \quad (IV.5)$$

Limits for LOCA scenario

The application, for the LOCA scenario, of the same limits as those for normal operating conditions would be excessively conservative since, in a LOCA, the duct has to be protected against catastrophic failure only, with no need of a safety margin from the yield stress. A core that has experienced a LOCA needs in fact to be completely replaced, and the assemblies will not be re-used. Hence, the stress intensity limit chosen for this accident scenario was simply the yield stress of unirradiated Zr-2.5Nb at the 600°C temperature assumed for LOCA, i.e. 84 MPa (per Eq. II-15 in Chapter II). The use of the unirradiated material yield stress is justified by the fact that at 600°C the duct material can be considered completely annealed. Hence, irradiation effects on the mechanical properties have disappeared.

⁹ Unirradiated conditions were conservatively chosen since yields stress increases with irradiation. Yield and ultimate strengths of irradiated Zr-2.5Nb are larger than those in unirradiated conditions by about 230 and 185 MPa respectively (Davies et al., 1994).

IV.1.3.1. 2 Lateral deformation limit

The differential pressure existing across the duct walls causes these walls to deform. In particular, they tend to deflect inward during normal operating conditions, and outward during transient and accident scenarios characterized by primary system depressurization (refueling, LOCA etc.). For the non-collapsible duct both these deflections need to be limited, for different reasons:

- inward deflection has to be limited to avoid fuel-duct gap closure, which would favor hydrogen pickup by the duct and consequent embrittlement of the latter;
- outward deflection has to be limited to avoid control blade interference.

For the collapsible duct, only the outward deflection has to be limited, since the inward deflection is designed as to cause extensive contact of the duct with the fuel.

When applied, the limit on maximum inward deformation is equal to the difference between the (pre-irradiation) width of the gap separating the fuel from the duct and the maximum lateral expansion expected for the fuel block, due to irradiation-induced swelling. Based on the gap sizing method described in Section III.2.1.2, this difference amounts to about 0.2 mm. The limit on maximum outward deformation is instead equal to the distance between the duct outer surface and the adjacent control blade. Since the width of the water gaps, i.e. of the channels between adjacent assemblies, and the thickness of the control blades were set equal to those of a typical BWR-5 (12.24 mm and 6.6 mm), the clearance between the duct and the blade is $0.5 \times (12.24 - 6.6) = 2.82$ mm. Due to the safety-related role of control rods, a safety factor of 2 is applied, and the maximum outward deformation was set to 1.4 mm.

IV.1.3. 2 Stress and deformation analysis

IV.1.3.2. 1 Analysis method for the non-collapsible duct design

Four duct flat-to-flat distances were initially considered for the non-collapsible duct: 100, 125, 150 and 219 mm. The latter value corresponds to an inverted assembly design having a footprint approximately equal to that of a typical 17×17 PWR assembly (~462 cm², Seabrook USAR, 2002). The other three were chosen as representative of possible smaller sizes. For each flat-to-flat distance, stress and deformation behavior was

investigated as a function of wall thickness using the COSMOSWorks code (SolidWorks, 2007). An example of COSMOSWorks output, for stresses, is shown in Figure IV- 3, while one on deformation is shown in Figure IV- 4.

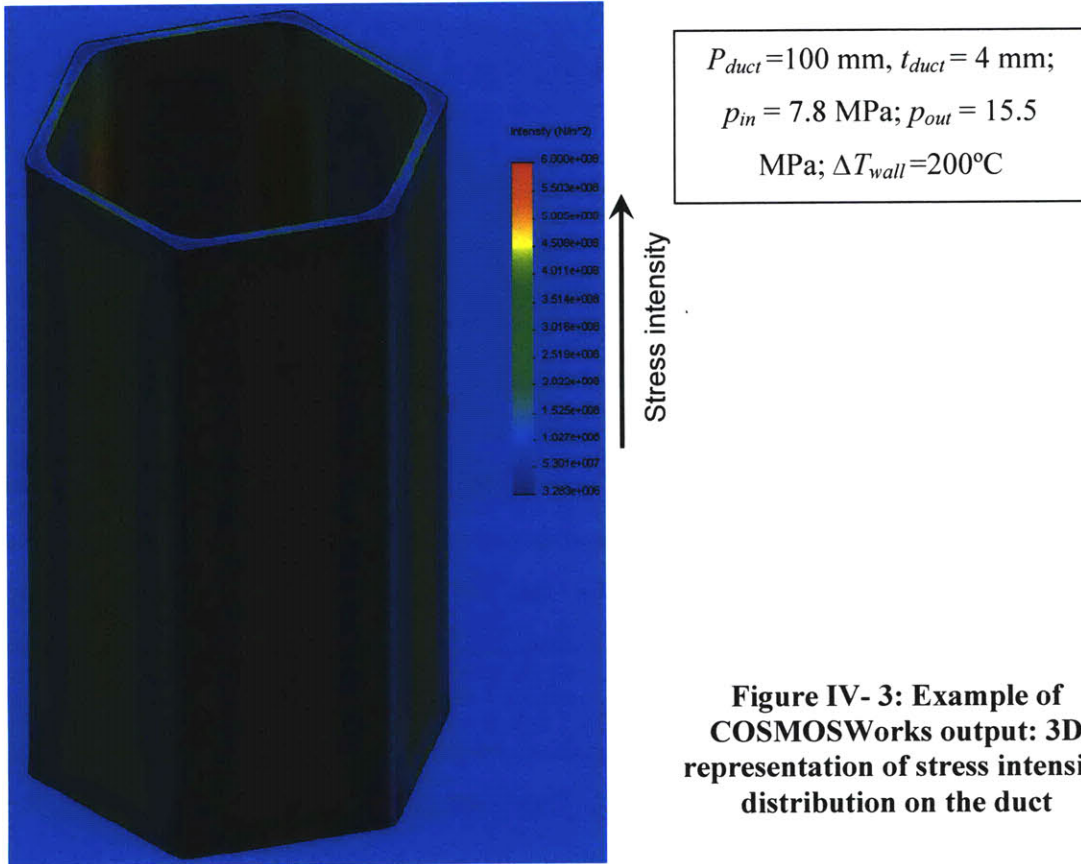


Figure IV- 3: Example of COSMOSWorks output: 3D representation of stress intensity distribution on the duct

In spite of the four sets of boundary conditions mentioned at the beginning of Section IV.1.3.1 ($p_{out} - p_{in} = \pm 7.7 \text{ MPa}$, each with and without thermal gradient across the duct walls¹⁰) only one boundary condition set was analyzed, i.e. $p_{out} - p_{in} = 7.7 \text{ MPa}$ with thermal gradient. This was done since, among the possible scenarios representing normal operating conditions, this is the most conservative from the stress intensity viewpoint, as discussed next and evident from Figure IV- 5 and Figure IV- 6. Conclusions on duct behavior during LOCA were inferred from results obtained for this scenario. Figure IV- 5

¹⁰ The scenarios without thermal gradient have to be analyzed since the COSMOSWorks code does not separate primary and secondary stresses, but gives a single stress intensity value for each spatial location. Therefore, in order to verify the safety criterion of Eq. IV.2, scenarios without thermal gradient have to be analyzed.

and Figure IV- 6, which derive from elaboration of plots similar to that shown in Figure IV- 3, show the variation of the stress intensity across, i.e. transversally, one of the six faces of a duct having flat-to-flat distance, P_{duct} , of 100 mm and wall thickness, t_{duct} , of 4 mm, for the four scenarios derived from the combination of the mentioned boundary conditions. It can be seen that:

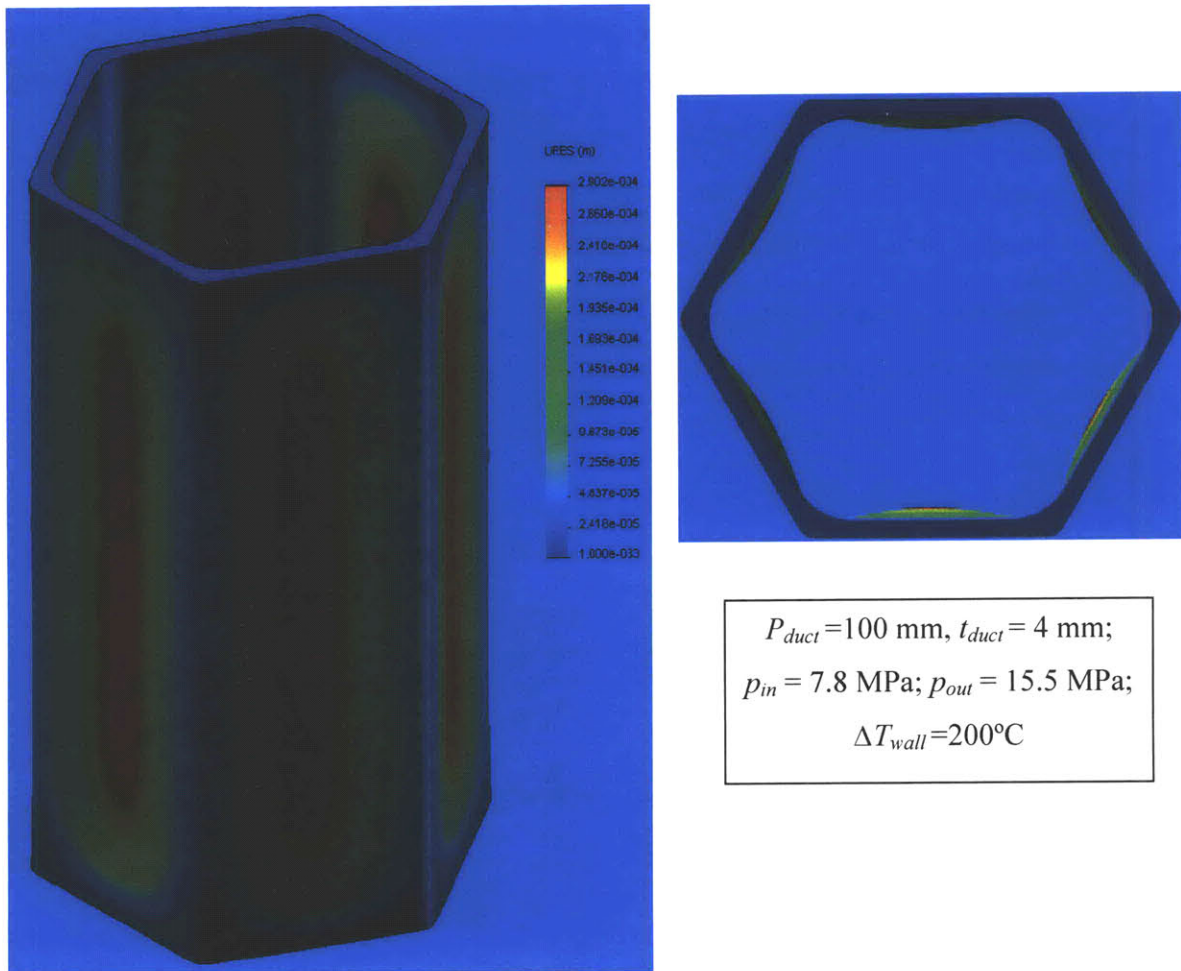


Figure IV- 4: Example of COSMOSWorks output: 3D representation of duct lateral deformation, enlarged 10 times. Max. deformation: $2.902 \times 10^{-4} \text{ m}$ (0.29 mm) inward

- the maximum stress intensity is that obtained in the compression scenario with thermal gradient ($\sim 330 \text{ MPa}$);
- when no thermal gradient is applied, i.e. in isothermal conditions, the maximum average stress intensity is almost independent on whether the duct is in

compression ($p_{out} - p_{in} = 7.7$ MPa) or in tension ($p_{out} - p_{in} = -7.7$ MPa). This implies that, if thermal gradient was not to be analyzed, from the average stress intensity viewpoint selecting the compression scenario or the tension one would not make any difference.

- the assumed thermal gradient generates compressive stresses on the outside surface of the duct and tensile ones on the inside surface: this is why the stress intensity on the outside surface is increased by the thermal gradient in the compression scenario, while it is decreased in the tension scenario. Vice versa, the assumed thermal gradient causes the stress intensity on the inside surface to decrease in the compression scenario, and to increase in the tensile scenario.
- as mentioned at the beginning of Section IV.1.3.1, the stress intensity peaks at the corners and, specifically, on their inside surface. This is evident in Figure IV- 3.

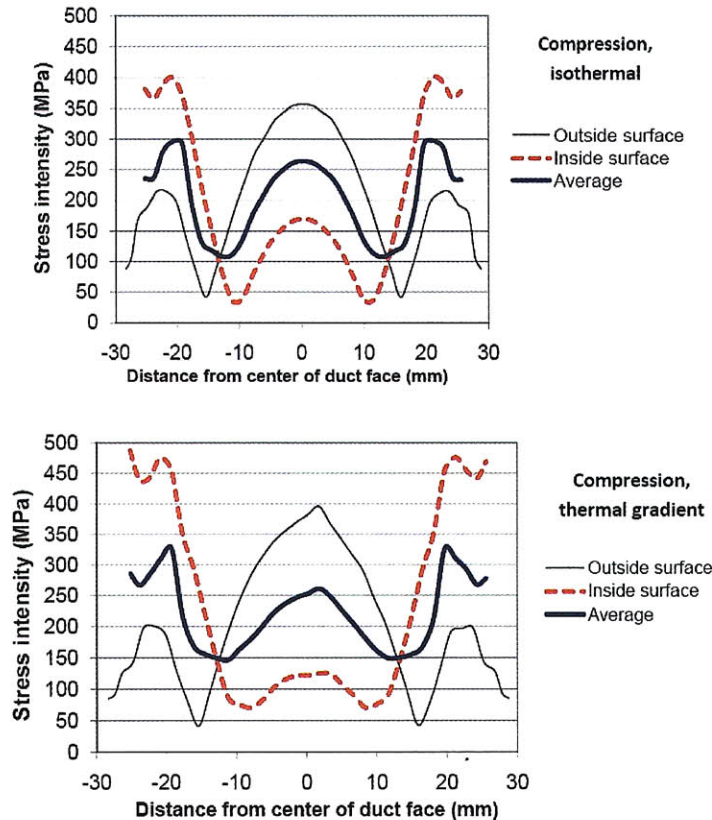


Figure IV- 5: Stress intensity distribution across a face of the duct ($P_{duct}=100$ mm, $t_{duct}=4$ mm; $p_{in} = 7.8$ MPa; $p_{out} = 15.5$ MPa; for thermal gradient case $\Delta T_{wall}=200^{\circ}\text{C}$)

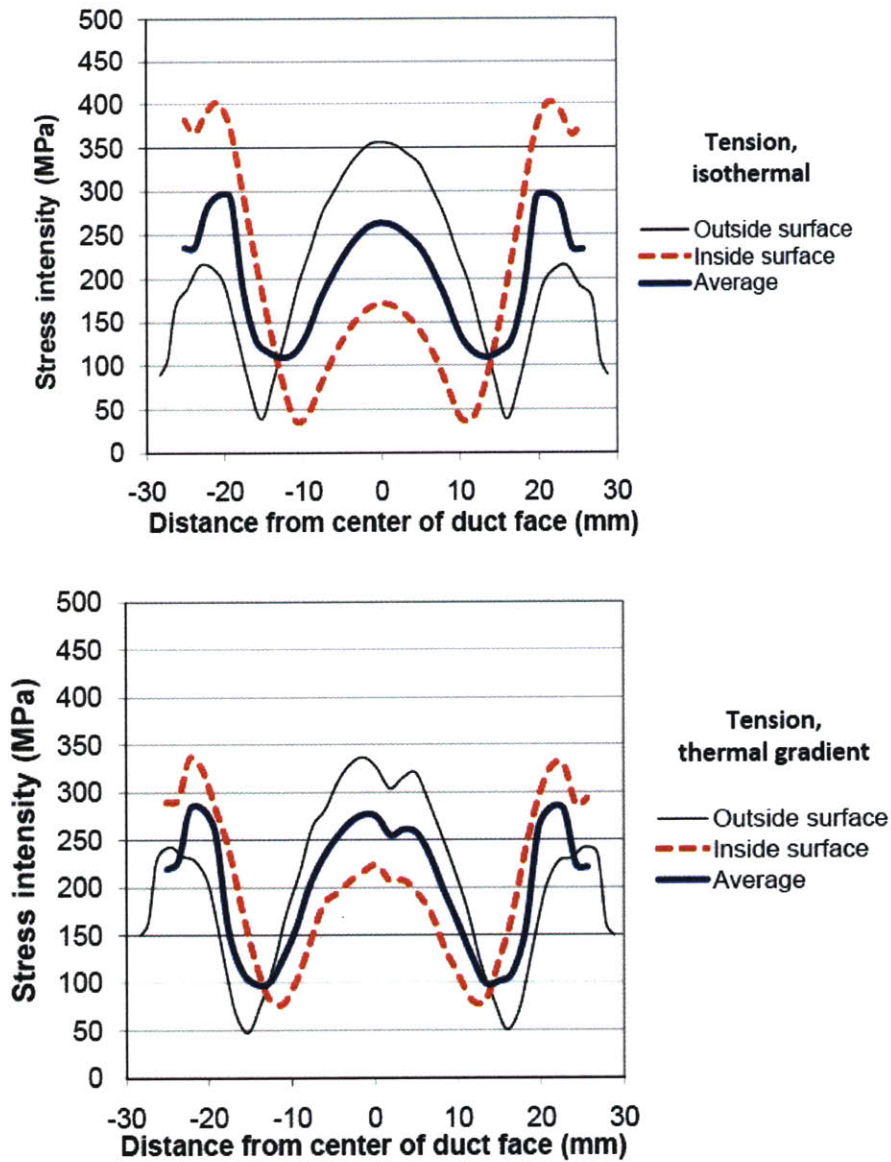


Figure IV- 6: Stress intensity distribution across a face of the duct ($P_{duct}=100$ mm, $t_{duct}=4$ mm; $p_{in} = 7.8$ MPa; $p_{out} = 0.1$ MPa; for thermal gradient case $\Delta T_{wall}=200^{\circ}\text{C}$)

IV.1.2.2. 2 Analysis method for the collapsible duct design

The collapsible duct design was analyzed with the same structural analysis code used for the non-collapsible design, i.e. COSMOSWorks (SolidWorks, 2007). However, only one duct size was considered, having a 9 mm wall thickness and a flat-to-flat distance that, to maximize the advantages of the collapsible duct concept, was the largest of the sizes

examined for the non-collapsible duct was considered, i.e. 219 mm. As mentioned before, this value results in an assembly footprint approximately equal to that of a typical 17×17 PWR assembly. For normal operating conditions, two fuel-duct gap widths were considered: 0.75 and 0.2 mm, representing two possible scenarios for the inward deformation allowed by the fuel prism. The latter was modeled as a hard body, incompressible, and no stress analysis was performed on it.

The LOCA analysis was instead performed by modeling the duct only, i.e. without the fuel prism, assuming an uniform temperature of 600°C and an internal and external pressure equal to 1 and 0.1 MPa respectively. To explore the feasibility of using IFBA as burnable poison, internal pressures of 2 and 3 MPa were also assumed.

IV.1.2.2. 3 Analysis results for the non-collapsible duct design

Figure IV- 7 summarizes the key results of the analysis performed to model the state of stress characterizing the non-collapsible duct during normal operating conditions. It shows that the two largest ducts, i.e. those having $P_{duct}=150$ mm and $P_{duct}=219$ mm, would require very thick walls ($t_{duct} > 12$ mm) to avoid the maximum average stress intensity to exceed the limit of 167 MPa established for normal operating conditions. This would negatively impact neutron economy, because of the extra-absorptions in the duct, and assembly thermal performance, because of the increased thermal resistance across the duct. These designs were therefore discarded for the non-collapsible duct concept. Regarding the two remaining duct sizes, the significant difference between them, in terms of minimum wall thickness satisfying the stress intensity constraint, i.e. $t_{duct}=5.8$ mm for $P_{duct}=100$ mm and $t_{duct}=8$ mm for $P_{duct}=125$ mm, drove the design of the IPWR ducts toward a flat-to-flat distance closer¹¹ to 100 mm than to 125 mm. In particular, based on the minimum duct wall thickness that, for the two smaller duct sizes examined, satisfies

¹¹ Saying that the duct flat-to-flat distance was fixed to a certain value, i.e. 100 mm for the non-collapsible design, would not be correct. In fact, the assembly sizing method discussed in Section IV. 2 requires, as input parameter, a “base” value for the fuel prism flat-to-flat distance. This value is only used for assembly construction, and the actual fuel prism flat-to-flat distance, P_{prism} , is lattice-dependent and slightly differs from it. This is because, given a $D_{ci}-t_{web}$ pair as input, the assembly construction is performed by searching for the number of fuel cell rings that more closely matches the “base” value selected for P_{prism} . This number of rings fixes the prism flat-to-flat distance which, consequently, will slightly differ from the base value. This, in turn, will lead to a value for P_{duct} close, but not exactly equal, to 100 mm.

the stress intensity criterion of Eq. IV.2, the following dependence on the fuel prism flat-to-flat distance has been identified¹²:

$$t_{duct} = 5.8 \left(\frac{P_{prism}}{85} \right)^{1.5} \quad (IV.6)$$

where t_{duct} , duct wall thickness, and P_{prism} , fuel prism flat-to-flat distance, are both expressed in mm. It is important to stress that this relation cannot be applied to fuel prisms having P_{prism} larger than about 110 mm, since it underpredicts the required wall thickness. This is not, however, a limitation for the design of the IPWR since, as discussed above, only non-collapsible designs having P_{prism} close to 85 mm (and therefore P_{duct} close to 100 mm) are analyzed.

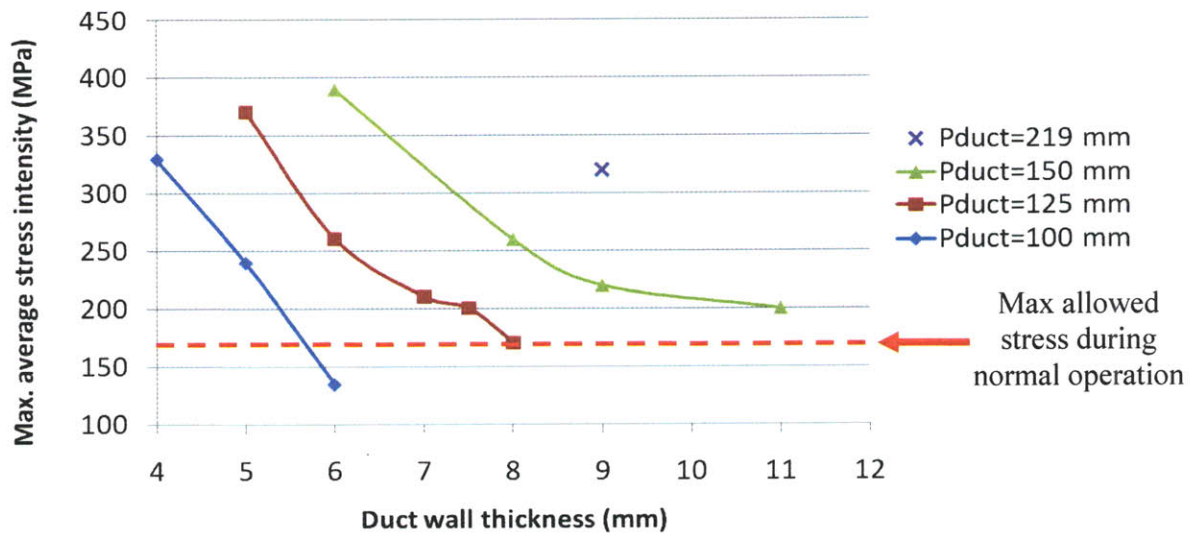


Figure IV- 7: Maximum average stress intensity for non-collapsible duct, as a function of wall thickness, for different duct sizes ($p_{in} = 7.8$ MPa; $p_{out} = 15.5$ MPa; $\Delta T_{wall} = 200^\circ\text{C}$)

Figure IV- 8 summarizes the key results of the deformation analysis performed on the non-collapsible duct. It shows the maximum duct lateral deformation as a function of wall thickness, for the four duct sizes examined. Since the state of stress considered for

¹² The dependence is on the prism flat-to-flat distance, P_{prism} , and not on the duct flat-to-flat distance, P_{duct} , since the precise value of the latter is not known a priori. As discussed in footnote 11, P_{prism} is determined first, and it is then used to calculate P_{duct} .

these calculations is compression ($p_{in} = 7.8$ MPa, $p_{out} = 15.5$ MPa), the lateral displacements shown are negative, i.e. inward. It has been verified, however, that the boundary conditions associated with a LOCA scenario, i.e. $p_{in} = 7.8$ MPa, $p_{out} = 0.1$ MPa, would yield outward displacements that, in absolute value, are very close to those shown in Figure IV- 8. This is because the absolute value of the pressure differential selected for the two scenarios analyzed, i.e. normal operating conditions and LOCA, is the same, i.e. 7.7 MPa.

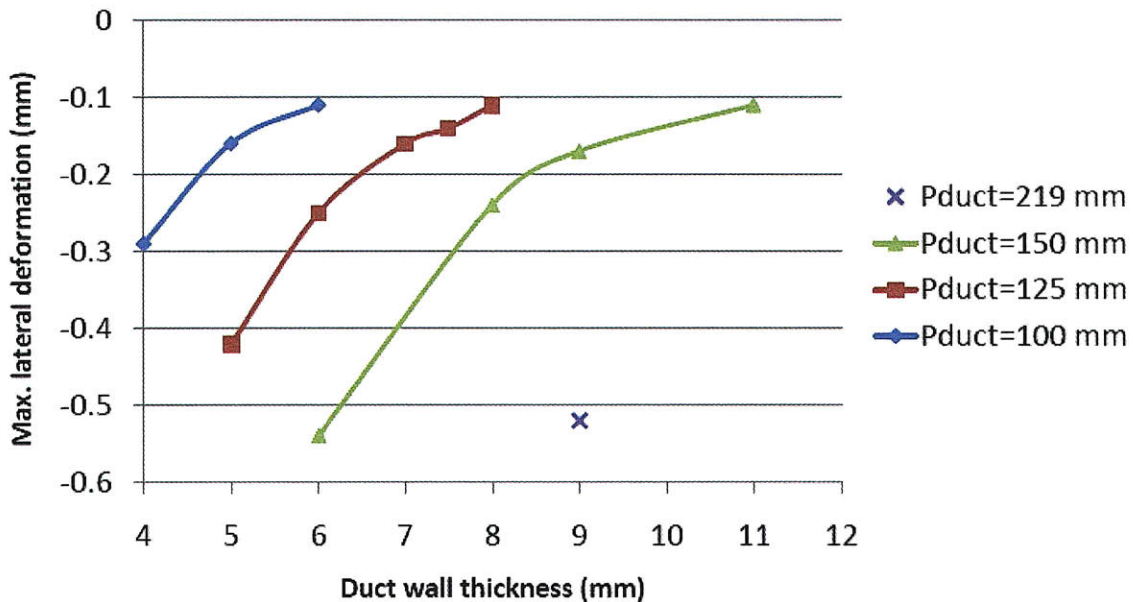


Figure IV- 8: Maximum duct lateral deformation for non-collapsible duct, as a function of wall thickness, for different duct sizes ($p_{in} = 7.8$ MPa; $p_{out} = 15.5$ MPa; $\Delta T_{wall}=200^{\circ}\text{C}$)

IV.1.2.2. 4 Analysis results for the collapsible duct design

The possibility for the duct to collapse onto the fuel prism allows a significant reduction in average-wall stress intensity. This is evident by comparing Figure IV- 9 to Figure IV- 10. The former shows the stress intensity in the duct if the fuel prism was not present. It can be seen that the average stress intensity significantly exceeds the limit value, i.e. 167 MPa, reaching values as high as 540 MPa near the duct corners. Figure IV- 10 shows the same plot, but referred to a real scenario in which the fuel prism is present, and the pre-

compression fuel-duct gap width is fixed to 0.75 mm. The maximum average stress intensity is now 330 MPa, i.e. it has decreased by about 40%.

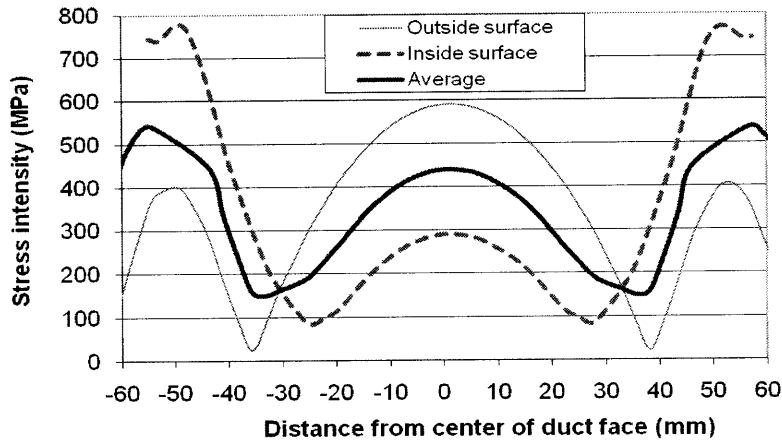


Figure IV- 9: Maximum average stress intensity for collapsible duct with no fuel prism present ($p_{in} = 0.1$ MPa, $p_{out} = 15.5$ MPa; $P_{duct}=219$ mm; $t_{wall}= 9$ mm)

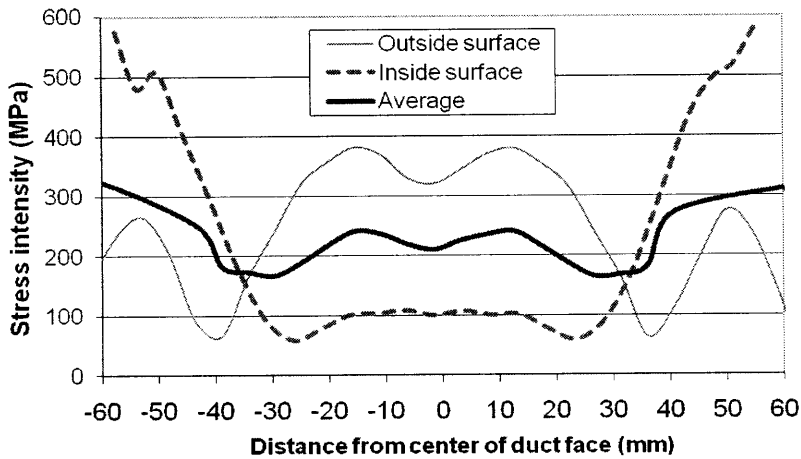


Figure IV- 10: Maximum average stress intensity for collapsible duct with fuel-duct gap width of 0.75 mm ($p_{in} = 0.1$ MPa, $p_{out} = 15.5$ MPa; $P_{duct}=219$ mm; $t_{wall}= 9$ mm)

The stress intensity can be reduced further, and below the stress intensity limit, if the pre-compression gap width is reduced to 0.2 mm, as shown in Figure IV- 11. In this scenario the section of duct internal surface that comes in contact with the fuel is very large, allowing for a more significant stress relief. The different extent with which the duct

touches the fuel, in this scenario relative to the previous one, can be inferred from Figure IV- 12, which shows the corresponding 3D representations of the components modeled (duct and incompressible fuel prism), in which a color scale is used to indicate different degrees of deformation. In particular, red is used to indicate the maximum allowed deformation, which coincides with the fuel-duct gap width. It can be seen that the narrower gap characterizing the model on the right causes the fuel-duct contact to extend over most of the duct face, while it is localized in the central region in the model on the left.

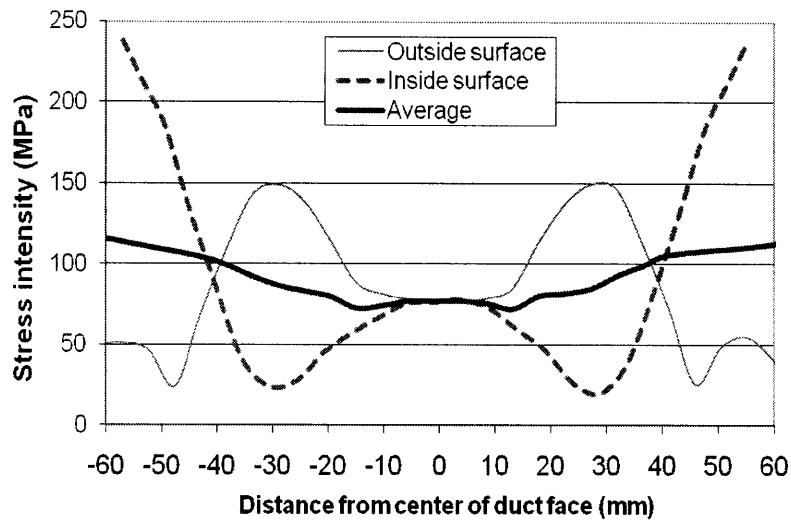


Figure IV- 11: Maximum average stress intensity for collapsible duct with fuel-duct gap width of 0.2 mm ($p_{in} = 0.1$ MPa, $p_{out} = 15.5$ MPa; $P_{duct} = 219$ mm; $t_{wall} = 9$ mm)

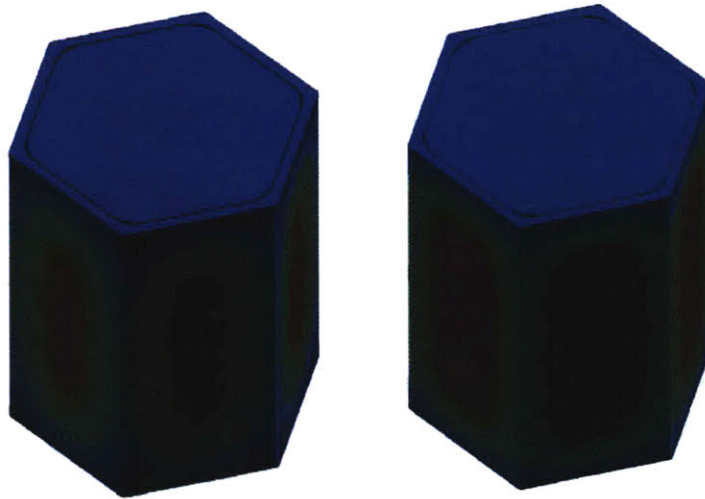


Figure IV- 12: Color scale showing regions of duct-fuel contact (red) and no-contact (other colors), for pre-compression gap widths of 0.75 mm (left) and 0.2 mm (right)

The results of the stress analysis for the LOCA scenario are shown in Figure IV- 13. It can be seen that the maximum average stress intensity is about 38 MPa, which is less than half the stress limit of 84 MPa fixed for LOCA. The corresponding outward lateral deformation was calculated to be 0.1 mm, which is well below the limit of 1.4 mm fixed in Section IV.1.2.1.2.

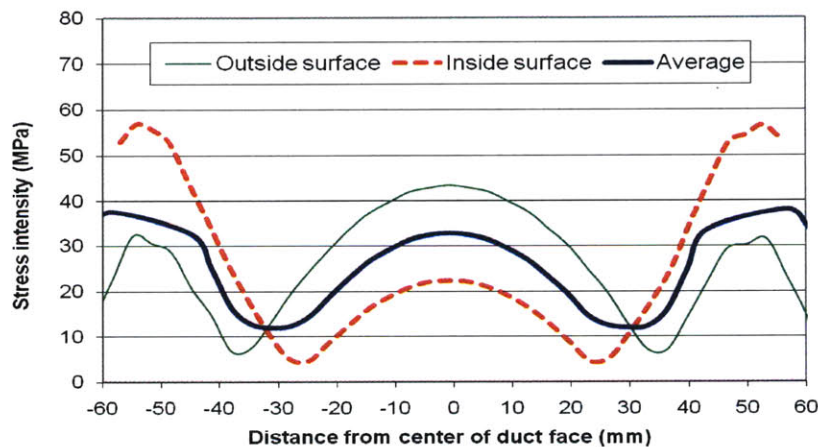


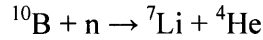
Figure IV- 13: Stress intensity profile for collapsible duct during LOCA scenario

As mentioned in Section IV.1.2.2.2, LOCA scenarios characterized by a higher duct internal pressure, i.e. 2 and 3 MPa, were also analyzed. The results are summarized in

Figure IV-14, which shows the variation of the maximum average stress intensity and of the maximum lateral displacement as a function of the internal pressurization. It can be seen that a margin of about 1.4 MPa exists between the expected duct internal pressurization (~0.7 MPa, from Figure IV-2) and the maximum allowed internal pressure which, as shown in Figure IV-14, is of about 2.1 MPa. This margin fixes the maximum amount of IFBA, which is one of the two types of burnable poisons investigated for the IPWR, that can be loaded in each assembly. Since, for the collapsible duct design, the upper plenum height is fixed to 10 cm, the number of moles of helium that, at an assumed temperature of 370°C, would lead to an extra-pressure of 1.4 MPa is:

$$\begin{aligned}
 n_{He} &= \frac{PV_{plenum}}{RT} \approx \frac{1.4 \times 10^6 \left[\left(\frac{\sqrt{3}}{2} P_{prism}^2 - \frac{N_{cells/A} \pi D_{co}^2}{4} \right) \times 0.1 \right]}{8.3145 \times (370 + 273)} = \\
 &= 26.2 \left(\frac{\sqrt{3}}{2} P_{prism}^2 - \frac{N_{cells/A} \pi D_{co}^2}{4} \right) \quad (IV.7)
 \end{aligned}$$

The maximum allowed IFBA loading can be obtained accounting for the fact that, in the He buildup reaction, one mole of ^{10}B generates one mole of He:



Thus, the maximum IFBA loading, expressed in mg ^{10}B per cm of fuel cell, is:

$$\begin{aligned}
 IFBA_{\max} &= \frac{\text{Max } ^{10}\text{B mass per assembly (mg)}}{N_{cells/A} \times L_{heated} \text{ (cm)}} \\
 &= \frac{n_{He} \times [^{10}\text{B atomic weight (mg/mol)}]}{N_{cells/A} \times L_{heated} \text{ (cm)}} \\
 &= \frac{26.2 \left(\frac{\sqrt{3}}{2} P_{prism}^2 - \frac{N_{cells/A} \pi D_{co}^2}{4} \right) \times 10012.9}{N_{cells/A} \times 367} \\
 &= \frac{715}{N_{cells/A}} \left(\frac{\sqrt{3}}{2} P_{prism}^2 - \frac{N_{cells/A} \pi D_{co}^2}{4} \right) \quad (IV.8)
 \end{aligned}$$

where both the prism flat-to-flat distance, P_{prism} , and the cooling channel outer diameter, D_{co} , are expressed in m. For a typical inverted assembly ($N_{cells/A}=169$; $P_{prism}=0.2$ m; $D_{co}=$

IV.1. 4 Conclusions on assembly duct design

The considerations presented in Sections IV.1. 1 and IV.1. 2, together with the stress and deformation analysis presented in Section IV.1. 3, allowed assessing two Zr-2.5Nb duct designs: a non-collapsible duct ($P_{duct} \sim 100$ mm; $t_{wall} \sim 5.8$ mm; $L_{duct} = 4.1-4.6$ m) and a collapsible duct ($P_{duct} \sim 219$ mm; $t_{wall} \sim 9$ mm; $L_{duct} = 3.8$ m). The former requires He to be introduced during manufacture, in an amount such that its compression due to fuel swelling and consequent liquid metal migration toward the upper plenum would result in an internal pressure of about 7.8 MPa. The latter does not require either initial pressurization or liquid metal bonding of the fuel-clad and fuel-duct gaps. The non-collapsible duct is designed to not come in hard contact with the fuel, which makes hydrogen uptake very unlikely. The collapsible duct, on the other hand, is allowed by design to touch the fuel, which makes its hydriding more likely. The latter phenomenon is however hindered by appropriate measures taken for both designs, consisting of duct internal surface oxidation or application of a ceramic coating.

Both designs meet the ASME design criteria on stresses during normal operation, as well as the deformation limits imposed to prevent assembly-control blade interference. They also meet the design criterion selected for LOCA.

IV. 2 Number of fuel cells per assembly

This section discusses the methodology used for the calculation of the number of fictitious¹⁴ fuel cells forming a fuel prism like that shown in Figure IV- 15. This parameter can be calculated only once the fuel cell geometry is known. Section IV.2. 1 is aimed at defining such geometry.

¹⁴ The term “fictitious” is used to stress the fact that the fuel prism is not made of fuel cells, i.e. it is manufactured as a single body. The division into cells is only performed to allow for its construction.

IV.1. 4 Conclusions on assembly duct design

The considerations presented in Sections IV.1. 1 and IV.1. 2, together with the stress and deformation analysis presented in Section IV.1. 3, allowed assessing two Zr-2.5Nb duct designs: a non-collapsible duct ($P_{duct} \sim 100$ mm; $t_{wall} \sim 5.8$ mm; $L_{duct} = 4.1-4.6$ m) and a collapsible duct ($P_{duct} \sim 219$ mm; $t_{wall} \sim 9$ mm; $L_{duct} = 3.8$ m). The former requires He to be introduced during manufacture, in an amount such that its compression due to fuel swelling and consequent liquid metal migration toward the upper plenum would result in an internal pressure of about 7.8 MPa. The latter does not require either initial pressurization or liquid metal bonding of the fuel-clad and fuel-duct gaps. The non-collapsible duct is designed to not come in hard contact with the fuel, which makes hydrogen uptake very unlikely. The collapsible duct, on the other hand, is allowed by design to touch the fuel, which makes its hydriding more likely. The latter phenomenon is however hindered by appropriate measures taken for both designs, consisting of duct internal surface oxidation or application of a ceramic coating.

Both designs meet the ASME design criteria on stresses during normal operation, as well as the deformation limits imposed to prevent assembly-control blade interference. They also meet the design criterion selected for LOCA.

IV. 2 Number of fuel cells per assembly

This section discusses the methodology used for the calculation of the number of fictitious¹⁴ fuel cells forming a fuel prism like that shown in Figure IV- 15. This parameter can be calculated only once the fuel cell geometry is known. Section IV.2. 1 is aimed at defining such geometry.

¹⁴ The term “fictitious” is used to stress the fact that the fuel prism is not made of fuel cells, i.e. it is manufactured as a single body. The division into cells is only performed to allow for its construction.

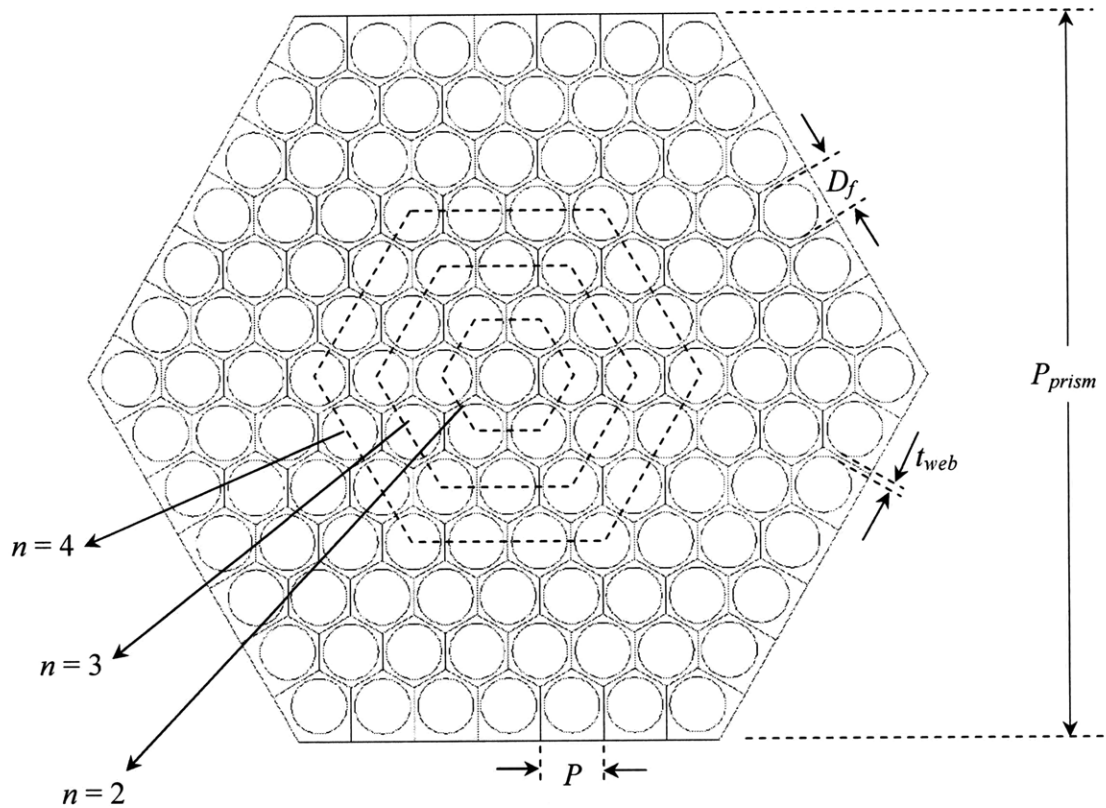


Figure IV- 15: Top view of a fuel prism, showing the fictitious division in fuel cells used for its construction

IV.2. 1 Fuel cell geometry

As indicated in Figure IV- 16 where, relative to Figure IV- 15, also the cooling channels cladding and the fuel-clad gaps are shown, the fuel prism can be seen as composed of three types of fictitious fuel cells: interior, side and corner cells. The interior cells are regular hexagons with flat-to-flat distance equal to the fuel cell pitch P and side length equal to:

$$L_{hex} = \frac{P}{\sqrt{3}} \quad (IV.10)$$

The side and corner cells are instead irregular pentagons with geometry completely defined by P and by the value chosen for the distance t_{border} . For all the assembly geometries examined, the latter parameter is fixed to 3 mm: a value that is considered large enough to allow manufacture of the fuel prism, i.e. the drilling of the outermost ring

of fuel holes, and small enough to avoid overheating of the fuel located at the prism periphery¹⁵. By looking at the side cells, it can be easily demonstrated that the length of their side perpendicular to the fuel prism external border is:

$$L_{pent,1} = \frac{1}{2}L_{hex} + \frac{D_f}{2} + t_{border} = \frac{1}{2} \frac{P}{\sqrt{3}} + \frac{P - t_{web}}{2} + t_{border} = P \frac{1 + \sqrt{3}}{2\sqrt{3}} - \frac{t_{web}}{2} + t_{border} \quad (IV.11)$$

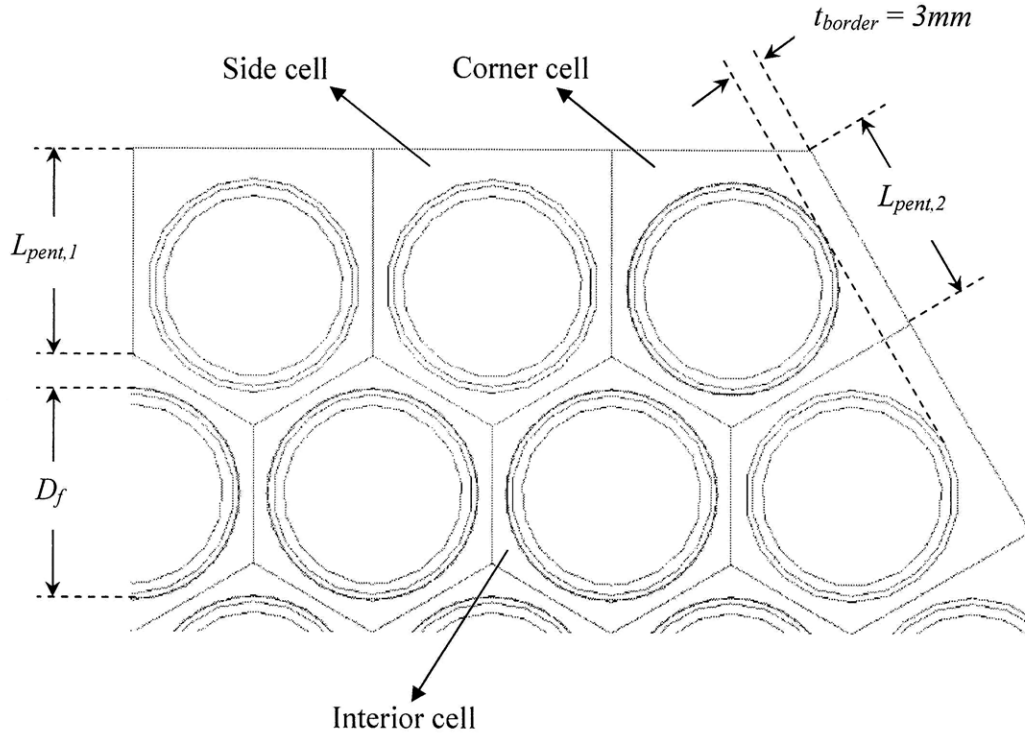


Figure IV- 16: Fuel prism corner region, showing interior, side and corner cells

As for the corner cells, the length of the side coinciding with the prism external border can be obtained by applying the Pythagorean theorem to the rectangular triangles ABC and ACD shown in Figure IV- 17. The length of the segment AC can in fact be expressed as:

$$\overline{AC} = \sqrt{L_{pent,1}^2 + L_{pent,2}^2} \quad (IV.12)$$

¹⁵ Unlike any other point in the fuel prism, those located at the prism periphery, i.e. in the fuel meat beyond the outermost hole ring, are cooled by one ring of channels only.

but also as:

$$\overline{AC} = \sqrt{(\overline{AD})^2 + (\overline{CD})^2} = \sqrt{\left(\frac{P}{\sqrt{3}} + \frac{D_f}{2} + t_{border}\right)^2 + (L_{pent,2} - 0.5P)^2} \quad (IV.13)$$

By equating the right hand sides of Eqs. IV.12 and IV.13 the pentagon side length $L_{pent,2}$ can be obtained:

$$\begin{aligned} L_{pent,2} &= \frac{1}{P} \left[\left(\frac{P}{\sqrt{3}} + \frac{D_f}{2} + t_{border} \right)^2 - L_{pent,1}^2 + \frac{P^2}{4} \right] = \\ &= \frac{1}{\sqrt{3}} \left[\frac{\sqrt{3}-2}{4} P + D_f + \frac{1+\sqrt{3}}{2} t_{web} + (1-\sqrt{3}) t_{border} \right] + \\ &\quad + \frac{1}{P} \left(\frac{D_f^2}{4} + D_f t_{border} - \frac{t_{web}^2}{4} + t_{web} t_{border} \right) \end{aligned} \quad (IV.14)$$

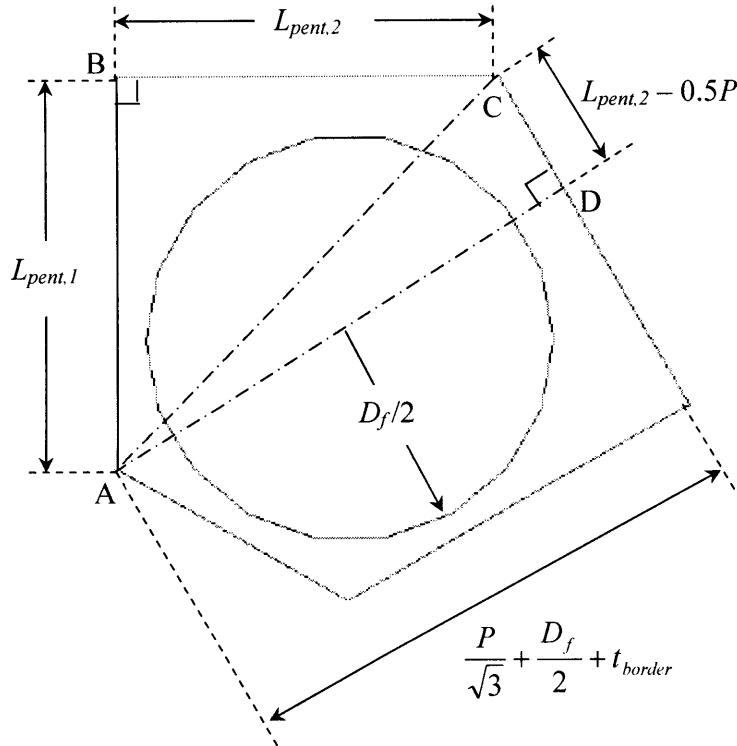


Figure IV- 17: Corner fuel cell: trigonometric considerations used to obtain $L_{pent,2}$

IV.2. 2 Computation of the number of fuel cells per assembly

The number of fuel cells per assembly is a function of three geometric parameters, shown in Figure IV- 15: fuel prism flat-to-flat distance, P_{prism} , fuel cell pitch, P , and fuel web thickness, t_{web} . Of these parameters P_{prism} and P are not input variables to the core construction algorithm, but derive from the application of some of the design constraints discussed in Chapter II. For simplicity, this section assumes that the application of those constraints has already been performed and that, therefore, these parameters are known¹⁶. Before discussing the methodology used to determine the number of fuel cells per assembly it is important to note that, in spite of being an input parameter for this calculation, P_{prism} can have a final value slightly different from the initial value used as input. This is because, as explained below, the values selected for the independent design variables used to construct the core, i.e. cooling channel diameter D_{ci} and fuel web thickness t_{web} , are likely to be incompatible with the value of P_{prism} resulting from the application of the structural constraints. The reason, simply geometrical, is that if P_{prism} was fixed a priori it is extremely unlikely that the modular repetition of the fuel cell defined by D_{ci} and t_{web} yields a fuel prism having a flat-to-flat distance equal to P_{prism} . Therefore, once D_{ci} and t_{web} have been selected, the resulting fuel cell is modularly repeated, ring by ring, until the fuel prism defined by a certain ring has a flat-to-flat distance close (either below or above) to the value of P_{prism} derived from the application of the structural constraints. At this point no more cell rings are added, and the fuel cell array so constructed defines the final fuel prism geometry, and therefore the actual value of P_{prism} .

By arranging hexagons side by side as to form a fuel prism like that shown in Figure IV- 15, and inspecting how the fuel prism flat-to-flat distance varies with the number of fuel

¹⁶ The fuel prism flat-to-flat distance derives from the application of (1) the stress and deformation constraints discussed in Section IV. 1, which determined the duct flat-to-flat distance and wall thickness, and (2) the constraint on fuel-duct gap thickness discussed in Section III.2.1.2, which determined the width of this gap. The fuel cell pitch is a function of the cooling channel inner diameter and fuel web thickness, which are independent design variables, fuel-clad gap width and clad thickness. The last two parameters are obtained from the cooling channel inner diameter using the structural constraint relations presented in Section III.2.1.1.

cell rings, n , the latter being defined as shown in Figure IV- 15, it can be demonstrated that:

$$P_{prism} = \begin{cases} P & \text{if } n = 1 \\ 2L_{pent,1} + (3n - 4)\frac{P}{\sqrt{3}} & \text{if } n > 1 \end{cases} \quad (IV.15)$$

By solving Eq. IV.15 for the number of fuel cell rings we get:

$$n = \begin{cases} 1 & \text{if } P_{prism} \leq P \\ \text{round} \left\{ \frac{1}{3} \left[(P_{prism} - 2L_{pent,1}) \frac{\sqrt{3}}{P} + 4 \right] \right\} & \text{if } P_{prism} > P \end{cases} \quad (IV.16)$$

where, in order to preserve the physical meaning of n , the function “round” has been added to the result of the mathematical derivation of n from Eq. IV.15. Eq. IV.16 is the key expression for the design of the fuel prism. In fact, once the value of P_{prism} , derived from the application of the structural constraints, is known, it is used in Eq. IV.16 to compute the number of fuel cell rings. Then, the resulting value of n is introduced in Eq. IV.15 to calculate the actual value of P_{prism} which, because of the use of the function “round” will be likely different, but close, to that deriving from the application of the structural constraints and used as input for this calculation. The number of fuel cell rings is also used to calculate the number of fuel cells forming the prism, as:

$$N_{cells/a} = 1 + \sum_{i=1}^n 6(i-1) \quad (IV.17)$$

which completes the sizing of the fuel prism.

IV. 3 Number of assemblies in the core

The number of assemblies that can be fit into the core is a function of three parameters: core shroud radius, R_{core} , assembly duct flat-to-flat distance, P_{duct} , and inter-assembly water gap width, t_{inter} . Of them, P_{duct} is the only parameter that was varied in the design of the IPWR, since the core radius was set equal to the radius of the smallest circle that, in

the reference core, encloses all the assemblies¹⁷, i.e. 1.831 m (Seabrook USAR, 2002), and t_{inter} was fixed to 12.24 mm to accommodate control rods, as discussed in Section III.2.1.7. Figure IV- 18 shows an example of possible assembly arrangement in the core.

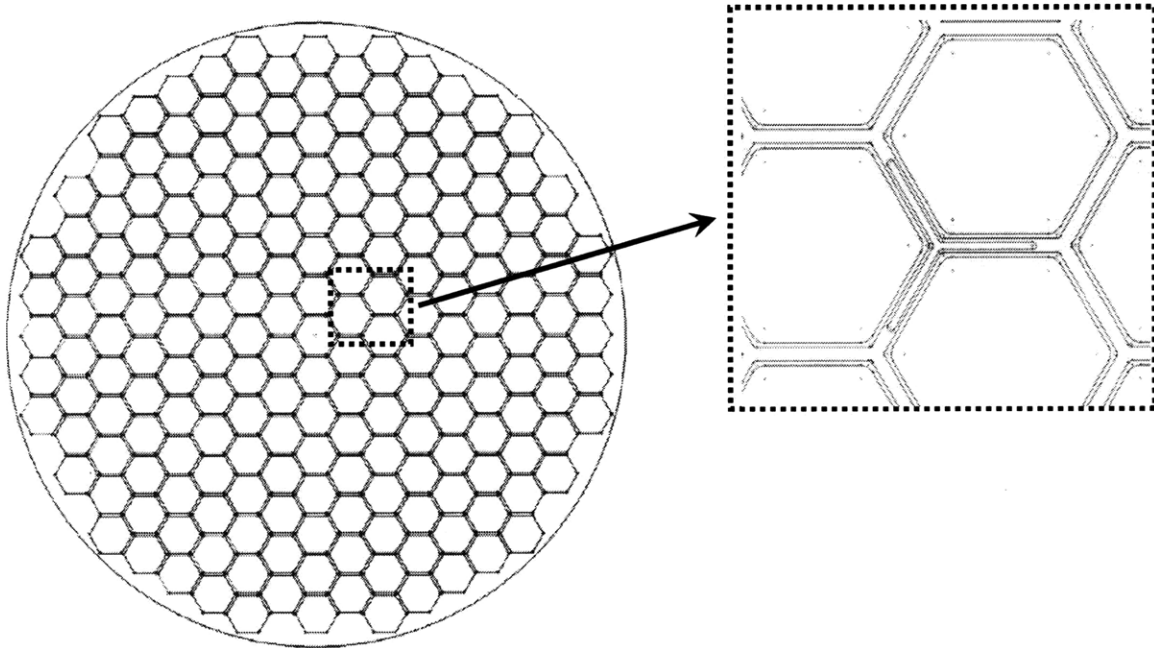


Figure IV- 18: Example of assembly arrangement in the core (left) and detail showing control rod (right)

The number of assemblies in the core is determined by means of a numerical algorithm that calculates the number of hexagons, each having flat-to-flat distance equal to:

$$P_{unit} = P_{duct} + t_{inter} \tag{IV.18}$$

that can be inscribed into a circle having radius equal to R_{core} . This algorithm was developed by inspection, i.e. by looking at the number of the mentioned hexagons that

¹⁷ This was done so that the IPWR core can fit into a vessel of the same size of that of the reference plant. This avoids the design of a larger core shroud, even though the shape of the shroud will be circular and not step-like as in typical LWRs.

can fit into a circle, whose radius is progressively increased. The algorithm has a recursive form that can be expressed as:

```

if  $R_{core} < R_1$             $\rightarrow N_{assy} = N_0$ 
else if  $R_1 \leq R_{core} < R_2$     $\rightarrow N_{assy} = N_1$ 
.....
else if  $R_i \leq R_{core} < R_{i+1}$   $\rightarrow N_{assy} = N_i$ 
...
else if  $R_{112} \leq R_{core} < R_{113}$   $\rightarrow N_{assy} = N_{112}$ 
end

```

where R_1, R_2 etc., which are functions of P_{unit} of the form:

$$R_i = \sqrt{\frac{K_i}{3}} P_{unit} \quad (IV.19)$$

are the radii of the circles that, starting from a radius equal to zero, determine the increase in the number of inscribed hexagons by an integer amount. The values of K_1, K_2 etc. as well as N_0, N_1, N_2 etc. are summarized in Table IV- 1 and Table IV- 2 respectively. As it can be seen, the algorithm can only be used for core geometries containing up to 1255 assemblies; extension of the algorithm beyond this limit is possible.

Table IV- 1: Coefficients K implemented in the algorithm for the calculation of the number of assemblies in the core

K ₁	1	K ₂₄	211	K ₄₇	427	K ₇₀	652	K ₉₃	892
K ₂	7	K ₂₅	217	K ₄₈	436	K ₇₁	673	K ₉₄	907
K ₃	16	K ₂₆	229	K ₄₉	439	K ₇₂	679	K ₉₅	919
K ₄	19	K ₂₇	247	K ₅₀	457	K ₇₃	700	K ₉₆	931
K ₅	31	K ₂₈	256	K ₅₁	469	K ₇₄	703	K ₉₇	961
K ₆	37	K ₂₉	259	K ₅₂	481	K ₇₅	709	K ₉₈	964
K ₇	49	K ₃₀	268	K ₅₃	484	K ₇₆	721	K ₉₉	973
K ₈	52	K ₃₁	271	K ₅₄	487	K ₇₇	733	K ₁₀₀	976
K ₉	61	K ₃₂	283	K ₅₅	496	K ₇₈	739	K ₁₀₁	988
K ₁₀	73	K ₃₃	304	K ₅₆	511	K ₇₉	763	K ₁₀₂	997
K ₁₁	79	K ₃₄	307	K ₅₇	532	K ₈₀	772	K ₁₀₃	1009
K ₁₂	91	K ₃₅	313	K ₅₈	547	K ₈₁	784	K ₁₀₄	1027
K ₁₃	100	K ₃₆	325	K ₅₉	553	K ₈₂	787	K ₁₀₅	1036
K ₁₄	103	K ₃₇	331	K ₆₀	559	K ₈₃	793	K ₁₀₆	1039
K ₁₅	112	K ₃₈	343	K ₆₁	571	K ₈₄	796	K ₁₀₇	1057
K ₁₆	127	K ₃₉	361	K ₆₂	589	K ₈₅	811	K ₁₀₈	1063
K ₁₇	133	K ₄₀	364	K ₆₃	592	K ₈₆	817	K ₁₀₉	1069
K ₁₈	139	K ₄₁	367	K ₆₄	613	K ₈₇	829	K ₁₁₀	1075
K ₁₉	151	K ₄₂	373	K ₆₅	625	K ₈₈	832	K ₁₁₁	1087
K ₂₀	169	K ₄₃	388	K ₆₆	628	K ₈₉	859	K ₁₁₂	1093
K ₂₁	172	K ₄₄	397	K ₆₇	631	K ₉₀	871	K ₁₁₃	1108
K ₂₂	181	K ₄₅	409	K ₆₈	637	K ₉₁	877		
K ₂₃	196	K ₄₆	421	K ₆₉	643	K ₉₂	889		

Table IV- 2: Parameter N implemented in the algorithm for the calculation of the number of assemblies in the core

N ₀	0	N ₂₃	211	N ₄₆	463	N ₆₉	733	N ₉₂	1015
N ₁	1	N ₂₄	223	N ₄₇	475	N ₇₀	745	N ₉₃	1027
N ₂	7	N ₂₅	241	N ₄₈	487	N ₇₁	757	N ₉₄	1039
N ₃	13	N ₂₆	253	N ₄₉	499	N ₇₂	769	N ₉₅	1045
N ₄	19	N ₂₇	265	N ₅₀	511	N ₇₃	781	N ₉₆	1069
N ₅	31	N ₂₈	271	N ₅₁	517	N ₇₄	793	N ₉₇	1081
N ₆	37	N ₂₉	283	N ₅₂	529	N ₇₅	805	N ₉₈	1093
N ₇	43	N ₃₀	289	N ₅₃	535	N ₇₆	823	N ₉₉	1105
N ₈	55	N ₃₁	301	N ₅₄	547	N ₇₇	835	N ₁₀₀	1117
N ₉	61	N ₃₂	313	N ₅₅	559	N ₇₈	847	N ₁₀₁	1129
N ₁₀	73	N ₃₃	325	N ₅₆	583	N ₇₉	859	N ₁₀₂	1141
N ₁₁	85	N ₃₄	337	N ₅₇	595	N ₈₀	871	N ₁₀₃	1153
N ₁₂	91	N ₃₅	349	N ₅₈	601	N ₈₁	877	N ₁₀₄	1159
N ₁₃	97	N ₃₆	361	N ₅₉	613	N ₈₂	889	N ₁₀₅	1171
N ₁₄	109	N ₃₇	367	N ₆₀	637	N ₈₃	901	N ₁₀₆	1183
N ₁₅	121	N ₃₈	379	N ₆₁	649	N ₈₄	913	N ₁₀₇	1195
N ₁₆	127	N ₃₉	385	N ₆₂	661	N ₈₅	925	N ₁₀₈	1207
N ₁₇	139	N ₄₀	397	N ₆₃	673	N ₈₆	931	N ₁₀₉	1219
N ₁₈	151	N ₄₁	409	N ₆₄	685	N ₈₇	943	N ₁₁₀	1231
N ₁₉	163	N ₄₂	421	N ₆₅	691	N ₈₈	955	N ₁₁₁	1243
N ₂₀	175	N ₄₃	433	N ₆₆	703	N ₈₉	967	N ₁₁₂	1255
N ₂₁	187	N ₄₄	439	N ₆₇	709	N ₉₀	991		
N ₂₂	199	N ₄₅	451	N ₆₈	721	N ₉₁	1003		

The calculation of the total number of assemblies completes the geometric design of the core.

Chapter V

Core pressure drop

The pressure drop experienced by the coolant flowing through an inverted channel is calculated as sum of four terms: gravity, acceleration, friction and form losses. Form losses, which include entry and exit losses only, are not embedded in the friction term but treated separately for clarity. The pressure drop across the generic i -th axial zone¹ is therefore calculated as:

$$(dp)_i = (dp_g)_i + (dp_a)_i + (dp_f)_i + (dp_l)_i \quad (V-1)$$

where the subscripts g , a , f and F identify gravity, acceleration, friction and form respectively.

While expressions for the gravity and acceleration terms are the typical ones, friction and form pressure drop contributions require particular attention since, in presence of twisted tapes (TTs), ad-hoc correlations must be used. For this reason, while for the gravity and acceleration terms only the corresponding formulas are shown (Section V. 1 and V. 2), a more detailed discussion is presented on friction factor (Section V. 3) and form loss calculation (Section V. 4).

V. 1 Gravity pressure drop

Gravity pressure drop across the i -th axial zone is computed as:

$$(dp_g)_i = (\rho_c)_i \times g \times dz \quad (V-2)$$

¹ In order to accurately capture the fluid property axial variation, the code developed for the thermal hydraulic study of the inverted core divides the cooling channel in about 500 axial zones, each having length dz .

where ρ_c is the bulk coolant density, equal to the density of the subcooled liquid, ρ_l , before Onset Of Significant Voids (OSV), and to the mixture density after OSV. In this latter case ρ_c is calculated as:

$$(\rho_c)_i = \alpha_i \rho_g + (1 - \alpha_i) \rho_l \quad (V-3)$$

where ρ_l is the liquid bulk density. The void fraction is calculated using the homogeneous model in saturated boiling and the Levy correlation (Levy, 1967) in subcooled boiling.

V. 2 Acceleration pressure drop

Acceleration pressure variations are due to coolant density and flow area changes. The pressure drop due to coolant density variation, across the i -th axial zone, is computed as:

$$(dp_a)_i = (G^2)_i \left(\frac{1}{(\rho_c)_i} - \frac{1}{(\rho_c)_{i-1}} \right) \quad (V-4)$$

The mass flux G is the actual mass flux at the axial zone under consideration, i.e. it is computed by dividing the mass flow rate by the actual flow area of axial zone i , which is the empty tube flow area where the TT is not present, or the reduced flow area where the TT is present.

For all the geometries considered, acceleration pressure drops/gains due to flow area changes (not inclusive of the associated unrecoverable pressure losses, treated separately in Section V. 4) are explicitly calculated only at the channel inlet (flow area contraction from the core lower plenum) and at the channel outlet (flow area expansion to the core upper plenum). The acceleration terms due to flow area contraction and expansion at the inlet and outlet of short-length twisted tapes (SLTTs) are assumed to reciprocally cancel; in fact, because of the short length of SLTTs, the coolant density variation between their two ends is negligible. The arithmetic sum of the pressure variations at the channel inlet and outlet is given by:

$$(\Delta p_a)_{area_change} = (\Delta p_a)_{contr_inlet} + (\Delta p_a)_{exp_outlet} = \left[\frac{G^2}{2\rho_c} \right]_{i=1} - \left[\frac{G^2}{2\rho_c} \right]_{i=last_node} \quad (V-5)$$

where the convention of a positive sign for a pressure drop and a negative sign for a pressure gain is used, as done in the rest of this work.

V. 3 Friction pressure drop

Friction pressure drop across the i -th axial zone is computed as:

$$(dp_f)_i = \begin{cases} (f \times V_{visc})_i \frac{dz}{D_{ci}} \frac{G_{empty}^2}{2(\rho_l)_i} & \text{if } z_i \leq z_{ONB} \\ (f)_i \frac{dz}{D_{ci}} \frac{G_{empty}^2}{2(\rho_c)_i} & \text{if } z_{ONB} < z_i < z_{OSB} \\ (f \times V_{visc})_i \frac{dz}{D_{ci}} \frac{G_{empty}^2}{2\rho_f} (\phi_{lo}^2)_i & \text{if } z_i \geq z_{OSB} \end{cases} \quad (\text{V-6})$$

where:

- f_i is the isothermal liquid-only Darcy's friction factor at axial location i , whose computation is discussed in detail in Section V.3.1 for all the designs examined;
- V_{visc} is the coolant viscosity correction factor, which accounts for the coolant viscosity difference between the heated walls and the bulk. In the present work, consistent with the vast majority of the literature consulted, this factor is expressed as:

$$V_{visc} = K \left(\frac{\mu_w}{\mu_b} \right)^n \left(\frac{D_e}{D_{ci}} \right) \quad (\text{V-7})$$

where μ_w and μ_b are the coolant dynamic viscosities at the wall and coolant bulk temperature, respectively, D_e and D_{ci} are the equivalent diameter and the tube inside diameter, and $K=1$. The value assigned to the exponent n is²:

$$n = \begin{cases} 0.28 & \text{where TTs are not present (empty tubes and between SLTTs)} \\ 0.35 & \text{where TTs are present (HLTT designs, and MSLTT designs where TTs are present)} \end{cases}$$

The value chosen for n in absence of TTs is that suggested by Leung et al. (2005)³, and derives from experiments performed with water flowing through

² The meaning of the acronyms is as follows: SLTTs (Short Length Twisted Tapes); HLTT (Half Length Twisted Tape); MSLTTs (Multiple Short Length Twisted Tapes).

tubular test sections at about 10 MPa. The value for n where TTs are present is instead that suggested by Lopina and Bergles (1969), who also introduced the exponent correction D_e/D_{ci} . Such correction is needed because, unlike in empty tubes where the entire wall surface in contact with the fluid is heated, in TT-provided tubes the two TT faces do not dissipate heat (less than 3% of the heat flowing through the tube walls is in fact dissipated through the TT) and consequently there is no difference in viscosity between the fluid bulk and the fluid in contact with the TT.

- G_{empty} is the coolant mass flux along the channel assumed to be TT-free (regardless of whether a TT is actually present in axial zone i or not⁴);
- z_{ONB} and z_{OSB} are the Onset of Nucleate Boiling and Onset of Saturated Boiling axial locations respectively;
- ϕ_{lo}^2 is the liquid-only two-phase multiplier, calculated using the EPRI-Columbia correlation (Reddy et al., 1982). The reasons that lead to the choice of this correlation, as well as the correlation itself, are presented in Section V.3.2.

It is important to note that, between ONB and OSB, i.e. in the subcooled boiling region, the friction pressure drop is calculated as if the channel was unheated. This was done for two reasons: (1) it is consistent with the pressure drop vs applied heat flux trend observed by Tong et al. (1996), shown in Figure V-A. 15 in Appendix A of this chapter and (2) the only two-phase multiplier correlation for subcooled boiling found in the literature, i.e. the Tarasova correlation (Tarasova et al., 1966) was found to slightly overpredict the pressure drop, especially at the high mass flux conditions characterizing the IPWR. The rationale behind this choice is that the extra-friction due to the bubbles at the wall is not

³ In the literature there is no universal agreement on the value to assign to the coefficient n , for liquids flowing in heated channels. Probably the most widely used value is $n=0.14$ (combined with $K=1.02$), which was suggested by Sieder and Tate (1936). Other authors are consistent in choosing a unity value for K , while for n they suggest different values. Rohsenow and Clark (1951) state that $n=0.14$ is mainly valid for the combination friction-acceleration pressure drops, rather than for the friction component alone, and suggest $n=0.6$ for this latter component. Maurer and LeTourneau (1963) use instead $n=0.25$. Dormer and Bergles use $n=0.35$.

⁴ The mass flux corresponding to the empty tube is also used where TTs are present to be consistent with the way the friction factor is defined in the TT correlation used to compute it, i.e. Eq. V-10.

modeled by means of a two-phase multiplier, but by neglecting the viscosity difference between the bulk of the coolant bulk and the coolant close to the walls.

V.3.1 Isothermal liquid-only friction factor calculation

The computation of the isothermal liquid-only friction factor for the generic i -th axial zone is performed in different ways depending on the channel configuration characterizing that axial zone (empty or TT-provided) and on the type of flow at that zone (axial or swirl). Also, because of the small influence that system pressure has on friction factor in single-phase (liquid), public available correlations developed from experimental data at low pressure are considered applicable to high pressure as well. The discussion on liquid-only friction factor is organized as follows:

- Section V.3.1.1 refers to TT-free axial zones characterized by purely axial flow (i.e. completely empty channels, bottom half of HLTT-provided channels and portion of MSLTT channels upstream of the first TT);
- Section V.3.1.2 refers to axial zones located within a region where a long TT is present (upper half of HLTT-provided channels);
- Section V.3.1.3 refers to MSLTT-provided channels.

V.3.1.1 TT-free axial zones with purely axial flow

When the portion of channel under consideration is an empty axial zone in which purely axial flow exists, the computation of the liquid-only Darcy friction factor across the i -th axial zone is performed using the Churchill equation (Churchill, 1973):

$$(f)_i = \frac{8}{6.0516} \left\{ \ln \left[\frac{1}{3.7} \frac{\lambda}{D_{ci}} + \left(\frac{7}{(Re_{empty,lo})_i} \right)^{0.9} \right] \right\}^{-2} \quad (V-8)$$

where:

- λ , depth of the cavities on the inside surface of the tubes, is set equal to 1.5×10^{-6} m, which is a typical value for drawn tubing (Todreas and Kazimi, 1993);
- $(Re_{empty,lo})_i$ is the liquid-only Reynolds number of the empty tube at axial zone i .

The friction factor obtained with the Churchill equation approximates that obtained through the well known Colebrook equation (Colebrook, 1939), i.e.:

$$\frac{1}{\sqrt{(f)_i}} = -2 \log_{10} \left(\frac{1}{3.7} \frac{\lambda}{D_{ci}} + \frac{2.51}{(\text{Re}_{empty,lo})_i \sqrt{(f)_i}} \right) \quad (\text{V-9})$$

with an error ranging between about -1% and +2% in the range: $10^{-5} \leq (\lambda/D_{ci}) \leq 5 \times 10^{-3}$ and $10^4 \leq \text{Re} \leq 10^7$, as shown in Figure V.1. Unlike the Colebrook equation, however, the Churchill equation has the advantage of being explicit in f , which makes the equation more practical to use and reduces computational time.

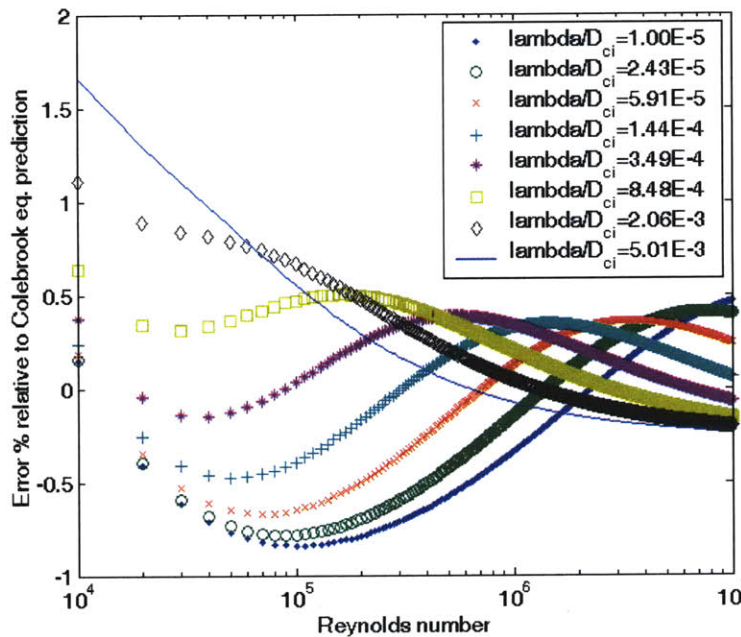


Figure V.1 – Error percentage of Churchill friction factor equation relative to Colebrook equation, for different values of the tube roughness λ/D_{ci}

V.3.1.2 Axial zones provided with a long TT

The public available literature is rich with friction factor correlations for fully developed flow in tubes containing a long TT, in single-phase liquid and typically low pressure conditions. In their overview paper on TTs, Manglik and Bergles (2002) summarize the most well known friction factor correlations, both for laminar and for turbulent flow. Since the inverted core operates in the highly turbulent regime, only this regime is

discussed here. Manglik and Bergles state that the correlation they developed in the early '90s, here referred to as the Manglik-Bergles correlation (Manglik and Bergles, 1993) “*is seen to describe within +/-5% most of the available data in the literature*”. Based on their thorough review and conclusions, this correlation was used for the upper half of the channel in HLTT configurations⁵. The correlation has the following form:

$$(f)_i = \frac{0.3164}{(\text{Re}_{\text{empty},lo})_i^{0.25}} \left(1 + \frac{2.752}{y^{1.29}} \right) \left(\frac{\pi}{\pi - \frac{4t_{TT}}{D_{ci}}} \right)^{1.75} \left(\frac{\pi + 2 - \frac{2t_{TT}}{D_{ci}}}{\pi - \frac{4t_{TT}}{D_{ci}}} \right)^{1.25} \quad (\text{V-10})$$

f is the Darcy friction factor, t_{TT} is the TT thickness, y is the TT twist ratio and $(\text{Re}_{\text{empty},lo})_i$ is computed as discussed in Section V.3.1.1. Even though it is already clear from the nomenclature used in Eq. V-6, it must be pointed out that the friction factor given by Eq. V-10 is defined with respect to the empty tube: this means that, once this factor is calculated, the computation of the friction pressure drop through Eq. V-6 must be performed using the nominal axial length of zone i (and not the larger length characterizing the helicoidal flow path) as dz , the tube inside diameter D_{ci} (and not the hydraulic diameter of the TT-provided channel), and the empty tube mass flux (and not the higher mass flux actually characterizing a TT-provided axial zone).

V.3.1.3 MSLTT-provided channels

Given a channel provided with a series of equally spaced SLTTs, the liquid-only friction factor is calculated in two ways, depending on the section of the channel under consideration. The methodology discussed in Section V.3.1.1 is used upstream of the first TT, i.e. where the flow is purely axial. Downstream of the first TT the friction factor is calculated as the empty tube friction factor multiplied by a coefficient determined experimentally during the pressure drop tests described in Volume 2, and shown in Table V- 1. This coefficient, which is a function of the twist ratio and of the SLTT spacing, was calculated by diving the experimental friction factor of a test section containing SLTTs

⁵ The use of a correlation for fully developed flow even at the TT inlet, i.e. where the flow is not fully developed, may seem unjustified and non conservative. However, the TT length for the HLTT IPWR design, i.e. 1.6 m, is much larger than the length required for the swirl flow to become fully developed (~0.1-0.3 m for a 10 mm diameter, see Appendix B of Volume 2). Further, a form loss (see Section V. 4) is applied at the TT inlet to account for the extra-pressure drop associated to the developing flow conditions.

having twist ratio y and spacing s and the experimental friction factor of an empty tube having the same diameter. For $Re > 30000$, this ratio was verified to be almost independent on Re , and was therefore calculated at the maximum Re obtained during the tests, i.e. ~ 85000 . The coefficients summarized in Table V- 1 are applicable to SLTTs having a number of 360° revolutions equal to 1.5. As discussed in Chapter VI and Volume 2, for the S-IPWR design this number was chosen to maximize CHF enhancement and minimize pressure drop.

s	y						
	1.5	2	2.5	3	4	5	6
30	3.33	2.55	2.28	2.04	1.92	1.90	1.92
40	2.83	2.30	2.14	1.87	1.83	1.79	1.68
50	2.66	1.86	1.85	1.69	1.50	1.58	1.58

V.3.2 Two-phase multiplier

As mentioned in Section V.3, the two-phase multiplier technique, for predicting pressure drop in two-phase flow, is only used in saturated conditions. In subcooled conditions the extra-friction due to the bubbles at the wall is accounted for by neglecting the viscosity difference between the bulk of the coolant and the coolant close to the walls (see Eq. V-6).

In the saturated region the liquid-only two-phase multiplier is calculated using the EPRI-Columbia correlation (Reddy et al., 1982). This correlation, presented below, was selected after noticing that, among the two-phase multiplier correlations available in the VIPRE code (Cuta et al., 1989), the EPRI-Columbia correlation is that yielding the greatest accuracy in reproducing the high-pressure two-phase pressure drop experimental data collected by Matzner et al. (1965). In spite of being recommended for any operating condition characterized by $\mu_f / \mu_g < 1000$ (Hewitt, 2008) (this ratio is about 3 at PWR operating conditions), the most well known two-phase multiplier correlation, i.e. the Friedel correlation, was not used since when compared to the Matzner data (Matzner et al., 1965) it exhibited a lower accuracy relative to that achieved using the EPRI-Columbia correlation (see Appendix V-A).

Notice that the use of the methods just described, to account for the pressure drop contribution due to the presence of steam, are also applied in swirl flow, which may seem inappropriate. In fact, it is reasonable to think that, especially in subcooled boiling before OSV, the presence of swirl tends to swipe bubble away from the wall, thus reducing the extra-friction that the coolant experiences near the wall because of the presence of stationary bubbles. The extent of this phenomenon is small and a detailed discussion, justifying the use of axial flow correlations, is presented in Section V-A.2.1 (Appendix A in this chapter).

EPRI-Columbia correlation

The EPRI-Columbia correlation (Reddy et al., 1982) has the following form:

$$\phi_{lo}^2 = 1 + x_{eq} \left(\frac{\rho_f}{\rho_g} - 1 \right) C \quad (V-11)$$

where x_{eq} is the equilibrium quality, ρ_f and ρ_g are the saturated liquid and steam densities, while C is a parameter to be computed as:

$$C = \begin{cases} 0.357 \left(1 + 10 \frac{p}{p_{cr}} \right) x_{eq}^{-0.175} (7.373257 \times 10^{-4} G)^{-0.45} & \text{for } 2.07 \leq p < 4.14 \text{ MPa} \\ 1.02 \times x_{eq}^{-0.175} (7.373257 \times 10^{-4} G)^{-0.45} & \text{for } p \geq 4.14 \text{ MPa} \end{cases}$$

where p is the operating pressure, p_{cr} is the critical pressure, and G is the mass flux expressed in kg/s m^2 .

The correlation was developed using 1533 experimental data referred to vertical upflows in round tubes having diameters ranging between 5.1 and 15.2 mm, and length between 12.7 and 254 cm, in the following operating conditions:

- $2.07 \leq p \leq 8.96$ MPa (the validity of the correlation between 13.8 and 15.2 MPa was also confirmed);
- $0 \leq x_{eq} \leq 1$;
- $447 \leq G \leq 4476$ kg/s m^2

Reddy et al. (1982) verified that Eq. V-11, when used in conjunction with the McAdams correlation for the liquid-only friction factor computation and the homogeneous model for the calculation of gravity and acceleration pressure drops, reproduces experimental two-phase multipliers with the following errors:

$$\text{Average ratio} = \frac{1}{N} \sum_{i=1}^N R_i = 1.00$$

$$\text{Relative Root Mean Square error} = \sqrt{\sum_{i=1}^N \frac{(R_i - 1)^2}{N}} = 0.097$$

$$\text{Relative standard deviation} = \sqrt{\sum_{i=1}^N \frac{(R_i - \bar{R})^2}{N}} = 0.097$$

where N is the total number of measurements, R_i is defined as:

$$R_i = \frac{(\phi_{lo}^2)_{pred}}{(\phi_{lo}^2)_{exp}}$$

and \bar{R} is the average of the R_i values. Reddy et al. (1982) compared the predictions resulting from Eq. V-11 with those derived from other well known two-phase multiplier correlations: Dukler, Martinelli-Nelson, Thom, Baroczy and Chisholm, and found that Eq. V-11 was the most accurate.

V. 4 Form losses

Form pressure drop across a generic “obstacle” located at the i -th axial node is computed as:

$$\Delta p_{form} = \begin{cases} K \frac{G_{empty}^2}{2(\rho_l)_i} & \text{if } z_i \leq z_{OSV} \\ K \frac{G_{empty}^2}{2\rho_f} (\phi_{lo}^2)_i & \text{if } z_i > z_{OSV} \end{cases} \quad (\text{V-12})$$

where K is the form loss corresponding to the obstacle of interest and G_{empty} is the mass flux in the empty channel . Three form losses are considered for the inverted core:

- the abrupt flow area contraction experienced by the coolant when flowing from the core lower plenum to the inside of the cooling channels. The corresponding form loss coefficient is $K=0.5$ (Todreas and Kazimi, 1993);
- the abrupt flow area expansion experienced by the coolant when flowing from the cooling channels to the core upper plenum. The corresponding form loss coefficient is $K=1.0$ (Todreas and Kazimi, 1993);
- the form loss “*due to swirl formation*” (Gambill et al., 1961) at the entrance of long TTs only, i.e. in the HLT design. According to Gambill et al. (1961), this form loss, defined with respect to the empty tube conditions, can be calculated as:

$$K = \frac{1}{8} \left(\frac{\pi}{y} \right)^2 \left(\frac{A_{empty}}{A_{with_TT}} \right) = \frac{1}{8} \left(\frac{\pi}{y} \right)^2 \left(\frac{0.25\pi D_{ci}^2}{0.25\pi D_{ci}^2 - t_{TT} D_{ci}} \right)^2 \quad (V-13)$$

This form loss is not computed for the MSLTT design since the friction factor obtained through the experimental tests discussed in Volume 2 already embeds such form loss.

Appendix V-A: Benchmark of pressure drop correlations against experimental data

This Appendix presents the procedure followed to choose the liquid-only two-phase multiplier correlation to be used in the pressure drop calculation for the inverted core. Such procedure consisted of comparing experimental pressure drop data, derived from Matzner et al. (1965), with pressure drop analytical predictions performed by means of different correlations and assumptions regarding primarily the liquid-only two-phase multiplier ϕ_{lo}^2 . The work by Matzner et al. (1965) was chosen as reference experimental work because the data presented in the corresponding paper were collected for operating conditions of system pressure, mass flux and geometry, rare to find simultaneously covered in an experimental study and similar to the conditions characterizing the inverted PWR. Particularly, the data were collected:

- at high pressure, i.e. 6.9 MPa;
- at high mass flux conditions ($1221 \leq G \leq 9765$ kg/s m²);
- with two-phase mixtures: $-0.6 \leq (x_{eq})_{in} \leq 0$ and $0.01 \leq (x_{eq})_{out} \leq 0.88$;
- with both empty tubes and tubes containing TTs of various geometric configuration (FLTTs and MSLTTs with $y=15$ and $y=5$ respectively). Particularly, of the 200 experimental runs, 104 refer to empty tubes while the other to TT-containing tubes.

Matzner et al. (1965) measured pressure drop and CHF for water flowing upward inside the six tube geometry configurations shown in Figure V-A. 1, all of which are 10.16 mm inner diameter tubes. Black regions indicate the presence of a full-length TT (geometry 2) and short-length TTs (geometries 3 and 4) respectively⁶.

⁶ The lengths shown in Figure V-A. 1 are the heated lengths. Pressure drop measurements were performed over tube lengths slightly larger than the overall tube lengths shown in the figure. Particularly, the inlet pressure tap was placed: 25.4 mm upstream the heated section inlet for all the geometries. The outlet pressure tap was placed: 38.1 mm downstream the heated section outlet for geometries 1, 2, 3, and 127 mm downstream the heated section outlet for geometries 4, 5 and 6.

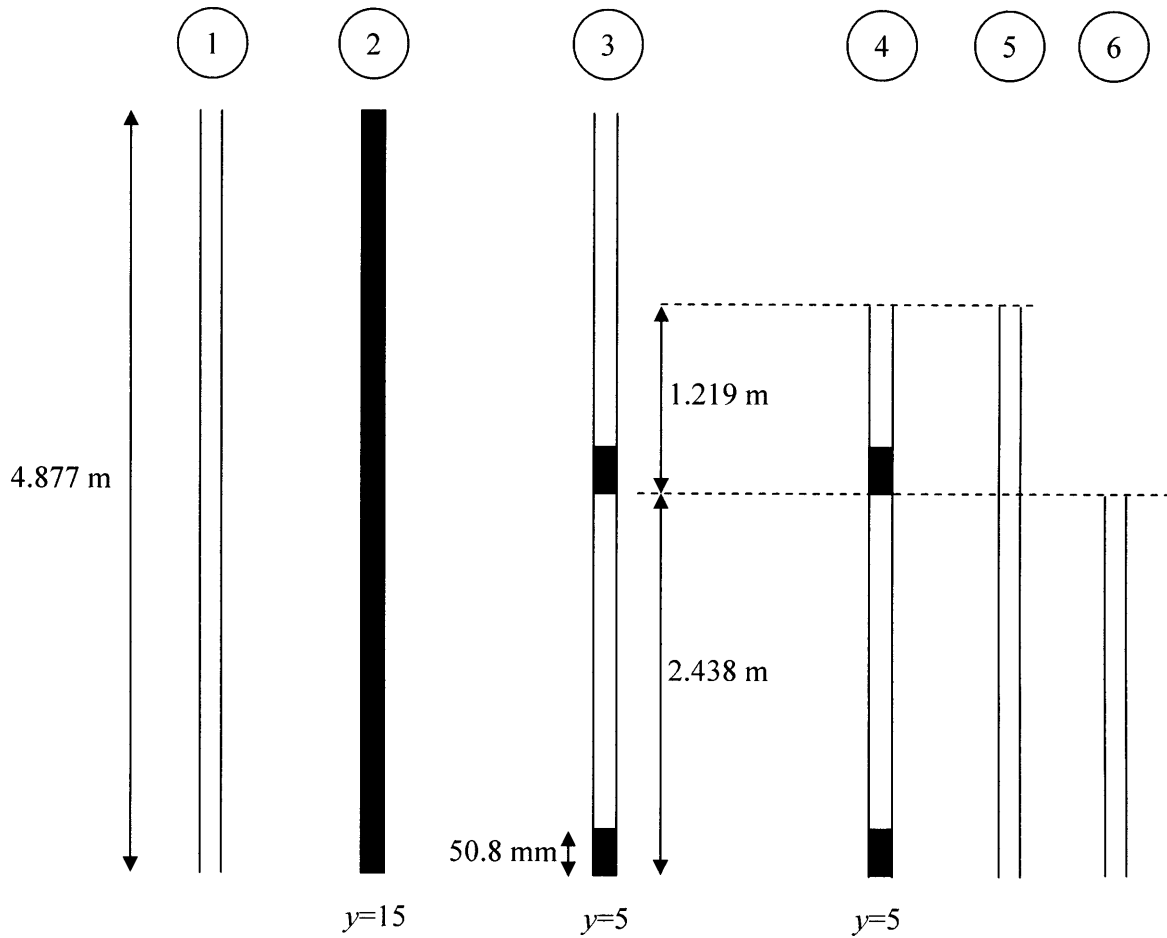


Figure V-A. 1– Geometric configurations examined in Matzner et al. (1965)

While, regarding pressure drop, Matzner et al. (1965) do not present correlations but only experimental data, on CHF they present both. However, the CHF correlations are of no use in the IPWR design since they are strictly geometry-specific. In fact, they were developed in the same general form for all the six geometries shown in Figure V-A. 1:

$$q''_{CHF} = \frac{(y_0 D_{ci}^{y_1} G^{y_2}) + 0.25 y_3 D_{ci}^{1+y_4} G^{1+y_5} (h_f - h_m)}{1 + y_3 D_{ci}^{y_4} G^{y_5} L} \quad (\text{V-A-1})$$

where q''_{CHF} is in MBtu/hr ft², D_{ci} is in ft, G is in Mlb/hr ft² and L , channel heated length, is in ft. Six sets of numerical coefficients y_0 to y_5 are provided for the six geometries: in other words, the CHF dependence on the test section geometric parameters is embedded in the y coefficients, and cannot be directly expressed in any way.

The pressure drop comparison against Matzner et al. (1965), which is the subject of this Appendix, was performed by reproducing, computationally, Matzner's runs and then comparing the pressure drop predictions with the experimental values. Two comparisons were performed:

- Empty-tube data comparison: analytical vs experimental pressure drop data for geometries 1, 5 and 6 (the numbering is that shown in Figure V-A. 1). A single comparison was made, in the sense that no distinction was made based on whether the data came from geometry 1, 5 or 6.
- Full-length TT data comparison: analytical vs experimental pressure drop data for geometry 2.

No comparisons were instead made for geometries 3 and 4.

In both comparisons, which are presented below, the following choices were made for some of the correlations that have a key role in pressure drop calculations:

- Eq.V-7 for the viscosity correction factor;
- Levy correlation (Levy, 1967), for the void fraction in subcooled boiling;
- Homogeneous model for the void fraction in saturated boiling;
- Friction pressure drop calculation performed according to Eq. V-6 in which, however, different formulations for the liquid-only friction factor, f , were used.

The correlations used for the liquid-only friction factor and, in saturated boiling, for the liquid-only two-phase multiplier are described in the following paragraphs.

V-A.1 Empty-tube data comparison

Matzner et al. (1965) present all the geometric characteristics of the test sections shown in Figure V-A. 1 except for the tube roughness. This parameter has a significant effect on the friction factor, as shown in Eq. V-8. Therefore, before deciding what two-phase multiplier correlation is best to use, it was necessary to estimate Matzner test section roughness by calculating the roughness value that, once entered in Eq. V-8, results in the smallest pressure drop error percentage relative to some of the experimental values. For

this purpose, not all Matzner experimental data were used, but only those, 24, derived from low steam quality runs ($x_{out} \leq 0.09$)⁷. This is because, in case a discrepancy existed between analytical predictions and experimental data, the higher is the steam quality the smaller is the contribution that the tube roughness would have on such discrepancy: errors in two-phase multiplier and void fraction prediction would in fact dominate uncertainties related to the tube roughness.

Figure V-A. 2 compares, for the low steam quality runs, the experimental measurements collected by Matzner et al. (1965) with predictions made through the use of (1) the Matlab code developed to analyze the IPWR and (2) the VIPRE code (Cuta et al., 1989)⁸. Particularly, in the Matlab code, two correlations were used for the isothermal friction factor:

- the Churchill equation (Eq. V-8) with, alternatively, three tentative values for the tube roughness:

$$\lambda = 0 \text{ m} \quad \rightarrow \lambda/D_{ci} = 0$$

$$\lambda = 10^{-7} \text{ m} \quad \rightarrow \lambda/D_{ci} = 9.84 \times 10^{-6}$$

$$\lambda = 10^{-6} \text{ m} \quad \rightarrow \lambda/D_{ci} = 9.84 \times 10^{-5}$$

- the McAdams correlation (Todreas and Kazimi, 1993):

$$f = 0.184 \text{ Re}^{-0.2} \quad . \quad \quad \quad (\text{V-A-2})$$

which is a correlation valid for smooth tubes.

The points corresponding to the predictions made, with the Matlab code, using the Churchill equation with $\lambda = 0$, are not visible in the figure because they almost coincide with those made, again with the Matlab code, using the McAdams correlation. As a consequence of such marker overlapping, of the two only the dark square markers corresponding to the use of the McAdams correlation are visible. Straight lines enclosing

⁷ As shown earlier in this section, all the Matzner experimental measurements had steam at the test section outlet. Therefore, it was not possible to choose entirely subcooled runs, and measurement characterized by an outlet quality lower than 9% were used for the roughness calculation.

⁸ Like the Matlab code written to analyze the IPWR (and in this appendix modified to reproduce Matzner's runs), a VIPRE input file was written to reproduce Matzner runs. The file specifications, in terms of correlations to be used by VIPRE, are consistent with those used in the Matlab code (e.g. the McAdams correlation for the isothermal friction factor and the EPRI-Columbia correlation (Reddy et al., 1982) for the liquid-only two-phase multiplier) with the exception of the heat transfer coefficient correlation to be used in saturated boiling: Thom plus the single phase correlation (in VIPRE), versus the Chen correlation used in the Matlab code.

the +/-20% error band are also shown. The overall error percentages characterizing each correlation-roughness combination are summarized in Table V-A. 1.

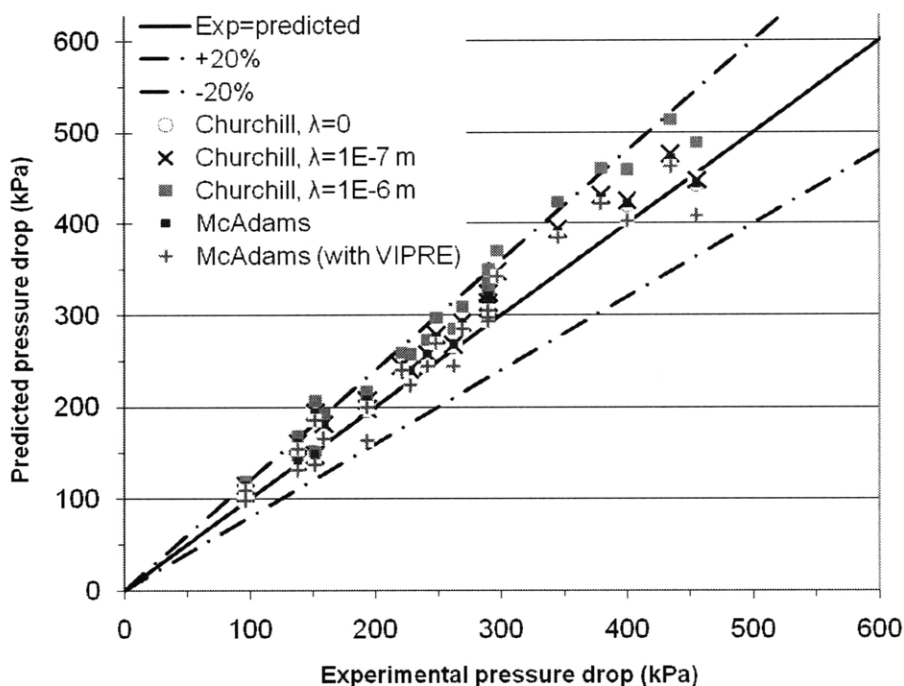


Figure V-A. 2– Comparison between analytical predictions and Matzner et al. (1965) exp. pressure drop data (low-quality runs only; Churchill $\lambda=0$ is not visible since Churchill $\lambda=10^{-7}$ and McAdams overlap it)

Code used	Isothermal friction factor correlation	Tube roughness (m)	RMS error (kPa)	RMS error %
Matlab	Churchill	0	25.0	7.0
		10^{-7}	27.4	7.6
		10^{-6}	46.0	12.8
	McAdams	0	26.2	7.3
VIPRE	McAdams	0	23.1	6.5

⁹ Root Mean Square (RMS) error is defined as: $RMS = \sqrt{\frac{1}{N} \sum_{j=1}^N (\Delta p_{predicted} - \Delta p_{exp})^2}$, where N is the number of experimental points, while $\Delta p_{predicted}$ and Δp_{exp} are the calculated and experimental pressure drops respectively. The RMS error percentage is defined as: $RMS\% = 100 \frac{RMS}{\max(\Delta p_{exp}) - \min(\Delta p_{exp})}$

Two important observations can be made:

- among the predictions made using the Matlab code, those which assume very smooth tubes, i.e. $\lambda = 0$ and $\lambda = 10^{-7}$ m, together with that using the McAdams correlation (which is equivalent to assuming zero roughness) result in the smallest RMS error percentages. Vice versa, the predictions made assuming $\lambda = 10^{-6}$ m are characterized by larger errors, and few times fall outside the +/-20% error band.
- predictions made using the Matlab code, with the Churchill correlation ($\lambda = 0$ and $\lambda = 10^{-7}$ m) and with the McAdams correlation chosen for the isothermal friction factor, are very close to the experimental values. Their accuracy is comparable to that obtained with the VIPRE code.

From these two observations it can be concluded, respectively, that:

- the tubes used by Matzner et al. (1965) were very smooth: it was therefore decided to assume a zero roughness in the pressure drop analysis discussed in this Appendix;
- from the pressure drop viewpoint, the Matlab code developed to analyze the thermal hydraulic behavior of the channels can be considered very accurate.

With the conclusion on the tube roughness drawn by examining the low-quality data only, the comparison prediction-experiment was then extended to all the Matzner et al. (1965) runs made on empty tubes, now with the purpose of discussing the accuracy of the liquid-only two-phase multiplier correlation. The 106 experimental runs were reproduced with the Matlab code and the VIPRE code. Particularly, two correlations for ϕ_{lo}^2 were used in the Matlab code:

- the EPRI-Columbia correlation presented as Eq. V-11 (Reddy et. al, 1982) (also used in the VIPRE code);

- the Friedel correlation (Friedel, 1979), presented as follows in its form for horizontal and vertical upflow in circular channels¹⁰:

$$\phi_{lo}^2 = E + \frac{3.24 \times F \times H}{Fr^{0.0454} We^{0.035}} \quad (V-A-3)$$

where:

$$E = (1 - x_{flow})^2 + x_{flow}^2 \frac{\rho_f}{\rho_g} \frac{f_{goF}}{f_{loF}}$$

$$f_{goF} = \begin{cases} \frac{64}{Re_{goF}} & \text{for } Re_{goF} \leq 1055 \\ \frac{1}{\left[0.86859 \ln \left(\frac{Re_{goF}}{1.964 \ln(Re_{goF}) - 3.8215} \right) \right]^2} & \text{for } Re_{goF} > 1055 \end{cases}$$

$$f_{loF} = \begin{cases} \frac{64}{Re_{loF}} & \text{for } Re_{loF} \leq 1055 \\ \frac{1}{\left[0.86859 \ln \left(\frac{Re_{loF}}{1.964 \ln(Re_{loF}) - 3.8215} \right) \right]^2} & \text{for } Re_{loF} > 1055 \end{cases}$$

$$Re_{goF} = \frac{GD_{eq}}{\mu_g}$$

$$Re_{loF} = \frac{GD_{eq}}{\mu_f}$$

$$F = x_{flow}^{0.78} (1 - x_{flow})^{0.224}$$

$$H = \left(\frac{\rho_f}{\rho_g} \right)^{0.91} \left(\frac{\mu_g}{\mu_f} \right)^{0.19} \left(1 - \frac{\mu_g}{\mu_f} \right)^{0.7}$$

¹⁰ The complete Friedel work (Friedel, 1979) includes correlations for ϕ_{lo}^2 referred to vertical upward and downward flow, and horizontal flow. Correlations also account for the channel geometry, making distinction between circular, rectangular and annular cross sections.

$$We = \frac{G^2 D_{eq}}{\sigma \rho_c}$$

$$Fr = \frac{G^2}{g D_{eq} \rho_c^2}$$

$$\rho_c = \frac{1}{\frac{x_{flow}}{\rho_g} + \frac{1-x_{flow}}{\rho_f}}$$

x_{flow} : steam flow quality

The Friedel correlations were developed using an experimental data body of approximately 25000 pressure drop results obtained with unheated single- and two-component mixtures flowing vertically upward, vertically downward and horizontally through channels having circular, rectangular and annular cross section. The vertical upflow runs were performed with a broad range of operating conditions, which are listed as follows together with the arithmetic mean of the data for each parameter:

- $0.01 \leq p \leq 21.2$ MPa (pressure arithmetic mean: 3.3 MPa for single-component mixtures, 0.7 MPa for two-component mixtures);
- $0 \leq x_{eq} \leq 1$ (quality arithmetic mean: 0.31);
- $20 \leq G \leq 8410$ kg/s m² (mass flux arithmetic mean: 1430 kg/s m² for single-component mixtures, 610 kg/s m² for two-component mixtures).

Ranges for other parameters, e.g. surface tension, density and viscosity ratio, are discussed in Friedel (1979). When compared to the experimental results referred to vertical upflows, the predictions made through the Friedel correlation were found to have the following deviations:

$$\text{Relative standard deviation} = \sqrt{\sum_{i=1}^N \frac{(R_i - 1)^2}{N - 1}} = 0.26 \text{ (single-component mixtures)}$$

$$= 0.52 \text{ (two-component mixtures)}$$

$$\text{Absolute standard deviation} = \sqrt{\sum_{i=1}^N \frac{[(\phi_{to})_{exp} - (\phi_{to})_{pred}]^2}{N - 1}} = 16 \text{ (single-comp. mixtures)}$$

= 39 (two-comp. mixtures)

where N is the total number of measurements, and R is defined as:

$$R = \frac{(\phi_{lo}^2)_{exp}}{(\phi_{lo}^2)_{pred}}$$

Figure V-A. 3 shows the comparison between the predictions made through these two correlations and the experimental data. It also shows how the predictions made using the Matlab code compare to those made through the VIPRE code. To better display the data in the bottom left hand corner, this region has been reproduced in Figure V-A. 4. The deviations of the analytical predictions relative to the experimental results are summarized in Table V-A. 2.

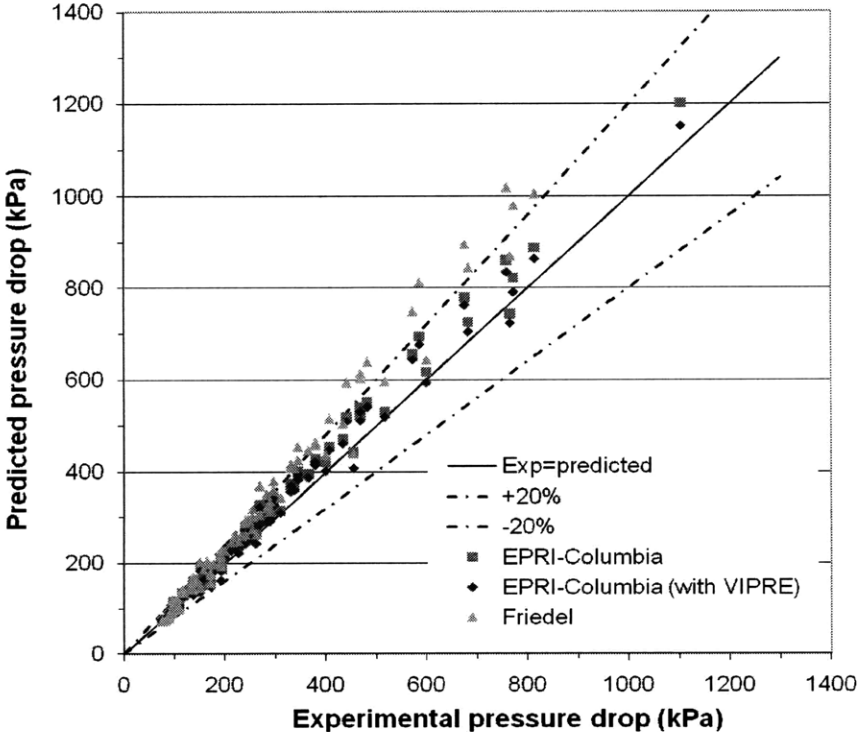


Figure V-A. 3– Comparison between analytical predictions and Matzner et al. (1965) experimental pressure drop data (empty tube)

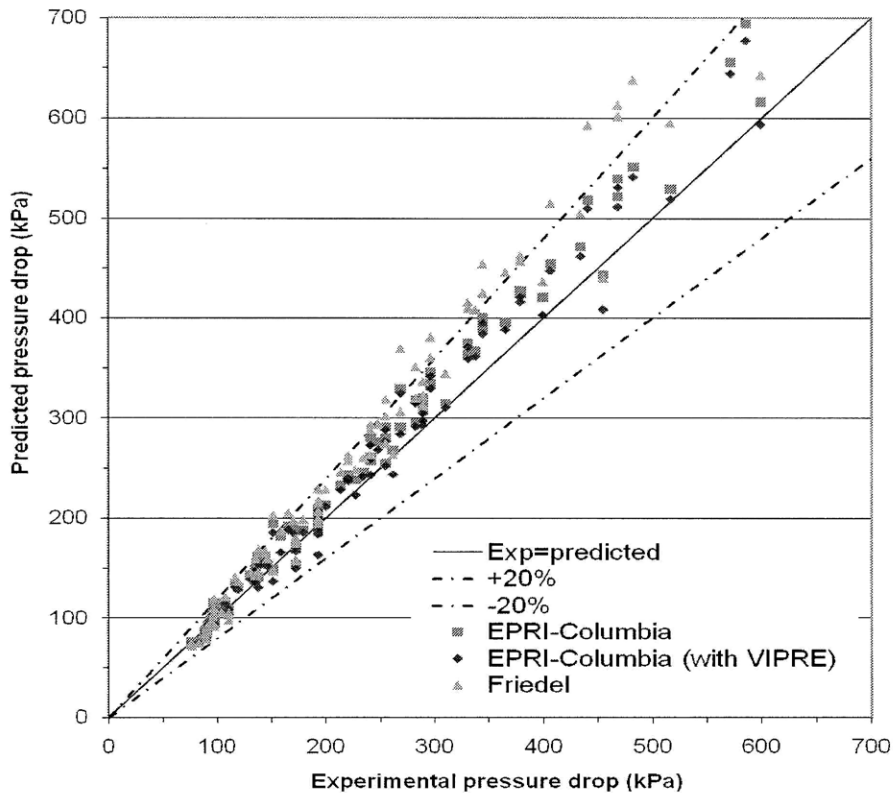


Figure V-A. 4— Comparison between analytical predictions and Matzner et al. (1965) experimental pressure drop data (empty tube, low pressure drop region)

Table V-A. 2— Error in pressure drop predictions against Matzner et al. (1965) experimental data			
Code used	Two-phase multiplier correlation	RMS error (kPa)	RMS error %
Matlab	EPRI-Columbia	34.2	3.3
	Friedel	82.6	8.0
VIPRE	EPRI-Columbia	29.1	2.8

From Figure V-A. 3 and Figure V-A. 4, as well as from Table V-A. 2, it can be seen that the predictions made through the EPRI-Columbia correlation are more accurate than those made through the Friedel correlation. In fact, while with the former most of the points fall within the +/-20% region, with the latter several points fall outside this region, particularly for the experimental runs characterized by high mass flux conditions. In fact, as shown in Figure V-A. 5 and Figure V-A. 6, the deviation percentages from the

experimental values tend to become bigger and bigger as the mass flux increases, while the dependence on the steam quality is more irregular. This behavior is consistent with the mass flux applicability range of the correlations (already discussed in Section V.3.2 and above for the EPRI-Columbia and Friedel correlation respectively): $447 \leq G \leq 4476$ kg/s m² for the EPRI-Columbia and $20 \leq G \leq 8410$ kg/s m² for Friedel (the latter, however, with an arithmetic mean of the mass flux values characterizing the database used for the correlation development of only 1430 kg/s m²).

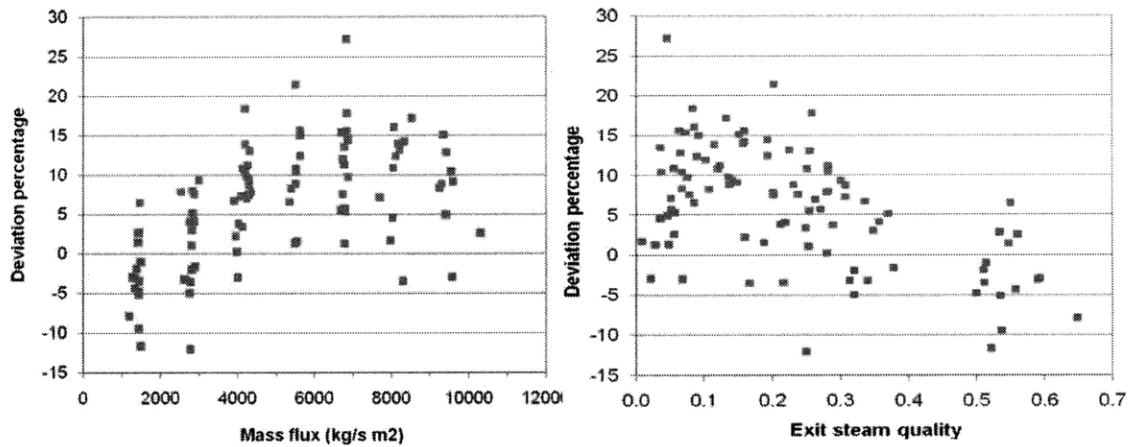


Figure V-A. 5– Deviation percentage, from Matzner et al. (1965) exp. data, of pressure drop predictions using EPRI-Columbia correlation in the Matlab code (empty tube)

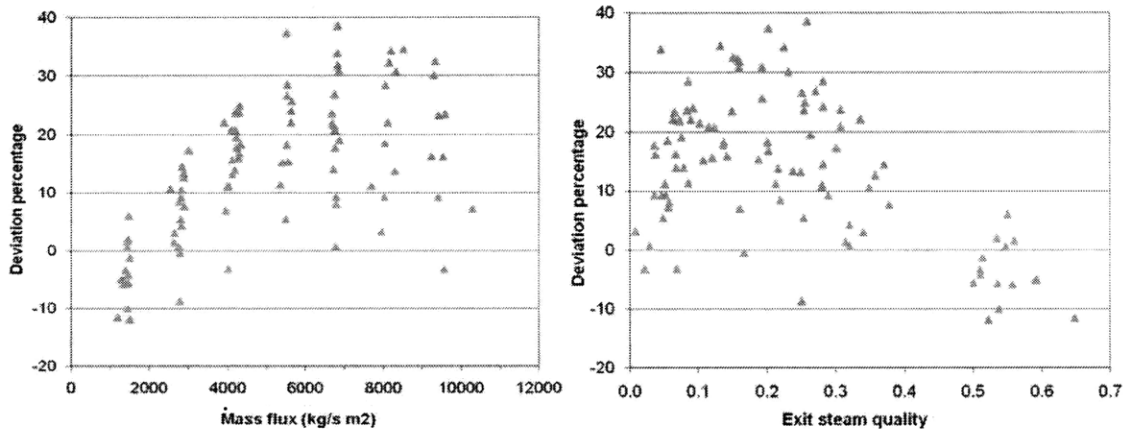


Figure V-A. 6– Deviation percentage, from Matzner et al. (1965) exp. data, of pressure drop predictions using Friedel correlation in the Matlab code (empty tube)

V-A.2 FLTT data comparison

Matzner et al. (1965) collected 27 data points for the FLTT geometry shown in Figure V-A. 1. These data points correspond to runs having inlet qualities between -0.52 and -0.04, and outlet qualities between 0.33 and 0.88. Such runs have been reproduced with the Matlab code, in which:

- the Manglik-Bergles correlation (Manglik and Bergles, 1993), i.e. Eq. V-10, was used for the liquid-only friction factor;
- the EPRI-Columbia correlation (Reddy et al., 1982), i.e. Eq. V-11, was used for the liquid-only two-phase multiplier in saturated boiling.

The comparison between the predictions and the experimental pressure drop values is shown in Figure V-A. 7. It can be seen that the Matlab code underpredicts, of about 10-15%, the experimental points; particularly, the RMS error is 100.6 kPa and the RMS error percentage is 10.9%. The accuracy in pressure drop prediction is however acceptable since, in two-phase conditions (which characterize all Matzner runs) inaccuracies of +/-30% in pressure drop prediction are typical; this conclusion is further reinforced by the fact that the mentioned +/-30% refers to empty tubes, while Matzner runs are for a tube containing a FLTT, which introduces additional inaccuracies. Unlike the runs performed on empty tubes, those on the FLTT geometry were all characterized by high steam quality at the outlet, i.e. $0.33 \leq (x_{eq})_{out} \leq 0.88$. Thus, it is not possible to verify the accuracy of the Matlab code, for FLTT geometries, in subcooled conditions only. Considerations on how swirl flow is expected to affect two-phase pressure drop are discussed in Section V-A.2.1.

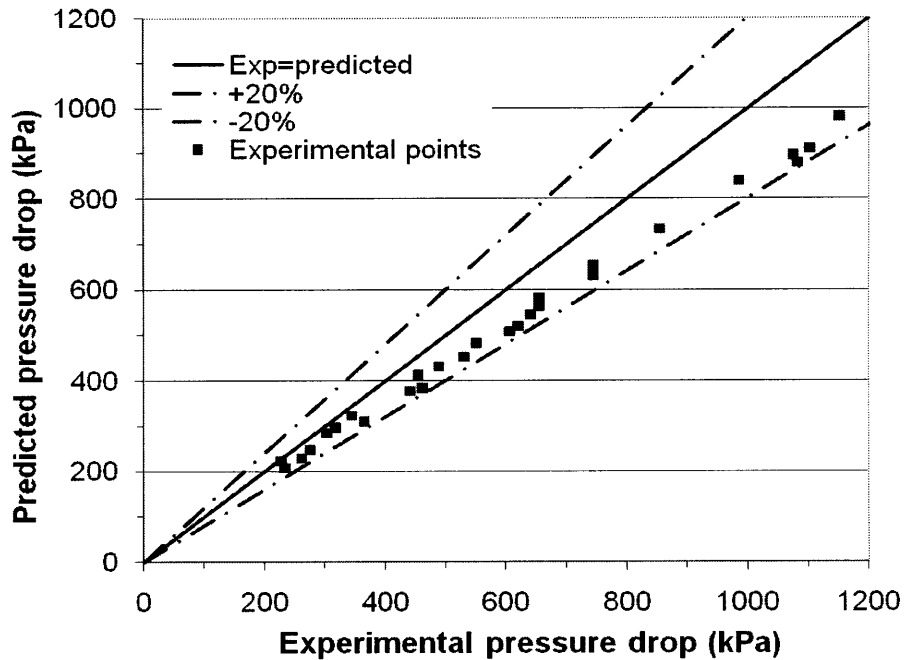


Figure V-A. 7– Comparison between analytical predictions and Matzner et al. (1965) experimental pressure drop data (FLTT geometry)

V-A.2.1 Effect of swirl flow on pressure drop in saturated and subcooled boiling

V-A.2.1.1 Saturated boiling

In saturated boiling the effect of swirl flow on pressure drop is small, and is well within the typical $\pm 20\%$ error bands characterizing pressure drop calculations of two-phase mixtures (see Figure V-A. 7). An interpretation of this fact is that the swirl nature of the flow seems not to significantly affect the extent with which the presence of steam, in saturated boiling conditions, causes the pressure drop to increase, relative to liquid-only flow conditions characterized by the same mass flux and steam quality. It can be noticed, however, that the analytical predictions in Figure V-A. 7 are always smaller than the corresponding experimental values. Using this observation to conclude that, when applied to swirl flow conditions, axial flow pressure drop correlations always underpredict pressure drops would be fundamentally wrong. This is because, while in single-phase all the features of swirl flow contribute to increasing pressure drop relative to a condition of axial flow with the same mass flux, in two-phase such features point in opposite

directions, and it is not easy to infer which effect prevails. In fact, relative to two-phase axial flow, in two-phase swirl flow:

- bubbles are more effectively removed from the wall, due to the tangential forces: this contributes to a reduction in pressure drop relative to axial flow;
- like in single-phase, (1) coolant does not flow parallel to the channel walls but impinges them with a certain angle and (2) the coolant travel path in contact with the walls is longer (due to the helicoidal trajectory): these two effects contribute to an increase in pressure drop relative to axial flow.

Since the presence of steam significantly increases pressure drop relative to all-liquid conditions, it may be reasonable to think that the bubble removal effect prevails over the other two phenomena. This has been verified by examining the work of Moussez et al. (1965) who, among other things, measured pressure drops of water-steam mixtures flowing through an empty tube and through a tube containing a FLTT, at atmospheric pressure. Particularly, they plotted the experimental liquid-only two-phase multiplier as a function of the Martinelli parameter for the empty tube (Figure V-A. 8) and for the FLTT tube (Figure V-A. 9). Of the two curves displayed in each figure (for our purposes the short straight line on the top left hand corner can be neglected) the lower one is the analytical curve, obtained using the Martinelli-Nelson model for the computation of ϕ_{lo}^2 , while the upper one (labeled as “Courbe SNECMA”) interpolates the experimental points. By comparing the “Courbe SNECMA” curve of Figure V-A. 8 with that of Figure V-A. 9 it can be noticed that, at the steam quality typical of a PWR hot channel exit, i.e. ~4% (corresponding Martinelli parameter at atmospheric pressure is 0.6), the multiplier is ~6.8 for pure axial flow (Figure V-A. 8) while it is ~6.2 for swirl flow (Figure V-A. 9). Thus, the swirl flow seems to be responsible for a reduction of about 10% in two-phase multiplier, with respect to axial flow. This deviation is small and within correlation inaccuracy bands.

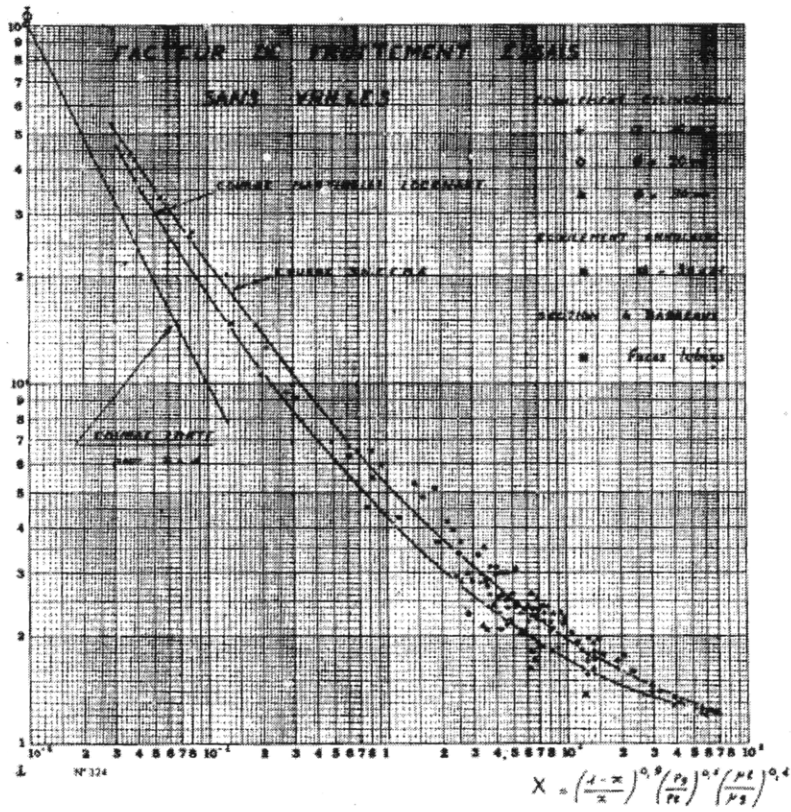


Figure V-A. 8— Experimental liquid-only two-phase multiplier as a function of the Martinelli parameter for an empty tube ($D_{ci}=10$ mm). From Moussez et al. (1965)

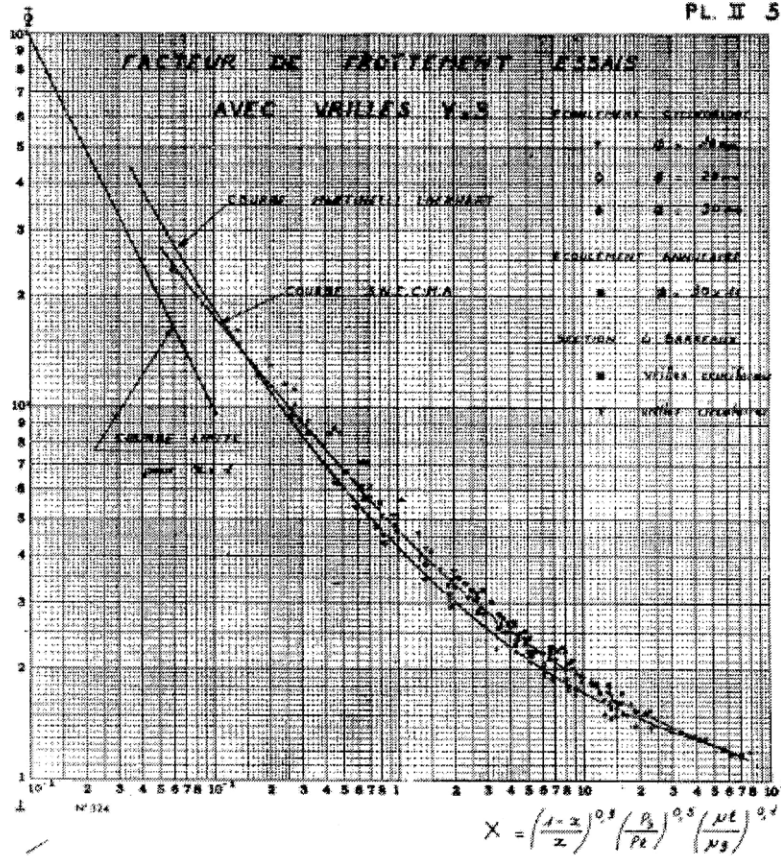


Figure V-A. 9– Experimental liquid-only two-phase multiplier as a function of the Martinelli parameter for a tube containing a FLTT ($D_{ci} = 10 \text{ mm}$; $y=3$). From Moussez et al. (1965)

Moussez et al. (1965) also state that the Martinelli-Nelson model was proven to be more accurate for swirl flow than for axial flow. In fact, while 97% of the swirl flow experimental points were predicted with an accuracy of $\pm 17\%$, the accuracy for the axial flow experimental points was only $\pm 30\%$. However, they also highlight the fact that, at high pressure, the Martinelli-Nelson method may not be valid, which is known to be the case¹¹. The evidence that the Martinelli-Nelson model can be used at low pressure, regardless of the presence of the TTs, is however an important point. In fact, from this it can be again inferred that the extent with which steam causes the pressure drop to increase, relative to an all-liquid situation characterized by same mass flux and steam quality, does not differ significantly between pure axial flow and swirl flow.

¹¹ The calculation of the two-phase multiplier at 15.5 MPa using the Martinelli-Nelson model has been verified, in this project, to yield values about 2.5 times higher than those using the Friedel and HEM models, which give instead similar results.

V-A.2.1.2 Subcooled boiling

Like in saturated boiling, in subcooled boiling the role played by the flow type (axial vs swirl) in determining ϕ_{lo}^2 can be considered small, and within the uncertainty margins that typically characterize two-phase pressure drop measurements. Relative to saturated boiling conditions, however, the effect that swirl flow has on subcooled boiling is, phenomenologically, more relevant for the IPWR and thus worth discussing. Before doing this, it is however convenient to list the conclusions that have resulted from the literature search performed on such phenomenology:

- ϕ_{lo}^2 in swirl flow subcooled boiling is slightly smaller than in axial flow subcooled boiling;
- the reason for the smaller ϕ_{lo}^2 in subcooled boiling is the lower concentration of bubbles at the wall, downstream the ONB location. While this is due to their extra-removal induced by the swirl, the wall superheat required for ONB is approximately the same in axial and swirl flow;
- no correlations are available for ϕ_{lo}^2 in swirl flow subcooled boiling, and no liquid-only two-phase multiplier was calculated in this region. Rather, the effect on pressure drop of the bubbles at the wall was accounted for by neglecting the viscosity difference between the bulk and the wall, i.e. by assuming that the channel was unheated.

The reasons why ϕ_{lo}^2 is smaller in subcooled swirl boiling than in subcooled axial boiling are essentially two, having however different importance. As shown in Figure V-A. 10, the swirl flow-induced fluid mixing yields:

- a smaller bubble concentration at the wall downstream the ONB location;
- an ONB location slightly downstream than that in axial flow (i.e. a slightly higher wall superheat required for ONB inception).

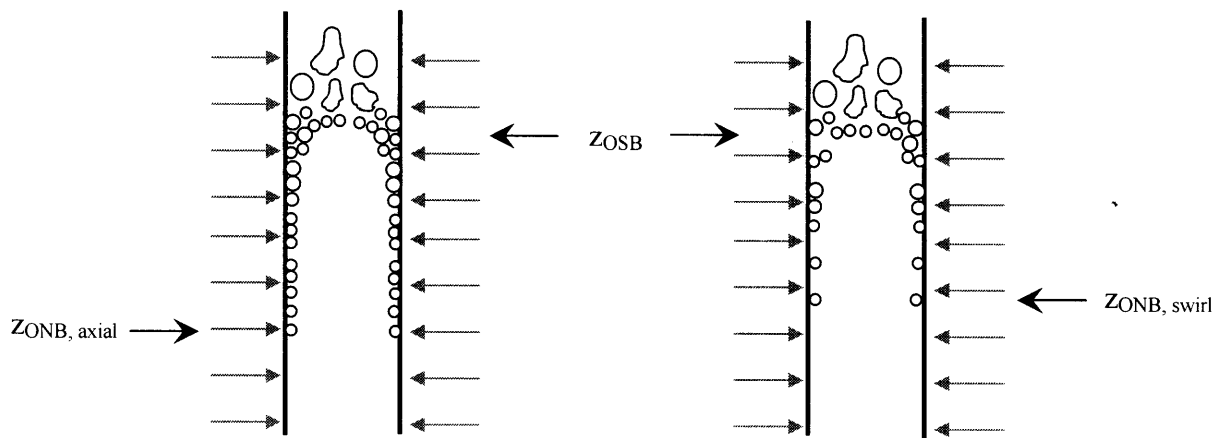


Figure V-A. 10– ONB in pure axial flow (left) and in swirl flow (right) (qualitative sketch)

While the reduced bubble concentration at the wall, downstream the ONB axial location, has been experimentally verified (and is discussed later in this section), the difference in wall superheating has been demonstrated to be negligible: this is why, in Figure V-A. 10, the ONB location in swirl flow has been drawn only slightly downstream that in axial flow. Lopina and Bergles (1973) came to this conclusion by studying boiling curves for water at about 0.2 MPa. In fact, referring to the swirl flow boiling curves of Figure V-A. 11, they state: *“it may be seen that the first visually observed bubbles occurred very close to the predicted boiling inception line of Bergles and Rohsenow”*. This can be reworded by saying that the Bergles and Rohsenow correlation, frequently used to predict the wall superheat at ONB in axial flow, is applicable to swirl flow conditions as well. Referring to Figure V-A. 12 they also say: *“no systematic effect of tape twist can be observed, and the superheats with twisted tapes are essentially the same as for straight flow. (...) It can thus be concluded that wall superheats for swirl flow are not any higher than those for straight flow”*.

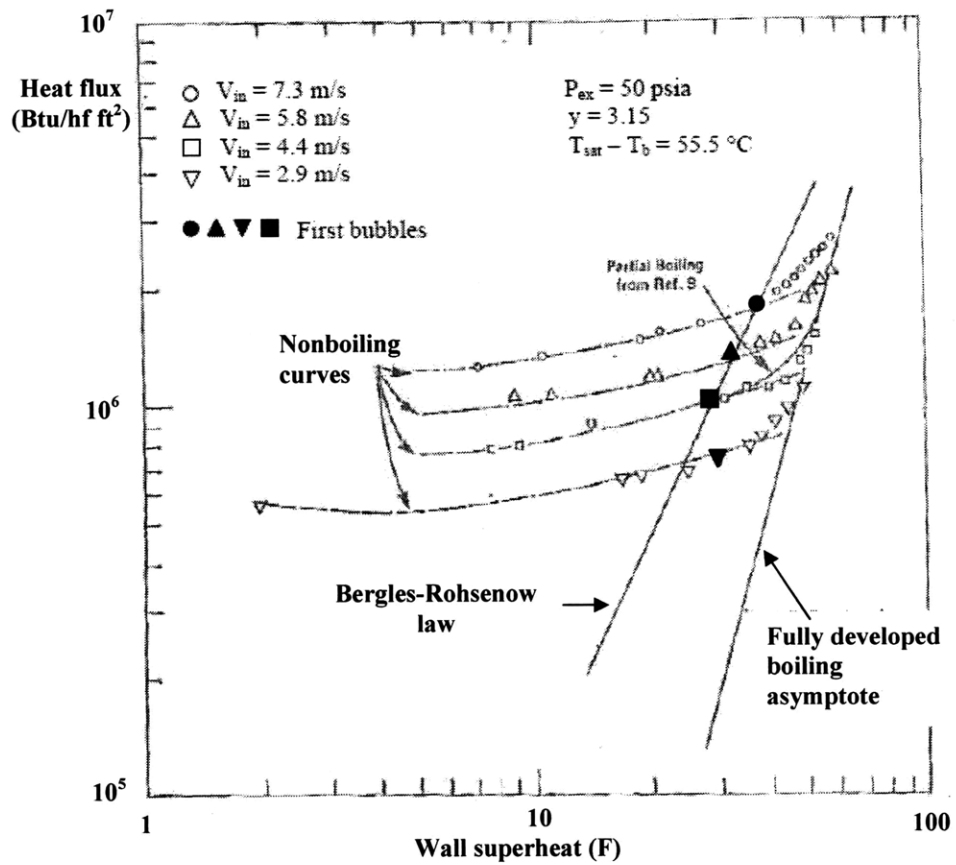


Figure V-A. 11- Subcooled boiling data for water in swirl flow (from Lopina and Bergles, 1973)

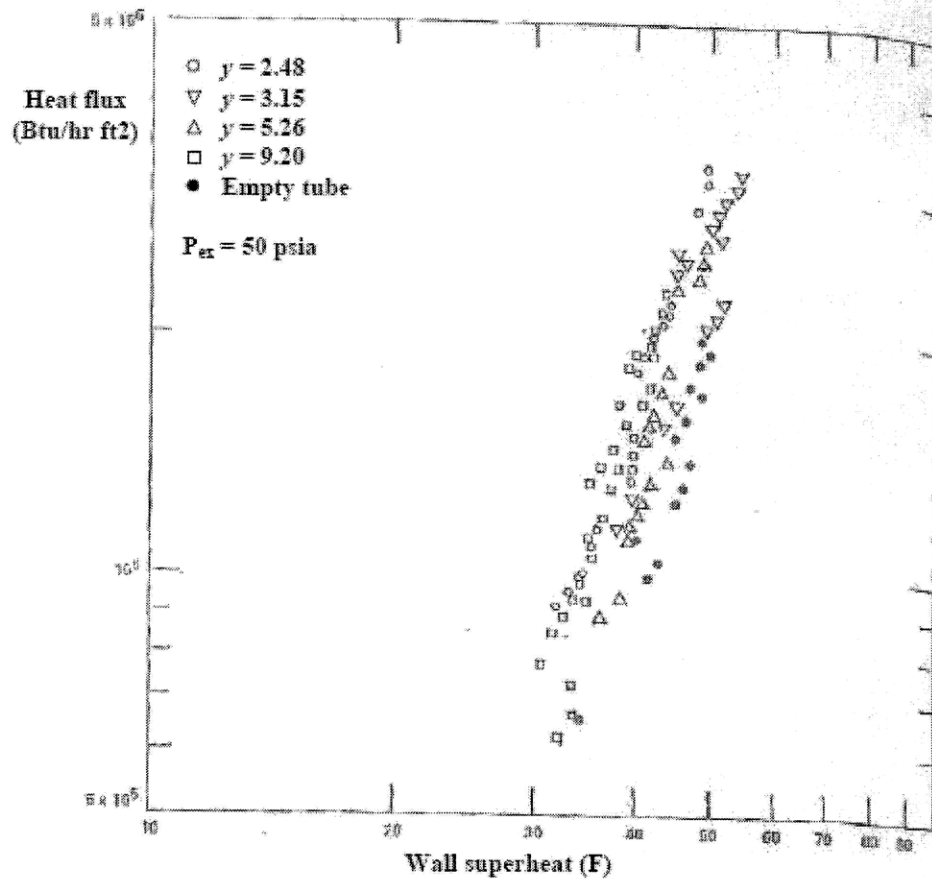


Figure V-A. 12– Composite of fully developed boiling data for axial and swirl flow (from Lopina and Bergles, 1973)

The same conclusion can be drawn by referring to the work by Novog et al. (2007), who analyzed boiling of high velocity water, in axial and swirl flow, at 3.5 MPa. Some of their results have been collected and plotted in Figure V-A. 13. It can be seen that, for the same mass flux, the change in slope of the boiling curves occurs at the same wall superheat regardless of whether the flow is purely axial or swirl.

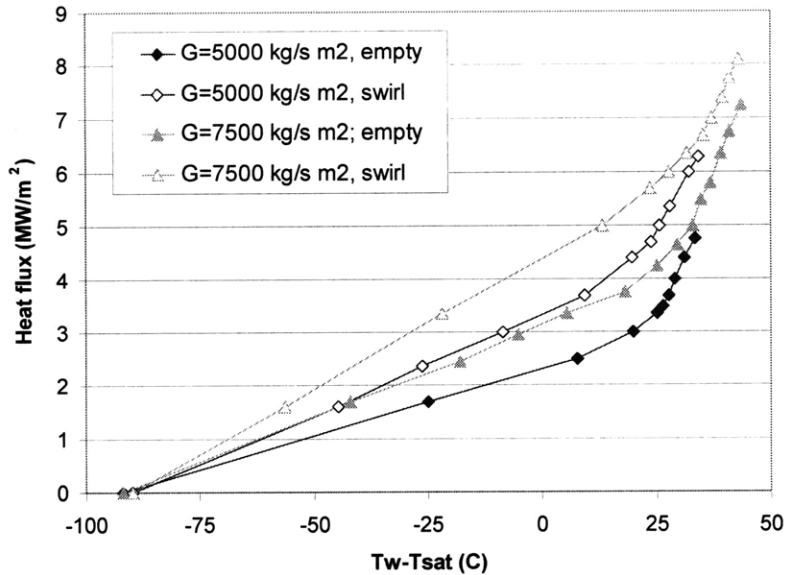


Figure V-A. 13– Boiling curves for water in axial and swirl flow ($\gamma = 2$) at 3.5 MPa (from Novog et al., 2007)

The evidence of the extra bubble removal at the wall, relative to an axial flow condition, was instead verified by both Lopina and Bergles (1973) and by Tong, Bergles and Jensen (1996). Lopina and Bergles (1973) plotted pressure drop versus heat flux for an empty tube and for tubes provided with TTs having three different twist ratios (see Figure V-A. 14). Referring to this figure they state: “*the swirl data seem to indicate a less pronounced increase in pressure drop than the empty-tube data. This increase is normally due to a rapid buildup of nonequilibrium vapor volume, which increases the momentum component of the pressure drop. The visual observations made in this study confirm that the swirl flow results in displacement of the bubbles from the wall*”.

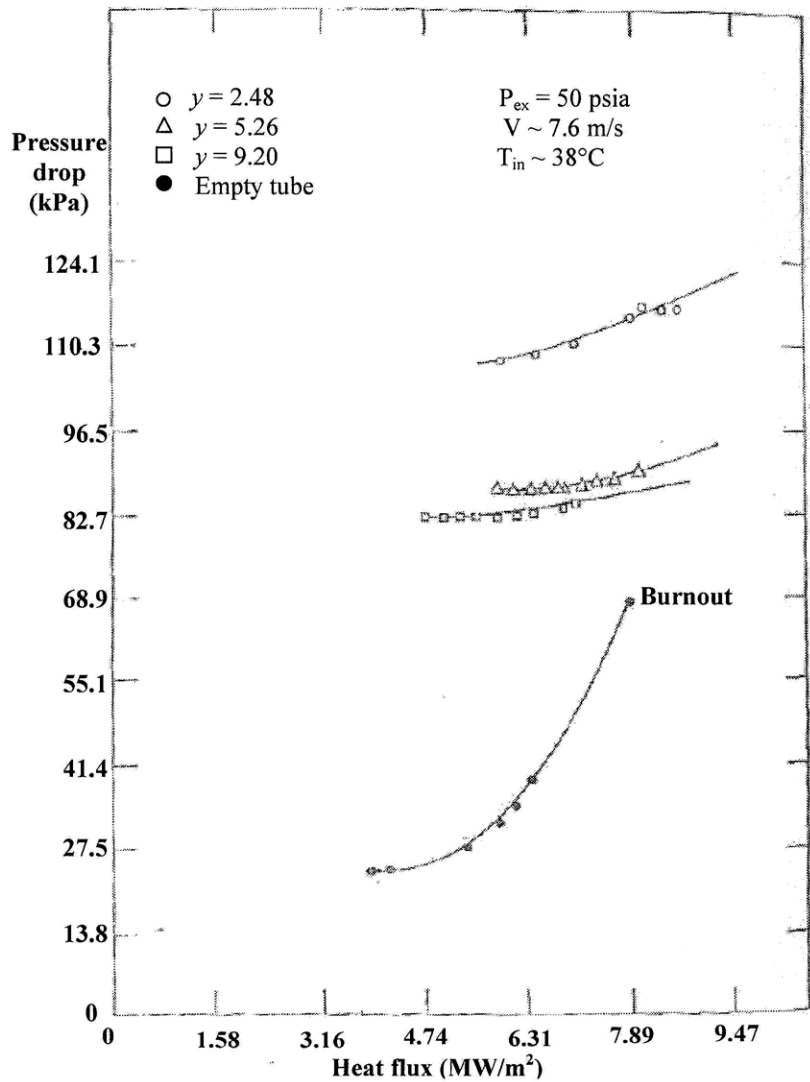


Figure V-A. 14– Overall pressure drop for subcooled boiling of water in axial and swirl flow (modified from Lopina and Bergles, 1973)

Like Lopina and Bergles (1973), Tong, Bergles and Jensen (1996) collected pressure drop data at different heat fluxes starting, however, from a condition of zero heat flux. This allowed them to study the trend pressure drop vs heat flux through both subcooled single phase and subcooled boiling. They show that, for a FLTT-provided tube under low-pressure subcooled boiling and constant mass flow rate, a higher heat flux is needed to invert the slope of the pressure drop vs heat flux curve, relative to an empty tube, and that this difference increases as the twist ratio decreases. This is shown in Figure V-A. 15.

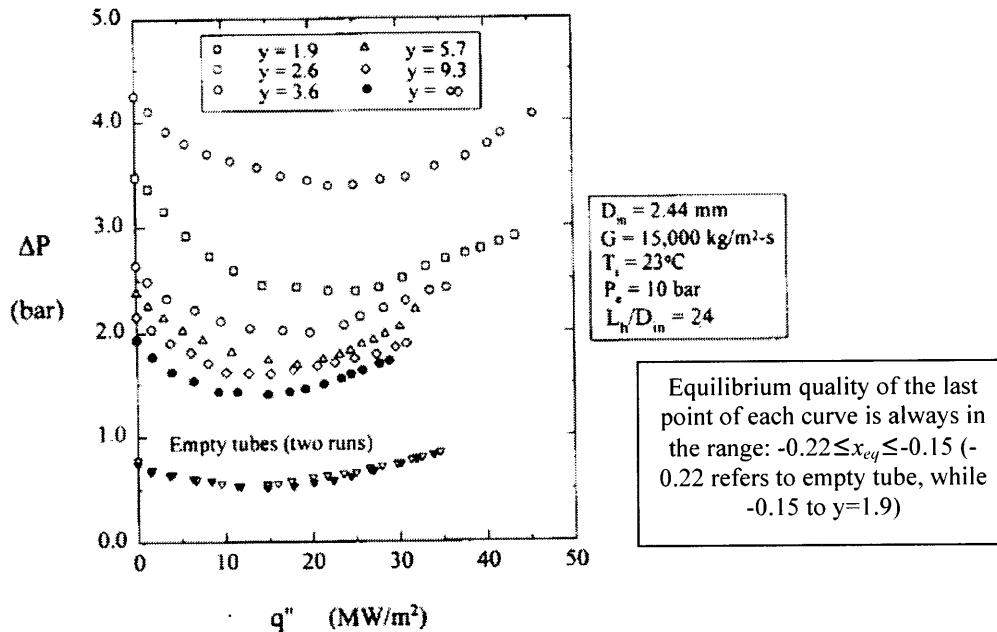


Figure V-A. 15– Effect of twist ratio on pressure drop (test sections burned out at the last point of each curve) (from Tong, Bergles and Jensen, 1966)

All curves in Figure V-A. 15 show the same pressure drop trend: as the heat flux is increased pressure drop decreases, reaches a minimum and then increases. This is due to the fact that, as the heat flux increases from the unheated condition:

- coolant viscosity at the wall decreases, yielding a reduction in friction pressure drop;
- at a certain heat flux bubbles start forming at the wall (ONB), yielding an increase in friction pressure drop.

However, two observations can be made regarding Figure V-A. 15:

- in swirl flow conditions the minimum is reached at a higher heat flux than for the empty tube, and that the smaller is the twist ratio the higher is the heat flux required to have such minimum. The delay in reaching the minimum is due to the enhanced fluid mixing resulting from the swirl, which causes the equilibrium between the friction increase at the wall, due to the bubble formation, and the friction reduction, due to the decreasing fluid viscosity, to be reached later. In other words, assuming that, regardless of the flow characteristics, the same bubble concentration is required to invert the curve slope, in swirl flow a higher

heat flux is needed to generate such bubble concentration¹². Also, this extra-wall loading becomes higher and higher as the fluid mixing is enhanced, i.e. as the twist ratio is decreased.

- After the inversion point is reached, the pressure drop for the empty tube increases and reaches the value corresponding to the unheated conditions. This trend is also shown by the twisted-tape provided tubes, for which however the pressure drop in heated conditions never reaches the unheated value. This is again a consequence of the extra-removal of bubbles, from the wall, characterizing swirl flow conditions: a phenomenon observed and discussed by also Lopina and Bergles (1973), as explained earlier.

The conclusions that can be drawn from the three experimental studies cited above are those listed at the beginning of Section V-A.2.1.2, which are repeated here for clarity:

- ϕ_{lo}^2 in swirl flow subcooled boiling is slightly smaller than in axial flow subcooled boiling;
- the reason for the smaller ϕ_{lo}^2 in subcooled boiling is the lower concentration of bubbles at the wall, downstream the ONB location. While this is due to their extra-removal induced by the swirl, the wall superheat required for ONB is approximately the same in axial and swirl flow.

Since (1) no correlations are available for ϕ_{lo}^2 in swirl flow subcooled boiling, (2) the difference in ϕ_{lo}^2 from axial flow is small and (3) such differences will probably become less and less significant as the system pressure increases¹³, for the inverted core project it was decided to predict friction pressure drop in subcooled boiling as done for axial flow subcooled boiling, i.e. using the second formula of Eq. V-6. This means that no ϕ_{lo}^2 was

¹² If experimental evidences were not available, another reason for the late inversion can be mentioned: the increase in wall superheat required to have ONB. However, as demonstrated by Lopina and Bergles (1973) and Novog et al. (2007) (and discussed earlier), the wall superheat required for ONB does not differ between swirl and axial flow conditions.

¹³ The inverted core operates at a much higher pressure than that for the experimental data of Figure V-A. 11 through Figure V-A. 15. As the heat flux is increased, a TT-provided tube operating at PWR pressure is not expected to experience pressure drop variations as significant as those shown in the figures since (1) water viscosity dependence from temperature is less pronounced at high pressure and (2) bubbles are smaller at high pressure, yielding a lower swirl-induced removal rate.

calculated, and the extra-friction due to the bubbles at the wall was accounted for by neglecting the viscosity reduction at the wall due to heating. This approach will therefore lead to results that, if not accurate, will probably fall on the conservative side.

Chapter VI

Critical Heat Flux

Accurate prediction of the Critical Heat Flux (CHF) in PWRs and the Critical Power Ratio (CPR) in BWRs is of extreme importance. The knowledge of these parameters, coupled with that of the actual conditions at which the cooling channels operate, allows determination of the margin from heat transfer crisis. In PWRs this margin is expressed by means of the Minimum Critical Heat Flux Ratio (MCHFR), which is defined as the minimum value that the ratio between the CHF and the operating heat flux has in the core. The calculation of the CHF is performed, for the inverted PWR, in different ways depending on the flow conditions, i.e. axial vs swirl flow, characterizing the location under investigation. Because of the design variants considered for the inverted PWR, three cases are possible:

- pure axial flow: it characterizes all the channels for the empty-channel PWR design, the bottom half of the channels in the HLTT design and the section of channels upstream the first SLTT in the MSLTT design;
- swirl flow through channel axial sections provided with a long TT: it characterizes the top half of the channels in the HLTT design;
- decaying swirl flow: it characterizes the swirl decay regions between SLTT in the MSLTT design.

The CHF calculation methods for these three cases, as well as CHF enhancement mechanisms in swirl flow, are presented in the following sections.

VI. 1 CHF in pure axial flow

In pure axial flow CHF is calculated using the 2006 Groeneveld look-up tables (Groeneveld et. al, 2007). This method is preferred over well-known CHF correlations

because these look-up tables were developed using an enormous experimental database of about 33000 data points, covering a very broad range of conditions in terms of pressure ($p \leq 21$ MPa), equilibrium quality ($-0.4 \leq x_{eq} \leq 1$), equivalent diameter ($3 < D_{eq} < 25$ mm) and especially mass flux ($0 < G < 8000$ kg/s m²). The inverted PWR operates in fact at mass flux values (~ 7000 kg/s m²) that make several well-known CHF correlations not applicable. The accuracy of the Groeneveld 2006 look-up tables is very good, as shown in Figure VI- 1, and is improved, especially for subcooled conditions, relative to the 1996 version of the same tables.

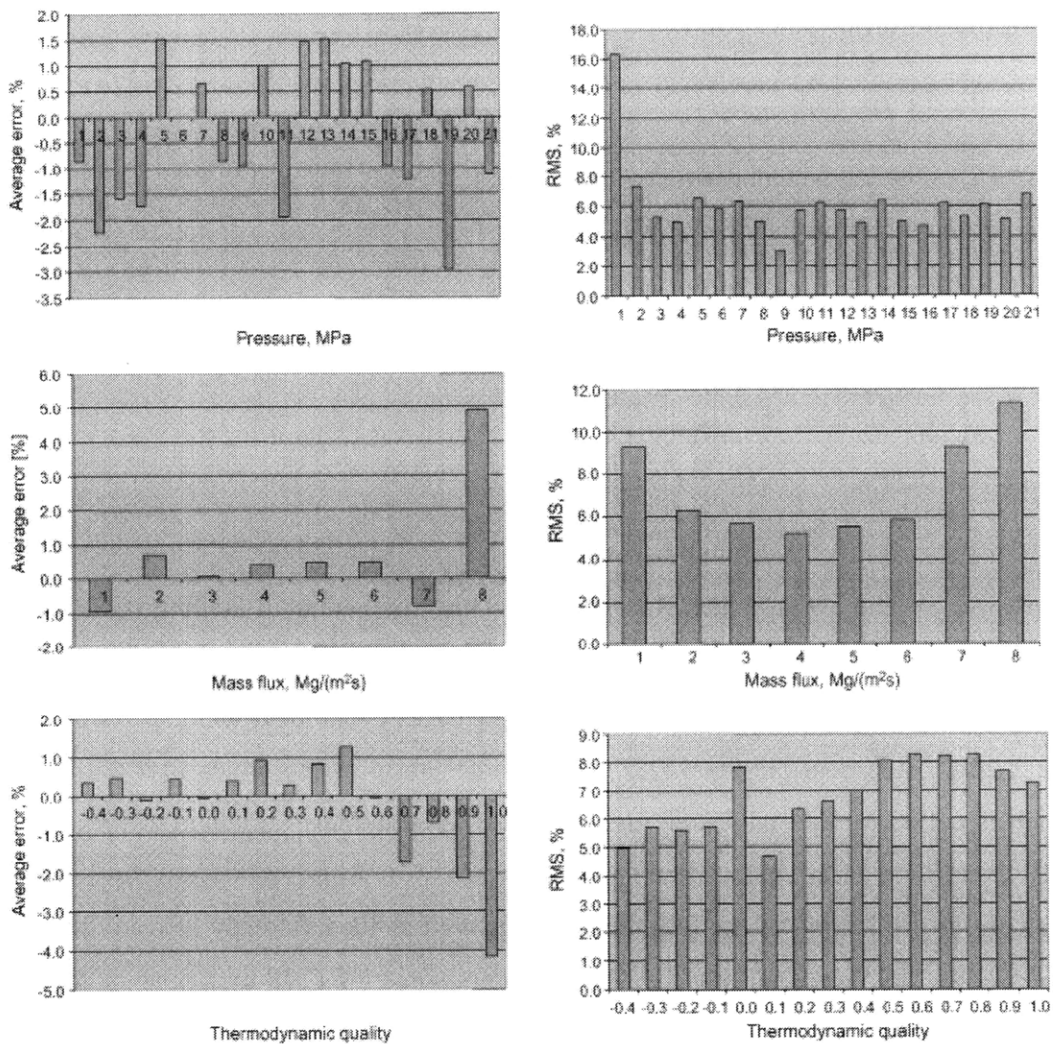


Figure VI- 1– Error distributions for the CHF look-up tables (from Groeneveld et al., 2007)

As well known, the Groeneveld look-up tables contain CHF values corresponding to triplets “pressure-mass flux-equilibrium quality”, which are however referred to an equivalent tube diameter of 8 mm and uniform axial flux distribution. Such values are therefore adjusted to the diameter and flux distribution under investigation by means of correction factors that multiply the values of the tables, i.e.:

$$q''_{CHF} = (q''_{CHF})_{LUT} K_D K_F \quad (VI-1)$$

where $(q''_{CHF})_{LUT}$ is the CHF from the look-up tables. The diameter correction factor, K_D , is given by Groeneveld et al. (2007) as:

$$K_D = \left(\frac{8}{D_{eq}} \right)^{0.5} \quad (VI-2)$$

where D_{eq} is the equivalent diameter under investigation, expressed in mm. The heat flux distribution correction factor, K_F , was obtained from a corrected¹ version of Groeneveld et al. (1986):

$$K_F = \begin{cases} \frac{q''}{\overline{q''_{BLA}}} & \text{if } x_{eq} > 0 \\ 1 & \text{if } x_{eq} \leq 0 \end{cases} \quad (VI-3)$$

where $\overline{q''_{BLA}}$ is the average heat flux from the Onset of Saturated Boiling (OSB) to the location of interest, q'' is the heat flux at the location of interest and x_{eq} is the steam equilibrium quality. The computational use of the Groeneveld look-up tables (Groeneveld et al., 2007) was possible thanks to the implementation of the tables in a Matlab file, which is called by the main code used to study the thermal-hydraulics of the inverted PWR every time a CHF calculation is needed.

The correct application of the look-up tables as well as their (already proven) accuracy, were verified by benchmarking the Matlab code against the CHF experiments described

¹ The formulation of the heat flux distribution factor in Groeneveld et al. (1986) contains two typos: the correction factor is incorrectly shown as the reciprocal of that presented in Eq. VI-3, and the parameter defining the two formulation ranges is defined, in the nomenclature table, as vapor weight fraction instead of steam equilibrium quality as it should be.

in Matzner et al. (1965). These experiments, very valuable for the inverted PWR project, consisted of CHF and pressure drop measurements on geometries and with operating conditions that resemble those of the inverted PWR more than any other experimental work found in the literature². The benchmark of the CHF tests is presented in Appendix A of this chapter.

VI. 2 CHF in swirl flow

With respect to axial flow, CHF in swirl flow is typically higher, and the extent of such enhancement is expressed by the ratio between the CHF in swirl flow and the CHF in purely axial flow, under the same conditions in terms of pressure, steam quality and mass flow rate³. To distinguish from the empty tube Critical Heat Flux Ratio (CHFR), this ratio is referred to as Twisted Tape Critical Heat Flux Ratio (TTCHFR):

$$TTCHFR = \left(\frac{q''_{cr,TT}}{q''_{cr,empty}} \right)_{p,x,\dot{m}} \quad (VI-4)$$

From the available literature on the subject, at LWR pressure, it is possible to conclude that swirl flow causes the TTCHFR to be generally larger than one, and to have the dependence on steam quality, mass flux G , twist ratio y and, for MSLTT designs, TT spacing, qualitatively sketched in Figure VI- 2. This figure does not derive from any experimental study in particular, and has purpose only to show the general trend of TTCHFR with the mentioned parameters. The magnitude of TTCHFR is also approximated, and should not be used for any quantitative evaluation. The main messages that should be taken from Figure VI- 2 are:

² Matzner et al. (1965) tests were performed with water flowing at high pressure and high mass flux through both empty tubes and tubes containing twisted tapes. A detailed description of the geometries and operating conditions examined by Matzner et al. (1965) is presented in Appendix A of Chapter V, which discusses the benchmark of the Matlab code against pressure drop data.

³ Mass flux, and not mass flow rate, is typically used for CHF comparison purposes. However, since the insertion of TTs is aimed at enhancing CHF while keeping the amount of coolant flowing through the channel constant, the comparison is made on same mass flow rate basis. For FLTT geometries, this is almost the same as fixing the mass flux since, for the same mass flow rate, a FLTT-provided tube is characterized by a mass flux which is less than 10% higher than the empty tube. This distinction is instead irrelevant for MSLTT geometries since the flow area of most of the channel is the same as that of the empty tube.

- the maximum gain in CHF with respect to axial flow conditions is not achieved in subcooled conditions, but in saturated boiling;
- TTCHFR increases with mass flux;
- TTCHFR increases as the twist ratio decreases or, equivalently, as the swirl intensity increases.

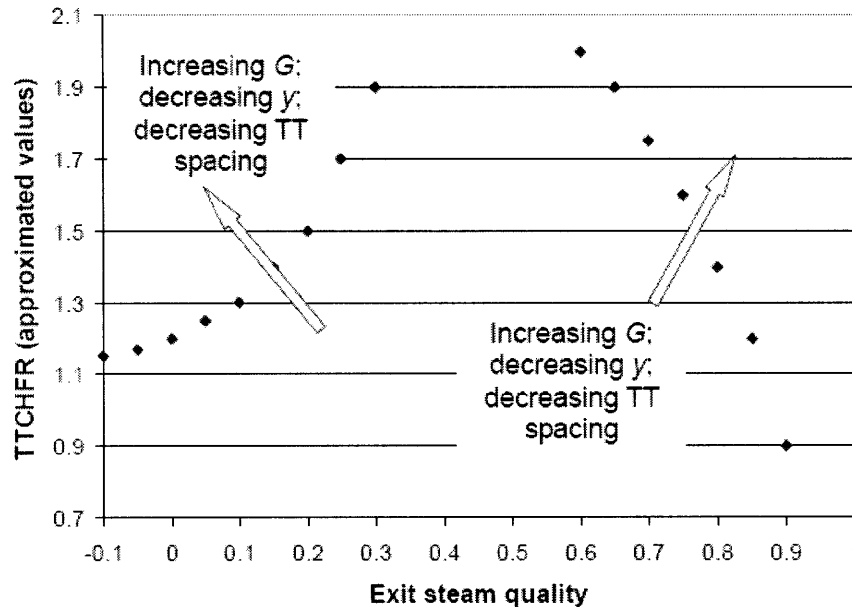


Figure VI- 2– Qualitative behavior of TTCHFR with quality, mass flux and twist ratio

The following subsections are aimed at covering the key aspects of swirl flow and of its analysis in the design of the IPWR. In particular:

- Section VI.2.1 discusses the mechanisms responsible for CHF enhancement in swirl flow;
- Section VI.2.2 presents experimental evidence of the effect that FLTTs and SLTTs have on CHF, relative to empty tubes in pure axial flow. It is important to note that only experimental work performed at high pressure ($p \geq 5$ MPa) have been considered. This is a key point since several studies on CHF with TTs at low pressure, often more complete than those at high pressure, are available in the literature. However, part of the swirl-induced CHF enhancement is related to the

density ratio between saturated liquid and saturated steam, which decreases as the system pressure increases. As pointed out by Inasaka et al. (1991): “*it is thought that the increase in CHF due to the twisted tape at the low pressure is larger than that at the high pressure. As the vapor-liquid density ratio at the low pressure is very large, the effect of making the bubbles collapse is also large*”.

- Section VI.2.3 and Section VI.2.4 present the CHF calculation methods adopted for channels provided with long TTs and for channels provided with MSLTTs, respectively.

VI.2.1 Phenomenology of the influence of swirl flow on CHF

VI.2.1.1 Subcooled boiling and low-quality saturated boiling

In subcooled boiling and low-quality saturated boiling, swirl flow CHF is typically higher than axial flow CHF (exceptions are discussed at the end of this section). The reason is the enhancement in bubble removal from the wall, which causes the heat flux required for steam blanketing of the walls to be higher. Such enhancement increases as the swirl intensity and/or the bubble collapse rate at the wall increase. Increasing the swirl intensity can be achieved by reducing the TT twist ratio, by increasing the mass flux and, in MSLTT designs, by reducing the spacing between TTs. Increasing bubble collapse rate at the wall can be achieved by reducing the degree of subcooling, which facilitates the formation of larger-, easier to remove-, bubbles and/or by reducing the system pressure⁴. The enhancement in bubble removal can be inferred from pressure drop data, as shown in Figure VI- 3. This figure presents the variation of pressure drop with imposed heat flux, for water flowing both in empty tubes and in FLTT-provided tubes. It can be seen that, starting from cold conditions, pressure drop decreases and then increases as the heat flux is increased, for both tube types. The initial reduction is due to the reduction of the viscosity at the wall, while the increase is due to extra-shear at the wall due to bubble

⁴ Reducing the system pressure has multiple effects on boiling-related parameters: it causes the surface tension and the liquid-to-steam density ratio to increase, while the vaporization heat decreases. The higher surface tension causes a reduction in size of the bubbles, which will therefore require more impact energy to be collapsed/swiped from the wall. The increase in liquid-to-steam density ratio offsets this phenomenon by making the impact of liquid being centrifugally diverted by the swirl more effective in collapsing/swiping the bubbles. The reduction in vaporization heat, instead, does not affect bubble collapsing effectiveness since it only increases their rate of formation.

formation, which starts offsetting the viscosity effect from a certain heat flux value. It can be noticed that:

- the slope inversion heat flux is higher for FLTT-provided tubes than for empty tubes;
- the slope inversion heat flux increases as the TT twist ratio decreases.

These are direct consequences of the extra-removal of bubbles that characterizes swirl flow with respect to axial flow. In addition to reducing bubble-induced shear stress at the wall, this extra-removal of bubbles clearly increases CHF.

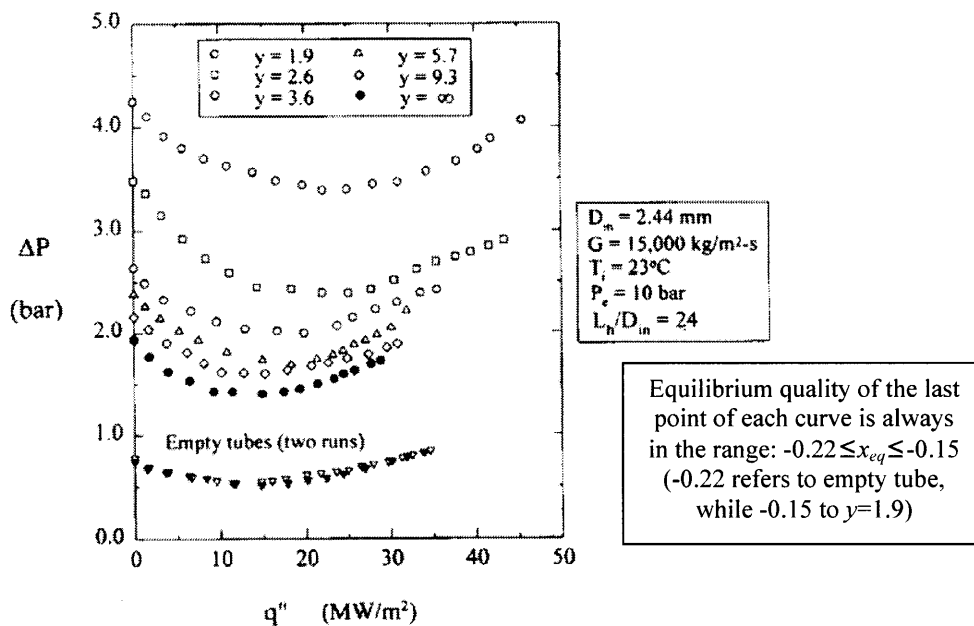


Figure VI- 3– Pressure drop vs heat flux for empty and FLTT-provided tubes (Tong et al., 1996)

Exceptions to the CHF enhancement by swirl flow, in subcooled boiling, have been demonstrated experimentally: they are linked to the use of FLTTs to generate the swirl, and do not occur if most of the tube characterized by swirl flow is actually empty, like in the case of MSLTT-provided tubes. Specifically, axial flow CHF has been verified to be higher than FLTT-induced swirl flow CHF in two scenarios:

- the FLTTs are inserted into small diameter tubes (~2.5 mm) at mass fluxes below about 5500 kg/s m² (Tong et al., 1996);

- gently twisted FLTTs ($y \geq 4$) fit snugly into the tubes (TT-tube diametral gap ≤ 0.6 mm) (Lee and Inoue, 1995).

In both cases the reason for the absence of CHF enhancement or, even, for CHF depression, is the thermal-insulating effect that the tape creates at the tape-wall contact points. If the tube diameter is reduced to very small values, the fraction of tube inner surface that is not cooled by the fluid becomes significant, causing spikes in the difference between the wall and the saturation temperature. In small diameter tubes this happens regardless of the TT twist ratio: Tong et al. (1996) observed this phenomenon for a very small twist ratio, i.e. $y=1.93$. For larger diameter tubes the same phenomenon occurs if the insulating effect, which is always present if the tape fits snugly into the tube, is not offset by a sufficient increase in heat transfer coefficient at the TT-wall contact points, which is the case when the TT twist ratio is large. Lee and Inoue (1995) noticed that CHF reduction, relative to empty tubes, no longer occurs in large y FLTTs when the clearance between the tape and the wall is increased above 0.7 mm, so that the insulating effects vanishes. Looser-fit FLTTs are however subjected to flow-induced fretting, which forces the designer to choose, for subcooled boiling, small twist ratio FLTTs, SLTTs or swirl generators that do not touch the channel walls.

VI.2.1.2 Medium and high-quality saturated boiling

Under medium and high steam quality conditions, i.e. in annular flow, CHF in swirl flow is generally higher than in axial flow. Like in subcooled boiling, however, exceptions exist, and are discussed at the end of this section.

The CHF increase at medium and high quality is due to an enhanced droplet deposition on the wall. The centrifugal field characterizing swirl flow causes liquid droplets to be diverted toward the wall, where they contribute to liquid film thickening thus delaying dryout. This has been experimentally verified, even though in a quite different context, by Hills et al. (1996). They tested gas-liquid mixtures flowing through a venturi followed by a short TT, and measured the fraction of liquid entrained, in the form of droplets, in the gas current, both before and after the TT. As shown in Figure VI- 4, referring to a throat velocity of 100 m/s, the insertion of a typical-geometry TT caused the percentage of liquid entrained as drops to decrease from about 27% (upstream the TT) to 11%

(downstream the TT). Hills et al. (1996) also noticed that the extent of entrained liquid abatement could be further reduced by adopting a fish-tail TT, i.e. a TT that instead of having the typical straight exit edge has a full-width V-notch, as shown in the bottom right hand corner of Figure VI- 4. This atypical fish-tail shape allowed a further 8% abatement in entrained drops. The reason for such further improvement, according to Hills et al., is that with typical shape TTs some liquid tends to run along the tape, accumulate at the tape exit edge, and re-atomize due to shear stress. If the tape downstream end is shaped with a full-width V-notch, the liquid film running on the tape and approaching its downstream end is diverted to the walls instead of accumulating there and being re-atomized.

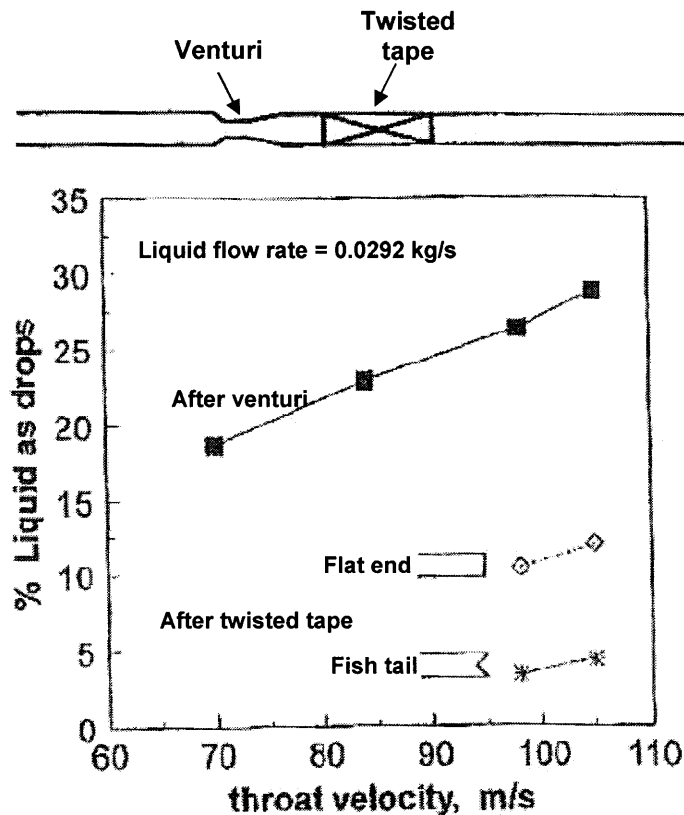


Figure VI- 4– Effect of twisted tape on liquid entrainment (from Hills et al., 1996)

However, circumstances exist in which a reduction in CHF relative to axial flow conditions is instead observed. Besides the obvious scenario, for MSLTT designs, of insufficient swirl due to excessive SLTT spacing, CHF reduction relative to the axial

flow case can affect FLTTs when too much liquid runs along the tape. There exists a tradeoff between enhanced droplet deposition on the wall and liquid running along the tape. In most cases the first phenomenon dominates, but under high quality and weak centrifugal field conditions (i.e. low mass flux and/or large twist ratio) the fraction of liquid running along a FLTT can be significant, thus causing early dryout. This was demonstrated by Moeck et al. (1964), as shown in Figure VI- 5, and highlighted by Hewitt (2003). Figure VI- 5 shows the ratio between the critical heat flux, q''_{CHF} , and the heat flux yielding unity steam quality at the exit, q''_{VAP} , as a function of mass flux, for different outlet steam qualities. It can be seen that, for a give steam quality, the smaller is the mass flux the more likely is that the FLTT-provided tube performs worse than the empty tube. The subtraction of liquid from the walls can be therefore avoided by employing small twist ratio FLTT, by increasing mass flux, or by generating swirl with non-continuous inserts, like SLTTs.

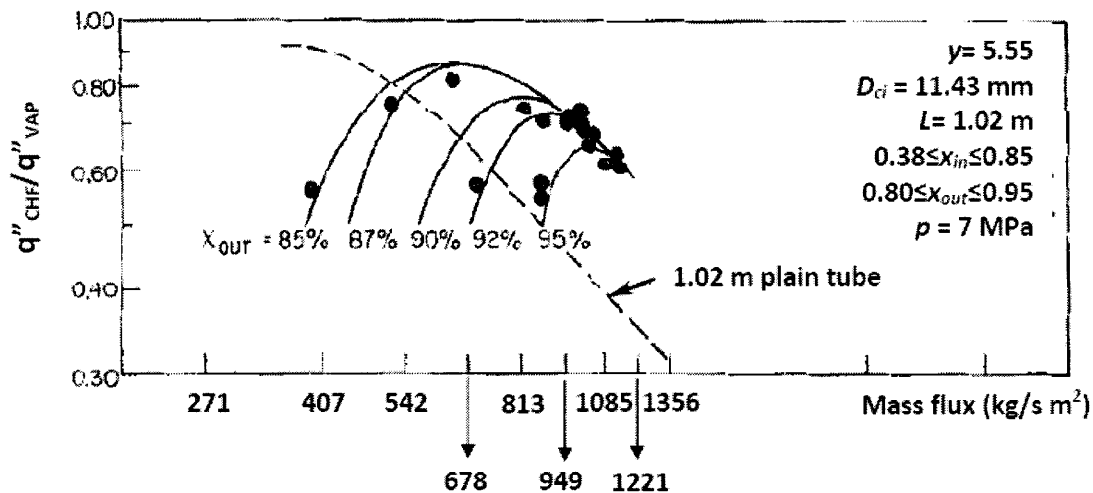


Figure VI- 5– Evidence of TTCHFR reduction below unity caused by liquid running along the tape (modified from Moeck et al., 1964)

Also, it is important to note that unlike in subcooled boiling, in saturated boiling the TT insulating effect discussed in Section VI.2.1.1 does not cause reduction in CHF, or at least not below the axial flow value (Lee and Inoue, 1995).

VI.2.2 Experimental evidence of swirl flow effect on CHF at high pressure

The available literature on CHF in TT-induced swirl flow, at high pressure, is very limited, and the few experimental works performed are summarized in Table VI-A- 1. Since the heat transfer crisis mechanism is very different between subcooled boiling and saturated boiling, it would be convenient to present CHF enhancement evidence separately between these two operating conditions. However, this is not possible since none of the studies listed in Table VI-A- 1 addresses subcooled boiling specifically and, when present, subcooled CHF data are a very small percentage of the CHF data actually collected. Therefore, conclusions about this boiling regime can be deduced by either using the few available data, or by extrapolating CHF vs steam quality curves toward near-zero and negative qualities. Section VI.2.2.1 presents results from experimental work performed on FLTT geometries, while Section VI.2.2.2 refers to SLTT geometries.

VI.2.2.1 FLTT geometries

Among the findings by the investigators shown in Table VI-A- 1, only those by Viskanta (1961), Matzner et al. (1965), Moussez et al. (1965A) and Staub (1969) are presented next. Results from the other experimental studies on CHF with FLTTs, i.e. Moeck et al. (1964) and Brevi et al. (1971) are not presented because they refer only to exit steam quality conditions close to pure steam.

Viskanta (1961)

Figure VI- 6 shows the TTCHFR as a function of the exit quality (coinciding with the critical quality since the heat flux was axially uniform) and of the mass flux, for the two twist ratios investigated by Viskanta (1961). To improve readability in the low TTCHFR region, and since few data fall above TTCHFR=3.5, the bottom part of this figure has been redrawn in Figure VI- 7, where interpolating lines have also been added. From Figure VI- 7 it can be seen the increase in TTCHFR with quality and mass flux, as well with decreasing twist ratio. More importantly, it can be inferred that, in subcooled boiling, the TTCHFR is between 1.3 and 1.5. Based on what is known about twist ratio and mass flux effect (see Figure VI- 2), higher values should be obtainable with $y < 2.5$ and/or $G > 2712 \text{ kg/s m}^2$.

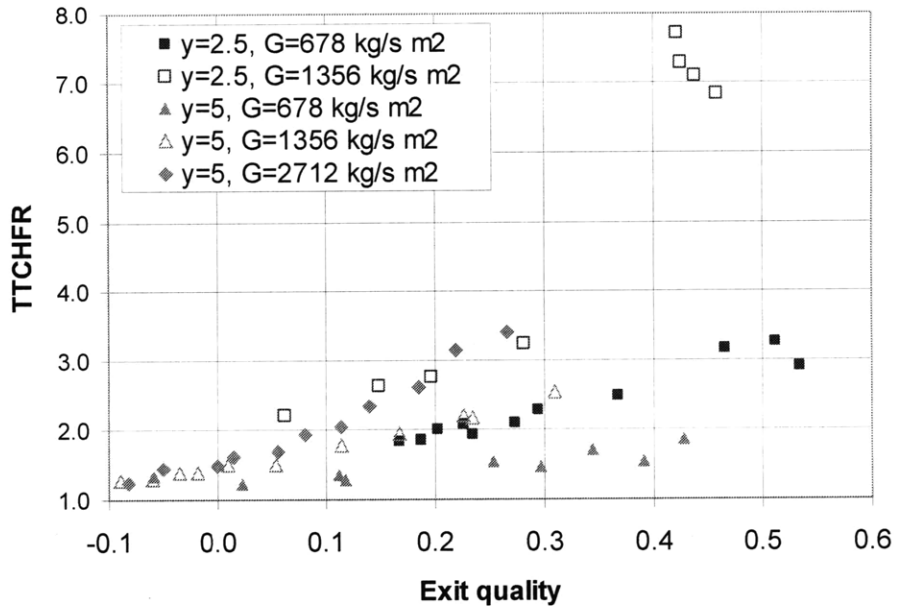


Figure VI- 6– TTCHFR vs exit quality for different values of twist ratio and mass flux, $p=13.8 \text{ MPa}$ (derived from Viskanta, 1961)

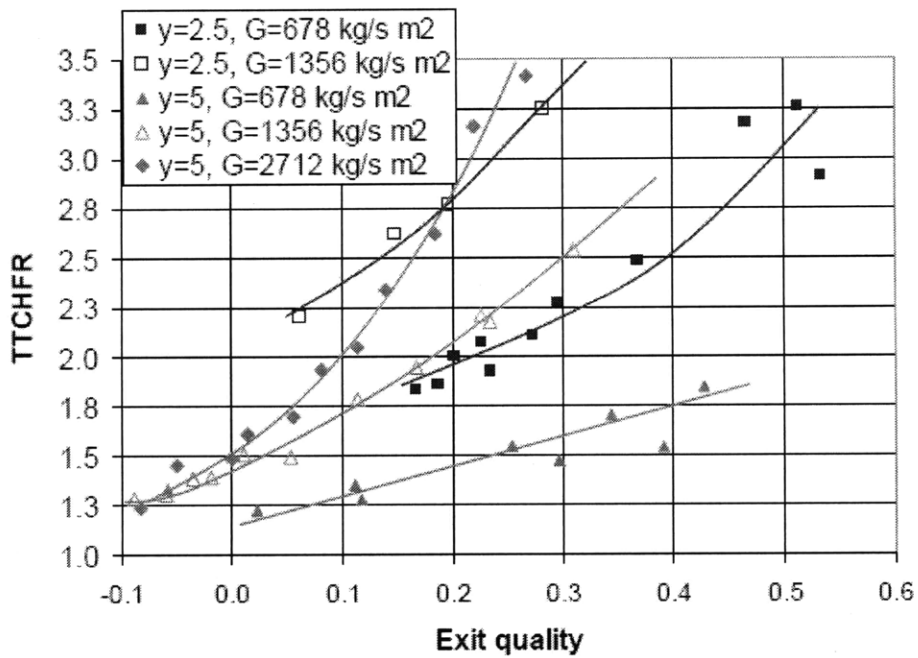


Figure VI- 7– TTCHFR vs exit quality for different values of twist ratio and mass flux (bottom part of Figure VI- 6, with interpolating line added)

However, unlike all the other investigators, Viskanta did not measure the CHF for the empty tubes, but analytically predicted this parameter by means of an unknown correlation⁵. Also, Viskanta's results for FLTTs show almost no dependence of the CHF on the mass flux, which is inconsistent with the findings by all the other investigators⁶.

Matzner et al. (1965)

Figure VI- 8 shows the TTCHFR as a function of exit steam quality and mass flux, for the FLTT (twist ratio equal to 15) used by Matzner et al. (1965). Their tests with FLTTs only covered the medium-high quality region, and no subcooled CHF data are available. Experimental points identified with the same marker type refer to runs performed with similar mass flux values, whose average value is that shown in the figure legend. Since runs performed with different mass fluxes did not yield comparable critical qualities, it is not possible to infer any trend of TTCHFR with mass flux. The only meaningful result deducible from the figure is that, even with a relatively little twisted FLTT (i.e. $\gamma=15$), a ~30-50% increase in CHF is achievable with a FLTT.

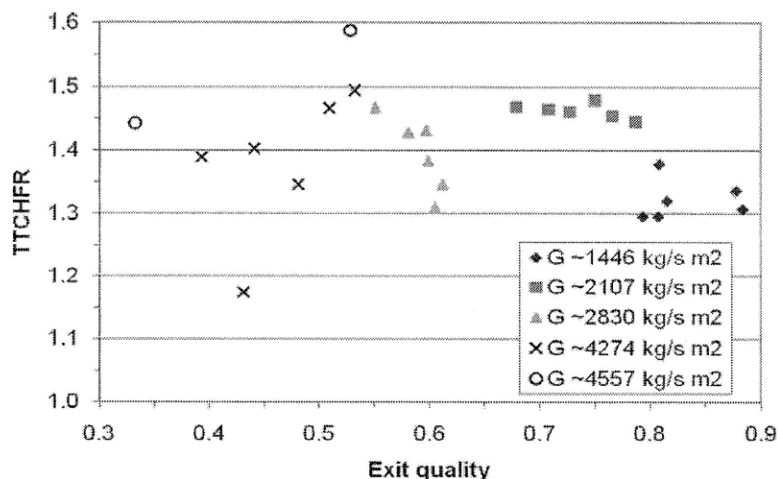


Figure VI- 8– TTCHFR vs exit quality for different mass flux values ($\gamma=15$, $p=6.89$ MPa) (derived from Matzner et al., 1965)

⁵ The correlation used by Viskanta in 1961 came from a private communication about which no details are provided. Its accuracy was confirmed by comparing the corresponding predictions to those obtained using the Groeneveld look-up tables (Groeneveld et al., 2007). Since the use of a correlation made the construction of Figure VI- 6 much easier, the TTCHFR was computed using, as empty tube CHF, the value obtained with the Groeneveld look-up tables.

⁶ The fact that, in Figure VI- 6, different mass flux values yield different curves is due to the dependence of the empty tube CHF on mass flux, not of the FLTT CHF on mass flux.

Moussez et al. (1965A)

Results from Moussez et al. (1965A) consist of only two⁷ experimental points which, in spite of their number, are presented anyway since the steam quality they refer is closer to zero than that of many other investigators. The CHF enhancement they observed, as shown in Figure VI- 9, was of the order of 20-30%.

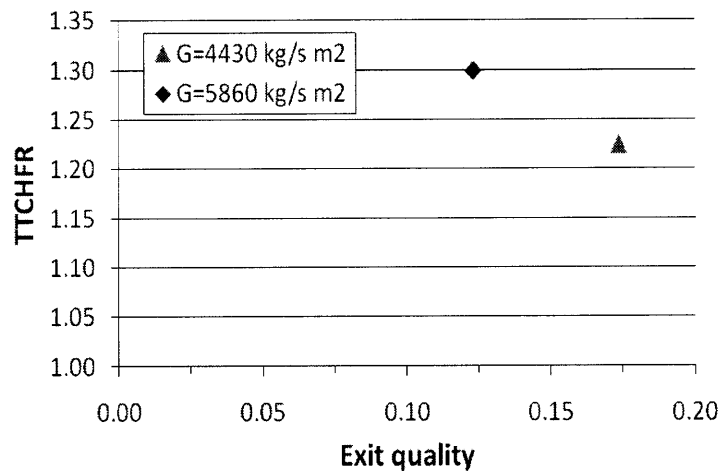


Figure VI- 9– TTCHFR vs exit quality ($\gamma=3$, $p=7$ MPa) (derived from Moussez et al., 1965A)

Staub (1969)

Results from Staub (1969) are shown in Figure VI- 10. The exit steam qualities characterizing his tests are high relative to typical PWR values, but not as high as those of Moeck et al. (1964) and Brevi et al., (1971). Staub's results are shown also to highlight their similarity to those obtained by Matzner et al. (1965) and shown in Figure VI- 8, in spite of the use of a different fluid, i.e. Freon 22 vs water.

⁷ Most of the CHF experimental data collected by Moussez et al. (1965A) refer to a 4-rod bundle containing turbulence promoters. Although interesting from a general CHF enhancement viewpoint, the involved geometry to which they refer does not allow using them for the assessment of the effectiveness of TTs in increasing CHF in a simple tube. Moussez, however, also collected two CHF experimental data point on a single 10 mm-diameter tube containing a FLTT.

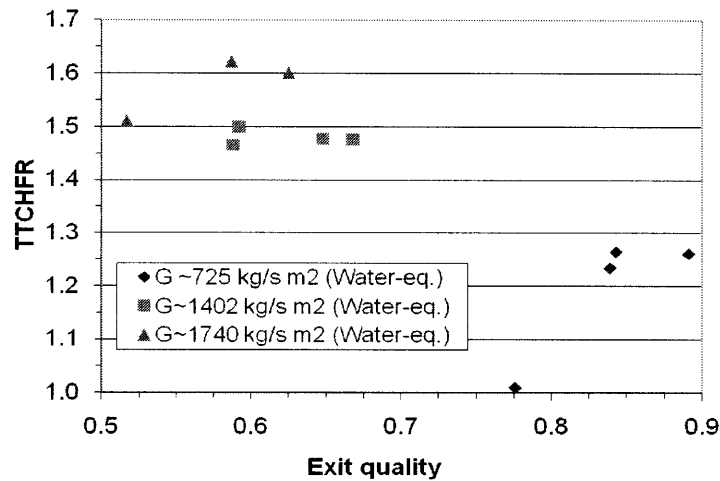


Figure VI- 10– TTCHFR vs exit quality for different mass flux values ($y=16.25$, H₂O-equivalent $p=6.5$ MPa) (derived from Staub, 1969)

VI.2.2.2 SLTT geometries

With respect to FLTT geometries, the complete understanding of CHF for SLTT geometries requires knowledge of the effect that an additional independent geometric variable, the TT spacing s , has on CHF. Unfortunately, no comprehensive studies have ever been performed on the effect that twist ratio, mass flux and TT spacing have on CHF, meaning that some or all the above parameters have either been kept constant during the tests, or have been varied over limited ranges. Moreover, like for FLTTs, no studies specifically referred to subcooled boiling at high pressure exist, and CHF in this boiling regime has to be inferred from few experimental points, or extrapolated from data collected at low, positive, steam qualities.

The key findings from two the two most relevant studies on SLTT geometries shown in Table VI-A- 1 are presented next: those from Hassid et al. (1966) and Peterlongo et al. (1964). More emphasis is given to the former since it is by far the most complete experimental work on CHF enhancement using SLTTs. Results from the other studies are not reported since:

- they refer only to geometries characterized by very long swirl decay regions (Matzner et al., 1965, for which $s \geq 115$);

- they refer to thermal hydraulic conditions characterized by instability-induced pulsed-type CHF, whose conversion into TTCHFR has been found difficult to perform (Henkel et al., 1965);
- they refer to high-quality conditions only (Bennett et al., 1967).

Also, it was not possible to present all the experimental data in a single representation since differences in geometry and operating conditions did not allow a consistent comparison. This did not prevent, however, gaining a quantitative understanding of the effect that some parameters have on CHF.

Hassid et al. (1966)

Hassid investigated the effect that twist ratio, number of revolutions, TT-wall gap width, mass flux and steam quality have on CHF. Only the lack of subcooled boiling data and data referred to medium and large twist ratios prevents their study from being considered comprehensive. They tested water flowing vertically through uniformly heated round tubes provided with one and multiple SLTTs. Among the types of twisted tapes analyzed, the most exhaustively tested was what they call “Promoter #9”, which was analyzed under different conditions in terms of mass flux and length of the downstream swirl decay region. Figure VI- 11 contains the key results concerning that promoter, in the form of TTCHFR as a function of exit quality, x_{out} , mass flux, G and length of the swirl decay region, s . It can be seen that:

- there are no data in the subcooled and zero quality regions;
- the TTCHFR increases as the steam quality increases (for constant G and s);
- the TTCHFR increases as the mass flux increases (for constant x_{out} and s);
- the TTCHFR increases as the length of the swirl decay region decreases (for constant x_{out} and G);
- extrapolation of existing data to $x_{out} \sim 0.05$ (typical value for a PWR at the exit of the hot subchannel) is feasible only for the case $G=3800 \text{ kg/s m}^2$, $s=50$, which yields a TTCHFR of about 1.4-1.5. It is reasonable to think that a larger TTCHFR could have been reached if a mass flux above 3800 kg/s m^2 had been tested.

Besides the results on CHF enhancement, Hassid et al. (1966) came to an important conclusion about the effect that the number of 360° revolutions of a SLTT, N_{rev} , has on CHF. They concluded that “*it can be inferred that from the point of view of heat transfer crisis the number of pitches can be limited to 1-1.5: any further increase should therefore be avoided since it would lead to a pressure drop increase across the promoter without any advantage*”. This conclusion motivated the choice, for the design of the IPWR, of using MSLTTs in place of a single FLTT, and of setting the number of revolutions of each tape to 1.5.

Peterlongo et al. (1964)

Peterlongo et al. (1964) investigated the CHF enhancement resulting from inserting a single SLTT with twist ratio 2.8 in a vertical round tube. Unlike Hassid et al. (1966), they only varied the length of the downstream heated swirl decay region and the mass flux. Investigations on the effect that twist ratio, number of revolutions, and TT-to-wall gap width have on CHF were not performed. Key results from Peterlongo et al. (1964) are summarized in Figure VI- 12. It is important to note that, although the heating was axially uniform, the CHF was not always detected at the exit of the heated length. In fact, when the swirl decay region was very short the extent of swirl at its exit was often high enough to cause the critical conditions to be reached just upstream of the TT where, in spite of a lower steam quality, the flow was purely axial. In these situations the measured CHF cannot be associated with the exit quality, since these parameters refer to different axial locations. Therefore, in the construction of Figure VI- 12, markers corresponding to the exit quality for those cases were enclosed with uparrow-provided circles, to stress the fact that the experimental TTCHFR corresponding to the steam quality of the marker is equal or greater than the TTCHFR at which the marker is located. This was done since this section discusses the maximum CHF enhancement attainable with SLTTs equally spaced along a channel: if Peterlongo had positioned a SLTT upstream of the SLTT he actually tested, the TTCHFR measured would have been higher than that he actually measured.

An interesting observation, on the effect that the increase of the swirl decay length has on TTCHFR, can be made by comparing the point $s=50$, $G=3800$, $x\sim 0.09$ in Figure VI- 11 with the point $s=105$, $G=3800$, $x\sim 0.09$ in Figure VI- 12. While a TT spacing equal to 50

diameters allows for a 75% enhancement in CHF, its increase beyond the swirl-to-axial transition results in no enhancement at all⁸.

⁸ The fact that Figure VI- 12 shows, for some experimental points, a TTCHFR below unity is probably due to uncertainties and scatter of experimental measurements. This is because, no matter how long the swirl decay region is, a SLTT-provided tube is not expected to have a CHF lower than that of an empty tube operating in the same conditions.

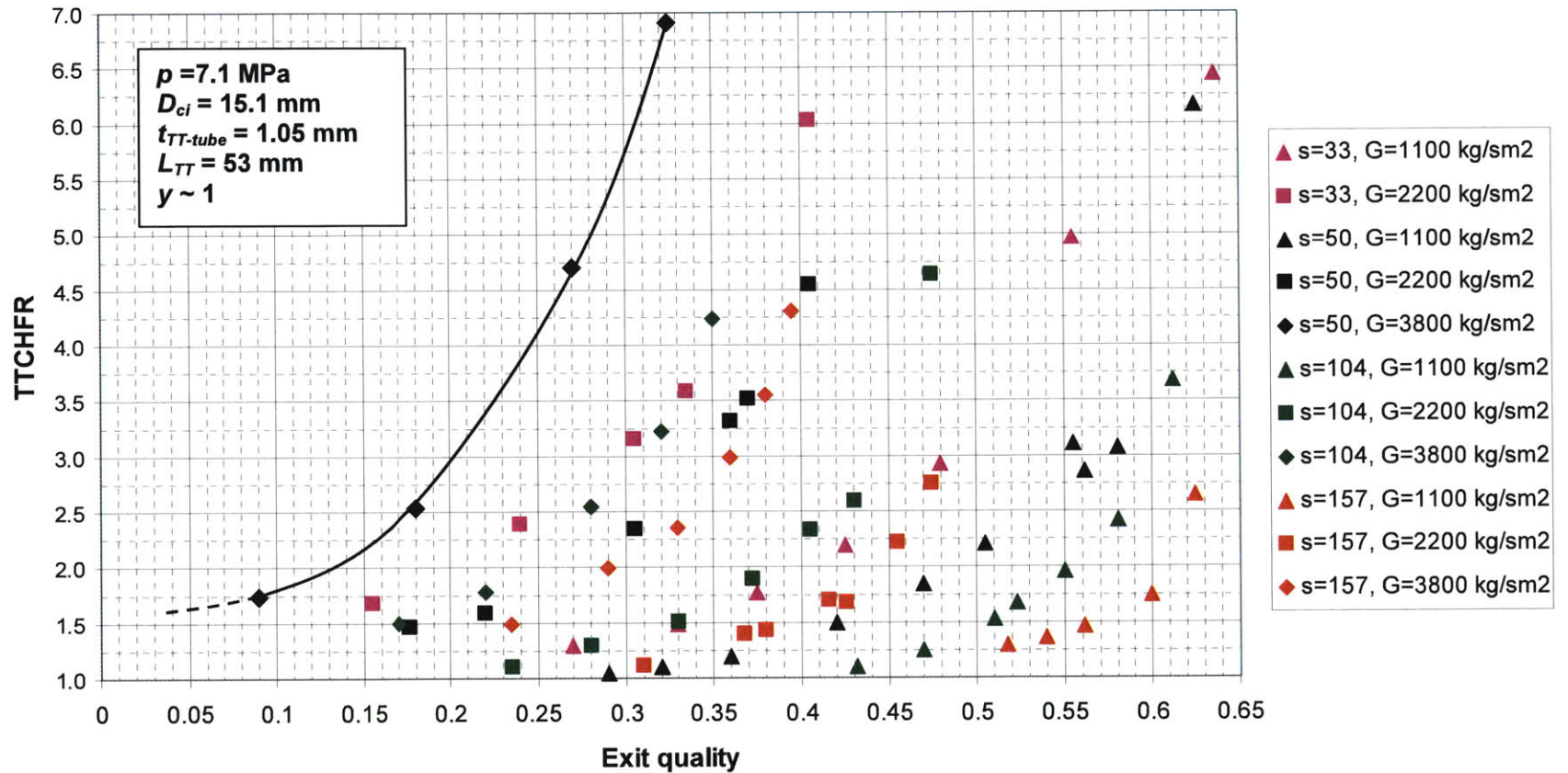


Figure VI- 11– TTCHFR vs exit quality for a single SLTT followed by a swirl decay region, with line interpolating the most interesting experimental points (obtained from Hassid et al., 1966)

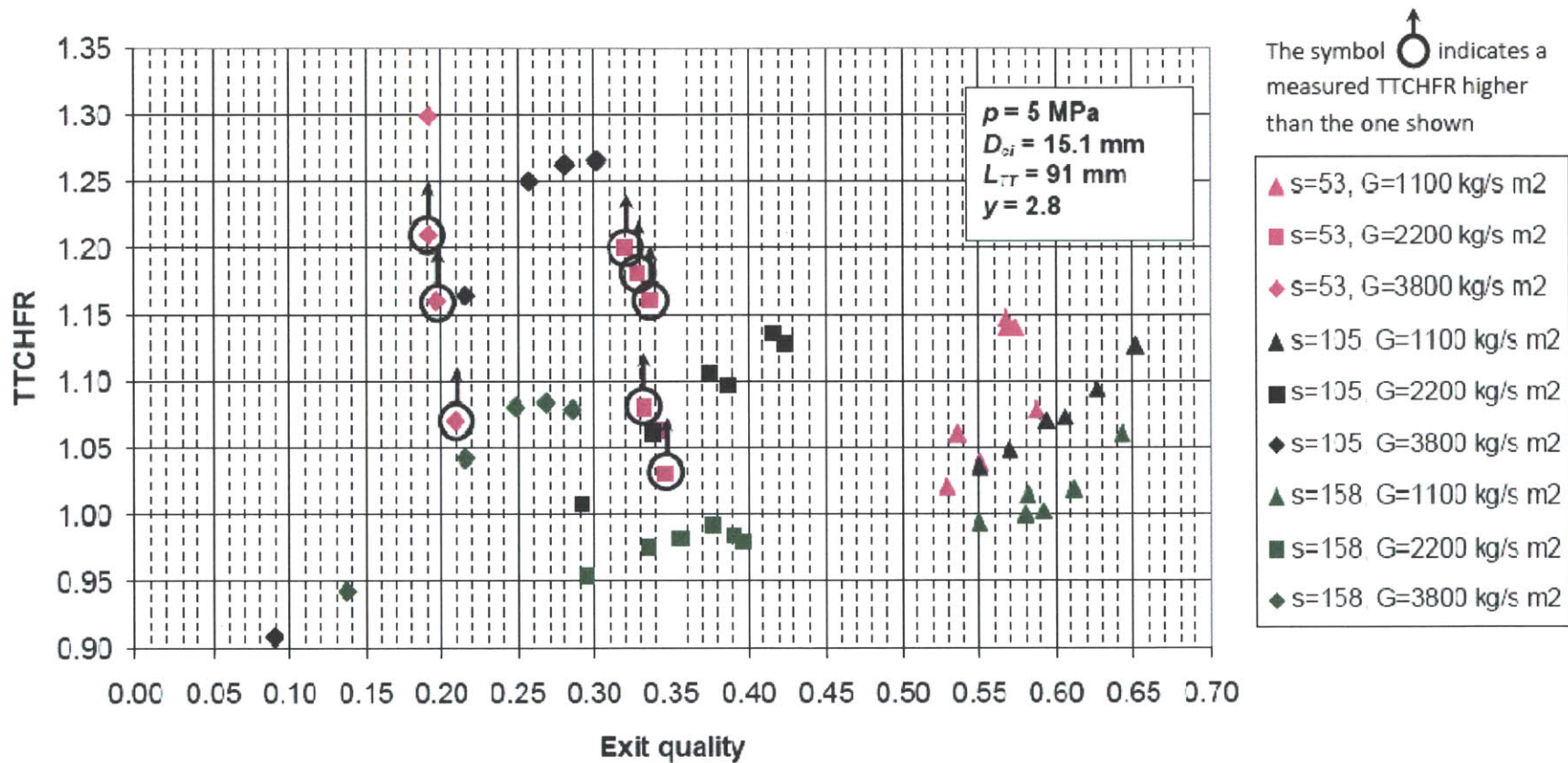


Figure VI- 12– TTCHFR vs exit quality for a single SLTT followed by a swirl decay region (from Peterlongo et al., 1964)

VI.2.3 CHF calculation method in presence of long TTs

Two CHF correlations for swirl flow in presence of long TTs have been found in the literature: the Jensen correlation (Jensen, 1984) and the Weisman correlation (Weisman et al., 1994). The former was obtained by a regression analysis of experimental data collected by various authors, while the latter is a phenomenological model. Even though phenomenological models are typically preferred over models developed by fitting experimental data, the Jensen correlation (actually a slightly modified version of it) was selected to calculate CHF in the axial zones provided with a long TT, for the following reasons:

- the Weisman correlation has been found too involved and several doubts arose in the selection of the parameters to be entered into the correlation itself;
- the Jensen correlation was developed using almost all the available experimental CHF data in swirl flow, which cover broad ranges in terms of mass flux and quality.

The modified Jensen correlation is presented next. A complete discussion on the original form of the Jensen correlation, the reason of the modification and the verification of its correct implementation in the Matlab code can be found in Appendix A of this chapter.

The modified Jensen correlation has the following form:

$$TTCHFR = \left(\frac{q''_{cr,FLTT}}{q''_{cr,empty}} \right)_{p,x,\dot{m}} = \begin{cases} A & \text{if } A \geq 1 \text{ and } y \leq y_{crit} \\ 1 & \text{if } A < 1 \text{ and } y \leq y_{crit} \end{cases} \quad (VI-5)$$

whereas for $y > y_{crit}$ the correlation is not applicable. Since, as discussed in Appendix A of this chapter, $y_{crit}(15.5 \text{ MPa}) = 4.7$, only HLTT designs with $y \leq 4.7$ are analyzed. Limiting the applicability of the original Jensen correlation to twist ratios less than the critical twist ratio y_{crit} is the modification mentioned above. The meaning of the parameters shown in Eq. VI-5 is:

$q''_{cr,FLTT}$: CHF at the taped axial location of interest;

$q''_{cr,empty}$: CHF in the tube assumed to be empty, at the same axial location, calculated using the Katto correlation (Katto, 1980);

$$A = (4.597 + 0.09254y + 0.004154y^2) \left(\frac{\rho_g}{\rho_f} \right)^{0.7012} + 0.09012 \ln \left(\frac{a}{g} \right) \quad (\text{VI-6})$$

$$y_{crit} = \begin{cases} 23.023p^{-0.4114} & \text{if } 0.1 \leq p \leq 3 \text{ MPa} \\ -5.6794 \ln(p) + 20.134 & \text{if } 3 < p \leq 21 \text{ MPa} \end{cases} \quad (\text{VI-7})$$

y : twist ratio;

ρ_g and ρ_f : saturated steam and liquid densities;

g : gravitational acceleration;

$$\frac{a}{g} = \text{nondimensional centrifugal acceleration} = \frac{2}{gD_{ci}} \left(\frac{V_{ax,TT} \pi}{2y} \right)^2 \quad (\text{VI-8})$$

D_{ci} : tube inside diameter;

$$V_{ax,TT}: \text{axial velocity in presence of the tape} = \frac{G_{TT}}{\alpha \rho_g + (1 - \alpha) \rho_f}$$

G_{TT} : mass flux in presence of the tape;

$$\alpha: \text{homogeneous void fraction} = \frac{1}{1 + \frac{\rho_g}{\rho_f} \frac{1-x}{x}}$$

The original Jensen correlation is claimed to predict CHF with an average deviation, relative to experimental data, of +/-10.2%. Particularly, of the 207 experimental points used by Jensen in the regression analysis, 81% are predicted to within +/-15% and 91% are predicted to within +/-20%.

VI.2.4 CHF calculation method in decaying swirl flow

As already pointed out, CHF experimental data in presence of SLTTs (1) are few, (2) never refer to near-zero quality operating conditions and (3) come from experimental tests performed under different geometric and operating conditions. This prevented both

the development of an experimentally-based CHF correlation for subcooled boiling in decaying swirl flow and the comparison between any CHF correlation and the experimental data, since zero- and near-zero experimental data are not available. Also, even if the obstacle, for the development of a correlation, of having saturated boiling CHF experimental data collected under very different operating conditions was neglected, and a correlation could indeed be developed, it would likely not be applicable to subcooled conditions. The reason for this is the different swirl-induced CHF enhancement mechanisms in saturated boiling, relative to subcooled boiling, which would likely cause subcooled CHF to be overestimated (see Section VI.2.1). Therefore, to predict CHF in zero- and near-zero quality conditions, in presence of SLTTs, a simple mechanistic model was developed. The model is based on two assumptions:

- the CHF enhancement at the exit of each SLTT is equal to that predicted using Eq. VI-5, i.e. it is equal to the CHF enhancement that would characterize that location if the channel was provided with a FLTT having a twist ratio equal to that of the SLTTs;
- in the swirl decay region the CHF increase percentage, relative to an empty tube in pure axial flow, decreases proportionally with the reduction of the velocity tangential component.

The first assumption is correct based on the fact that the decision to set the number of 360°-revolutions of each SLTT to 1.5 derived from experimental observations, by Hassid et al. (1966), according to which any further increase in number of revolutions, i.e. any further increase of the TT length toward the FLTT configuration, is not accompanied by an increase in CHF (see Section VI.2.2.2 and Appendix B of Volume 2). The second assumption, although not verified experimentally, is reasonable since:

- the tangential velocity is the parameter responsible, in subcooled boiling, of the enhancement, relative to pure axial flow, of the bubble removal at the wall;
- the tangential velocity is maximum at the TT exit and decreases as the distance from the tape increases. In particular, when the swirl has decayed completely, the tangential velocity is zero and consequently also the CHF enhancement is zero.

Quantitatively, the CHF at any position downstream of a TT is calculated as:

$$q''_{cr,SLTT} = q''_{cr,empty} + (q''_{cr,FLTT} - q''_{cr,empty}) S_f \quad (VI-9)$$

where $q''_{cr,empty}$ is the CHF of the empty tube in pure axial flow, computed using the Groeneveld look-up table (Groeneveld et al., 2007), $q''_{cr,FLTT}$ is the CHF of the FLTT-provided channel and S_f is the swirl fraction. The latter parameter, which is a function of the distance from the TT exit, is proportional to the fraction of the tangential velocity relative to the TT exit (=1 at the TT exit and =0 beyond the location of complete swirl decay). From Eq. VI-9 it follows that the CHF enhancement, relative to an empty tube in axial flow, is:

$$TTCHFR = \left(\frac{q''_{cr,SLTT}}{q''_{cr,empty}} \right)_{p,x,\dot{m}} = 1 + \left(\frac{q''_{cr,FLTT}}{q''_{cr,empty}} - 1 \right) S_f \quad (VI-10)$$

where the ratio $\frac{q''_{cr,FLTT}}{q''_{cr,empty}}$ is calculated using the modified Jensen correlation, i.e. Eq. VI-5,

while S_f is computed as recommended⁹ by Kreith and Sonju (1965):

$$S_f(z_T) = \sqrt{\frac{\int_0^{R_{ci}} [W(r, z_T)]^2 r dr}{\int_0^{R_{ci}} [W(r, 0)]^2 r dr}} \quad (VI-11)$$

where R_{ci} is the tube inner radius, z_T is the distance of the axial location of interest from the TT exit, while W , which is a function of both the radial coordinate r and the axial coordinate z_T , is a dimensionless velocity defined as the ratio between the tangential velocity and the axial velocity (the latter being the same for axial and swirl flow). Using results from Algifri and Bhardwaj (1985), which are discussed in detail in Appendix B of this chapter, W can be predicted using the following expression:

$$W(r, z_T) = \frac{7.73}{4y} J_1 \left(7.664 \frac{r}{D_{ci}} \right) \exp \left[- \frac{29.368(1 + \varepsilon_d)}{N_R} \frac{z_T}{D_{ci}} \right] +$$

⁹ Kreith and Sonju (1965) used this expression to calculate an angular velocity fraction. The angular velocity was that of a movable blade used to measure the degree of swirl and, like in the present investigation, the corresponding fraction was defined as relative to the exit of the swirl-generating device.

$$\begin{aligned}
& -\frac{5.26}{4y} J_1\left(14.032 \frac{r}{D_{ci}}\right) \exp\left[-\frac{98.448(1+\varepsilon_d)}{N_R} \frac{z_T}{D_{ci}}\right] + \\
& +\frac{4.04}{4y} J_1\left(20.346 \frac{r}{D_{ci}}\right) \exp\left[-\frac{206.98(1+\varepsilon_d)}{N_R} \frac{z_T}{D_{ci}}\right] + \\
& -\frac{3.38}{4y} J_1\left(26.648 \frac{r}{D_{ci}}\right) \exp\left[-\frac{355.06(1+\varepsilon_d)}{N_R} \frac{z_T}{D_{ci}}\right] + \\
& +\frac{3.00}{4y} J_1\left(32.928 \frac{r}{D_{ci}}\right) \exp\left[-\frac{542.12(1+\varepsilon_d)}{N_R} \frac{z_T}{D_{ci}}\right] + \\
& -\frac{3.06}{4y} J_1\left(39.232 \frac{r}{D_{ci}}\right) \exp\left[-\frac{769.58(1+\varepsilon_d)}{N_R} \frac{z_T}{D_{ci}}\right] + \\
& +\frac{3.33}{4y} J_1\left(45.520 \frac{r}{D_{ci}}\right) \exp\left[-\frac{1036.04(1+\varepsilon_d)}{N_R} \frac{z_T}{D_{ci}}\right] + \\
& -\frac{5.43}{4y} J_1\left(50.612 \frac{r}{D_{ci}}\right) \exp\left[-\frac{1280.8(1+\varepsilon_d)}{N_R} \frac{z_T}{D_{ci}}\right]
\end{aligned} \tag{V-A-1}$$

where:

$$W(r, z) = \text{dimensionless tangential velocity} = \frac{w(r, z_T)}{v_{ax}};$$

$w(r, z_T)$: tangential velocity at a point distant z_T from the TT exit and r from the tube axis;

v_{ax} = axial velocity in pure axial flow = G_{empty}/ρ ;

y = twist ratio of the SLTT generating the swirl;

J_1 : Bessel function of order 1;

D_{ci} = tube inner diameter;

$N_R = \text{Re}_{empty}/2$;

ε_d = dimensionless eddy diffusivity = $4.15 \times 10^{-3} N_R^{0.86}$

It is important to note that, even though the swirl decay regions lie between the outlet of a TT and the inlet of the successive TT, the CHF analysis assumes they exist between the outlets of successive TTs, i.e. the swirl buildup characterizing the taped region is neglected. This assumption, which is conservative from the CHF viewpoint, was made to avoid the need to compute the CHF differently in the taped regions, where the understanding of the complex fluid behavior would require an effort which is not justified in view of the small percentage of axial length actually occupied by the taped regions.

Eqs. VI-11 and V-A-1 accurately predict the swirl fraction variation downstream a swirl-generating device. As discussed in Appendix B of this chapter, this was demonstrated by Kreith and Sonju (1965), who compared analytical predictions with experimental data. A discussion on how accurate these equations are, when combined with Eq. VI-10, for predicting CHF is presented in Appendix A of this chapter (Section VI-A.3).

Appendix VI-A: Benchmark of CHF predictions against experimental data

This Appendix presents the benchmark of the CHF calculation methods used for the inverted PWR against experimental data available in the literature. The benchmark is organized in three sections:

- Section VI-A.1: CHF in axial flow. Experimental data used for the benchmark are from Matzner et al. (1965).
- Section VI.A.2: CHF in swirl flow generated by a FLTT. Experimental data used for the benchmark are from Matzner et al. (1965).
- Section VI.A.3: CHF in subcooled boiling swirl flow generated by a SLTT. Because of the lack of experimental data under these conditions, only a brief discussion on the applicability of the selected CHF calculation method in subcooled boiling is presented. Only two experimental points, from Hassid et al. (1966) and Peterlongo et al. (1964) are considered for this discussion.

Among the numerous experimental CHF values available in the world database, those collected by the mentioned authors have been selected since they derive from experimental measurements performed on geometries and with operating conditions that resemble those of the inverted PWR, i.e. TT-induced swirl flow of two-phase mixtures at high (water-equivalent) pressures (≥ 5 MPa). Table VI-A- 1 shows the parameter ranges of these experimental studies, as well as those characterizing some other experimental work found in the literature. All the studies were performed with an axially uniform power distribution. It is likely that the table is comprehensive, and that no studies are missing. Other experimental works on CHF enhancement with TTs are available in the literature, but they refer to low pressures and have not been considered.

Study	Type of test section	D_{ci} (mm)	y	Heated lengths ¹⁰		N_{rev}	t_{TT} (mm)	TT-tube diametral gap (mm)	Mass flux (kg/s m ²)	x_{in}	x_{out}	Fluid type and pressure (MPa)
				Total	Downstream the TT exit							
Viskanta (1961)	FLTT	7.94	2.5 and 5	0.457 (57)	N.A. ¹¹	N.R. ¹²	0.13	~0	678 to 2712	-1.51 to 0.089	-0.089 to 0.53	Water; 13.8
Peterlongo et al. (1964)	One SLTT at the inlet	15.10	2.8	4.1 (272); 3.3 (218); 2.4 (159)	2.4 (158); 1.6 (106); 0.8 (53)	~1.2	? ¹³	0.4	1100 to 3800	-0.24 to 0.06	0.09 to 0.65	Water; 5 and 6.5
Moeck et al. (1964)	FLTT	11.43	5.55 and 34.5	1.02 (89)	N.A.	N.R.	0.25	~0	390 to 1145	0.38 to 0.85	0.80 to 0.95	Water; 7
Henkel et al. (1965) (work also cited in Mayinger et al., 1966)	One SLTT at the inlet	7.0	2.32 and 5.71	?	0.28 (40);	1 and 2	0.5	?	2300 to 3500	-0.2 to 0	-0.023 to 0.23	Water; 7.1 and 10.1
Matzner et al. (1965)	FLTT and MSLTTs	10.16	15 (FLTT); 5 (SLTT)	FLTT: 4.88 (480); SLTT: 4.88 (480); 3.66 (360)	2.39 (235); 1.17 (115)	SLTT: 0.5	0.38	~0	1261 to 9792	-0.52 to -0.03	0.04 to 0.88	Water; 6.89
Moussez et al. (1965A)	FLTT	10.00	3	0.8 (80)	N.A.	N.R.	0.2 to 0.8	?	4480 and 5840	0.01 to 0.04	0.15 to 0.19	Water; 7
Hassid et al. (1966)	SLTTs connected with a solid rod	15.10	~0.57 to ~2.72 ¹⁴	≤2.4 (159)	0.23 (15) to 2.3 (153)	0.7 to 3.5	2.5	0.6 to 6.1	1100 to 3800	-0.39 to 0.69	0.02 to 0.73	Water; 5 and 7

¹⁰ Heated lengths are expressed in meters and, in parenthesis, in number of tube inner diameters.

¹¹ N.A.: Not Applicable

¹² N.R.: Not a Relevant parameter for FLTTs.

¹³ Question marks indicate unknown values, either because they are not specified in the article consulted or because it was not possible to consult the article itself.

¹⁴ The twist ratios shown for Hassid et al. (1966) are obtained using the TT peripheral angle, α , which is the geometric parameter used by Hassid to express the extent of twisting characterizing each TT. This angle is defined as the complementary of the angle between the TT profile and the tube axis and is related to the twist ratio through the geometric law: $y = \frac{\pi}{2tg(90-\alpha)}$ (Wang and Sunden, 2002). However, some discrepancy exists between the values so obtained and those

calculable by measuring the TT pitch and diameter from the pictures that Hassid et al. (1966) shows for some of the TTs they used. In particular, the smallest twist ratio seems to be closer to 0.7 than to 0.57.

Table VI-A-1 (cont'd): Experimental studies on CHF in swirl flow at high pressure (both FLTT and SLTT designs)												
Study	Type of test section	D_{ci} (mm)	y	Heated lengths ¹⁵		N_{rev}	t_{77} (mm)	TT-tube diametral gap (mm)	Mass flux (kg/s m ²)	x_{in}	x_{out}	Fluid type and pressure (MPa)
				Total	Downstream the TT exit							
Bennett et al. (1967)	One SLTT	12.62	4	3.66 (290)	0 to 2 (0 to 158)	0.5	0.25	2.22	2712	-0.2 to -0.09	0.32 to 0.46	Water; 6.9
Staub (1969)	FLTT	10.16	16.25	1.54 (151)	N.A.	N.R.	0.24	0.08	511 to 1275 (water-equivalent: 706 to 1762)	-0.29 to -0.025	0.52 to 0.89	Freon-22; 1.2 (water-equivalent: 6.5 MPa)
Brevi et al. (1971)	FLTT	10.00	3	2.0 (200)	N.A.	N.R.	0.8	-0	758 to 1038	-0.2 to 0	0.92 to 0.99	5.1

¹⁵ Heated lengths are expressed in meters and, in parenthesis, in number of tube inner diameters.

VI-A.1 Benchmark in axial flow

Matzner et al. (1965) measured CHF for water flowing upward in axially uniformly heated empty tubes having lengths: 4.87 m (16 ft), 3.66 m (12 ft) and 2.43 m (8 ft). Several CHF calculation methods/correlations have been benchmarked against Matzner data. Such methods/correlations were implemented in the Matlab code used to study the thermal hydraulics of the IPWR¹⁶. Two of them, i.e. the EPRI-1 correlation and the W3 correlation, were also tested by running the VIPRE code. In this way, not only the comparison of the CHF predictions by the Matlab code with Matzner data was possible, but also a cross-comparison between the Matlab code and the VIPRE code. Methods and correlations are summarized in Table VI-A- 2 together with the corresponding validity ranges.

Table VI-A- 2: CHF correlations benchmarked against Matzner et al. (1965) experimental data				
Correlation	Mass flux (kg/s m ²)	Pressure (MPa)	Steam equilibrium quality	Equivalent diameter (mm)
Groeneveld look-up table (Groeneveld et al., 2007)	0<G<8000	$p \leq 21$	$-0.4 \leq x_{eq} \leq 1$	$3 < D_{eq} < 25$
EPRI-1 (EPRI-NP-2609, 1982), as reported in Eq. D-36 by Cuta et al. (1985)	271<G<6103	$1.38 < p < 16.9$	$-0.25 \leq x_{eq} \leq 0.75$	Typical PWR and BWR
Tong-68 modified by Inasaka-Nariai (Inasaka-Nariai, 1987; Tong, 1968)	1300<G<20000	$0.1 < p < 20$	$-0.46 \leq x_{eq} \leq -0.001$	$2 < D_{eq} < 20$
W3 (Tong, 1972) as reported in Eq. D-5 of Cuta et al. (1985)	1356<G<6781	$6.89 < p < 15.86$	$-0.15 \leq x_{eq} \leq 0.15$	$5.1 < D_{eq} < 17.8$
Katto-80 (Katto, 1980)	$3 \times 10^{-9} \leq \frac{\sigma \rho_f}{L_h G^2} \leq 8 \times 10^{-4}$ (See footnote ¹⁷)		Not given	$1 < D_{eq} < 80$
MacBeth (MacBeth and Thompson, 1964; MacBeth, 1965) as reported in Cuta et al. (1985)	10<G<18581	$0.1 < p < 12.1$	$-0.45 \leq x_{eq} \leq -0.99$	$1 < D_{eq} < 37.5$

¹⁶ An ad-hoc Matlab code was developed since the study of the IPWR thermal hydraulics required correlations and models that are not available in a standard code, such as VIPRE (Cuta et al., 1985). Swirl flow-related correlations, as well as the most recent version of the Groeneveld look-up table (Groeneveld, 2007) are examples of tools that are not available in VIPRE.

¹⁷ Katto (1980) does not explicitly state the validity range of his correlation. The range shown here for the dimensionless number $\frac{\sigma \rho_f}{L_h G^2}$ is obtained from the plots he extensively uses to explain how the correlation

has to be used.

Prediction errors have been computed both for all the Matzner's experimental points combined (Table VI-A- 3) and, separately, for the experimental points characterized by the lowest outlet qualities ($0.8\% \leq x_{out} \leq 8.9\%$) (Table VI-A- 4). The latter calculation allows assessment of the correlation accuracy for the thermal hydraulics conditions that, among all those considered by Matzner et al. (1965), are closer to those characterizing a PWR hot subchannel¹⁸. Referring to the results shown in the two tables, the following observations can be made:

- the Katto correlation (Katto, 1980) and the Groeneveld look-up tables are the most accurate CHF prediction methods. When all Matzner's points are considered, the RMS percentage error is 7.1% for both methods. When only the low-quality points are considered ($0.8\% \leq x_{out} \leq 8.9\%$) the RMS percentage error is 12.1% for the Katto correlation, and 18.7% for the Groeneveld look-up tables.
- the EPRI-1 and the MacBeth correlations are also quite accurate, with RMS error percentages below 23%;
- the Tong-68 correlation (version modified by Inasaka and Nariai) shows a good RMS error of 17.6% over the whole experimental point spectrum, while it is not as accurate when the low quality points only are considered (RMS=47.7%);
- the W3 correlation is characterized by large errors. This is probably due to the high mass flux and high steam quality characterizing most of the experimental tests (only about 25% of the low-quality tests have $G < 6700 \text{ kg/s m}^2$).
- the W3 and EPRI-1 correlations give the same CHF predictions regardless of whether they are used through the Matlab code or through the VIPRE code. This is a further proof of the accuracy of the Matlab code written to study the thermal hydraulics of the inverted PWR.

¹⁸ The steam quality at the exit of the hot subchannel of a typical PWR is about 4-8%. These values can be derived from the hot subchannel exit void fraction reported in the Seabrook Power Station UFSAR (2002), i.e. 21%.

Table VI-A- 3–Errors¹⁹ in CHF predictions against Matzner et al. (1965) experimental data (all data for empty tubes)			
Code used	CHF correlation	RMS error (kW/m ²)	RMS error %
Matlab code	Groeneveld look-up tables	253	7.1
	Katto	253	7.1
	EPRI-1	452	12.7
	Tong-68 (Inasaka and Nariai version)	625	17.6
	W3	1576	44.3
VIPRE	EPRI-1	450	12.7
	W3	1217	34.2
	MacBeth	669	18.8

Table VI-A- 4–Errors in CHF predictions against Matzner et al. (1965) experimental data (empty tubes; low-quality points only)			
Code used	CHF correlation	RMS error (kW/m ²)	RMS error %
Matlab code	Groeneveld look-up tables	318	18.7
	Katto	205	12.1
	EPRI-1	387	22.8
	Tong-68 (Inasaka and Nariai version)	810	47.7
	W3	1155	68.0
VIPRE	EPRI-1	385	22.7
	W3	1185	69.8
	MacBeth	375	22.1

Figure VI-A- 1 shows the distribution of the CHF predictions relative to the experimental values, for three of the correlations listed in Table VI-A- 2. As it can be seen, the CHF predictions through the Katto correlation (Katto, 1980) and through the Groeneveld look-up tables (Groeneveld et al., 2007) are within the +/-15% error band most of the times. Even though the Katto correlation was proved to be slightly more accurate than the look-up tables in the subcooled region (see Table VI-A- 4), the latter is preferred due to the

¹⁹ Root Mean Square (RMS) error is defined as: $RMS = \sqrt{\frac{1}{N} \sum_{j=1}^N (q''_{CHF, predicted} - q''_{CHF, exp})^2}$, where N is the number of experimental points, while $q''_{CHF, predicted}$ and $q''_{CHF, exp}$ are the calculated and experimental CHFs respectively. The RMS error percentage is defined as: $RMS\% = 100 \frac{RMS}{\max(q''_{CHF, exp}) - \min(q''_{CHF, exp})}$

larger database used for its development, and was therefore selected for the prediction of the CHF in the sections of the core characterized by purely axial flow.

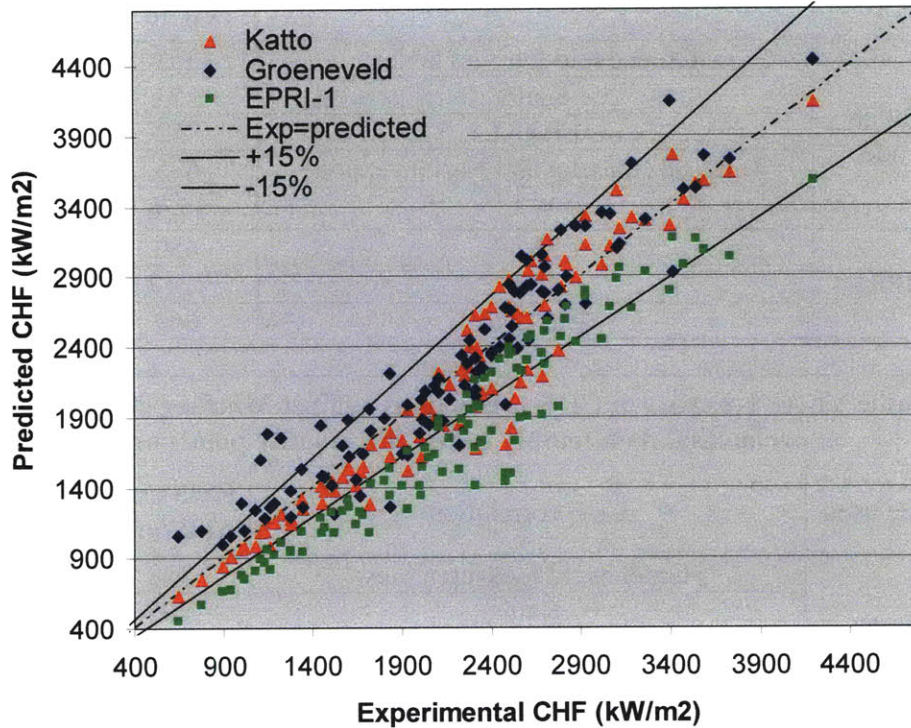


Figure VI-A- 1: Experimental vs predicted CHF for some of the correlations benchmarked against Matzner et al. (1965) empty tube experimental data

VI-A.2 Benchmark in FLTT-induced swirl flow

Two CHF correlations for swirl flow have been found in the literature: the Jensen correlation (Jensen, 1984) and the Weisman correlation (Weisman et al., 1994). The former was obtained by a regression analysis of experimental data collected by various authors, while the latter is a phenomenological model. Even though phenomenological models are typically preferred over models developed by fitting experimental data, the Jensen correlation (actually a slightly modified version of it) was selected to calculate CHF in the axial zones provided with a long TT, for the following reasons:

- the Weisman correlation has been found too involved and several doubts arose in the selection of the parameters to be entered into the correlation itself;

- the Jensen correlation was developed using almost all the available experimental CHF data in swirl flow, which cover broad ranges in terms of mass flux and quality.

Section VI-A.2.1 presents the Jensen correlation in its original form, Section VI-A.2.2 discusses an anomaly found in its application, and Section VI-A.2.3 presents the modified version of this correlation, which was implemented in the Matlab code for the analysis of the inverted PWR.

VI-A.2.1 Original Jensen correlation

The Jensen correlation was obtained through a nonlinear regression analysis on the CHF experimental data collected by some of the investigators shown in Table VI-A- 1. The only experimental data not considered in the regression were those by Peterlongo et al. (1964) and Hassid et al. (1966), which are both referred to SLTT geometries. The original Jensen correlation has the following form:

$$\frac{q''_{CHF,FLTT}}{q''_{CHF,empty}} = \begin{cases} A & \text{if } A \geq 1 \\ 1 & \text{if } A < 1 \end{cases} \quad (\text{VI-A-1})$$

where:

$q''_{CHF,FLTT}$: CHF at the axial location of interest in the FLTT-provided tube;

$q''_{CHF,empty}$: CHF in the tube assumed to be empty, at the same axial location, calculated using the Katto correlation (Katto, 1980);

$$A = \left(4.597 + 0.09254y + 0.004154y^2\right) \left(\frac{\rho_g}{\rho_f}\right)^{0.7012} + 0.09012 \ln\left(\frac{a}{g}\right) \quad (\text{VI-A-2})$$

y : FLTT twist ratio;

ρ_g and ρ_f : saturated steam and liquid densities;

g : gravitational acceleration;

$$\frac{a}{g} = \text{nondimensional centrifugal acceleration} = \frac{2}{gD_{ci}} \left(\frac{V_{ax,IT} \pi}{2y}\right)^2 \quad (\text{VI-A-3})$$

D_{ci} : tube inside diameter;

$$V_{ax,TT}: \text{axial velocity in presence of the tape} = \frac{G_{TT}}{\alpha\rho_g + (1-\alpha)\rho_f}$$

G_{TT} : mass flux in presence of the tape;

$$\alpha: \text{homogeneous void fraction} = \frac{1}{1 + \frac{\rho_g}{\rho_f} \frac{1-x}{x}}$$

The Jensen correlation is claimed to predict CHF with an average deviation, relative to experimental data, of +/-10.2%. Particularly, of the 207 experimental points used in the regression, 81% are predicted to within +/-15% and 91% are predicted to within +/-20%.

Figure VI-A- 2 compares the CHF predictions obtained using the Jensen correlation to the FLTT experimental data collected by Matzner et al. (1965). This comparison cannot be considered a benchmark since Jensen used all the available experimental data on CHF for FLTT geometries, including those by Matzner et al. (1965), to develop his correlation, and the good accuracy evident from Figure VI-A- 2 is therefore expected. Rather, this comparison was performed to verify the correct implementation of the Jensen correlation in the Matlab code²⁰.

²⁰ In spite of having an apparent simple formulation, the Jensen correlation is complicated by the need to compute $q''_{CHF,empty}$ using the Katto correlation (Katto, 1980). The implementation of this correlation in the Matlab code was found quite involved due to the fact that the Katto correlation computes CHF in different ways depending on the location of the operating point inside regime maps having the dimensionless numbers $\frac{\sigma\rho_f}{G^2L_h}$ and $\frac{L_h}{D_{ci}}$ as abscissa and ordinate respectively.

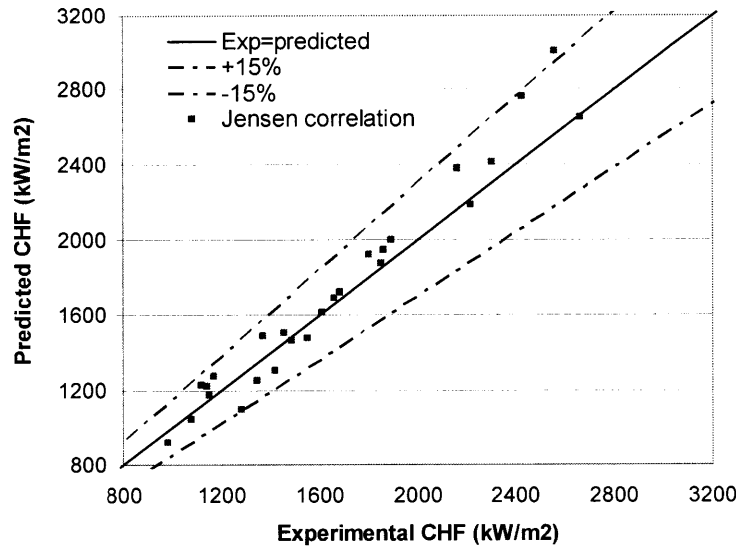


Figure VI-A- 2: Experimental vs predicted CHF using the Jensen correlation, against Matzner et al. (1965) experimental data

Even though the accuracy claimed for the Jensen correlation is quite good, its use is not recommended for comparing CHF performance of FLTTs having twist ratios spanning broad ranges. The following section discusses the reason for such inadequacy, while Section VI-A.2.3 presents the modified version of the Jensen correlation, which was used for the study of the axial zones provided with long TTs.

VI-A.2.2 Jensen correlation anomaly

A nonphysical behavior has been observed when plotting $\frac{q''_{CHF,FLTT}}{q''_{CHF,empty}}$, from Eq. VI-A-1, as a function of y , with all the other parameters fixed. It was expected that, at least at low quality²¹, the CHF ratio decreased as y increased, and that eventually it reached an

²¹ With respect to axial flow conditions, the effect that swirl flow has on CHF depends mainly on the TT twist ratio, steam quality and mass flux. In single-phase liquid as well as at low-quality conditions, swirl flow increases CHF by enhancing bubble removal near the wall, and the smaller is the twist ratio the higher is the CHF increase. At high quality conditions the effect that swirl flow has on CHF is more complex, since on one hand it causes liquid droplets to move to the walls, therefore thickening the liquid film that prevents dryout from occurring, but on the other, if the mass flux is sufficiently high, it tends to make that film thinner by favoring droplet entrainment. In the latter case, it may be expected that a reduction in twist ratio results in a reduction in CHF.

asymptotic value at high y . This was proved to be the case at low y , while from a certain twist ratio, here called critical twist ratio y_{crit} , the CHF ratio increases as y increases. As a consequence of this behavior, if applied to scenarios where $y > y_{crit}$, the original form of the Jensen correlation yields unphysical results, like that shown in Figure VI-A-3, where a FLTT with twist ratio 11 has better CHF performance than a FLTT with twist ratio 1.5, at all steam quality conditions.

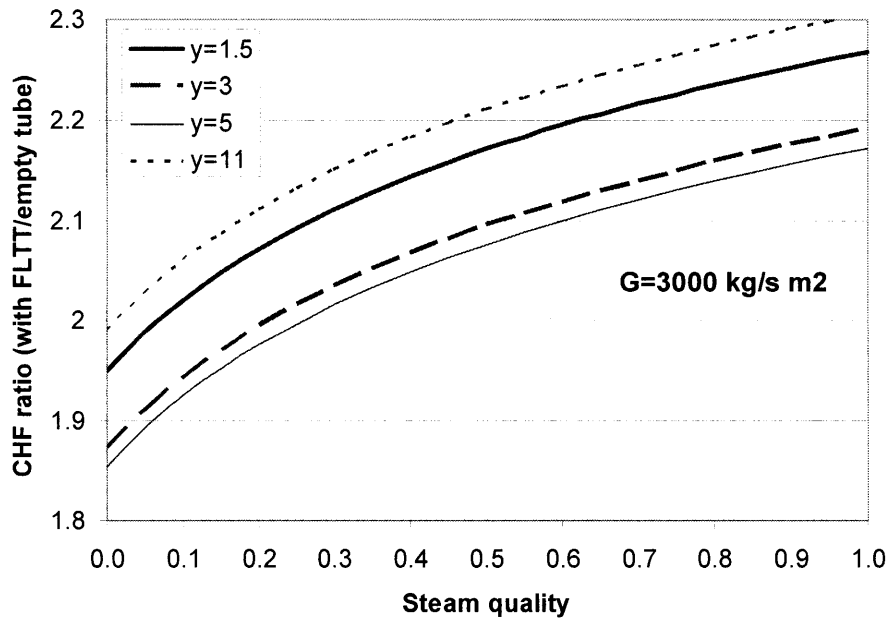


Figure VI-A-3: CHF ratio vs steam quality, for different twist ratios, as predicted by the Jensen correlation (FLTT geometry, $G=3000 \text{ kg/s m}^2$; $D_{ci}=10 \text{ mm}$; $p=15.5 \text{ MPa}$)

The critical twist ratio is a function of the density ratio ρ_g/ρ_f , and therefore of the operating pressure, and can be calculated by differentiating the RHS of Eq. VI-A-2 and by equating the resulting derivative to zero, i.e.:

$$\frac{d\left(\frac{q''_{CHF,FLTT}}{q''_{CHF,empty}}\right)}{dy} = 0 \quad \Rightarrow \quad \left(9.254 \times 10^{-2} + 8.308 \times 10^{-3} y\right) \left(\frac{\rho_g}{\rho_f}\right)^{0.7012} - \frac{0.18024}{y} = 0$$

$$\Rightarrow y_{crit} = -5.569 + \sqrt{31.017 + 21.695 \left(\frac{\rho_f}{\rho_g} \right)^{0.7012}}$$

Figure VI-A- 4 shows the critical twist ratio as a function of the operating pressure. To improve readability, the pressure range 0.1-22 MPa has been divided in two: 0.1-2 MPa (shown in the small plot on the top right hand side) and 2-22 MPa (shown in the large plot). At typical PWR pressure, i.e. 15.5 MPa, $y_{crit} = 4.7$.

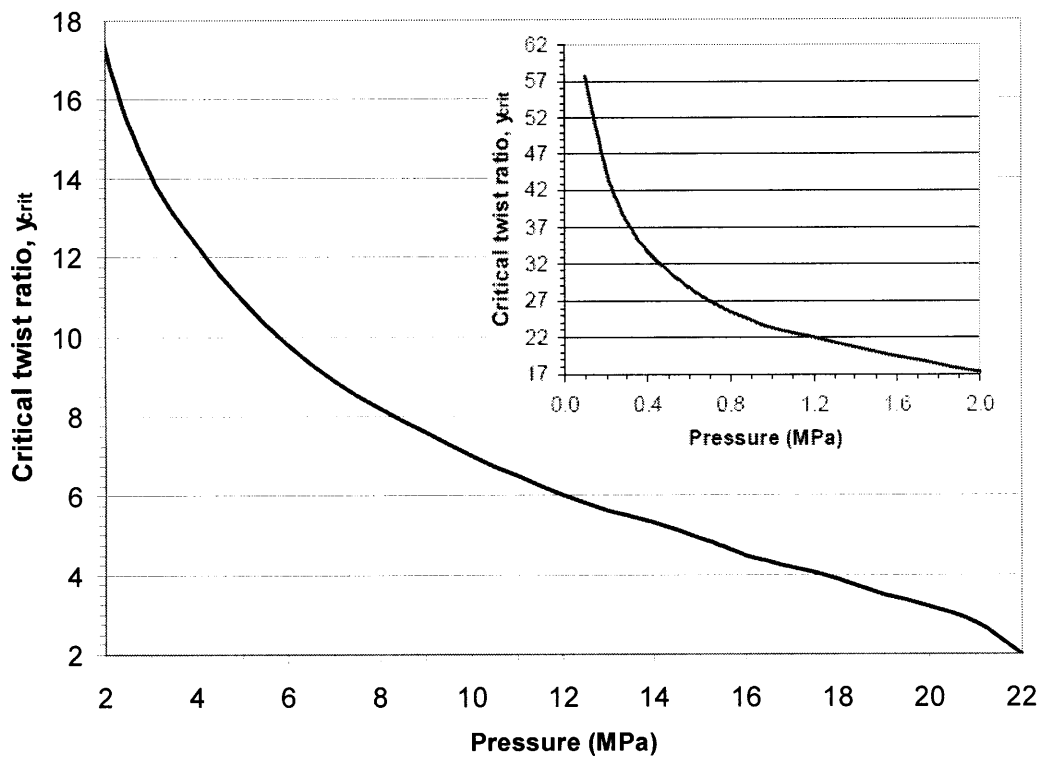


Figure VI-A- 4: Critical twist ratio for the Jensen correlation

The unphysical behavior of the original Jensen correlation cannot be explained by saying that y values larger than y_{crit} were not part of the experimental data used by Jensen to develop the correlation, since of the 207 experimental points he examined, about 20% had twist ratios larger than y_{crit} . As shown in Table VI-A-5, these points are: all those from Matzner et al. (1965) for FLTTs ($y=15$ vs $y_{crit}=9$), all those from Staub (1969) ($y=16.25$ vs $y_{crit}=9.4$) and some of those from Moeck et al. (1964) ($y=34.5$ vs $y_{crit}=9$).

Interestingly enough, the accuracy with which the Jensen correlation reproduces these experimental points is not different from that characterizing other points that instead satisfy the criterion $y < y_{crit}$, as shown in Figure VI-A- 5.

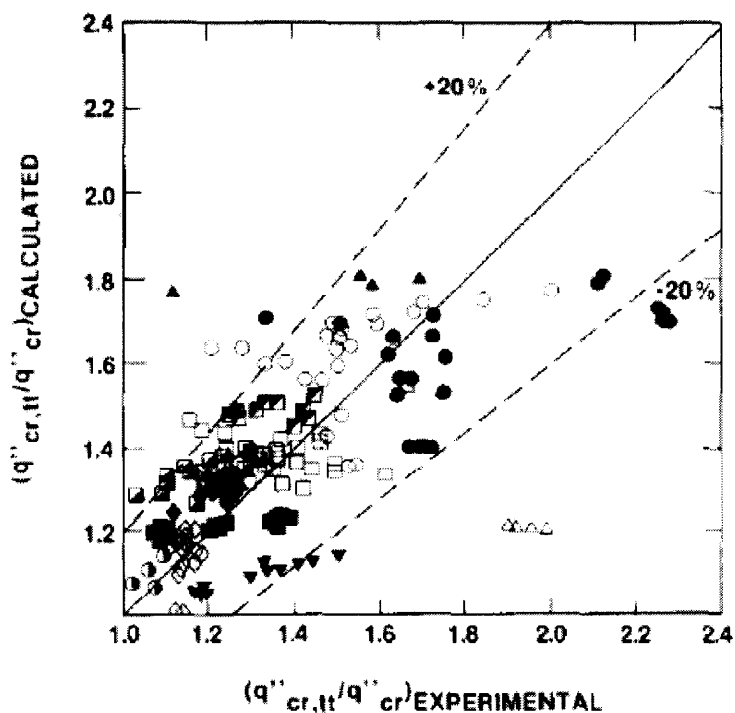


Figure VI-A- 5: Experimental vs predicted CHF ratio using the Jensen correlation (from Jensen, 1984). Symbol legend shown in Table VI-A- 5.

Table VI-A- 5– Legend for markers used in Figure VI-A- 5			
	p (MPa)	y	y_{crit}
□	Matzner et al. (1965)	6.89	15
■	Brevi et al. (1971)	5.1	3
○	Viskanta (1961)	13.8	2.5
●		5	5.4
▼	Staub (1969)	6.5 (H ₂ O-equivalent)	16.25
△	Moeck et al. (1964)	6.9	5.55
▲			34.5
◐	Rosuel and Sourieux (1961)	0.1	3
◑			6
◆	Henkel et al. (1965)	7.1	2.32
◼		10.1	7
◻		7.1	5.71
◻	Moussez et al. (1965A)	10.1	7
▽		7	3

The behavior of the Jensen correlation is a consequence of the way the correlation was developed, i.e. through a regression analysis of experimental points derived from tests during which the twist ratio was, most of the times, fixed, whereas mass flux was varied. No apparent anomaly has been found, in fact, in the variation of the CHF ratio with mass flux.

VI-A.2.3 Modified Jensen correlation for long TTs

The anomalous behavior discussed in the previous section required the Jensen correlation to be modified. However, because of the absence of other FLTT experimental data besides those already collected by Jensen (which yielded the development of the correlation itself), and since no complete study exists on the effect that twist ratio has on CHF at high pressure, it was not possible to modify the Jensen correlation in such a way that the new correlation gives consistent and accurate results for all geometries and operating conditions. Rather, the purpose of the modification was to exclude its application whenever inconsistent results would otherwise be obtained. The modified Jensen correlation for use in taped regions is:

$$\frac{q''_{CHF,FLTT}}{q''_{CHF,empty}} = \begin{cases} A & \text{if } A \geq 1 \text{ and } y \leq y_{crit} \\ 1 & \text{if } A < 1 \text{ and } y \leq y_{crit} \end{cases} \quad (\text{VI-A-4})$$

where:

$$A' = (4.597 + 0.09254y + 0.004154y^2) \left(\frac{\rho_g}{\rho_f} \right)^{0.7012} + 0.09012 \ln \left(\frac{a}{g} \right) \quad (\text{VI-A-2})$$

$$y_{crit} = \begin{cases} 23.023p^{-0.4114} & \text{if } 0.1 \leq p \leq 3 \text{ MPa} \\ -5.6794 \ln(p) + 20.134 & \text{if } 3 < p \leq 21 \text{ MPa} \end{cases} \quad (\text{VI-A-5})$$

whereas for $y > y_{crit}$ the correlation is not applicable. Since the inverted PWR operates at 15.5 MPa, only HLTT designs with $y \leq y_{crit}(15.5 \text{ MPa}) = 4.7$ are analyzed.

An additional modification of the Jensen correlation, to include TTCHFR dependence on steam quality, would be advisable if CHF calculations in saturated boiling were of

interest. In fact, as it can be seen from Eq. VI-A-1, the predicted TTCHFR is independent on steam quality, which is inconsistent with experimental observations, according to which TTCHFR increases as the steam quality increases (see Figure VI- 7 for FLTT-induced swirl and Figure VI- 11 for SLTT-induced swirl). This modification was not, however, performed for the IPWR design since this reactor does not operate in saturated boiling.

VI-A.3 Benchmark in SLTT-induced swirl flow

As discussed in Section VI.2.4, the CHF calculation method developed for the SLTT-provided IPWR consists of the combination of Eqs. VI-11 and V-A-1 with Eq. VI-10, and refers to subcooled boiling only. CHF experimental data for this boiling regime, at high pressure, are not available, and a comprehensive benchmark cannot be performed. However, comparisons between analytical predictions and (1) extrapolations, toward the zero-quality region, of saturated boiling CHF experimental points and (2) the few experimental points referred to small positive qualities, can be made, and used to confirm that the CHF calculation method discussed in Section VI.2.4 is reasonably accurate. This is presented next.

Figure VI-A-6 shows an example of prediction of swirl fraction variation along a SLTT-provided tube, performed by means of Eqs. VI-11 and V-A-1. The swirl fraction, i.e. the fraction of tangential velocity with respect to that at the exit of each tape, is shown on the y-axis, while the dimensionless axial coordinate (z/D_{ci}) is on the x-axis. The graph refers to a 15.1 mm inner diameter tube containing 3 SLTTs having $y=1$ and spaced 50 diameters from each other, of which the first one is located at 1.5 m from the tube inlet (dimensionless axial location = $1.5/1.51 \times 10^{-2} = 99.3$). Two key observations can be made about this graph:

- the swirl fraction at the end of the swirl decay regions, for $Re=6.3 \times 10^5$, is about 0.28. This means that the CHF predicted with Eq. VI-10, at those axial locations, would be 1.28 times higher than the axial flow CHF (see Section VI.2.4). This degree of enhancement is consistent, and probably conservative, with respect to that obtainable, in Figure VI- 11, by extrapolating the solid line toward the zero

quality region. The solid line interpolates experimental points, collected by Hassid et al. (1966), on a SLTT-provided, 15.1 mm inner diameter tube in which the tape twist ratio and the tape spacing were the same as those used to obtain Figure VI-11, and the Reynolds number was about 6.3×10^5 .

- the swirl fraction decay rate decreases as the Reynolds number increases. Based on the CHF calculation method of Eq. VI-10, this implies that the CHF enhancement at a fixed axial location of a swirl decay region increases as the Reynolds number increases, i.e. as mass flux increases. This is consistent with the experimental evidence, as shown in Figure VI- 11.

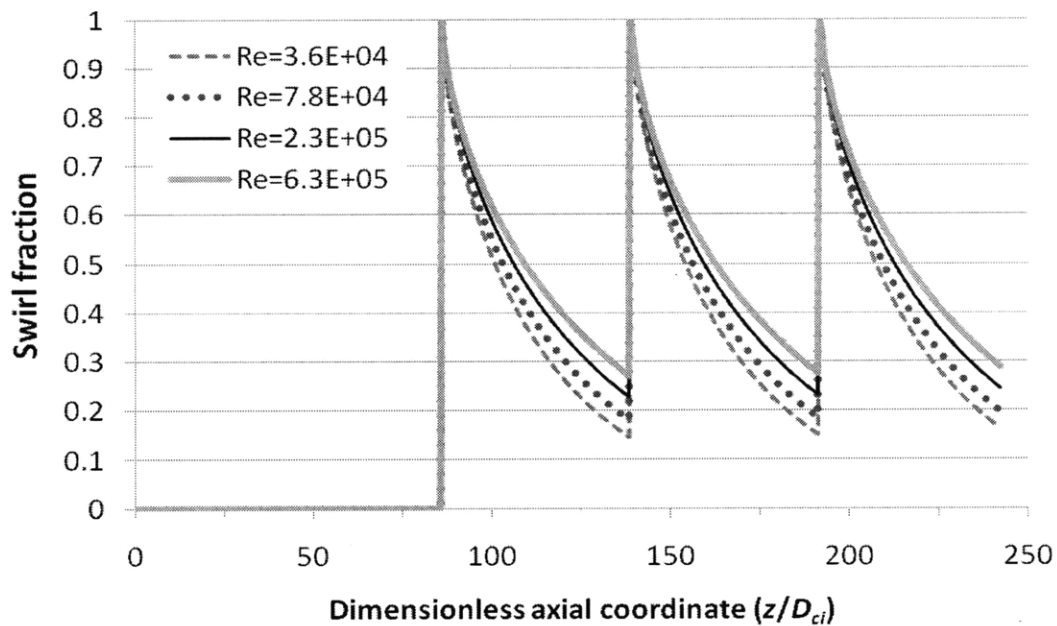


Figure VI-A- 6– Swirl fraction profile as a function of the dimensionless axial coordinate, for different Reynolds numbers ($y = 1, s = 50$)

An analogous swirl fraction study was performed to compare the CHF enhancement predicted analytically with that measured by Peterlongo et al. (1964) for the case of a very long swirl decay region. Specifically, the Peterlongo’s experimental point considered for this comparison is that corresponding to $y=2.8, s=158, G=3800 \text{ kg/s m}^2$ in Figure VI- 12. Because of the large length of the swirl decay region, the swirl completely decays and no CHF enhancement, relative to the empty tube in axial flow, was

measured²². Figure VI-A-7 shows that the analytical prediction is consistent with the experimental evidence since the swirl fraction predicted for the end of the decay region is only 0.03.

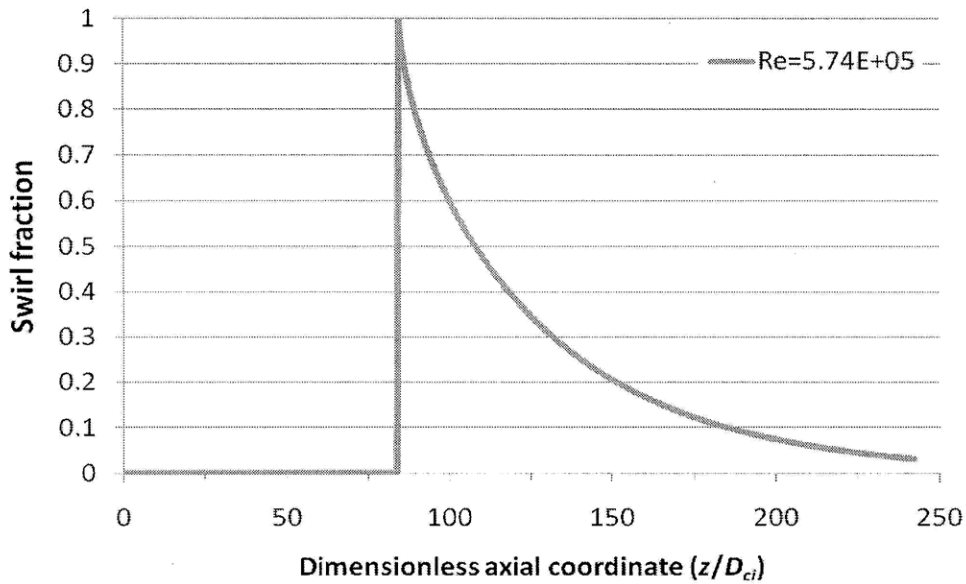


Figure VI-A- 7– Swirl fraction profile as a function of the dimensionless axial coordinate ($y=2.8, s=158$)

Based on these observations, it can be concluded that the CHF calculation method adopted for the SLTT-provided IPWR is expected to yield reasonably accurate results.

²² The fact that Figure VI- 12 shows, for some experimental points, a TTCHFR below unity is probably due to uncertainties and scatter of experimental measurements. This is because, no matter how long the swirl decay region is, a SLTT-provided tube is not expected to have a lower CHF than an empty tube.

Appendix VI-B: Swirl decay analysis

This Appendix presents analytical techniques found in the literature for analyzing the swirl decay downstream of a swirl generator device, e.g. a SLTT. In particular, it presents the methodology used for calculating the tangential velocity component in the swirl decay region downstream of a SLTT. This velocity, as discussed in Section VI.2.4, was used for predicting the CHF in the IPWR SLTT-provided channels.

Two main studies have been performed on the decay of a swirl flow downstream a swirl-generator device: Kreith and Sonju (1965) and Algifri et al. (1987). The Kreith and Sonju solution was actually revised by Algifri and Bhardwaj (1985): such revision simply consisted of a more precise mathematical treatment of the swirl decay problem, but no modifications either to the method developed by Kreith and Sonju (1965) or to the assumptions they adopted were made.

The studies by Kreith and Sonju (1965) and Algifri et al. (1987) were aimed at predicting the spatial variation of the tangential velocity component, both in the axial direction, i.e. axially downstream the swirl-generator device, and in the radial one, i.e. at various distances from the tube axis. The analytical solutions obtained in the two studies were both very accurate in predicting the axial variation of the tangential velocity component. However for the radial variation, the work by Algifri et al. (1987) provided more accurate results, particularly at distances from the exit of the swirl-generator device greater than 20 diameters. For this reason, the methodology developed by Algifri et al. (1987) was adopted in the study of the inverted core. Both works are described below.

V-B.1 Swirl decay: Kreith and Sonju study

Using simplifying assumptions and choosing appropriate boundary conditions, Kreith and Sonju (1965) solved the continuity and the Navier-Stokes equations for a flow exiting a swirl generator device and progressively decaying downstream. Their solution was in the form of an analytical expression for the dimensionless tangential velocity, $W(r, z_T)$, for a generic location having radial coordinate r (distance from the tube axis) and axial coordinate z_T (distance from the swirl generator device). This dimensionless tangential velocity is defined as:

$$W(r, z_T) = \frac{w(r, z_T)}{v(0, \infty)} \quad (\text{V-B-1})$$

where $w(r, z_T)$ is the dimensioned tangential velocity at location (r, z_T) , while $v(0, \infty)$ is the maximum velocity in fully developed axial flow²³. The analytical solution developed by Kreith and Sonju (1965) consists of the summation of infinite terms, of which only the dominant ones are shown in their paper²⁴ as:

$$\begin{aligned} W(r, z_T) = & \frac{7.78}{4y} J_1 \left(7.664 \frac{r}{D_{ci}} \right) \exp \left[-\frac{33.4(1 + \varepsilon_d)}{N_R} \frac{z_T}{D_{ci}} \right] + \\ & - \frac{5.26}{4y} J_1 \left(14.032 \frac{r}{D_{ci}} \right) \exp \left[-\frac{111.4(1 + \varepsilon_d)}{N_R} \frac{z_T}{D_{ci}} \right] + \\ & + \frac{3.93}{4y} J_1 \left(20.348 \frac{r}{D_{ci}} \right) \exp \left[-\frac{235.8(1 + \varepsilon_d)}{N_R} \frac{z_T}{D_{ci}} \right] + \\ & - \frac{3.16}{4y} J_1 \left(26.648 \frac{r}{D_{ci}} \right) \exp \left[-\frac{407.4(1 + \varepsilon_d)}{N_R} \frac{z_T}{D_{ci}} \right] + \dots \end{aligned} \quad (\text{V-B-2})$$

where N_{Re} is defined as half of the axial flow Reynolds number calculated with respect to the maximum axial velocity defined above:

$$N_R = \frac{\rho \times v(0, \infty) \times D_{ci}}{2\mu} \quad (\text{V-B-3})$$

while for ε_d , which is the dimensionless eddy diffusivity defined as the ratio between the eddy diffusivity and the kinematic viscosity (μ/ρ):

$$\varepsilon_d = \frac{\varepsilon\rho}{\mu} \quad (\text{V-B-4})$$

Kreith and Sonju (1965) proposed the experimentally-deducted expression²⁵:

²³ In fully developed axial flow the radial velocity profile is parabolic, with a maximum at the tube axis and a minimum (zero) at the tube wall. The notation $v(0, \infty)$ is used since, at an infinite distance from the swirl generator device, the flow is purely axial and fully developed.

²⁴ By comparing Equation V-B-2 with Equation 16 of the Kreith and Sonju (1965) paper, it can be noticed that they look different. The reason is the different definition of the twist ratio ($y = P_{180}/D_{ci}$ in the inverted core project, $H = 4P_{180}/D_{ci}$ in Kreith and Sonju (1965)) and in the use of the tube inner diameter (inverted core project) in place of the radius (Kreith and Sonju (1965)) to nondimensionalize the distance from the TT exit. Quantitatively, the two equations are identical.

²⁵ The way Kreith and Sonju (1965) handle the parameter they call "Reynolds number" is confusing. They in fact (1) refer to the parameter N_R as "axial flow Reynolds number", (2) define it as in Equation V-B-3 and (3) use the symbol N_R in all the expressions throughout the paper. However, in describing experimental tests, Kreith and Sonju (1965) say that the tests were performed at a certain Reynolds number, and give the corresponding value, but they do not specify whether that number is the actual Reynolds number ($\rho v D/\mu$) or

$$\varepsilon_d = 4.15 \times 10^{-3} N_R^{0.86} \quad (\text{V-B-5})$$

The method used by Kreith and Sonju (1965) is based on the assumption that the radial profile of the dimensionless tangential velocity at the exit of the swirl generator device, which is used as initial condition for solving the swirl flow differential equation, is axisymmetric and has the form that Smithberg and Landis (1964) obtained by experimentally measuring such velocity for twisted tapes having twist ratios in the range $1.8 \leq y \leq 11$:

$$W(r,0) = \frac{1}{4y} \left[12.6 \frac{r}{D_{ci}} - 0.013 \left(1.1 - \frac{2r}{D_{ci}} \right)^{-2.68} \right] \quad (\text{V-B-6})$$

This profile is shown in **Error! Reference source not found.** as a function of the dimensionless radial coordinate $r_d = 2r/D_{ci}$. The figure also shows the maximum deviations from the axisymmetric curve, which are due to the secondary flows created by the swirl.

half of that, i.e. N_R . From one of these experiments, performed by Musolf (1963), it is possible to clarify this issue: Figure 9 of Kreith and Sonju (1965) shows the experimental points obtained by Musolf (1960) and the curves interpolating them. The caption of the figure cites a “*Reynolds number of 48000*” and “*axial velocity: 6.24 ft/s*” (1.90 m/s). Since Musolf (1963) used a 50.8 mm inner diameter tube, such diameter together with the specified velocity and the water properties at room conditions can be used to compute the actual Reynolds number ($\rho v D / \mu$), which results to be 96000. This means that, when referring to the Reynolds number for Figure 9, Kreith and Sonju (1965) actually mean $Re/2$. The authors’ tendency to use $Re/2$ and call it “Reynolds number” can also be proved by reasoning on the definition they give to the dimensionless diffusivity ε_d . They define such diffusivity as shown in Equation V-B-5, i.e. using the parameter N_R , and say that the expression for ε_d was chosen in order to match “*the decay characteristics predicted by theory and those which were observed experimentally*” during a test in which the “*axial flow Reynolds number*” was 61000 and ε_d had to have a value equal to 54 to result in such matching. From Equation V-B-5, ε_d is equal to 54 if the parameter elevated to the 0.86 power has a numerical value of 61000, which means the “*axial flow Reynolds number*” they cite is, consistently with their notation, N_R or, in other words, $Re/2$. This has a repercussion on the interpretation of Figures 7 and 8 of Kreith and Sonju (1965), which are reproduced here in Figure V-B. 2 (bottom and top figure respectively). In Kreith and Sonju (1965) the captions of these figures state “Reynolds numbers” of 61000 and 18000. The reader would likely interpret such Reynolds numbers as actual Reynolds numbers ($\rho v D_{ci} / \mu$), while they are instead half of those. This is why, when reporting Figures 7 and 8 of Kreith and Sonju (1965) in this Appendix (Figure V-B. 2), the Reynolds numbers have been doubled.

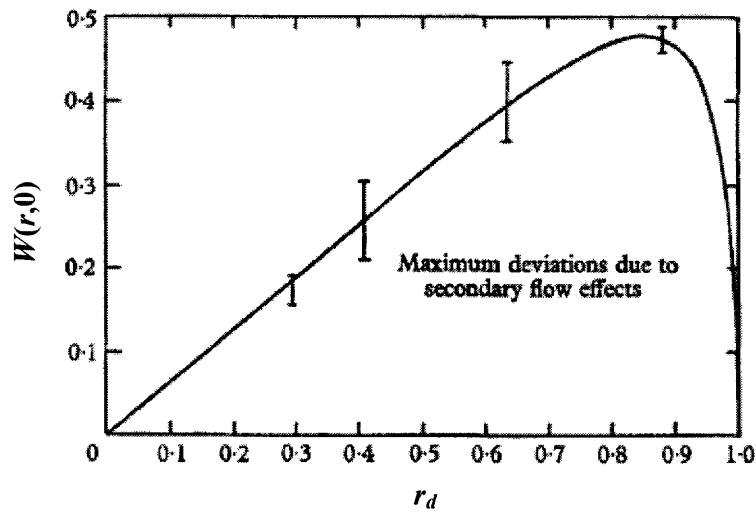


Figure V-B. 1 - Radial profile of the dimensionless tangential velocity at the exit of a twisted tape with $\gamma=2.5$ (Kreith and Sonju, 1965, citing Smithberg and Landis, 1964)

From Figure V-B. 1 it can be seen that the tangential component of the velocity is zero at the tube axis, increases almost linearly with radius until the boundary layer is reached, and then drops rapidly to zero at the tube wall. Qualitatively, this profile is the same regardless of the twist ratio considered. Quantitatively, for a twist ratio equal to 2.5, it can be seen that the maximum tangential velocity is about half of the maximum velocity that the fluid would have if the swirl generator device was not present.

Kreith and Sonju (1965) compared their analytical results with experimental measurements, in two ways:

- they compared, at various locations downstream the swirl generator device, the measured (radially-averaged) dimensionless tangential velocity, which they call “swirl intensity”, with that obtainable from Eq. V-B-2. This comparison gives an indication of the accuracy of Eq. V-B-2 in predicting the axial swirl decay, without however providing information on how accurate is the prediction of the radial profile of the tangential velocity at each location downstream the swirl generator device.

- They compared, at various locations downstream the swirl generator device, the radial profile of the dimensionless tangential velocity, obtained experimentally, with that obtained with Eq. V-B-2. This comparison, more complete than the previous one, gives indications of the accuracy with which Eq. V-B-2 predicts the variation of the tangential velocity both axially and radially.

Figure V-B. 2 is the first comparison discussed above. The two plots, which only differ in the Reynolds number, show the experimental swirl decay points and the analytical swirl decay curve, as a function of the dimensionless distance, z_d , from the TT exit. The “percentage of initial swirl” on the y-axis is defined as:

$$\% \text{ of initial swirl at location } z_T = 100 \frac{\int_0^{R_{ci}} [W(r, z_T)]^2 r dr}{\int_0^{R_{ci}} [W(r, z_T = 0)]^2 r dr} \quad (\text{V-B-7})$$

where $W(r, z_T)$ is from Eq. V-B-2 and R_{ci} is the tube inner radius.

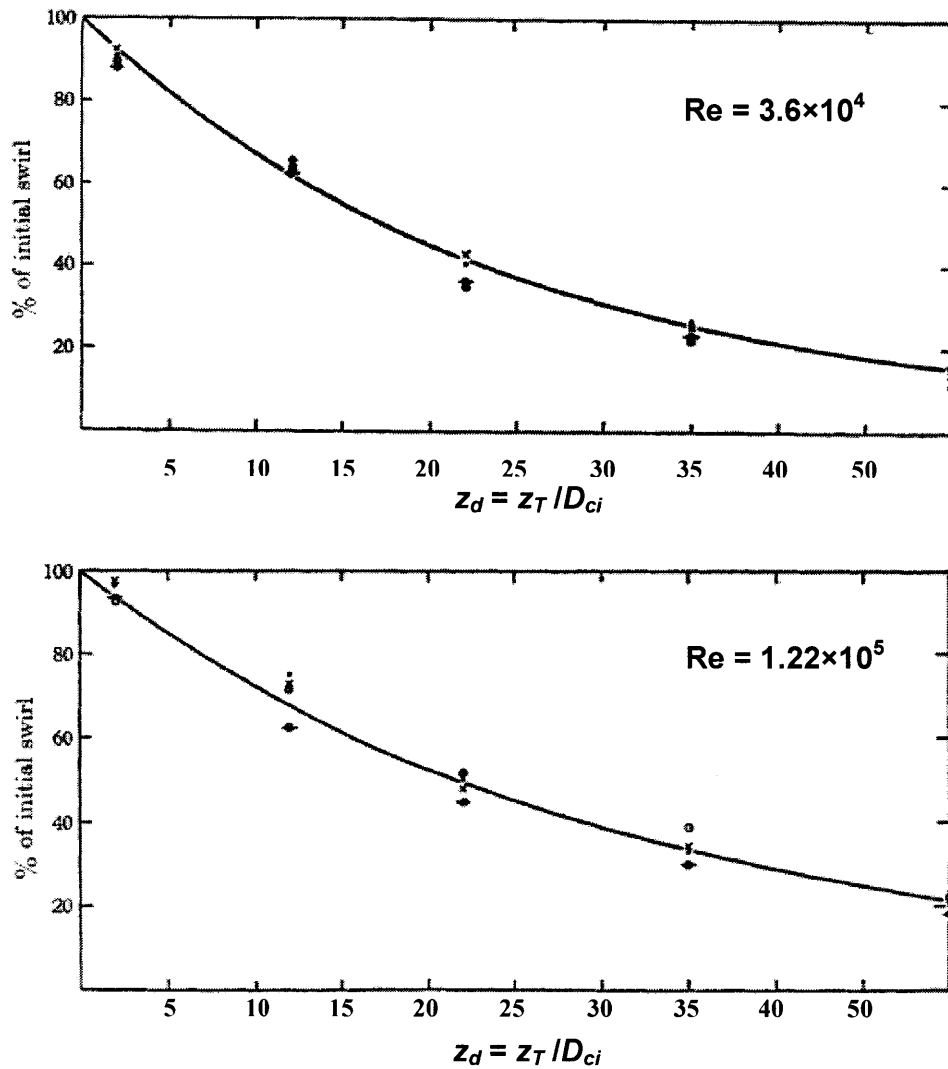


Figure V-B. 2– Comparison, by Kreith and Sonju (1965), of experimentally measured (markers) and theoretically predicted (curve) swirl decay. $D_{ci} = 25.4$ mm. Four TT geometries: $y=2.25$, $L_{TT} = 457$ mm; $y=2.25$, $L_{TT} = 762$ mm; $y=3.75$, $L_{TT} = 457$ mm; $y=3.75$, $L_{TT} = 762$ mm

Note, from Figure V-B. 2, that the axial profile of the swirl percentage is not a function of the TT twist ratio, y , but only of the Reynolds number.

To make sure about the correctness of the interpretation given to the parameter Kreith and Sonju call “Reynolds number” (see footnote 25), the two plots shown in Figure V-B. 2 have been reproduced using Eq. V-B-2 and imposing, as boundary condition, both the Reynolds numbers 3.6×10^4 and 1.22×10^5 and half of those, i.e. 1.8×10^4 and 6.1×10^4 .

Figure V-B. 3 shows that the analytical predictions are closer to the experimental values when the Reynolds number ($\rho v D_{ci}/\mu$) assumed for the two plots is the largest, i.e. 3.6×10^4 in the left plot and 1.22×10^5 in the right plot, which confirms the conclusion drawn about how Kreith and Sonju define the Reynolds number²⁶.

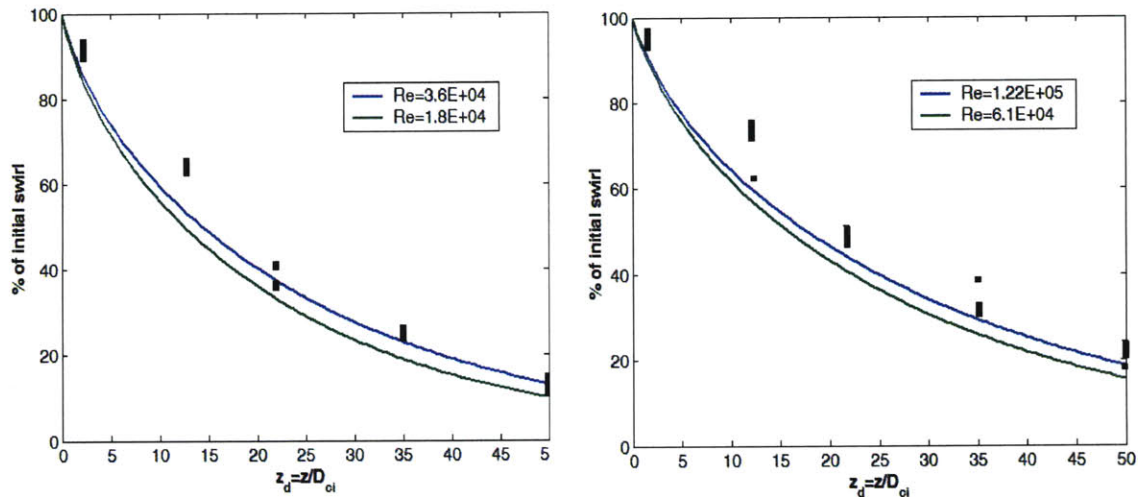


Figure V-B. 3– Comparison of experimentally measured swirl decays (markers, from Kreith and Sonju, 1965) with reproduction of Kreith and Sonju theoretical prediction (curves) using two interpretations of the Reynolds number cited in Kreith and Sonju (1965)

Important observations can be made about the analytical method developed by Kreith and Sonju (1965). Particularly, from Figure V-B. 2 it can be concluded that:

- the analytical solution obtained by Kreith and Sonju (1965), i.e. Eq.V-B-2, predicts quite satisfactorily the decay of a swirl flow;
- the swirl flow decays to 20% of the initial value at about 40-50 diameters downstream from the TT exit;
- the rate of swirl decay does not depend on the TT twist ratio, i.e. the tangential velocity component decreases with the same speed regardless of the twist ratio

²⁶ The reason why the upper curves in Figure V-B. 3 match the experimental points less closely than the Kreith-Sonju curves shown in Figure V-B. 2 is unknown. However, for the purposes of the swirl decay study for the IPWR design, the accuracy of the upper curves in Figure V-B. 3 is considered acceptable.

(the absolute value of the tangential component does, however, depend on twist ratio);

- the rate of swirl decay depends on the Reynolds number, and decreases as Re increases.

Unlike the prediction of the axial variation of the tangential velocity, the prediction of the radial profile of the tangential velocity by means of Eq. V-B-2 is not always accurate. In fact, as Kreith and Sonju note, there is a “*general agreement near the swirl inducer, i.e. within a distance less than about 20 diameters downstream from the outlet of the inducer section*”. Further downstream of this distance, however, Eq. V-B-2 predicts tangential velocity profiles that have a maximum near $R_{ci}/2$, while experimental profiles are peaked closer to the tube wall. This is shown in Figure V-B. 4, where both the analytical predictions obtained using Eq. V-B-2 and those obtained with Eq. V-B-10 (which is a version of Equation V-B-2 mathematically more complete and accurate) are represented. It can be also noted that, in spite of the radial shift of the predicted tangential velocity profile with respect to the experimental one, the analytical prediction of the maximum absolute value of the dimensionless tangential velocity across the tube is very accurate at any distance downstream of the swirl generator device.

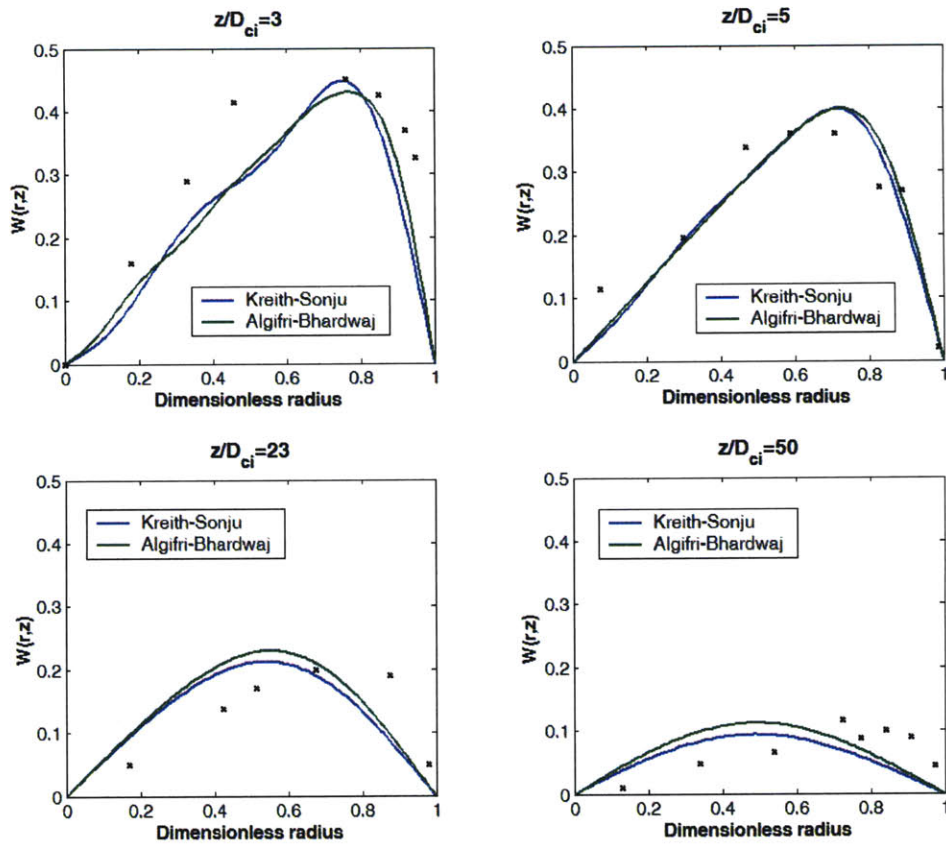


Figure V-B. 4– Comparison of experimental radial profiles of the dimensionless tangential velocity (markers, from Kreith and Sonju, 1965) with reproductions of the analytical predictions developed by Kreith-Sonju and Algifri-Bhardwaj (curves), at various distances downstream the exit of the swirl-inducer device ($Re=9.6 \times 10^4, y=2.5$)

V-B.1.1 Swirl decay: more accurate version of Equation V-B-2 (Algifri-Bhardwaj study)

As mentioned above, the methodology developed by Kreith and Sonju (1965) was revised, in the accuracy of its mathematical treatment, by Algifri and Bhardwaj (1985). Their objective was not, however, to investigate the swirl decay itself, but the heat transfer in swirl decay. They in fact solved the same set of differential equations solved by Kreith and Sonju (1965), with the same assumptions and boundary conditions but a higher mathematical accuracy (more terms in the series of Eq. V-B-2) and used the solution found (similar to Equation V-B-2) to develop a heat transfer coefficient correlation for swirl flow. It should be noted, however, that the way they defined the

dimensionless tangential velocity was slightly different from that shown by Kreith and Sonju (1965), i.e. from Equation V-B-1. Algifri and Bhardwaj (1985) defined such dimensionless velocity as:

$$W'(r, z_T) = \frac{w(r, z_T)}{\bar{v}(z_T = \infty)} \quad (\text{V-B-8})$$

where $\bar{v}(z_T = \infty)$ is the radial average of the axial velocity in fully developed axial flow. Since, in axial turbulent flow, the velocity at the tube axis is only slightly larger than the radially-averaged axial velocity, we can reasonably assume that the two definitions are quantitatively similar, i.e.:

$$W'(r, z_T) \cong W(r, z_T) \quad (\text{V-B-9})$$

and use the notation $W(r, z_T)$ to identify the dimensionless tangential velocity used by Algifri and Bhardwaj (1985). The expression they developed for this velocity is similar to Equation V-B-2:

$$\begin{aligned} W(r, z_T) = & \frac{7.73}{4y} J_1 \left(7.664 \frac{r}{D_{ci}} \right) \exp \left[-\frac{29.368(1 + \varepsilon_d) z_T}{N_R D_{ci}} \right] + \\ & - \frac{5.26}{4y} J_1 \left(14.032 \frac{r}{D_{ci}} \right) \exp \left[-\frac{98.448(1 + \varepsilon_d) z_T}{N_R D_{ci}} \right] + \\ & + \frac{4.04}{4y} J_1 \left(20.346 \frac{r}{D_{ci}} \right) \exp \left[-\frac{206.98(1 + \varepsilon_d) z_T}{N_R D_{ci}} \right] + \\ & - \frac{3.38}{4y} J_1 \left(26.648 \frac{r}{D_{ci}} \right) \exp \left[-\frac{355.06(1 + \varepsilon_d) z_T}{N_R D_{ci}} \right] + \\ & + \frac{3.00}{4y} J_1 \left(32.928 \frac{r}{D_{ci}} \right) \exp \left[-\frac{542.12(1 + \varepsilon_d) z_T}{N_R D_{ci}} \right] + \\ & - \frac{3.06}{4y} J_1 \left(39.232 \frac{r}{D_{ci}} \right) \exp \left[-\frac{769.58(1 + \varepsilon_d) z_T}{N_R D_{ci}} \right] + \\ & + \frac{3.33}{4y} J_1 \left(45.520 \frac{r}{D_{ci}} \right) \exp \left[-\frac{1036.04(1 + \varepsilon_d) z_T}{N_R D_{ci}} \right] + \\ & - \frac{5.43}{4y} J_1 \left(50.612 \frac{r}{D_{ci}} \right) \exp \left[-\frac{1280.8(1 + \varepsilon_d) z_T}{N_R D_{ci}} \right] \dots \end{aligned} \quad (\text{V-B-10})$$

The parameters shown in Equation V-B-10 are the same as those defined for Equation V-B-2. However, it must be noticed that, when defining the dimensionless diffusivity ε_d ,

Algifri and Bhardwaj (1985) in spite of referencing the expression developed by Kreith and Sonju, i.e. Equation V-B-5, they use Re in place of N_R in that equation. It is likely that such inconsistency was not due to the choice, by Algifri and Bhardwaj, to use Re in place of N_R , but rather to an erroneous interpretation of the misleading notation used by Kreith and Sonju (see footnote 25). Since Algifri and Bhardwaj did not check the accuracy of Equation V-B-10 (with Re in place of N_R in Equation V-B-5) against experimental swirl decay data, but only used the equation in that form to develop a heat transfer coefficient correlation, Equation V-B-10 (with ε_d calculated as Equation V-B-5 prescribes) can be considered their solution to the swirl decay problem. The accuracy with which such solution predicts the radial and axial variation of the dimensionless tangential velocity is shown in Figure V-B. 4 and in Figure V-B. 5 respectively. The accuracy in predicting the radial profile is similar to that of Equation V-B-2 (very accurate for $z_T \leq 20D_{ci}$ and less and less accurate as z_T increases), while the accuracy in predicting the axial variation is slightly superior to that of Equation V-B-2.

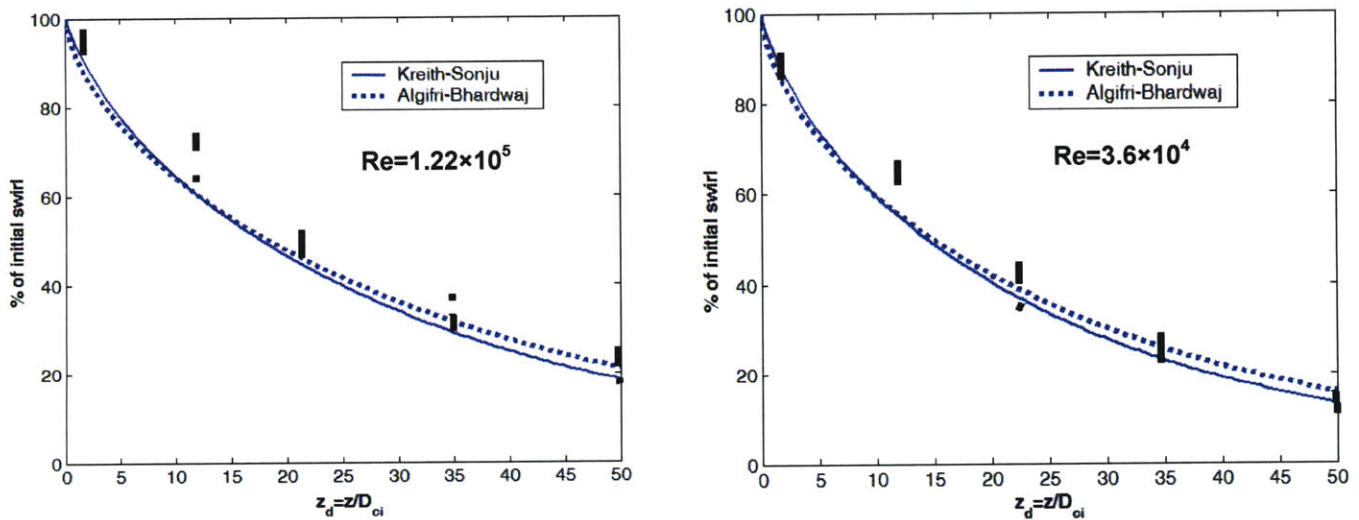


Figure V-B. 5— Comparison of experimentally measured swirl decays (markers, from Kreith and Sonju, 1965) with reproductions of Kreith-Sonju and Algifri-Bhardwaj analytical predictions (curves)

Chapter VII

Fuel temperature and heat transfer coefficient calculation methods

This chapter describes the calculation methods used for the peak fuel temperature (Section VII. 1), for the heat transfer coefficient between coolant and cladding (Section VII. 2) and for the thermal resistance across the cladding and the clad-fuel gap (Section VII. 3).

VII. 1 Maximum fuel temperature: the corrected equivalent annulus approximation

In the IPWR design the peak fuel temperature is reached at the corners of the fictitious¹ hexagonal contours enclosing the cells. Because of the hexagonal geometry, heat conduction equations typically used to predict temperature profiles across cylindrical rods cannot be used. Prediction of the temperature at the corners of a hexagonal annulus is often performed through the so-called equivalent-annulus approximation (EAA). This method consists of approximating the hexagonal annulus with a cylindrical annulus having the same inner diameter and cross sectional area, as shown in Figure VII- 1. By requiring these equalities to be satisfied, it can be easily demonstrated that the outer diameter of the equivalent annulus is a function of only the inverted cell pitch, and it is given by:

$$D_{EA} = P_i \sqrt{\frac{2\sqrt{3}}{\pi}} \quad (\text{VII-1})$$

¹ The term “fictitious” is used to stress the fact that the fuel prism is not made of fuel cells, but is manufactured as a single body. The division into cells is only performed to simplify the analysis.

Figure VII- 1, in which the cladding has been omitted to improve readability, also shows two important geometric parameters of an inverted fuel cell: the fuel web thickness, t_{web} , and the in-fuel maximum heat path length, t_{HF} . The latter represent the maximum thickness that the heat has to travel, in the fuel, to go from a point of generation to the point of removal. It is evident that the larger is this thickness the larger is the maximum fuel temperature.

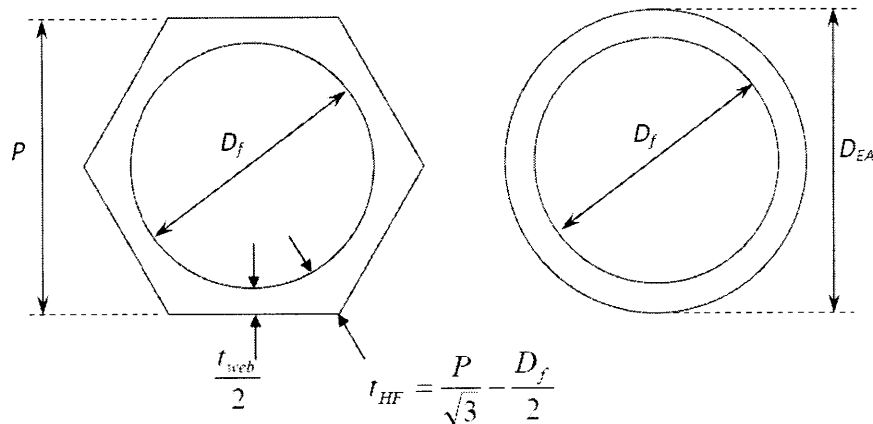


Figure VII- 1: Inverted fuel cell (left) and equivalent annulus (right)

In the equivalent annulus the maximum temperature is reached on the outside diameter. By solving the heat conduction equations in cylindrical coordinates, it can be easily demonstrated that this temperature, $T_f(D_{EA})$, is equal to:

$$T_f(D_{EA}) = T_f(D_f) + \frac{q'}{2\pi k_f} \left(-\frac{1}{2} + \frac{D_{EA}^2}{D_{EA}^2 - D_f^2} \ln \frac{D_{EA}}{D_f} \right) \quad (VII-2)$$

where $T_f(D_f)$ is the temperature on the inside surface of the fuel hole. The EAA sets the maximum temperature in the inverted cell equal to $T_f(D_{EA})$. For a fixed thermal conductivity, the error resulting from this approximation becomes larger and larger as P/D_f decreases, and for the same P/D_f ratio it increases as the fuel thermal conductivity decreases and as the linear heat generation increases. This is clearly evident from Figure VII- 2, which shows the difference between the actual maximum fuel temperature, obtained using the COSMOSWorks code (SolidWorks, 2007) and the prediction using the EAA. As it can be seen, for low-conductivity materials the error can reach hundreds of degrees.

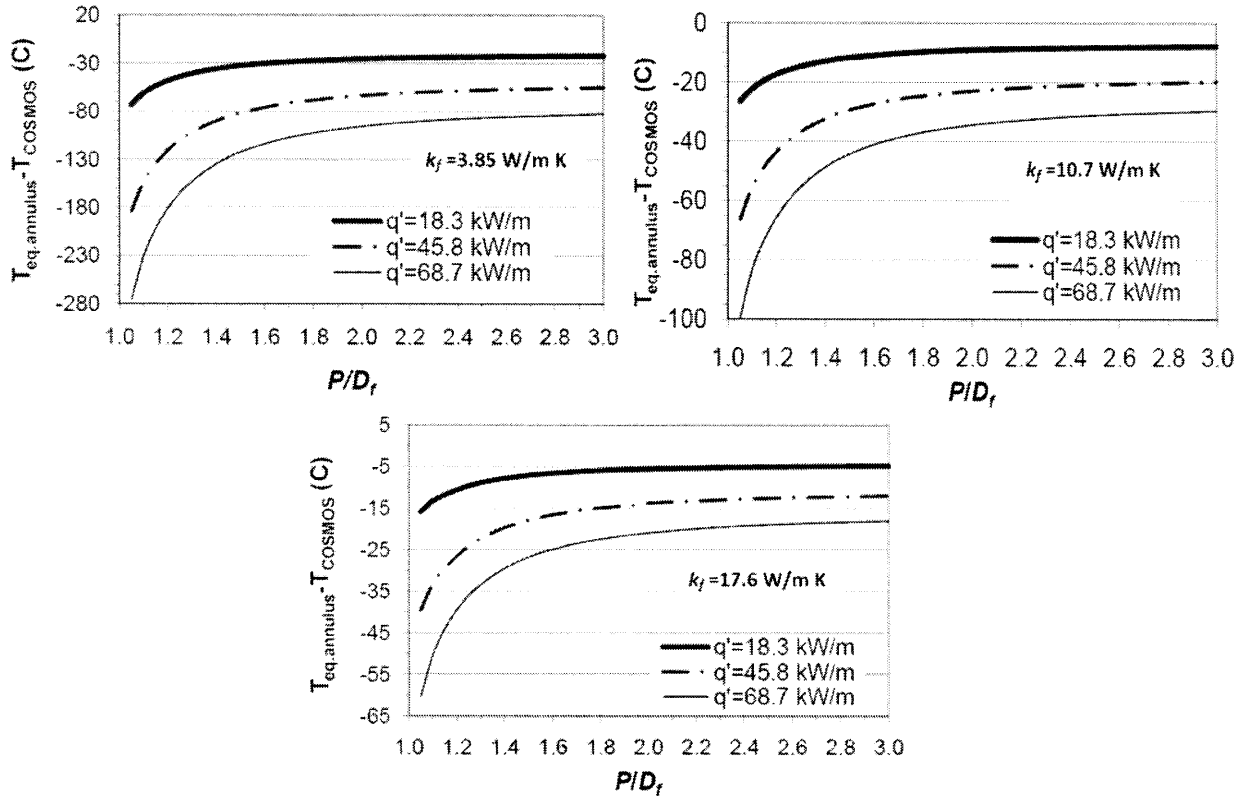


Figure VII- 2: Error on maximum fuel temperature resulting from using the equivalent annulus approximation

Since (1) the error resulting from using the EAA does not fall on the conservative side, i.e. the EAA underestimates the peak temperature of the inverted cell, and (2) the fuel temperature is a key parameter for hydride fuels, for the design of the IPWR it was decided to correct the EAA by introduction a correction factor, ΔT_{EA} , which is added to the right hand side of Eq. VII-2, as:

$$T_f(D_{EA}) = T_f(D_f) + \frac{q'}{2\pi k_f} \left(-\frac{1}{2} + \frac{D_{EA}^2}{D_{EA}^2 - D_f^2} \ln \frac{D_{EA}}{D_f} \right) + \Delta T_{EA} \quad (\text{VII-3})$$

The correction factor ΔT_{EA} was developed in the form of a function of three variables: thermal conductivity k_f of the material composing the cell, linear heat generation rate q' and P/D_f ratio:

$$\Delta T_{EA} = -K_{EA} \frac{q'}{k_f} \quad (\text{VII-4})$$

where ΔT_{EA} is expressed in K, q' in W/m, k_f in W/m K. K_{EA} is a function of the P/D_f ratio, as shown in Figure VII- 3, for which the following expression can be used:

For $1.05 \leq P/D_f \leq 1.8$:

$$K_{EA} = 0.162976 \left(\frac{P}{D_f} \right)^5 - 1.23514 \left(\frac{P}{D_f} \right)^4 + 3.74211 \left(\frac{P}{D_f} \right)^3 +$$

$$- 5.67627 \left(\frac{P}{D_f} \right)^2 + 4.32485 \left(\frac{P}{D_f} \right) - 1.33684 \quad (\text{VII-5})$$

while for $1.8 < P/D_f \leq 3$:

$$K_{EA} = -6.19612 \times 10^{-4} \left(\frac{P}{D_f} \right)^2 + 3.87355 \times 10^{-3} \left(\frac{P}{D_f} \right) - 1.06359 \times 10^{-2} \quad (\text{VII-6})$$

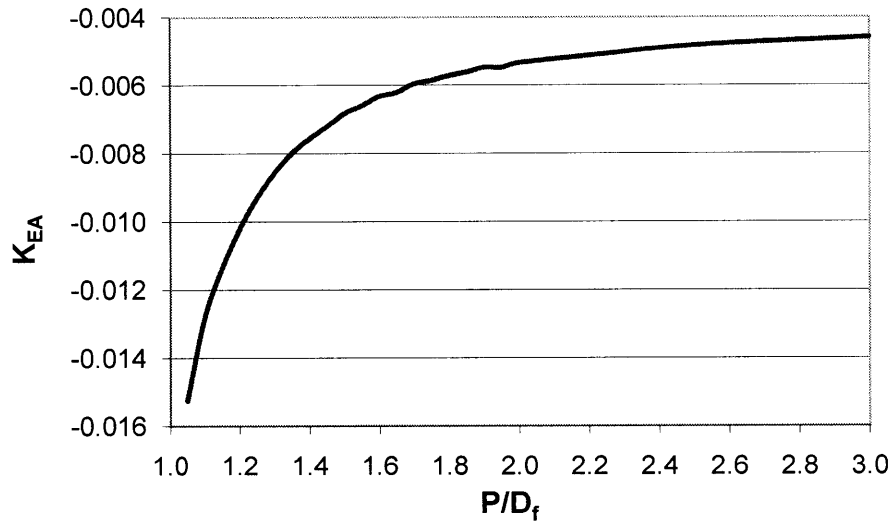


Figure VII- 3: Dimensionless parameter for the correction of the equivalent annulus approximation

The method resulting from the modification of the EAA is termed here “corrected equivalent annulus approximation” (CEAA). It was developed by comparing the results obtained with the equivalent annulus approximation with those obtained using the COSMOSWorks code (SolidWorks, 2007), and then by finding an expression for ΔT_{EA} to correct such an approximation. The comparison was made for fuel cells having geometries in the range $1.05 \leq$

$P/D_f \leq 3$, with linear heat rates of 18.3, 45.8 and 68.7 kW/m and with three values for the thermal conductivity: 3.85, 10.7 and 17.6 W/m K. The wide ranges selected for q' and k_f guarantee that the CEAA can be applied in a variety of operating conditions, not limited to those of the IPWR. For the examined operating conditions, the error associated with the corrected equivalent annulus approximation is of about $\pm 0.7\%$ which, for a high-conductive fuel like $UTh_{0.5}Zr_{2.25}H_{5.625}$ is equivalent to $\pm 3^\circ\text{C}$, as shown in Figure VII- 4.

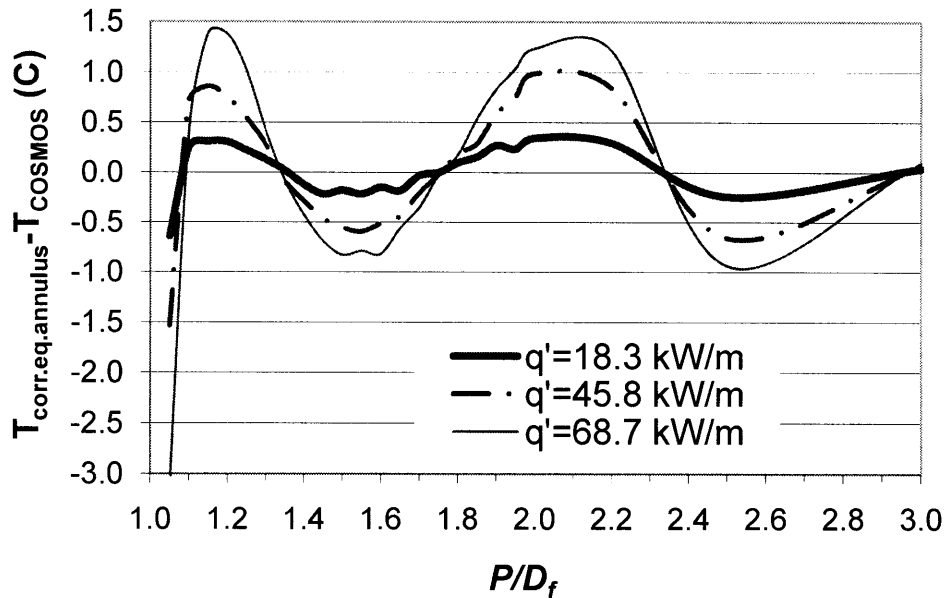


Figure VII- 4: Error on maximum fuel temperature for IPWR fuel resulting from using the corrected equivalent annulus approximation

VII. 2 Coolant-cladding heat transfer coefficient

The heat transfer coefficient (htc) between coolant and cladding inner surface is calculated in different ways depending on the type of flow, i.e. axial or swirl, and on the heat transfer regime. Section VII.2. 1 discusses axial flow correlations, while Section VII.2. 2 concerns swirl flow correlations. Correlations aimed at determining the axial location at which transition between flow regimes occurs, e.g. Onset of Nucleate Boiling, are also presented.

VII.2. 1 Axial flow htc correlations

Pure axial flow characterizes the following cooling channels or fraction of cooling channels:

- the entire length of the E-IPWR channels;
- the bottom half of the H-IPWR channels;
- the regions upstream of the first SLTT in the S-IPWR channels.

The htc correlations used for these channel regions are correlations typically adopted in the thermal hydraulic analysis of LWRs. They are listed as follows:

- Single-phase liquid forced convection: Sieder and Tate (1936) correlation

$$Nu = 0.023 Re^{0.8} Pr^{0.4} \left(\frac{\mu}{\mu_w} \right)^{0.14} \quad (VII-7)$$

where μ and μ_w indicate the coolant viscosity at the bulk and wall respectively.

- Saturated boiling: Chen² (1963)

$$Nu = \frac{D_e}{k_c} (h_c + h_{NB}) \quad (VII-8)$$

where:

$$h_c = 0.023 \left[\frac{G(1-x_{flow})D_e}{\mu_f} \right]^{0.8} (Pr_f)^{0.4} \frac{k_f}{D_e} F \quad (VII-9)$$

$$F = \begin{cases} 1 & \text{if } \frac{1}{X_u} < 0.1 \\ 2.35 \left(0.213 + \frac{1}{X_u} \right)^{0.736} & \text{if } \frac{1}{X_u} \geq 0.1 \end{cases} \quad (VII-10)$$

$$\frac{1}{X_u} = \left(\frac{x_{flow}}{1-x_{flow}} \right)^{0.9} \left(\frac{\rho_f}{\rho_g} \right)^{0.5} \left(\frac{\mu_g}{\mu_f} \right)^{0.1} \quad (VII-11)$$

$$h_{NB} = 0.00122S \left[\frac{(k^{0.79} C_p^{0.45} \rho^{0.49})_f}{\sigma^{0.5} \mu_f^{0.29} h_{fg}^{0.24} \rho_g^{0.24}} \right]^{0.8} (T_w - T_{sat})^{0.24} [p_{sat}(T_w) - p_{sat}(T_{sat})]^{0.75} \quad (VII-12)$$

² Chen gives a graphical representation of the suppression factor S. The analytical expression used for this parameter, shown in Eq. VII-13, is from NRTSC (1990).

$$S = \begin{cases} \frac{1}{1 + 0.12 \left(\frac{\text{Re}_{TP}}{10^4} \right)^{1.14}} & \text{if } \text{Re}_{TP} < 32.5 \times 10^4 \\ \frac{1}{1 + 0.42 \left(\frac{\text{Re}_{TP}}{10^4} \right)^{0.78}} & \text{if } 32.5 \times 10^4 \leq \text{Re}_{TP} < 50.9 \times 10^4 \\ 0.1 & \text{if } \text{Re}_{TP} \geq 50.9 \times 10^4 \end{cases} \quad (\text{VII-13})$$

$$\text{Re}_{TP} = \left[\frac{G(1 - x_{flow})D_e}{\mu_f} \right] F^{1.25} \quad (\text{VII-14})$$

- Subcooled boiling: the approach suggested by Collier and Thom (2001) of extending the use of the Chen correlation to subcooled boiling is used. Specifically, the htc is expressed as sum of the single-phase and two-phase convective parts, each weighted with the corresponding temperature difference, i.e.

$$q_w'' = h_C(T_w - T_c) + h_{NB}(T_w - T_{sat}) \quad (\text{VII-15})$$

where h_C and h_{NB} are calculated using Eq. VII-9 through Eq. VII-14, in which the factor F is set to unity and the boiling suppression factor S is calculated with the flow quality set to zero. Also, the steam flow quality between OSV and Onset of Saturated Boiling (OSB) is calculated using the Levy (1967) correlation is used:

$$x_{flow} = x_{eq} - (x_{eq})_{OSV} \exp \left[\frac{x_{eq}}{(x_{eq})_{OSV}} - 1 \right] \quad (\text{VII-16})$$

The locations of the Onset of Nucleate Boiling (ONB) and of the Onset of Significant Voids (OSV) are determined using the following correlations:

- Onset of Nucleate Boiling (ONB): Bergles and Rohsenow (1963) correlation

$$(T_w - T_{sat})_{ONB} = 0.556 \left(\frac{q_w''}{1082 p^{1.156}} \right)^{0.463 p^{0.0234}} \quad (\text{VII-17})$$

where T_w and T_{sat} are the wall and saturation temperatures (K), q_w'' is the heat flux at the wall (W/m²) and p is the system pressure (bar).

- Onset of Significant Voids (OSV): Saha and Zuber (1974) correlation

$$(T_{sat} - T_c)_{OSV} = \begin{cases} \frac{1}{455} \frac{q_w'' D_e}{k_c} & \text{if } Pe \leq 70000 \\ \frac{1}{0.0065} \frac{q_w''}{GC_p} & \text{if } Pe > 70000 \end{cases} \quad (\text{VII-18})$$

where T_c is the coolant bulk temperature (K), q_w'' is the heat flux at the wall (W/m²), D_e is the equivalent diameter (m), k_c and C_p are the coolant bulk thermal conductivity (W/m K) and specific heat (J/kg K) and G is the coolant mass flux.

VII.2. 2 Swirl flow htc correlations

The literature does not provide all the correlations needed for the thermal hydraulic analysis of swirl flow. When no swirl-flow specific correlations are available, axial flow correlations are used. Because of heat transfer enhancement characterizing swirl flow, this approach is clearly conservative. Correlations are presented below, for flow in presence of Full Length Twisted Tapes (FLTTs) and for flow in the swirl decay regions between Short Length Twisted Tapes (SLTTs). The axial locations corresponding to ONB and OSV, as well as the steam flow quality between ONB and OSV are calculated in the same way as done for axial flow conditions. As discussed in Chapter V (Section V.A.2.1.2) the swirl flow does not appreciably change the ONB location, but only slightly changes the concentration of bubbles at the wall between ONB and OSV.

Correlations for FLTTs

- Single-phase liquid forced convection: Manglik and Bergles (1993) correlation

$$Nu = 0.023 Re^{0.8} Pr^{0.4} \left(1 + \frac{0.769}{y}\right) \left(\frac{\pi}{\pi - \frac{4t_{TT}}{D_{ci}}}\right)^{0.8} \left(\frac{\pi + 2 - \frac{2t_{TT}}{D_{ci}}}{\pi - \frac{4t_{TT}}{D_{ci}}}\right)^{0.2} \left(\frac{\mu}{\mu_w}\right)^{0.18} \quad (\text{VII-19})$$

where y and t_{TT} are the FLTT twist ratio and thickness respectively.

- Subcooled boiling: no correlation is available for subcooled boiling in presence of FLTTs. Eq. VII-15 is used.
- Saturated boiling: Jensen and Bensler (1986) correlation. This correlation has the same form of Eq. VII-8, in which however the definitions of the term h_C and of the suppression factor S are slightly different:

$$h_c = 0.020 \left[\alpha_t \frac{G(1-x_{flow})D_e}{\mu_f} \right]^{0.8} (\text{Pr}_f)^{0.4} \frac{k_f}{D_e} \quad (\text{VII-20})$$

$$S = \frac{k_f}{h_f FX_0} \left[1 - \exp\left(-\frac{h_f FX_0}{k_f}\right) \right] \quad (\text{VII-21})$$

where:

$$\alpha_t = \frac{1}{2y} \sqrt{4y^2 + \pi^2} \quad (\text{VII-22})$$

$$X_0 = 0.041 \sqrt{\frac{\sigma}{g(\rho_f - \rho_g)}} \quad (\text{VII-23})$$

Correlations for swirl decay regions between SLTTs

- Single-phase liquid forced convection: Jensen and Bensler (1986) correlation for single-phase convection, adapted to single-phase swirl flow decay³:

$$Nu = 0.020(\alpha_t \text{Re})^{0.8} \text{Pr}^{0.4} \quad (\text{VII-24})$$

where:

$$\alpha_t(z_T) = \sqrt{1 + \left[\int_0^{0.5D_c} \frac{W(r, z_T)}{r} dr \right]^2} \quad (\text{VII-25})$$

$W(r, z_T)$: dimensionless coolant tangential velocity, calculated using Eq. V-B.10 shown in Chapter V. In particular, z_T is the distance from the exit of the upstream TT.

³ The ratio between the resultant velocity and the axial velocity which, in Eq. VII-20, is expressed by the term α_t , in decaying swirl flow is calculated using the theory of swirl decay discussed in Appendix VI-B of Chapter VI.

r : radial coordinate inside the cooling channel.

- Subcooled boiling: no correlation is available for subcooled boiling in decaying swirl flow. Eq. VII-15 is used.
- Saturated boiling: the same correlation used for saturated boiling in presence of FLTTs is used. The only difference is the use of Eq. VII-25 in place of Eq. VII-22 for the calculation of the parameter α_t .

VII. 3 Temperature drop across clad and clad-fuel gap

The temperature drop across the Zr-2.5Nb clad is calculated as (Todreas and Kazimi, 1993):

$$T_{co} - T_{ci} = \frac{q'}{2\pi k_c} \ln\left(\frac{D_{co}}{D_{ci}}\right) \quad (\text{VII-26})$$

where q' is the linear heat generation rate, which varies axially according to a chopped cosine axial profile, while k_c is the Zr-2.5Nb thermal conductivity discussed in Chapter II.

The temperature drop across the clad-fuel gap is calculated as (Todreas and Kazimi, 1993):

$$T_f - T_{co} = \frac{q'}{2\pi\left(\frac{D_f + D_{co}}{4}\right)h_{gap}} \quad (\text{VII-27})$$

where h_{gap} is the thermal conductance of the gap determined as:

$$h_{gap} = \frac{k_{LM}}{t_{gap}} \quad (\text{VII-28})$$

In Eq. VII-28 the thermal conductivity at the denominator is that of the Pb-Sn-Bi eutectic liquid metal (35 W/m K, see Chapter II), while t_{gap} is the as-designed gap width, i.e. without accounting for fuel swelling. It must be pointed out that, for the non collapsible duct design⁴, this formula is an approximation since (1) the gap width decreases during fuel burnup and (2) clad and fuel surfaces may not be completely wetted by the liquid metal (LM) because of local voids, thus creating localized hot spots. While, with respect to point (1), the present analysis is conservative,

⁴ Even though, in the collapsible duct IPWR assembly the gaps are not liquid metal bonded, Eq. VII-28 is used anyway. This is justified by the fact that the instantaneous gap closure, coupled with the hard contact between the fuel and the clad/duct, makes the thermal resistance across the gap very small.

it may not be so with respect to point (2). Complete wettability of the fuel and clad surfaces, by the LM, cannot be guaranteed, but can be improved by adopting the manufacture method suggested by Wongsawaeng and Olander (2007). They verified that, if no measures are taken to address this issue, voids are created when stacking UO_2 pellets into a Zircaloy tube filled with LM, at atmospheric pressure. They were able to eliminate the voids by first evacuating the tube loaded with the pellets and the solid eutectic, then by melting the latter and finally by applying at least 0.5 MPa of He overpressure. This technique is included in the assembly manufacture method proposed in Chapter X for the IPWR non-collapsible duct assembly which, in order to not collapse onto the fuel prism, has in fact to be pressurized with He.

Chapter VIII

LBLOCA analysis

This chapter describes the methodology used to determine the Peak Cladding Temperature (PCT) and its evolution in time during a Large Break Loss-of-Coolant Accident (LBLOCA) assumed to occur at an IPWR plant. The time evolution of this temperature will be used for the calculation of the thickness of oxide forming on the cladding inside surface during the accident, which will be performed using the methodology described in Section III.2.2.6 of Chapter III. While this chapter only discusses the LBLOCA analysis methodology (Section VIII. 1) and differences, in terms of the physical parameters that determine the core thermal hydraulics during a LBLOCA, between inverted and pin geometries (Section VIII. 2), actual results regarding PCT and oxide thickness will be presented in Chapter XI. In this chapter, in fact, the LBLOCA analysis methodology will be applied to a promising IPWR design/geometry selected upon application of structural and steady-state thermal hydraulic constraints.

VIII. 1 Analysis methodology

The LBLOCA analysis was performed with the RELAP5-3D[®] code (RELAP5, 2005a) on core geometries approximating the IPWR configuration. The approximation consisted of modeling the inverted assemblies as pin geometry assemblies, without duct, in which equivalent inverted annuli were used in place of hexagonal inverted cells, as shown in Figure VIII- 1. In particular, the inverted annuli are only internally cooled, and a symmetry boundary condition is applied to the outer surface of the fuel. While cooling channel inner diameter, as well as clad thickness and clad-fuel duct width are the same in the two geometries, the diameter of the equivalent inverted annulus, D_{EA} , is obtained by preserving the fuel area. It can be easily demonstrated that this requirement, as already discussed in Chapter VII, leads to the following expression for D_{EA} :

$$D_{EA} = P_I \sqrt{\frac{2\sqrt{3}}{\pi}} \quad (\text{VII-1})$$

The reason for this approximation is that RELAP was developed for pin geometry cores, and inverted geometries are difficult¹ to model. However, it is reasonable to think that this model, although inappropriate for fuel temperature calculation and for the analysis of most of the core thermal hydraulic parameters, can give a reasonable approximation of the PCT during a LOCA scenario.

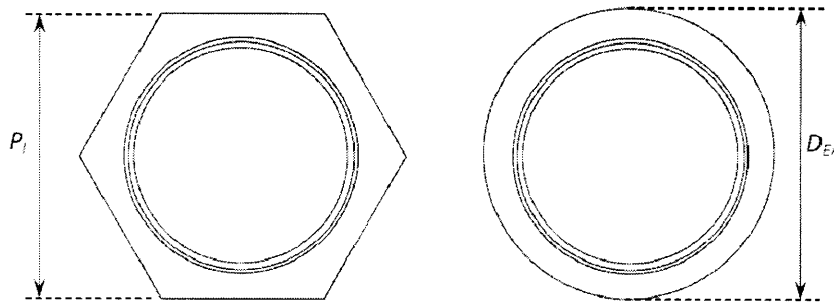


Figure VIII- 1: Actual fuel cell (left) and equivalent annulus used for LOCA analysis (right)

VIII.1. 1 RELAP plant nodalization and pre-accident power distribution

The RELAP input file used for the LOCA analysis models the primary system and the steam generators of the IPWR. Except for the core, all the plant components are those of a typical Westinghouse 4-loop PWR. The plant nodalization implemented in the file is shown in Figure VIII- 2. It is worth noting that:

- the break is assumed to be of double ended guillotine type, located in the cold leg between the primary pump discharge and the vessel inlet nozzle;
- the three intact loops are lumped together, while the broken loop is modeled separately;
- the axial modeling of the core is performed using 16 axial zones: the bottom and the top zones are 45.3 cm long each, while the remaining 14 zones are 22.6 cm long each. The

¹ Analyzing non-conventional assembly geometries with RELAP requires an extensive use of RELAP control variables to solve 2D heat conduction equations. An example of the feasibility of this approach is given by Memmott et al. (2009). They used RELAP5-3D to perform subchannel analysis of sodium-cooled fuel assemblies with non-conventional geometries.

active part of the core includes all the 14 central zones plus a fraction of the two outermost ones;

- the radial modeling of the core consists of three channels:
 - channel 335 represents the cooling channels of the hot assembly, lumped together;
 - channel 333 represents the cooling channels of the remaining assemblies, lumped together;
 - channel 320 represents the water gaps between assemblies, lumped together.
- two heat structures are embedded in channel 335: the hottest inverted annulus and a dummy annulus representing the remaining fuel cells of the hot assembly.
- mixing between channels is not allowed;
- heat transfer through the duct wall to inter-assembly water gaps is neglected.

The power distribution inside the core, just before the transient initiation, was defined by means of three peaking factors:

- an axial peaking factor equal to 1.515 (in a chopped cosine axial power profile);
- an assembly radial power peaking, defined as the ratio between the power of the hot assembly and the power of the average assembly, equal to 1.515;
- a unit cell radial power peaking, defined as the ratio between the power of the hottest cell and the power of the average cell, equal to 1.09.

These values were not calculated, but taken the same as typical peaking factors used in safety analysis of PWRs (Seabrook USAR, 2002).

VIII.1. 2 Plant response model

The plant response to the LBLOCA event consists of a series of actions actuated with a certain delay time with respect to the first of the following two signals being detected:

- S1 (low pressurizer pressure): pressurizer pressure drops below 1935 psia (13.34 MPa);
- S2 (low core flow): coolant flow rate at core inlet drops below 87% of the nominal value.

The protective actions are summarized in Table VIII- 1, together with the corresponding delay times which are consistent with those used in Chapter 15 of Seabrook USAR (2002) for the LBLOCA analysis.

Table VIII- 1: Sequence of events following the occurrence of the break		
	Delay with respect to S-signals (s), or actuation setpoint	Notes
Main Steam Line Isolation Valves start closing	2 s after S1 1 s after S2	5 s are needed for complete closure
RCP trip. coastdown starts	2 s after S1	
Main Feedwater Isolation Valves start closing	2 s after S1	10 s are needed for complete closure
Auxiliary Feedwater Pumps start injecting	75 s after S1	
PRZ Power Operated Valves open	PRZ pressure > 2425 psia	They close after PRZ pressure has decreased below 2330 psia
Safety injection signal	31 s after PRZ pressure has dropped below 1867 psia	CCP, SIP and RHRP flow rates vary based on RCS pressure
Accumulators start injecting	Cold leg pressure < 600 psia	

Conservative assumptions that are also made to reduce the ECCS capability to mitigate the event are consistent with those used in Chapter 15 of Seabrook USAR (2002). They can be summarized as follows:

- a) Reactor trip is not credited, i.e. control rods are assumed completely withdrawn during the whole transient.
- b) Boron contained in the Emergency Core Cooling System (ECCS) water is not credited.
- c) 1 out of 4 accumulators is not credited.
- d) 1 out of 2 ECCS trains is assumed not available, i.e. 1 Centrifugal Charging Pump, 1 Safety Injection Pump and 1 Residual Heat Removal Pump are not credited. The capacity of the remaining train is 10% degraded.

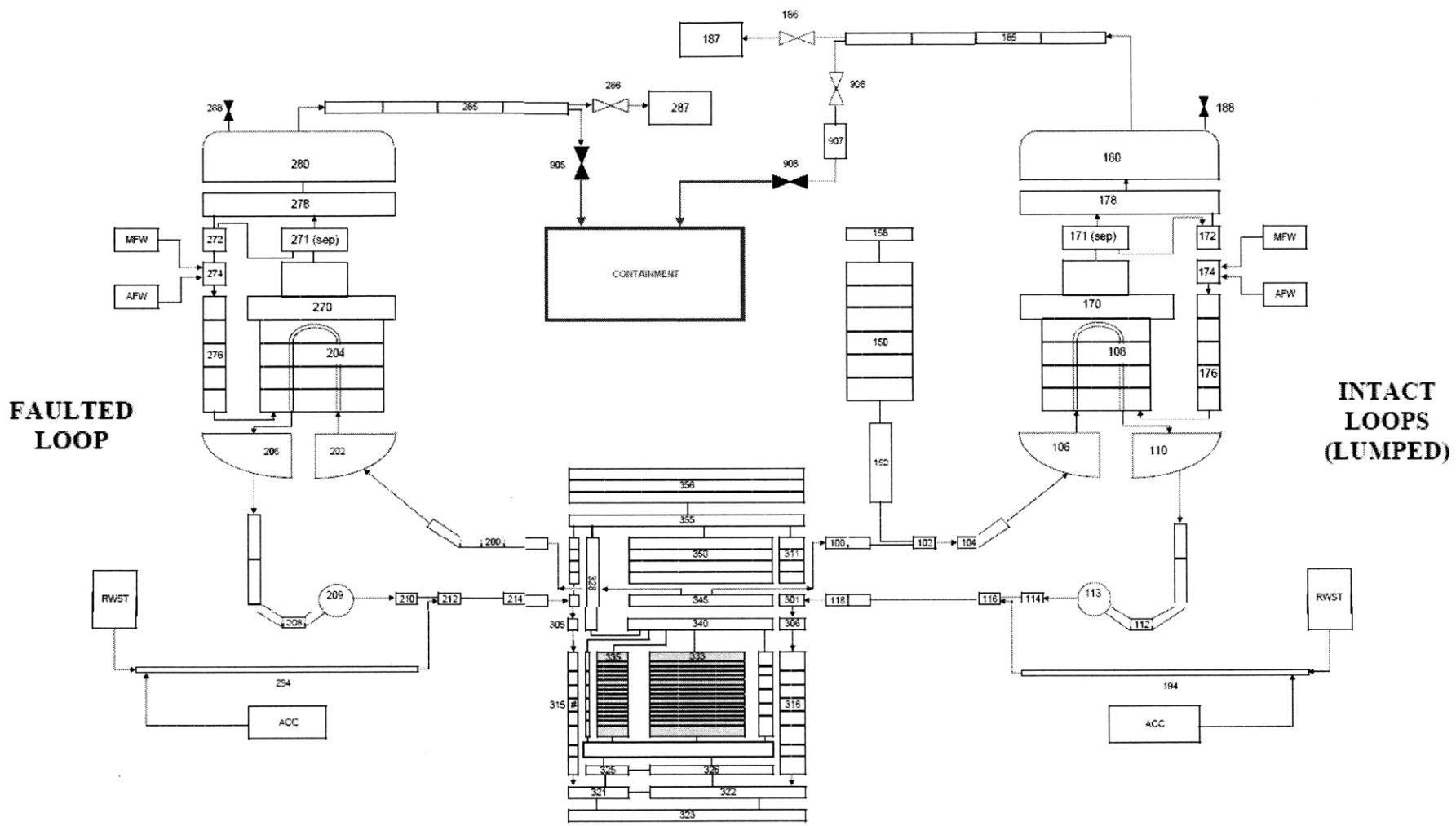


Figure VIII- 2: RELAP plant nodalization for LBLOCA analysis

In addition, the containment pressure variation assumed² during the LBLOCA corresponds to that of a transient in which the containment atmosphere cooling system is perfectly working. In this way, the backpressure is maintained quite low and the flow through the break, after the period when it is choked, is higher. Figure VIII- 3 compares the containment pressure evolution assumed in the LBLOCA analysis to that used in Seabrook USAR (2002) for containment design purposes. In spite of being different, they are both conservative since the ECCS cooling capability is challenged by a low backpressure, while the containment isolation is challenged by a high backpressure.

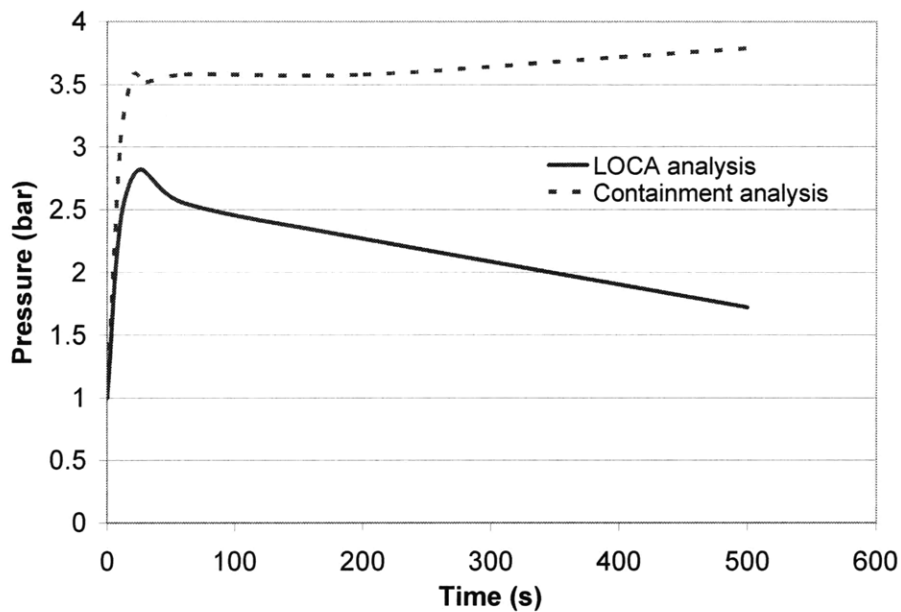


Figure VIII- 3: Containment pressure evolution used for LBLOCA analysis compared to that used for containment design purposes (from Seabrook USAR, 2002)

Technical specifications regarding the LBLOCA mitigation capability are shown in Table VIII- 2 and derived from the Seabrook USAR (2002).

When applied to typical pin geometry PWR cores, the LBLOCA analysis method discussed in this section was confirmed to be accurate. This was done by making the core model contained in the RELAP input file consistent with the geometry of the Seabrook PWR core, and by modeling

² Since the containment atmosphere is not modeled explicitly but simply plays the role of a fixed boundary condition for the reactor coolant system, the evolution of the containment backpressure is entered as input data.

the occurrence of a LBLOCA at this plant. The time evolution of key plant parameters (primary system pressure, collapsed liquid level in the core etc.) was compared with that presented in the Seabrook USAR (2002), and good agreement was found (Greenspan et al., 2007).

Table VIII- 2: Nominal and simulated ECCS capability to mitigate LBLOCA event (from Seabrook USAR, 2002)			
	Units	Nominal	Simulated
Accumulators			
Number of units		4	3 (one is not credited)
Water volume in each unit	m ³	24.07	24.07
Nitrogen volume in each unit	m ³	14.16	14.16
Accumulator water temperature	°C	38-65	52
Boron concentration	ppm	2600-2900	0 (boron not credited)
Injection pressure setpoint	MPa	4.83	4.14
Centrifugal Charging Pumps (CCPs)			
Number of units		2	1 (one is not credited)
Discharge head at shutoff	MPa	18.54	18.54
Discharge head at max flow rate	MPa	4.18	4.18
Max flow rate	m ³ /s	0.03470	0.0312 (10% degraded)
High pressure Safety Injection Pumps (SIPs)			
Number of units		2	1 (one is not credited)
Discharge head at shutoff	MPa	10.60	10.60
Discharge head at max flow rate	MPa	5.08	5.08
Max flow rate	m ³ /s	0.04164	0.03748 (10% degraded)
Residual Heat Removal Pumps (RHRPs)			
Number of units		2	1 (one is not credited)
Discharge head at shutoff	MPa	1.37	1.37
Discharge head at max flow rate	MPa	0.822	0.822
Max flow rate	m ³ /s	0.2965	0.2668 (10% degraded)

VIII. 2 Peak cladding temperature and quenching time for pin and inverted core geometries

Hydride-fueled inverted cores were found to have a different PCT time evolution than typical oxide-fueled pin geometry cores operating at the same power. In particular, they were found to have lower PCTs but longer quenching times³, t_Q . Understanding the reason for the different

³ The quenching time is defined, for a certain axial location on a cladding, as the time from LBLOCA initiation when the cladding temperature at that location drops abruptly. Physically, this is due to the fact that, at a certain time during the reflood phase of a LBLOCA, coolant starts wetting the cladding at the axial location of interest, causing its temperature to decrease significantly. Before that time, i.e. during the reactor bottom head refill phase as well as during the reflood of the axial locations below that of interest, the cladding is cooled first by a dispersed two-phase mixture of superheated steam and entrained droplets, rising from the lower sections of the assembly, and then by

PCTs would require multiple comparisons, each performed while varying a single parameter. In this way it would be possible to identify the parameter that contributes most to the difference in PCT. Also, the comparisons should be performed both at cell level and at whole core level since, as discussed in Chapter I, the IPWR is not a continuous inverted geometry and the presence of discontinuities, i.e. thick ducts and wide inter-assembly water gaps, causes comparison performed at cell level to yield different results from those, more realistic, performed at whole core level. For the IPWR study it was therefore decided to only investigate the effect that the different geometry and fuel type have on the energy stored in the fuel, which is discussed in Section VIII.2. 1. The stored energy, because of the energy redistribution occurring almost instantaneously after the break, is responsible for the rapid cladding temperature increase that characterizes the first seconds after accident initiation, which lead to the so-called blowdown peak cladding temperature. It is important to note that this peak temperature may or may not coincide with the actual PCT: the latter is in fact defined as the maximum temperature reached by the cladding during the entire transient, and not only during blowdown. The speed with which the Emergency Core Cooling System (ECCS) is able to activate, refill the vessel lower head and reflood the core, determines whether the maximum temperature reached during blowdown is the actual PCT.

The delay in quenching characterizing the IPWR, with respect to typical PWRs, is mainly⁴ due to the smaller flow area of the former which, for the same ECCS injection flow rate, yields a larger pressure drop through the core. This is briefly discussed in Section VIII.2. 2.

VIII.2. 1 Stored energy comparison between pin and inverted cell having same fuel volume

Before accounting for the differences in fuel type and linear power existing between hydride-fueled inverted geometries and oxide-fueled pin geometries, it is useful to compare inverted and pin geometries on a fair basis, i.e. assuming same material composition, fuel volume, cladding-coolant heat transfer area and heat transfer coefficient, and linear power. With these boundary conditions, it can be easily demonstrated that the amount of energy stored in the fuel in an

film boiling: two heat transfer mechanisms that, relative to the post-quenching nucleate boiling, are much less effective in removing decay heat.

⁴ Another reason, although less important, is the absence of inter-channel mixing. In fact, in pin geometry assemblies, coolant moves from cool pins to hot pins, thus enhancing assembly cooling.

inverted cell, relative to 0 K, is lower than that stored in the fuel in a pin geometry. For a pin geometry, the energy stored in the fuel, per unit length, is given by:

$$\begin{aligned}
 E_{f,p} &= \int_0^{R_f} 2\pi r \rho_f C_{pf} T_f(r) dr = 2\pi \rho_f C_{pf} \int_0^{R_f} r \left(T_{f,peak} - \frac{q'''}{4k_f} r^2 \right) dr = \\
 &= \pi R_f^2 \rho_f C_{pf} \left\{ T_{f,peak} - \frac{q'''}{8\pi k_f} \right\} \quad \text{(VIII-1)}
 \end{aligned}$$

where R_f is the pellet radius, $T_{f,peak}$ is the pellet centerline temperature, q''' is the pin linear power, ρ_f , C_{pf} and k_f are the fuel density, specific heat and thermal conductivity respectively. For an inverted cell, approximated using the equivalent annulus discussed in Chapter VII (without correction factor on the temperature), the energy stored in the fuel, per unit length, is given by:

$$\begin{aligned}
 E_{f,i} &= \int_{R_f}^{R_{EA}} 2\pi r \rho_f C_{pf} T_f(r) dr = 2\pi \rho_f C_{pf} \int_{R_f}^{R_{EA}} r \left[T_{f,R_{EA}} + \frac{q'''}{4k_f} \left(R_{EA}^2 - r^2 + 2R_{EA}^2 \ln \frac{r}{R_{EA}} \right) \right] dr = \\
 &= 2\pi \rho_f C_{pf} \left\{ \left(T_{f,R_{EA}} + \frac{q'''}{4k_f} R_{EA}^2 - \frac{q'''}{2k_f} R_{EA}^2 \ln R_{EA} \right) \frac{(R_{EA}^2 - R_f^2)}{2} - \frac{q'''}{16k_f} (R_{EA}^4 - R_f^4) + \right. \\
 &\quad \left. + \frac{q'''}{4k_f} R_{EA}^2 \left[-\frac{(R_{EA}^2 - R_f^2)}{2} + R_{EA}^2 \ln(R_{EA}) - R_f^2 \ln(R_f) \right] \right\} = \\
 &= \pi (R_{EA}^2 - R_f^2) \rho_f C_{pf} \left\{ T_{f,R_{EA}} - \frac{q'''}{2\pi k_f (R_{EA}^2 - R_f^2)} \left[\frac{R_{EA}^2 + R_f^2}{4} + \frac{R_{EA}^2 R_f^2}{R_{EA}^2 - R_f^2} \ln \frac{R_f}{R_{EA}} \right] \right\} \quad \text{(VIII-2)}
 \end{aligned}$$

where R_f is the fuel hole radius, R_{EA} is the equivalent annulus outer radius and $T_{f,R_{EA}}$ is the temperature reached at the annulus outer surface. Figure VIII- 4 shows the ratio between the

energy stored in the fuel pellet and that stored in the fuel belonging to the equivalent annulus⁵. It can be seen that this ratio is always ≥ 1 , and gets larger and larger as the linear power increases and the thermal conductivity decreases. The reason for this behavior is that in the inverted annulus the average temperature in the fuel is lower, as can be easily demonstrated using Eqs. VIII-1 and VIII-2. In fact, in these equations the term in braces is the fuel average temperature, which is multiplied by a term that has the same value in the two geometries, i.e. $[\pi R_f^2 \rho_f C_{pf}]_p = [\pi(R_{EA}^2 - R_f^2) \rho_f C_{pf}]_i$.

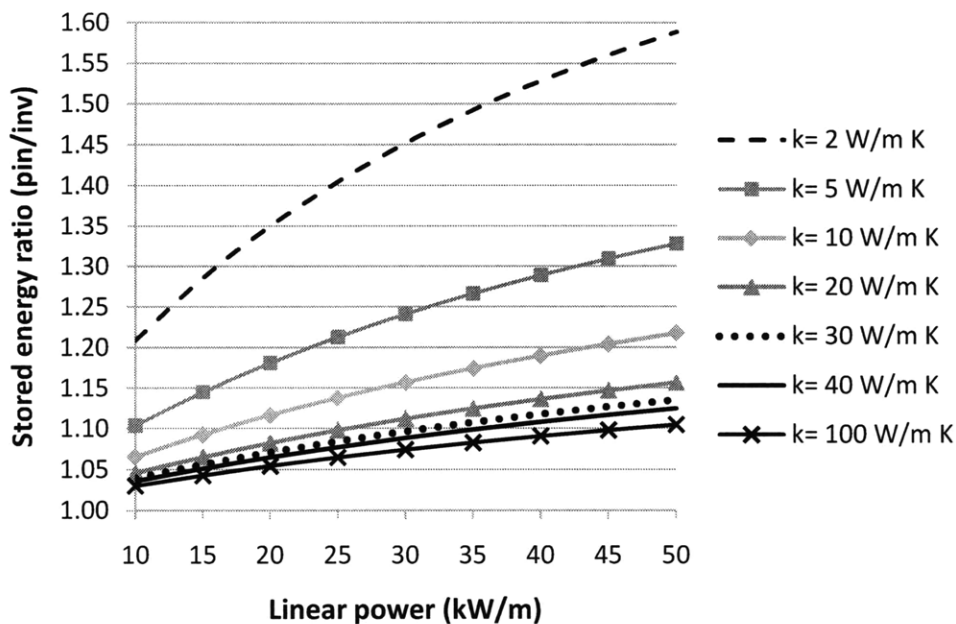


Figure VIII- 4: Stored energy ratio (pin/inverted) for same material, fuel cross sectional area and heat transfer area, as a function of linear power and thermal conductivity

The boundary conditions used for the comparison presented above are not representative of the actual conditions characterizing a typical oxide-fueled pin geometry PWR core and a hydride-fueled inverted PWR core. Even if assumed to operate at the same linear power, the fuel type is

⁵ The annulus is assumed to be cooled internally only. Therefore, the cladding outside diameter of the pin geometry is set equal to the cladding inside diameter of the inverted geometry. Also, the same coolant-cladding heat transfer coefficient (45000 W/m² K), fuel-clad gap thermal conductance (5682 W/m² K) and cladding thermal conductivity (16.6 W/m K) are used in the two geometries.

different. $UTh_{0.5}Zr_{2.25}H_{5.625}$ density is about 14% lower than that of UO_2 , while its thermal conductivity and specific heat are higher, as shown⁶ in Figure VIII- 5.

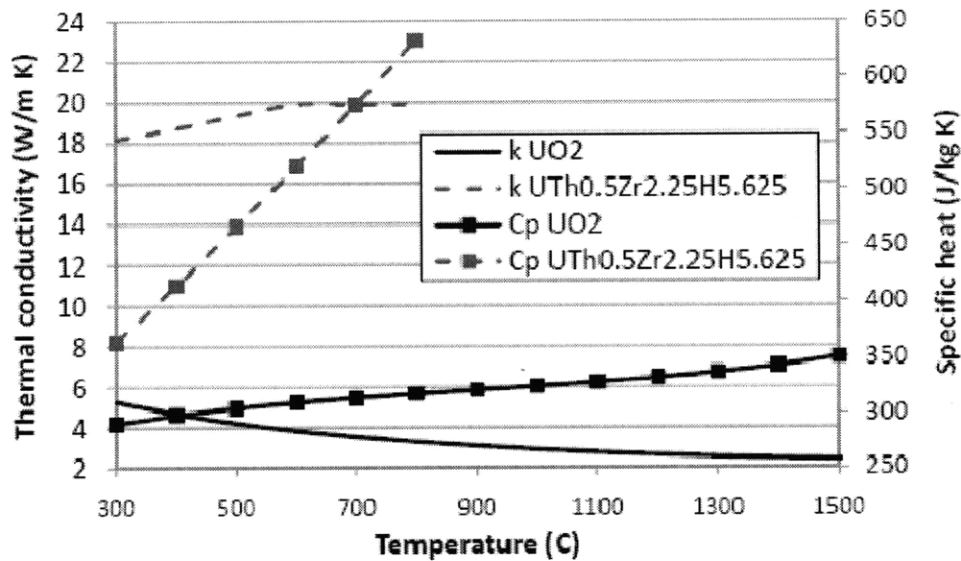


Figure VIII- 5: Thermal conductivity and specific heat for UO_2 (from NUREG/CR-6150, 1993) and $UTh_{0.5}Zr_{2.25}H_{5.625}$ (from Chapter II)

The effect of these differences in fuel properties on the stored energy is to cause an increase of the stored energy in the inverted cell, thus leading to a reduction of the stored energy ratio, as shown in Figure VIII- 6. Of the three properties affecting the stored energy, i.e. fuel density, specific heat and thermal conductivity, density and specific heat clearly dominate the beneficial effect that a higher thermal conductivity has on average fuel temperature, thus causing the stored energy ratio to decrease, relative to that shown in Figure VIII- 4. The rapid increase in $UTh_{0.5}Zr_{2.25}H_{5.625}$ specific heat with temperature, shown in Figure VIII- 5, causes the stored energy ratio to be practically independent of the linear power. Therefore, from the stored energy point of view, a $UTh_{0.5}Zr_{2.25}H_{5.625}$ -fueled inverted cell does not behave very differently from an UO_2 -fueled pin, when both have same fuel cross sectional area and linear power. This last condition, although useful to guarantee a fair comparison between pin and inverted geometries, is not necessarily true when comparing an IPWR with a typical PWR. In fact, as discussed in Chapter I, the cell-level fuel volume fraction of IPWRs is typically higher than in PWRs, due to

⁶ This figure does not show $UTh_{0.5}Zr_{2.25}H_{5.625}$ properties above 800°C since hydrogen release is expected to occur, and no data are available in this regard. In the analysis, it is assumed that at temperatures above 800°C thermal conductivity and specific heat remain constant at the 800°C values.

the larger flow area of the latter. For example, the cell-level fuel volume fraction of a promising IPWR design selected in Chapter XI is 0.397, versus 0.332 of the reference PWR. This contributes to an increase in stored energy with respect to pin geometry.

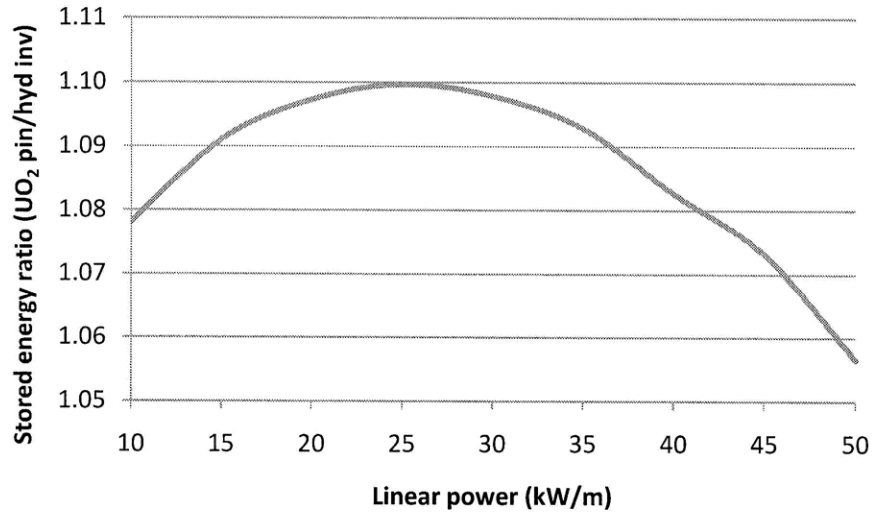


Figure VIII- 6: Stored energy ratio (UO₂ pin/ UTh_{0.5}Zr_{2.25}H_{5.625} inverted)

VIII.2. 2 Quenching time comparison between pin and inverted cores

Figure VIII- 7 shows the time evolution of the hot rod cladding temperature during a LBLOCA event, for the reference pin geometry PWR. It can be seen that, as expected, axial zones above mid core are quenched later, while those at core mid height (8th and 9th axial zones in Figure VIII- 7) reach higher temperatures but are quenched earlier in the transient.

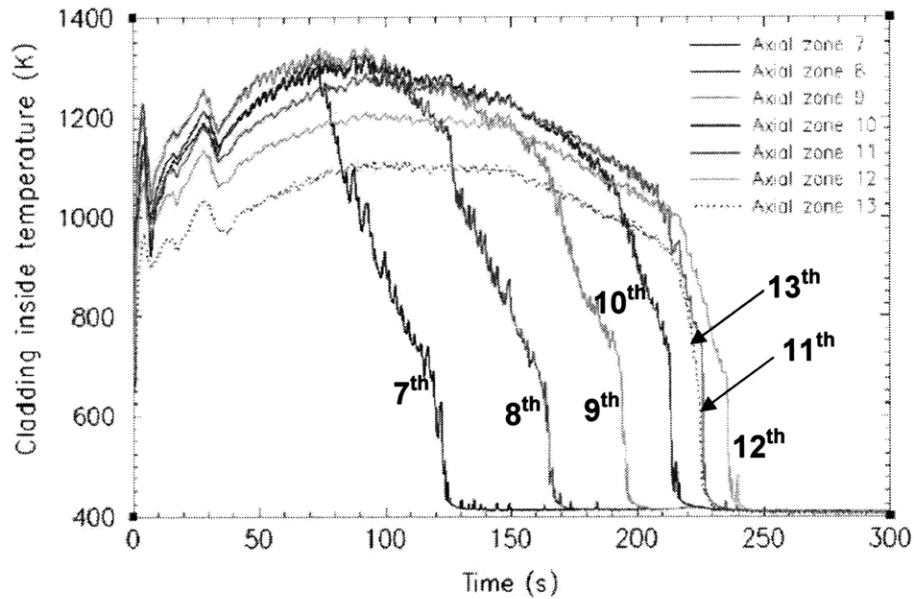


Figure VIII- 7: Hot rod cladding temperature during LBLOCA, at different axial locations (UO₂-fueled PWR, 3479 MW_t)

The temperature variation of the 8th axial zone of Figure VIII- 7 is redrawn in Figure VIII- 8 together with the hot spot cladding temperature profiles of other core geometries/fuels. The temperature profiles refer to:

- two pin geometry PWRs having the same geometry as the reference PWR (Seabrook USAR, 2002), one oxide-fueled and the other hydride-fueled;
- four IPWRs, all hydride-fueled, which differ in the diameter of the cooling channels: 7, 9, 11 and 13 mm diameter channels have been considered;

all having the same thermal power, i.e. 3479 MW_t. It can be noticed that:

- the hydride-fueled PWR has a PCT much lower than the oxide-fueled PWR, which is mainly due to the lower pre-accident fuel temperature;
- IPWRs have higher PCT than the hydride-fueled PWR, but lower than the oxide-fueled PWR;
- IPWRs have longer quenching time, and such a time increases as the cooling channel diameter decreases.

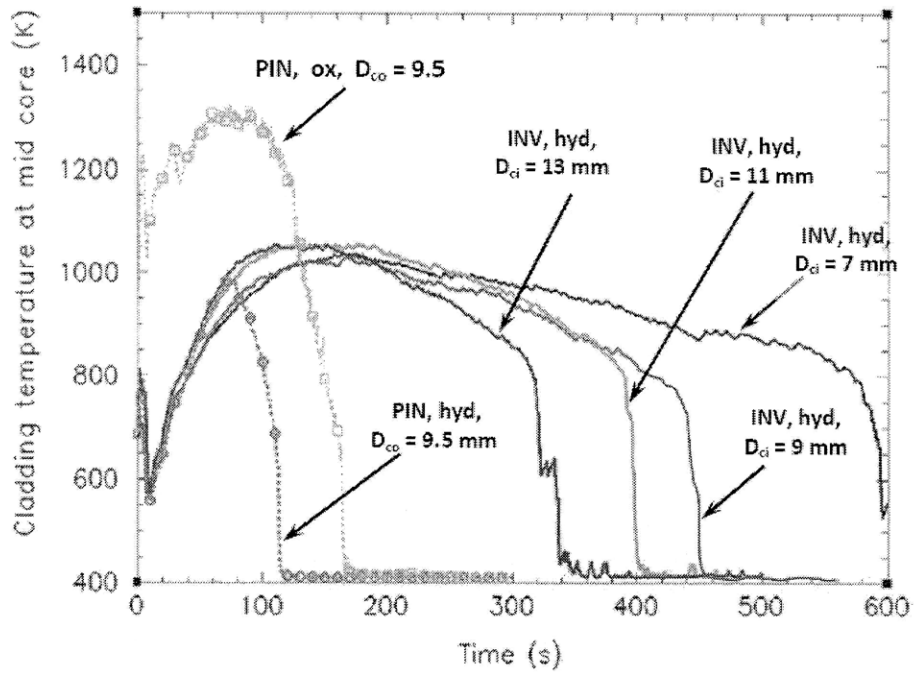


Figure VIII- 8: Hot spot cladding temperature during LBLOCA for different cores analyzed at the same total power (3479 MW_t)

The most interesting observation from Figure VIII- 8 is that about the longer quenching time of inverted PWRs with respect to pin geometry PWRs. The reason is the larger pressure drop characterizing IPWR cores. As demonstrated in Appendix I-A of Chapter I, for constant mass flow rate conditions, which is the case of a post-LBLOCA scenario during which ECCS injects into the vessel, friction pressure drop is inversely proportional to $A_{flow}^{1.8} D_e^{1.2}$, where A_{flow} is the active flow area while D_e is the equivalent diameter. Because of the presence of thick walled ducts and inter-assembly water gaps, the active flow area of IPWRs is typically smaller than that of pin geometry PWRs. Figure VIII- 9 shows the ratio:

$$\frac{\left(A_{flow}^{1.8} D_e^{1.2}\right)_{Pin,ref}}{\left(A_{flow}^{1.8} D_e^{1.2}\right)_{Inv}} \quad \text{(VIII-3)}$$

which can be interpreted as an indication of how much resistance the flow injected by the ECCS experiences in flowing through the IPWR relative to the reference PWR. It can be seen that this ratio ranges between about 1.8 and 15. IPWR geometries of interest, as discussed in Chapter XI,

are those located in the middle of the left part of the plot, therefore having a ratio ~ 2.3 with the area effect dominant.

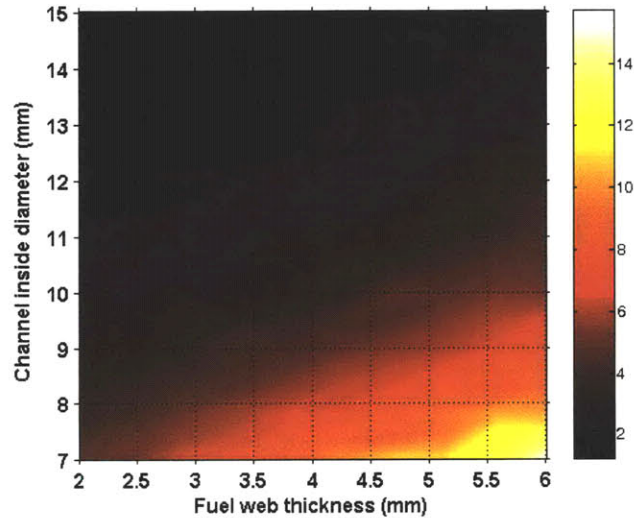


Figure VIII- 9: Graphical representation of the ratio expressed by Eq. VIII-3 (collapsible duct IPWR design)

A further indication of the effect that hydraulic resistance has on quenching time can be obtained by adding, in each cooling channel, localized pressure losses. These losses, from the pressure drop viewpoint, can be imagined as associated with short-length twisted tapes inserted in the cooling channels to enhance CHF performance. Assuming an arbitrary form loss value for illustration purposes their effect, shown in Figure VIII- 10, is clearly a lengthening of the quenching time.

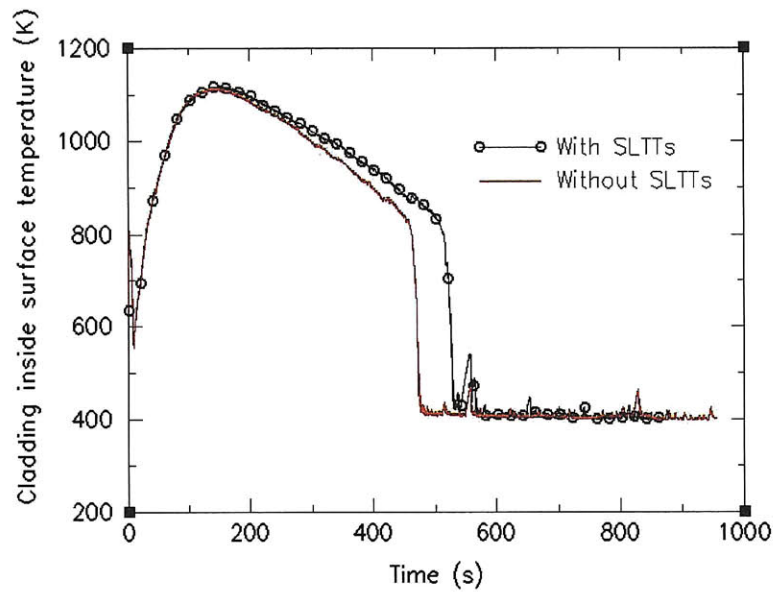


Figure VIII- 10: Effect of short-length twisted tapes on quenching time

As demonstrated in Chapter XI, as long as the cladding temperature remains low, the lengthening of the quenching time for IPWRs relative to typical PWRs does not cause an increase of the extent of cladding oxidation.

Chapter IX

Neutronic analyses

This chapter discusses the methodologies used for the neutronic analysis of the IPWR. Final results of this analysis are presented in Chapter XI since most of them are geometry-specific, and the selection of the most promising IPWR geometry is performed in that chapter.

The organization of this chapter is as follows:

- Section IX. 1: void reactivity coefficient (VRC) analysis method;
- Section IX. 2: findings, from Ganda and Greenspan (2010), on fuel temperature reactivity coefficient (FTRC);
- Section IX. 3: cycle length and fuel enrichment calculation methods;
- Section IX. 4: considerations on shutdown margin.

IX. 1 Determination of VRC sign

The IPWR is required to have a negative void reactivity coefficient (VRC). This constraint is extremely important from the safety viewpoint since the VRC defines the reactor power behavior upon a change in coolant density. The analysis of the IPWR focuses on the sign of this parameter, rather than on its actual value: a positive VRC means that a reduction in coolant density yields an increase in core power, while a negative VRC means that the core response to a coolant density reduction is a reduction in power. The prediction of the VRC sign is performed by locating the hydrogen-to-

heavy metal ratio (H/HM), computed at cell level¹, on the k_{∞} vs H/HM curve, where k_{∞} is the infinite multiplication factor. As mentioned in Section III.2.3.1 of Chapter III, in order for the VRC requirement to be met, the operating H/HM must be located on the left of the H/HM value at which that curve has a maximum. In the present analysis, this H/HM limit is referred to as L_{HM} . This criterion, when applied to the hydride fuel type originally investigated for the IPWR, i.e. U(45% w/o)ZrH_{1.6}, led to its rejection since this fuel, regardless of the lattice geometry, cannot have an H/HM below about 5, which is higher than the corresponding L_{HM} .

IX.1. 1 Calculation of H/HM

For an inverted cell, like that shown in Figure IX- 1, the H/HM ratio can be expressed as a function of geometry- and fuel and coolant composition-related parameters:

$$\frac{H}{HM} = \frac{H_{coolant} + H_{fuel}}{HM} = \frac{\left[\left(\pi \frac{D_{ci}^2}{4} \right) \frac{2\rho_c}{M_{H_2O}} N_A \right] + \left[\left(\frac{\sqrt{3}}{2} P^2 - \pi \frac{D_f^2}{4} \right) \frac{\rho_f w_H}{M_H} N_A \right]}{\left(\frac{\sqrt{3}}{2} P^2 - \pi \frac{D_f^2}{4} \right) \left(\frac{\rho_f w_U}{M_U} + \frac{\rho_f w_{Th}}{M_{Th}} \right) N_A} \quad (IX-1)$$

where the meaning of the geometric parameters is that shown in Figure IX- 1, ρ_c and ρ_f are the coolant and fuel densities (kg/m³), w_x is the weight fraction of element x in the fuel, M_x is the atomic (or molecular) weight of element (or compound) x , expressed in kg/mol, and N_A is the Avogadro number. For the analysis of the IPWR, the coolant is assumed to have a density of 705 kg/m³, which corresponds to the operating conditions: $T_c = 310^\circ\text{C}$ and $p = 15.5$ MPa.

¹ VRC analysis at cell level is, relative to that at assembly-level, conservative since neutron leakage is not accounted for.

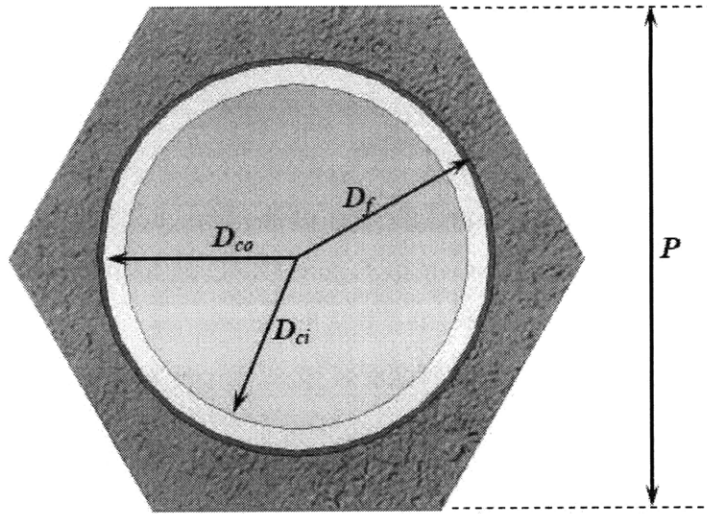


Figure IX- 1: Example of inverted cell

Before showing how the H/HM ratio changes when key cell geometric parameters are varied, it is interesting to calculate the contribution given by the coolant to the total amount of hydrogen contained in a fuel cell which, as discussed below, has important implications on the self-shielding effect². This contribution fraction, given by:

$$\begin{aligned} \frac{H_{coolant}}{H_{coolant} + H_{fuel}} &= \frac{\left(\pi \frac{D_{ci}^2}{4} \right) \frac{2\rho_c}{M_{H_2O}}}{\left[\left(\pi \frac{D_{ci}^2}{4} \right) \frac{2\rho_c}{M_{H_2O}} \right] + \left[\left(\frac{\sqrt{3}}{2} P^2 - \pi \frac{D_f^2}{4} \right) \frac{\rho_f w_H}{M_H} \right]} = \\ &= \frac{1}{1 + \left(\frac{2\sqrt{3}P^2 - \pi D_f^2}{D_{ci}^2} \frac{w_H \rho_f}{2\pi \rho_c} \frac{M_{H_2O}}{M_H} \right)} = \end{aligned}$$

² In typical fuels, e.g. UO₂, moderation only occurs in the coolant. After being born, neutrons travel through the fuel without being substantially absorbed or slowed down, reach the coolant, slow down and re-enter the fuel in a thermal or epithermal state. Those in thermal state create fissions, while those in epithermal state will be probably absorbed by ²³⁸U, in the outermost layers of the pellet. This is the self-shielding effect.

$$= \frac{1}{1 + \left[\frac{2\sqrt{3}(D_f + t_{web})^2 - \pi D_f^2 w_H \rho_f M_{H_2O}}{D_{ci}^2 2\pi \rho_c M_H} \right]} \quad (\text{IX-2})$$

where t_{web} is the fuel web thickness and the rest of the nomenclature is the same as that used for Eq. IX-1. The result is shown in Figure IX- 2 as a function of the two key geometric parameters used to identify the IPWR geometries, i.e. the cooling channel inner diameter, D_{ci} , and the fuel web thickness³, t_{web} . It can be seen that the maximum coolant contribution to the total hydrogen content is of about 65%, and that for the geometries of interest (small t_{web} and intermediate D_{ci} , examined in Chapter XI), it is about 50%. These high percentages imply that, relative to a fuel which does not contain hydrogen, the self-shielding effect in hydride fuels is less pronounced.

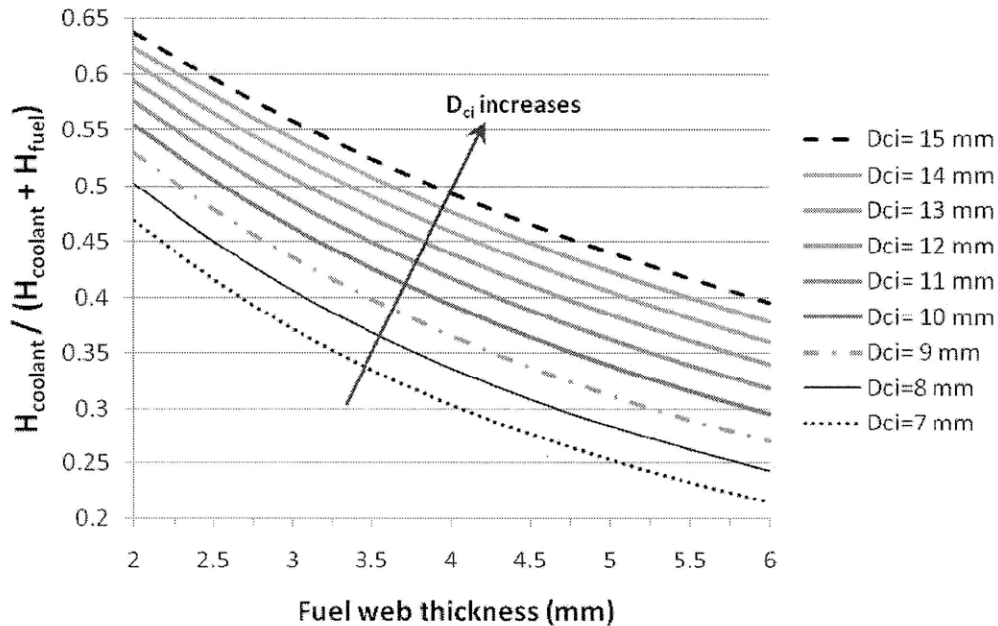


Figure IX-2: Coolant contribution fraction to total number of hydrogen atoms
 $(\rho_c=705 \text{ kg/m}^3)$

³ Figure IX- 2 was generated by modifying Eq. IX-2 so that the fractional contribution was a function of D_{ci} and t_{web} only. This was possible by calculating, for each value of D_{ci} , the cladding thickness t_{clad} and clad-fuel gap width t_{gap} using the relations introduced in Section III.2.1.1 of Chapter III, and by noting that $D_f = D_{ci} + 2(t_{clad} + t_{gap})$.

Even though Eq. IX-1 cannot be reduced to a form in which the P/D_{ci} ratio (or the P/D_f ratio) is the only geometric parameter, i.e. D_{ci} (or D_f) will still appear alone, it has been verified that once P/D_{ci} (or P/D_f) is fixed, the influence of varying D_{ci} (or D_f) on H/HM is very small, and negligible for the cooling channel diameter range of interest ($7 \leq D_{ci} \leq 15$ mm). This is shown in Figure IX- 3. This figure shows both the H/HM vs P/D_f curves and the H/HM vs P/D_{ci} curves, drawn for cooling channel diameters ranging between 5 and 15 mm, and fuel web thicknesses between 1 and 20 mm. Figure IX- 4, which is an enlargement of the region of Figure IX- 3 included between pitch-to-diameter ratios of 1.3 and 2.3, more clearly shows the diameter dependence of H/HM .

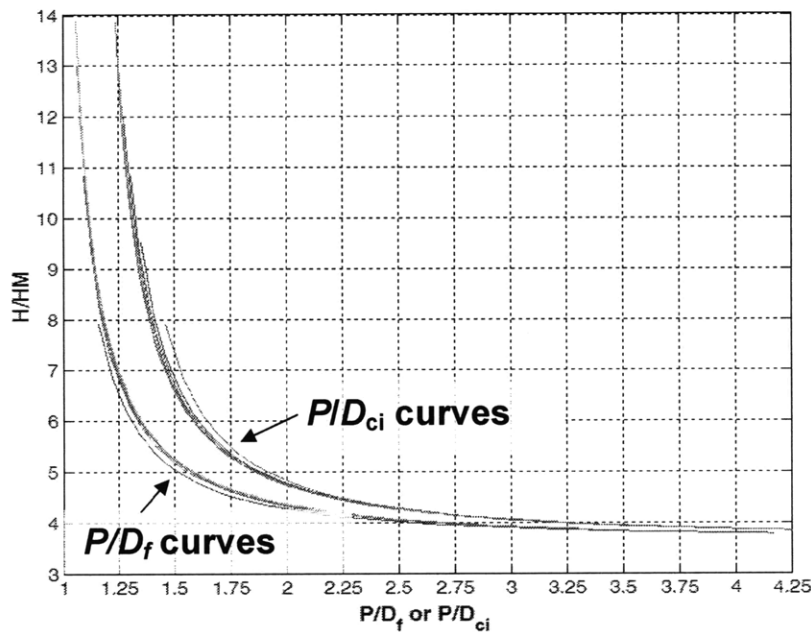


Figure IX- 3: H/HM vs pitch-to-diameter ratio ($UTh_{0.5}Zr_{2.25}H_{5.625}$ unit cell calculation, see Figure IX- 4 for enlargement)

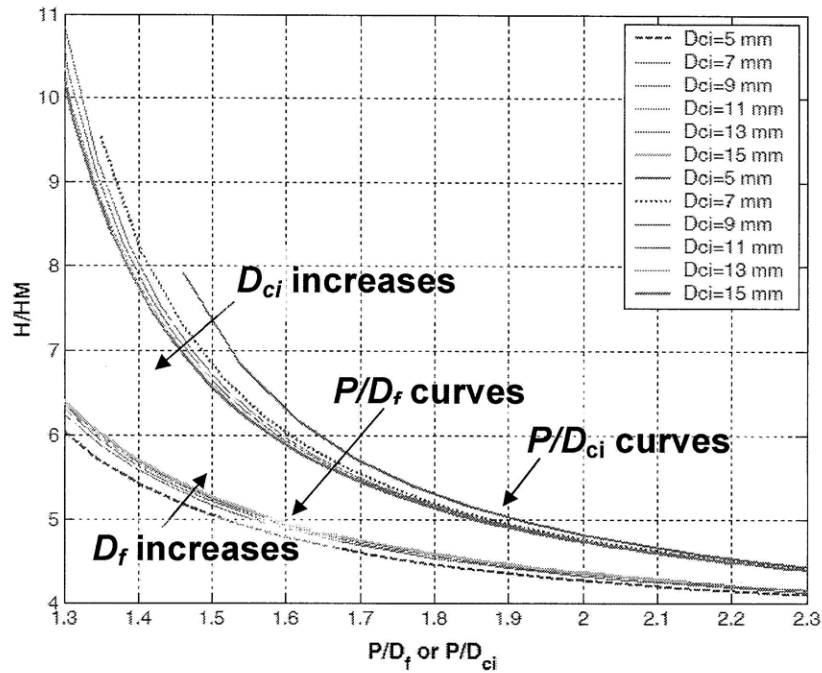


Figure IX- 4: H/HM vs pitch-to-diameter ratio (enlargement of Figure IX- 3 with indication of diameter effect)

From Figure IX- 3, it can be seen that inverted-, $UTh_{0.5}Zr_{2.25}H_{5.625}$ -fueled cells can have H/HM ratios as low as about 3.8. However, geometries of practical interest for the IPWR have higher H/HM values, generally above 6, due to the fact that the web thickness cannot be too large to avoid exceeding the limit imposed on fuel temperature. For this reason, Figure IX- 3 was redrawn to show the dependence of H/HM on the two geometric parameters more often used to identify the IPWR lattice geometry, i.e. D_{ci} and t_{web} . This is shown in Figure IX- 5. It can be seen that H/HM increases as the channel diameter increases, and as the fuel web thickness decreases, as expected.

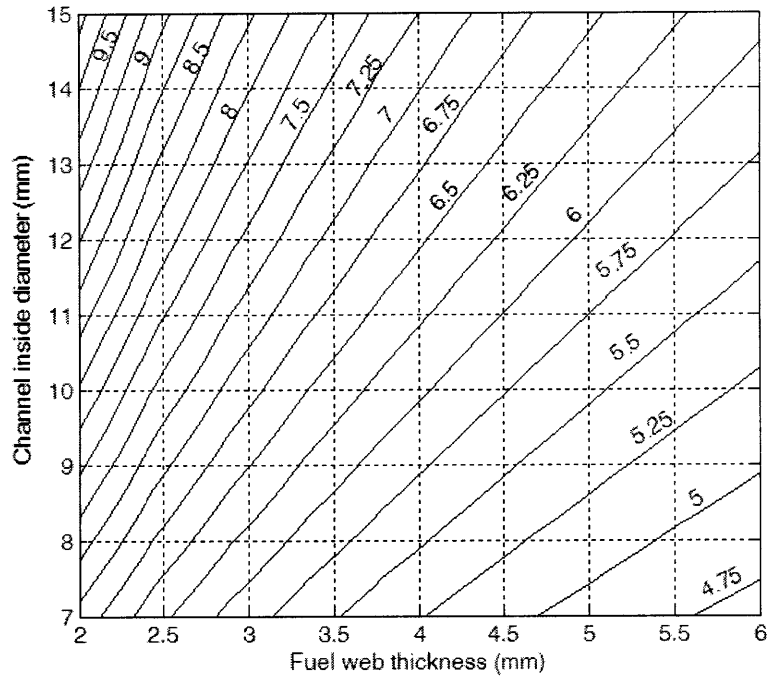


Figure IX- 5: H/HM ratio vs D_{ci} and t_{web} ($UTh_{0.5}Zr_{2.25}H_{5.625}$ unit cell calculation)

While, for a given inverted geometry, the operating H/HM is fixed, and can be found by applying Equation IX-1, the H/HM value with which it has to be compared, i.e. L_{HM} , depends on the soluble boron concentration, which varies during the life of the core. The concentration to be used to calculate L_{HM} is the critical boron concentration, B_{crit} , i.e. the concentration required, at any time during the cycle, to compensate for the reactivity excess and make the reactor critical. As mentioned in Section III.2.3.1, the higher this concentration the smaller is L_{HM} , and therefore the smaller is the margin from a positive VRC. Therefore, the verification of the sign of the VRC must be referred to the phase of the fuel cycle characterized by the maximum critical boron concentration, which is Beginning Of Cycle (BOC). The value of B_{crit} at BOC depends on the fuel composition (which is fixed for the IPWR), on the enrichment and on the burnable poison loading. Since these two last parameters are not fixed a priori, instead of optimizing them to calculate B_{crit} , it was decided to assume different soluble boron concentrations B , and, for each, to calculate L_{HM} . The resulting L_{HM} vs B trend is extremely useful since it allows

associating each inverted geometry, i.e. each operating H/HM, with a maximum allowed boron concentration, B_{max} . Once this concentration is known, the enrichment and the burnable poison loading can then be adjusted so that (1) the resulting B_{crit} is lower than B_{max} and (2) the constraints on maximum fuel enrichment and duct internal pressurization are met. The strategy used to determine the mentioned L_{HM} vs B trend is discussed in Section IX.1.2, while the method used to calculate the BOC critical boron concentration is described in Section IX.3. 4.

IX.1. 2 Effect of soluble boron concentration on maximum allowed H/HM

The effect of the soluble boron concentration, B , on the maximum allowed H/HM ratio, L_{HM} , was investigated using the MCNP4C code (LANL, 2000). This code was used to model inverted-, $UTh_{0.5}Zr_{2.25}H_{5.625}$ -fueled cells like that shown in Figure IX- 1, to determine the corresponding infinite multiplication factor, k_{∞} , as a function of the H/HM ratio. For each fuel cell geometry, H/HM was varied by changing the coolant density.

Since the analysis of the IPWR was not focused on a single fuel cell geometry, but spans different values of cooling channel diameter and fuel web thickness, it was decided to verify first whether L_{HM} is sensitive to the fuel cell geometry chosen for the MCNP model. To do this, four fuel cells having the same fuel composition ($UTh_{0.5}Zr_{2.25}H_{5.625}$, 10% enriched) and fuel web thickness (=2.5 mm) but different cooling channel inside diameter⁴, have been modeled, without and with soluble boron. For the boron-free case, the maximum of the k_{∞} vs H/HM curve was verified to be the same regardless of the cell geometry, as shown in Figure IX- 6. In particular, it can be seen that this maximum is associated with an H/HM value of about 14.5, which is therefore the value of L_{HM} for the boron-free scenario.

⁴ Because of the geometric relations presented in Section III.2.1.1, the four cells also differ in cladding thickness, fuel-clad gap and pitch.

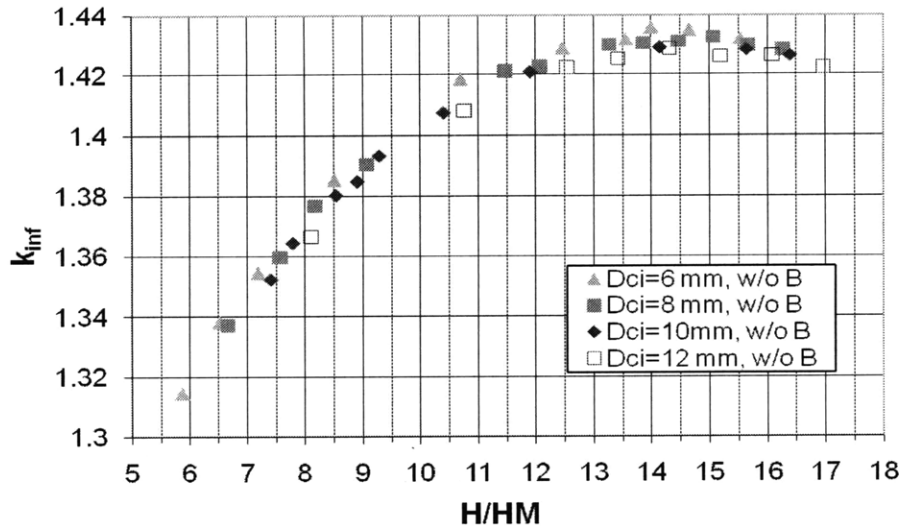


**Figure IX- 6: k_{∞} vs H/HM for 4 inverted cell geometries, with no soluble boron
($UTh_{0.5}Zr_{2.25}H_{5.625}$, 10% enriched)**

When boron is accounted for, the curve shifts to the left, i.e. L_{HM} decreases, and the degree of this reduction increases as the boron concentration increases. Like for the boron-free case, also when boron is modeled L_{HM} was demonstrated to be practically independent of the fuel cell geometry. This is shown in Figure IX- 7, which presents the k_{∞} vs H/HM curves corresponding to a natural boron concentration of 2000 ppm. With respect to Figure IX- 7, in this figure the curves are, vertically, more spaced from each other since the scale on the k_{∞} -axis is enlarged. The peaking of all the curves at an H/HM value of about 6.25 is evident. Analogous figures were obtained for boron concentrations equal to 1800, 1600, 1400, 1100, 800, 500 and 250 ppm. The values of L_{HM} corresponding to each concentration are plotted in Figure IX- 8.

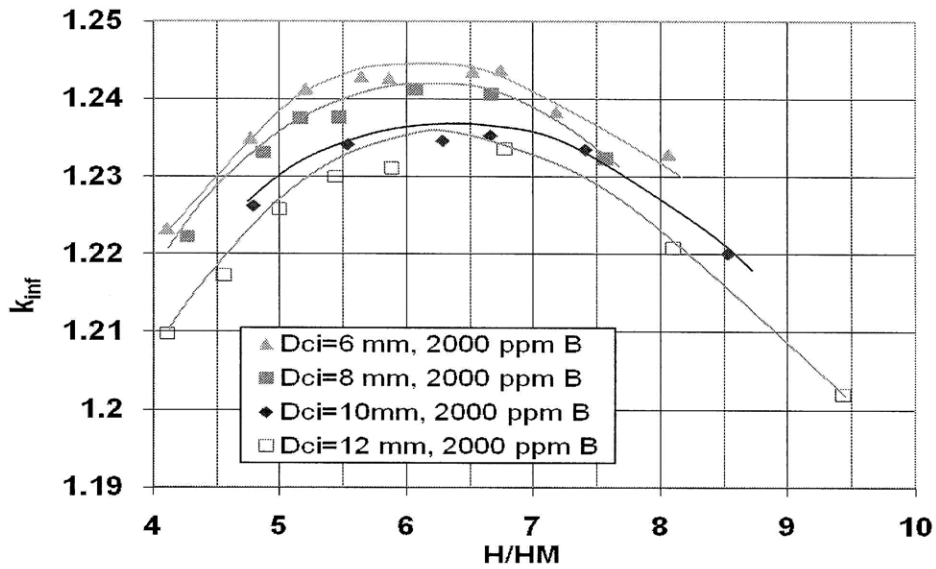


Figure IX- 7: k_{∞} vs H/HM for 4 inverted cell geometries, with 2000 ppm B

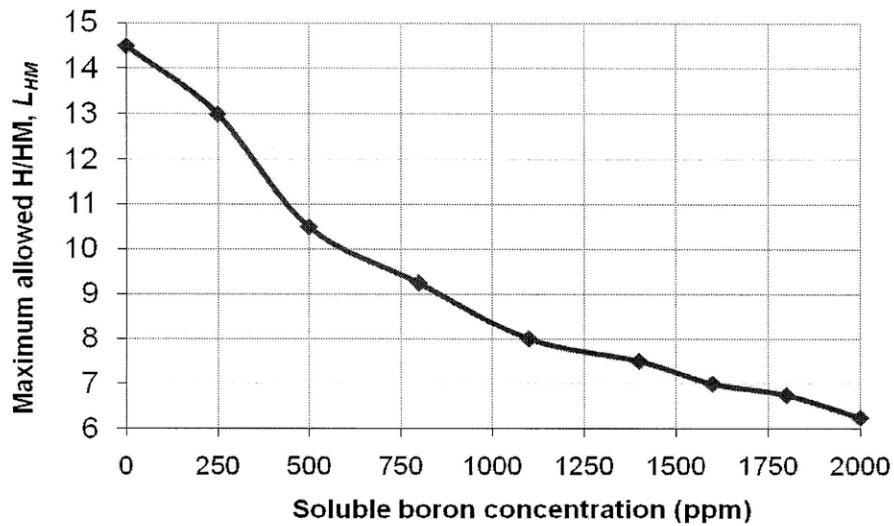


Figure IX- 8: Maximum allowed H/HM as a function of soluble boron concentration

The objective of the VRC analysis is to verify at what boron concentrations a certain inverted geometry, and therefore a certain operating H/HM, has a negative VRC. Therefore, for design purposes it is useful to invert the axes of Figure IX- 8, as done in Figure IX- 9, and interpret the H/HM not as a limit but as an operating value, and the

boron concentration not as an operating concentration, but as a maximum allowed value. In this way, given a certain inverted geometry, it is possible to calculate the maximum allowed boron concentration, beyond which the VRC would become positive.

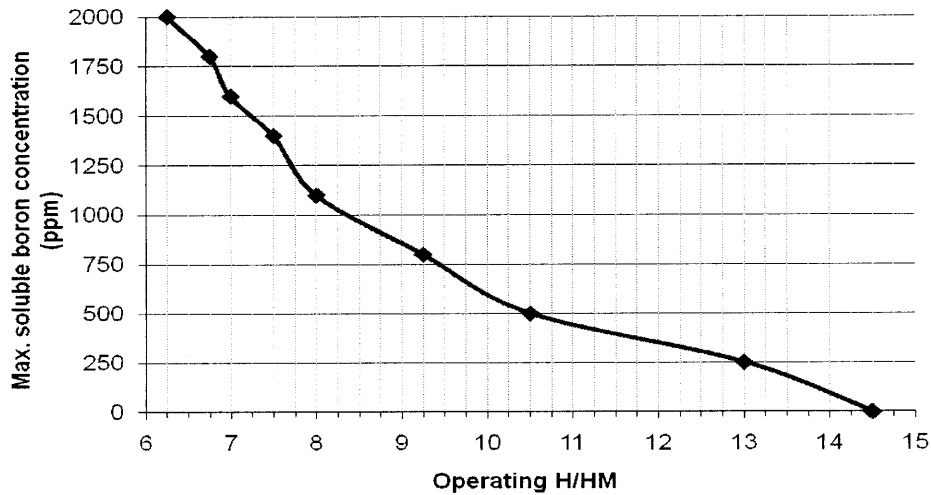


Figure IX- 9: Max. allowed soluble boron concentration as a function of operating H/HM

If the maximum allowed soluble boron concentration from Figure IX- 9 is applied to the H/HM map of Figure IX- 5, Figure IX- 10 is obtained. In obtaining this figure, H/HM ratios smaller than 6.25 which, per Figure IX- 9 would be associated with boron concentration above 2000 ppm, were instead associated with a maximum allowed value of 2000 ppm. This is because, as discussed in Section III.2.3.3, 2000 ppm was selected as the maximum allowed boron concentration to limit boron-induced corrosion and to avoid challenging the Chemical and Volume Control System capabilities. Figure IX- 10 is the key result of the analysis presented in this section, since it allows calculating, for each inverted geometry, the corresponding maximum soluble boron concentration. This parameter will also set the minimum amount of burnable poison (both IFBA and Er_2O_3 are considered) required to compensate the BOL reactivity excess. The latter will then need to be compared with other limits eventually imposed on burnable poison loading like, for example, the maximum IFBA loading to avoid excessive duct internal pressurization.

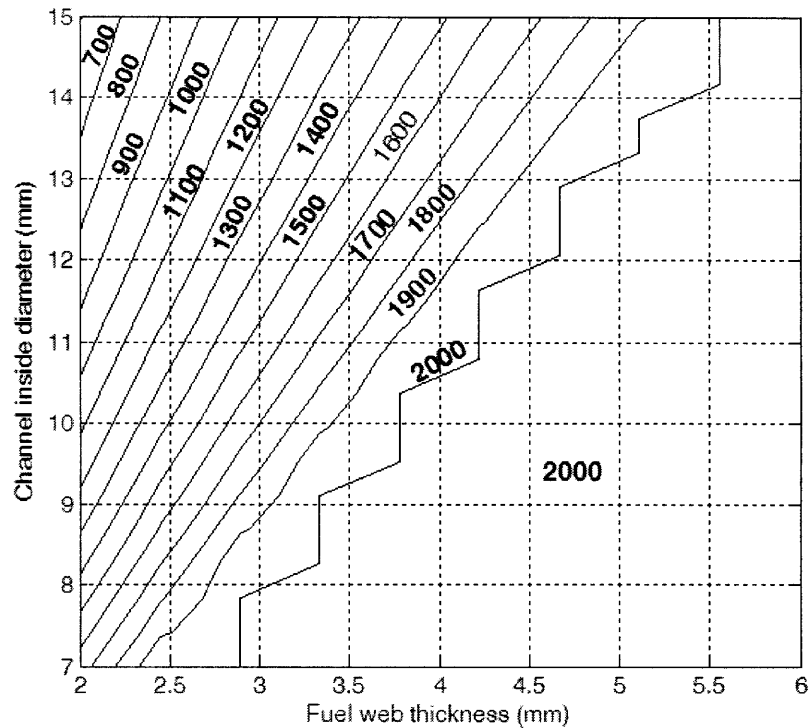


Figure IX- 10: Max. allowed soluble boron concentration as a function of D_{ci} and t_{web}

It is important to note that Figure IX- 10 was obtained with data referred to unpoisoned, 10% enriched inverted cells while, as discussed in Section IX. 3, the cycle length calculations that will make use of it are performed on poisoned cells having an enrichment not necessarily equal to 10%. This method is however conservative since:

- the burnable poisons examined for the IPWR either have negligible influence on the VRC (IFBA) or make it more negative (Er_2O_3 , since it is a resonant absorber);
- the final enrichment for the IPWR is larger than 10% (see Chapter XI). The higher the enrichment, the higher is L_{HM} and therefore the higher is the maximum allowed soluble boron concentration. This is evident from Figure IX- 11, which shows the shift of the curve maximum to higher H/HM values as the enrichment increases.

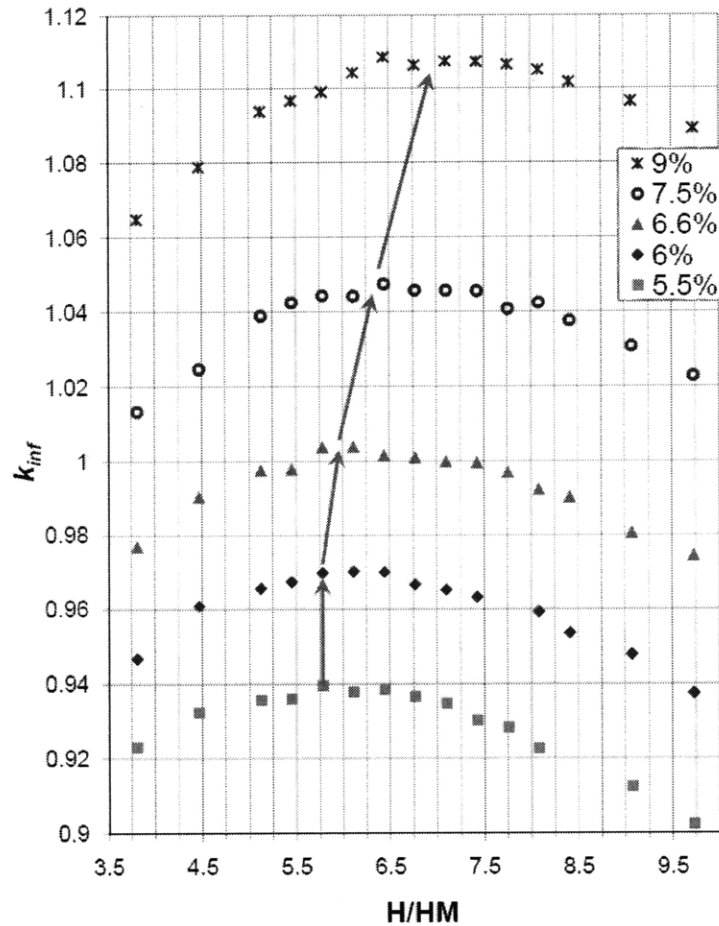


Figure IX- 11: Enrichment-induced L_{HM} shift to higher H/HM values
 ($UTh_{0.5}Zr_{2.25}H_{5.625}$, 1400 ppm B, IFBA = 0.3 mg $^{10}B/cm$)

IX. 2 FTRC sign

The IPWR is designed to have a negative fuel temperature reactivity coefficient (FTRC). This allows the reactor to respond, as the fuel temperature increases, with a reduction in power, which results in a reduction in temperature and consequent re-equilibrating effect. The FTRC is a property of the fuel, and for $UTh_{0.5}Zr_{2.25}H_{5.625}$ it is negative. This conclusion was not obtained within the IPWR project, but is contained in the work by Ganda and Greenspan (2010). They demonstrated that FTRC for $UTh_{0.5}Zr_{2.25}H_{5.625}$ is negative throughout the cycle, and it is more negative than that of UO_2 at Beginning Of

Life (BOL) (-5.9 vs -2 pcm/K) while it tends to be less negative at End Of Life⁵ (EOL) (-0.7 vs -3.2 pcm/K). The reason for this behavior is that, while for typical UO₂ fuel the FTRC is negative due to the resonance broadening effect only (Doppler effect), for hydride fuel another phenomenon has to be accounted for: neutron upscattering by hydrogen. In fact, in hydride fuels, temperature increase causes an enhancement of hydrogen atom vibration motions and, as consequence, instead of being slowed down by hydrogen, thermal neutrons can be actually accelerated, leading to a reduction in moderation and therefore in reactivity. This allows TRIGA reactors to be operated in pulsing mode. The evidence of hydrogen upscattering upon fuel temperature increase is shown in Figure IX- 12. This figure contains two plots: that on the left refers to typical UO₂ fuel, while that on the right to the most well known hydride fuel, i.e. U_{0.32}ZrH_{1.6}. The fact that hydrogen upscattering is associated with hydride fuels in general allows the conclusions that can be drawn from Figure IX- 12 to be applicable to the IPWR fuel as well, even though its composition differs from that of U_{0.32}ZrH_{1.6}. Each graph shows the variation in neutron flux (perturbed minus nominal), per unit of lethargy and normalized with respect to the total flux, resulting from a 100 K fuel temperature increase, as a function of neutron energy. The major⁶ difference between the two graphs is in the thermal region ($E_n \leq 1$ eV), where an increase in temperature does not cause any appreciable variation in normalized neutron flux for UO₂, while for U_{0.32}ZrH_{1.6} it causes a reduction in normalized flux below 0.1 eV and an increase between 0.1 and 1 eV. This is the evidence of neutron upscattering: neutrons with thermal energy (~0.025 eV) are upscattered by the enhanced hydrogen vibrations resulting from the temperature increase, leaving this part of the energy spectrum. As a consequence, the region below 0.1 eV becomes less neutron-rich, while the region between 0.1 and 1 eV becomes more neutron rich. Since, in the thermal region, the ²³⁵U fission cross section follows a $1/\sqrt{E_n}$ law, the

⁵ For UTh_{0.5}Zr_{2.25}H_{5.625} the burnup corresponding to EOL is ~90 MWD/kg_{HM} (Ganda, 2009).

⁶ The two graphs also differ in the fast region ($E_n \sim 1$ MeV), where UO₂ shows an increase in normalized flux, while U(45% w/o)ZrH_{1.6} a reduction. This is not caused by variations of the absolute fast neutron flux, since temperature changes do not affect this region of the spectrum. The reason is instead related to the flux normalization performed in constructing the graphs. Since the area subtended by the curve has to be unity, a reduction in epithermal flux will cause a reduction in the corresponding fraction of total flux, with consequent increase of the fraction, over all the neutrons, of fast neutrons. This happens for UO₂, since for this fuel the only significant consequence of a temperature increase is the enhancement of epithermal neutron resonance captures. For hydride fuel the thermal neutron upscattering dominates over the broadening of the resonances, and the normalized fast flux decreases.

spectral shift toward higher energies causes a reduction in fission cross section, and therefore a reduction in reactivity. This contributes to making the FTRC, which would already be negative because of the Doppler effect, even more negative in general.

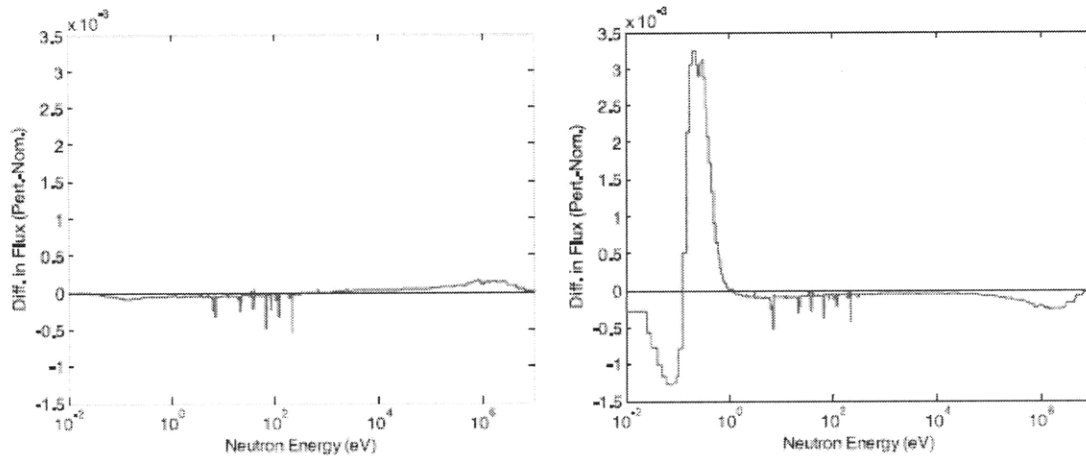
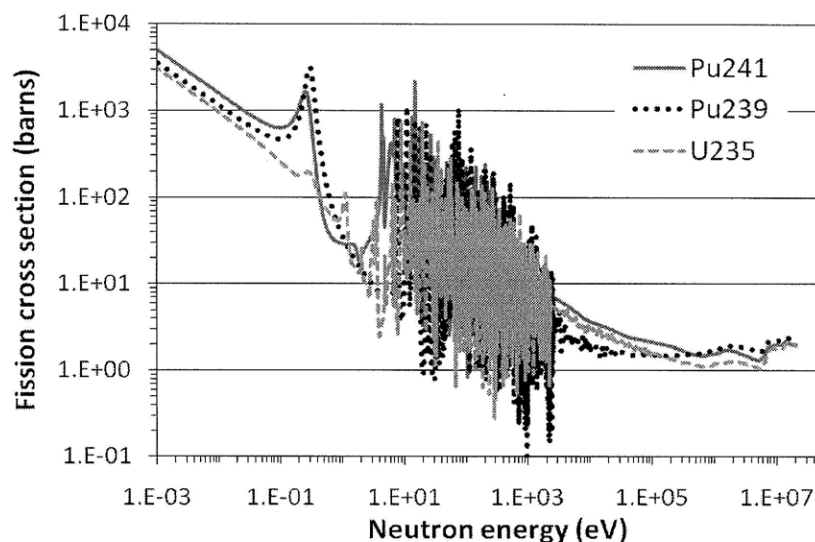


Figure IX- 12: BOL difference in the normalized neutron spectrum, per unit lethargy, in UO_2 -fueled (left plot) and $\text{U}_{0.32}\text{ZrH}_{1.6}$ -fueled (right plot) unit cells due to 100 K fuel temperature increase (Ganda and Greenspan, 2010)

As mentioned earlier, however, the FTRC for hydride fuels becomes less and less negative as the fuel burns. This is because, as explained by Ganda and Greenspan (2010), fuel burning causes Pu production and both ^{239}Pu and ^{241}Pu , unlike ^{235}U , have fission resonances at about 0.3 eV, i.e. in the region of the spectrum that is enriched in neutrons by hydrogen upscattering. This is shown in Figure IX- 13. Therefore, as fuel burns and fissile Pu isotopes build up, the FTRC becomes less and less negative due to the competition between the reduction in ^{235}U fissions and the increase in Pu fissions.



**Figure IX- 13: Fission cross section for ^{235}U , ^{239}Pu and ^{241}Pu vs neutron energy
(from KAERI, 2000)**

Besides Doppler and hydrogen-induced neutron upscattering, hydride fuels are characterized by an additional negative feedback on FTRC which, unlike those just mentioned, is not prompt but delayed: hydrogen release-induced negative feedback. In fact, if the fuel temperature increase is significant (above $\sim 750^\circ\text{C}$) and long-lasting, hydrogen is released from the fuel, moves in the fuel-clad gaps and collects in the assembly upper plenum, causing loss of moderation and thus power reduction. This effect, not included in the results by Ganda and Greenspan (2010), is an additional safety feature of hydride fuels.

IX. 3 Cycle length and enrichment

The IPWR core is designed to have a cycle length of about 18 months and an enrichment not higher than 20%. The constraint on cycle length is to limit plant downtime, and the value chosen is typical of US PWRs. The 20% limit on enrichment is motivated by the need of using Low Enriched Uranium (LEU) fuel, which is in fact defined as fuel with enrichment lower than 20%. This section discusses how these two constraints are calculated and imposed in the design of the IPWR.

IX.3. 1 Formula for the cycle length calculation

The cycle length, expressed in months, is calculated as:

$$T_c = \frac{BU_d \times M_{HM}}{\dot{Q}_{core} \times L \times n \times 30.42} \quad (IX-3)$$

where n , number of batches, and L , plant capacity factor, are constant in the analysis, equal to 3 and 0.9 respectively. The coefficient 30.42 is used to convert days into months.

The other three parameters, which instead vary, are defined as follows:

- M_{HM} (heavy metal mass in the core, kg): it is a function of the fuel composition, which is fixed, and of the core geometry, which is an analysis variable;
- \dot{Q}_{core} (maximum attainable steady-state core thermal power, MW): once the power-limiting constraints are established, it is a function of the core geometry;
- BU_d (reactivity-limited discharge burnup, MWD/kg_{HM}): since fuel element composition is fixed, it only depends on its enrichment and on core power.

IX.3. 2 Method of application of cycle length and enrichment constraints

Unlike thermal hydraulic constraints, cycle length and enrichment constraints are not applied here to all the geometries, i.e. to all the D_{ci} - t_{web} combinations, since an automatic methodology able to scan all of them, simultaneously optimizing their burnable poison loading and soluble boron concentration, was not developed. Instead, cycle length and enrichment constraints are only applied to the geometries that (1) based on the thermal hydraulic analysis, have the best power performance and (2) have a negative void reactivity coefficient.

Given a core geometry, and therefore a value for M_{HM} , the constraint on cycle length is applied once the value of \dot{Q}_{core} corresponding to that geometry is known. Based on Eq. IX-3, the only parameter missing for predicting the cycle length is the reactivity-limited discharge burnup⁷. Its calculation is performed iteratively: increasing values for the

⁷ Because of lack of experimental data on irradiated UTh_{0.5}Zr_{2.25}H_{5.625}, an exact calculation of the fuel performance-limited burnup was not performed. The relations for irradiation-induced fuel swelling (Lillie et al., 1973) and fission gas release (Langer and Baldwin, 1971) introduced in Chapter II were developed using U-ZrH_{1.6} fuel specimens irradiated up to about 200 MWD/kg_{HM}. The fuel performance-limited burnup for UTh_{0.5}Zr_{2.25}H_{5.625} is however smaller than this value, since the heavy metal loading of this fuel,

enrichment are tested, and for each a combination of IFBA (or Er_2O_3) loading and soluble boron concentration leading to a negative VRC is used. A depletion analysis (see Section IX.3. 3) of the fuel cell derived from the combination of these three parameters (enrichment, burnable poison loading and B concentration) is performed and the discharge burnup is calculated. The introduction of this burnup into Eq. IX-3 allows determining T_c , which is then compared to the imposed limit: if $T_c \sim 18$ months the procedure stops, while if it is smaller or larger the enrichment is, respectively, increased or decreased until the 18 month constraint is matched. In case the enrichment required to meet the fuel cycle constraint is above 20%, it is set to 20% and the geometry under investigation is recorded as not able to provide the maximum achievable power and meet the cycle length constraint simultaneously.

IX.3. 3 Depletion analysis of an inverted cell

Single cell depletion analyses using⁸ CASMO-4 (Edenius et al., 1995) are performed to determine the reactivity-limited discharge burnup to enter in Eq. IX-3 and thus to obtain the cycle length. The output of each of these analyses is a single-batch k_∞ vs burnup plot, in which the discharge burnup, BU_{dl} , is identified as the burnup value corresponding to $k_\infty=1.03$. A Δk_∞ equal to 0.03, which is typical for LWRs, is used to account for leakages, since the calculated multiplication factor refers to an infinite system. The actual discharge burnup, which accounts for the fact that the core is not composed of single batch, but has n batches, is calculated using the linear reactivity model (Driscoll et al., 1990), supplemented with a 1/R CASMO-to-MCODE correction factor explained later in this section:

$$BU_d = \left(\frac{2n}{n+1} BU_{dl} \right) \frac{1}{R} \quad (\text{IX-4})$$

which typically enhances swelling and fission gas release, is larger than that of $\text{U-ZrH}_{1.6}$. Irradiation tests, never performed for $\text{UTh}_{0.5}\text{Zr}_{2.25}\text{H}_{5.625}$, would be needed to calculate the corresponding value.

⁸ For simplicity, CASMO-4 will be referred to as CASMO in the rest of this chapter.

Since, for the IPWR, the number of batches is 3, Eq. IX-4 becomes:

$$BU_d = (1.5 \times BU_{d1}) \frac{1}{R} \quad (\text{IX-5})$$

which is the formula used for the calculation of the discharge burnup to enter into Eq. IX-3. The 1/R correction factor was used to account for the error in predicting the single-batch discharge burnup, derived from the use of a neutronic code, i.e. CASMO, that is not suited for inverted geometry modeling. In fact, although CASMO was developed to analyze solid pin geometries only, it was used for the IPWR design to take advantage of the very short computational time it requires for a complete depletion analysis (order of tens of seconds). In principle, depletion of inverted configurations could have been analyzed with MCODE, a linkage program developed at MIT that couples MCNP4C and ORIGEN22 (Xu and Hejzlar, 2008). The computational time required by MCODE is however hundreds of times larger than that of CASMO, which makes its use unpractical when multiple geometries need to be analyzed. For this reason it was decided to use CASMO using a solid-pin-geometry that is neutronicly equivalent to the inverted geometry. In this context, “neutronicly equivalent” means that it has the same, or roughly the same, k_∞ vs burnup curve as the inverted geometry from which it was constructed, particularly the same BU_{d1} . The conversion of each inverted cell into the inverted-equivalent solid pin cell was based on the conservation of three parameters:

- hydrogen to heavy metal ratio (H/HM);
- fuel surface to volume ratio (S/V);
- ^{10}B (in IFBA) or Er (in Er_2O_3) to ^{235}U atom ratio

while no fuel composition change was needed. The verification of the match between the k_∞ vs burnup curves was performed by benchmarking CASMO against MCODE, for a single inverted cell geometry. The results of this benchmark, as well as details on the inverted-to-pin conversion method, are presented in Appendix A of this chapter.

IX.3. 4 Critical boron concentration at BOC

As discussed in Section IX.1.2 the determination of the sign of the Void Reactivity Coefficient (VRC) requires knowledge of the concentration of soluble boron in the primary coolant. In particular, since the higher this concentration the less negative is VRC, for design purposes it is important to be able to calculate the maximum concentration expected during the fuel cycle, i.e. the critical boron concentration at Beginning Of Cycle (BOC). This calculation can be performed only once the inverted assembly geometry, as well as a value for the burnable poison loading, are known⁹. The method, which is based on the application of the linear reactivity model (Driscoll et al., 1990), consists of two phases: first the BOC core average multiplication factor and burnup are determined, and then the critical boron concentration corresponding to these core-average values is calculated. The first phase consists of calculating the BOC core average k_{∞} as arithmetic average of the three BOC k_{∞} values corresponding to the three batches. This is performed in four steps, which are listed below and graphically represented in Figure IX- 14:

- depletion analysis, performed with CASMO, of the (poisoned) pin geometry assembly neutronically equivalent to the inverted assembly of interest, and generation of a k_{∞} vs burnup table;
- calculation of the discharge burnup, BU_d , using Eq. IX-5 (for the example presented in Figure IX- 14 it is assumed this calculation gives $BU_d=BU_{90}$);
- calculation of the burnup evolution corresponding to each fuel batch, performed by dividing the k_{∞} vs burnup table, up to BU_d , in three blocks, each characterized by the same burnup increment;
- placement of the three blocks side to side (see Figure IX- 14) and calculation of core average values by averaging k_{∞} and burnup values of each row: the first pair of average values correspond to the searched BOC conditions.

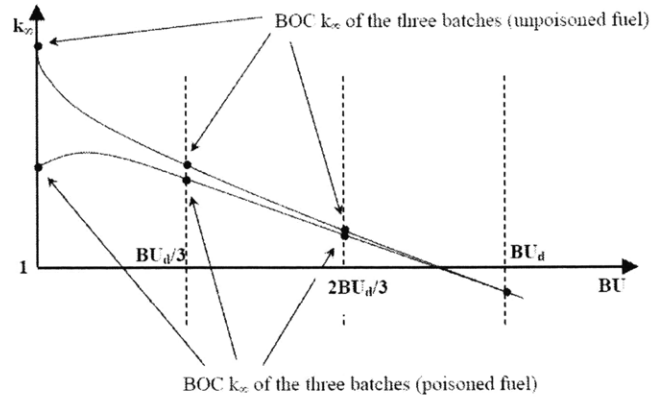
⁹ Different burnable poison loadings needed to be tested, until the corresponding BOC critical boron concentration decreases below the value shown in Figure IX- 10 and corresponding to the inverted geometry of interest. This procedure was followed only after identifying the most promising IPWR design, and it is therefore described in Chapter XI.

Once the BOC core average k_{∞} is calculated, the burnup corresponding to this value in the original k_{∞} vs burnup table is identified. Branch calculations, at this value of burnup, are then performed with CASMO, assuming different soluble boron concentrations. The concentration that leads to $k_{\infty} = 1.03$ is the BOC critical boron concentration.

It must be stressed that the procedure to determine the BOC critical boron concentration uses the following approximations:

- although the linear reactivity model (Driscoll et al., 1990), uses the reactivity as base parameter to associate with each batch, in this study the multiplication factor is instead used;
- the three fuel batches are assumed to have the same power.

Depletion step	k_{∞} value	Burnup value
1	$k_{\infty 1}$	BU ₁
2	$k_{\infty 2}$	BU ₂
3	$k_{\infty 3}$	BU ₃
...
30	$k_{\infty 30}$	BU ₃₀
31	$k_{\infty 31}$	BU ₃₁
32	$k_{\infty 32}$	BU ₃₂
33	$k_{\infty 33}$	BU ₃₃
...
60	$k_{\infty 60}$	BU ₆₀
61	$k_{\infty 61}$	BU ₆₁
62	$k_{\infty 62}$	BU ₆₂
63	$k_{\infty 63}$	BU ₆₃
...
90	$k_{\infty 90}$	BU ₉₀ (=BU _d)
91	$k_{\infty 91}$	BU ₉₁
92	$k_{\infty 92}$	BU ₉₂
...



First batch			Second batch			Third batch			Core average values	
Dep. step	k_{∞} value	Burnup value	Dep. step	k_{∞} value	Burnup value	Dep. step	k_{∞} value	Burnup value	Average k_{∞}	Average burnup
1	$k_{\infty 1}$	BU ₁	31	$k_{\infty 31}$	BU ₃₁	61	$k_{\infty 61}$	BU ₆₁	<i>Average($k_{\infty 1}, k_{\infty 31}, k_{\infty 61}$)</i>	<i>Average(BU_{1}, BU_{31}, BU_{61}})}}</i>
2	$k_{\infty 2}$	BU ₂	32	$k_{\infty 32}$	BU ₃₂	62	$k_{\infty 62}$	BU ₆₂	<i>Average($k_{\infty 2}, k_{\infty 32}, k_{\infty 62}$)</i>	<i>Average(BU_{2}, BU_{32}, BU_{62}})}}</i>
3	$k_{\infty 3}$	BU ₃	33	$k_{\infty 33}$	BU ₃₃	63	$k_{\infty 63}$	BU ₆₃	<i>Average($k_{\infty 3}, k_{\infty 33}, k_{\infty 63}$)</i>	<i>Average(BU_{3}, BU_{33}, BU_{63}})}}</i>
...
30	$k_{\infty 30}$	BU ₃₀	60	$k_{\infty 60}$	BU ₆₀	90	$k_{\infty 90}$	BU ₉₀ (=BU _d)	<i>Average($k_{\infty 30}, k_{\infty 60}, k_{\infty 90}$)</i>	<i>Average(BU_{30}, BU_{60}, BU_{90}})}}</i>

Figure IX- 14: Schematic of the method used to determine BOC core average k_{∞} and burnup (grey cells correspond to BOC values)

IX. 4 Considerations on shutdown margin

In any reactor, control rods must be designed as to be able to guarantee subcriticality, with some margin, at any time during the life of the reactor. This margin, referred to as shutdown margin, must be guaranteed in the worst case scenario of the most reactive control rod stuck in withdrawn position while the reactor experiences sudden transition from Hot Full Power (HFP) to Cold Zero Power (CZP). A precise control rod design would require a whole core analysis that, for the IPWR, was not performed. A partial indication of the control rod worth required to guarantee a certain shutdown margin can be obtained by comparing the reactivity variation resulting from the HFP to CZP transition in the IPWR to that characterizing a typical pin geometry PWR. The CASMO neutronic code (Edenius, 1995) was used for this purpose. Since, as discussed in Section IX.3. 3, this code cannot model inverted geometries, the geometric characteristics of the inverted assembly of interest will be used to generate a neutronic equivalent pin geometry assembly, using the methodology developed and tested in Appendix A of this chapter. CASMO will then be used to calculate the HFP-to-CZP reactivity insertion characterizing this assembly, which will be compared to that of the reference PWR assembly and conclusions will be drawn.

All scenarios (CZP, HZP, HFP) were analyzed at Beginning of Life (BOL) and at End Of Life (EOL), with All Rods Out (ARO) and no soluble boron in the coolant. In spite of not being realistic for BOL, this latter assumption was made since this analysis is only aimed at comparing the neutronic behavior of the two assembly designs upon changes in reactor temperature conditions. Table IX- 1 shows the temperature assumed for the various conditions.

	HFP		HZP		CZP	
	Fuel	Coolant	Fuel	Coolant	Fuel	Coolant
Reference core assembly	627	310	310	310	25	25
Inverted-equivalent assembly	500	310	310	310	25	25

Results of the HFP-CZP reactivity insertion analysis are presented in Chapter XI. This is because the calculation requires knowledge of the assembly geometry, which will be identified only after all the design constraints have been applied.

Appendix IX-A: CASMO-MCODE benchmark

This Appendix presents the benchmark performed between CASMO-4 (Edenius et al., 1995) and MCODE (Xu and Hejzlar, 2008)¹⁰. This benchmark was necessary to verify whether CASMO, which is computationally very fast but can only model solid-pin geometries, can actually be used in place of MCODE, which can model any geometry but is computationally very intensive.

IX-A. 1 Analysis methodology: the inverted-pin equivalence

For pin geometries, depletion calculations are typically performed with codes such as CASMO which, for an assembly, requires a relatively short computational time (order of tens of seconds). However, CASMO was developed for solid pin-geometries only, and cannot handle inverted configurations. Depletion for these configurations could, in principle, be analyzed with MCODE, a linkage program developed at MIT that couples MCNP4C and ORIGEN22. The computational time required by MCODE is however hundreds of times larger than that of CASMO, which makes its use unpractical for the IPWR, since several geometries needed to be analyzed. For this reason it was decided to use CASMO, using an input that, however, models a solid-pin-geometry that is equivalent to the inverted geometry. A solid-pin-geometry is defined “equivalent” to an inverted geometry when its depletion, performed with CASMO, closely reproduces the depletion, performed with MCODE, of the inverted geometry. Once the method through which an inverted geometry can be converted into its equivalent pin geometry is known, it can be applied to any inverted geometry, i.e. to any D_{ci} - t_{web} combination, and the resulting equivalent pin geometries can be analyzed with CASMO. This strategy was successfully applied to the neutronic analysis of another non-solid-pin geometry of interest, i.e. annular fuel, and was found to be successful (Kazimi et al., 2006).

For a complete understanding of the rationale behind the conversion of an inverted geometry into the equivalent pin geometry, which is discussed below, it is important to first mention that two burnable poisons were examined for the IPWR: IFBA (Integral Fuel Burnable Poison), in the form of a thin layer of ZrB_2 applied to the inner surface of the fuel holes, and Er_2O_3 uniformly dispersed in the fuel. For simplicity, and because of

¹⁰ For simplicity, CASMO-4 will be referred to as CASMO in the rest of this Appendix.

the small width of the gap separating the fuel from the cladding, both in CASMO and in MCODE, IFBA is modeled as ZrB_2 uniformly distributed in such a gap, rather than segregated in an even thinner layer on the fuel surface.

IX-A.1. 1 Rationale behind the pin-inverted cell equivalence

The rationale behind the conversion of an inverted geometry into the equivalent pin geometry is the conservation of three parameters:

- hydrogen to heavy metal ratio (H/HM);
- fuel surface to volume ratio (S/V);
- ^{10}B (in IFBA) or Er (in Er_2O_3) to ^{235}U atom ratio.

The H/HM ratio is representative of the extent of moderation characterizing the lattice, and plays a key role in determining the sign of the void reactivity coefficient.

The fuel surface to volume ratio is representative of the resonance absorptions which, in fuel types like UO_2 , are responsible for the so-called self-shielding effect. In hydride-fueled geometries this effect is not localized on the fuel periphery, but is more uniformly distributed in the fuel due to the fact that neutrons start to slow down in the fuel, thus increasing ^{238}U resonance absorptions. An indication of the less important role played by self-shielding in hydride fuels can be inferred, as discussed in Section IX.1.1, from the significant contribution of the fuel to the total moderation which, for the geometries of interest, is of about 50% (see Figure IX- 2). The resonance absorptions responsible for the self-shielding effect, regardless of its degree, occur both in pin and in inverted geometry, but their extent could be different depending on the fuel surface to volume ratio characterizing the two configurations.

The third criterion mentioned above, i.e. the equivalence of the ^{10}B (or Er) to ^{235}U atom ratio, is applied to preserve the extent of neutron absorptions, by burnable poisons, relative to the amount of fissile material. This criterion allows calculating the number density of the IFBA components, mainly ^{10}B , to be used in the inverted-equivalent pin cell. In fact, because of the segregation of the ZrB_2 in the fuel-clad gap, and because of the difference between the diameter of the hole in the inverted cell and the diameter of the pellet in the pin geometry, the use of the same ^{10}B atom density in the two cells would

lead to different ^{10}B -to- ^{235}U atom ratios. When Er_2O_3 is used as burnable poison, this criterion is automatically satisfied since it is uniformly dispersed in the fuel.

IX-A.1. 2 Construction of the inverted-equivalent pin cell

Figure IX-A. 1, which shows an inverted geometry (on the left) and the equivalent pin geometry (on the right), helps to understand how the inverted-equivalent pin geometry is constructed. For a fuel with generic stoichiometry $\text{UTh}_t\text{Zr}_z\text{H}_h$, the relations between the H/HM and S/V ratios used for the conversion of the inverted geometry to the equivalent pin geometry and the key geometric parameters are as follows:

$$\left(\frac{S}{V}\right)_I = \left(\frac{\text{fuel surface}}{\text{fuel volume}}\right)_I = \left(\frac{\frac{1}{2}\pi D_f}{\frac{\sqrt{3}}{4}P^2 - \frac{\pi}{8}D_f^2}\right)_I = \frac{4\pi D_{f,I}}{2\sqrt{3}P_I^2 - \pi D_{f,I}^2} \quad (\text{IX-A-1})$$

$$\left(\frac{S}{V}\right)_P = \left(\frac{\text{fuel surface}}{\text{fuel volume}}\right)_P = \left(\frac{\frac{1}{2}\pi D_f}{\frac{\pi}{8}D_f^2}\right)_P = \frac{4}{D_{f,P}} \quad (\text{IX-A-2})$$

$$\left(\frac{H}{HM}\right)_I = \frac{\frac{\pi}{8}D_{c,I}^2\rho_c\frac{2}{M_c} + \left(\frac{\sqrt{3}}{4}P_I^2 - \frac{\pi}{8}D_{f,I}^2\right)\frac{\rho_f}{M_f}h}{\left(\frac{\sqrt{3}}{4}P_I^2 - \frac{\pi}{8}D_{f,I}^2\right)\frac{\rho_f}{M_f}m} \quad (\text{IX-A-3})$$

$$\left(\frac{H}{HM}\right)_P = \frac{\left(\frac{\sqrt{3}}{4}P_P^2 - \frac{\pi}{8}D_{c,P}^2\right)\rho_c\frac{2}{M_c} + \frac{\pi}{8}D_{f,P}^2\frac{\rho_f}{M_f}h}{\frac{\pi}{8}D_{f,P}^2\frac{\rho_f}{M_f}m} \quad (\text{IX-A-4})$$

where, besides the nomenclature already shown in Figure IX-A. 1, ρ_c and ρ_f are the coolant and fuel densities (kg/m^3), M_c is the water molecular weight (kg/mol), while M_f , h and m are parameters chosen consistently with the stoichiometry of the fuel, i.e. $\text{UTh}_t\text{Zr}_z\text{H}_h$: M_f is the fuel molecular weight (kg/mol), h is the hydrogen stoichiometry index in the fuel while m is the heavy metal stoichiometric index ($m=1+t$). It can be easily verified that, once the inverted cell geometry has been fixed, the fuel pellet diameter in the pin geometry follows from Eq. IX-A-2, while the pin pitch follows from Eq. IX-A-1. The two geometric parameters remaining to uniquely identify the pin geometry, i.e. the

thicknesses of the fuel-clad gap and of the cladding, are obtained from $D_{f,p}$ by virtue of the relations discussed in Section III.2.1.1. This completes the construction of the inverted-equivalent pin geometry for the case of Er_2O_3 used as burnable poison. However, when IFBA is instead used, a third criterion must be applied. In fact, the geometric relations used to determine clad and gap thickness for the pin geometry do not come from neutronic considerations: hence if the ^{10}B loading in the fuel-to-clad gap of the pin geometry was set to the same value as that in the fuel-to-clad gap of the inverted geometry, different ^{10}B to ^{235}U atom ratios in the two configurations would be obtained. To avoid this, the mentioned geometric relations are still applied, but when IFBA is examined as burnable poison the ^{10}B atom density in the fuel-clad gap of the pin cell is varied in such a way that the ^{10}B to ^{235}U atom ratio in the pin cell is the same as that in the inverted cell. It can be easily demonstrated that the ^{10}B atom density in the pellet-clad gap of the pin cell that satisfies this requirement is:

$$(N_{B10})_p = (N_{B10})_i \left(\frac{D_f^2 - D_{co}^2}{\frac{2\sqrt{3}}{\pi} P^2 - D_f^2} \right)_i \frac{1}{\left(\frac{D_{cl}}{D_f} \right)_p^2 - 1} \quad (\text{IX-A-5})$$

where $(N_{B10})_i$ is the ^{10}B atom density in the fuel-clad gap of the inverted geometry. The application of Eq. IX-A-5 concludes the construction of the inverted-equivalent pin geometry.

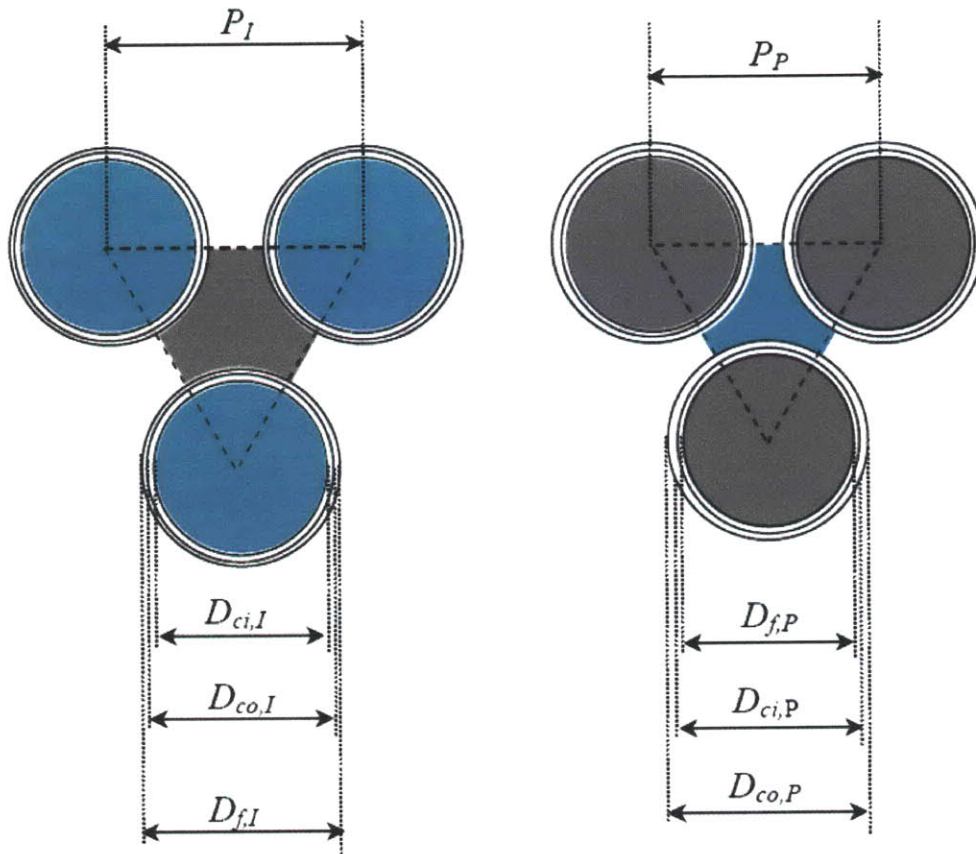


Figure IX-A. 1 – Example of inverted cell (left) and its equivalent pin cell (right)

IX-A. 2 Benchmark between MCODE and CASMO

IX-A.2. 1 Cases analyzed and parameters compared

Three benchmarks have been performed, all referred to the inverted cell with geometry:

$$D_{ci} = 10 \text{ mm};$$

$$D_{co} = 11.271 \text{ mm};$$

$$D_f = 11.615 \text{ mm};$$

$$P = 14.600 \text{ mm}$$

The first benchmark, referred to as Case 1, refers to unpoisoned fuel; the second benchmark, Case 2, to the scenario of IFBA-provided fuel¹¹ (0.513 mg ¹⁰B/cm); the third benchmark, Case 3, to fuel containing 1.7% w/o of Er₂O₃. In all three cases the fuel is UTh_{0.5}Zr_{2.25}Hf_{5.625} 17.5% enriched.

¹¹ Non-enriched IFBA is assumed for this analysis.

The objective of the MCODE-CASMO benchmark is to compare the evolution, with burnup, of the infinite multiplication factor and of the atom density of the major nuclides: ^{232}Th , ^{233}U , ^{234}U , ^{235}U , ^{236}U , ^{238}U , ^{239}Pu , ^{240}Pu , ^{241}Pu and, when applicable, ^{10}B or ^{167}Er .

IX-A.2. 2 Results

Results are presented in the form of plots comparing the variations, with burnup, of:

- infinite multiplication factor (Figure IX-A. 2 through Figure IX-A. 3);
- atom density of major nuclides (Figure IX-A. 5 through Figure IX-A. 10)

obtained with CASMO with those obtained with MCODE. The plots also show, on the secondary y-axis, the error percentage of CASMO relative to MCODE.

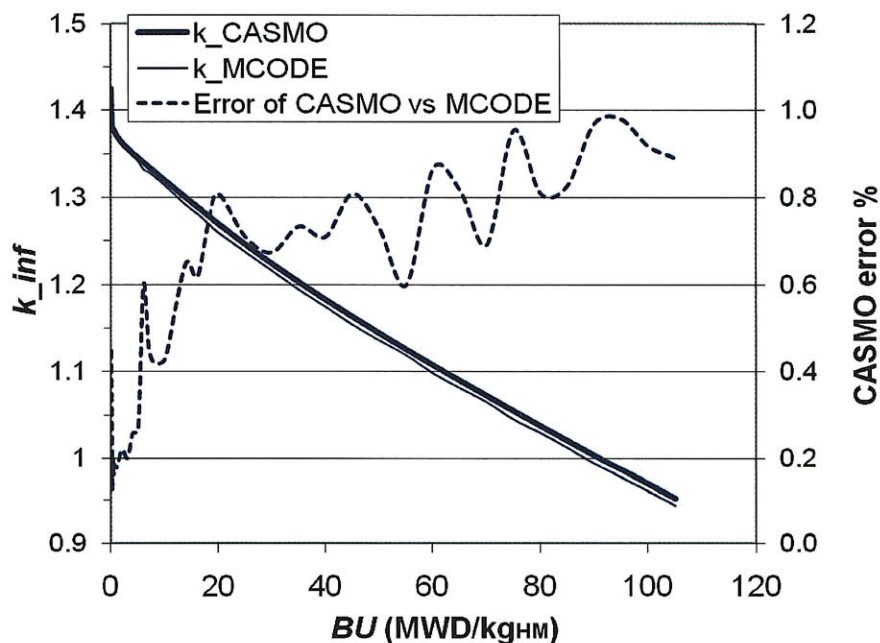
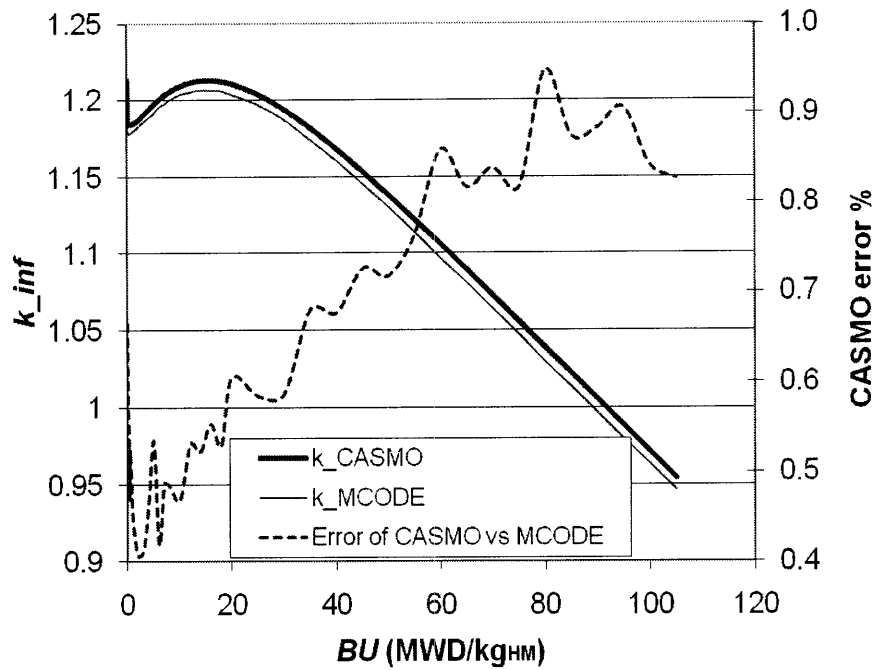
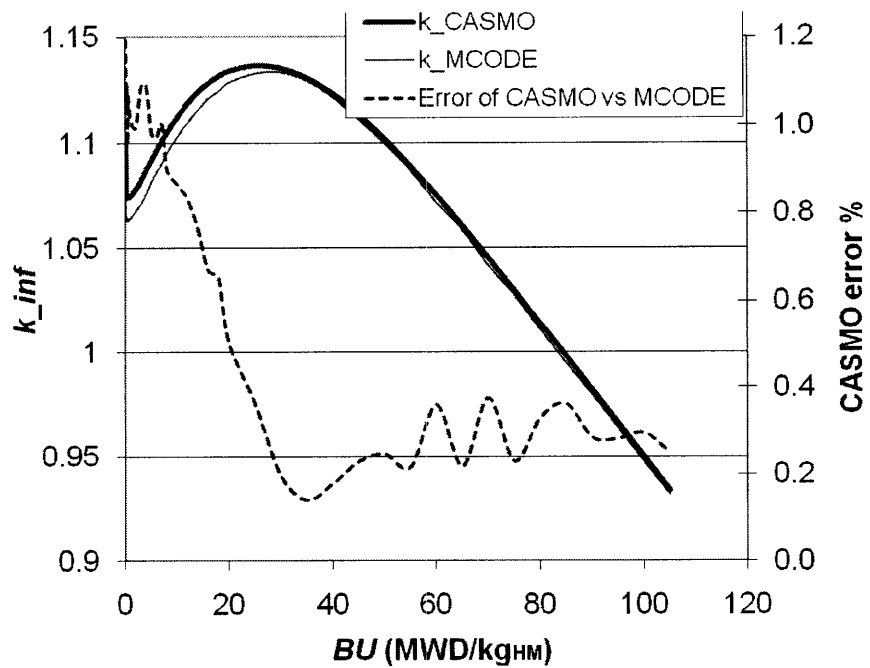


Figure IX-A. 2 – Multiplication factor vs burnup: comparison CASMO-MCODE (unpoisoned cell)



**Figure IX-A. 3 – Multiplication factor vs burnup: comparison CASMO-MCODE
(IFBA-provided cell)**



**Figure IX-A. 4 – Multiplication factor vs burnup: comparison CASMO-MCODE
(Er_2O_3 -containing fuel)**

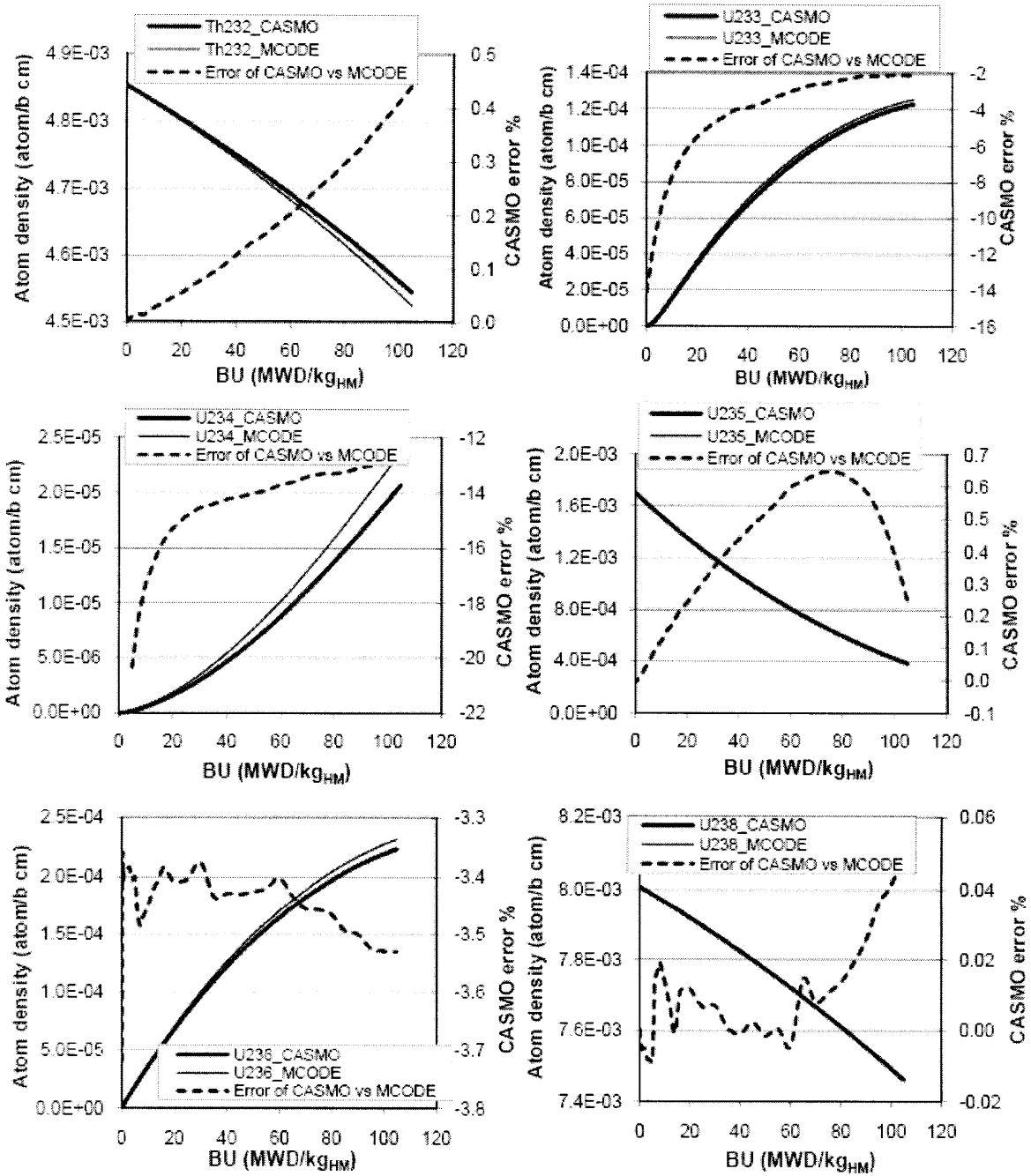


**Figure IX-A. 5 – Atom density variation with burnup for major nuclides:
comparison CASMO-MCODE (unpoisoned cell)**

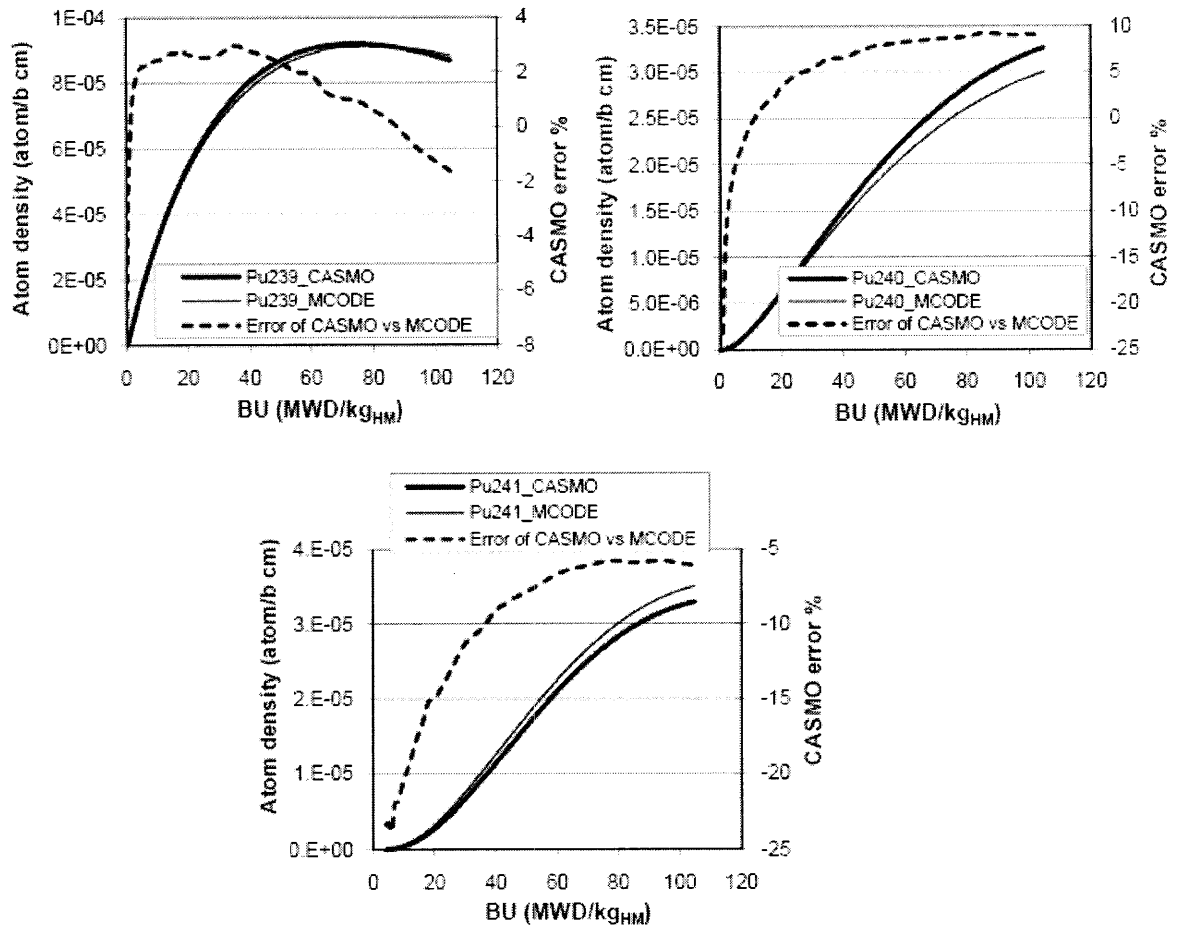


**Figure IX-A. 6 – Atom density variation with burnup for major nuclides:
comparison CASMO-MCODE (unpoisoned cell)**

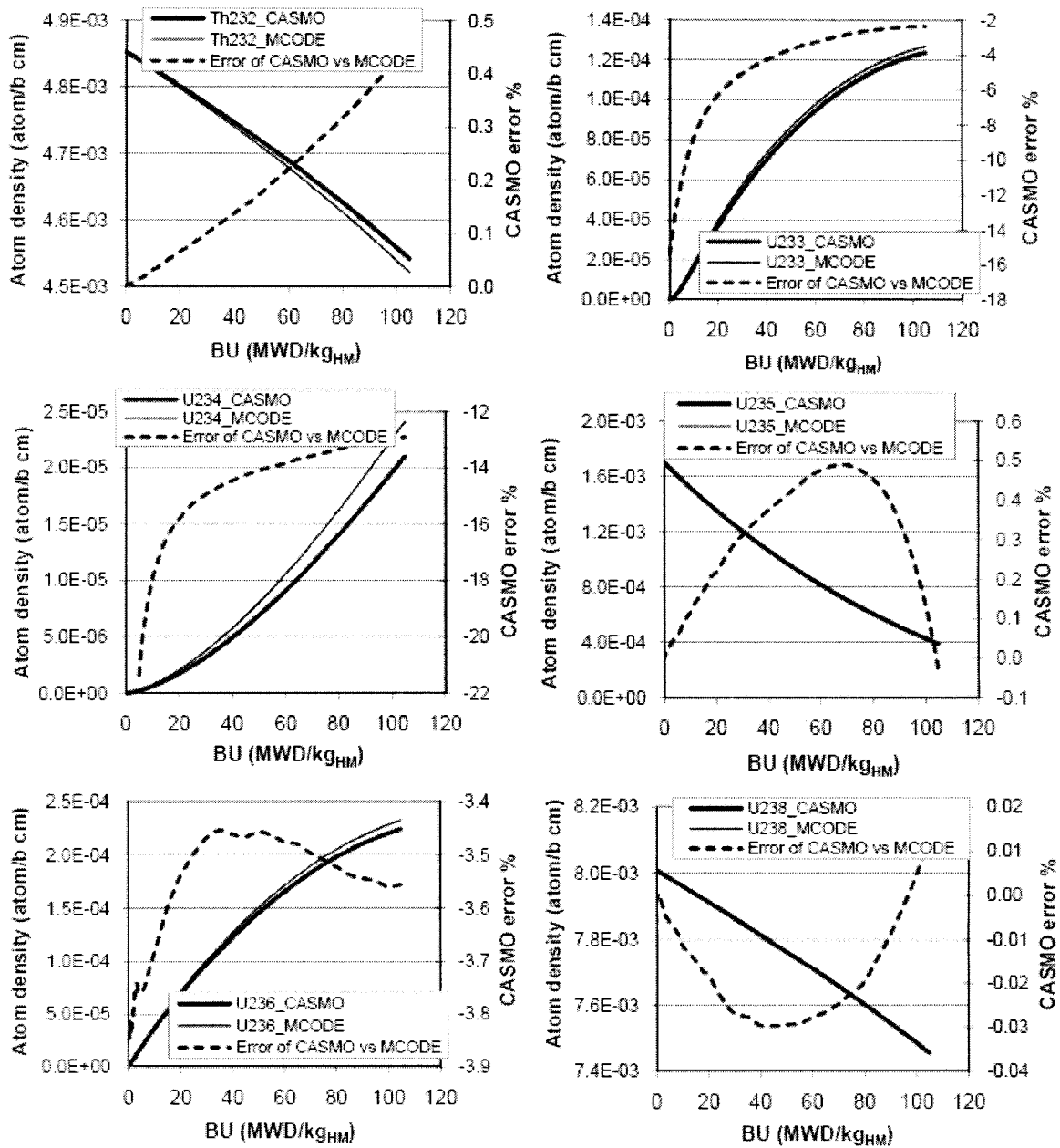


Figure IX-A. 7 – Atom density variation with burnup for major nuclides: comparison CASMO-MCODE (IFBA-provided cell)

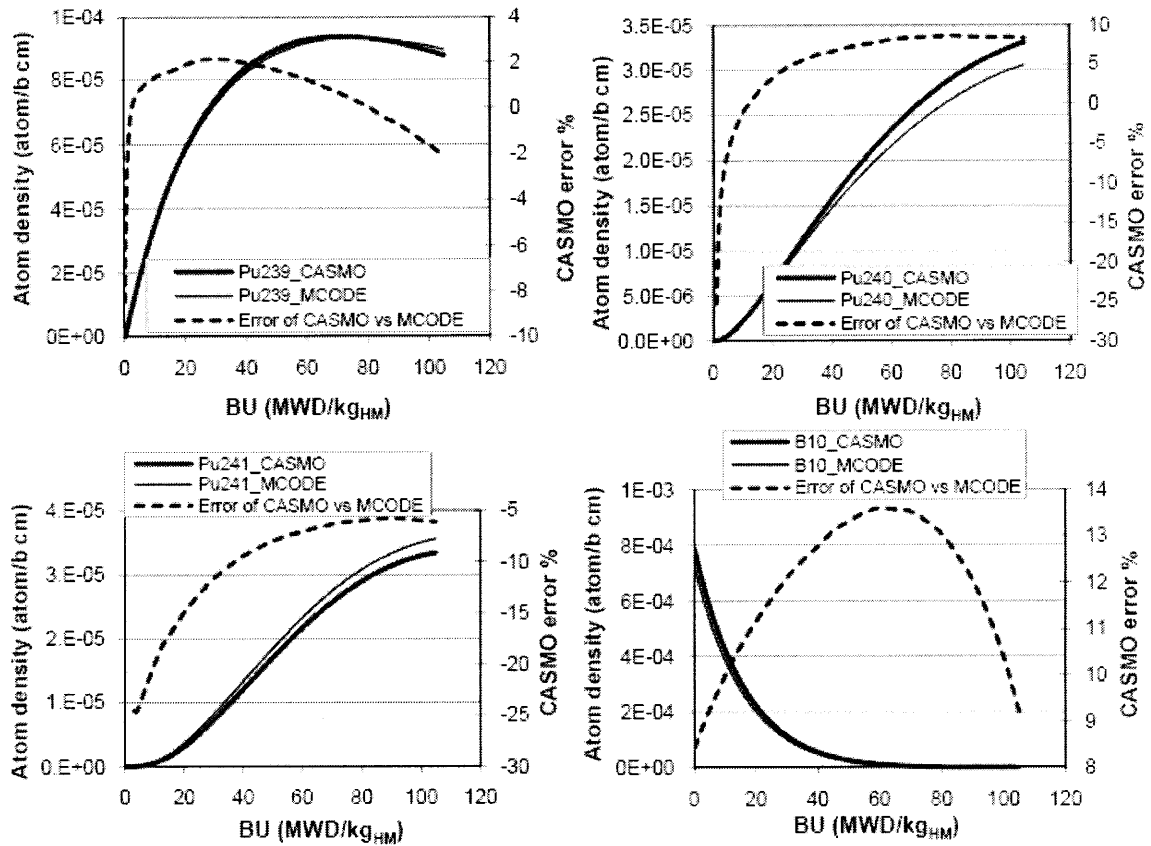
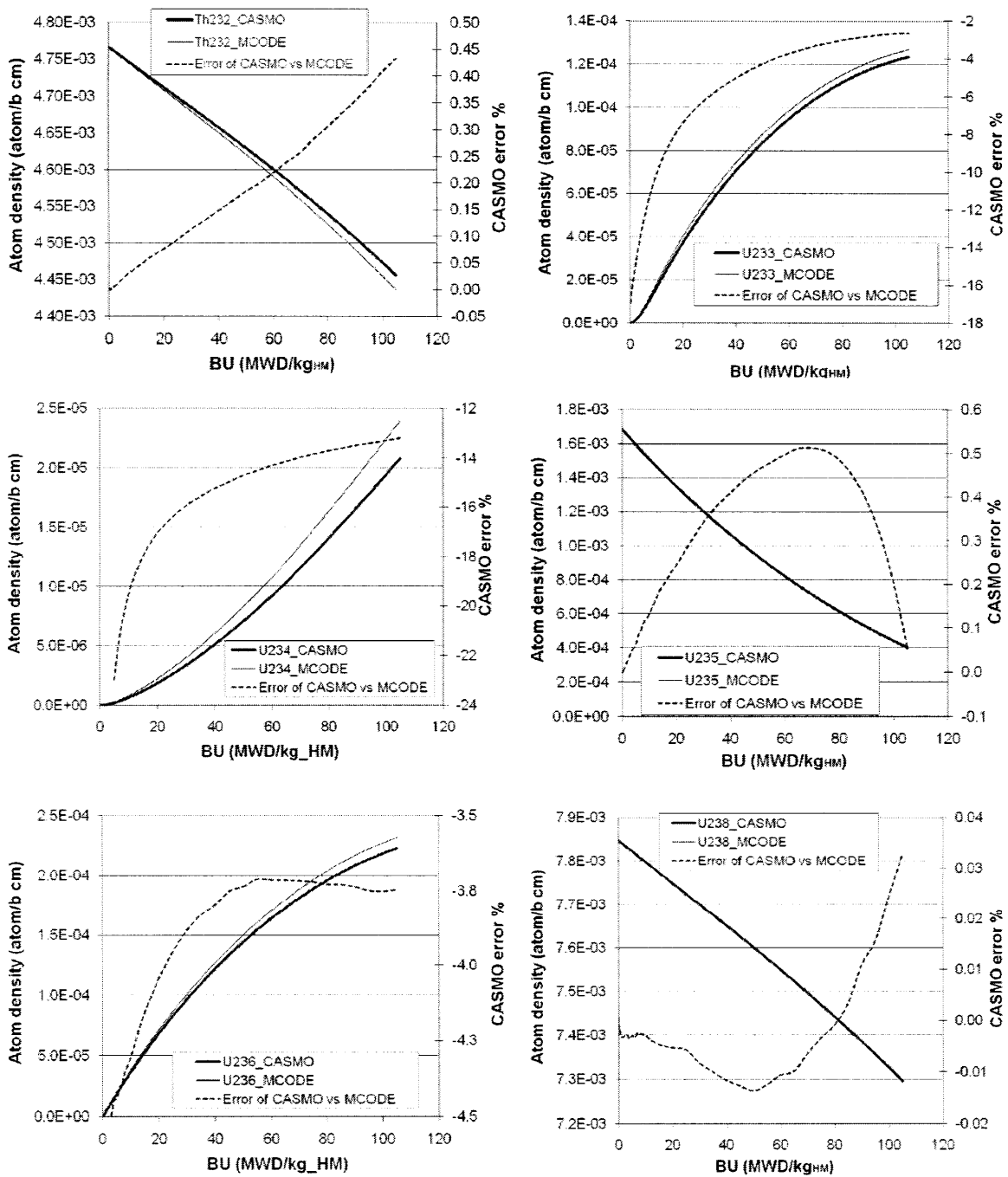


Figure IX-A. 8 – Atom density variation with burnup for major nuclides: comparison CASMO-MCODE (IFBA-provided cell)



**Figure IX-A. 9 – Atom density variation with burnup for major nuclides:
comparison CASMO-MCODE (Er₂O₃-containing fuel)**

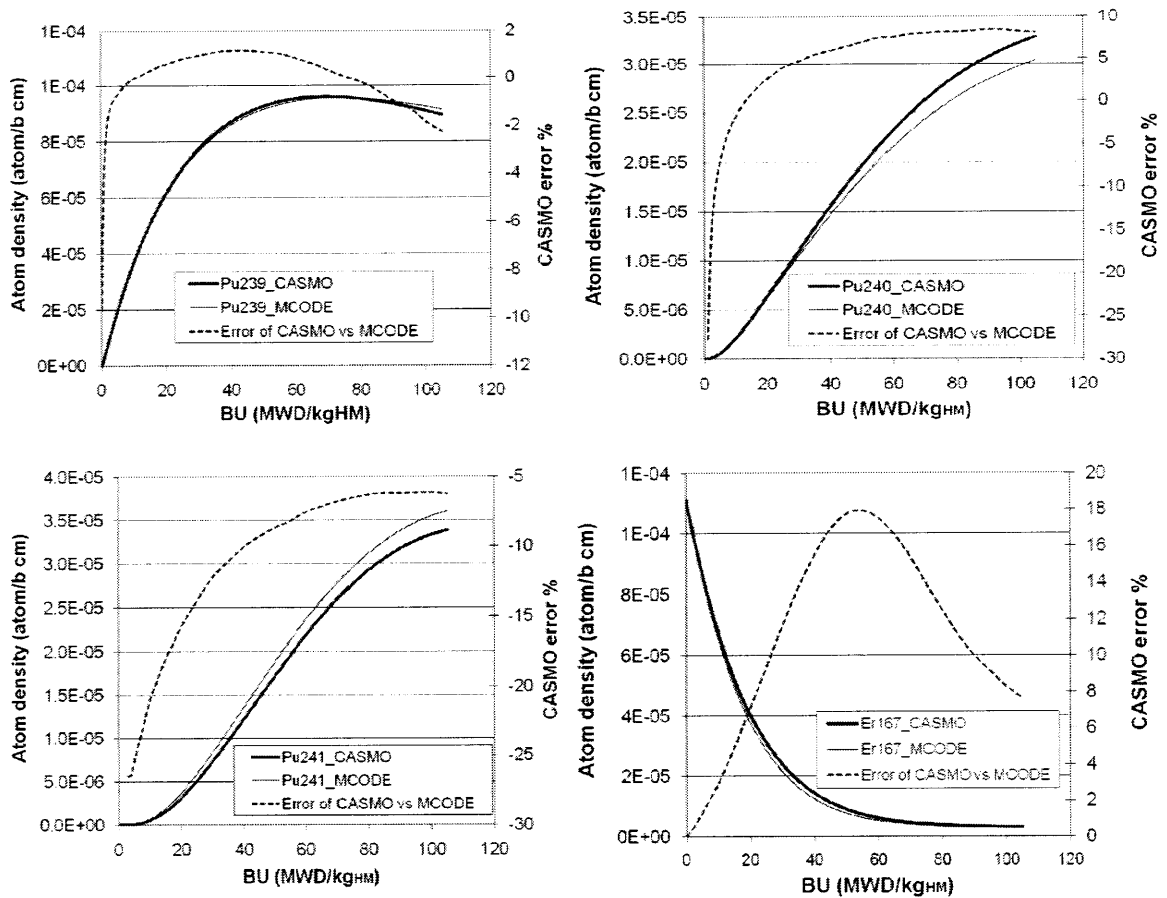


Figure IX-A. 10 – Atom density variation with burnup for major nuclides: comparison CASMO-MCODE (Er₂O₃-containing fuel)

IX-A.2. 3 Interpretation of results

Figure IX-A. 2 through Figure IX-A. 4 compare the infinite multiplication factor obtained with CASMO to that obtained with MCODE. It can be seen that the modeling of the equivalent pin geometry with CASMO slightly overestimates the multiplication factor, with an error ranging, when $k_{\infty} \sim 1$, between 0.5% (Er₂O₃-containing fuel case) to about 1% (unpoisoned cell case and IFBA-provided cell case). For comparisons between neutronic codes modeling the same geometry, an error of this magnitude would be significant, denoting poor code performance. However, in the present case, getting an error of about 1% while modeling an inverted geometry using a pin geometry can be considered acceptable. An estimate of the maximum cycle length difference resulting

from the difference in multiplication factor can be easily calculated by using the linear reactivity model (Driscoll et al., 1990). According to this model, the discharge burnup BU_d for a core composed by n batches of fuel can be approximated as:

$$BU_d = \frac{2n}{n+1} BU_{d1}$$

where BU_{d1} is the single-cycle discharge burnup. To account for neutron leakages, BU_{d1} can be estimated as the burnup corresponding to $k_{\infty} = 1.03$. Thus, for the IFBA-provided cell from Figure IX-A. 3:

$$\text{CASMO: } BU_{d1} \sim 82.6 \text{ MWD/kg}_{\text{HM}} \quad \rightarrow \quad (BU_d)_{\text{CASMO}} = 123.9 \text{ MWD/kg}_{\text{HM}}$$

$$\text{MCODE: } BU_{d1} \sim 79.8 \text{ MWD/kg}_{\text{HM}} \quad \rightarrow \quad (BU_d)_{\text{MCODE}} = 119.7 \text{ MWD/kg}_{\text{HM}}$$

The cycle length, in months, can be computed as:

$$T_c = \frac{BU_d \times M_{\text{HM}}}{\dot{Q}_{\text{core}} \times L \times n \times 30.42} \quad (\text{IX-2})$$

where M_{HM} is the heavy metal mass in the core, \dot{Q}_{core} is the core thermal power and L is the plant capacity factor. Thus, the cycle length overestimate resulting from modeling the IFBA-provided inverted geometry with an equivalent pin geometry is:

$$\frac{(T_c)_{\text{CASMO}}}{(T_c)_{\text{MCODE}}} = \frac{(BU_d)_{\text{CASMO}}}{(BU_d)_{\text{MCODE}}} = 1.035 \quad (\text{unpoisoned and IFBA-containing cell})$$

i.e. of about 3.5%.

For the Er_2O_3 -containing fuel case, the same procedure gives:

$$\text{CASMO: } BU_{d1} \sim 75 \text{ MWD/kg}_{\text{HM}} \quad \rightarrow \quad (BU_d)_{\text{CASMO}} = 112.5 \text{ MWD/kg}_{\text{HM}}$$

$$\text{MCODE: } BU_{d1} \sim 74.2 \text{ MWD/kg}_{\text{HM}} \quad \rightarrow \quad (BU_d)_{\text{MCODE}} = 111.3 \text{ MWD/kg}_{\text{HM}}$$

from which it follows that:

$$\frac{(T_c)_{\text{CASMO}}}{(T_c)_{\text{MCODE}}} = \frac{(BU_d)_{\text{CASMO}}}{(BU_d)_{\text{MCODE}}} = 1.011 \quad (\text{Er}_2\text{O}_3\text{-containing fuel})$$

To get more accurate results, a 3.5% reduction is therefore applied to the cycle length calculated when modeling unpoisoned and IFBA-provided inverted-equivalent pin

geometries with CASMO. A 1.1% reduction is instead applied when modeling inverted-equivalent pin geometries containing Er_2O_3 .

The comparison between the nuclide depletions predicted by CASMO and those by MCODE is shown in Figure IX-A. 5 and Figure IX-A. 6 for the poison-free case, in Figure IX-A. 7 and Figure IX-A. 8 for the IFBA-provided cell and in Figure IX-A. 9 and Figure IX-A. 10 for the Er_2O_3 -containing fuel. It can be seen that in all cases the depletion study performed with CASMO, for the inverted-equivalent pin geometry, closely matches that by MCODE for the heavy nuclides composing the fresh fuel, i.e. ^{232}Th , ^{235}U and ^{238}U . For these nuclides, the error percentages are below 1%. Particularly important is the very good agreement obtained for the depletion of ^{238}U (error percentages between -0.03% and 0.06%), which is the nuclide responsible for most of the resonance absorptions and self shielding effect. This is the result of having preserved the fuel surface to volume ratio when constructing the inverted-equivalent pin geometry. A disagreement between the two codes, ranging between 0 and 25% depending on the nuclide considered, exists instead for the atom densities of the nuclides generated during fuel burning. In particular, the CASMO error percentages in predicting the atom density of the main fissile nuclides generated during fuel burning, i.e. ^{233}U and ^{239}Pu , range between -18% and -2% for ^{233}U , and between -10% and +3% for ^{239}Pu . Except for ^{236}U , whose depletion is modeled quite accurately by CASMO, the depletion of the heavier nuclides ^{240}Pu and ^{241}Pu is characterized by larger error percentages, ranging between -25% and +10%. It is important to note that the plot referred to ^{10}B , which is the last plot of Figure IX-A. 8, has to be interpreted differently than the others. In fact, the discrepancy between the outputs of the two codes was expected since, unlike for the actinides, the initial ^{10}B atom density is different in the two geometries, by virtue of Equation E. Particularly, that in the pin cell is ~8% higher than that in the inverted cell: this motivates the initial ~8% overprediction by CASMO.

IX-A. 3 Conclusions on using CASMO for cycle length calculation of inverted geometries

The main conclusions from the CASMO-MCODE comparison presented in Section IX-A. 2 are:

- CASMO can be used to accurately predict the cycle length of an inverted geometry by modeling an equivalent pin geometry, having the same H/HM and fuel surface to volume ratio as the inverted geometry. For unpoisoned and IFBA-provided cells, when reduced by 3.5% the cycle length of this equivalent pin geometry closely matches that of the inverted geometry under investigation. A smaller reduction, of 1.1%, is instead needed for cells containing Er_2O_3 as burnable poison.
- The CASMO model of the pin geometry discussed above allows to accurately predict the depletion of ^{232}Th , ^{235}U and ^{238}U of an inverted geometry, while larger errors are obtained for the depletion of heavier nuclides, like ^{239}Pu and ^{241}Pu . These errors, which have eventually to be reduced if fuel depletion analyses become needed, are not important at this stage of the IPWR project since the only depletion analysis output data currently used is the cycle length, which can be accurately predicted through the selected methodology.

Chapter X

Inverted assembly manufacture

This chapter describes the method of fabrication proposed for the IPWR assemblies. The chapter is written to address the most obvious, but sometimes neglected, concern that arises when an innovative design is presented, that is whether its components can actually be manufactured. Since the most innovative, and atypical, component of the IPWR is the assembly, efforts were made to assess its manufacturability, with particular focus on the fuel prism fabrication. Figure X- 1 and Figure X- 2, which show two views of a generic¹ inverted assembly, are presented to support the discussions made throughout the chapter. Figure X- 1 is a top view of the assembly, before the top lid is welded to the duct and tubes: it clearly shows the internal structure of the inverted assembly. Figure X- 2 shows instead the final product.

¹ The manufacture processes described in this chapter are not geometry-specific, i.e. they were not developed specifically for a single inverted assembly geometry. Whenever reference to a geometry was necessary, e.g. in the numerical example comparing the degree of hydriding homogeneity obtainable with a fuel prism relative to a fuel pellet (see Table X- 3), typical inverted geometries were considered.

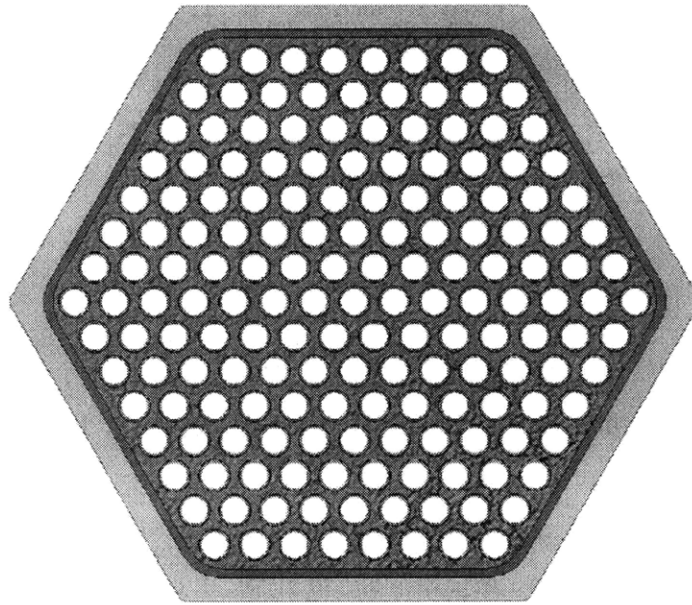


Figure X- 1: Top view of inverted assembly before welding of top lid²

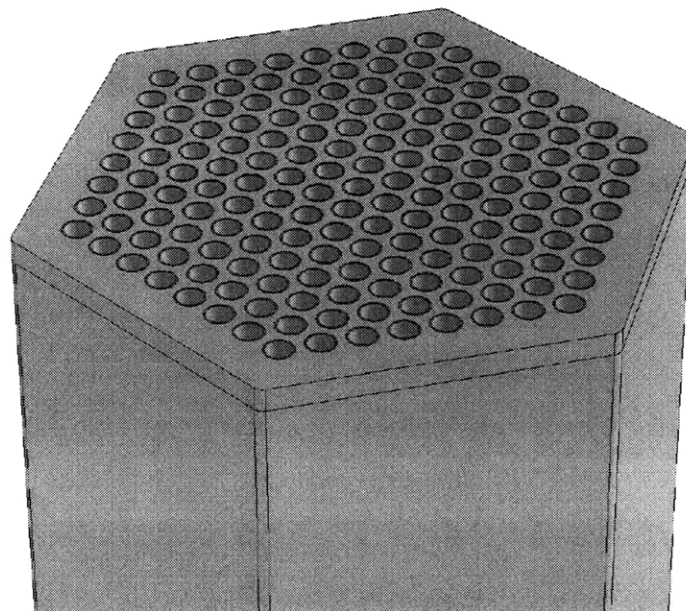


Figure X- 2: 3D view of top part of finished assembly

² This top view refers to an E-IPWR assembly design, i.e. the assembly design having empty tubes as cooling channels. Twisted tapes would be visible if the assembly depicted was of the S-IPWR or H-IPWR design type. These designs employ twisted tapes (short-length twisted tapes the former, long twisted tapes the latter) to enhance CHF performance.

X. 1 Manufacture phases and concerns

The manufacture of the inverted assembly consists of three phases, which are listed below and discussed more in detail in the section indicated:

- 1) Manufacture of the fuel prism (Section X.1. 1);
- 2) Insertion and securing of the twisted tapes to the cooling tubes, only for S-IPWR and H-IPWR designs (Section X.1. 2);
- 3) Final assembling phase (Section X.1. 3).

Of these, the first is the most challenging, and most of this chapter is devoted to it.

X.1. 1 Manufacture of the fuel prism

Manufacture of U-ZrH_{1.6} components has often been performed in the past, but only for relatively small components of simple geometry, i.e. pellets and slugs, used in TRIGA and SNAP reactors. More massive components made of zirconium hydride only, and consisting of 1 m long extrusions of tubular cross section, roughly 10 cm in diameter and weighing about 27 kg, were manufactured through powder compacting at GE-ANDP in the late '50s (Alexander, 1960). What is known about the hydriding technology developed for those projects can be used to assess the manufacturability of a fuel prism made³ of UTh_{0.5}Zr_{2.25}H_{5.625}. This assessment is performed by analyzing the fabrication process for U-ZrH_{1.6} pellets, which was patented by Simnad and colleagues (Simnad, 1964), and by discussing the applicability of each process to a short fuel prism, instead of a simple pellet.

The fabrication of U-ZrH_{1.6} pellets consisted of the following processes:

- 1) fabrication of base metal (U-Zr) ingots (Section X.1.1. 1);
- 2) ingot cleaning (Section X.1.1. 2);
- 3) ingot hydriding (Section X.1.1. 3);
- 4) ingot shaping/sizing (Section X.1.1. 4).

³ Important considerations on whether drawing conclusions on U-Th-Zr-H systems using data and experience acquired in the past on the manufacture of U-Zr-H or Zr-H specimens is reasonable or not, are discussed in Section X.1.1.3. 1.

An additional process, referred to as ingot superficial oxidation, is recommended for the fuel prisms, even though it was not part of the process patented by Simnad and typically performed for U-ZrH_{1.6} pellets. This process, suggested by Eggers (Eggers, 1978) is discussed in Section X.1.1. 5.

X.1.1. 1 Base metal ingot fabrication

From the chemistry standpoint, U-Zr hydride fuel was obtained by first producing the base metal, i.e. a U-Zr alloy, which was subsequently hydrided. The U-Zr alloy was produced by arc melting the pure metals, as shown in Figure X- 3, which refers to the manufacturing of U-Zr-H pellets. “Once homogenized in the liquid phase, the U-Zr alloy is released from the crucible and flows into the molds (called moules in the figure) which are roughly the diameter of the fuel pellet” (Olander, 2009).

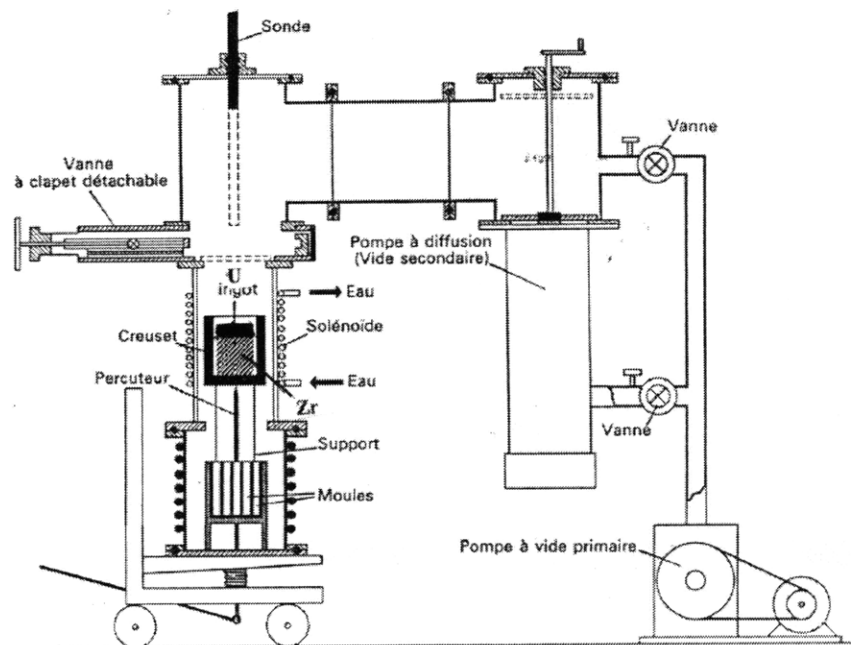


Figure X- 3: Induction-melting furnace for producing U-Zr ingots (Olander, 2009)

It is reasonable to think that this technology can be used to manufacture U-Zr specimens more massive than a fuel pellet, like the fuel prism shown in Figure X- 1. It is important to point out, however, that the fuel prism must be pierced with holes before hydriding is performed, for three reasons:

- a) the presence of the holes significantly increases the surface-to-volume ratio of the specimen, which is extremely beneficial to achieve an effective and homogeneous hydriding;
- b) once hydrided, the specimen becomes brittle, and precise drilling is more challenging to perform. Only minor finishing processes can be performed on a hydrided specimen;
- c) material removed from the hydrided specimen cannot easily be recycled since the hydrided form is not suitable for return into the melting furnace shown in Figure X- 3.

Reason c) suggests planning hydriding as well as earlier manufacture processes so that the specimens leaving the hydriding furnace have dimensions as close as possible to the final fuel prism design.

There are two options to obtain a perforated U-Zr prism before hydriding:

- OPTION 1: using, for the process sketched in Figure X- 3, a mold provided with solid cylinders, so that each cylinder will generate a hole. An example of such a mold, for circular-shaped instead of hexagonal-shaped prisms however, is shown in Figure X- 4.
- OPTION 2: using, for the process sketched in Figure X- 3, an empty mold, i.e. a mold not provided with solid cylinders. The U-Zr hexagonal prism obtained after solidification will be then drilled to generate the holes.

The descriptions of Options 1 and 2 are presented in Section X.1.1.1. 1 and Section X.1.1.1. 2 respectively. The two options are compared in Section X.1.1.1. 3 and recommendations are given.

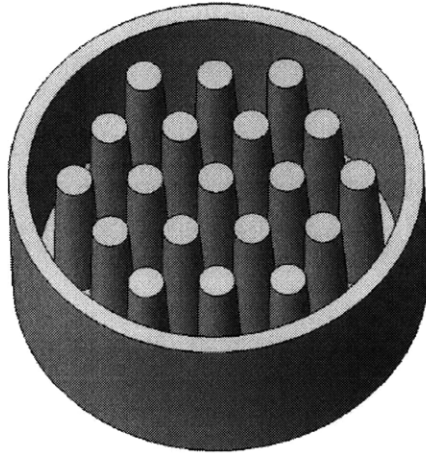


Figure X- 4: Example of mold usable to generate a perforated specimen (Ales, 2008)

X.1.1.1. 1 OPTION 1: holes generated through casting

This process has the advantage of minimizing the amount of uranium content fuel that is removed from the specimen and therefore needs to be recycled back into the melting furnace shown in Figure X- 3. To allow mold removal, the surfaces of the mold that are to come in contact with the liquid U-Zr alloy should not be parallel to the vertical axis, but inclined of about 1° with respect to it. This angle, referred to as draft angle, affects the maximum height that the fuel prism can have, since the taller is the mold, the larger is the difference in dimensions between the lower base and the upper base of the prism. The process is quite involved, since casting must be followed by drilling because of the need to remove the mold after solidification. Therefore Figure X- 5 shows a not-to-scale frontal view of part of a mold in which:

- the draft angle, identified with α , is 1° ;
- the casted specimen height is L ;
- the casted specimen will be provided with holes having a maximum diameter⁴ D_f and a minimum diameter $D_{f,MIN}$.

⁴ Since hydriding causes the cast specimen to swell about 20% in volume, D_f is designed to be equal to the as-designed hole diameter, i.e. to the diameter that the holes are supposed to have in the finished inverted assembly. This means that, after hydriding, the holes will need to be bored out, more in the upper part (that having a pre-hydriding diameter $D_{f,MIN}$) and less in the lower part.

Once the mold is removed, the cast specimen will be provided with holes having an axially variable diameter. However, the holes may or may not be through holes, i.e. holes passing completely through the specimen, depending on the specimen height. In fact, if L is greater than a certain height L_{MAX} , then $\Delta R = D_f/2$, which means that the hole will not go through the whole specimen, but only up to a certain depth (see Figure X- 7). If this was the case, post-casting processes would not only consist of boring the holes out (which would be needed anyway also for $L < L_{MAX}$), but also in drilling a solid specimen thickness equal to $L - L_{MAX}$.

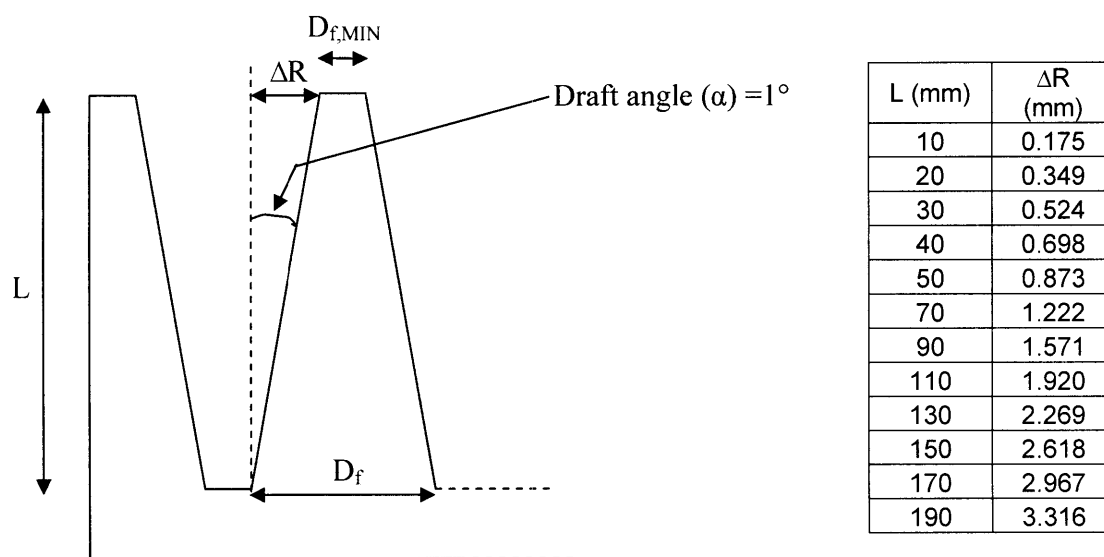


Figure X- 5: Simplified sketch of a mold showing the dimension difference between the top and the bottom of the casted specimen

In order to avoid drilling the solid specimen thickness and only boring out passing holes, it is important to cast specimens having a height smaller than L_{MAX} . How much smaller depends on a trade-off between (1) minimizing the amount of material that, after casting, needs to be removed and (2) minimizing the cost and the time needed to perform the casting. These two aspects are discussed as follows. For simplicity, the calculation of the height of the casted specimen that minimizes the amount of material to be removed is

performed assuming that this removal is performed soon after casting, instead of after hydriding. In this way the hydriding-induced volume changes can be neglected⁵.

Given an inverted assembly height equal to L_{target} , the fuel prism contained in it can be either a single fuel prism of the same height, or it can be composed by n fuel prisms each having a height equal to L_{target}/n . Figure X- 6 is a sketch of these options, where for the latter $n = 2$ was chosen for simplicity. In both cases, the material that needs to be removed is represented by the areas between the dashed lines and the hole profile lines.

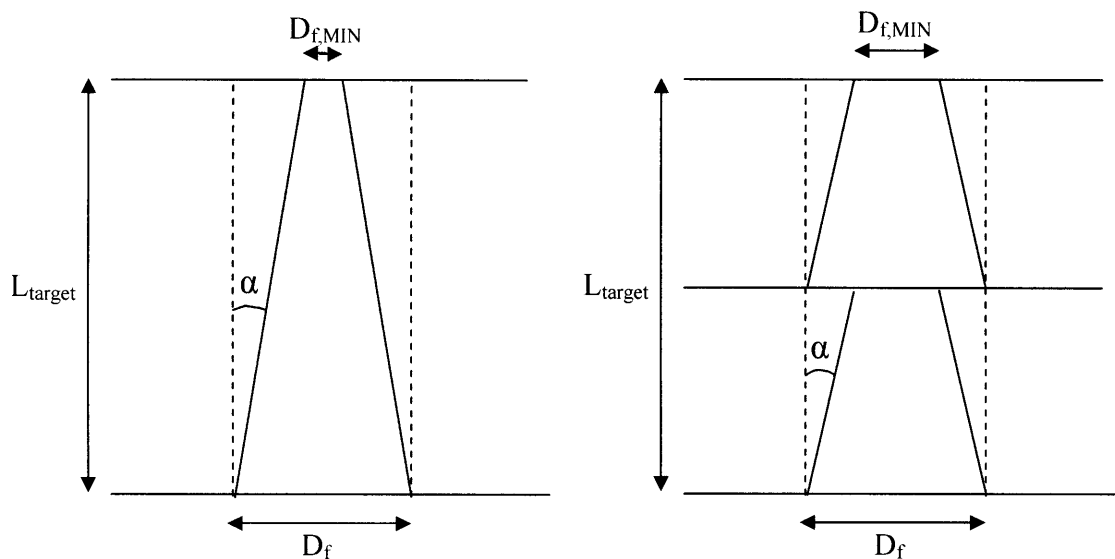


Figure X- 6: Base metal ingot casting options: casting of a ingot (left); casting of n shorter ingots that will be stacked one above the other (right, for $n=2$)

⁵ Since at this stage we are not interested in the actual amount of material that has to be removed, this assumption is reasonable. In fact, the result we are searching is the same regardless of whether the minimization is performed accounting for volume swelling or not.

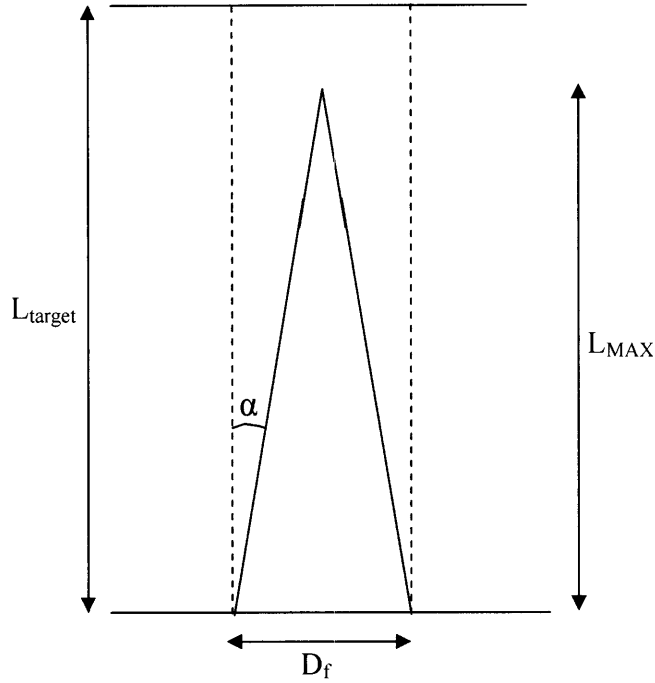


Figure X- 7: Cast specimen having height greater than L_{MAX}

Recalling that $D_{f,MIN} = D_f - 2\Delta R = D_f - 2\frac{L_{target}}{n}tg\alpha$, the volume of material to be removed is:

if $\frac{L_{target}}{n} \leq L_{MAX}$ (see Figure X- 6):

$$\begin{aligned}
 V_{to_be_removed} &= \frac{\pi}{4} D_f^2 L_{target} - n \times \text{Truncated_cone_volume} \\
 &= \frac{\pi}{4} D_f^2 L_{target} - n \times \left[\frac{\pi}{12} \frac{L_{target}}{n} (D_f^2 + D_{f,MIN}^2 + D_f D_{f,MIN}) \right] \\
 &= \frac{\pi}{4} D_f^2 L_{target} - n \times \left[\frac{\pi}{12} \frac{L_{target}}{n} \left(3D_f^2 + 4\frac{L_{target}^2}{n^2} (tg\alpha)^2 - 6D_f \frac{L_{target}}{n} tg\alpha \right) \right] \\
 &= \pi \frac{L_{target}^2}{n} tg\alpha \left(\frac{D_f}{2} - \frac{1}{3} \frac{L_{target}}{n} tg\alpha \right)
 \end{aligned}$$

while if $\frac{L_{target}}{n} > L_{MAX}$ (see Figure X- 7):

$$\begin{aligned}
V_{to_be_removed} &= \frac{\pi}{4} D_f^2 L_{target} - n \times Cone_volume \\
&= \frac{\pi}{4} D_f^2 L_{target} - n \times \frac{\pi}{3} \frac{D_f^2}{4} L_{MAX} = \frac{\pi}{4} D_f^2 L_{target} - n \times \frac{\pi}{3} \frac{D_f^2}{4} \frac{D_f}{2tg\alpha} \\
&= \frac{\pi D_f^2}{4} \left(L_{target} - n \frac{D_f}{6tg\alpha} \right)
\end{aligned}$$

The four plots in Figure X- 8 show the volume of material that, using a mold configuration analogous to that shown in Figure X- 5, should be removed after casting to bring the hole to an axially uniform diameter⁶ $D_f = 11.63$ mm. The four plots refer to the same draft angle of 1° but to different inverted assembly heights, $L_{targets}$, equal to 0.5, 1.5, 2.5 and 3.5 m respectively. It can be seen that the volume of material to be removed decreases as the number of stacked fuel prisms increases. However, such reduction is not uniform, and for this reason the plots have a secondary y-axis, which shows the material saving percentage relative to the case of a single fuel prism having a height equal to that of the inverted assembly, i.e.:

$$Vol. \text{ saving } \% = 100 \frac{(Vol. \text{ removed})_n - (Vol. \text{ removed})_{n=1}}{(Vol. \text{ removed})_{n=1}}$$

The volume saving percentage increases (in absolute value) very rapidly in the n -range from $n=1$ to $n \sim 15-30$, while increases more slowly as n is increased further. This means that, relative to the casting of a single fuel prism per assembly, the extra-costs required to cast 15-25 fuel prisms per assembly would be accompanied by a significant reduction in volume of removed material, while those required to further increase the number of fuel prisms per assembly would not be accompanied by a comparable saving.

⁶ The value of 11.63 mm for the hole diameter was arbitrarily chosen, and it is used as an example. The value of L_{MAX} corresponding to this diameter is $L_{MAX} = 333$ mm.

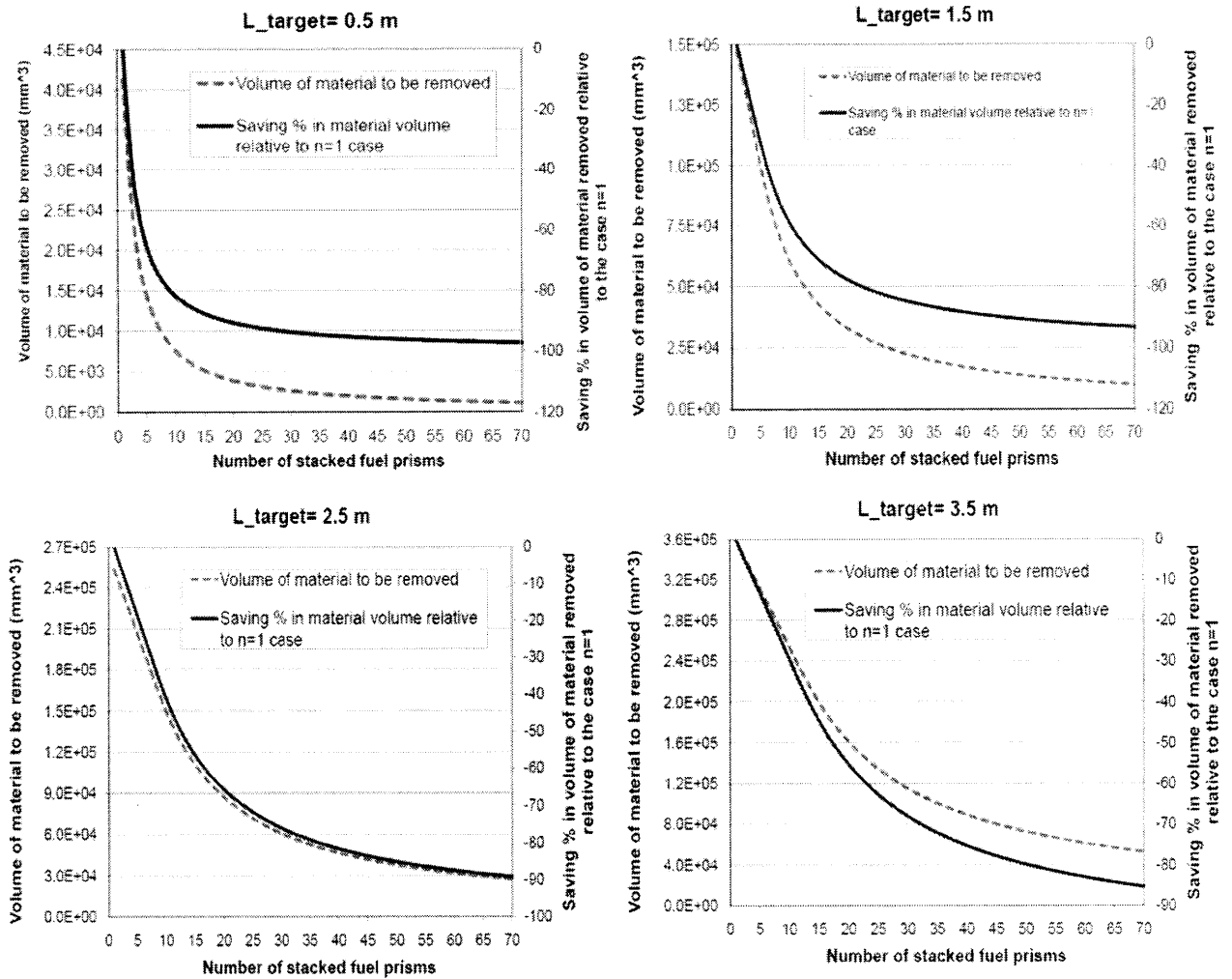


Figure X- 8: Material removed vs number of stacked fuel prisms

If 15, 20, 25 and 30 were the numbers of fuel prisms to stack inside inverted assemblies having L_{target} of 0.5, 1.5, 2.5 and 3.5 m respectively, the height of each prism would be:

- 3.3 cm for $L_{target} = 0.5$ m;
- 7.5 cm for $L_{target} = 1.5$ m;
- 10 cm for $L_{target} = 2.5$ m;
- 11.7 cm for $L_{target} = 3.5$ m;

In spite of not being final results for the casted specimen height, the above values give an idea about the range of heights to be considered for the specimens to cast.

X.1.1.1. 2 OPTION 2: holes generated through drilling

The casting of a solid prism, i.e. a prism without holes, would undoubtedly be less challenging than the casting process discussed above as “Option 1”. Choosing this process would imply the need of a subsequent drilling of solid thicknesses and not just boring out passing holes. The material removed through drilling would be recycled back into the melting furnace of Figure X- 3 to produce new U-Zr ingots. The limitation of this method is again related to the height of the fuel prisms since the precision with which holes can be drilled decreases as the hole L/D_f ratio increases. During drilling the hole axis inevitably tends to move away from its as-designed position, with a radial displacement rate that is, for conventional drilling, up to about 2.5 mm/m (Ales, 2008). Conventional drilling of deep holes would also require a multi-step drilling, in the sense that first the drill perforates the block up to a certain depth, then it needs to be extracted to allow chip removal and subsequently re-inserted to drill further (Ales, 2008).

Another type of drilling, the so-called gun drilling, allows means to solve the chip removal issue and to reduce the hole axis displacement rate. This alternative technique consists of using hollow drills, through which a liquid flows to lubricate/cool the drill tip and to remove chips. For gun drilling the deviation of the hole axial position relative to the as-designed position is about three times smaller than that characterizing conventional drilling, i.e. ~ 0.8 mm/m (Ales, 2008). The hole axis radial displacement from the entrance position is shown in Figure X- 9 for both conventional and gun drilling.

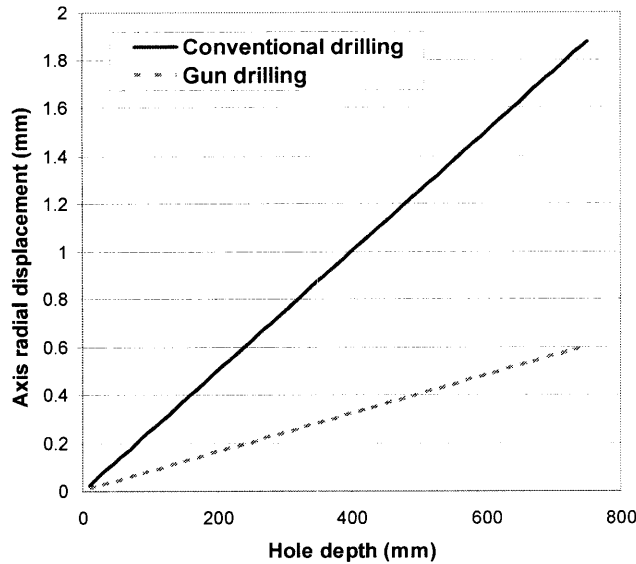


Figure X- 9: Hole axis radial displacement as a function of hole depth

The deviation of the hole axis position with respect to the as-designed position becomes unacceptable when the Zr-2.5Nb tube, inserted vertically from the prism lower base, touches the hole walls near the prism upper base. This would cause, in fact, additional stresses on the fuel, as well as possible fretting that would accelerate fuel cracking and crumbling during operation⁷. If the tube is assumed perfectly straight, the displacement, *dis*, becomes unacceptable when:

$$dis \geq t_{gap}$$

where t_{gap} is the width of the gap between the tube outer surface and the hole inner surface. For inverted assemblies, as discussed in Chapter III, t_{gap} is a function of the cladding inside diameter and discharge burnup. If the latter is assumed equal to 125 MWD/kg_{HM}, using Eq. III.3 in Chapter III can be used to calculate the gap thickness corresponding to various possible cladding diameters and, using the bottom line of Figure X- 9, the maximum allowed height of the base metal ingot can be obtained. Results of this procedure are summarized in the third column of Table X- 1. It can be seen that the maximum height to prevent tube-hole interference ranges between 25 and 54 cm. These

⁷ As in the discussion about casting, also for drilling the maximum acceptable fuel prism height is calculated assuming no swelling during hydriding. This is acceptable at this stage since considering swelling would only add a multiplicative factor to all dimensions, which would cancel out in the search of the maximum acceptable fuel prism height.

maximum heights are only bounding values, and do not correspond to the actual heights of the metal ingot to be drilled. This is because they do not account for hole manufacture tolerances. In other words, the condition $dis < t_{gap}$ is used only to avoid tube-hole interference, and does not embed any requirement in terms of minimum allowed tube-fuel gap width. In this regard, the fabrication tolerance of typical PWR fuel pellets (~0.15% of their diameter, i.e. 0.5 mills, from DiGrande and Lambert, 1991), which establishes the tolerance on the fuel-clad gap for pin geometry, can be used as fabrication tolerance on the fuel-clad gap width of inverted fuel prisms. In this way, the maximum allowed ingot height that meets fabrication tolerances can be easily calculated⁸. The results of this calculation are shown in the last column of Table X- 1. It can be seen that metal ingots, and therefore inverted fuel prisms, have to be fabricated in heights ranging between about 8 and 16 mm.

Cladding inside diameter (mm)	As-designed fuel-clad gap width (mm)	As-designed hole diameter (mm)	Maximum prism height allowed by tube-hole interference (mm)	Deviation from as-designed gap width based on 0.15% diametral fabrication tolerance (mm)	Maximum prism height to meet fabrication tolerance (mm)
7	0.202	8.4	250	6.3×10^{-3}	7.9
8	0.231	9.6	290	7.2×10^{-3}	9.0
9	0.260	10.5	320	7.8×10^{-3}	9.7
10	0.288	11.8	360	8.9×10^{-3}	11.1
11	0.317	13.0	400	9.7×10^{-3}	12.1
12	0.346	14.1	430	10.6×10^{-3}	13.2
13	0.375	15.2	470	11.4×10^{-3}	14.2
14	0.404	16.4	500	12.3×10^{-3}	15.4
15	0.433	17.5	540	13.1×10^{-3}	16.4

X.1.1.1. 3 Comparison between Option 1 and Option 2

Table 2 summarizes the two options highlighting pros and cons of both. The color pattern uses green for a pro, red for a con and yellow for a condition that would be preferable to avoid but that, if present, penalizes the corresponding option only slightly.

⁸ If, for example, the fuel prism has to be provided with 10 mm diameter cooling channels, the as-designed diameter of the holes in the fuel prism can be calculated using Eqs. III.2 and III.3 in Chapter III. The resulting diameter is 11.8 mm. The application of the 0.15% tolerance to this diameter yields the maximum hole diameter deviation, i.e. 17.8×10^{-3} mm which, divided by two, gives the maximum allowed radial deviation, 8.9×10^{-3} mm. By dividing this number by the drill bit deviation, i.e. by 0.8×10^{-3} mm/mm, a maximum prism height equal to 11.1 mm can be obtained.

Table X- 2: Options for pre-hydriding base metal ingot manufacture		
	Option 1	Option 2
	U-Zr alloy is casted into perforated prisms. Holes only need to be bored out before hydriding. Material removed is recycled back.	U-Zr alloy is casted into solid prisms, i.e. prisms without holes. The solid prisms are then drilled through their entire thickness. Material removed is recycled back.
For a given prism height and hole diameter, volume of U-Zr alloy that needs to be recycled back	Y	3Y to 10Y ^(a)
For a fixed assembly height, suggested minimum number of prisms that need to be stacked one above the other inside the assembly	X	2X to 16X ^(b)
Level of technical challenge	Somewhat high	Somewhat low

- (a) The range of recycled volume ratios between the two options, i.e. from 3 to 10, is obtained by dividing the volume of material removed during the drilling of a 11.63 mm diameter hole through solid prisms having the heights shown in Figure X- 8, and the volumes of material removed through Option 1 and shown by the four plots in Figure X- 8.
- (b) The ratios between the number of stacked prisms, i.e. from 1/16 to 1/2, is obtained by dividing the prism heights listed after Figure X- 8 by the prism heights, calculated for Option 2, and summarized in the last column of Table X- 1.

As long as the recycling of U-Zr burr material produced during drilling does not pose particular challenges, Option 2 is recommended for the manufacture of base metal ingots for IPWR assemblies. This conclusion is mainly based on the relative ease with which casting of a non-perforated metal ingot as well as its drilling can be performed. Based on the much larger number of fuel pellets that have to be handled in the manufacture of the assemblies forming a typical PWR core, i.e. ~19 millions, the fact that Option 2 requires from 2 to 14 times more prisms per assembly is not considered a showstopper for this method. For a core composed by 200 assemblies, in fact, the number of prisms would be of only 60000-70000.

X.1.1. 2 Base metal ingot cleaning prior to hydriding

In the manufacture of hydride fuel pellets, the U-Zr ingots are extracted from the mold and subjected to a series of cleaning processes aimed at removing hydrogen permeation barriers, generally oxide and nitride layers, that easily form on the specimen surface. Depending on the temperature at which these layers form, which range “*from well below*

ambient to 500 or 600°C and higher” (Van Houten, 1974), the oxide layers impede hydrogen permeation with a different extent. Particularly, for Zr hydriding, oxide layers formed at room temperature impede hydrogen permeation more than thicker layers formed at high temperatures (Mueller, 1968). This is shown in Figure X- 10, in which the slowest weight gain, i.e. the slowest hydrogen absorption, corresponds to the case of an oxide layer formed at room temperature.

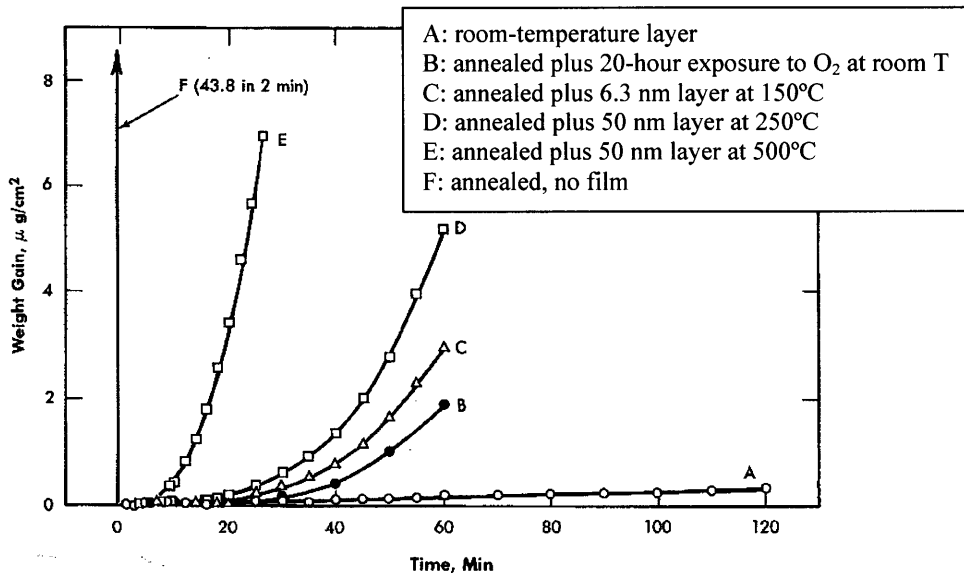


Figure X- 10: Effect of oxide film on hydrogen absorption speed (measured as weight gain vs time) (Mueller, 1968)

Oxide layers act as barriers both against hydrogen absorption and against hydrogen loss. Thus, on one hand their presence on the specimen surface is to be avoided before hydriding, while on the other it is beneficial after hydriding to enhance the specimen hydrogen retaining capabilities. Superficial post-fabrication oxidation is in fact recommended for fuel prisms and it is discussed in Section X.1.1. 5. For U-Zr pellets/slugs, the removal of possible hydrogen permeation barriers before hydriding was performed through the following cleaning processes:

- degreasing in liquid trichloroethylene;
- abrading;

- pickling with a solution of nitric and fluoridric acid to remove mainly oxides;
- washing in distilled water to remove traces of acids;
- rinsing in an alcohol bath, followed by drying.

It is reasonable to think that a short U-Zr fuel prism can be subjected to these processes as well. Relative to the cleaning of non-perforated geometries, like pellets, the cleaning of a perforated fuel prism will require additional abrading tools, like cylindrical tools covered with steel wool, to be inserted into the holes. As for pellets, this procedure should be performed while the specimen is still immersed in the trichloroethylene bath. As for the treatment with chemicals, a fuel prism, like a pellet, does not have hidden surfaces, e.g. crevices, and therefore the attack with chemicals should be as effective without posing any additional challenge.

X.1.1. 3 Base metal ingot hydriding

Section X.1.1.3. 1 discusses the general features of the hydriding mechanisms, particularly Zr hydriding, without addressing the question of how hydriding is actually performed. Section X.1.1.3. 2 discusses, specifically, the hydriding process and its applicability to fuel prisms for inverted assemblies.

X.1.1.3. 1 Hydriding mechanisms and consequences

Hydrogen absorption by hydride-forming transition metals is accompanied by either lattice expansion or structure transformation into a new structure, in both cases with an increase in internal stresses. Such stresses can cause the specimen to crack, either because hydriding is performed at a temperature below that required for the relief of the internal stresses or because, although the temperature is high, hydriding is performed too fast, and the material is not able to stress-relieve itself rapidly enough. Thus, it is important for hydriding to be performed slowly and at high temperature. A slow hydriding is needed not only to avoid material cracking during the process, but also to obtain a hydrided specimen with a fine grain structure, which favors mechanical properties. Figure X- 11 shows the grain size obtained through a fast hydrogen absorption rate (left) and through a slow absorption rate (right): the difference is evident. A fine grain size can be obtained by controlling hydrogen partial pressure in vacuum or inert atmosphere. It has to be pointed

out, however, that no matter how well hydriding is performed, the resulting hydride will be brittle, somewhat resembling “cast iron in regard to brittleness and resistance to thermal shock“ (Mueller, 1968). “Its brittleness at both room temperature and at elevated temperatures makes machining and hot-working nearly impossible” (Vetrano, 1962).

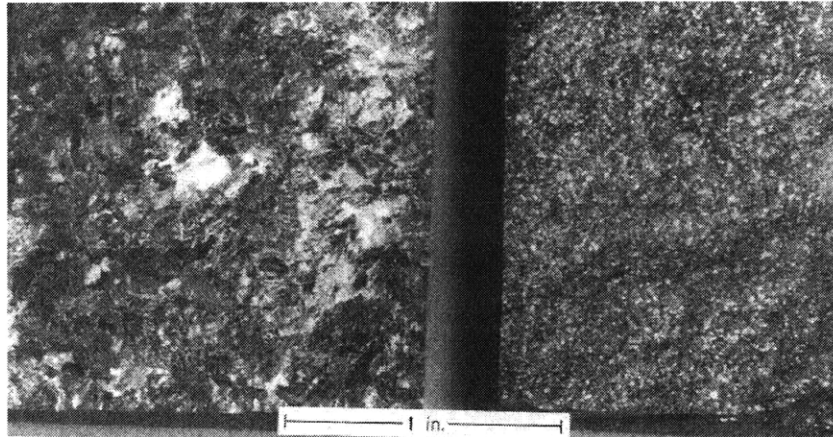


Figure X- 11: Effect of hydrogen absorption rate on grain size in hydrided yttrium: fast absorption rate (left) vs slow absorption rate (right). (Mueller, 1968)

It is important to note, however, that in this discussion the applicability of the hydriding methods to the U-Th-Zr base metal prisms for inverted cores is assessed based on properties and behaviors of Zr and U-Zr specimen subjected to hydriding, i.e. specimens not containing Th. This is because most of the experience gained in hydriding nuclear fuels and moderators refers to Zr-H and U-Zr-H systems, while fewer studies have been performed on the hydriding of U-Th-Zr specimens: initially in Japan (e.g. Yamamoto et al., 1998), and more recently at University of California at Berkeley (Terrani et al., 2009). Extending the conclusions on the hydriding of Zr and U-Zr specimens to U-Th-Zr specimens is therefore questionable, but only because of the presence of Th. In fact, while for Th no explicit statements have been found about its influence on U-Zr-H systems, neglecting the presence of uranium by studying the hydriding of U-Zr specimens as if they were made of Zr only is done very often, and justified by the fact that uranium has little effect on the hydriding process. In particular, when present with an atom percentage less than about 10% (like in the inverted assembly fuel) uranium has a negligible effect on the Zr-H phase relations, consisting of slightly shifting the boundaries of the $(\alpha\text{-Zr})+(\delta\text{-hydride})$ two-phase region and that of the $\delta\text{-hydride}$ region

toward the hydrogen-poor end of the phase diagram shown in Figure X- 12⁹ (Mueller, 1968). Also, uranium has a relatively minor effect on the physical and mechanical properties of the final U-Zr-H specimen (Mueller, 1968). This small influence is due to the fact that the dissociation pressure of uranium hydride is so high relative to that of zirconium hydride that uranium hydride does not form under normal hydrogen pressures. This means that hydriding a U-Zr (or U-Th-Zr) base metal (at typical hydrogen pressure) does not yield the formation of U-hydride. As for the presence of other alloying elements beside U and Zr, like Th, a statement by Simnad (Simnad, 1964) could be used to justify extending the conclusions drawn for U to Th: “*where a zirconium alloy is utilized, the hydriding conditions of this method are such that the hydriding is essentially that of the zirconium in the alloy*”. However, Simnad was not referring to any alloy element in particular, and he probably had in mind uranium, with which he had gained significant experience. A different and more reliable conclusion can be drawn if, as done for U, the dissociation pressure of Th-hydride is used to establish the extent with which Th influences the behavior of a U-Th-Zr-H system relative to that of a U-Zr-H system. Hydrogen dissociation pressure in ThH₂ is of the same order of that in ZrH_{1.6} at all temperatures of practical interest (Garkisch, 2003), which means that hydriding a U-Th-Zr metal base will also yield the formation of a thorium hydride which, according to Terrani et al. (2009) is ThZr₂H_{7-x}. The formation of the ThZr₂H_{7-x} phase, which is known to be significantly stable, would make relying on data and information referred to U-Zr-H systems not advisable, in the sense that while the final product could indeed be obtained, the process characteristics (mainly pressure and temperature) could be substantially different from those, discussed here, for U-ZrH_{1.6} specimens. The optimism on the possibility to obtain the final product, i.e. a UTh_{0.5}Zr_{2.25}H_{5.625} fuel prism, is justified by the fact that U-Th-Zr-H pellets, with different compositions in terms of atom percentage of each component, have been manufactured in Japan in the late ‘90s (Yamamoto et al., 1998) and, with the exact fuel composition selected for the IPWR, by Terrani et al. (2009) at University of California at Berkeley. The related literature is however more focused on the thermo-mechanical properties of the specimens obtained and on the pellet

⁹ In alloys containing 15 to 40% at.% uranium, instead, the (α -Zr)+(δ -hydride) two-phase region is eliminated, and there is a rather high solubility of hydrogen in the δ -hydride phase (Mueller, 1968).

manufacture processes rather than on the possibility to extend such processes to more massive specimens. In the absence of this information, the manufacturability of a U-Th-Zr-H fuel prism is assessed based on what is known about U-Zr-H systems. Further studies are needed to verify how severe are the implications of this approximation.

The hydriding of zirconium for nuclear applications is typically performed until the H/Zr atom ratio reaches about 1.65-1.75. This is because the phase corresponding to this value, i.e. the δ -Zr hydride phase, is stable at all the temperatures of practical interest, as shown in Figure X- 12. In this figure the phases are indicated with greek letters having the following meaning (Domain, 2002, and Mueller, 1968):

- α : metal phase having zirconium in HCP (Hexagonal Close Packed) structure and interstitially dissolved H
- β : metal phase having zirconium in BCC (Body Centered Cubic) structure and interstitially dissolved H
- δ : hydride phase, $ZrH_{1.3-1.7}$, in which Zr has FCC (Face Centered Cubic) structure and H is in tetrahedral sites
- ϵ : hydride phase, $ZrH_{x \geq 2}$, in which Zr has FCT (Face Centered Tetragonal) structure and H in tetrahedral sites.

The preference for the δ -Zr hydride phase is also due to the significant irradiation-induced swelling characterizing the β -Zr phase (Birney, 1967). This is because, relative to the δ -Zr hydride phase, the β -Zr phase has a much lower resistance to fission gas bubble growth, which contributes to swelling. Another consequence of this fact is the difference in creep rate: β -Zr phase creep rate is several orders of magnitude higher than that of δ -Zr hydride phase (Birney, 1967).

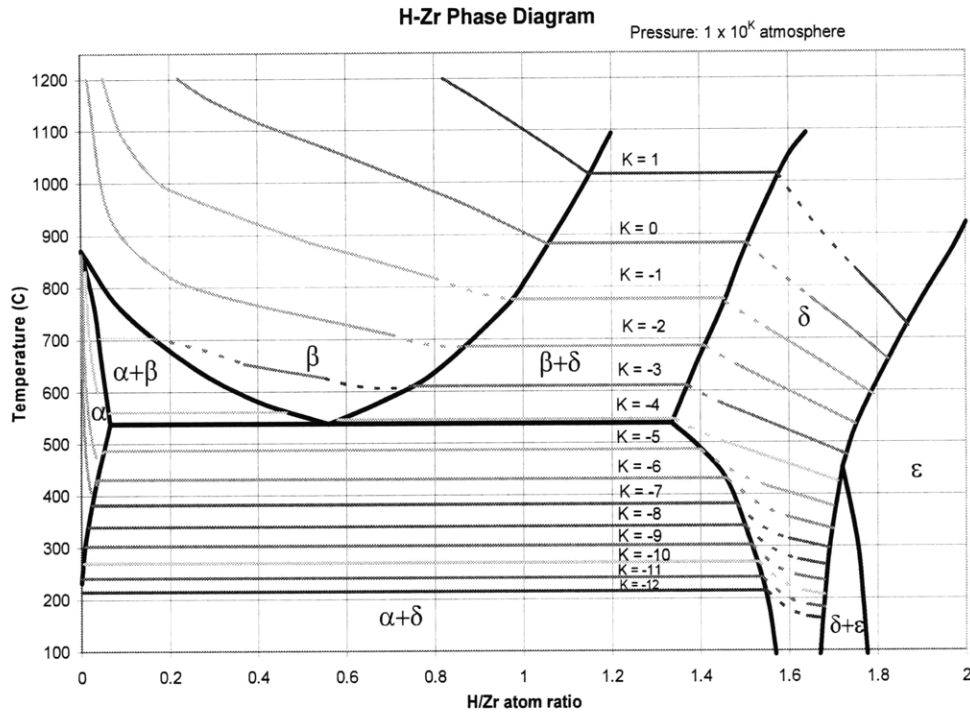
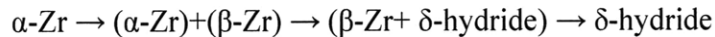


Figure X- 12: H-Zr phase diagram with isobars of equilibrium H_2 pressure superposed (Olander, 2009)

Even though the phase obtained through hydriding, i.e. the δ -hydride phase, is relatively stable, during hydriding significant phase changes occur. When hydriding is performed at about 800°C , as the hydrogen atom percentage increases the system moves through several phases:



These transformations cause the specimen density to decrease from 6550 kg/m^3 of α -Zr to about 5650 kg/m^3 of δ -hydride, i.e. a $\sim 16\%$ reduction, which implies a volume growth of the same percentage. This volume growth must be accounted for, not only in the design of the components that are in contact with the specimen during hydriding but especially in relation to the final dimensions that the specimen is supposed to achieve. According to Van Houten (Von Houten, 1974), by using particular expedients aimed at inducing as much isotropic growth as possible, it is possible to predict the specimen final dimensions to 0.1%. These expedients mainly consist of adding elements, like carbides or borides,

that prevent large-scale non-isotropic grain growth¹⁰. In fact, without such additions hydriding-induced swelling may or may not be isotropic depending on the material that is hydrided and on the hydriding methodology: “*one combination of raw materials and processes may yield a 9% growth in the x and y directions and a 1% growth in the z direction on one occasion, and yet, with other starting materials and hydriding procedures, the growth along each of the three axes may be substantially identical*” (Von Houten, 1974). Isotropic grain growth is typically achieved by guaranteeing the hydrided structure to be composed of small grains, i.e. by hydriding slowly, and by using the mentioned additives which allow a randomly oriented grain growth. The selection of the best additive to be used for the IPWR metal ingots is not possible at this stage, since experimental verification would be needed. The knowledge of the existence of such additives, and of their effect, is however very important.

X.1.1.3. 2 The hydriding process and its applicability to inverted assembly fuel prisms

Before the ‘60s, due to less advanced technology and to a lack of understanding of the factors affecting the quality of hydriding, metal hydrides were produced “*primarily in granular and powder form and, when required in solid form, they were compacted by powder metallurgical techniques*” (Mueller, 1968). Manufacturing of relatively large hydride specimens from hydride powders has three main disadvantages:

- more time needed to obtain the final product since extra-processes, like powder compacting, are needed;
- possibility of de-hydriding: “*when carrying out conventional forming and shaping operations on the hydride, the hydrogen in the hydride has the pronounced tendency to dissociate from the zirconium or zirconium alloy*” (Simnad, 1964);

¹⁰ The additive used for SNAP reactor fuel was carbon. Studies on fuel growth during irradiation (Birney, 1967) recommended a carbon content of about 0.15% in weight since, above this range, carbon was found to yield an excessive fuel growth upon irradiation. Besides preventing large-scale non-isotropic grain growth, carbon was also found to have beneficial effects on the fuel mechanical properties. A 0.15-carbon weight percentage was found to (Birney, 1967):

- increase the compressive strength (of about 5 times relative to a C-free fuel at room temperature);
- increase the yield stress (of about 1.5 times relative to a C-free fuel at room temperature);
- increase the ultimate tensile strength (of about 3 times relative to a C-free fuel at 790°C);
- decrease the creep rate (of at least two times under 10 MPa stress at 700°C).

- reduced thermal conductivity: powder compacting yields specimens with low thermal conductivity, relative to that of a specimen obtained through casting, even though the density can be close to the theoretical density. This is shown in Figure X- 13, where lithium hydride powder pressed to 99.4% of theoretical density has, depending on the temperature, a thermal conductivity as low as half of that of the cast material.

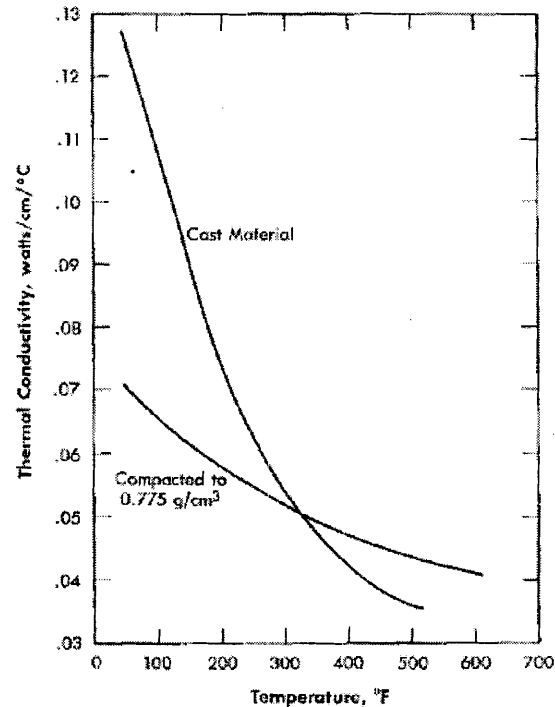


Figure X- 13: Thermal conductivity of lithium hydride in compacted and cast forms (Mueller, 1968)

More recently, U-Zr hydride slugs/pellets were fabricated by hydriding the casted U-Zr ingots discussed in Section X.1. 1, after they have been cleaned. The ingots, in which zirconium is in α -phase, are inserted into a hydriding furnace like that shown in Figure 14, which was previously flushed with a solvent to eliminate any possible hydriding-polluting chemical. Before hydriding takes place, the hydriding chamber, which is contained in an Inconel vessel (referred to as “retort” in Figure X- 14), is evacuated to a

pressure of about 0.1-1 Pa and is heated¹¹ to 760-800°C over a period of time that minimizes the possibility of thermal expansion-induced cracking. The period suggested by Simnad is 1-3 hours (Simnad, 1964), while 20 hours is the recommendation by Eggers (Eggers, 1978). A three-step hydriding is then performed, which can be qualitatively¹² followed in Figure X- 15:

- 1) hydrogen is admitted into the furnace quite rapidly until its pressure reaches about 30 kPa: in this way the H/Zr atom ratio is brought to about unity, which is the terminal solubility of hydrogen in β -Zr, without however having allowed any δ -hydride to form. The pressure during this first phase is about 13 kPa above the equilibrium pressure of the β -Zr/ δ -hydride two phase region, which is 17.3 kPa at this temperature (see Figure X- 12): this is because some hydriding rate-depressing contaminants are normally present in the chamber, and a certain overpressure is needed to compensate for their slowing down effect on the reaction rate.
- 2) hydrogen is then further added, but in smaller pulses, until pressure reaches about 100 kPa. The slow hydrogen admission, which causes formation of δ -hydride, is motivated by the needs to:
 - reduce as much as possible the stresses that generate between the more superficial hydride layers (which are formed first) and the internal metal layers (which progressively turn from ductile β -Zr to brittle δ -hydride);
 - guarantee a continuous equilibrium between the amount of hydrogen supplied to the chamber and the amount of hydrogen diffusing into the specimen, so that an overloading of δ -hydride with hydrogen cannot occur before all the β -Zr is converted into δ -hydride.

¹¹ As can be seen in Figure X- 12, the transition from α -Zr to δ -hydride can in principle be performed below 550°C or between 550 and 860°C. Hydriding below 550°C is not advisable since the system would pass directly from the α -Zr single phase region to the (α -Zr)+(δ -hydride) two-phase region, likely cracking due to the coexistence of a ductile material (α -Zr) with a brittle material (δ -hydride). Conversely, hydriding between 550°C and 860°C has the advantage of reaching a quite high H/Zr atom ratio, i.e. ~1 (Figure X- 12), before any δ -hydride has been formed.

¹² The pressure-hydrogen concentration isotherm diagram that could be drawn using Figure X- 12 would look slightly different from that in Figure X- 15. This is because the Zr-H phase diagram used by Simnad (Simnad, 1964) is a more qualitative diagram than that shown in Figure X- 12.

The H/Zr atom ratio at the end of this phase is about 1.5.

- 3) hydrogen supply is continued but the temperature of the chamber is simultaneously reduced. This is because for the δ -hydride phase the only way to attain a higher H/Zr atom ratio is by increasing the hydrogen solubility, which is a consequence of lowering the temperature. In this way, once a temperature of about 450-500°C is reached, the H/Zr atom ratio has reached a value in the range 1.6-1.8. A period of about 25 hours has passed from the beginning of the hydriding.

The chamber is then reduced to a pressure of about 0.15-0.3 Pa to prevent further hydriding¹³, but the temperature is maintained approximately constant at 450-500°C for about 2 hours to anneal out internal stresses in the specimen. After that, the chamber is allowed to cool to room temperature over a period of about 12 hours and the specimens are removed and are ready for assembling.

¹³ Even though, by increasing the pressure, ratios as high as 2 could in principle be obtained, this is not done since high hydrogen concentrations make cracking more likely to occur (Eggers, 1978).

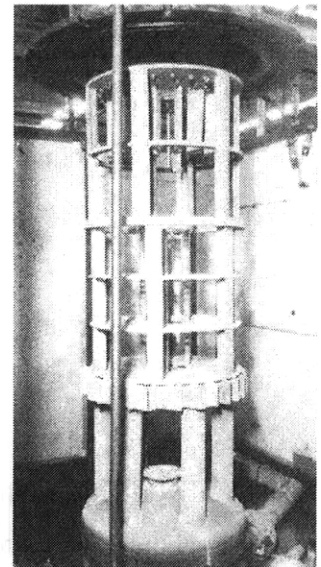
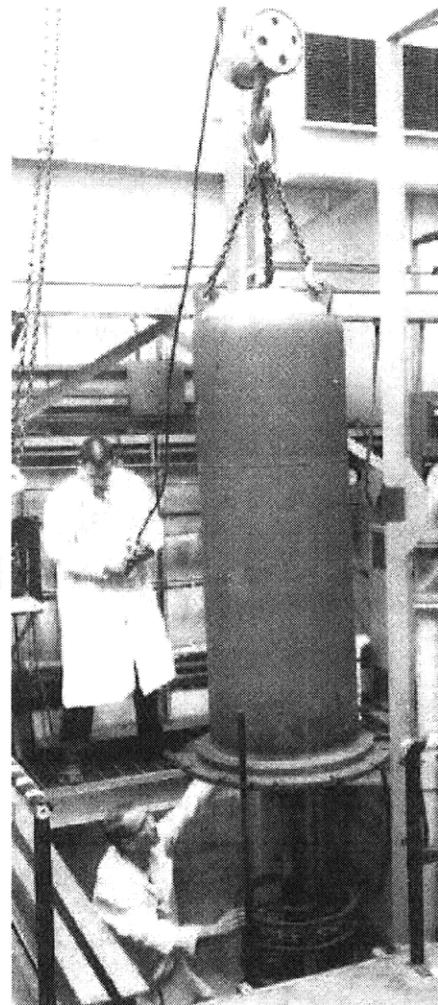
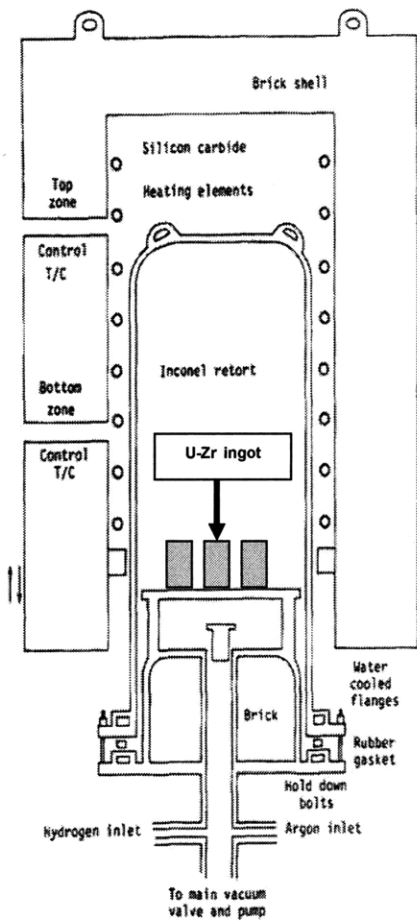


Figure X- 14: Hydriding furnace: complete sketch (left); lifting of Inconel retort from base when the brick shell is removed (centre); inner fixture with zirconium specimens as the Inconel retort is completely lifted (Von Houten, 1974)

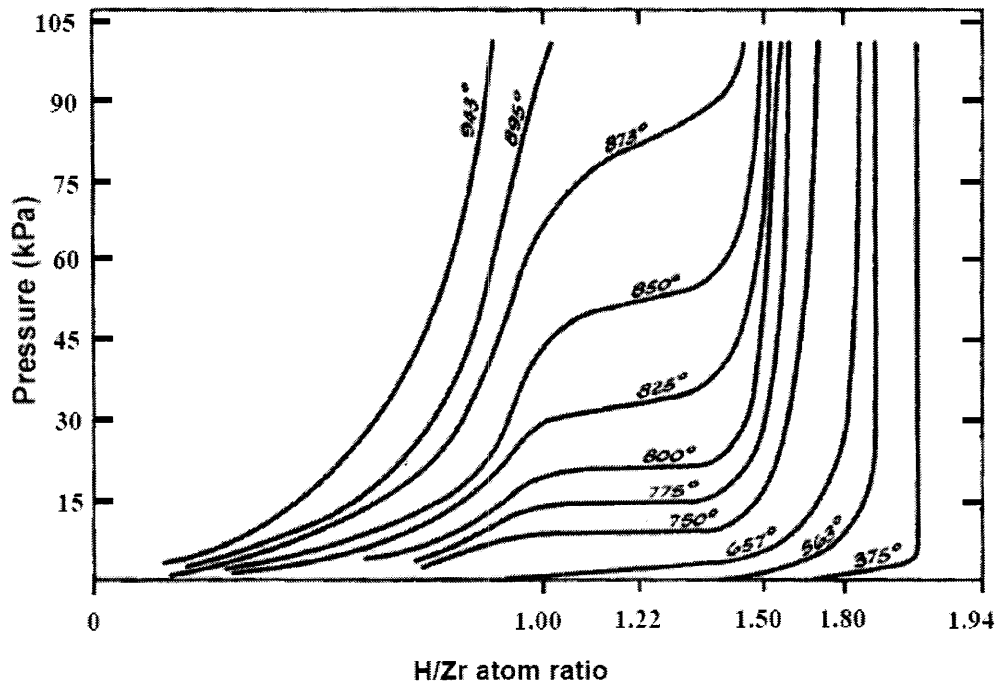


Figure X- 15: Pressure-hydrogen concentration isotherm for U-Zr system, with temperature in °C (adapted from Simnad, 1964)

The two main concerns that typically arise when the hydriding of fuel prisms instead of small pellets is proposed are the volume swelling and the hydriding effectiveness and homogeneity. They have been studied and turned out to be manageable, if not a concern at all, and are discussed as follows.

X.1.1.3.2. 1 Hydriding-induced swelling

As described by Von Houten (Von Houten, 1974), a concern of hydriding large specimens is handling the strain resulting from the swelling. According to the same source, for a base metal of pure Zr brought to zirconium hydride with a hydrogen atom density of 7.1×10^{22} atoms/cm³, the volumetric growth is 18.2%. This volume growth, rounded to 20%, can be used to estimate the dimension changes that a fuel prism would experience during hydriding¹⁴. Since there is no guarantee that swelling will be perfectly

¹⁴ Similar values for the hydriding-induced swelling percentage, i.e. 17.7% and 22.4%, were measured by Terrani et al. (2009A) during the fabrication of Th-containing hydride fuels. Particularly, the 17.7% value was measured for the hydride fuel proposed for the IPWR, i.e. $UTh_{0.5}Zr_{2.25}H_{5.625}$.

isotropic, bounding cases are worth to be examined. The bounding cases assume that, of the prism dimensions that determine the prism volume, i.e. side-to-side distance P_{prism} , height L and hole diameter D_f , only one at a time can actually vary. In this way it is possible to estimate the maximum variation that each dimension would experience during a 20% volume hydriding-induced swelling. The methodology is shown below, where:

- primed parameters refer to post-hydriding conditions, while non-primed parameters to pre-hydriding conditions;
- the dimensions used for the pre-hydriding conditions are those of an inverted assembly design having $N_{holes} = 169$; $P_{prism} = 194.24$ mm; $D_f = 11.63$ mm, while L is left unspecified.

$$\text{Prism volume before hydriding} = V_{prism} = \left(\frac{\sqrt{3}}{2} P_{prism}^2 - N_{holes} \frac{\pi}{4} D_f^2 \right) L$$

$$\text{Prism volume after hydriding} = V'_{prism} = 1.2 \times V_{prism}$$

BOUNDING CASE 1: only P_{prism} varies

$$V'_{prism} = 1.2 \times V_{prism} = 1.2 \left(\frac{\sqrt{3}}{2} P_{prism}^2 - N_{holes} \frac{\pi}{4} D_f^2 \right) L = \left(\frac{\sqrt{3}}{2} P'^2_{prism} - N_{holes} \frac{\pi}{4} D_f^2 \right) L$$

$$\Rightarrow P'_{prism} = 202.80 \text{ mm} \Rightarrow \Delta P_{prism} \% = +4.4\%$$

BOUNDING CASE 2: only D_f varies

$$V'_{prism} = 1.2 \times V_{prism} = 1.2 \left(\frac{\sqrt{3}}{2} P_{prism}^2 - N_{holes} \frac{\pi}{4} D_f^2 \right) L = \left(\frac{\sqrt{3}}{2} P_{prism}^2 - N_{holes} \frac{\pi}{4} D'^2_f \right) L$$

$$\Rightarrow D'_f = 10.63 \text{ mm} \Rightarrow \Delta D_f \% = -8.6\%$$

BOUNDING CASE 3: only L varies

$$V'_{prism} = 1.2 \times V_{prism} = 1.2 \left(\frac{\sqrt{3}}{2} P_{prism}^2 - N_{holes} \frac{\pi}{4} D_f^2 \right) L = \left(\frac{\sqrt{3}}{2} P_{prism}^2 - N_{holes} \frac{\pi}{4} D_f^2 \right) L'$$

$$L' = 1.2 \times L \Rightarrow \Delta L \% = +20\%$$

If the way in which swelling proceeds during hydriding was known with certainty, the pre-hydriding specimen could be designed to be undersized by a preestablished amount

(e.g. -20% in volume), so that hydriding would bring it exactly to the dimensions that the fuel prism is supposed to have just before insertion into the duct, i.e. just before the final assembly. Vice versa, if it was conservatively assumed that the quantitative aspects of swelling are unknown, or not predictable, the pre-hydriding prisms could be designed to be close to the final dimensions, i.e. those they are supposed to have before the final assembly, and hydriding should be followed by removal of the amount of fuel that causes the prism to be “oversized” relative to the as-designed dimensions. Such an amount of fuel is not recyclable as easily as for the material removed during drilling because it is hydrided and cannot be put back into the melting furnace directly. To be recycled it should be de-hydrided, by heating it for example, and only then recycled. Since at this stage nothing is known about the behavior of hexagonal perforated prisms during hydriding, it is not possible to specify the pre-hydriding prism dimensions, and experimental tests are the only way to gain familiarity with the technique.

X.1.1.3.2. 2 Hydriding effectiveness and homogeneity

There are no evident reasons to think that the hydriding effectiveness and homogeneity attainable for U-Zr fuel prisms will be poorer than that for U-Zr slugs/pellets. In the comparison between hydriding a fuel pellet and hydriding a fuel prism, both made of the same U-Zr alloy, it is reasonable to think that hydriding effectiveness and homogeneity mainly depend on the following factors:

- a) effectiveness of hydrogen barrier (e.g. oxides) removal performed before hydriding.
- b) the maximum distance, from the surface of the specimen, that hydrogen needs to travel to hydride the specimen: the larger is this distance the longer is the time to complete hydriding. Also, if some locations inside the specimen are too far from the surface, they may not be hydrided at all. For a fuel pellet, this distance is equal to the pellet radius, while for a fuel prism it is equal to the maximum heat path length in the fuel, introduced in Chapter I:

$$t_{Hf} = \frac{P_f}{\sqrt{3}} - \frac{D_f}{2}$$

where P_f is the fuel cell pitch while D_f is the diameter of the holes in the prism.

- c) the surface to volume ratio of the specimen. The higher is this ratio the higher will be the concentration of hydrogen atoms per unit of volume of specimen.

Point a) was discussed in Section X.1.1. 2, and it was concluded that hydrogen barriers can be removed from a U-Zr prism as effectively as from a U-Zr pellet without the need of any significant addition to the equipment already used in the past for that purpose.

As for point b), the evidence that the mentioned maximum distance does affect hydriding performance was noticed by Vetrano (1962) while comparing hydriding times for solid cylindrical zirconium specimen of different sizes. He defined the hydriding time as the time the hydrogen pressure must be maintained above a certain level in order to reach a satisfactory hydriding. By testing cylindrical specimens having $\frac{1}{4}$, $\frac{1}{2}$ and 1-inch diameter¹⁵, he developed the following empirical equation to predict the hydriding time for those specimens:

$$\Delta t_{\text{hydriding}} = -0.24D^2 + 12.44D - 65.3$$

This hydriding time, which is graphically represented in Figure X- 16, does not include the cooling period and it depends on the temperature/pressure variation steps performed during hydriding. Thus, from the inverted assembly manufacture standpoint, the time-vs-diameter trend should be given more importance than the hydriding time itself, which should be instead interpreted as a ballpark number.

¹⁵ As for more massive specimens, Simnad (1964) states that: “it has been found that if the diameter of the piece is greater than about 1 inch, satisfactory hydriding to hydrogen-to-zirconium atom ratios of 1.5 or more cannot be carried out in a reasonable amount of time”. Specimens of this size needs to be center drilled so that hydriding can progress through the inside surface as well as through the outside surface.

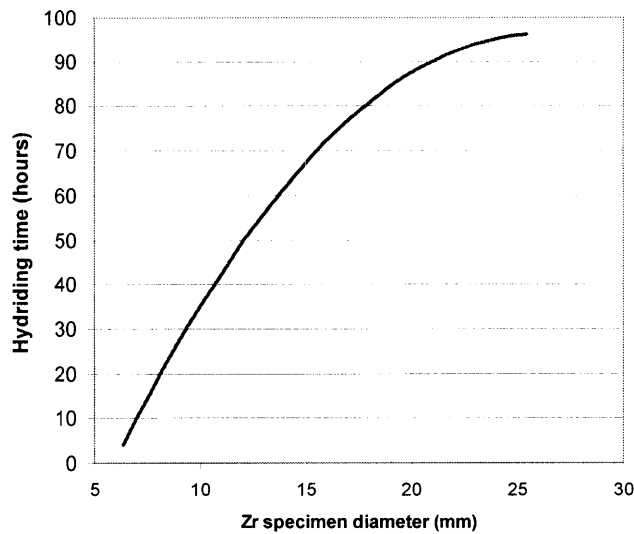


Figure X- 16: Hydriding time vs cylindrical specimen diameter (Vetrano, 1962)

It is evident, from Figure X- 16, that hydriding time is sensitive to the thickness to be hydrided. This is particularly true at small thicknesses where a doubling in thickness implies a 10-fold increase in hydriding time. Table X- 3 compares the maximum hydrogen penetration depth, t_{Hf} , as well as the specimen area to volume ratio mentioned at point c) above, between a pellet and two fuel prisms. The pellet is assumed to have a diameter of 12.94 mm, which is typical of TRIGA reactors, while for the prisms the following two geometries are considered:

- Prism A (representative of a prism for non-collapsible duct design)
 - flat-to-flat distance: 91 mm;
 - number of holes in the prism: 37;
- Prism B (representative of a prism for collapsible duct design)
 - flat-to-flat distance: 195 mm;
 - number of holes in the prism: 169;

both with holes having diameter of 11.85 mm and fuel web thickness of 2.75 mm. The comparison of the surface to volume ratio is made for two different heights of the

specimen: 8 and 16 mm (to bind the heights recommended for the fuel prism and listed in Table X- 1). It can be seen that:

- the maximum distance that hydrogen needs to travel to fully hydride the prism is about 2.5 times smaller than for the TRIGA pellet;
- the prisms considered have a surface to volume ratio 30% to 40% larger than a TRIGA pellet.

Maximum distance from the surface, t_{Hf} (mm)		Specimen height (mm)	Surface to volume ratio (mm^{-1})		
Pellet	Prism A and B		Pellet	Prism A	Prism B
6.47	2.50	8	0.559	0.744	0.737
		16	0.434	0.619	0.612

Based on these observations, and based on the fact that a homogeneous hydriding of TRIGA pellets was achieved in the past, hydriding a prism for inverted assembly should not pose any particular challenge and may be even easier to perform. This is consistent with the description that Simnad (Simnad, 1964) gives of the process he and his colleagues patented: “*by utilizing the method of the present invention, any desired forming operations can be performed on the relatively easily fabricable zirconium metal or zirconium alloy and the necessity of carrying out such operations on the difficultly fabricable hydrides is obviated*”.

X.1.1. 4 Fuel prism shaping/sizing

Because of the density changes occurred during hydriding, the post-hydriding specimens have extra-material that needs to be removed in order to bring the specimen to the as-designed dimensions. In the particular case of the inverted assembly fuel prism, the cooling channel holes need to be bored out and the hexagonal flats as well as the two bases need to be machined. Shaping/sizing processes were performed at GE-ANDP for Zr-hydride hollow bars, from 76 to 91 cm in length and with an inner diameter of about 6 cm (see Figure X- 17), which required removal of as much as 3 mm of thickness from both the inner and the outer surfaces. The circular inner contour was bored out using

high-speed tool bits, and very precise dimensions were easily obtained. The outer surfaces were machined with fly cutters, milling cutters and silicon carbide and diamond grinding wheels (Mueller, 1968).

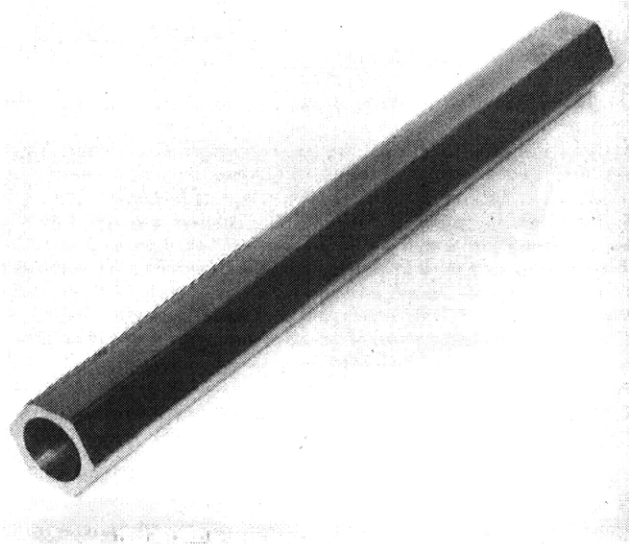


Figure X- 17: Machined section of hydrided zirconium (Mueller, 1968)

Relative to those described above, shaping/sizing processes would not differ in the case of a fuel prism for inverted assembly. Because of the large number of surfaces to finish, only a longer time would be required relative to that required for a specimen like that shown in Figure X- 17.

X.1.1. 5 Fuel prism superficial oxidation

Superficial oxidation is aimed at improving the hydrogen retaining capability of the hydrided specimen. Hydrogen loss during operation is to be avoided for several reasons:

- it can cause phase changes and consequent additional mechanical stresses in the fuel due to lattice expansion/contraction;
- it can cause swelling (Stadnik, 1988);
- it causes the fuel to have a lower moderation power. Although the reactivity loss consequent to the de-hydriding is a negative neutronic feedback typically used to highlight the inherent safety of hydride fuels, the hydrogen lost cannot re-hydrate the fuel at a later time because of the presence of a) the oxide layers on the

surface and b) the liquid metal bond (the latter only in assemblies adopting the non-collapsible duct design);

- it can cause embrittlement of the clad in case the hydrogen lost diffused into it¹⁶;
- it causes internal overpressurization of the assembly.

Even though superficial oxidation was not performed during the manufacture of pellets/slugs for TRIGA reactors, it is recommended for fuel prisms based on the arguments supported by Eggers (Eggers, 1978). According to Eggers, as oxides act as barriers against hydrogen permeation during hydriding, they also act as barriers against hydrogen loss from a hydrided specimen. This would allow increasing the maximum temperature at which fuel can safely operate in the reactor, since hydride-fueled reactors are protected against fuel de-hydriding by limiting the fuel temperature. Hydrogen loss from U-ZrH_{1.6} becomes significant above about 765°C, that is when hydrogen partial pressure approaches one atmosphere. TRIGA reactors are designed to operate at fuel temperatures between about 300°C and 500°C, except for pulsing operation during which higher temperatures are momentarily reached. Continuous operation of TRIGA fuel above 500°C should be avoided *“because there should be some leeway in the case of emergency situations so that any unexpected rise in temperature can be arrested before such a large amount of dissociation takes place”* (Eggers, 1978). As a measure of the enhanced hydrogen retaining capability of an oxidized specimen, Eggers states that a 5-10 mils (0.127-0.254 mm) thick zirconium oxide layer on the surface of a ZrH_{1.56} specimen reduces the hydrogen dissociation pressure at 1100°C from 40 atmospheres to only 4 atmospheres. *“Testing shows the fuel element is suitable for use in a nuclear reactor operating at a temperature of above 800°C”* (Eggers, 1978).

Eggers suggests several ways to oxidize the specimen outer surface: some seem feasible, like the insertion of the hydrided specimens into an oxygen atmosphere at 300°C for 15

¹⁶ In the SNAP reactor design, the inside surface of the cladding was covered with a 0.05-0.075 mm thick ceramic coating made of a mixture of silicon, barium, titanium and aluminum oxides, aimed at minimizing hydrogen permeation (Stadnik, 1988). The presence of this coating was necessary in the SNAP design, more than it actually is in the PWR inverted design under examination. This is because the fuel-clad gap could not be too wide, otherwise the thermal resistance of the gap, which was hydrogen-bonded, would have caused the fuel to reach excessive temperatures (Birney, 1967). In the IPWR the gap is either filled with liquid metal (non-collapsible duct design) or it closes right after the reactor is brought to nominal pressure (collapsible duct design).

minutes, while some others do not seem applicable (e.g. introduction of oxygen-providing chemicals, such as water or solid CO₂, between the fuel and the clad during fuel rod assembling). Based on the results shown in Figure X- 10, and based on the strong tendency of zirconium (and zirconium hydride) to spontaneously oxidize when exposed to air, it is recommended to let the hydrided specimens spontaneously oxidize, at room temperature in an oxygen-rich atmosphere, after they have been hydrided and brought to room temperature.

X.1. 2 Securing of the short-length twisted tapes (for S-IPWR design only)

The CHF performance of two of the three proposed IPWR designs, i.e. the H-IPWR and the S-IPWR, are enhanced by means of twisted tapes (TTs).

In the H-IPWR a ~1.6 m long tape is inserted in the top region of each cooling channel, and welded to it at the channel exit. This securing technique should not pose particular challenges since (1) long TTs are widely used in heat transfer devices (see Manglik and Bergles, 2002) and a lot of experience has been gained about their securing to the tubes, and (2) the exit of the channels, i.e. where the TTs need to be secured, is a low neutron flux region and irradiation-induced deformation of the TTs and of the tubes is expected to be negligible.

The S-IPWR design employs short-length twisted tapes (SLTTs) which, relative to full-length TTs, have the advantage of providing the same, or nearly the same CHF enhancement, but with a 1.5-2 times lower pressure drop (see Chapter V in this Volume or Section 10 in Volume 2). This advantage comes, however, with more challenging installation and securing methods, as well as with concerns during reactor operation. Concerning installation, the solution proposed consists of securing the SLTTs by swaging down the tube outer diameter. Specifically, the tapes have to be manufactured with a width as close as possible to the tube inside diameter, inserted up to the desired axial location and secured by swaging down the tube outer diameter locally, i.e. either along the whole TT length, or just in correspondence to the two TT ends. This technique, applied to the manufacture of the test sections used for the pressure drop measurements described in Volume 2, was verified to be feasible, easy to perform and inexpensive. Technical improvements are possible, especially if the implementation is performed at an

industrial scale, and may include, for example, the selection for the tapes of a material softer than the tube material. This, together with carefully controlling the tube diameter compression and choosing the right tube wall thickness, would allow the TT-tube contact to result in a controlled penetration of the tape profile into the tube wall. Also, optimization of the tube compression technique would be advisable: due to limited financial resources, for the test section manufacture described in Volume 2 the tube compression was performed with compression fittings. Tube swagers, widely used in the mechanical industry, can be adapted to the needs of the IPWR design.

Two other TT securing techniques, which were envisioned but not verified experimentally, are:

- inside tube surface threading: the tube inside surface is threaded through the whole length, so that the thread pitch coincides with the TT pitch. The thread vane is then locally blocked, at the axial location where the terminal edge of the last tape will be located. A TT is then screwed inside the tube, until its axial progression stops due to the vane blockage. Vane blockage is then performed at the tape inlet edge. The same procedure is then repeated for the other tapes. This technique, although more involved than the one suggested for the IPWR assembly manufacture, would allow for an increase in TT spacing, with consequent pressure drop reduction, thanks to the contribution to swirl flow generation given by the thread.
- TT welding to the tube inside surface.

An important issue, which needs to be addressed through experimental work, concerns the safe operation of SLTTs during reactor operation. In fact, even if the tapes are well secured at Beginning Of Life (BOL), they may become loose during fuel burning because of irradiation-induced deformation of the tubes. Because of the high coolant velocities characterizing the IPWR (~9-10 m/s), they may be expelled from the cooling channels as high-speed projectiles. This is an important safety concern that, if confirmed, will cause the S-IPWR design to be rejected.

X.1.3 Final assembling

Once the fuel prisms are fabricated, the cooling channels eventually assembled (for H-IPWR and S-IPWR designs only, while they are simply empty tubes in the E-IPWR design) and the hexagonal duct and perforated upper and lower cap manufactured, the final assemble can be performed. The assemble procedure differs depending on whether helium is used as gap filling material (collapsible duct design) or if liquid metal (Pb-Sn-Bi eutectic) is used for this purpose (non-collapsible duct design). For IPWR assemblies provided with collapsible ducts which, based on power performance considerations, is the preferred design, the assembly consists of the following phases:

- a) welding of assembly lower cap to hexagonal duct;
- b) insertion of cooling tubes into lower cap holes and welding of the tubes lower end to the cap;
- c) stacking of ~ 1 cm tall fuel prisms inside the duct, with the cooling tubes into the fuel prism holes;
- d) evacuation of the assembly and placement in low pressure He atmosphere;
- e) welding of the assembly upper cap to the duct and to the upper end of the cooling tubes.

For the IPWR assemblies provided with non-collapsible ducts the procedure is more challenging, and consists of the following phases:

- a) same as a) above;
- b) same as b) above;
- c) stacking of fuel prisms inside the duct, with the cooling tubes into the fuel prism holes;
- d) evacuation of the assembly and heating up to about 130°C ;
- e) liquid metal (LM), at about 130°C , is poured on top of the last fuel prism, and it is allowed to flow down through the fuel-duct gaps; vibrations are induced throughout the assembly body as to favor liquid metal distribution.

- f) slight pressurization with helium followed by welding of the assembly upper cap to the duct and to the upper end of the cooling tubes, and cooling down.

Alternatively, instead of pouring LM onto the fuel prism stack, solid Pb-Sn-Bi can be placed on the duct lower cap, fuel prisms then stacked above it, the assembly evacuated and then heated. This is the method recommended by Wongsawaeng and Olander (2007) to prevent formation of potential hot spots. They verified that, if no measures are taken to address this issue, voids are created when stacking UO₂ pellets into a Zircaloy tube filled with LM, at atmospheric pressure. They were able to eliminate the voids by first evacuating the tube loaded with the pellets and the solid eutectic, then by melting the latter and finally by applying at least 0.5 MPa of He overpressure.

X. 2 Conclusions on inverted assembly manufacture

The phases leading to the manufacture of the inverted assembly have been examined, and manufacture methods have been presented.

Assembly components such as cooling channel tubes and assembly duct can be easily fabricated, and do not require customized techniques relative to components routinely fabricated in the mechanical industry.

For the S-IPWR assemblies, a method for inserting and securing the short-length twisted tapes has been experimentally tested, and confirmed to be feasible. Concerns arose however about the stability of the tapes during reactor operation since, due to irradiation-induced deformation of the tubes, tapes may become loose and be expelled from the cooling channels as projectiles.

Fuel prism fabrication was found to be the most challenging phase of the inverted assembly manufacture. The following fabrication phases have been proposed:

- 1) casting base metal (U-Th-Zr) ingots;
- 2) ingot gun drilling;
- 3) ingot cleaning;
- 4) ingot hydriding;

- 5) ingot shaping/sizing;
- 6) ingot superficial oxidation,

A detailed literature review was performed, to understand hydriding techniques developed in the past for the manufacture of U-ZrH_{1.6} pellets and slugs, and of more massive hollow bars made of ZrH_{1.6}. Their extension to U-ZrH_{1.6} fuel prisms was concluded to be feasible. Unlike pellet and slugs, the IPWR fuel prisms are provided with holes which, in the ingot fabrication phase, require drilling. Pre-hydriding gun drilling of ~0.7 to 1.6 cm tall prisms (depending on the hole diameter), followed by recycling of burr material into the melting furnace, was verified to be the best way to create the holes. Appropriate tools would be required for the pre-hydriding cleaning phase because hole inner surfaces, in addition to the typical outer ones, will have to be cleaned to enhance hydrogen permeation. Relative to the hydriding of small pellets, the hydriding of perforated prisms was concluded to be attainable in less time and with a higher degree of homogeneity, due to their larger surface-to-volume ratio.

The same conclusions can be extended to the manufacture of Th-containing fuel prisms. However, while nothing would change for most of the manufacture phases, the behavior of the specimen during hydriding will be different, therefore requiring different pressure/temperature variation steps, and would probably be characterized by hydriding-induced swelling of a different extent. Manufacture of small U-Th-Zr-hydride specimens is documented in the literature, which proves the feasibility of the hydriding phase. More experimental work would however be needed to optimize the manufacture of massive prisms.

Methods for assembling the various components and thus obtaining the final product, i.e. the IPWR assembly, have been proposed. They were found to be feasible for the IPWR assembly with collapsible duct. Because of the need to liquid metal bond the gaps, the assembly of the same product but provided with a non-collapsible duct was instead found to be challenging. This aspect, together with the power performance degradation resulting from the small assembly size and thick duct walls, significantly compromises the competitiveness of the latter assembly design.

Chapter XI

IPWR design selection

This chapter presents the performance of the IPWR resulting from the application of all the design constraints summarized in Chapter III and described in Chapter IV through Chapter X. Most of the details on constraint calculation methods are not presented here, and can be found in the previous chapters.

The main objective of this chapter is to identify a promising IPWR design, and to fully characterize it in terms of geometry, power performance, fuel enrichment and cycle length. To do this, the various IPWR designs examined throughout the analysis will be compared to each other. Also, their power performance will be compared to those of pin geometry PWRs examined by Shuffler et al. (2009), using the same pressure drop limit for both designs. For convenience, the acronyms used for the IPWR designs as well as the main features characterizing each are summarized as follows¹:

- E-IPWR: IPWR design in which the cooling channels are empty tubes, i.e. tubes not provided with turbulence promoters;
- H-IPWR: IPWR design in which a long twisted tape (TT) is located in the top 1.6 m of each cooling channel;
- S-IPWR: IPWR design in which multiple short-length twisted tapes (MSLTTs) are located in the top half of each cooling channel (geometric details are given later).

Each of these designs can adopt a non-collapsible or a collapsible duct. As a consequence, a total of six IPWR designs can potentially be presented. However, not all of them will be examined with the same level of detail since some showed poor power performance and, consequently, are not analyzed in all the aspects needed for the complete reactor characterization. Such

¹ The first letter of the acronyms used indicates the type of channel: “E” stands for “Empty” and “S” stands for “Short length TTs”. “H” is used to indicate “Half-length TTs” even though the length of the corresponding tapes, i.e. 1.6 m, is slightly smaller than half of the heated length (1.83 m).

characterization, as discussed in Section III.1.1 of Chapter III, was performed through four analysis phases, which are repeated here for convenience:

- Phase 1: application of structural constraints;
- Phase 2: application of steady-state thermal hydraulic constraints;
- Phase 3: LBLOCA analysis of an IPWR design/geometry that, among those attaining the highest power levels upon application of the constraints of Phases 1 and 2, is considered promising, and determination of the maximum power satisfying LBLOCA constraints;
- Phase 4: application of neutronic constraints to the selected IPWR design/geometry, using the power level determined in Phase 3.

The results of each analysis phase are presented in Section XI. 1 (Phase 1), Section XI. 2 (Phase 2), Section XI. 3 (Phase 3) and Section XI. 4 (Phase 4). Section XI. 5 concisely characterizes the final IPWR design.

XI. 1 IPWR core geometry characterization

The application of the structural constraints (see Table III-1 in Chapter III) allowed characterizing the core geometry, in terms of number of assemblies, number of fuel cells and consequently heavy metal loading. Since the presence of CHF enhancement devices, i.e. twisted tapes, only affected the core power performance but not the core construction, distinction between core geometry maps is only made depending on whether the IPWR adopts collapsible or non-collapsible ducts. Because of the different flat-to-flat distance and wall thickness, the type of duct has an important effect on the core geometry. These differences, obtained through the methodology discussed in Chapter IV, are summarized in Table XI- 1.

Table XI- 1: Duct key characteristics				
	Base values ²			
	P_{duct} (mm)	t_{duct} (mm)	Duct-fuel gap width, $t_{gap,out}$ (mm)	L_{duct} (m)
Collapsible duct	219	9	0.2	3.8
Non-collapsible duct	100	5.8	2	4.1-4.6

Figure XI- 1 and Figure XI- 2 show the total number of fuel cells contained in the core (left plots), and the ratio, $N_{c, ratio}$, between this number and the number of subchannels contained in the reference, pin geometry PWR (Seabrook USAR, 2002) (right plot), for the collapsible and non-collapsible duct design respectively. The right plots also show, with the dashed line, the D_{ci} - t_{web} combinations corresponding to inverted cells having the same cross sectional area as that of the pin geometry cell of the reference PWR³. It can be seen that the number of fuel cells that can be fit into the core ranges between 1.4×10^4 and 6.9×10^4 for the collapsible design, and between 1.1×10^4 and 5.2×10^4 for the non-collapsible design. Therefore, the non-collapsible design suffers from a 30% reduction in amount of fuel that can be loaded into the core, with respect to the collapsible one. This reduction significantly penalizes any IPWR adopting the non-collapsible duct design. As can be inferred from Table XI- 1, this is due to the small size and, in proportion to such size, thicker walls characterizing the non-collapsible duct relative to the wider collapsible one. Because of this, and since the inter-assembly water gap width is fixed to 12.24 mm in both designs, the fuel prisms occupies ~72% of the core cross section in the collapsible design, while only 59% in the non-collapsible design.

² The “base” values are, as discussed in Chapter IV, the values used for constructing the assembly. The final duct dimensions, which depend on the duct design (collapsible or non-collapsible) and, with a less extent, on the D_{ci} - t_{web} pair of interest, do not coincide with these base values but are very close to them. This is because the assembly sizing method was performed, for each D_{ci} - t_{web} combination, by searching for the fuel prism size that more closely matches that corresponding to a duct having geometry identified by the base values. Since an assembly can only contain an integer number of fuel cell rings, the number of rings was rounded up or down to satisfy this requirement, thus leading to duct sizes that are close, but not equal, to those associated with the specified “base” values.

³ The cross sectional area of the pin geometry cell is simply equal to the fuel rod pitch squared.

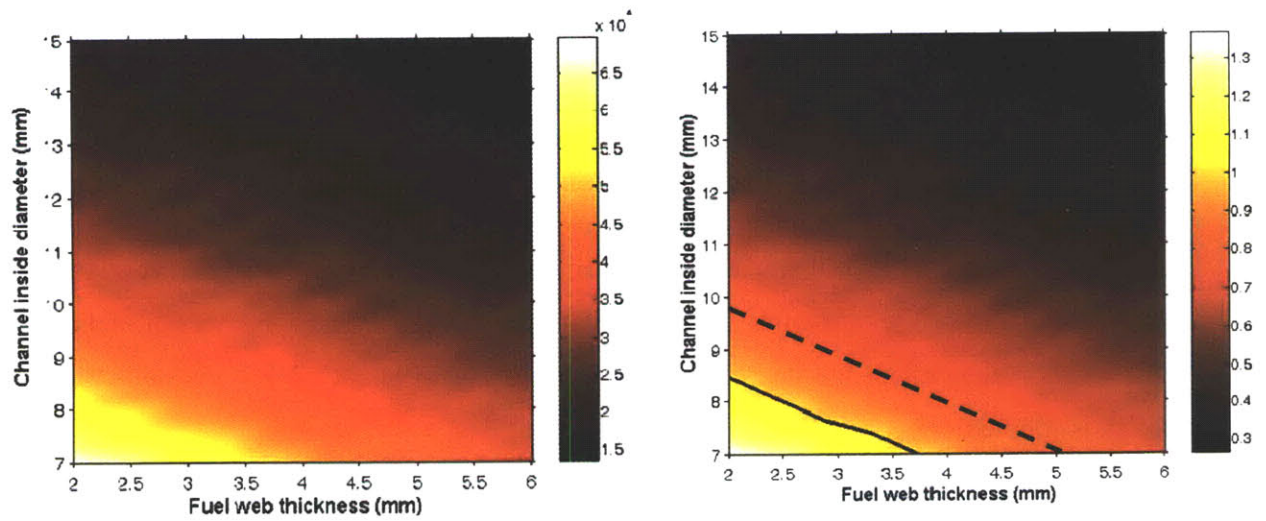


Figure XI- 1: Number of fuel cells in the core (left) and $N_{c,ratio}$ (right) for collapsible duct design (solid line indicates $N_{c,ratio}=1$, dashed line indicates $A_{cell}=A_{cell,ref_pin}$)

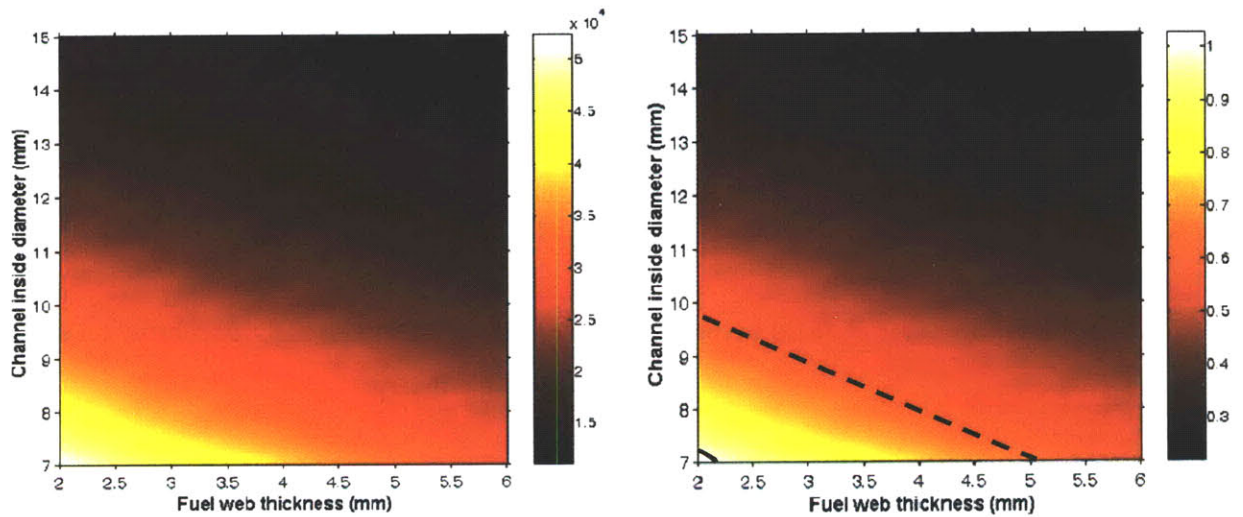


Figure XI- 2: Number of fuel cells in the core (left) and $N_{c,ratio}$ (right) for non-collapsible duct design (solid line indicates $N_{c,ratio}=1$, dashed line indicates $A_{cell}=A_{cell,ref_pin}$)

The inverted geometries laying between the solid and the dashed line in the right plots of Figure XI- 1 and Figure XI- 2 have an important feature: in spite of occupying a smaller area than the pin cell of the reference PWR, their total number in the core is smaller than the number of cells contained in the reference PWR. This is the effect of the discontinuities (thick wall ducts and wide inter-assembly water gaps) introduced in Chapter I. For the inverted cells laying on the

dashed lines, $N_{c,ratio}$ is equal to about 0.8 for the IPWRs adopting the collapsible duct design, while it is about 0.6 for those adopting a non-collapsible duct. If the IPWR did not have large discontinuities, $N_{c,ratio}$ would be unity for these geometries. The effect of the discontinuities characterizing the IPWR is clearly shown in Figure XI- 3, which presents the ratio, averaged over all the $D_{ci}-t_{web}$ combinations, between the actual number of fuel cells contained in the core and the number of fuel cells that would be contained if the inverted geometry was continuous⁴. It can be seen that the discontinuities are responsible for a reduction, in the number of fuel cells, of about 29% if the collapsible duct design is adopted, and of about 50% if the non-collapsible design is adopted.

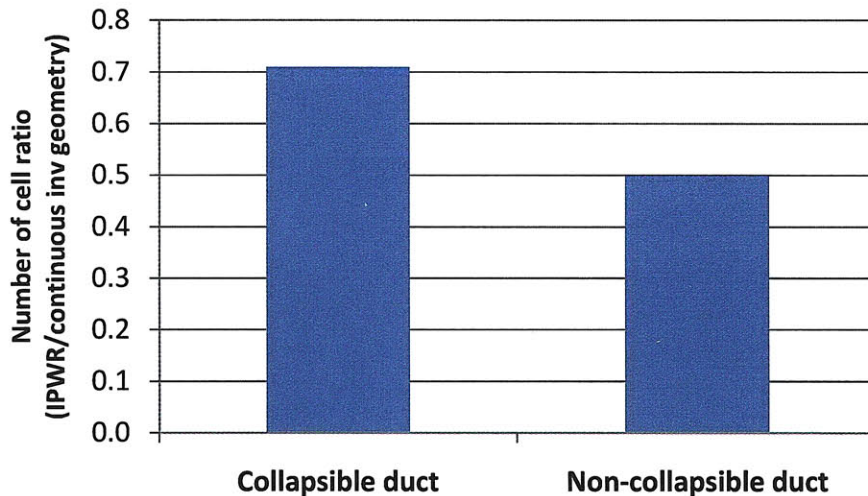


Figure XI- 3: Average ratio between total number of fuel cells and number of cells of a continuous inverted geometry

It is important to note that the IPWR adopting non-collapsible ducts is penalized, relative to that with collapsible ducts, not only by the fewer cells, but also by the increased height of the ducts which, as shown in Table XI- 1, ranges between 4.1 and 4.6 m versus 3.8 m of the collapsible design⁵. The smaller number of cells, 29% less on average throughout the geometry spectrum considered, has two consequences on the reactor performance: a smaller fuel loading, which translates in either a shorter cycle length or in a higher enrichment, and a reduced flow area

⁴ The number of fuel cells of a continuous inverted core was calculated by dividing the core area (not including the area between the outermost assembly ring and the core shroud) by the area of the unit cell.

⁵ As discussed in Chapter IV, the longer height of the non-collapsible duct is required to provide a plenum large enough to accommodate the liquid metal that, upon fuel swelling and duct creepdown, is squeezed out from the fuel-duct and fuel-clad gaps.

which, together with the increased height, impacts pressure drop. Since, as demonstrated in Appendix I-A of Chapter I, the friction pressure drop is proportional to $A_{flow}^{1.8}$, for the same active mass flow rate and neglecting the difference in height an IPWR with non-collapsible ducts has a pressure drop about $1.29^{1.8}=1.58$ times larger than that of the design adopting collapsible ducts. If an average height equal to 4.3 m is considered for the non-collapsible ducts, and the difference in height with respect to the collapsible ducts is accounted for, the pressure drop penalty increases to $1.58 \times 4.3 / 3.8 = 1.79$.

In addition to the cycle length and/or enrichment penalty and the pressure drop penalty, the non-collapsible duct design was also found much more challenging to manufacture than the collapsible design, due to the need of bonding the fuel-clad and fuel-duct gaps with a liquid metal. For all these reasons, the IPWR design adopting non-collapsible ducts was not examined further, and the attention was focused on the collapsible duct design only.

Figure XI- 4 and Figure XI- 5 show the fuel and coolant volume fraction respectively. In each figure, the plot on the left refers to a volume fraction calculated at cell level, i.e. without accounting for the duct and the inter-assembly water gap, while the plot on the right refers to the whole core. Since the water gaps contribute to the whole core coolant volume fraction, the reduction in volume fraction resulting from moving from cell-level to whole-core is larger for the fuel than for the coolant. For example, the geometry having $D_{ci}=10.79$ mm, $t_{web}=2.9$ mm has cell-level fuel and coolant volume fractions equal to 0.397 and 0.432, while the corresponding whole-core values are 0.318 and 0.405.

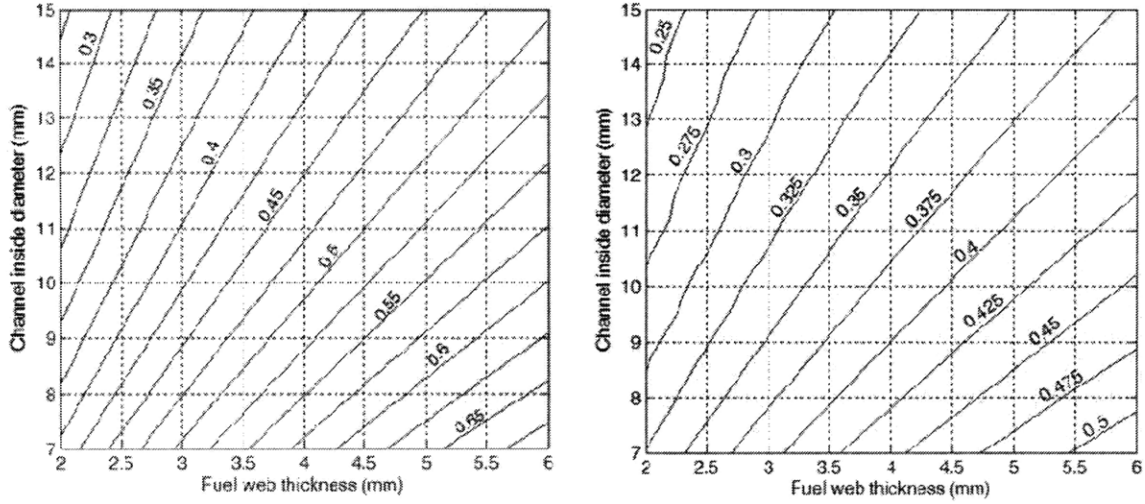


Figure XI- 4: Fuel volume fraction at cell level (left) and at whole core level (right, for collapsible duct design)

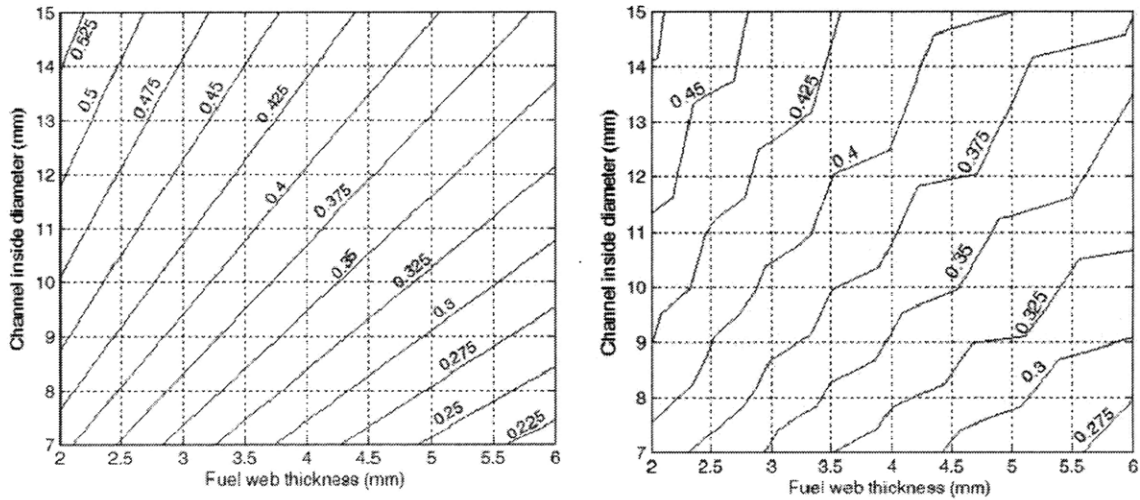


Figure XI- 5: Coolant volume fraction at cell level (left) and at whole core level (right, for collapsible duct design)

XI. 2 Power maps

The key result of the steady-state analysis performed on the IPWR designs is the maximum achievable core power. This power is a function of:

- the IPWR design considered: E-IPWR, H-IPWR or S-IPWR;

- the pressure drop value chosen as limit;
- the lattice geometry, i.e. the $D_{ci}-t_{web}$ combination.

As mentioned in Chapter III, the core pressure drop is not a hard constraint, i.e. limit values were not chosen to prevent failure mechanisms (like instead for MCHF or maximum fuel temperature limits), but rather to comply with the current pump technology and to investigate the power performance enhancement that would result from a near-term advancement in such technology. This is why three core pressure drop limits were considered: the reference core pressure drop (X), 1.5 times this value (1.5X) and 2 times this value (2X).

The following sections show the power maps corresponding to the three IPWR designs. When present, a dashed line separates IPWR geometries having higher power than the reference PWR, i.e. 3.411 GW_{th} (Seabrook USAR, 2002), from those with lower power. Each power map is presented together with the corresponding limiting constraint map, which shows the constraints that limit the power, and the region where they act. The steady-state cladding temperature, which was used as constraint, is never limiting and thus it does not appear in any of the constraint maps.

XI.2. 1 E-IPWR power maps

Figure XI- 6, Figure XI- 7 and Figure XI- 8 are the power maps for the E-IPWR design, referred to the X, 1.5X and 2X pressure drop limits respectively.

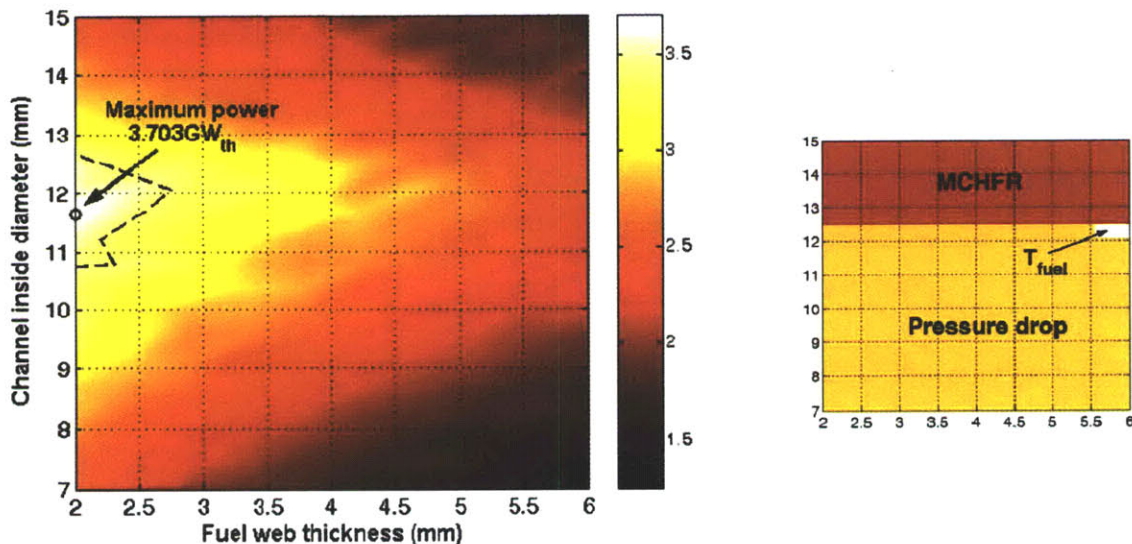


Figure XI- 6: Power map and limiting constraint map for E-IPWR ($\Delta p=X$)

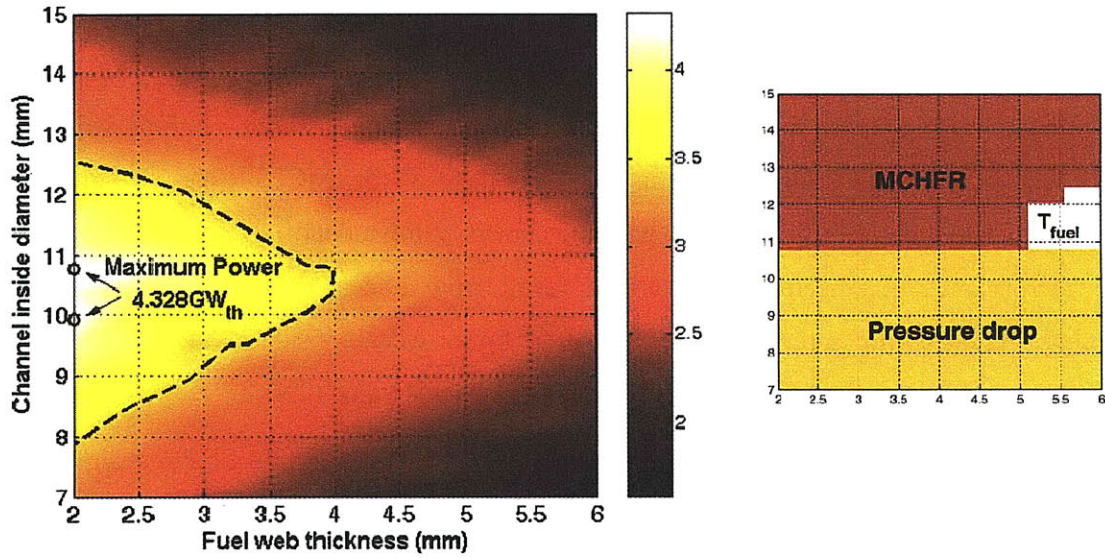


Figure XI- 7: Power map and limiting constraint map for E-IPWR ($\Delta p=1.5X$)

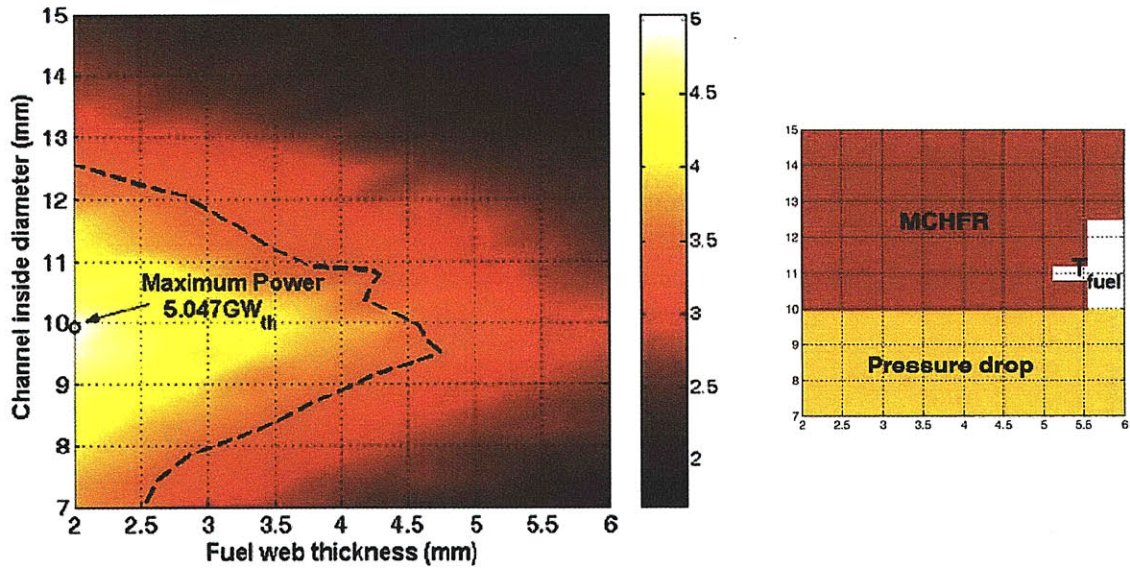


Figure XI- 8: Power map and limiting constraint map for E-IPWR ($\Delta p=2X$)

XI.2. 2 H-IPWR power maps

Figures XI-9 through XI-11 are the H-IPWR power maps, referred to X, 1.5X and 2X pressure drop limits. The TT occupying the last 1.6 m of each channel has a twist ratio equal to 2.5.

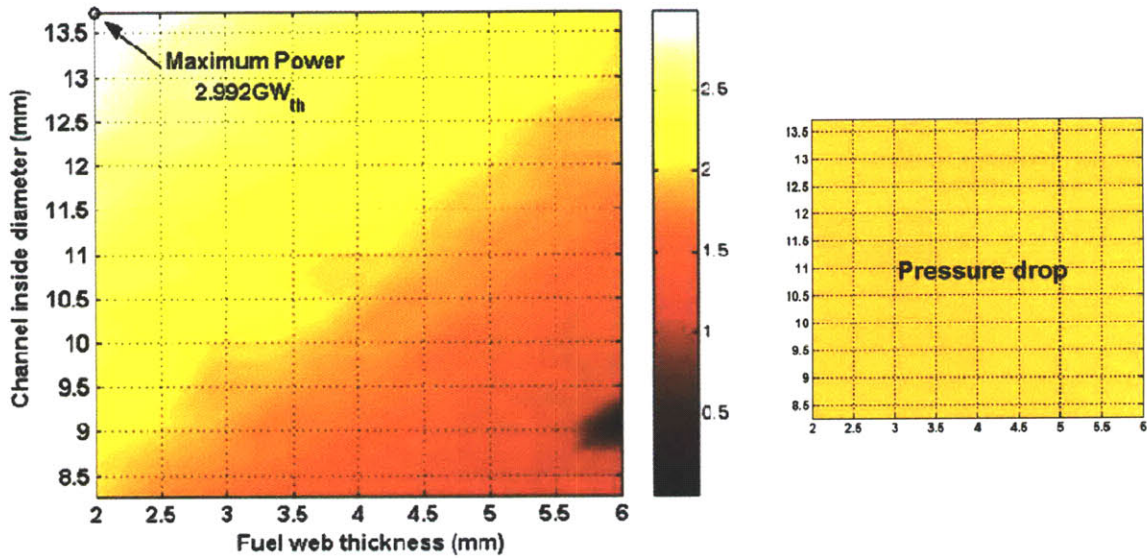


Figure XI- 9: Power map and limiting constraint map for H-IPWR ($\Delta p=X$)

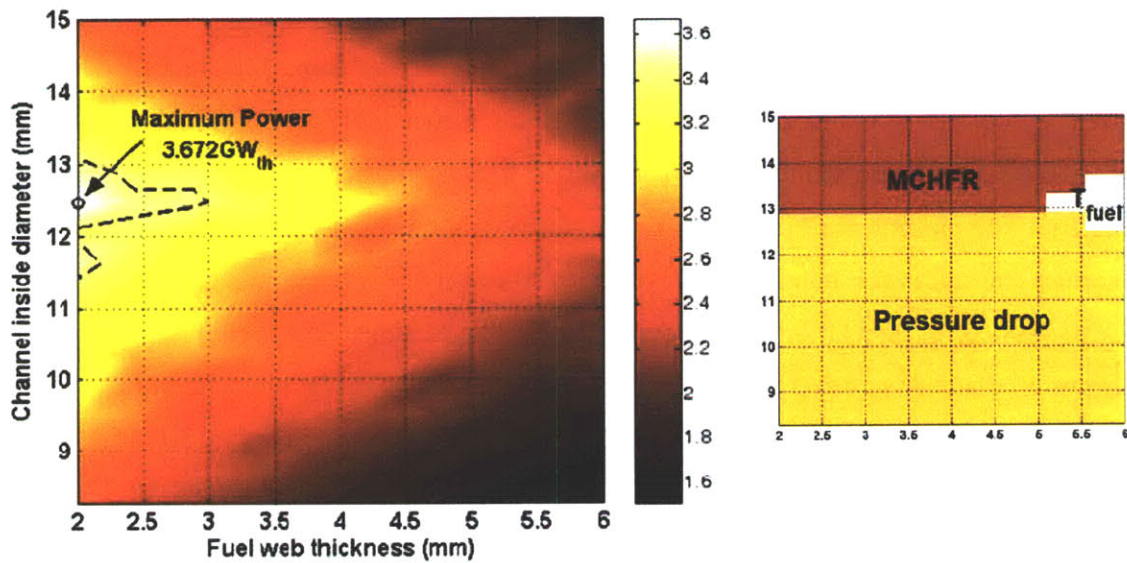


Figure XI- 10: Power map and limiting constraint map for H-IPWR ($\Delta p=1.5X$)

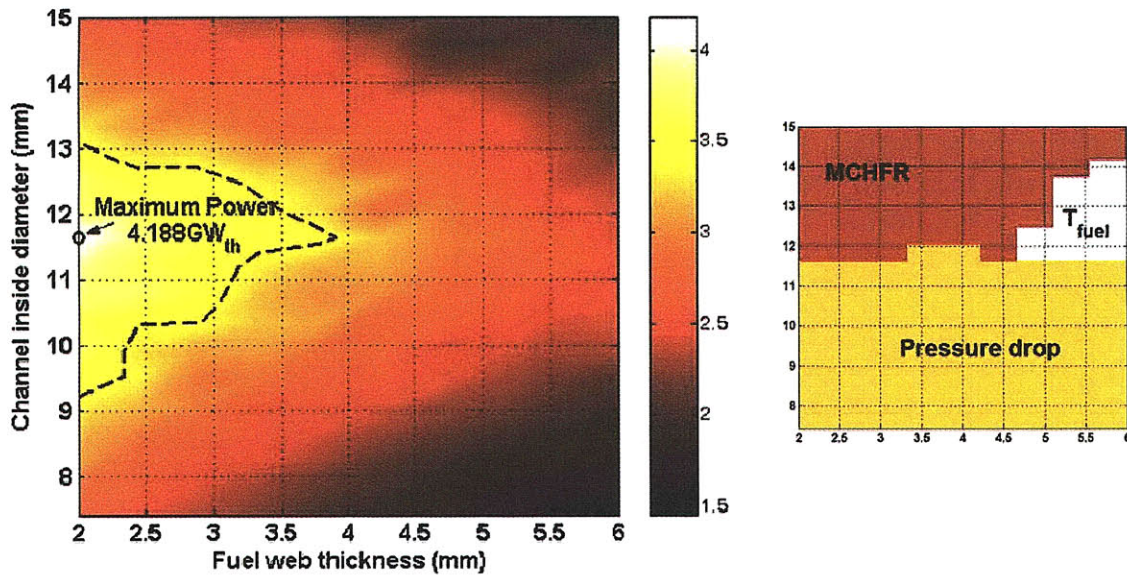


Figure XI- 11: Power map and limiting constraint map for H-IPWR ($\Delta p=2X$)

XI.2. 3 S-IPWR power maps

Figure XI- 12, Figure XI- 13 and Figure XI- 14 are the power maps for the S-IPWR design, referred to the X, 1.5X and 2X pressure drop limits respectively. The S-IPWR to which the figures refer is provided with SLTTs having twist ratio equal to 1.5 and spacing equal to 50 diameters⁶. The placement of the first TT is performed automatically by the Matlab code, which determines the minimum number of TTs needed to cover the top 1.6 m of the core. Since, to allow pressure drop calculations⁷, fractions of swirl decay regions are not allowed, the last SLTT is always 50 diameters away from the channel exit. Since the channel diameter varies across the power maps, the number of SLTTs per channel also varies, as shown in Figure XI- 15.

⁶ 1.5 and 50 are the minimum twist ratio and the maximum spacing, respectively, tested during the pressure drop measurements discussed in Volume 2. SLTTs having smaller twist ratio or larger spacing are outside the geometry range to which pressure drop data collected during the tests can be applied.

⁷ The pressure drop measurements discussed in Volume 2 were always performed between integer numbers of SLTT modules. A SLTT module is defined as the length of channel comprised between the inlets of two successive SLTTs.

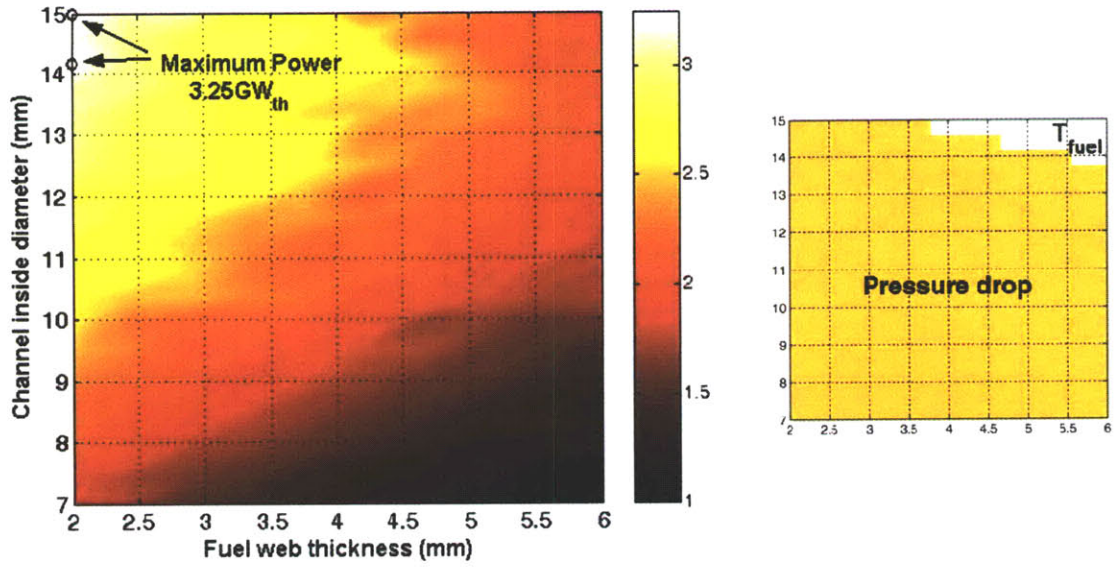


Figure XI- 12: Power map and limiting constraint map for S-IPWR ($\Delta p=X$)

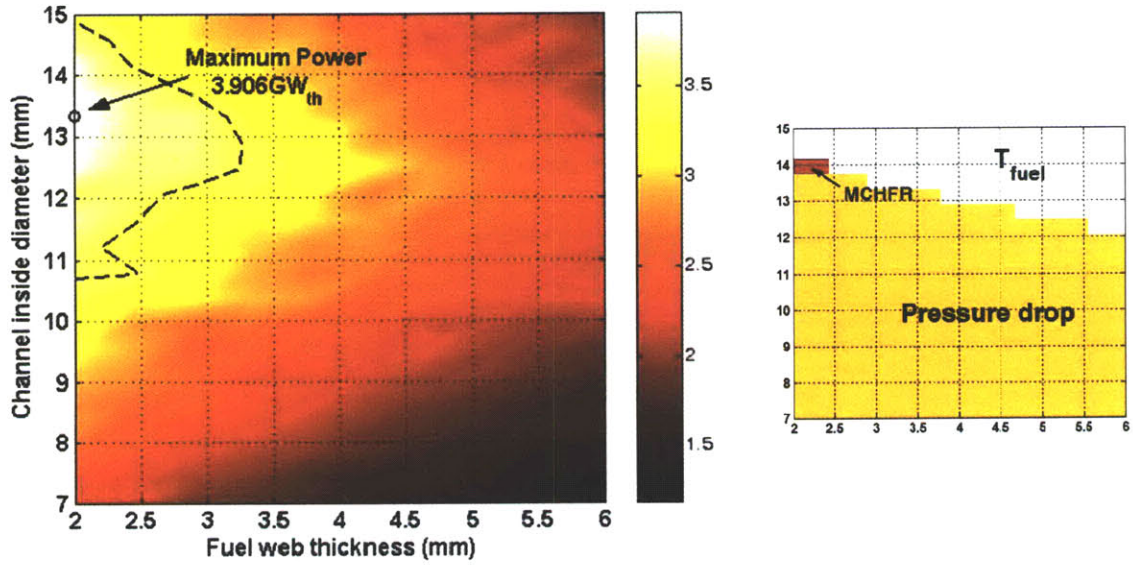


Figure XI- 13: Power map and limiting constraint map for S-IPWR ($\Delta p=1.5X$)

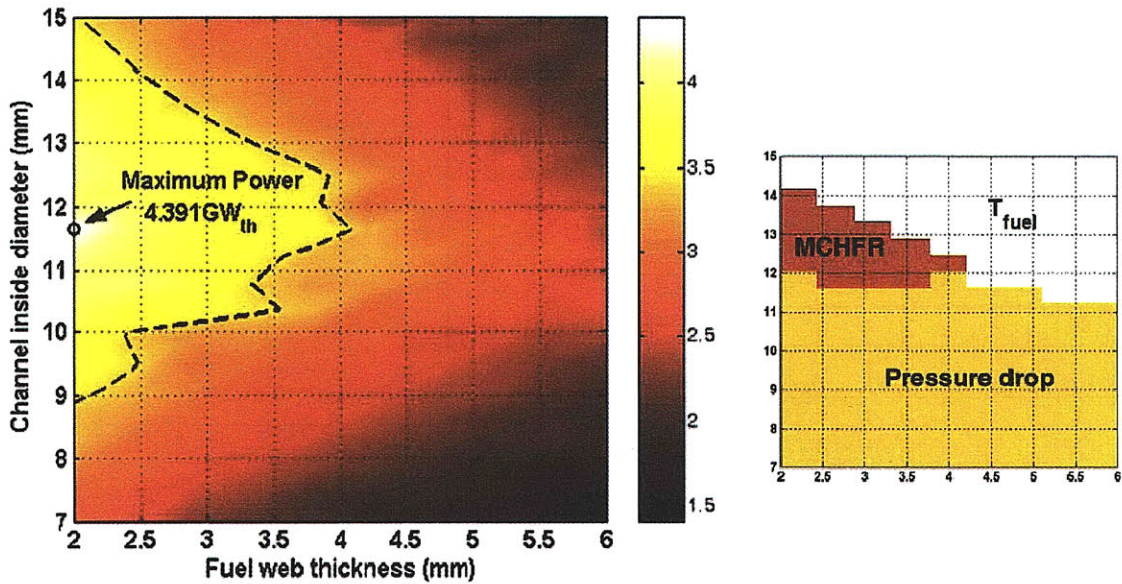


Figure XI- 14: Power map and limiting constraint map for S-IPWR ($\Delta p=2X$)

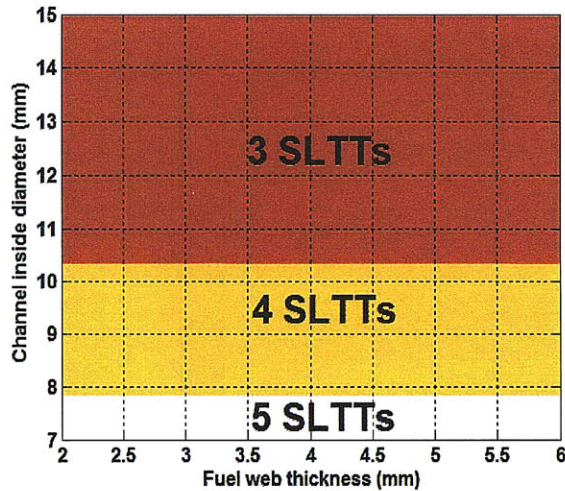


Figure XI- 15: Number of SLTTs in each channel (S-IPWR, $y = 1.5$, $s = 50$)

XI.2. 4 Power map comparison

XI.2.4. 1 Maximum powered IPWR designs

By comparing the power maps shown in Sections XI.2. 1 through XI.2. 3 it can be noticed that the E-IPWR design outperforms both the H-IPWR and the S-IPWR. For the TT-provided

designs, the insertion of the turbulence promoters does not lead to an increase in maximum achievable power, but to a shift of the maximum power region toward wider channels. In fact, as shown in Figure XI- 6 through Figure XI- 8, for the E-IPWR:

- the maximum power is always reached with channel diameters between 9.95 and 10.79 mm;
- the maximum power geometries is always limited by pressure drop. For two of these geometries, i.e. the $t_{web}=2$ mm $D_{ci}=10.79$ mm geometry in Figure XI- 7 and the $t_{web}=2$ mm $D_{ci}=9.95$ mm geometry in Figure XI- 8, power is limited simultaneously by pressure drop and MCHFR;
- as the channel diameter increases, the pressure drop becomes less and less limiting, while the MCHFR becomes more and more limiting.

Therefore, if TTs are implemented in the maximum powered E-IPWR geometries:

- the pressure drop of these geometries will be further penalized, thus causing their maximum achievable power to decrease;
- the CHF performance of large channel geometries will be enhanced, thus shifting the high power region toward the top of the power maps. This is evident from Figure XI- 16, which shows the ratio between the maximum powers attainable with the S-IPWR design and those attainable with the E-IPWR design. The largest ratio is of about 1.43.

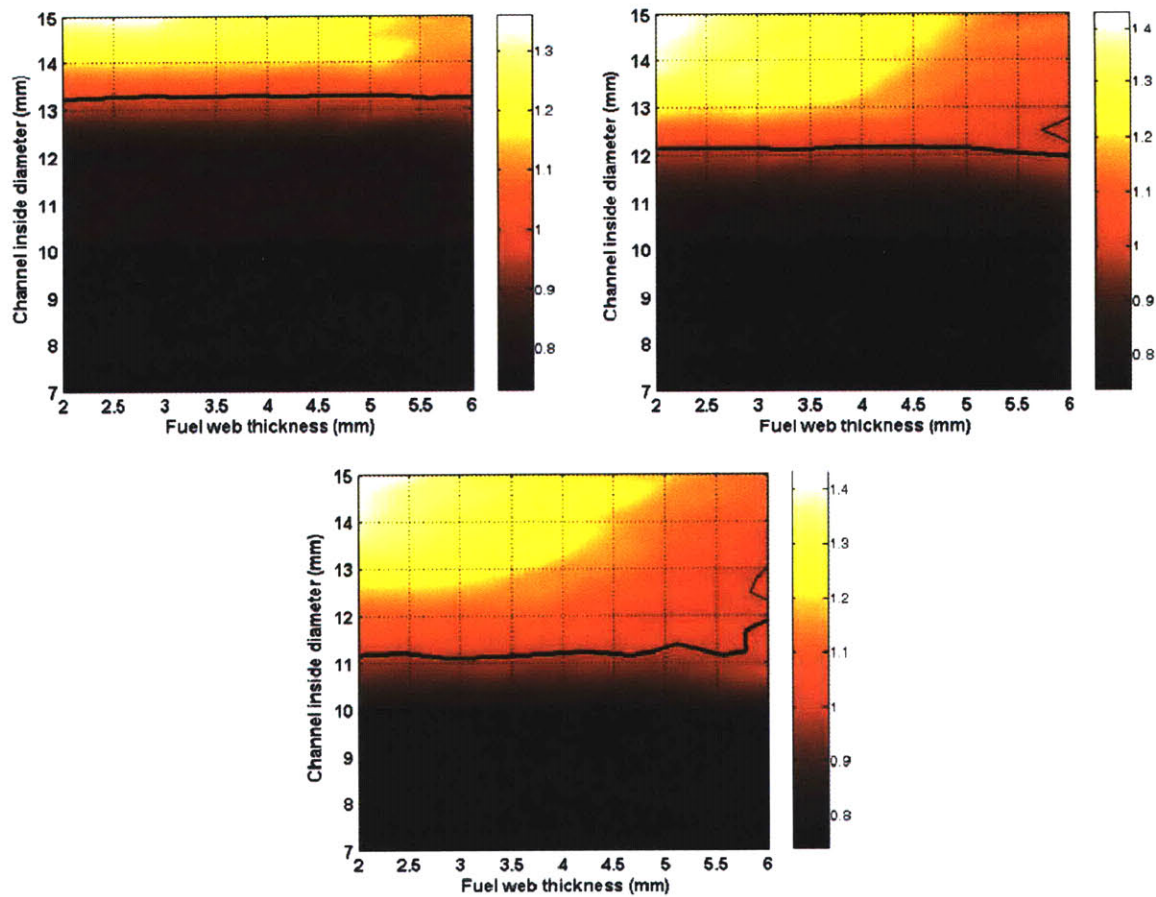


Figure XI- 16: S-IPWR to E-IPWR maximum achievable power ratio (clockwise from the top left plot: X, 1.5X and 2X pressure drop limit; solid line indicates unity ratio)

The best power performance of the three IPWR designs are compared in Figure XI- 17, in the form of power gain/loss relative to pin geometry PWRs obtained by Shuffler et al. (2009) in their investigation on the effect that changes in fuel rod diameter and pitch have on power performance. In particular:

- for each comparison, the pressure drop limit imposed on the IPWR designs is the same as that imposed by Shuffler on the PWR designs;
- the left plot shows the IPWR power performance relative to the maximum powered pin geometry PWR (fuel rod outer diameter ~ 6.5 mm; pitch-to-diameter ratio 1.4-1.5);
- the right plot shows the IPWR power performance relative to the reference pin geometry (fuel rod outer diameter = 9.5 mm; pitch-to-diameter ratio = 1.326);

- for the left plot, the comparison at 1.5X pressure drop limit is not shown since this limit was not examined⁸ by Shuffler et al. (2009).

IPWR power performance is expressed relatively to two pin geometry PWRs since the maximum powered pin geometry PWR:

- has very thin fuel rods which are challenging to manufacture and susceptible to vibrations, and
- was not verified to meet neutronic constraints in the earlier hydride fuel project.

For these reasons using, as the only base of comparison, the maximum powered PWR, would overestimate the power performance actually attainable by pin geometry PWRs, thus unjustly penalizing the IPWR design competitiveness. From Figure XI- 17 it can be seen that:

- the E-IPWR design always outperforms the H-IPWR and the S-IPWR designs;
- the maximum powered E-IPWR delivers about 2% less power than the maximum powered PWR when the pressure drop is fixed at the reference value, while about 13% more power when the pressure drop limit is doubled;
- the maximum powered E-IPWR always outperforms the reference PWR, with power gain percentages equal to 8, 27 and 48% for the X, 1.5X and 2X pressure drop limit respectively.

The reason for the increasing power gain of the maximum powered IPWR relative to the reference pin geometry PWR, as the pressure drop limit is increased, is the type of constraint that limits the power of these reactors. The maximum powered E-IPWR is pressure drop limited, while the reference PWR is MCHFR- and fretting-limited. Therefore, relaxation of the pressure drop limit is beneficial for the E-IPWR, while it does not offer any power benefit for the reference PWR. The high mass flux characterizing all the IPWR designs with respect to pin geometry PWRs is the physical reason of their lower susceptibility to heat transfer crisis.

⁸ In spite of not being examined by Shuffler, the 1.5X pressure drop limit case is shown in the right plot. This is because, unlike the maximum powered PWR geometry, the PWR geometry relative to which the power gain/loss is expressed in this plot, i.e. the reference PWR, was demonstrated by Shuffler to be MCHFR- and fretting-limited. Hence, any pressure drop allowance beyond the reference core pressure drop does not result in any increase in maximum achievable power.

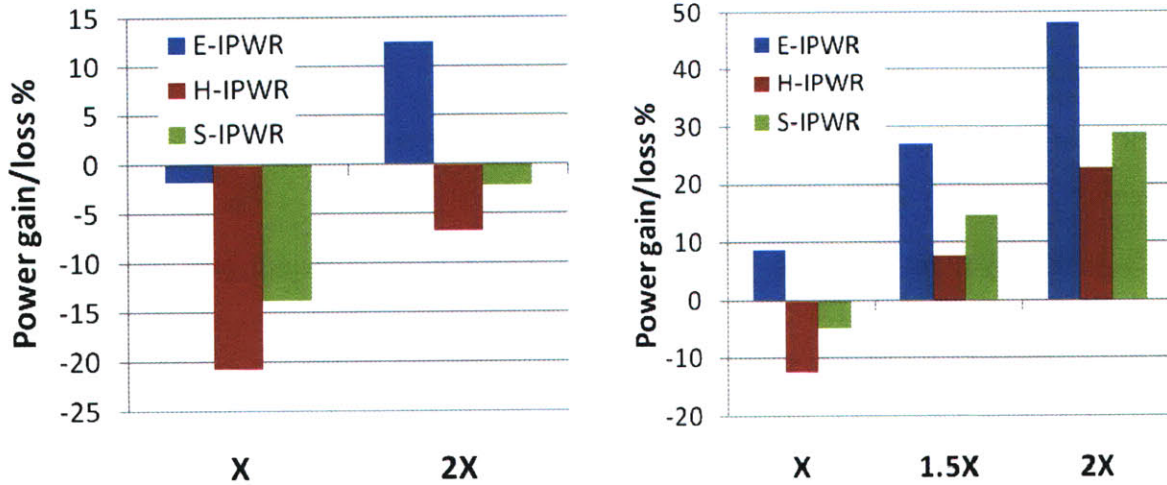


Figure XI- 17: Power gain/loss percentage of maximum powered IPWRs with respect to maximum powered pin geometry PWR (left) and reference PWR (right), for X, 1.5X and 2X pressure drop limits

XI.2.4. 2 Selected E-IPWR design

Because of the better power performance of the E-IPWR with respect to H-IPWR and S-IPWR, the former was analyzed further, and subjected to the application of the remaining design constraints, i.e. LOCA-related and neutronic constraints. However, this analysis could not be performed over the whole geometry spectrum, i.e. for all the D_{ci} - t_{web} combinations examined to generate the power maps, and a point design was selected. This point design is shown in Figure XI- 18, and corresponds to the pair: $D_{ci} = 10.79$ mm, $t_{web} = 2.9$ mm, subjected to intermediate pressure drop limit, i.e. that equal to 1.5 times the pressure drop of the reference core. The decision to consider this point, instead of those associated with the maximum power, was made in order to leave some margin from the minimum web thickness considered in this analysis, i.e. 2 mm, since this latter value may be too small thus making fuel prism manufacture very difficult to perform. As discussed in Chapter X, the fuel prisms are initially casted in the form of solid metal prisms, about 1 cm tall, which are then gun drilled, hydrided and finished to the final dimensions. Since hydriding causes the material to swell of about 20%, the web thickness before hydriding has to be smaller than the design value, and a pre-hydriding web thickness of 20% less than the 2 mm post-hydriding web thickness, i.e. $2 \times 0.8 = 1.6$ mm, may be difficult to preserve intact during swelling. The choice of a 50% thicker web makes the prisms stiffer, even though a confirmation

of whether this thickness is enough can only come from experimental tests performed on $UTh_{0.5}Zr_{2.25}H_{5.625}$.

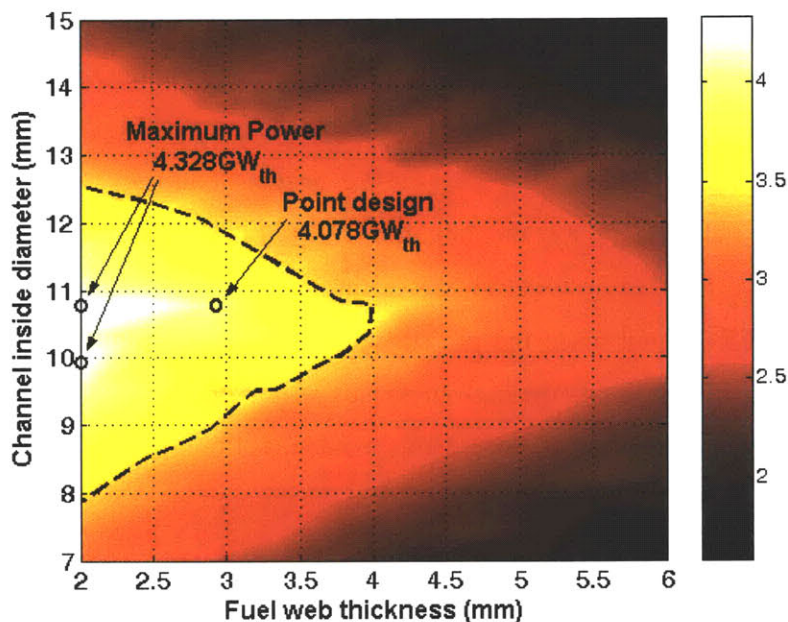


Figure XI- 18: Power map for E-IPWR ($\Delta p=1.5X$) with indication of selected point design

Analogously to what has been done for the maximum powered IPWR designs, i.e. Figure XI- 17, Figure XI- 19 compares the power performance of the IPWR designs adopting the selected D_{ci} - t_{web} pair. Again, this performance is expressed as power gain/loss with respect to the power of the maximum powered and of the reference pin geometry PWRs, evaluated with the same pressure drop limit. It can be seen that:

- unlike the maximum powered E-IPWR, the selected E-IPWR geometry never outperforms the maximum powered pin geometry PWR. The reason for this is the larger fuel web thickness, which penalizes the selected E-IPWR geometry with respect to the maximum powered E-IPWR, i.e. 2.9 vs 2 mm.
- the selected E-IPWR attains about 5% less power than the reference pin geometry PWR when the pressure drop limit is fixed to the reference value, while it can deliver about 19% more power when the pressure drop constraint is relaxed.

It is interesting to note that the power gain of the selected E-IPWR geometry does not increase when the pressure drop limit is increased from 1.5X to 2X, whereas an increase in power gain was verified for the maximum powered E-IPWR (see Figure XI- 17). This is because the geometry, i.e. the D_{ci} - t_{web} combination, corresponding to the maximum powered IPWR, changes depending on the pressure drop limit adopted (see Figure XI- 6, Figure XI- 7 and Figure XI- 8) and MCHFR becomes the limiting constraint (in addition, eventually, to pressure drop) only⁹ when the pressure drop limit is fixed at 2X (see the limiting constraint map in Figure XI- 8). Instead, the selected E-IPWR D_{ci} - t_{web} combination ($D_{ci} = 10.79$ mm, $t_{web} = 2.9$ mm) is pressure drop-limited when the limit value is set to X (see limiting constraint map in Figure XI- 6), but becomes also MCHFR-limited when the pressure drop limit is increased to 1.5X (see limiting constraint map in Figure XI- 7). At the high mass flux values characterizing the E-IPWR (6500 - 7000 kg/s m^2), CHF does not increase appreciably with mass flux. Hence, any further increase in pressure drop limit beyond the 1.5X value does not yield appreciable power benefits.

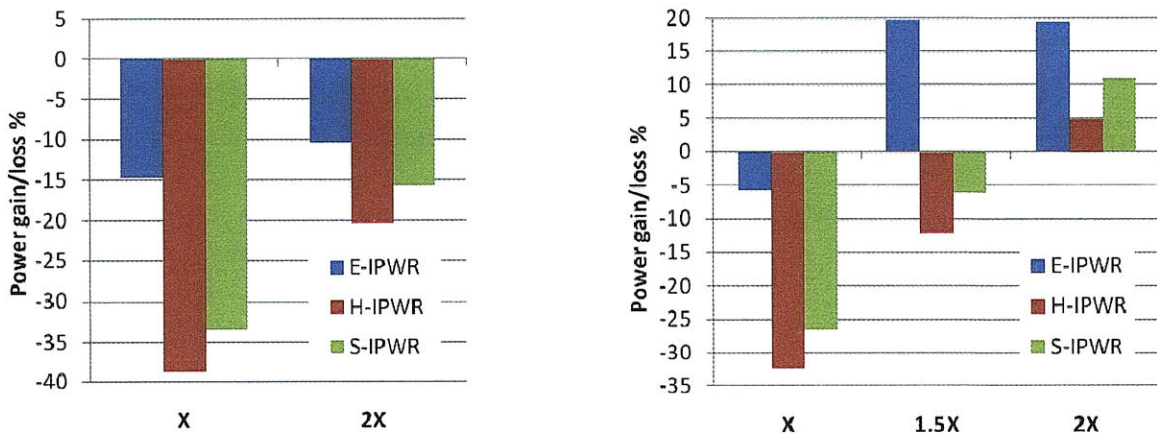


Figure XI- 19: Power gain/loss percentage of $t_{web} = 2.9$ mm $D_{ci} = 10.79$ mm IPWR geometry with respect to maximum powered pin geometry PWR (left) and reference PWR (right), for X, 1.5X and 2X pressure drop limits

⁹ MCHFR is the limiting constraint (for the maximum powered geometry) also in Figure XI- 7, but only for one of the two maximum powered geometries shown. Thus, when the pressure drop limit is increased from 1.5X to 2X, the attainable power of the other geometry can increase, thus leading to the increasing power gain shown, for the E-IPWR design, in Figure XI- 17.

XI. 3 LBLOCA analysis of the selected E-IPWR geometry

RELAP5-3D[®] code (RELAP5, 2005a) was used to model the occurrence of a Large Break Loss-Of-Coolant Accident (LBLOCA) for the E-IPWR having the $D_{ci}-t_{web}$ combination selected as point design in the previous section. The scenario boundary conditions, as well as the analysis method and assumptions, are described in detail in Chapter VIII. This section only shows how the reactor behaves concerning the two LOCA-related constraints used in the IPWR design, i.e. the peak cladding temperature (PCT) and the percentage of initial clad thickness converted to oxide, P_{OX} . The limit values for these parameters are, as discussed in Chapter III, 1204°C and 17% respectively.

Figure XI- 20 shows the variation of the cladding inside surface temperature during the LBLOCA event, at various axial locations across the core. Of the 16 axial zones in which RELAP divides the core (see Chapter VIII), the figure only shows the temperature evolution for those included between the 6th and the 13th. The axial zones below the 6th have low decay linear power and, being close to the bottom of the core, are quenched much earlier than those located higher in the core. Concerning the axial zones above the 13th, in spite of being quenched relatively late, they are not limiting since their linear power is small (see later in this section). Figure XI- 20 shows that the PCT is 863°C (1136 K), and it is reached at the 9th axial location, which is consistent with the pre-accident axial power profile assumed in the analysis, i.e. a chopped cosine. Therefore, a margin of more than 300°C exists from the maximum allowed PCT.

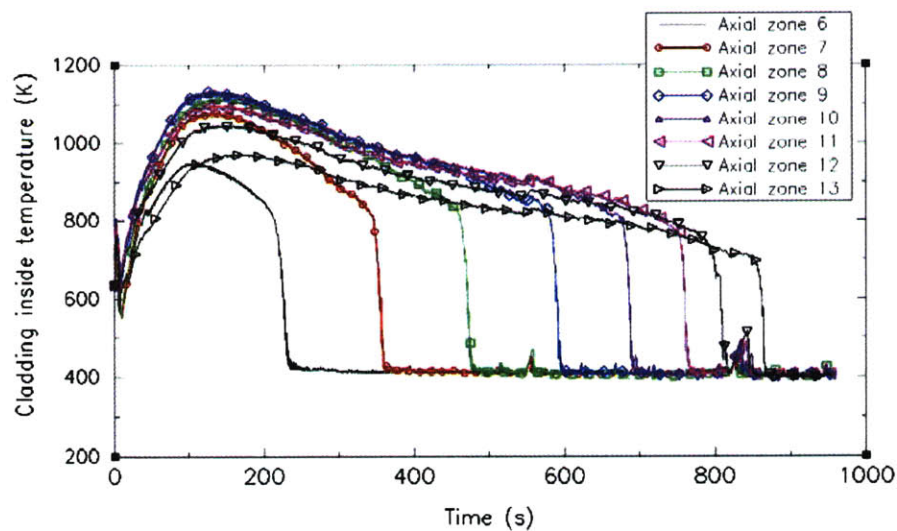


Figure XI- 20: Cladding inside surface temperature during LBLOCA, at various heights

Figure XI- 21 shows the time variation of the percentage of cladding thickness that is oxidized during the accident, calculated using the Baker-Just correlation (Baker and Just, 1962) introduced in Chapter III. It can be seen that:

- the maximum oxide thickness is only 0.63% of the original, i.e. as-designed, clad thickness, and it is reached at the axial location with the highest temperature, i.e. the 9th.
- the oxide thickness increases during the first 300 seconds and then remains constant. This means that, provided the cladding temperature is of the order of those shown in Figure XI- 20, the quenching time does not affect the degree of oxidation.

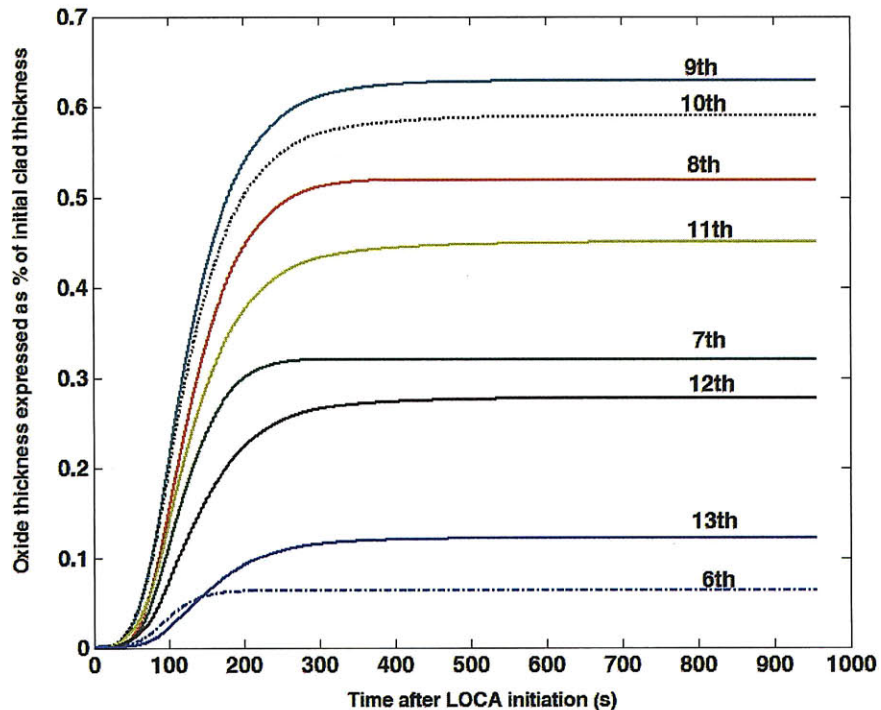


Figure XI- 21: Oxide thickness expressed as percentage of as-designed clad thickness, for various axial locations in the core

Since both the PCT and the oxide thickness are significant smaller than the corresponding limits, it can be concluded that the maximum power attainable by the E-IPWR point design having $D_{cl}=10.79$ mm and $t_{web}=2.9$ mm is 4078 MW_t, i.e. the application of the LOCA constraints did not require the power calculated through the steady-state analysis to be reduced. The next and

last step in the analysis of the E-IPWR is represented by the application of the neutronic constraints, which is presented in the next section.

XI. 4 Neutronic analysis of the selected E-IPWR geometry

The neutronic analysis presented here is aimed at designing, from the neutronic viewpoint, the selected E-IPWR geometry, in such a way that the neutronic constraints introduced in Chapter III are met. These constraints, with the corresponding limits, are:

- Fuel Temperature Reactivity Coefficient (FTRC) < 0 ;
- Void Reactivity Coefficient (VRC) < 0 ;
- Soluble boron concentration based on Chemical and Volume Control System (CVCS) capabilities < 2000 ppm;
- fuel enrichment $< 20\%$;
- cycle length ~ 18 months;
- shutdown margin: similar to reference PWR.

The characterization, from the neutronic viewpoint, of the selected E-IPWR geometry will complete the E-IPWR design.

Of the constraints listed above, the FTRC, which is a characteristic of the fuel, was verified to be negative by Ganda and Greenspan (2010) (see Section IX.2 in Chapter IX) and it is not examined further here. Section XI.4. 1 examines the other constraints, except for the shutdown margin which is discussed separately in Section XI.4. 2. Those constraints cannot, in fact, be analyzed individually since they are interdependent.

XI.4. 1 E-IPWR neutronic characterization

The neutronic characterization of the E-IPWR consists of selecting the fuel enrichment and the burnable poison type, as well as its loading, yielding a negative VRC, a Beginning Of Cycle (BOC) soluble boron concentration < 2000 ppm and a cycle length of about 18 months.

Two burnable poison types were considered: Integral Fuel Burnable Absorber (IFBA) and Er_2O_3 . The former is in the form of a thin layer of ZrB_2 deposited on the inner surface of the fuel prism holes, while the latter is uniformly dispersed in the fuel. The neutronic design consisted of the following three steps:

- 1) assembly-level analysis, performed with CASMO-4 (Edenius et al., 1995), in search for the minimum enrichment needed to achieve a 18.5 month cycle;
- 2) search for the minimum burnable poison loading needed to reduce the BOC critical boron concentration below 1511 ppm, which is the threshold that, based on the analysis discussed in Section IX.1.2 of Chapter IX, guarantees a negative VRC;
- 3) comparison, for the IFBA-provided design only, between the calculated IFBA loading and the maximum loading allowed to avoid excessive duct internal pressurization.

Input data for the neutronic/ fuel cycle analysis were:

- fuel composition: $U_{0.5}Zr_{2.25}H_{5.625}$;
- inverted assembly geometry: since CASMO-4C does not model inverted geometries, a pin geometry assembly neutronically equivalent¹⁰ to the selected E-IPWR assembly was constructed. This was done using the methodology discussed in Section IX.3 of Chapter IX. The key geometric characteristics of the E-IPWR assembly and of the equivalent pin assembly are summarized in Table XI- 2.
- reactor power level: 4078 MW_t;
- number of assemblies in the core¹¹: 187;
- number of fuel batches and plant capacity factor: 3 and 0.9 respectively.

¹⁰ As discussed in Chapter IX, an inverted-equivalent pin geometry is a pin geometry having approximately the same k , vs burnup curve of the inverted geometry from which it was generated. The small difference between the depletion characteristics of the two geometries was accounted for by means of a correction factor applied to the CASMO-4 runs.

¹¹ The number of assemblies is needed to calculate the core heavy metal loading, which is used to compute the cycle length.

Table XI- 2: Assembly geometry key characteristics			
	Ref. assembly (Seabrook USAR, 2002)	IPWR assembly	Pin-geometry assembly neutronically equivalent to E-IPWR assembly
Geometry	Pin	Inverted	Pin
Array	Square (17×17)	Hexagonal (8 rings)	Hexagonal (8 rings)
Cladding OD, mm	9.50	12.12	10.12
Cladding ID, mm	8.36	10.79	8.93
Fuel diameter (pellet OD for pin, D_f for inverted)	8.19	12.74	8.41
Fuel pin/cell pitch, mm	12.60	15.63	12.75
Heated length, m	3.67	3.67	3.67
Fuel pins/cells per assembly	264	169	169
Fuel type	UO ₂	UTh _{0.5} Zr _{2.25} H _{5.625}	UTh _{0.5} Zr _{2.25} H _{5.625}
Control rod guide thimbles (ID, OD in mm)	24 (11.43, 12.24)	N.A.	None
Instr. tubes (ID, OD in mm)	1 (11.38, 12.29)	N.A.	N.A.
Fuel prism flat-to-flat distance (mm)	N.A.	208	N.A.
Duct wall thickness (mm)	N.A.	9.8	Modeled as extra row of 12.70 mm diameter solid pins ¹²

The minimum enrichment required to achieve an 18.5-month cycle was found to be 15%. This value was found by simply modeling the depletion of a burnable poison-free assembly in which the fuel enrichment was iteratively increased from 5% until a cycle length equal to 18.5 months was achieved¹³. The 0.5 months in excess of the ~18 month target was used to account for possible cycle length reductions resulting from the addition of burnable poisons, which is discussed next.

The depletion of the inverted-equivalent pin geometry assembly, 15% enriched, was modeled assuming increasing amounts of burnable poison present. Figure XI- 22 and Figure XI- 23 show the k_{∞} vs burnup curves for IFBA- and Er₂O₃-loaded assemblies respectively. It can be seen that IFBA burns more quickly than Er₂O₃ and no reactivity penalty exists at the single batch discharge burnup¹⁴, BU_{dl} . Consequently, the cycle length corresponding to the various IFBA loadings analyzed is the same as that of the unpoisoned assembly, i.e. 18.5 months. Instead, small amounts of Er₂O₃ are still present at BU_{dl} thus leading to a shorter cycle length.

¹² The “HEX” card in CASMO (Edenius et al., 1995) was used to model a pin-geometry assembly with hexagonal lattice. This card, however, does not allow modeling fuel channels thicker than about 5 mm. The 9.8 mm thick duct was therefore modeled as an extra-ring of solid pins.

¹³ The cycle length computation was performed using the method discussed in Section IX.3 of Chapter IX.

¹⁴ The single batch discharge burnup was defined in Chapter IX as the burnup corresponding to $k_r = 1.03$. The Δk margin of 0.03 from criticality was used to account for leakages which, in single assembly analyses, are not accounted for.

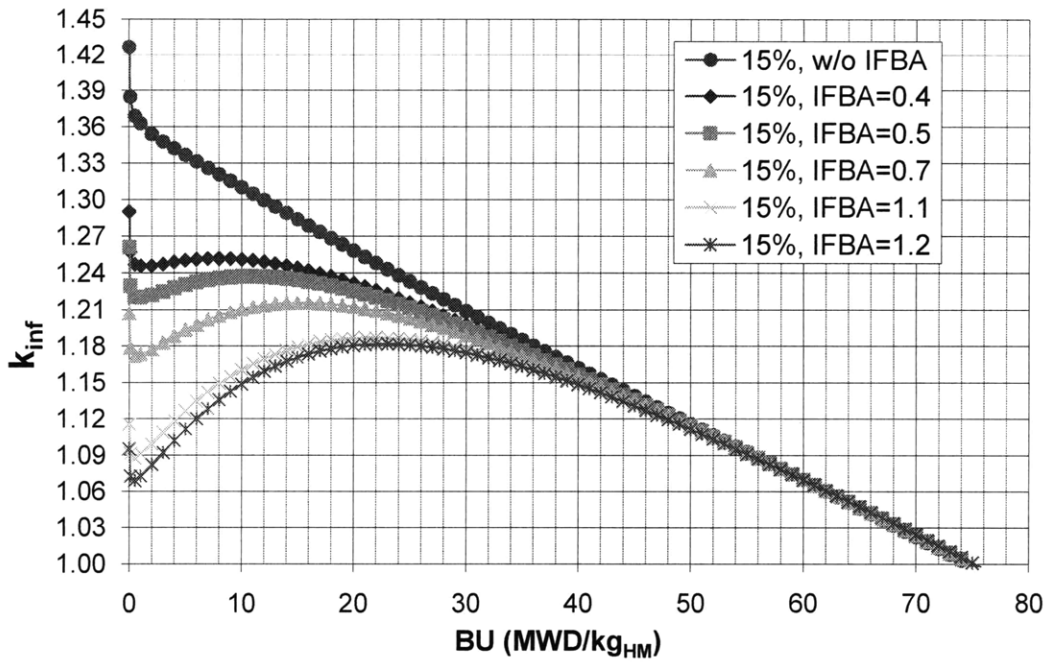


Figure XI- 22: Single-assembly depletion for 15% enrichment and different IFBA loadings (expressed as $\text{mg } ^{10}\text{B/cm}$)

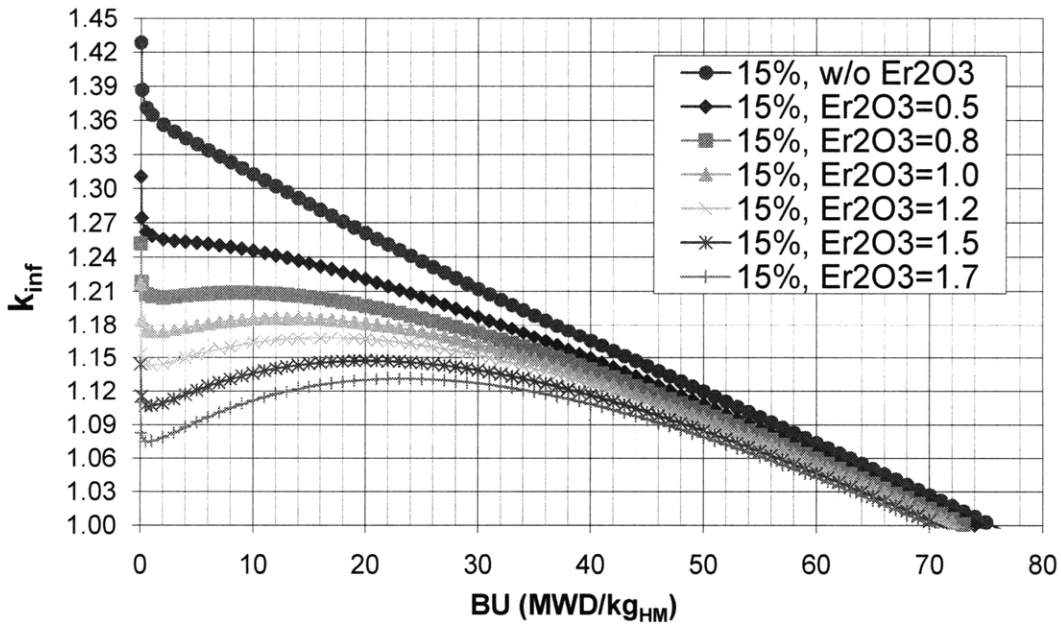


Figure XI- 23: Single-assembly depletion for 15% enrichment and different Er_2O_3 loadings (expressed as Er_2O_3 weight percentage in the fuel)

The dependence of cycle length and BOC critical boron concentration on the burnable poison loading is shown in Figure XI- 24. It can be seen that the minimum IFBA loading required to meet the VRC constraint (through the maximum soluble boron concentration limit) is of about 1.25 mg ¹⁰B/cm, while for Er₂O₃ it is of about 1.7 w/o %. For the latter, the corresponding cycle length is 17.2 months which, although slightly shorter than the prescribed 18 months, is considered acceptable. IFBA, in spite of being superior to Er₂O₃ in terms of cycle length performance, has to be discarded since the 1.25 mg ¹⁰B/cm loading is much larger than the limit required to avoid He-induced duct internal pressurization This limit is given by the following expression (see Chapter IV):

$$IFBA_{\max} = \frac{715}{N_{\text{cells}/A}} \left(\frac{\sqrt{3}}{2} P_{\text{prism}}^2 - \frac{N_{\text{cells}/A} \pi D_{\text{co}}^2}{4} \right) \quad (\text{IV.8})$$

which, applied to the E-IPWR assembly geometry of interest ($N_{\text{cells}/A}=169$; $P_{\text{prism}}=0.208$ m; $D_{\text{co}}=12.12 \times 10^{-3}$ m), gives 0.076 mg ¹⁰B/cm.

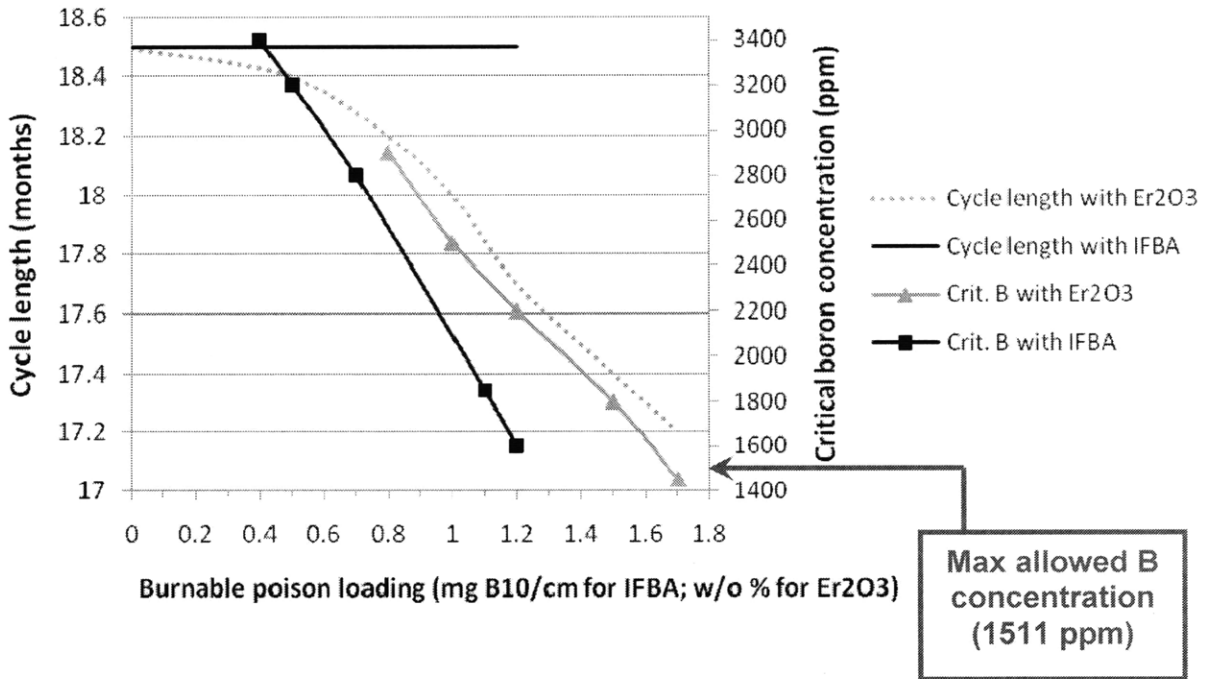


Figure XI- 24: Cycle length and BOC critical boron concentration as a function of burnable poison loading

XI.4. 2 Shutdown margin

The methodology discussed in Section IX.4 of Chapter IX was used to estimate the reactivity insertion resulting from the Hot Full Power (HFP) to Cold Zero Power (CZP) transition. Table XI- 2 summarizes the key geometric characteristics of the inverted assembly of interest, of the neutronically-equivalent pin geometry assembly on which the HFP-CZP reactivity insertion calculation was performed, and of the reference PWR assembly, which was also subjected to the same type of analysis in order to have a measure of comparison. Table XI- 3 shows the results of this analysis. It can be seen that:

- the two assemblies show reactivity insertions, resulting from the HFP-CZP transition, of the same order of magnitude;
- both assemblies show a HFP-CZP reactivity insertion that is about 30-40% larger at EOL than BOL;

unlike for the reference assembly, for the inverted assembly there is no variation in HFP-HZP reactivity insertion between BOL and EOL. This may be due to the competing effect between the extra-absorptions that characterize burnt fuel, with respect to fresh fuel, and the extra-fissions in ^{239}Pu and ^{241}Pu due to hydrogen-induced neutron upscattering, as discussed in Section IX.2 of Chapter IX.

	BOL (0.1 MWD/kg _{HM})			EOL (40 MWD/kg _{HM} for ref; 100 MWD/kg _{HM} for inv)		
	HFP to HZP	HZP to CZP	HFP to CZP	HFP to HZP	HZP to CZP	HFP to CZP
Reference core assembly	+650	+2809	+3459	+978	+3579	+4557
Inverted-equivalent pin geometry assembly	+667	+2081	+2748	+669	+3252	+3921

A single-assembly analysis does not provide all the information required to calculate the control rod worth needed to satisfy shutdown margin requirements. However, from the values shown in Table XI- 3 it is reasonable to conclude that the selected E-IPWR design should be able to meet shutdown margin requirements by means of a control rod design that, in terms of total worth, will not be significantly different from that of a typical PWR.

XI. 5 Complete characterization of selected IPWR

Table XI- 4 summarizes the characteristics, mainly geometric, of the selected IPWR. Table XI- 5 summarizes instead the IPWR performance as well as the operating conditions that were assumed to characterize this reactor during normal operation.

Table XI- 4: Final IPWR design: geometry		
Characteristic	Unit	Value
IPWR design	-	E-type
Duct design	-	Collapsible-type
Fuel		
Stoichiometry	-	UTh _{0.5} Zr _{2.25} H _{5.625}
Total density	kg/m ³	9096
U density	kg/m ³	3829
Th density	kg/m ³	1870
Zr density	kg/m ³	3308
H density	kg/m ³	89
Enrichment in ²³⁵ U	%	15
Assembly geometry		
Heated length	m	3.67
Upper plenum height	m	0.1
Total height	m	3.8
Duct outer flat-to-flat distance	mm	228
Duct wall thickness	mm	9.8
Fuel prism flat-to-flat distance	mm	208
Cooling channel inner diameter	mm	10.79
Cladding thickness	mm	0.67
Clad-fuel gap width	mm	0.3
Fuel hole diameter	mm	12.74
Cooling channel pitch	mm	15.63
Fuel web thickness	mm	2.9
Number of fuel cells per assembly	-	169
Fuel volume fraction (unit-cell level)	-	0.397
Coolant volume fraction (unit-cell level)	-	0.432
Clad volume fraction (unit-cell level)	-	0.113
Core		
Shroud diameter	m	3.66
Number of assemblies	-	187
Inter-assembly water gap width	mm	12.24
Fuel volume fraction (whole core)	-	0.318
Coolant volume fraction (whole core)	-	0.405
Clad+duct volume fraction (whole core)	-	0.229
Miscellaneous		
BOC critical boron concentration	ppm	1450
Er ₂ O ₃ loading	w/o % in the fuel	1.7

Table XI- 5: Final IPWR design: performance and operating conditions			
Characteristic	Unit	Value	Calculated (C) or assumed (A)
Steady-state performance			
Core thermal power	MW	4078	C
Core thermal power increase % with respect to reference PWR evaluated at the same pressure drop limit	%	+19%	C
Core power density	MW/m ³	119	C
Specific power	kW/kg _{HM}	73.6	C
Core flow rate	kg/s	20891	C
Core pressure drop	kPa	222	C
Maximum fuel temperature	°C	597	C
Maximum cladding inside surface temperature	°C	358	C
MCHFR	-	1.79	C
Cycle length	months	17.2	C
Discharge burnup	MWD/kg _{HM}	92	C
Fuel enrichment at discharge	%	3.7	C
Fuel temperature reactivity coefficient	-	<0	C
Void reactivity coefficient	-	<0	C
LBLOCA performance			
Peak cladding temperature	°C	863	C
Maximum oxide thickness	% of as-designed clad thickness	0.63	C
Steady-state operating conditions			
Reactor pressure	MPa	15.5	A
Core inlet temperature	°C	295	A
Percentage of coolant flowing through inter-assembly water gaps	%	10	A
Core enthalpy rise	kJ/kg	195.2	A
Axial power profile	-	Chopped cosine	A
Axial peaking factor	-	1.515	A
Assembly radial peaking factor	-	1.515	A
Fuel cell peaking factor	-	1.089	A

Chapter XII

Conclusions and future work

XII. 1 Conclusions

The power performance attainable by implementing a $UTh_{0.5}Zr_{2.25}H_{5.625}$ -fueled inverted geometry in a PWR was assessed. Six Inverted Pressurized Water Reactor (IPWR) designs were examined, differing in the assembly duct and cooling channel designs. Among them, the IPWR adopting collapsible ducts and twisted tape-free cooling channels, i.e. the E-IPWR design, was found to have the best power performance. While the comparison inverted vs pin, performed at cell level, clearly shows better performance of the former, when inverted geometry is adapted to the operating conditions characterizing a PWR its performance degrades, due to the need of adopting thick walled ducts enclosing the fuel prisms, as well as wide inter-assembly water gaps for control rod insertion. These components cause the inverted geometry to lose continuity, i.e. to deviate from the ideal case of a modular repetition of the unit cell throughout the core, which instead holds during the transition unit cell-whole core in pin geometry PWRs. As a consequence of this, active flow area decreases, yielding an increase in mass flux which penalizes pressure drop.

The fuel web thickness was found to significantly affect the maximum power attainable by the IPWR. In particular, the smaller this thickness, the larger is the power. However, fuel assemblies with very small fuel web thickness are challenging to manufacture.

The competitiveness of the E-IPWR, relative to typical pin geometry PWRs, depends on the E-IPWR considered (maximum powered or selected point design) and on the pin geometry PWR relative to which the E-IPWR is compared (maximum powered, but with very thin fuel rods, or reference geometry, with 9.5 mm OD rods). The maximum powered and selected E-IPWR

geometries differ in the fuel web thickness. For the maximum powered geometry it is equal to 2 mm while for the selected point design it is equal to 2.9 mm.

Table 2 summarizes the power gain/loss corresponding to each scenario. Table XI-4 and Table XI-5 in Chapter XI summarize the key characteristics and performance of the selected E-IPWR design.

Based on Table 2, it can be concluded that, from the power performance viewpoint, the E-IPWR design is competitive against pin geometry PWRs if:

- fuel prisms with small fuel web thickness are confirmed to be manufacturable, or
- small diameter fuel rod PWRs are confirmed to be unfeasible due to fabrication and flow-induced vibration concerns.

	Pressure drop limit	Maximum powered E-IPWR ($t_{web} = 2\text{mm}$, $9.94 \leq D_{ci} \leq 10.79\text{ mm}$)	Selected point design E-IPWR ($t_{web} = 2.9\text{mm}$, $D_{ci} = 10.79\text{ mm}$)
Relative to maximum powered PWR ($D_{co} = 6.5\text{ mm}$, $1.4 \leq P/D_{co} \leq 1.5$)	X	-2	-14
	2X	+13	-11
Relative to reference PWR ($D_{co} = 9.5\text{ mm}$, $P/D_{co} = 1.326$)	X	+8	-5
	1.5X	+27	+19
	2X	+48	+19

The competitiveness of the E-IPWR design against typical PWRs does not depend on achievable power only, but also on the cost of the fuel and plant components. In this regard, the E-IPWR would be penalized by the extra cost due to the higher enrichment, i.e. 15% vs 5% of typical PWRs.

Irradiation tests on $\text{UTh}_{0.5}\text{Zr}_{2.25}\text{H}_{5.625}$, which are not documented in the literature, need to be performed to assess the performance of this fuel regarding irradiation-induced swelling and fission gas release (FGR). This study relies on experimental data collected on hydride fuels of different composition and, particularly, lower heavy metal density. It is known that the higher the heavy metal density, the larger is swelling and FGR. An excessive swelling may cause the collapsible duct design to fail, while an excessive FGR will prevent the implementation of non-vented inverted assemblies. Both these aspects deserve particular attention.

XII. 2 Future work

Future work is recommended in three areas:

- IPWR performance enhancement;
- investigation of aspects, identified while studying the inverted design concept, which may compromise its feasibility or degrade its performance;
- investigation of aspects that may lead to either performance enhancement or performance degradation;
- economic analysis.

Work in these areas is summarized below.

Aspects leading to performance enhancement

- Optimization of geometry, number and location of MSLTTs: variation of the MSLTT design may enhance the achievable power performance of the S-IPWR. An optimization of this design would therefore be useful to assess whether S-IPWR power performance are always poorer than E-IPWR performance or if they may become better.
- Void reactivity coefficient (VRC) calculations accounting for Er_2O_3 : VRC calculations were performed neglecting the burnable poison. Er_2O_3 , through resonance captures, makes VRC more negative. This results in an increase of the maximum allowable soluble boron concentration which, in turn, reduces the amount of Er_2O_3 needed for reactivity control, with consequent cycle length benefit.

Aspects leading to performance degradation

- Limited data on hydride fuel swelling: swelling data used throughout the project refer to a hydride fuel, but of a different type than that proposed for the IPWR, i.e. U-Zr-hydride vs U-Th-Zr-hydride. The higher heavy metal density of U-Th-Zr-hydride, although beneficial from the cycle length and void reactivity coefficient viewpoints, is likely to result in (1) a larger irradiation-induced fuel swelling, which can result in failure of the collapsible duct and (2) a larger fission gas release, which may prevent the use of non-vented ducts and thus act as a showstopper for the IPWR concept. Fuel swelling

measurements for burnups up to about 225 MWD/kg_{HM} are needed to confirm behavior of the peak burnup fuel.

- Assessment of minimum fuel web thickness: IPWR power performance quickly degrades as fuel web thickness increases. Experimental tests on fuel prism drilling and hydriding are needed to determine the minimum obtainable fuel web thickness;
- Assessment of collapsible duct feasibility: the hard contact between fuel and duct was assumed to not yield extensive hydriding of the latter, due to the low hydrogen pickup of Zr-2.5Nb alloy, low fuel temperature and measures taken to hinder hydrogen diffusion in the duct (superficial oxidation or application of coating). Verification of the ineffectiveness of these measures would prevent the collapsible duct design to be implemented.
- Limited data on hydrogen release during LOCA: hydrogen release during transients characterized by fuel temperature increase, e.g. LOCA, results in duct pressurization. Data on hydrogen release by UTh_{0.5}Zr_{2.25}H_{5.625}, which are not currently available, are needed to establish a fuel temperature limit to apply in LOCA and transient analysis. Although unlikely, this limit may constrain the attainable core power.
- Assessment of short-length twisted tapes (SLTTs) securing method and stability: swaging the outer diameter for the cooling channels was proposed as preferred method for SLTT securing. The technique, experimentally tested, needs to be improved to be able to control the degree of tube compression. Also, irradiation-induced deformation of the tubes may cause the tapes to become loose and to be expelled from the channels as projectiles. Confirmation of this phenomenon would result in S-IPWR design rejection.
- Assessment of assembly liftoff potential: because of the small flow area, the IPWR mass flux is about twice of that of a typical PWR. The liftoff force exerted by the coolant on the assemblies may require strengthening of the hold-down springs and/or implementation of additional components on the core upper plate.
- Assessment of parallel channel instability: upon core flow rate reduction, some inverted cooling channels operating in single-phase flow will undergo subcooled boiling, with consequent increase in pressure drop due to bubble-induced extra-friction at the wall. The disequilibrium between those channels and the rest of the core which, vice versa, will experience a reduction in pressure drop, may lead to parallel channel instability. An

extra-orificing of the core, often used as solution to flow instabilities, will increase the core pressure drop with consequent penalty on attainable core power.

Aspects with unpredictable outcome

- Investigation of CHF enhancement due to MSLTTs: the CHF calculation method adopted in this work could not be benchmarked against a comprehensive set of data, since they are not available. Even though considerations led to think that it is a conservative model, experimental tests are needed.
- Assessment of primary pump performance enhancement: the maximum limit on core pressure drop adopted in the IPWR study was equal to 2 times the reference core pressure drop. Development in pump technology and/or reduction of ex-vessel primary circuit pressure losses (e.g. through adoption of pumps integrated in the vessel and consequent elimination of cross over leg) may allow larger core pressure drop to be accommodated.
- Adoption of cylindrical assemblies: stress concentration at the corners of the hexagonal ducts was demonstrated to require duct wall thickening. Adoption of cylindrical ducts would allow thinner duct walls, which would reduce the total volume occupied by these structures. At the same time large inter-assembly gaps would be generated, with consequent reduction in space available for the assemblies and localized extra-moderation. However, some of these inter-assembly gaps could be utilized for control rods albeit of unique shape. A tradeoff analysis between these two factors would be needed to assess the net benefit, if any, resulting from the duct shape modification.

Economic analysis

Cost of electricity analysis is needed to assess the competitiveness of the IPWR design against typical PWRs. Economic saving resulting from the power density uprate demonstrated in this study must be combined with (1) the higher fuel cycle cost resulting from the higher fuel enrichment and (2) the higher capital cost due to the need of adapting primary and secondary side components to operation at higher power, e.g. turbine upgrade, to assess the net economic performance of this concept.

References for Volume 1

AEC, 1973. Atomic Energy Commission Rule-Making Hearing, Opinion of the Commission, Docket RM-50-1, 28 December.

AECL (Atomic Energy of Canada Limited), 1997. *Canada Enters the Nuclear Age*. Published for AECL by McGill-Queen's University Press.

AER, 1999. Atomic Energy Research Benchmark Book. Budapest.

Ales, M., 2008. Personal communication with M. Ales, VP Engineering, Novatech, Lynchburg, VA, USA. September 2008.

Alexander, A.J., Huffine, C.L., 1960. Preparation of Solid Massive Shapes in Hydrided Zirconium. USAEC Report APEX-546. General Electric Company. March 1960.

Algifri A.H., Bhardwaj R.K., 1985. Prediction of the heat transfer for decaying turbulent swirl flow in a tube. *International Journal of Heat and Mass Transfer*. Vol. 28, No. 9, 1637-1643.

Algifri A.H., Bhardwaj R.K., Rao Y.V.N., 1987. Prediction of the decay process in turbulent swirl flow. *Proc. Insts. Mech. Engineers*. Vol. 201 No C4 (1987) 279-283.

Andersson, T., Almberger, J., Bjornkvist, L., 2004. A decade of assembly bow management at Ringhals. *2004 International Meeting on LWR Fuel Performance*. Orlando, Florida.

Anness, M., 2010. Westinghouse Electric Company LLC. Personal communication. January 6th.

ASME, 1969. Criteria of the ASME boiler and pressure vessel code for design by analysis in sections III and VIII, Division 2. American Society of Mechanical Engineers.

ATI Wah Chang, 2003. Reactor Grade Zirconium Alloys for Nuclear Waste Disposal. Technical Data Sheet.

Atomic Energy of Canada Limited, AECL, 1997. *Canada Enters the Nuclear Age*. McGill-Queen's University Press.

Baker, L., Jr., Just, L.C., 1962. Studies of metal-water reactions at high temperatures. III. Experimental and theoretical studies of the zirconium-water reaction. Argonne National Laboratory. Report ANL-6548.

Baldwin, N.L., Foushee, F.C., Greenwood, J.S., 1980. Fission product release from TRIGA-LEU reactor fuels. *General Atomic Report No. GA-A16287*.

Bennett, A.W., Hewitt, G.F., Kearsley, H.A., Keeys, R.K.F., 1967. Unpublished information successively reported in Whalley, P.B., The effect of swirl on critical heat flux in annular two-phase flow. Brief communication in *International Journal of Multiphase Flow*, Vol. 5, 211-217, 1979.

Bergles, A.E., Rohsenow, W.M., 1963. The determination of forced convection surface boiling heat transfer. Paper 63-HT-22 presented at 6th National Heat Transfer Conference of the ASME-AIChE, Boston, 11-14 August.

Birney, K.R., 1967. An empirical study of SNAP reactor fuel irradiation behavior. Atomic International. Contract AT(04-3)-701.

Bowring, R.W., 1979. WSC-2: a subchannel dryout correlation for water-cooled clusters over the pressure range 3.4-15.9 MPa (500-2300 psia). Winfrith, England: United Kingdom Atomic Energy Authority, AEEW-R983.

Brevi, R., Cumo, M., Palmieri, A., Pitimada, D., 1971. Forced convection heat transfer and burn-out measurements with twisted tapes. *La Termotecnica*. Vol. 25, No. 2, 619-625.

Burfoot, D., Rice, P., 1983. Heat transfer and pressure drop characteristics of short lengths of swirl flow inducers interspaced along a circular duct. *Chem. Eng. Res. Des.*, Vol. 61, 253-258.

Capana, R.J., Lindgren, J.R., 1974. Irradiation testing of design models for the GCFR fuel pressure equalization (vent) system. *Nuclear Engineering and Design*, Vol. 26, 201.

Cheong, Y.-M., Kwon, S.-C, Jung, H.-K., 2000. Determination of anisotropic elastic moduli of Zr-2.5Nb CANDU pressure tube materials. *Journal of Materials Science*, Vol. 35, 1195-1200.

Chen, J.C., 1963. A correlation for boiling heat transfer to saturated fluids in convective flow. ASME paper 63-HT-34.

Churchill, S.W. 1973. Empirical expressions for the shear stress in turbulent flow in commercial pipe. *AIChE Journal*. Vol. 19, No. 2, 375-376.

Colebrook, C.F., 1939. Turbulent flow in pipes with particular reference to the transition region between the smooth and rough pipe laws. *Journal of The Institute of Civil Engineering London*. Vol. 11, 133-156.

Collier, J.G., Thome, J.R., 2001. *Convective Boiling and Condensation*. Oxford Science Publications. Clarendon Press, Oxford. Third edition.

Combustion Engineering, 1977. CE critical heat flux: critical heat flux correlation for CE fuel assemblies with standard spacer grids: Part I, uniform axial power distribution. CENPD-162-P-A, Supplement 1-A.

Cuta, J.M., Koontz, A.S., Stewart, C.W., Montgomery, S.D., Nomura, K.K., 1985. VIPRE-01: A Thermal Hydraulic Code for Reactor Cores. Volume 2: User's Manual. Revision 2. EPRI-NP-2511-CCM-A.

Date, A.W., Saha, S.K., 1990. Numerical prediction of laminar flow and heat transfer characteristics in a tube fitted with regularly spaced twisted-tape elements. *International Journal of Heat and Fluid Flow*, Vol. 11, No. 4, 346-354.

Davies, P.H. Hosbons, R.R., Griffiths, M., Chow, C.K., 1994. Correlation between irradiated and unirradiated fracture toughness of Zr-2.5Nb pressure tubes. *Zirconium in the Nuclear Industry: Tenth International Symposium*, ASTM STP 1245, A.M. Garde and E.R. Bradley, Eds., American Society for Testing and Materials, Philadelphia, 1994, pp. 135-167.

Davis, E.J. and Anderson G.H., 1966. The incipience of nucleate boiling in forced convection flow. *AIChE Journal* 14(12), 774-780.

De Hoffmann, F., Rickard, C.L., 1965. High Temperature Gas-cooled Reactors. *Proceedings of the 3rd International Conference on the Peaceful Uses of Energy*. Vol. 5.

- DiGrande, J.T., Lambert, D.V., 1991. Pellet diameter measurement apparatus and method detecting non-orthogonally to the common axis of the pellets. US Patent 5043588.
- Domain, C., Besson, R., Legris, A., 2002. Atomic-scale Ab-initio study of the Zr-H system: I. Bulk properties. *Acta Materialia* 50 (2002) 3513-3526.
- Dormer Jr. T., Bergles A.E., 1969. Pressure drop with surface boiling in small diameter tubes. *International Journal of Heat and Mass Transfer*. Vol. 12, 459-470.
- Driscoll, M.J., Downar, T.J., Pilat, E.E., 1990. *The Linear Reactivity Model for Nuclear Fuel Management*. American Nuclear Society, La Grange Park, Illinois.
- Driscoll, M.J., 2009. Personal communication. July.
- Edenius, M., Ekberg, K., Forssen, B.H., Knott, D., 1995. CASMO-4: A fuel assembly burnup program. User's manual. Studsvik of America, Inc, and Studvisk Core Analysis AB.
- Eggers, G.H., 1978. Method of Making ZrH Fuel Element. United States Patent 4,071,587. Filed on September 25, 1975. Patented on January 31, 1978.
- Eiamsa-ard, S., Thianpong, C., Promvonge, P., 2004. Experimental investigations of heat transfer and pressure drop characteristics of flow through circular tube fitted with regularly-spaced twisted tape. *The Joint International Conference on "Sustainable Energy and Environment"*. 1-3 December, Hua Hin, Thailand.
- EPRI, 1982. EPRI-NP-2609. Parametric Study of CHF Data, Volume 2: A Generalized Subchannel CHF Correlation for PWR and BWR Fuel Assemblies. Electric Power Research Institute, Palo Alto, California. Prepared by Heat Transfer Research Facility, Department of Chemical Engineering, Columbia University, New York.
- ESBWR DCD, 2006. ESBWR Design Control Document, Tier 2, Chapter 4, Reactor. GE Nuclear Energy. Report 26A6642AP, Revision 1.

Ferroni, P., Handwerk, C.S., Todreas, N.E., 2009. Steady state thermal-hydraulic analysis of hydride-fueled grid-supported BWRs. *Nuclear Engineering and Design*, Vol. 239, Issue 8, 1544-1559.

Friedel, L., 1979. Improved friction pressure drop correlations for horizontal and vertical two phase pipe flow. European Two Phase Flow Group Meeting, Ispra, 5-8 June 1979. Paper E2. Subsequently published in the German journal *3R International*, Volume 18, No. 7, July 1979.

Gambill, W.R., Bundy, R.D., Wansbrough, R.W., 1961. Heat transfer, burnout, and pressure drop for water in swirl flow through tubes with internal twisted tapes. *Chemical Engineering Progress, Symposium Series*, 57 (32) 127-137.

Ganda, F., Greenspan, E., 2008. Plutonium and Minor Actinides multi-recycling in PWR using hydride fuels. *PHYSOR 2008*. Interlachen, Switzerland.

Ganda, F., Greenspan, E., 2009. Plutonium recycling in hydride fueled PWR cores. *Nuclear Engineering and Design*, Vol. 239, 1489-1504.

Ganda, F., 2009. Personal communication. December 30th.

Ganda, F., Greenspan, E., 2010. Analysis of reactivity coefficients of hydride-fueled PWR cores. *Nuclear Science and Engineering*, Vol. 164, 1-32.

Garkisch, H.D., Petrovic, B., 2003. Reference data and constraints for uranium-zirconium-hydride and uranium-thorium hydride fuels for Light Water Reactors. Westinghouse Electric Company LLC. Prepared for NERI Project: Use of solid hydride fuel for improved long-life LWR core designs.

Gellerstedt, J.S., Lee, R.A., Oberjohn, W.J., Wilson, R.H., Stanek, L.J., 1969. Correlation of critical heat flux in a bundle cooled by pressurized water. *Two-phase flow and heat transfer in rod bundles*. ASME, Los Angeles, 63-71.

Glaser, A., 2005. About the enrichment limit for research reactor conversion: why 20%? *The 27th International Meeting on Reduced Enrichment for Research and Test Reactors (RERTR)*, November 6-10, Boston, MA.

Greenspan, E., et al., 2006. Use of Solid Hydride Fuel for Improved LWR Core Designs. Final Summary Report. NERI Award No. DE-FG07-02SF22615.

Greenspan, E., et al., 2007. Feasibility of recycling plutonium and minor actinides in Light Water Reactors using hydride fuel. NERI Project No. DE-FC07-06ID14736. Quarter 3 Report. October-December 2006. Submitted on February 5, 2007.

Greenspan, E., et al., 2009. Hydride fuel for LWRs—Project overview. *Nuclear Engineering and Design*, Vol. 239, Issue 8, 1374-1405.

Groeneveld, D.C., Cheng, S.C., Doan, T., 1986. 1986 AECL-UO Critical Heat Flux Lookup Table. *Heat Transfer Engineering*. Vol. 7, No. 1-2, 46-62.

Groeneveld, D.C., Shan, J.Q., Vasic, A.Z., Leung, L.K.H., Durmayaz, A., Yang, J., Cheng, S.C., Tanase, A., 2007. The 2006 CHF look-up table. *Nuclear Engineering and Design*. Vol. 237, 1909-1922.

Groeneveld, D.C., 2008. CHF and CCP enhancement in nuclear fuel bundles – revisiting the past 45 years. Plenary session of the *CNS 2008 Simulation Conference*, Ottawa, November 2-4.

Groeneveld, D.C., 2009. Personal communication. November 26th.

Hache, G., Chung, H.M., 2001. The history of LOCA embrittlement criteria. Available online at: <http://www.ipd.anl.gov/anlpubs/2001/12/41086.pdf>. Also in *Proceedings of the 28th Water Reactor Safety Meeting*, Washington, DC. Page 205.

Hassid, A., Manzoni, G.C., Ravetta, R., 1966. Heat transfer crisis with steam-water mixtures: an experimental study on the increase of critical power with local swirl promoters in round tubes. *Energia Nucleare*. Vol. 13, No. 11, 589-610.

Henkel, D., Mayinger, F., Schad, O., Weiß, E., 1965. Untersuchung der kritischen Heizflächenbelastung (Burnout) bei siedendem Wasser (Investigations Into the Critical Heat Flux in Boiling Water). Maschinenfabrik Augsburg Nurnberg AG (MAN). Quarterly report Nr.1 (April 1st to June 30th, 1965). Contract No. 057-61-RDD. Q.D. Nr. III.1.8.

Hesson, J.C. et al., 1970. Laboratory Simulations of Cladding-Steam Reactions Following Loss-of-Coolant Accidents in Water-Cooled Power Reactors, ANL-7609.

Hewitt, G.F., 2003. Boiling enhancement: response to Professor A.E. Bergles. *Rohsenow Symposium*, Massachusetts Institute of Technology. May 16.

Hewitt, G.F., 2008. Multiphase fluid flow and pressure drop, in *Heat Exchanger Design Handbook*. Begell House, Inc. Vol.2, 2.3.2-14.

Hills, J.H., Azzopardi, B.J., Barhey, A.S., 1996. Spatial unsteadiness – A way towards intensive gas-liquid reactors. *Chemical Engineering Research and Design*, Vol. 74, Part A, 567-574.

Hobson, D.O., Rittenhouse, P.L., 1972. Embrittlement of Zircaloy clad fuel rods by steam during LOCA transients. ORNL-4758, Oak Ridge National Laboratory.

Huang, J., Tsuchiya, B., Konashi, K., Yamawaki, M., 2000. Estimation of hydrogen redistribution in zirconium hydride under temperature gradient. *Journal of Nuclear Science and Technology*, Vol.37, No.10, 887-892.

Hunt, C.E.L., Foote, D.E., 1977. High temperature strain behavior of Zircaloy-4 and Zr-2.5Nb fuel sheaths. *Zirconium in the Nuclear Industry*, ASTM STP 633. A.L. Lowe, Jr. and G.W. Parry, Eds., American Society for Testing and Materials, 50-65.

IAEA-TECDOC-643, 1992. Research reactor core conversion guidebook. Volume 4: Fuels (Appendices I-K).

IAEA, 2002. International Atomic Energy Agency, Safeguards Glossary, 2001 edition. *International Nuclear Verification Series*, No.3, Section 4.12, Vienna.

IAEA-TECDOC-1410, 2004. Delayed hydride cracking in zirconium alloys in pressure tube nuclear reactors. Final report of coordinated research project, 1998-2002. Page 22.

Inasaka, F., Nariai, H., 1987. Critical heat flux and flow characteristics of subcooled flow boiling in narrow tubes, *Japan Society of Mechanical Engineering (JSME) International Journal*. Vol. 30, 1595–1600.

Inasaka, F., Nariai, H., Fujisaki, W., Ishiguro, H., 1991. Critical heat flux of subcooled flow boiling in tubes with internal twisted tape. *ASME/JSME Thermal Engineering Proceedings*, Vol. 2, 65-70.

Ingersoll, D.T., et al., 2004. Status of Preconceptual Design of the Advanced High-Temperature Reactor (AHTR). Oak Ridge National Laboratory. ORNL/TM-2004/104.

INSC, International Nuclear Safety Center, 1998. Enthalpy and Heat Capacity of Zr-2.5%Nb. Available at: <http://www.insc.anl.gov/matprop/zr-25nb/zr25nbh.pdf> and at: <http://www.insc.anl.gov/matprop/zr-25nb/zr25nbk.pdf>

Iorgulis, C., Ciocanescu, M., Preda, M., Mladin, M., 1998. Neutronic calculations regarding the new LEU 6x6 fuel bundle for the 14 MW TRIGA-SSR, in order to increase the reactor power up to 21 MW. *International Meeting on Reduced Enrichment for Research and Test Reactors*. San Paulo, Brazil, October 18-23.

Jensen, M.K., 1984. A correlation for predicting the critical heat flux condition with twisted-tape generators. *International Journal of Heat and Mass Transfer*. Vol. 27, No. 11, 2171-2173.

KAERI, 2000. Korea Atomic Energy Research Institute, Nuclear Data Evaluation Lab. Available at: <http://atom.kaeri.re.kr/>

Karve, A., et al., 2006. A process for analyzing channel-control blade interference. ANS Summer Meeting, Reno, NV, June 8.

Katto, Y., 1980. Critical heat flux of forced convection boiling in uniformly heated vertical tubes (correlation for CHF in HP-regime and determination of CHF-regime map). *International Journal of Heat and Mass Transfer*. Vol. 23, 1573-1580.

Kazimi, K., Hejzlar, P., et al., 2006. High Performance Fuel Design for Next Generation PWRs: Final Report. Center for Advanced Nuclear Energy Systems (CANES). Massachusetts Institute of Technology. Report MIT-NFC-PR-082.

Kim, Y.-J., Kwak, S.-L., Lee, J.-S., Park, Y.-W., 2003. Integrity evaluation system of CANDU reactor pressure tube. *KSME International Journal*, Vol. 17, No. 7, 947-957.

- Kim, H.T., Rhee, B.W., Park, J.H., 2007. Application of a Zircaloy/Steam oxidation model to a CFD code and its validation against a CANDU fuel channel experiment: CS28-2. *Journal of Nuclear Science and Technology*, Vol. 44, No. 11, 1385-1394.
- Klaczak, A., 1996. Heat transfer and pressure drop in tubes with short turbulators. *Heat and Mass Transfer*, Vol. 31, 399-401.
- Klepper, O.H., 1975. Heat transfer performance of short twisted tapes. *A.I.Ch.E. Symposium Series* (Heat transfer No. 131), Vol.8, 87-93.
- Konashi, K., Yamawaki, M., 2004. "The development of thorium hydride fuel", *Characterization and quality control of nuclear fuels*, edited by C. Ganguly and R.N. Jayaraj, Allied Publishers Pvt. Ltd. 2004, 92-106.
- Konashi, K., Pudjanto, B.A., Terai, T., Yamawaki, M., 2005. Thermodynamic stability of ThZr_2H_x at high temperature. *Journal of Physics and Chemistry of Solids*, Vol.66, 625-628.
- Kreith, F., Sonju, O.K., 1965. The decay of a turbulent swirl in a pipe. *Journal of Fluid Mechanics*, Vol. 22, part 2, 257-271.
- Lahoda, E.J., 2007. Personal communication. November 1st.
- Langer, S., Baldwin, N.L., 1971. Fission product release experiments on uranium-zirconium hydride fuels. *General Atomic Report Gulf-GA-A10781*.
- LANL (Los Alamos National Laboratory), 2000. MCNPTM- A General Monte Carlo N-Particle Transport Code. Version 4C. J.F. Briesmeister, Editor. Report No. LA-13709-M.
- Lee, S., Inoue, A., 1995. Critical heat flux characteristics of R-113 boiling two-phase flow in twisted-tape-inserted tubes. *Heat Transfer Japanese Research*, Vol. 24, No.3, 272-287.
- Leung, L.K.H., Groeneveld, D.C., Teysseidou, A., Aubé, F., 2005. Pressure drops for steam and water flow in heated tubes. *Nuclear Engineering and Design*, Vol. 235, 53-65.
- Levy, S., 1967. Forced convection subcooled boiling – prediction of vapor volumetric fraction. *International Journal of Heat and Mass Transfer*, Vol. 10, 951-965.

- Lillie, A.H., Rooney, V.L. Jr., 1971. Findings of the SNAP 8 Developmental Reactor (S8DR) Post-test examination. *Atomics International Division. AI-AEC-13003*. June 30.
- Lillie, A.H., McClelland, D.T., Roberts, W.J., Walter, J.H., 1973. Zirconium hydride fuel element performance characteristics. *Atomics International Division. AI-AEC-13084*. June 19.
- Lopina, R.F., Bergles, A.E., 1969. Heat transfer and pressure drop in tape-generated swirl flow of single-phase water. *Journal of Heat Transfer*, 91 (434-442).
- Lopina, R.F., Bergles, A.E., 1973. Subcooled boiling of water in tape-generated swirl flow. *Journal of Heat Transfer*, 95 (281-283).
- MacBeth, R.V., 1965-1966. An appraisal of forced convection burnout data. *Proceedings of the Institute of Mechanical Engineers*. Vol. 180, 47-48.
- Malen, J.A., Todreas, N.E., Hejzlar, P., Ferroni, P., Bergles, A., 2009. Thermal hydraulic design of a hydride-fueled inverted PWR core. *Nuclear Engineering and Design*, Vol. 239, 1471-1480.
- Manglik, R.M., Bergles, A.E., 1992. Heat transfer enhancement and pressure drop in viscous liquid flows in isothermal tubes with twisted-tape inserts. *Wärme- und Stoffübertragung* 27, 249-257.
- Manglik, R.M., Bergles, A.E., 1993. Heat transfer and pressure drop correlations for twisted-tape inserts in isothermal tubes: Part II – Transition and turbulent flows. *Transactions of the ASME*. Vol. 115, 890-896.
- Manglik, R.M., Bergles, A.E., 2002. Swirl flow heat transfer and pressure drop with twisted-tape inserts. *Advances in Heat Transfer*. Vol.36, 183-266.
- Massih, A.R., 2006. Models for MOX fuel behavior: A selective review. Swedish Nuclear Power Inspectorate Report 2006:10.
- Matzner, B., Moeck, E.O., Casterline, J.E., Wikhammer, G.A., 1965. Critical heat flux in long tubes at 1000 psi with and without swirl promoters. ASME-Paper No. 65-WA/HT- 30, Presented at the *Winter Annual Meeting of the ASME*, Chicago, IL, November 7–11, 1965.

Maurer, G.W., LeTourneau, B.W., 1963. Friction factors for fully developed turbulent flow in ducts with and without heat transfer. *ASME paper No. 63-WA-98*.

Mayinger, F., Schad, O., Weiß, E., 1966. Der Einfluß der hydrodynamischen Bedingungen auf die kritische Heizflächenbelastung beim Sieden. *Sonderdruck aus Brennstoff-Warme-Kraft (BWK)* Vol. 18, No. 6. 288-294.

Memmott, M. J., Hejzlar, P., Buongiorno, J., 2009. Thermal-hydraulic analysis of innovative fuel configurations for the Sodium Fast Reactor. Center for Advanced Nuclear Energy Systems (CANES). Massachusetts Institute of Technology. Report No. MIT-ANP-TR-123.

Moeck, E.O., Wikhammer, G.A., MacDonald, I.P.I., Collier, J.G., 1964. Two methods of improving the dryout heat flux for high pressure steam/water flow. Chalk River Ontario, *AECL 2109*.

Morita, T., 1988. Nuclear fuel cladding containing a burnable absorber. United States Patent 4,717,534.

Moussez, C., Rosuel, A., Sourieux, G., du Boucheron, G., Eidelman, G., 1965. Ecoulements giratoires dans l'eau bouillante. EUR 1785.f. *Communaute Europeenne De L'Energie Atomique-Euratom*.

Moussez, C., Rosuel, A., Sourieux, G., du Boucheron, G., Eidelman, D., 1965A. Ecoulements giratoires dans l'eau bouillante. *EURAECE Report 1114*. Euratom Contract No. 058-61-7 RDF.

Mueller, W.M., Blackledge, J.P., Libowitz, G.G., 1968. *Metal Hydrides*. Academic Press. New York and London.

Musolf, A.O., 1963. An experimental investigation of the decay of a turbulent swirl flow in a pipe. Thesis, University of Colorado.

Novog, D.R., Yin, S.T., Chang, J.S., 2007. Recent advances in high heat flux smooth and swirl flow boiling of water. *Fusion Science and Technology*, Vol. 52, 880-884.

NRTSC, 1990. FLOWTRAN-TF Code Description (U). *Nuclear Reactor Technology and Scientific Computations. Westinghouse Savannah River Company. WSRC-TR—90-413.*

NUREG/CR-6150, 1993. SCDAP/RELAP5/MOD3.1 Code Manual. Volume IV: MATPRO--A library of materials properties for light water reactor accident analysis. Idaho National Engineering Laboratory.

Olander, D.R., Ng, M., 2005. Hydride fuel behavior in LWRs. *Journal of Nuclear Materials*, No.346, 98-108.

Olander, D.R., 2006A. Personal communication. June 1st.

Olander, D.R., 2006. Personal communication. December 18th.

Olander, D.R., Greenspan, E., Garkisch, H.D., Petrovic, B., 2009. Uranium-zirconium hydride fuel properties. *Nuclear Engineering and Design*, Vol.239, Issue 8, 1406-1424.

O'Neill, G.E., et al., 1965. A technical and economic evaluation of vented fuel for Sodium-cooled Fast Ceramic Reactors. GEAP-4770.

Pawel, R.E., 1974. Oxygen diffusion in beta Zircaloy during steam oxidation, *Journal of Nuclear Materials*, Vol. 50, 247-258.

Peterlongo, G., Ravetta, R., Riva, B., Rubiera, L., Tacconi, F.A., 1964. Large scale experiments on heat transfer and hydrodynamics with steam-water mixtures: further critical power and pressure drop measurements in round vertical tubes with and without internal obstacles. CISE report R122.

Pope, M.A., Yarsky, P., Driscoll, M.J., Hejzlar, P., Saha, P., 2005. An advanced vented fuel assembly design for GFR application. *Transactions of the American Nuclear Society*, San Diego, USA.

Pope, M.A., Lee, J.I., Hejzlar, P., Driscoll, M.J., 2009. Thermal Hydraulic Challenges of Gas Cooled Fast Reactors with Passive Safety Features. *Nuclear Engineering and Design*, 239, 840-854.

Rand, M., Fuger, J., Grenthe, I., Neck, V., Rai, D., 2008. *Chemical Thermodynamics – Chemical Thermodynamics of Thorium*. Vol. 11. Federico J. Mompean Ed. OECD Nuclear Energy Agency.

Rao, K.R., 2006. Companion Guide to the ASME Boiler & Pressure Vessel Code. Criteria and Commentary on Select Aspects of the Boiler & Pressure Vessel and Piping Codes. Second edition. Volume 1. ASME, Three Park Avenue, New York, NY 10016.

Reddy, D.G., Sreepada, S.R., Nahavandi, 1982. Two-phase friction multiplier correlation for high-pressure steam-water flow. NP-2522. Research Project 813. Prepared by Columbia university for Electric Power Research Institute (EPRI).

RELAP5, 2005a. RELAP5-3D[®] Code Manual. Volume 1: Code Structure, System Models, and Solution Methods. Idaho National Laboratory. Report INEEL-EXT-98-00834, Revision 2.3.

RELAP5, 2005b. RELAP5-3D[®] Code Manual. Volume IV: Models and Correlations. Idaho National Laboratory. Report INEEL-EXT-98-00834, Revision 2.3.

Rosuel, A., Sourieux, G., 1961. Influence de tourbillons induits dans l'eau bouillante a la pression atmospherique sur les flux de calefaction. *Euratom report No. 5*, SNECMA, Division Atomique.

Saha, P., Zuber, N., 1974. Point of net vapor generation and vapor void fraction in subcooled boiling. Proceedings of the 5th *International Heat Transfer Conference*, Tokyo. Vol. 4, Paper B4.7. September 3-7.

Saha S.K., Gaitonde U.N., Date A.W., 1990. Heat transfer and pressure drop characteristics of turbulent flow in a circular tube fitted with regularly spaced twisted-tape elements. *Experimental Thermal and Fluid Science*, 3, 632-640.

Schultz, R.R., et al., 2005. Very High Temperature Reactor – Design Methods Development and Validation Research & Development Program Plan. INEEL/EXT-04-02293. Revision 2. Idaho National Laboratory. September.

Seabrook USAR, 2002. Seabrook Power Station Updated Safety Analysis Report, Revision 8, 2002.

Shenoy, A., 1996. Gas Turbine-Modular Helium Reactor (GT-MHR) Conceptual Design Description Report. Revision 1, GA-910720, July.

Shi, S.-Q., Puls, M.P., 1994. Criteria for fracture initiation at hydrides in zirconium alloys. *Journal of Nuclear Materials*, Vol. 208, 232-242.

Shi, S.-Q., Puls, M.P., 1999. Fracture strength of hydride precipitates in Zr-2.5Nb alloys. *Journal of Nuclear Materials*, Vol. 275, 312-317.

Shuffler, C., Trant, J., Malen, J., Todreas, N., 2009. Thermal hydraulic analysis for grid supported pressurized water reactor cores. *Nuclear Engineering and Design*, Vol. 239, 1442-1460.

Sieder, E. N., Tate, C. E., 1936. Heat transfer and pressure drop of liquids in tubes. *Ind. Eng. Chem.* 28, 1429-1435.

Simnad, M.T., Bokros, J.C., Sleeper, H.P. Jr., 1964. Method of Hydriding. United States Patent 3135697. Filed on June 09, 1960. Patented on June 02, 1964.

Simnad, M.T., 1981. The U-ZrH_x alloy: its properties and use in TRIGA fuel. *Nuclear Engineering and Design*, Vol.64, 403-422.

Smithberg, E., Landis, F., 1964. Friction and forced convection heat transfer characteristics in tubes with twisted tape swirl generators. *Journal of Heat Transfer, Transactions of ASME*. Vol. 86, Series C, 39-49.

SolidWorks, 2007. SolidWorks Corporation COSMOS. 12121 Wilshire Blvd., Suite 700 Los Angeles, CA 90025.

Stadnik, A.G., Page, J.P., 1988. Uranium-zirconium hydride fuel performance in the SNAP-DYN space power reactor. *Proceedings of the Intersociety Energy Conversion Engineering Conference*, Vol. 3.

Staub, F.W., 1969. Two-phase fluid modeling – the critical heat flux. *Nuclear Science and Engineering*. Vol. 35, 190-199.

Tarasova, N.V., Leontiev, A.I., Hlopushin, V.I., Orlov, V.M., 1966. Pressure drop of boiling subcooled water and steam-water mixture flowing in heated channels. *Proceedings of the Third International Heat Transfer Conference*. Chicago, IL, August 7-12, 1966.

Terrani, K.A., Chinthaka Silva, G.W., Yeaman, C.B., Balooch, M., Olander, D.R., 2009A. Fabrication and characterization of uranium-thorium-zirconium hydrides. *Journal of Nuclear Materials*, Vol. 392, 151-157.

Terrani, K.A., Balooch, M., Olander, D.R., Greenspan, E., 2009B. Investigation of liquid metal bonded hydride fuels for LWRs - A review. *Technical Meeting on Advanced Fuel Pellet Materials and Fuel Rod Designs for Water Cooled Reactors*. PSI, Villigen, Switzerland, 23-26 November.

Thompson, B., Macbeth, R.V., 1964. Boiling water heat transfer - burnout in uniformly heated round tubes: a compilation of world data with accurate correlations. AEEW-R 356, United Kingdom Atomic Energy Authority, Winfrith, UK.

Todreas, N.E., Ferroni, P., 2009. Enhancing Reactor Core Performance through Inverted Fuel Design. *The 13th International Topical Meeting on Nuclear Reactor Thermal Hydraulics (NURETH-13)*. Kanazawa City, Ishikawa Prefecture, Japan, September 27-October 2.

Todreas, N.E., Kazimi, M.S., 1993. *Nuclear Systems I: Thermal Hydraulic Fundamentals*. Taylor and Francis. Second printing.

Toma, C., Parvan, M., Tuturici, I.L., 2002. Characterization of TRIGA LEU fuel behavior, irradiated in 14 MW core. Institute for Nuclear Research, 0300 Pitesti, Romania. Un-numbered report.

Tong, L.S., 1968. Boundary-layer analysis of the flow boiling crisis. *International Journal of Heat and Mass Transfer*. Vol. 11, 1208-1211.

Tong, L.S., 1972. Boling crisis and critical heat flux. *AEC Review Series*, USAEC Washington, DC.

Tong, W., Bergles, A.E., Jensen, M.K., 1996. Critical heat flux and pressure drop of subcooled flow boiling in small-diameter tubes with twisted-tape inserts. *Journal of Enhanced Heat Transfer*, Vol. 3, No. 2, 95-108.

Tsuchiya, B., Huang, J., Konashi, K., Saiki, W., Onoue, T., Yamawaki, M., 2000. Thermal diffusivity measurement of uranium-thorium-zirconium hydride. *Journal of Alloys and Compounds*. Vol. 312, 104-110.

Urbanic, V.F., 1977. Oxidation of zirconium alloy in steam at 1000 to 1850°C. *Zirconium in the Nuclear Industry*, ASTM STP 633, A.L. Lowe, Jr. and G.W. Parry, Eds., American Society for Testing and Materials, 168-181.

Urbanic, V.F., Warr, B.D., Manolescu, A., Chow, C.K., Shanahan, M.W., 1989. Oxidation and deuterium uptake of Zr-2.5Nb pressure tubes in CANDU-PHW reactors. *Zirconium in the Nuclear Industry: Eighth International Symposium*, ASTM STP 1023, L.F.P. Van Swam and C.M. Eucken, Eds., American Society for Testing and Materials, Philadelphia, 20-34.

US FCR10-50.46, 1974. Acceptance Criteria for Emergency Core Cooling Systems for Light-Water Nuclear Power Reactors, U.S. Code of Federal Regulations, Title 10, Part 50, Section 46, 4 January, Amended.

Van Houten, R., 1974. Selected Engineering and Fabrication Aspects of Nuclear Metal Hydrides (Li, Ti, Zr, and Y). *Nuclear Engineering and Design* 31 (1974) 434-448.

Vetrano, J.B. 1959. Method of making Delta Zirconium Hydride Monolithic Moderator Pieces. United States Patent 3018169. Filed on January 07, 1959. Patented on January 23, 1962.

Viskanta, R., 1961. Critical heat flux for water in swirling flow. Letter to the Editor. *Nuclear Science and Engineering*. Vol. 10, 202-203.

Wang, L., Sunden, B., 2002. Performance comparison of some tube inserts. *Int. Comm. Heat Mass Transfer*, Vol. 29, No. 1, 45-56.

Weaver, K.D., et al., 2004. Gen IV Nuclear Energy Systems: Gas-Cooled Fast Reactor (GFR), FY-04 Annual Report, INEEL/EXT-04-02361, September.

Weisman, J., Yang, J.Y., Usman, S., 1994. A phenomenological model for boiling heat transfer and the critical heat flux in tubes containing twisted tapes. *International Journal of Heat and Mass Transfer*. Vol. 37, No. 1, 69-80.

West, G.B., Simnad, M.T., Copeland, G.L., 1986. Final results from TRIGA LEU fuel post-irradiation examination and evaluation following long term irradiation testing in the ORR. General Atomics document LIZR-22. Presented at the *International Meeting on Reduced Enrichment for Research and Test Reactors*, Gatlinburg, Tennessee, USA, November 3-6. Also available as Appendix I-7.1 of *IAEA-TECDOC-643: Research Reactor Core Conversion Guidebook*, Volume 4, 1992.

Wongsawaeng, D., Olander, D., 2004. Effect of replacing helium with a liquid metal in the fuel-cladding gap on fission gas release. *Nuclear Technology*, Vol. 146, 211-220.

Wongsawaeng, D., Olander, D., 2007. Liquid-metal bond for LWR fuel rods. *Nuclear Technology*, Vol. 159, 279-291.

Wright, R.F., Tulenko, J.S., Schoessow, G.J., 1996. Thermal bonding of Light Water Reactor fuel using non alkaline liquid-metal alloy. *Nuclear Technology*, Vol. 115, 281-292.

Xu, Z., 2003. Design Strategies for Optimizing High Burnup Fuel in Pressurized Water Reactors. PhD thesis. Massachusetts Institute of Technology.

Xu, Z., Hejzlar, P., 2008. MCODE, Version 2.2: An MCNP-ORIGEN depletion program. MIT-NFC-TR-104. CANES (Center for Advanced Nuclear Energy Systems), Massachusetts Institute of Technology, Cambridge, MA, USA.

Yamamoto, T., Suwarno, H., Kayano, H., Yamawaki, M., 1995. Development of new reactor fuel materials: hydrogenation properties of U-Th-Zr alloys and neutron irradiation effects on their hydrides. *Journal of Nuclear Materials*, Vol. 247, 339-344

Yamamoto, T., Suwarno, H., Ono, F., Kayano, H., Yamawaki, M., 1998. Preparation, analysis and irradiation of hydrided U-Th-Zr alloy samples for a new fuel. *Journal of Alloys and Compounds*, Vol. 271-273, 702-706.

Yamawaki, M., et al., 1999. Development of U-Th-Zr alloy hydrides as alternative thorium-base fuel and MA burning target fuel. *Proceedings of the International Conference on Future of Nuclear Systems*, GLOBAL 1999. Jackson Hole, WY.

VOLUME 2
Pressure drop tests

Table of contents

Table of contents	404
Introduction to Volume 2	406
1. Twisted tapes: an introduction	407
2. Motivation for the test and existing literature on the subject	410
2.1 Available literature on SLTTs	411
3 Objectives of the tests and definition of SLTT module	417
4. Test planning	418
4.1 Choice of the geometric variables	419
5. Experimental apparatus	421
5.1 Test sections	422
5.1.1 Test section geometry	422
5.1.2 Test section manufacture.....	426
5.1.3 Pressure tap geometry and manufacture	429
5.2 Pump.....	430
5.3 Differential pressure transducer	431
5.4 Flow meter.....	431
5.5 Pressurizer	432
5.6 Heat exchanger.....	432
5.7 Data acquisition system.....	432
5.8 Other components	432
6. Test methodology description	433
7. Data scatter and error propagation analysis	434
7.1 Data scatter at constant pump speed	434
7.1 Error propagation analysis.....	436
8. Tube roughness determination and pressure drop measurement accuracy	442
8.1 Determination of test section inner surface roughness.....	443
8.1 Determination of pressure drop measurement accuracy	444

9. Data elaboration method: definition of friction factor and directions for using friction factor correlation.....	446
9.1 Friction factor: definition.....	446
9.2 Method for using friction factor correlation to predict pressure drops	447
10. Results	447
10.1 Result elaboration and interpretation.....	452
Appendix A: Calculation of the pressure drop penalty due to the use of a full-length tape ...	456
Appendix B: Criteria for the selection of N_{rev}	464
Appendix C: Investigation of swirl flow development.....	473
Appendix D: Effect of water deaeration on pressure drop.....	487
References for Volume 2.....	489

Introduction to Volume 2

Volume 2 describes the pressure drop tests performed to support the analysis of one of the design proposed for the Inverted Pressurized Water Reactor (IPWR), referred to as S-IPWR. This design employs multiple short-length twisted tapes (MSLTTs), equally spaced along the cooling channels, as a mean to increase the Critical Heat Flux (CHF). The tests were aimed at measuring the pressure drop of a MSLTT-provided tube, and the corresponding results were used for predicting the pressure drop of the S-IPWR design. The experimental work described in this Volume is valuable not just because of its usefulness for the IPWR design but also, and especially, because it was performed on designs that were never tested before. Therefore, it supplements the literature with new data, which are valuable for both nuclear and non-nuclear applications.

1. Twisted tapes: an introduction

Twisted tapes (TTs) are often employed in heat exchangers as turbulence promoters. By enhancing fluid mixing and increasing the absolute fluid velocity, TTs increase the heat transfer performance at the expense, however, of an increased pressure drop. The most well known TT design¹ is the full-length TT (FLTT), which consists of a TT having a length equal to that of the channel in which it is inserted. This TT design has been studied extensively in the past and, as a result, several correlations are available for the calculation of the heat transfer coefficient (htc) and pressure drop in the presence of such a device. Correlations for critical heat flux (CHF) are also available, even if they are less numerous. Manglik and Bergles (2002) summarize most of the available correlations in their overview on FLTTs.

As mentioned earlier, the drawback² of using FLTTs is the increase in pressure drop that accompanies the enhancement in htc and CHF performance. The extent of this increase, which is quantitatively evaluated and discussed in Appendix A of this volume, depends on the FLTT geometry and is always larger than 1.85 times for any FLTT geometry. The main reasons for this pressure drop penalty in decreasing order of importance are:

- the reduction in hydraulic diameter due to the presence of the tape;
- the increase in friction factor due to the fact that the fluid does not flow parallel to the walls, but impinges them with a certain angle;
- the increase in fluid velocity due to the reduction in flow area;

¹ The term “TT design” refers to the combination of the parameters that completely identify the TT geometry: diameter, thickness, twist ratio (γ), number of revolutions and, if applicable, spacing between successive TTs, s .

² Besides pressure drop-related drawbacks, there are three other problems encountered when using FLTTs. The first is that, as discussed by Hewitt (2003), if the flow is two-phase at high quality “*water can run along the tape itself, denying this water access to the surface and in some cases leading to a reduction in CHF*”. The second problem is the thermal-insulating effect at the contact points between the tape and the wall which, for FLTTs, are located throughout the tube length. This insulation effect makes the contact points more susceptible to CHF (Tong et al., 1996, and Lee and Inoue, 1995). A more detailed discussion on these CHF-related drawbacks of FLTTs is presented in Chapter VI of Volume 1. The last drawback is related to flow oscillations that can take place due to the flow instability characterizing the pair of parallel channels partitioned by the tape (Lee and Inoue, 1995).

- the increase in fluid-wall contact travel path length, per unit of tube axial length (because of the helicoidal motion, the length of the fluid particle trajectory is larger than the length of the tube).

Figure A- 1 in Appendix A shows the extent of each contribution.

The need to reduce the extra-pressure drop, relative to an empty tube, associated with the use of FLTTs, induced some researchers (see Table 1) to examine a different TT design, consisting of either a single short-length TT located at the inlet of a short channel or multiple short-length TTs inserted into a long channel and spaced by an empty length, s . Both these designs, which are conceptually equivalent, rely on the persistence of swirl flow downstream the TT, where heat transfer coefficient (h_{tc}) and CHF performance can therefore be enhanced, without having the hydraulic diameter reduced. In this chapter, as done in the rest of this document, this design is referred to as the short-length twisted-tape (SLTT) design and, in the particular case of multiple TTs along a tube, as the multiple short-length twisted-tape (MSLTT) design. Two dimensionless parameters define the geometry of a MSLTT design: the twist ratio y , which, as described in Section 4.1, is the ratio between the length of TT corresponding to a 180° revolution around its own axis and the tube inner diameter, and the TT spacing, s , given by the length of the empty region between SLTTs divided by the tube inner diameter.

It is important to note, however, that the mentioned pressure drop benefits of MSLTTs relative to FLTTs may not be sufficient to make the former design preferable over the latter when pressure drop and heat transfer performance are considered simultaneously. In fact, although in most³ cases MSLTTs yield a lower pressure drop than a FLTT having

³ The friction factor of a MSLTT design does not approach asymptotically that of the FLTT design as the SLTTs get closer and closer to each other. Instead, it can exceed the FLTT friction factor when the tapes are closely packed and have a large twist ratio. Saha et al. (1990) tested MSLTT designs having twist ratio between 3.46 and 10, and spacing between tapes between 2.5 and 10. They demonstrated that, in turbulent regime, the pressure drop characterizing these closely packed MSLTT designs is smaller than that of a FLTT design having the same twist ratio only when such twist ratio is below 5. Instead, for $y \geq 5$, the friction factor of closely packed SLTTs is larger than that of a FLTT. A possible explanation for this, according to Saha et al. (1990), is the strongly nonaxisymmetric velocity profile characterizing the flow issuing from a tape having large twist ratio. For these TT designs, therefore, a long mixing region, downstream of the tape exit is needed for the axisymmetric decaying swirl flow to set in. If such mixing region is short (closely packed SLTTs) the axisymmetry is not reached and the pressure drop will be higher than that characterizing a FLTT. Conversely, in a MSLTT design with small twist ratio (3.46 in Saha et al., 1990) the flow requires a very short mixing length downstream of the tapes to reach axisymmetry, and only when the tapes are extremely packed ($s \leq 2.5$) is the pressure drop experienced by the MSLTT design larger than that of the FLTT design.

the same twist ratio, y , inconsistent results have been found in the literature regarding whether MSLTTs are able to transfer more heat than FLTTs for the same pumping power. Saha et al. (1989) and Saha et al. (1990) state that MSLTTs perform better than FLTTs only in laminar regime, while in turbulent regime they perform worse. However, they did not test physically separated MSLTTs, but MSLTTs connected with a solid rod, which has a detrimental impact on pressure drop. If that rod had not been present, their results would have shown better, in an absolute sense, performance for the MSLTT design. Whether or not such performance would have been better than that of FLTTs cannot be known with certainty. Results by Klepper (1975) may however help in this regard. Klepper, who used nitrogen as working fluid, tested a single SLTT followed by a 50 diameter long swirl decay region, and compared the heat transfer coefficient of this design with that of a FLTT design having same twist ratio and pressure drop. Particularly, he defined an effectiveness parameter:

$$E = \left(\frac{\bar{h}_{TT}}{h_{empty}} \right)_{\text{constant pumping power}} \quad (1)$$

where \bar{h}_{TT} and h_{empty} are the heat transfer coefficients in a tube provided with a TT (either FLTT, or SLTT followed by a swirl decay region) and in an empty tube respectively. Particularly, for SLTT geometries the heat transfer coefficient is averaged over the TT module, i.e. over the combination of the taped and untaped regions. His findings are summarized in Figure 1. It can be seen that, in the ranges $2 \times 10^4 \leq Re \leq 3 \times 10^5$ and $2.38 \leq y \leq 8.05$, a SLTT design having a 50 diameter long swirl decay region performs slightly better than a FLTT design. Also, relative to an empty tube, the extra-amount of heat that can be transferred at constant pumping power ranges between 6 and 22% and between 9 and 29% for the FLTT and for the SLTT design respectively.

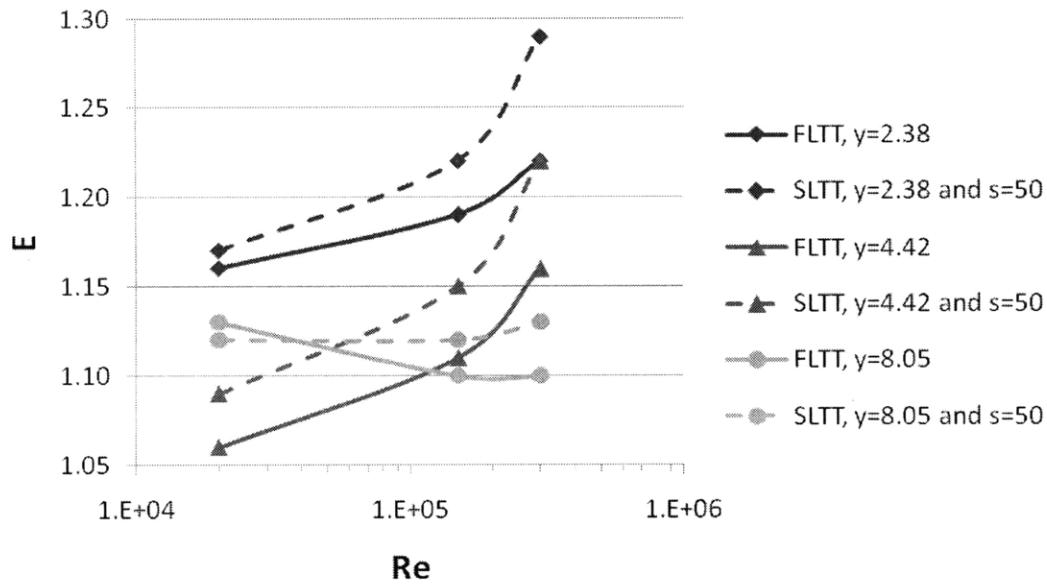


Figure 1 – Effectiveness parameter for FLTTs and for SLTTs having a swirl decay region 50 diameters long (from Klepper, 1975)

It must be stressed, however, that the comparison between the heat transfer performance of FLTTs and MSLTTs, on the basis of constant pumping power, is not a universally applicable tool to decide which design is better. In fact, ease of installation and maintenance, but especially CHF enhancement performance is not accounted for in that comparison. In the inverted PWR investigated in this project twisted tapes are used with the purpose of augmenting CHF, while the simultaneous enhancement in heat transfer coefficient, although beneficial, has a marginal importance. Unfortunately, no comparison between FLTT and MSLTT designs, accounting for CHF enhancement, has been found in the literature, and CHF data for TT-provided channels are very limited.

2. Motivation for the tests and existing literature on the subject

Designs employing SLTTs have not been studied as extensively as those using FLTTs. As a consequence, pressure drop, htc and CHF data and correlations for SLTT-provided systems are either not available or are applicable to very limited operating conditions. An overview of the experimental work performed on SLTTs is presented in Section 2.1. The tests performed for the inverted core project are aimed at supplementing the literature

with isothermal friction factor experimental data and correlations for MSLTT designs, under no-boiling conditions.

2.1 Available literature on SLTTs

Table 1 summarizes the studies on SLTTs (and similar turbulence promoters⁴) that have been found in the literature, listed in chronological order. This coincidentally places the studies in the turbulent regime first (except for Saha et al., 1990), followed by those in the laminar regime. The experimental study performed for the inverted core project is shown at the bottom of the table. It can be noticed that:

- interest for SLTTs seems to be born in turbulent regime applications and then shifted towards laminar regime applications, for which studies are ongoing even in recent years;
- the first experimental work on SLTTs was performed by the Italian research team CISE for their implementation in LWRs; particularly, as done for the inverted core project, interest for MSLTTs was motivated by the need to enhance CHF, while the increase in heat transfer coefficient, although real, was not subject to investigation. In fact, in LWRs the heat transfer coefficient is already quite high, due to subcooled and/or saturated boiling, and CHF is a much more limiting thermal hydraulic constraint.
- most of the studies on MSLTTs employed tapes that are not physically separated, but connected by means of a solid rod. This arrangement allows the tapes to be easily inserted and removed, without being fixed to the tubes. However, it does not take full advantage of their short length since, due to the presence of the solid rod, the swirl decay region is still characterized by a reduced equivalent diameter relative to the empty tube. For example, the swirl decay region in Saha et al. (1990) experiments suffered, because of the presence of a 3 mm rod diameter, of an equivalent diameter reduction of 23%, i.e. from 13 mm (value if the rod was not present) to 10 mm. It can be easily demonstrated that, with respect to the case

⁴ Note that, while most of the studies listed in Table 1 refer to twisted tapes, some refer to turbulence promoters that, geometrically speaking, are not short-length twisted tapes, e.g. short-length helical tapes. Their design is however based on the same principle as SLTTs, i.e. achieving heat transfer and/or CHF enhancement while minimizing pressure drop.

of an empty swirl decay region and assuming same mass flow rate and a friction factor dependence on Reynolds number of the form $Re^{-0.2}$, Saha's solid rod-provided swirl decay region was characterized by a pressure drop about 50% higher.

- 10 out of 20 of the studies listed in the table refer to turbulent regime; also, the pressure drop data collected in these ten studies are not sufficient to fully characterize the pressure drop characteristics of the MSLTT design. In fact, of these ten studies, only Peterlongo et al. (1964), Matzner et al. (1965), Blackwelder and Kreith (1970), Zozulya and Shkuratov (1974), Klepper (1975), Burfoot and Rice (1983) and Saha et al. (1990) actually measured pressure drops, and with some limitations. Peterlongo et al. (1964), Blackwelder and Kreith (1970) and Zozulya and Shkuratov (1974) used test sections containing a single SLTT, and not multiple SLTTs. The same for Klepper (1975), whose data were taken with nitrogen and only along the TT-provided region, i.e. the swirl decay region was excluded from pressure drop measurements. Matzner et al. (1965) tested two SLTTs, but very widely separated. The study by Burfoot and Rice (1983), although on MSLTT design, used tightly packed SLTTs, and few pressure drop data are presented. Saha et al. (1990) also tested closely packed SLTTs, which were however connected by means of a solid rod.

Based on the above observations, it can be concluded that the experimental work performed for the IPWR project supplements the literature with valuable data, since the geometries and the operating conditions tested have never been subjected to experimental investigation before.

Study	SLTT design	D_{ci} (mm)	y	Swirl decay region length ⁵	N_{rev}	t_{TT} (mm)	$t_{TT-tube}$ (mm) ⁶	Fluid	Re^7 , G (ton/s m^2) ⁸ and, if applicable, steam quality ranges	Experimental data collected and indication on correlation development		
										Δp	htc	CHF
Peterlongo et al. (1964)	One SLTT at the inlet ⁹	15.1	2.8	~158	~1.2	? ¹⁰	0.4	2-phase water at 5 and 6.5 MPa	2×10^5 to 6×10^5 $1.1 \leq G \leq 3.8$ $-0.24 \leq x_{in} \leq 0.06$ $0.09 \leq x_{out} \leq 0.65$	Yes (no corr.)	No	Yes (no corr.)
Henkel et al. (1965)	One SLTT at the inlet	7	1.4 and 3.3	40	1, 2	0.5	?	2-phase water at 7.1 and 10.1 MPa	3×10^5 to 5×10^5 $2.3 \leq G \leq 3.5$ $-0.2 \leq x_{in} \leq 0$ $-0.03 \leq x_{out} \leq 0.23$	No	No	Yes (no corr.)
Matzner et al. (1965)	Two SLTTs	10.2	5	115 and 235	0.5	0.38	~0	2-phase water at 6.89 MPa	$\sim 10^5$ to 10^6 $1.4 \leq G \leq 9.7$ $-0.6 \leq x_{in} \leq 0$ $0 \leq x_{out} \leq 0.88$	Yes (no corr.)	No	Yes (with corr.) ¹¹
Hassid et al. (1966)	SLTTs connected with a solid rod	15.1	0.5 to 2.5	15 to 153	0.7 to 3.5	2.5	0.6 to 6.1	2-phase water at 5 and 7 MPa	2×10^5 to 7×10^5 $1.1 \leq G \leq 3.8$ $-0.39 \leq x_{in} \leq 0.69$ $0.02 \leq x_{out} \leq 0.73$	No	No	Yes (with corr.)

⁵ The length of the swirl decay region is expressed in number of tube inner diameters.

⁶ $t_{TT-tube}$ is the diametral gap between the TT and the tube inside surface.

⁷ Reynolds number refers to empty tube conditions. For tests performed with two-phase water, it refers to saturated liquid conditions, i.e. it is equal to Re_f .

⁸ Even though the mass flux can be estimated using the Reynolds number, for the experimental studies on CHF it was decided to also show it explicitly.

⁹ The Peterlongo et al. (1964) test section consisted of a 4 m long round tube containing a single SLTT. The SLTT was positioned at about 1.6 m from the test section inlet, by means of a 10 mm diameter solid rod having the tape fixed at its downstream end. The length of the swirl decay region was kept fixed, while the length of the heated section region following the SLTT was varied. Pressure drop measurements were always taken across the whole 4 m long test section, therefore including the annular section (because of the presence of the solid rod), the SLTT, the heated part of the swirl decay region and the unheated part of it.

¹⁰ Question marks indicate parameters for which the numerical value is not specified in the articles consulted.

¹¹ The CHF correlation developed by Matzner et al. (1965) was design-specific, and therefore not applicable to MSLTT geometries and operating conditions different from those they tested.

Table 1 (cont'd) – Available literature on short-length TTs												
Study	SLTT design	D_{ci} (mm)	y	Swirl decay region length	N_{rev}	t_{TT} (mm)	$t_{TT-tube}$ (mm)	Fluid	Re, G (ton/s m ²) and, if applicable, steam quality ranges	Experimental data collected and indication on correlation development		
										Δp	htc	CHF
Bennett et al. (1967)	One SLTT	12.62	4	0 to 158	0.5	0.25	2.22	2-phase water at 6.9 MPa	3.7×10^5 $G = 2.712$ $-0.2 \leq x_{in} \leq -0.09$ $0.32 \leq x_{out} \leq 0.46$	No	No	Yes (with corr. ¹²)
Blackwelder and Kreith (1970)	One SLTT at the inlet	27.0	1.77; 4.25; 11	80	6.4; 2.6; 1	0.51	?	Air	2×10^4 to 6×10^4	Yes (no corr.)	Yes (no corr.)	No
								Subc. water	4.2×10^4 and 7.5×10^4			
Zozulya and Shkuratov (1974)	One SLTT at the inlet	21 and 24	4	63	~7	?	?	Subc. water	10^4 to 7×10^4	Yes (no corr.)	Yes (no corr.)	No
Klepper (1975)	One SLTT + swirl decay region	10.6, 11.0	2.38 to 8.05	66.8 to 81.4 ¹³	3, 6, 8	0.38	~0	N ₂ at 1.4 MPa	2×10^4 to 3.8×10^5	Yes (corr. and data only for TT-provided region)	Yes (with corr. valid also in the swirl decay region)	No
Burfoot and Rice (1983)	Physically separated SLTTs	20	2.02	~4 to ~22	0.5, 1	2.8, 3.2	~0	Subc. water	1.55×10^4 to 1.04×10^5	Yes, both, but few (no correlations)		No

¹² Bennett did not develop any CHF correlation. Whalley (1979) reported the originally unpublished data collected by Bennett and discuss a method for the prediction of CHF in annular flow.

¹³ Klepper's (1975) test sections consisted of ~1.5 m long tubes, in which a single short TT was inserted up to a location about 22 diameters from the tube inlet. Downstream of the TT, a swirl decay region having a variable length between 66.8 and 81.4 diameters was present.

Study	SLTT design	D_{ci} (mm)	y	Swirl decay region length	N_{rev}	t_{TT} (mm)	$t_{TT-tube}$ (mm)	Fluid	Re	Experimental data collected and indication on correlation development		
										Δp	htc	CHF
Saha et al. (1989)	SLTTs connected with a solid rod	13 (pres drop tests); 11 (htc tests)	3.46 to 10 (pres drop tests); 3.18 to 10 (htc tests)	2.5 to 10	0.5	0.4	1	Subc. water	5×10^2 to 2.3×10^3	Yes, both (correlations developed)	No	
Saha et al. (1990)			5×10^3 to 4.3×10^4	Yes, both (correlations developed)	No							
Date and Saha (1990)			3.18 to 5	2.5 to 10	0.5	0.4	1	Subc. water	5×10^2 to 2.3×10^3	Yes, both (no correlations, but a method to solve Navier-Stokes and energy equations was developed)	No	
Klaczak (1996)	One SLTT + swirl decay region	6.8	1.47 to 2.2	25.6 to 27^{14}	1	?	?	Subc. water	1.3×10^3 to 8×10^3	Yes, both (no correlations)	No	
Lokanath (1997)	One SLTT at the inlet ¹⁵	15.5	4.2, 5.2	39	4.6 and 3.7	0.35	?	Subc. water at 0.1 MPa	2.4×10^2 to 2.3×10^3	Yes, both (no correlations)	No	
Saha et al. (2001)	SLTTs connected with a solid rod ¹⁶	13 (pres drop tests); 11 (htc tests)	2.5, 5	2.5, 5	0.5	0.5	4 and 7 (for pres. drop tests); 3 and 6 (for htc tests)	Mineral oil	45 to 1150	Yes, both (no correlations)	No	

¹⁴ Klaczak's (1996) test sections consisted of tubes of length equal to $30 \times D_{ci}$, having a single short TT at the inlet. Even though the concept of TT spacing does not apply for this geometry, a swirl decay region downstream the TT was present, and its length ranged between $25.6 \times D_{ci}$ and $27 \times D_{ci}$.

¹⁵ Lokanath's (1997) test section consisted of a 1.2 m long heated tube, of which the first half contained a TT while the second half was the swirl decay region.

¹⁶ Saha et al. (2001) performed a thorough investigation on TT in laminar flow, which included the effect of the solid rod diameter, TT-tube gap width and TT phase angle on heat transfer coefficient and pressure drop.

Table 1 (cont'd) – Available literature on short-length TTs												
Study	SLTT design	D_{ci} (mm)	y	Swirl decay region length	N_{rev}	t_{TT} (mm)	$t_{TT-tube}$ (mm)	Fluid	Re	Experimental data collected and indication on correlation development		
										Δp	htc	CHF
Saha and Dutta (2001)	SLTTs connected with a solid rod ¹⁷	13 (Δp tests); 11 (htc tests)	2.5 to 10	2.5, 5	0.5, 1, 1.5	0.5	1	Mineral oil	45 to 1150	Yes, both (no correlations)		No
Eiamsa-ard et al. (2004)	Physically separated SLTTs	20	1	2 to 4	1	1	~0	Air	2.3×10^3 to 7.5×10^3	Yes, both (no correlations)		No
Eiamsa-ard and Promvonge (2005)	Physically separated short-length helical tapes ¹⁸	19	0.47	5.3 to 21.1	11	1	2	Air	2.3×10^3 to 8.8×10^3	Yes, both (no correlations)		No
Eiamsa-ard et al. (2006)	SLTTs connected with a wire	25.8	6	1 to 3	0.5	1	1	Subc. water	2×10^3 to 1.2×10^4	Yes, both (correlations developed)		No
Sivashanmugam (2007)	Helical tapes wrapped around an 8 mm solid rod	25.4	0.98 to 2.44	3.9 to 15.7	1, 1.5, 2, 2.5 and 3	?	0.45	Subc. water	6×10^3 to 1.3×10^4	Yes, both (with correlations)		No
This study (2009)	Physically separated SLTTs	10.9	1.5 to 6	30, 40, 50	1.5	0.74	~0.3	Subc. water	9×10^3 to 9×10^4	Yes (with corr.)	No	No

¹⁷ In addition to the geometries examined by Saha et al. (2001), Saha and Dutta (2001) also tested a full-length TT having axially decreasing twist ratio.

¹⁸ Eiamsa-ard and Promvonge (2005) did not test SLTTs, but short-length helical tapes. These tapes are different from twisted tapes since they do not fill the whole tube cross sectional area. Rather they are wrapped around a central rod which creates an annulus in which the tape spirals. The rod (1) improves the stiffness of the series of helical tapes and (2) allows an easier fixing of the resulting structure to the tube, with respect to physically separated, non-wrapped, helical tapes. Eiamsa-ard and Promvonge (2005) also tested the geometrical configuration resulting from removing the rod and leaving the tapes. No details are however provided on how the tapes are secured to the tube walls.

3. Objectives of the tests and definition of SLTT module

The pressure drop tests are aimed at collecting experimental data and at developing a correlation for the prediction of the pressure drop experienced by non-boiling water while flowing through an unheated circular tube containing multiple short-length twisted tapes. Because of reasons explained later, this objective is achieved by testing both test sections containing multiple SLTT modules, and test sections consisting of a single SLTT module.

A SLTT module can be defined as (see Figure 2):

- the length of test section between the inlet of a SLTT and the inlet of the successive SLTT, or
- the length of test section between the midpoint of a swirl decay region and the midpoint of the successive swirl decay region.

From the pressure drop viewpoint, and except for the Entry Module, these definitions are equivalent. This equivalence, graphically represented in Figure 2, is extremely important for the understanding of the results obtained, and especially for their application to any MSLTT design. In fact, although most of the results presented in Section 10 derive from experimental measurements taken between middle points of swirl decay regions, they are directly applicable to the sections between the inlets of successive SLTTs¹⁹.

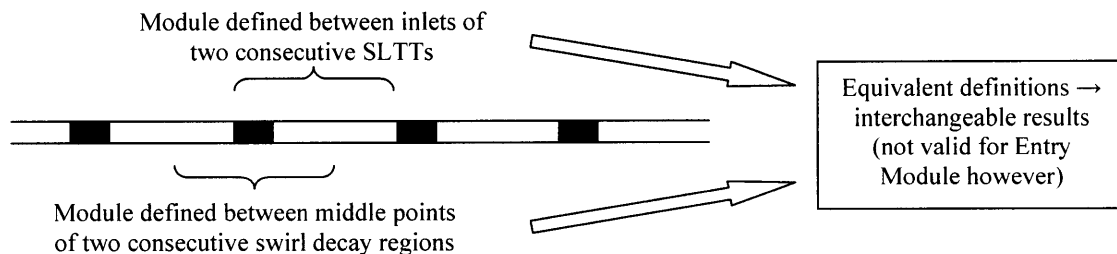


Figure 2 – Graphical representation of Module Equivalence concept

¹⁹ When the results of the pressure drop tests are used to calculate the pressure drop across a tube containing multiple SLTTs, the definition of SLTT module as the section between the inlets of two successive SLTTs is more convenient to use. In fact, if the tube is divided in modules consistently with that definition, the total pressure drop can be easily calculated by applying a typical axial flow friction factor formulation upstream the Entry Module, and the results of Section 10 for the remaining part of the tube.

4. Test planning

The pressure drop tests were preceded by a planning phase during which the operating conditions as well as the geometric variables were fixed. Particularly, liquid water was chosen as operating fluid, with no need of heating systems since pressure drop tests were decided to be performed in single-phase liquid conditions. Although testing water under both single-phase and two-phase conditions would have made the study more complete, it was decided to only test liquid water for the following reasons:

- the reactor type investigated for the inverted configuration implementation, i.e. a PWR, operates mostly in subcooled conditions;
- pressure drops in two-phase can be calculated using results obtained in single-phase by applying typical liquid-only two-phase multiplier correlations available in the literature. This is because, as discussed in Section V-A.2.1 of Volume 1, once steam quality and eventually mass flux are known, the liquid-only two-phase multiplier is approximately the same regardless of whether the flow is purely axial or swirl²⁰;
- in case two-phase flow conditions were to be chosen, the maximum mass flux chosen as target for the pressure drop tests, i.e. $\sim 7000 \text{ kg/s m}^2$, would have implied the need to upgrade the laboratory power supply system, which was found to be economically unfeasible. An alternative path, which would not have required an extensive power supply upgrade, is the use of a low-boiling refrigerant in place of water. The reasons discussed previously, together with toxicity and flammability issues, motivated the choice to not test two-phase mixtures.

Also, since the inverted PWR operates with an average mass flux about twice that of typical LWR, a mass flux target of about 7000 kg/s m^2 was fixed.

The choice of the geometric variables is discussed in the following section.

²⁰ The possibility to apply single-phase to two-phase correction methods developed for axial flow to swirl flow is not a general rule. In fact, while it is valid for pressure drop, it is not for heat transfer coefficient and CHF: this is because the way the presence of steam changes these parameters, relative to single-phase conditions, differs depending on whether the flow is purely axial or swirl. This is discussed, for CHF, in Section VI.2.1 of Volume 1.

4.1 Choice of geometric variables

Once the total length of a MSLTT test section is fixed, for pressure drop calculation purposes five other parameters are needed to completely define the test section:

- twist ratio y : the ratio between the length of TT corresponding to a 180° revolution around its own axis and the tube inner diameter;
- TT spacing s : the ratio between the length of the empty section comprised between two successive TTs and the tube inner diameter;
- number of 360° revolutions N_{rev} : the number of times each TT makes a 360° revolution around its axis;
- TT phase angle θ_{TT} ($0 \leq \theta_{TT} < 180^\circ$): the angle between the inlet edges of consecutive tapes. If zero, tapes are not rotated with respect to each other.
- TT thickness t_{TT} ;
- tube diameter D_{ci} ;
- TT width D_{TT} ;

If time and economic constraints did not apply, all these parameters should be varied, to allow the development of a correlation having y , s , N_{rev} , θ_{TT} , t_{TT} , D_{ci} and D_{TT} as independent geometric variables. However, time and economic constraints did affect the test planning and, as a consequence, it was decided to vary y and s , while the other five parameters were kept constant, at the values discussed below:

- $N_{rev} = 1.5$. It was decided to fix this parameter, instead of y or s , and to fix it at the value 1.5, because of the conclusion by Hassid et al. (1966): “*it can be inferred that from the point of view of heat transfer crisis the number of pitches can be limited to 1-1.5: any further increase should therefore be avoided since it would lead to a pressure drop increase across the promoter without any advantage*”. Further details about the choice of this numerical value can be found in Appendix B.
- $\theta_{TT} \sim 0^\circ$. For simplicity and because, according to the laminar regime study by Saha et al. (2001) “*higher-than-zero phase angle is of no use*”, the test sections

were fabricated with no relative rotation between successive SLTTs²¹. Saha et al. (2001) showed that the phase angle has a small influence on friction factor and Nusselt number, but their study only referred to the laminar regime. In particular, they showed that for MSLTTs having twist ratio and spacing both equal to 2.5, the friction factor increases by 5% when θ_{TT} is changed from 0 to 90°, and by 12% when θ_{TT} is changed from 0 to 180°. The same phase angle changes result in an increase of the Nusselt number by 8% and 15% respectively. This conclusion, i.e. the small effect that the phase angle has on friction factor and Nusselt number, cannot be used to justify the decision to fix θ_{TT} to 0°, since both the MSLTT design and the operating conditions characterizing the tests discussed in this chapter are different from those examined in Saha et al. (2001). However, the fact that the small dependence of the friction factor and Nusselt number was demonstrated for extremely packed SLTTs ($s = 2.5$) can be used to infer that its effect could be even smaller when the spacing is increased to 30, 40 or 50 (i.e. the spacings used in the pressure drop tests discussed in this chapter) since the swirl at the inlet of each tape will be much more decayed than in the case of $s=2.5$. The only factor that prevents us to state this for sure is the difference in flow regime: laminar in Saha et al. (2001) and turbulent here. As is well known, the higher the Reynolds number the slower is the decay of the swirl flow exiting a TT: a phenomenon that may counterbalance the swirl flow decay due to the larger spacing. Unfortunately, studies on the effect of θ_{TT} in the turbulent regime have not been found in the literature.

- $t_{TT} = 0.74$ mm. Varying this parameter would not provide any useful information since, both from the heat transfer and from the pressure drop viewpoint, it is always desired to have a thickness as small as possible. The minimum TT thickness is dictated by the need of preserving the TT shape both during manufacture and during operation. Typical TT thicknesses from experimental works documented in the literature are in the range 0.25-1 mm.

²¹ The notation “~0°” is used for the phase angle since, especially for the small twist ratio tapes, it was not possible to check their orientation very accurately. This is explained more in detail in Section 5.1.2.

- $D_{ci} = 10.92$ mm. The decision to not vary the test section diameter was made because the diameter-dependence of pressure drop is not expected to differ from that of empty tubes.
- $D_{TT} \approx 10.6$ mm. For the tube inside diameter chosen for the pressure drop tests, the TT width could in principle be varied. However, it was decided to manufacture the TTs so that they fit snugly into the tubes, for two reasons: first and foremost because Hassid et al. (1966) experimentally demonstrated that, for CHF increase purposes, it is preferable to have the gap between the TT profile and the tube inside surface as narrow as possible. Also, if the gap was designed to be wide, challenges in TT fixing would arise – particularly, the method used here to secure the TTs could not have been used.

5. Experimental apparatus

Figure 3 shows a schematic of the loop used to perform the pressure drop tests. The loop has a total capacity of about $8.5 \times 10^{-3} \text{ m}^3$ and consists of several components which, with the exception of the data acquisition system, are showed in the figure. They are also described in the following sections.

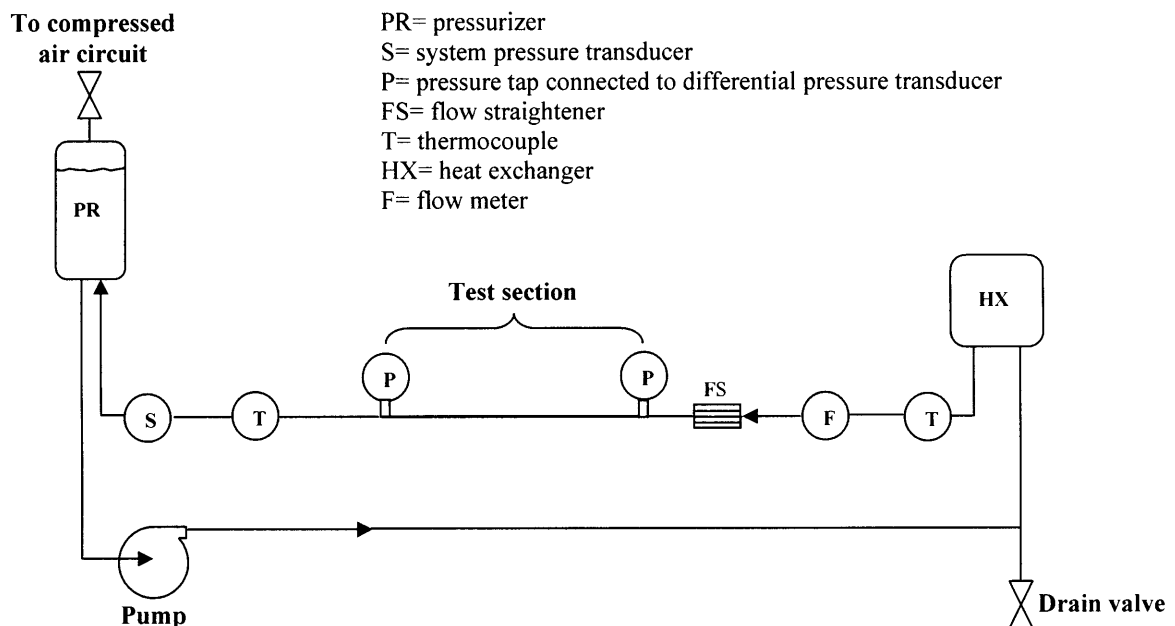


Figure 3– Schematic of loop for pressure drop tests

5.1 Test sections

The following three sections discuss test section geometry (Section 5.1.1), test section manufacture (Section 5.1.2) and pressure tap description and manufacture (Section 5.1.3). In spite of being part of the test sections, pressure taps deserve particular attention and are therefore discussed separately.

5.1.1 Test section geometry

The test sections examined are listed in Table 2. They consist of 316 stainless steel seamless tubes with the following geometric characteristics:

- Tube outside diameter: 12.7 mm;
- Wall thickness: 0.889 mm;
- Inner surface roughness²² $\approx 4.5 \mu\text{m}$ (type 1 tube), $5.2 \mu\text{m}$ (type 2 tube);
- Length:
 - variable between ~ 2 and ~ 3 m (depending on the TT design) for the test sections containing multiple short-length TTs; for these test sections the length is defined as the distance between the two pressure taps (see Figure 4);
 - variable between ~ 38 and ~ 74 cm (depending on the TT design) for the test sections containing a single short-length TT module; for these test sections the length is not the distance between the pressure taps, but instead coincides with the module length (see Figure 5).

Except for test sections E1 and E2, which are the empty tubes used as the base case, all the other test sections contain SLTTs. The tapes, which are 0.74 mm thick and ~ 10.6 mm wide, are made of 410 stainless steel and each makes 1.5 revolutions around its own axis. Test section length varies, depending on the TT design, and can be calculated by multiplying the number of hydraulically identical TT modules by the module length. It is important to note that the inlet of the test sections containing MSLTTs does not coincide

²² Unlike tube outer diameter and wall thickness, the inner surface roughness was not provided by the tube manufacturer, but was measured using a confocal microscope, as discussed in Section 8.1.

with the actual inlet of the tubes: as shown in Figure 4, a test section consists of the succession of geometrically and hydraulically identical TT modules, i.e. TT modules that have same geometry and hydraulic conditions at the inlet. In Figure 4, the TT module labeled as “Entry module” is not part of what is called “test section” since, relative to the other TT modules, it has purely axial flow at the inlet (because no TTs are located upstream), which is not instead the case for the other TT modules, whose inlet is in the middle of a swirl decay region. This difference between hydraulic conditions at the inlet was thought to cause the pressure drop associated with the entry TT to be significantly different from that associated with the downstream TTs: this motivated the need of manufacturing the short test sections, of which a qualitative sketch is shown in Figure 5.

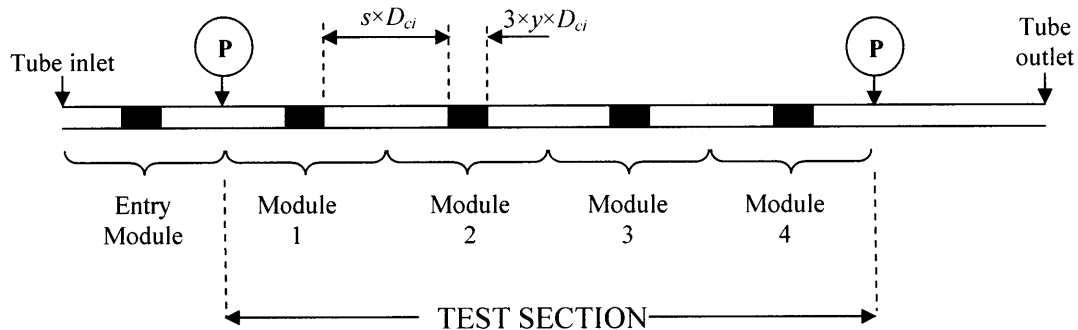


Figure 4 – Sketch of Multiple Short Length TT test section (black rectangles represent SLTTs, P ≡ pressure tap; not in scale)

The short test sections were used to obtain the pressure drop associated with the first module of a succession of SLTT modules. Such pressure drop should be measured between the inlet of the TT and the outlet of the swirl decay region: however, since locating the inlet pressure tap at the TT inlet could have resulted in recording pressure perturbations due to the vicinity of the tape, it was decided to locate the inlet pressure tap at a fixed distance from the TT inlet, equal to 20 diameters (~22 cm). The pressure drop associated with the TT module alone is then calculated as difference between the measured pressure drop and the pressure drop between the inlet pressure tap and the inlet of the TT which, being referred to a straight tube with purely axial flow, is easily

calculable. As shown in Figure 5, each short test section is used to test three TT configurations, which have same twist ratio but different swirl decay region length.

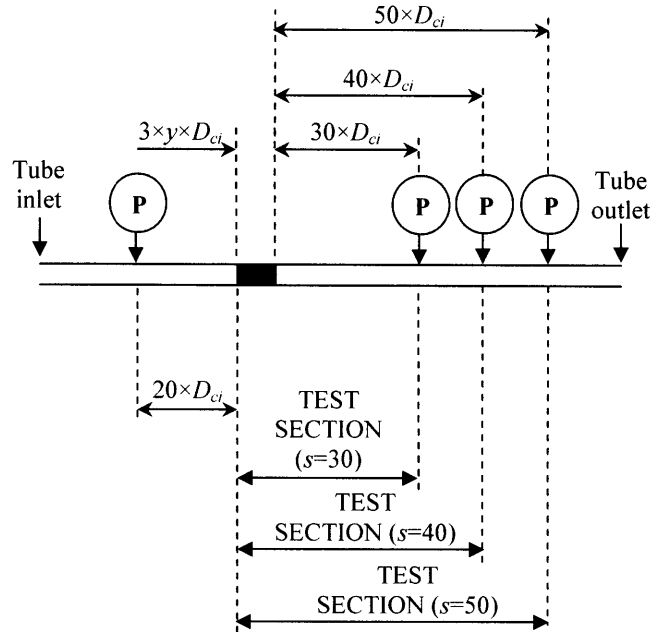


Figure 5 – Sketch of Single Short Length TT test section (black rectangle represents the SLTT, P ≡ pressure tap; not in scale)

Table 2 – Test section summary							
Test section	Tube type	y	s (tube inner diameter)	TT length ²³ (cm)	Module length ²⁴ (cm)	Number of modules per test section	Test section length ²⁵ (m)
<i>Empty tubes</i>							
E1	1	N.A.	N.A.	N.A.	N.A.	N.A.	2.981
E2	2	N.A.	N.A.	N.A.	N.A.	N.A.	2.981
<i>Multiple short-length TT test sections</i>							
MS 1.5-30	2	1.5	30	4.9	37.7	6	2.261
MS 2-30	1	2		6.5	39.3	6	2.359
MS 2.5-30	1	2.5		8.2	41.0	6	2.457
MS 3-30	1	3		9.8	42.6	6	2.556
MS 4-30	1	4		13.1	45.9	5	2.293
MS 5-30	2	5		16.4	49.2	5	2.457
MS 6-30	2	6	19.7	52.4	5	2.622	
MS 1.5-40	2	1.5	40	4.9	48.6	5	2.430
MS 2-40	2	2		6.5	50.2	5	2.512
MS 2.5-40	2	2.5		8.2	51.9	5	2.594
MS 3-40	1	3		9.8	53.5	5	2.676
MS 4-40	2	4		13.1	56.8	4	2.272
MS 5-40	2	5		16.4	60.1	4	2.403
MS 6-40	2	6	19.7	63.4	4	2.534	
MS 1.5-50	2	1.5	50	4.9	59.5	4	2.381
MS 2-50	1	2		6.5	61.2	4	2.446
MS 2.5-50	1	2.5		8.2	62.8	4	2.512
MS 3-50	1	3		9.8	64.4	4	2.578
MS 4-50	1	4		13.1	67.7	3	2.031
MS 5-50	1	5		16.4	71.0	3	2.129
MS 6-50	2	6	19.7	74.3	3	2.228	
<i>Single TT test sections</i>							
S 1.5	2	1.5	N.A.	4.9	37.7 ($s=30$); 48.6 ($s=40$); 59.5 ($s=50$)	1	Same as TT module length
S 2	2	2		6.5	39.3 ($s=30$); 50.2 ($s=40$); 61.2 ($s=50$)	1	Same as TT module length
S 2.5	1	2.5		8.2	41.0 ($s=30$); 51.9 ($s=40$); 62.8 ($s=50$)	1	Same as TT module length
S 3	2	3		9.8	42.6 ($s=30$); 53.5 ($s=40$); 64.4 ($s=50$)	1	Same as TT module length
S 6	2	6		19.7	52.4 ($s=30$);	1	Same as TT module length
					63.4 ($s=40$); 74.3 ($s=50$)		

²³ The length of a TT making N_{rev} revolutions is: $L_{TT}=2 \times D_{ci} \times y \times N_{rev}$.

²⁴ A TT module is defined as the length of test section between the midpoint of a swirl decay region and the midpoint of the successive swirl decay region. This yields pressure drop equivalent to the length of test section between the inlet of a TT and the inlet of the successive TT. The length of a module is therefore equal to: $L_{mod}=2 \times D_{ci} \times y \times N_{rev}+s \times D_{ci}$.

²⁵ For test sections containing MSLTTs, the test section length coincides with the distance between the two pressure taps. For test sections containing a single TT, the length coincides with the TT module length.

5.1.2 Test section manufacture

Test section fabrication begins with shearing a large metal sheet into ~11 mm wide strips; each strip is then converted into the final TT form through the following steps:

- strip is filed down to a width of about 10.7 mm;
- strip is cut to a length that exceeds the desired final length ($3 \times y \times D_{ci}$) by about one centimeter;
- strip is twisted with a lathe. The strip is inserted into a tube, slightly shorter than the strip itself, so that the two strip ends are visible. The function of the tube is to keep the strip straight during the twisting. One end of the strip is fixed to a stationary vice, while the other is fixed to the lathe chuck, which is manually rotated. During the rotation both the stationary vice and the chuck are locked against axial displacements. The only sections of the strip that do not rotate during twisting are the two 5mm-long end sections: this is why the strip was cut to a length larger than the desired final length. Twisting causes the TT width to decrease to about 10.5-10.6 mm.
- the strip length is brought to the final desired value by removing the untwisted ends with a cutting chisel and an hammer;
- TT ends are worked with a file in order to change their lateral profile from rectangular to triangular, and successively sandpaper. In this way turbulence due to the impingement of the flow on the tape front end is reduced.

Figure 6 shows the TTs, with the seven twist ratios listed in Table 2, obtained through the procedure just described. Twist ratios below 1.5 could not be obtained without buckling the tape; this is consistent with the statement by Smithberg and Landis (1964): “*Practical manufacturing difficulties limit the extreme pitch of the twisted tape to about the minimum value used in the present investigation*”, which was $y= 1.81$, and with that by Seymour (1966): “*at the maximum twists that were possible*” ($y= 1.83$) “*failure occurred by lateral buckling of the strip*”. Smaller twist ratios could probably have been obtained by using strips having a larger thickness-to-width ratio, or by choosing a material having

a smaller Young's modulus, which would have allowed large extensions not accompanied by high stresses (Seymour, 1966).



Figure 6 – Short-length TTs manufactured to conduct the pressure drop tests

The test section manufacture is completed by inserting the desired number and type of TTs inside a tube, and by securing them to it. These activities are discussed below.

The insertion is performed by pushing each TT, with a solid rod, inside the tube, up to the desired axial location. The solid rod has a notch at the end, in which the TT end is inserted to prevent TT rotation during the insertion (and therefore the phase angle deviation from 0°). The position of the tape as well as the phase angle are further checked by moving a $5 \times 5 \times 10$ mm neodymium magnet on the tube outside surface, a procedure allowed by the fact that the tape material, unlike the tube material, is magnetic. Especially for small twist ratio tapes, however, the check of the phase angle using the magnet could not be performed very accurately since these tapes make a 180° rotation

within 1-3 cm: a distance which is too short to allow the tape azimuthal orientation to be easily determined. This is why, in Section 4.1, the phase angle was not stated to be 0° , but $\sim 0^\circ$.

After being inserted, each TT is secured to the tube by swaging the tube outer diameter down, at the axial locations corresponding to the two TT ends. This procedure is performed using tube compression fittings (see Figure 7): from one end of the test section, a fitting with a male end (on the right in Figure 7) is slid along the tube, up to the axial location where one of the two TT ends is located²⁶. From the other end of the test section, a ferrule set (front and back ferrule) followed by a nut are slid along the tube, and the nut is screwed onto the male fitting. The screwing pushes the ferrules against the fitting and, because of the inclined ferrule lateral profile, the front ferrule compresses the tube outer diameter, yielding TT locking. The procedure is then repeated at the axial location corresponding to the other TT end.

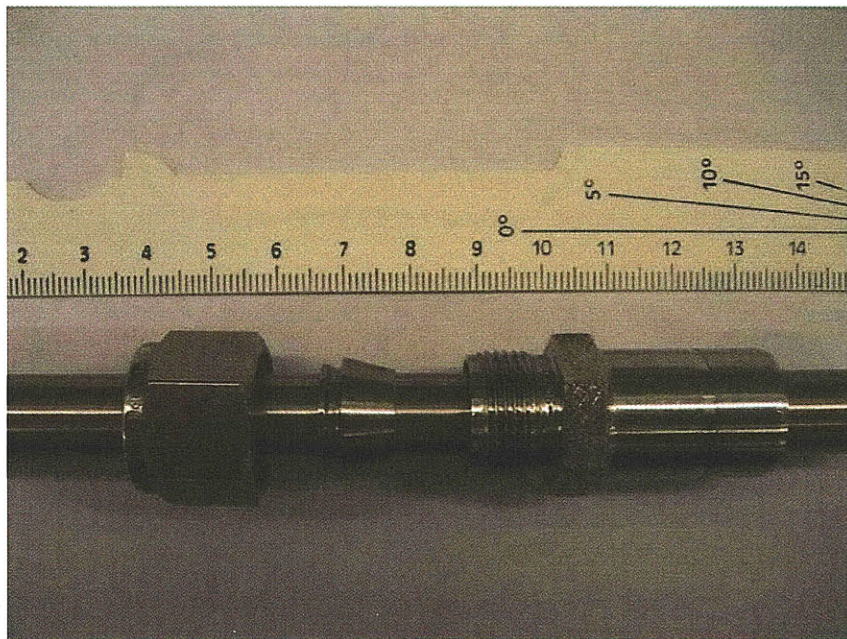


Figure 7– Compression fitting used to secure TTs (from left to right: nut, back ferrule, front ferrule, male fitting, all slid on the tube)

²⁶ The male compression fittings used to secure the TTs are sized for the outer diameter of the test section. Therefore, in their “as received” geometry, they cannot slide along the tube since their inner diameter only allows a short section of the tube end, about 1 cm long, to be inserted into the fitting. To allow the fittings to slide along the entire length of the tube, their inner diameter was uniformly enlarged using a drill press.

5.1.3 Pressure tap geometry and manufacture

After being fabricated, each test section needed to be provided with two pressure taps, which were to be connected to the high and low pressure side of the differential pressure transducer. Each pressure tap was made starting with a plastic adapter, whose lower base was reshaped to make it fit on the tube outer surface (see Figure 8). The reshaping was performed by heating a short section of a scrap tube with a torch, and by pushing the plastic adapter on the tube outer surface. The high temperature caused the plastic to melt, while the pressure exerted on the adapter allowed the lower base of the adapter to assume a semicircular profile. The hole inside the adapter was then redrilled, since some melted material tends to fill the hole. The adapter was then glued to the tube, just above a 1.15 mm diameter hole previously drilled through the test section wall and deburred. To get accurate pressure drop data, two experimental practices must in fact be followed:

- the hole through the test section wall must be small, about $1/10^{\text{th}}$ of the tube inside diameter. In fact, the larger the hole, the more significant is the perturbation to the flow caused by the hole opening, and therefore the inaccuracy of the pressure drop measurements (Rayle, 1959). This phenomenon was verified with the original loop setup, in which tees were used both as pressure taps and as connectors of the section to the rest of the loop. The tee hole perpendicular to the test section axis, which was connected to the differential pressure transducer, had a diameter of about 4 mm. With this setup, later abandoned, it was noticed that for an empty tube, the error percentages between the experimental pressure drops and the analytical predictions were acceptable, i.e. within $\pm 10\%$, only at Reynolds number above about 2.8×10^4 , while they increased up to $\sim 50\%$ as Re decreased to $\sim 10^4$.
- After being drilled, the holes through the test section wall must be deburred. Drilling causes burrs to form on the inside surface of the tube which, if not properly removed, perturb the flow by generating extra turbulence, yielding inaccuracies in pressure drop measurements. According to Rayle (1959), failure in removing the burrs can result in errors of the order of 15-20%. Burrs are removed using a hone, which consists of a metal stem with a rotating abrasive tip, which is

mounted on a portable drill and inserted into the tube up to the axial location where the hole is located.

The plastic adapters mounted on the tube are then connected to the two ports of the differential pressure transducer through two flexible clear plastic tubes. These tubes have an inside diameter of 4 mm and a length of about 1.5 m, and are connected to the plastic adapters and to the differential pressure transducer ports using compression fittings.

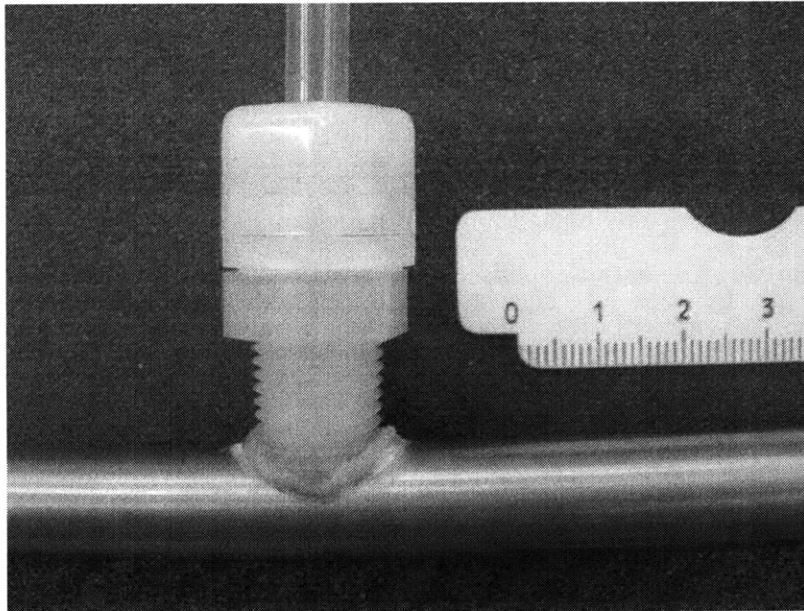


Figure 8 – Pressure tap

5.2 Pump

A Goulds 7GBS0715N4 pump is used to circulate water through the loop. This 13-stage pump allows testing the loop under high mass flux conditions, i.e. up to about 7000 kg/s m². The pump performance curve is shown in Figure 9: the curve referred to the pump in use is that identified with 7GB07-13 STAGE.

7GB PERFORMANCE CURVES

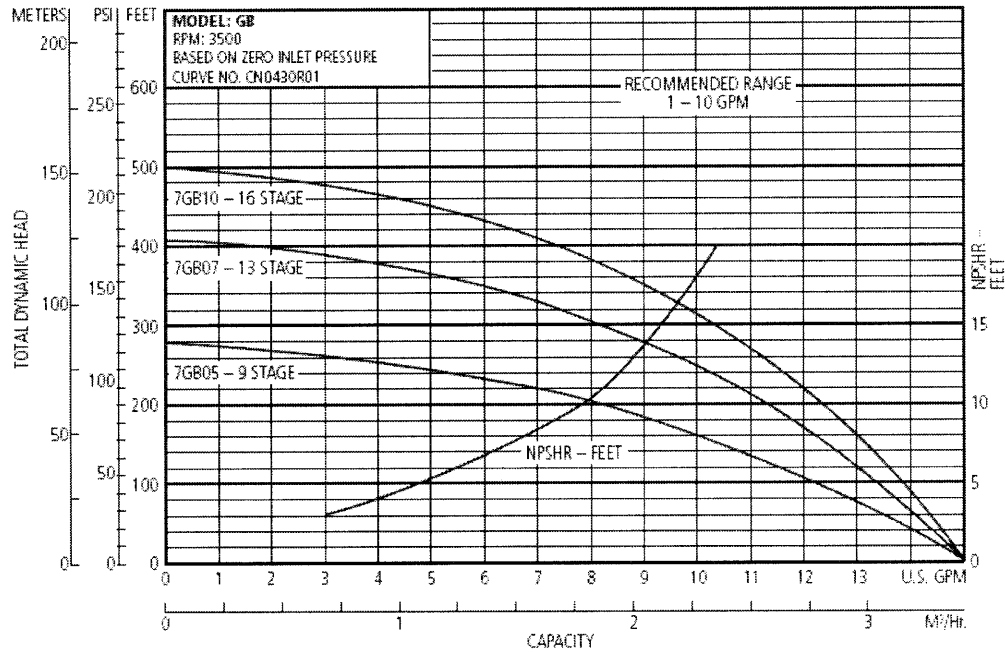


Figure 9 – Pump performance curve (pump in use is 7GB07-13STAGE) (From ITT 2008)

5.3 Differential pressure transducers

Two differential pressure drop transducers were used: an Omega PX2300-50DI (Serial Number 3933703), rated for measuring differential pressures between 0 and 50 psi (0 to 345 kPa), and an Omega PX2300-10DI (Serial Number 3970589) rated for pressure differentials between 0 and 10 psi (0 to 69 kPa). The former was used for measurements across the long test sections, while the latter for those across the short ones. The accuracy of these instruments is +/-0.25% of the full scale value, which corresponds to +/- 0.125 psi for the Omega PX2300-50DI and +/- 0.025 psi for the Omega PX2300-10DI.

5.4 Flow meter

An Omega FTB904 (Serial Number 238854) flow meter was used for the volumetric flow rate measurements. This instrument is capable of measuring volumetric flow rates in the range 1.75-16 gpm (1.1×10^{-4} - 1.0×10^{-3} m³/s) with an accuracy of +/-0.5% of the reading. At the loop operating conditions, this range corresponds to a mass flow rate

range of about 0.1-1 kg/s. The pump performance curve shown in Figure 9 allowed reaching mass flow rates up to ~ 0.7 kg/s, a value corresponding to a mass flux of about 7000 kg/s m^2 , consistent with the target value set during the test planning phase

5.5 Pressurizer

This component is used to fill the loop and to pressurize it. In fact, at the top it has a hole through which water is poured, and a small nozzle connected to the compressed air system. The pressurization, performed at the beginning of each run, is at about 30 psia (207 kPa), and it is needed to reach the minimum NPSH required by the pump. If no pressurization is performed, the pump cannot deliver the maximum flow rate shown in Figure 9.

5.6 Heat exchanger

The heat exchanger is used to maintain the temperature of the fluid approximately constant, and equal to that of the laboratory (which ranged between 23 and 25°C depending on the day). This is done by manually regulating the flow rate of cooling fluid (chill water at about 8°C) entering in the shell side of the heat exchanger, so that the heat removal by the cooling fluid compensates for the heating of the fluid due to friction.

5.7 Data acquisition system

Pressure drop, volumetric flow rate, temperature and system pressure are measured by the loop instrumentation and, in the form of electric signals (voltage or frequency), sent to the HP3852A data acquisition system. The latter is connected to a computer, in which a Visual Basic program is used to (1) convert the electric signals to actual values of pressure drop, volumetric flow rate, temperature and pressure, (2) display such values through a graphic interface and (3) control pump speed.

5.8 Other components

Fluid properties of interest, i.e. density and viscosity, are determined by pressure and temperature in the system. Pressure is recorded using an OMEGA PX302-200GV (Serial Number 040708) pressure gauge located downstream of the test section. The operating

temperature is calculated as the average between the test section inlet and the outlet temperatures, which are measured using two thermocouples.

6. Test methodology description

Pressure drop tests were performed with tap water as working fluid, at a temperature ranging between 23 and 25°C and an initial pressure (before running the pump) of about 200 kPa. The actions performed before each run are as follows:

- test section is mounted;
- loop is filled with tap water at room temperature, poured through the hole at the top of the pressurizer, up to about 90% of the loop capacity;
- pump is turned on and run for about 2 minutes. This allows air, initially trapped in the loop tubing, to vent through the hole at the top of the pressurizer (air eventually still present after such procedure does not have any effect on pressure drop measurements, as demonstrated in Appendix D);
- pump is turned off;
- pressurizer hole is plugged, and the loop is pressurized up to about 200 kPa using compressed air;
- differential pressure transducer lines are bled by turning three bleeding screws located on the differential pressure transducer body. This (1) allows air trapped inside the pressure lines to vent and (2) causes the loop internal pressure to decrease below 200 kPa. Pressure is then restored to about 200 kPa.

After completing the actions mentioned above, the loop is ready for a pressure drop test. All the tests are performed by recording data at incremental pump speeds: pump speed is in fact increased, step-wise, and a test is composed of about 10 steps. Each step lasts about 3-4 minutes, during which data are taken about 90 times. Measurements taken during the transition between steps are rejected, so that all the recorded data refer to steady-state operating conditions. For each test section about 700 data sets are collected.

7. Data scatter and error propagation analysis

7.1. Data scatter at constant pump speed

As discussed in Section 6, the pressure drop tests were performed by collecting about 70 experimental data sets for each of the 9-10 pump speeds selected for each run. When the pump is running at constant speed, however, neither the measured flow rate nor the measured pressure drop are constant, but fluctuate around an average value. The amplitude of such data scatter was investigated:

- for the test sections characterized by the smallest and by the largest pressure drop, i.e. test section E1 and test section MS1.5-30 respectively;
- using both the PX2300-50DI and the PX2300-10DI differential pressure transducer²⁷.

The parameter chosen to express this amplitude was the relative standard deviation percentage: given a series of N measurements performed at constant pump speed, the volumetric flow rate and pressure drop relative standard deviation percentages are defined as:

$$\left(\sigma_{\dot{Q}}\right)_{rel} = 100 \frac{\sigma_{\dot{Q}}}{\bar{\dot{Q}}} \quad (2)$$

$$\left(\sigma_{\Delta p}\right)_{rel} = 100 \frac{\sigma_{\Delta p}}{\bar{\Delta p}} \quad (3)$$

where σ_j is the standard deviation of the parameter j :

$$\sigma_j = \sqrt{\frac{1}{N} \sum_{i=1}^N (j_i - \bar{j})^2} \quad (4)$$

and \bar{j} is the mean value of j . As shown in Figure 10 and Figure 11, the volumetric flow rate relative standard deviation percentages are always below 2.5%, over the whole

²⁷ The PX2300-50DI instrument was tested while measuring pressure drops across the actual test sections, E1 and MS1.5-30, having length 2.981 m and 2.261 m respectively (see Table 2). Because of the limitation in maximum measurable pressure drop, i.e. 10 psid, the PX2300-10DI instrument could not be used over the same lengths. For test section E1, an additional pressure tap hole, 1.2 m away from the inlet pressure tap already present, was therefore drilled. For test section MS1.5-30, instead, the pressure drop measurement was performed across a single SLTT module.

Reynolds number range. As for the pressure drop, the relative standard deviation percentages are less than 4% for $Re > 20000$ ²⁸, and reach 10% at $Re \sim 10000$ but only with the PX2300-10DI differential pressure transducer²⁹.

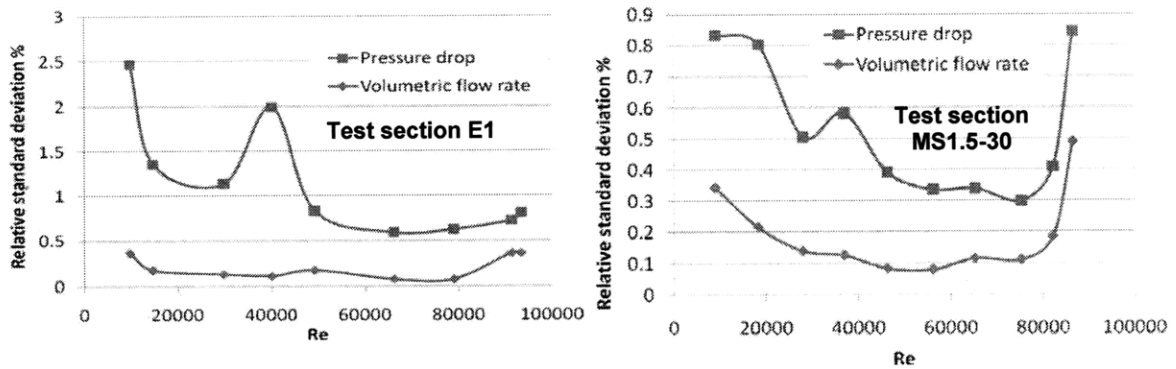


Figure 10– Data scatter at constant pump speed. PX2300-50DI

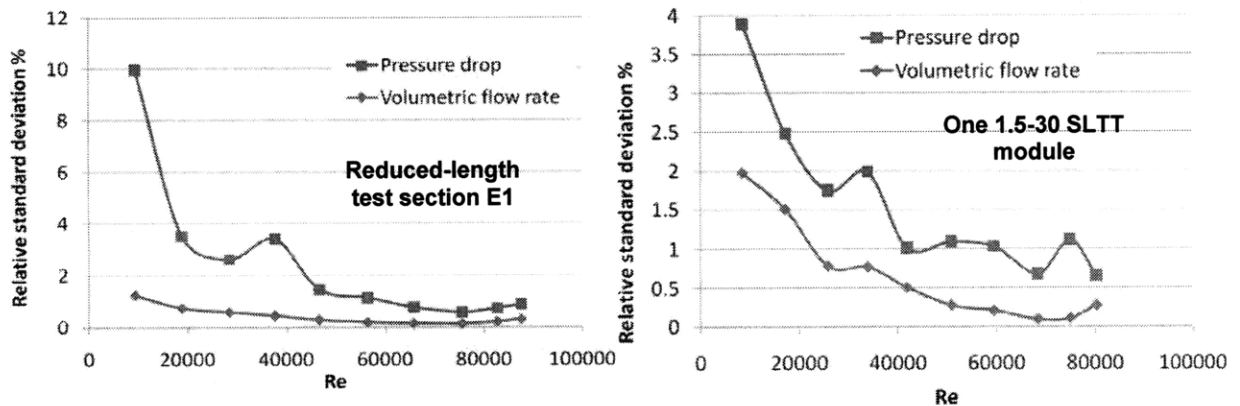


Figure 11– Data scatter at constant pump speed. PX2300-10DI

²⁸ As it can be noticed from Figure 10, the volumetric flow rate relative standard deviation percentage has the same magnitude regardless of the test section employed. Instead, the deviation percentage corresponding to the pressure drop is much higher for the empty test section (left plot). This is because, even though the two test sections are tested over the same Reynolds number range, the inaccuracy of the differential pressure transducer is higher at the pressure drops characterizing test section E1. In fact, the pressure drops corresponding to each Reynolds number are much smaller for test section E1 than for test section MS1.5-30 (e.g. ~ 2.7 kPa vs ~ 5.9 kPa at $Re \sim 9700$ and ~ 150 kPa vs ~ 327 kPa at $Re \sim 87000$).

²⁹ The peak in data scatter at $Re \sim 37000$ is due to the pump which, at this Re as well as at that corresponding to the maximum speed, was noticed to deliver a flow rate less constant than in the remaining regions of the Re spectrum.

7.2 Error propagation analysis

Error propagation analysis is an important part of any experimental investigation since instrumentation readings, often treated as true values, should be interpreted as associated with an uncertainty band. For the pressure drop measurements performed in this work, the major source of uncertainties is the instrumentation inaccuracy, particularly that of the differential pressure transducer and of the flow meter. Other instruments, i.e. the two thermocouples, the pressure gauge and the data acquisition system, are used as often as those just mentioned but do not significantly contribute to pressure drop reading errors. Instrumentation accuracy, from instrument manuals, is presented in Table 3.

Table 3 – Instrumentation accuracy			
Instrument type	Model	Accuracy	Reference
Differential pressure transducer	Omega PX2300-50DI	+/-0.25% of Full Scale value (= +/-0.125 psia = +/-862 Pa)	OMEGA PX2300
	Omega PX2300-50DI	+/-0.25% of Full Scale value (= +/-0.025 psia = +/-172 Pa)	
Flow meter	Omega FTB904	+/-0.5% of reading	OMEGA FTB-900

The error analysis discussed here was performed on the empty test section E1 and uses, as the parameter to which error bands are applied, the Darcy friction factor. This is because the friction factor can be related to pressure drop and flow rate readings, using the well-known relation:

$$f = \Delta p \frac{D_{ci}}{L} \frac{2\rho}{G^2} \quad (5)$$

where uncertainties on the tube inside diameter D_{ci} , on the tube length L and on the water density ρ are neglected³⁰. Since the mass flux G is not measured, but calculated from the

³⁰ The values used for L and D_{ci} are not actually exact since they are provided with manufacture tolerances. However, relative to the effect that inaccuracies on differential pressure and flow rate readings have on the friction factor error, the effect of the mentioned tolerances can be reasonably assumed to be very small. The same consideration applies to water density, which is not a parameter known with certainty since it is obtained by entering two experimental values, i.e. temperature and system pressure, into the NIST/ASME steam tables (Harvey et al., 1996). Both temperature and pressure measurements are affected by inaccuracy, and interpolation inaccuracies are also present in the steam tables. However, even assuming error bands for temperature and pressure readings, water density does not change appreciably within these bands since the density variation with small changes in temperature and/or pressure is very small.

measured volumetric flow rate, it is convenient to rewrite Equation 5 in the following form:

$$f = \Delta p \frac{D_{ci}}{L} \frac{2\rho}{\left(\frac{\dot{Q}\rho}{0.25\pi D_{ci}^2} \right)^2} = \frac{0.125\pi^2 D_{ci}^5 \Delta p}{L\rho \dot{Q}^2} \quad (6)$$

Equation 6 is useful to estimate the way errors in pressure drop and volumetric flow rate measurements affect the knowledge of the friction factor f . Particularly, given a run in which pressure drop and flow rate are measured, it is important to know what is the magnitude of the error band characterizing the friction factor. Such magnitude is typically expressed using the concept of variance, σ^2 , which is defined, for a single measurement of a generic variable g , as:

$$\sigma_g^2 \equiv (g - g_{true})^2$$

where g is the measured value, or the value obtained using the values of the measured variables, while g_{true} is the true value, which is unknown. According to error propagation theory, if g is function of multiple variables x_1, x_2, \dots, x_N , each of which is measured with a certain accuracy, the variance of g can be approximated as (Ang and Tang, 1975):

$$\sigma_g^2 = \sum_{j=1}^N \left(\frac{\partial g}{\partial x_j} \right)^2 \sigma_{x_j}^2 + \sum_{j=1}^N \sum_{i=1, i \neq j}^N \frac{\partial g}{\partial x_j} \frac{\partial g}{\partial x_i} Cov(x_j, x_i) \quad (7)$$

The covariance of two variables, which is zero in case of statistically independent variables (also said to be “uncorrelated”), can be expressed through the so called correlation coefficient, C , as (Blumenfeld, 2001):

$$Cov(x_j, x_i) = \langle (x_j - \langle x_j \rangle)(x_i - \langle x_i \rangle) \rangle = \langle x_j x_i \rangle - \langle x_j \rangle \langle x_i \rangle = C \sqrt{\sigma_j^2 \sigma_i^2} \quad (8)$$

where C can be either be calculated with a code, as done here, or estimated as (Ang and Tang, 1975):

$$C \cong \frac{1}{n-1} \frac{\sum_{k=1}^n [(x_i)_k - \langle x_i \rangle][(x_j)_k - \langle x_j \rangle]}{\sigma_i \sigma_j} \quad (8a)$$

where n is the number of data points in the sample. In our case, the parameter g in Equation 7 is the friction factor which, based on Equation 6, is a function of Δp and \dot{Q} . These two variables are correlated, since an increase in flow rate causes a (predictable) increase in pressure drop. The correlation coefficient between \dot{Q} and Δp is therefore 1³¹. By inserting Equation 8 into Equation 7 we get:

$$\sigma_f^2 = \left(\frac{\partial f}{\partial \dot{Q}}\right)^2 \sigma_{\dot{Q}}^2 + \left(\frac{\partial f}{\partial \Delta p}\right)^2 \sigma_{\Delta p}^2 + 2\left(\frac{\partial f}{\partial \dot{Q}}\right)\left(\frac{\partial f}{\partial \Delta p}\right)\sqrt{\sigma_{\dot{Q}}^2 \sigma_{\Delta p}^2} \quad (9)$$

Since, from Equation 5,

$$\frac{\partial f}{\partial \dot{Q}} = -\frac{0.25\pi^2 D_{ci}^5}{L\rho} \frac{\Delta p}{\dot{Q}^3} \quad (10)$$

$$\frac{\partial f}{\partial \Delta p} = \frac{0.125\pi^2 D_{ci}^5}{L\rho\dot{Q}^2} \quad (11)$$

and since (from Table 3):

$$\sigma_{\dot{Q}}^2 = \left(\frac{0.5}{100} \dot{Q}\right)^2 = 2.5 \times 10^{-5} \dot{Q}^2 \quad (\text{dimension: m}^6/\text{s}^2)$$

$$\sigma_{\Delta p}^2 = \begin{cases} (861.8 \text{ Pa})^2 = 742776.1 \text{ Pa}^2 & \text{for } PX2300-50DI \\ (172.4 \text{ Pa})^2 = 29711.0 \text{ Pa}^2 & \text{for } PX2300-10DI \end{cases}$$

when the measurement is taken with the Omega PX2300-50DI differential pressure transducer, Equation 9 can be rewritten in the form:

$$\begin{aligned} \sigma_f^2 &= \left(-\frac{0.25\pi^2 D_{ci}^5}{L\rho} \frac{\Delta p}{\dot{Q}^3}\right)^2 (2.5 \times 10^{-5} \dot{Q}^2) + \left(\frac{0.125\pi^2 D_{ci}^5}{L\rho\dot{Q}^2}\right)^2 742776.1 + \\ &+ 2\left(-\frac{0.25\pi^2 D_{ci}^5}{L\rho} \frac{\Delta p}{\dot{Q}^3}\right)\left(\frac{0.125\pi^2 D_{ci}^5}{L\rho\dot{Q}^2}\right)\sqrt{(2.5 \times 10^{-5} \dot{Q}^2)742776.1} = \\ &= 1.5625 \times 10^{-2} \left(\frac{\pi^2 D_{ci}^5}{L\rho\dot{Q}^2}\right)^2 \left[10^{-4} (\Delta p)^2 - 4\Delta p \sqrt{2.5 \times 10^{-5} \times 742776.1} + 742776.1\right] \quad (12) \end{aligned}$$

³¹ This has been verified using the Matlab code. A series of about 700 experimental \dot{Q} - Δp pairs was entered in the code and the Matlab function *corr2* delivered a correlation coefficient of 0.98.

while when the measurement is taken with the Omega PX2300-10DI differential pressure transducer it has the form:

$$\begin{aligned}\sigma_f^2 &= \left(-\frac{0.25\pi^2 D_{ci}^5 \Delta p}{L\rho \dot{Q}^3} \right)^2 (2.5 \times 10^{-5} \dot{Q}^2) + \left(\frac{0.125\pi^2 D_{ci}^5}{L\rho \dot{Q}^2} \right)^2 29711 + \\ &+ 2 \left(-\frac{0.25\pi^2 D_{ci}^5 \Delta p}{L\rho \dot{Q}^3} \right) \left(\frac{0.125\pi^2 D_{ci}^5}{L\rho \dot{Q}^2} \right) \sqrt{(2.5 \times 10^{-5} \dot{Q}^2) 29711} = \\ &= 1.5625 \times 10^{-2} \left(\frac{\pi^2 D_{ci}^5}{L\rho \dot{Q}^2} \right)^2 \left[10^{-4} (\Delta p)^2 - 4\Delta p \sqrt{2.5 \times 10^{-5} \times 29711} + 29711 \right] \quad (13)\end{aligned}$$

The square root of the variance, i.e. the standard deviation, is the key result of the error propagation analysis. In fact, the friction factor standard deviation is the amplitude of the friction factor error band associated with each measured $\dot{Q} - \Delta p$ pair. From Equation 12 it follows that the standard deviation of the friction factor, when the measurement is taken with the Omega PX2300-50DI differential pressure transducer, is:

$$\sigma_f = \pm 0.125 \frac{\pi^2 D_{ci}^5}{L\rho \dot{Q}^2} \sqrt{10^{-4} (\Delta p)^2 - 4\Delta p \sqrt{2.5 \times 10^{-5} \times 742776.1} + 742776.1} \quad (14)$$

while, with the Omega PX2300-10DI it is:

$$\sigma_f = \pm 0.125 \frac{\pi^2 D_{ci}^5}{L\rho \dot{Q}^2} \sqrt{10^{-4} (\Delta p)^2 - 4\Delta p \sqrt{2.5 \times 10^{-5} \times 29711} + 29711} \quad (15)$$

It must be stressed that, in Equation 14 and 15, D_{ci} and L are expressed in m, ρ in kg/m^3 , \dot{Q} in m^3/s and Δp in Pa.

Equation 14 and 15 are applicable to any pressure drop measurement, provided that they are used consistently with the differential pressure transducer actually used. In particular, they were applied to two runs performed on test section E1 (one using the PX2300-50DI instrument, the other using the PX2300-10DI connected across a 1.2 m long section of test section E1), in order to graphically show the amplitude of the error band associated with the experimental friction factor. In particular, each of the ~ 700 data sets (each consisting of Δp , \dot{Q} , T and p) of each run was used to calculate the friction factor (by

means of Equation 6) and the corresponding standard deviation (by means of Equation 14 or 15). These results are shown in Figure 12 and in Figure 13, where:

- the solid line represents the experimental friction factor, f_{exp} ³²;
- the dashed lines bound the uncertainty area, i.e. the area in which $f = f_{exp} \pm \sigma_f$;
- the dotted line represents the friction factor analytical prediction, obtained with the Churchill equation³³ presented in Section V.3.1.1 of Volume 1.

The following observations can be made:

- the amplitude of the experimental uncertainty area is very large at low Re, and decreases dramatically as Re increases: this is a direct consequence of the inaccuracies of the differential pressure transducers, which are larger at low Re.
- the analytical prediction of the friction factor is within the experimental uncertainty area for $Re < 20000$. The fact that it falls outside this area for $Re > 20000$ must not be interpreted as a poor accuracy of the experimental measurements since, as shown in Section 8.2, the experimental measurements are always within the analytical prediction $\pm 10\%$, and within the analytical prediction $\pm 5\%$ for $Re > 50000$.

³² Since measurements were performed at about 9-10 Reynolds numbers, and for each Re about 70 measurements were collected, the continuous line connects the average friction factors corresponding to each Re.

³³ A tube roughness equal to $4.5 \mu\text{m}$ was used in the Churchill equation. This roughness was measured using a confocal microscope, as discussed in Section 8.

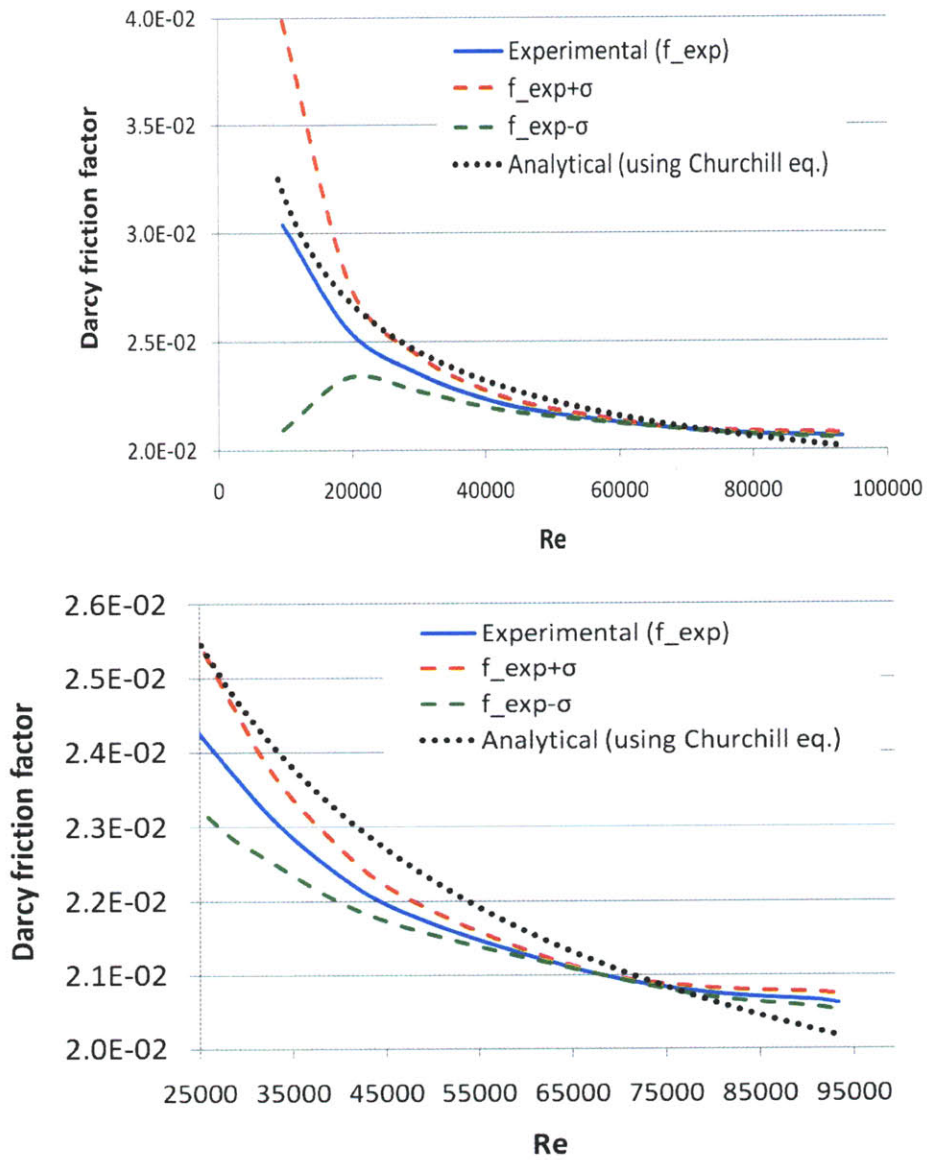


Figure 12– Experimental friction factor for test section E1 (empty tube) with error band curves, compared to analytic prediction (top: whole Re-range; bottom: $Re \geq 25000$ only). PX2300-50DI used.

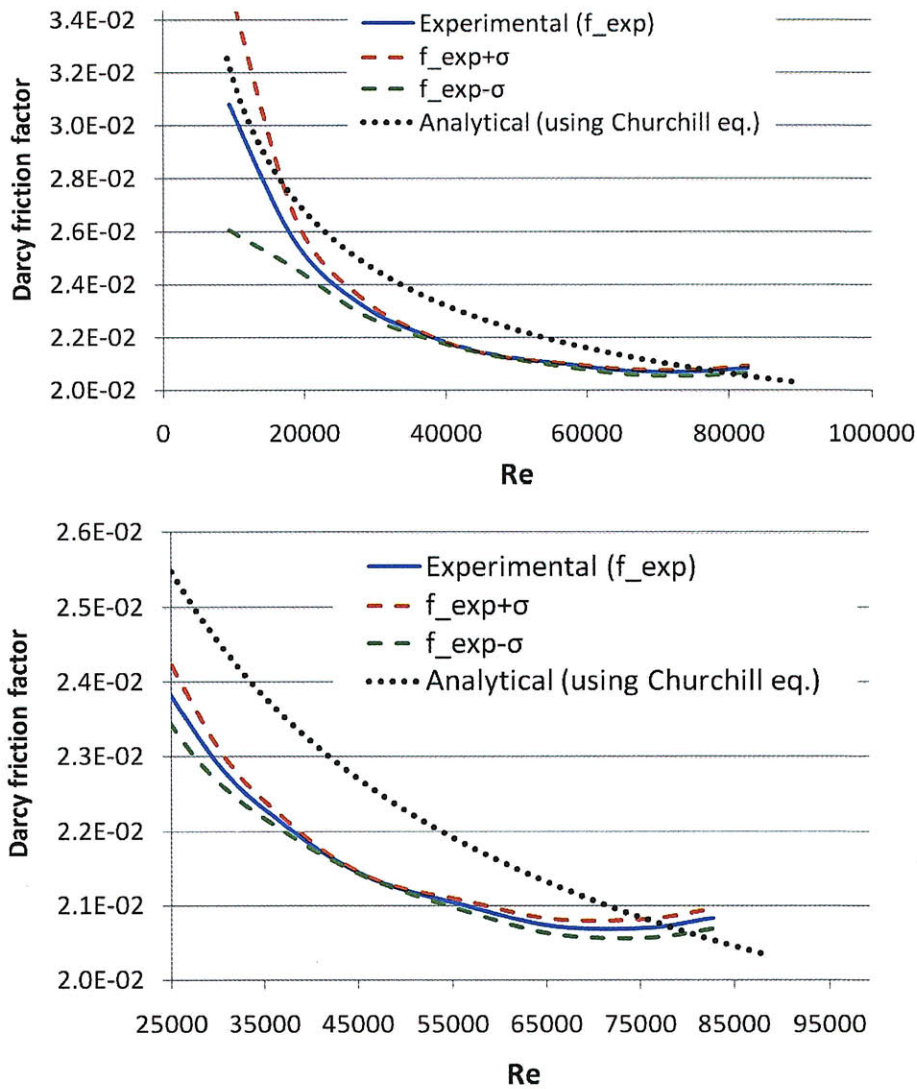


Figure 13– Experimental friction factor for a 1.2 m long section of test section E1 (empty tube) with error band curves, compared to analytic prediction (top: whole Re-range; bottom: $Re \geq 25000$ only). PX2300-10DI used.

8. Tube roughness determination and pressure drop measurement accuracy

Test sections E1 and E2 consisted of two 2.98 m long empty tubes, which were tested to verify the accuracy of the pressure drop measurements: for such simple geometry, in fact, pressure drop can be analytically predicted, and the prediction then compared to the

experimental measurements. This comparison required first, however, to determine the tube inner surface roughness, which is an input to the analytical pressure drop prediction. Roughness determination and comparison between experimental and analytical pressure drop are discussed in Sections 8.1 and 8.2 respectively.

8.1 Determination of test section inner surface roughness

A confocal microscope Olympus Lext OLS3000 was used to measure the surface roughness of several samples cut from test sections E1 and E2. For each sample, the microscope was set to examine an area of about 1.28×1.28 mm, and to automatically provide the average roughness along straight lines oriented perpendicularly to the sample curvature. The microscope also provided images of the surface, of which an example is shown in Figure 14.

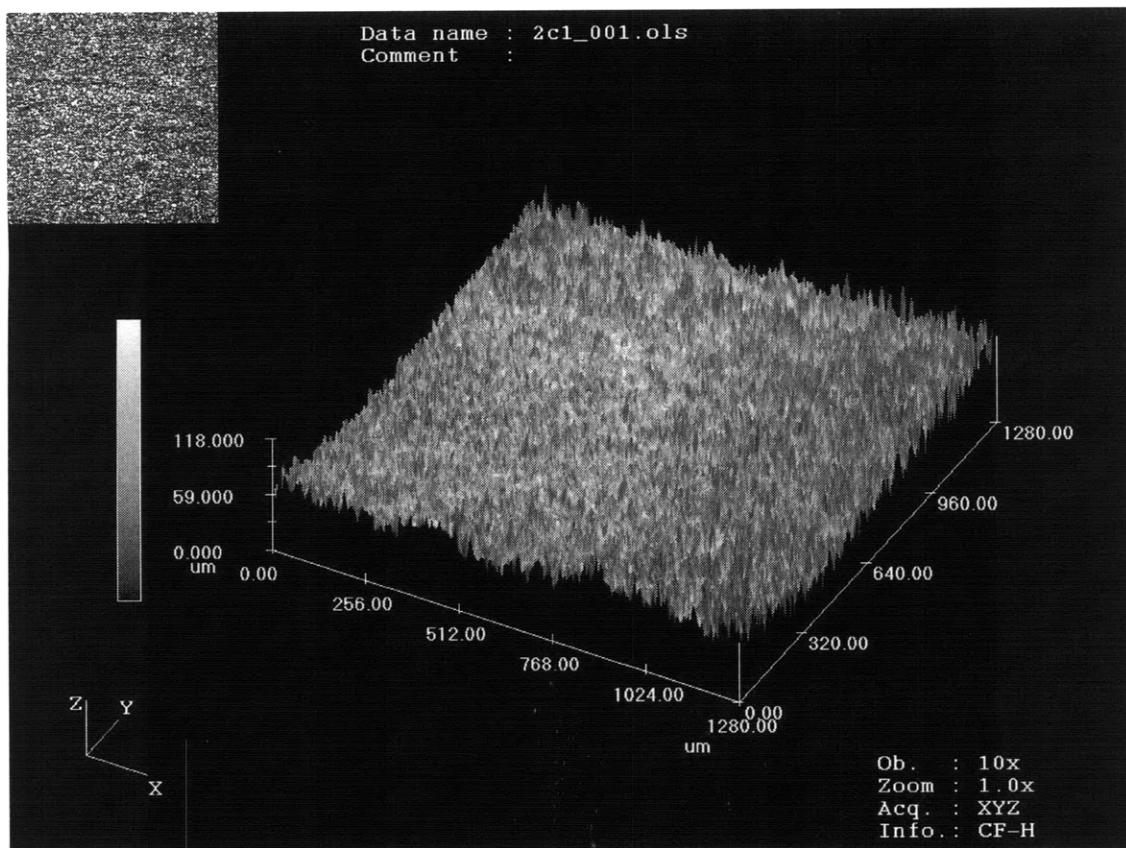


Figure 14– Tube inner surface image provided by confocal microscope

The average roughness was found to be of about 4.5 and 5.2 μm for tube Type 1 and Type 2 respectively.

8.2 Determination of pressure drop measurement accuracy

Figure 15 compares, for test section E1, the experimental friction factors to the analytical predictions of the same parameter obtained using the Churchill equation presented in Section V.3.1.1 of Volume 1. The top plot refers to about 700 measurements performed with the PX2300-50DI differential pressure transducer, while the bottom one to other 700 measurements performed, over a portion of test section E1, with the PX2300-10DI instrument. For the roughness to be entered, as input, in the Churchill correlation, the measured value of 4.5×10^{-6} m was used (see Section 8.1). It can be seen that, with the exception of the low Reynolds number region ($\text{Re} < 20000$), the experimental friction factors agree with the analytical predictions within a margin of $\pm 10\%$ over the range $20000 < \text{Re} < 95000$, and within a $\pm 5\%$ margin for $50000 < \text{Re} < 95000$. It can be therefore concluded that the pressure drop measurement technique yields accurate results.

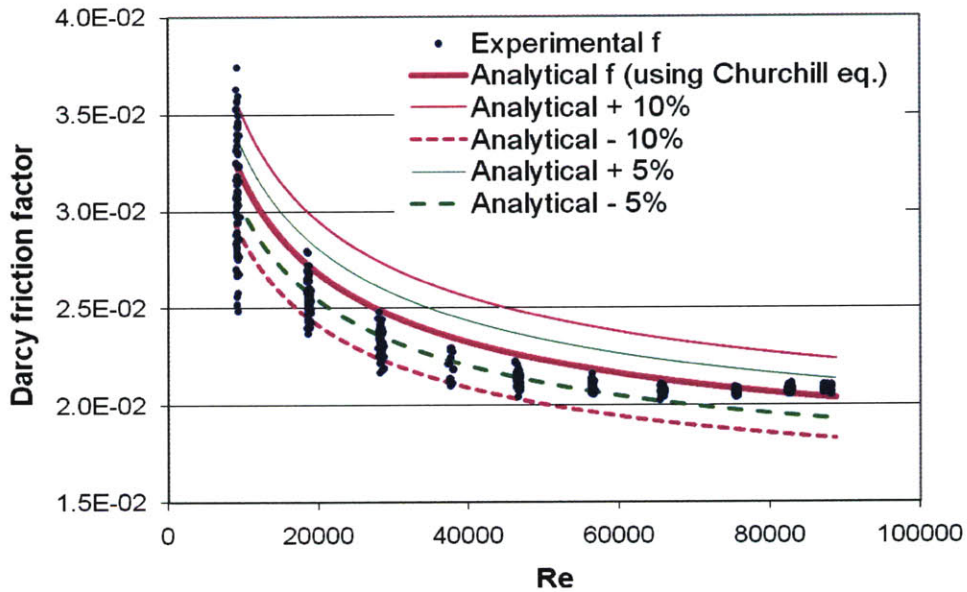
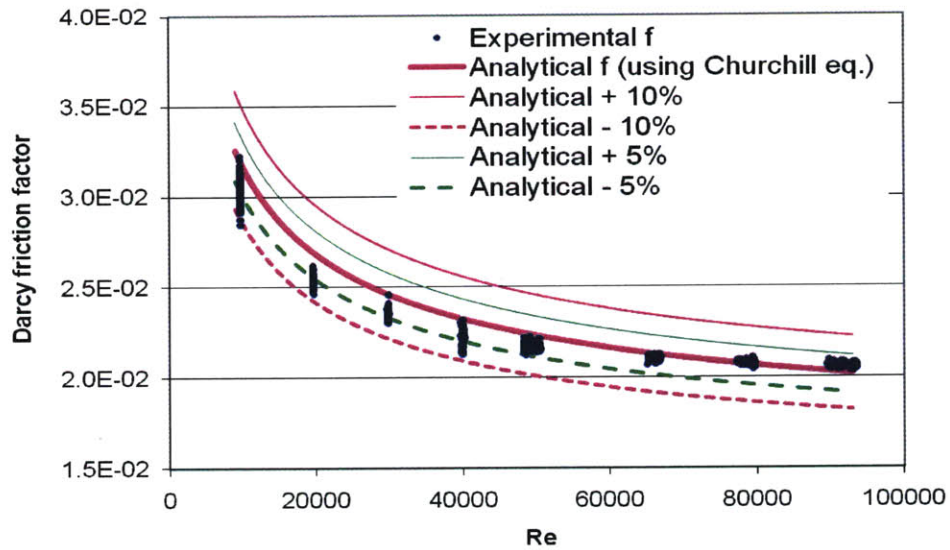


Figure 15– Accuracy of pressure drop measurements: experimental vs analytical friction factor for test section E1 (top plot: PX2300-50DI; bottom plot: PX2300-10DI)

9. Data elaboration method: definition of friction factor and directions for using friction factor correlation

The objectives of the pressure drop tests was to collect experimental pressure drop data and to develop a correlation for predicting the friction pressure drop across a tube containing multiple short-length TTs, having twist ratio y and spacing s . Since the correlation was developed in the form of a friction factor correlation, it is fundamental to define the selected form of the friction factor and to explain how the correlation has to be interpreted and used. These aspects are discussed in the following two sections.

9.1 Friction factor: definition

Given a tube containing multiple short-length TTs with twist ratio y and spacing s , the experimental Darcy friction factor is defined as:

$$f = (\Delta p_{\text{module}}) \frac{D_{ci}}{L_{\text{module}}} \frac{2\rho}{G_{\text{empty}}^2} \quad (16)$$

where:

Δp_{module} : TT module pressure drop, calculated as the ratio between the pressure drop measured between the two pressure taps shown in Figure 4, and the number of TT modules included between the two pressure taps.

D_{ci} : tube inside diameter;

G_{empty} : experimental mass flux calculated as

$$G = \frac{\dot{Q}_{\text{exp}} \rho}{0.25 \pi D_{ci}^2} \quad (17)$$

where the volumetric flow rate \dot{Q}_{exp} is a measured value, while the water density ρ is obtained using the NIST/ASME steam tables (Harvey et al., 1996). Input data to the steam tables are the test section average temperature (computed as average between the inlet and outlet temperatures, which are measured during each of the ~700 runs) and the test section average absolute pressure. The latter is calculated as:

$$p_{test\ section} = p_{exp}^{gauge} + \frac{(\Delta p)_{exp}}{2} + p_{atm} \quad (18)$$

where p_{exp}^{gauge} is the system pressure measured, in each run, by the pressure gauge shown in Figure 3, Δp_{exp} is the measured test section pressure drop, and p_{atm} is the atmospheric pressure.

L_{module} : TT module length, given by:

$$L_{module} = L_{TT} + L_{swirl\ decay\ region} = 2yD_{ci}N_{rev} + sD_{ci} = 3yD_{ci} + sD_{ci} \quad (19)$$

9.2 Method for using friction factor correlation to predict pressure drop

This section explains how the friction factor correlation developed in this work is to be used. It allows predicting the pressure drop across N SLTT modules having twist ratio y and spacing equal to s , where the term “module” is here to be intended as the section of tube between the inlets of two successive SLTTs. Since no clear trend has been found for the pressure drops associated with successive TT modules, and all are distributed within +/-10% of an average value, the pressure drop across N SLTT modules has to be calculated as:

$$\Delta p = N\Delta p_{module} \quad (18)$$

where Δp_{module} is the pressure drop associated to the average TT module:

$$\Delta p_{module} = f \frac{L_{module}}{D_{ci}} \frac{G_{empty}^2}{2\rho} = f \left(\frac{3yD_{ci} + sD_{ci}}{D_{ci}} \right) \frac{G_{empty}^2}{2\rho} \quad (19)$$

where f has to be computed using the friction factor correlation developed in this study and presented in Section 10.

10. Results

Experimental results are presented in Figure 16 through Figure 22. Each plot refers to one of the six twisting ratios tested, and shows the experimental SLTT friction factors as a function of the Reynolds number. According to the recommendations given by Marner et al. (1983), the latter is defined with respect to the empty tube, i.e. the tube inside diameter is used as equivalent diameter and the mass flux is calculated using the empty tube cross

sectional area. Log-log scale is used to conform to friction factor plot practice. The plots also show:

- the experimental friction factor of the empty tube;
- the uncertainty bars associated with each experimental point. The amplitude of the bars is equal to the friction factor standard deviation given by Eqs. 14 and 15. Whenever the error bar is not shown, its amplitude is very small and, graphically, the bar is covered by the marker used to indicate the experimental point.
- the analytical prediction of the friction factor of a tube provided with a FLTT having same twist ratio as the SLTTs to which each plot refers, obtained using the Manglik-Bergles correlation presented in Section V.3.1.2 of Volume 1.

It has to be stressed that the SLTT experimental friction factors shown in Figure 16 through Figure 22 derive from the tests performed on the MSLTT test sections. The results obtained with the short test sections are not relevant since they confirmed (see Appendix C) that the very first TT of a series does not behave differently from the others.

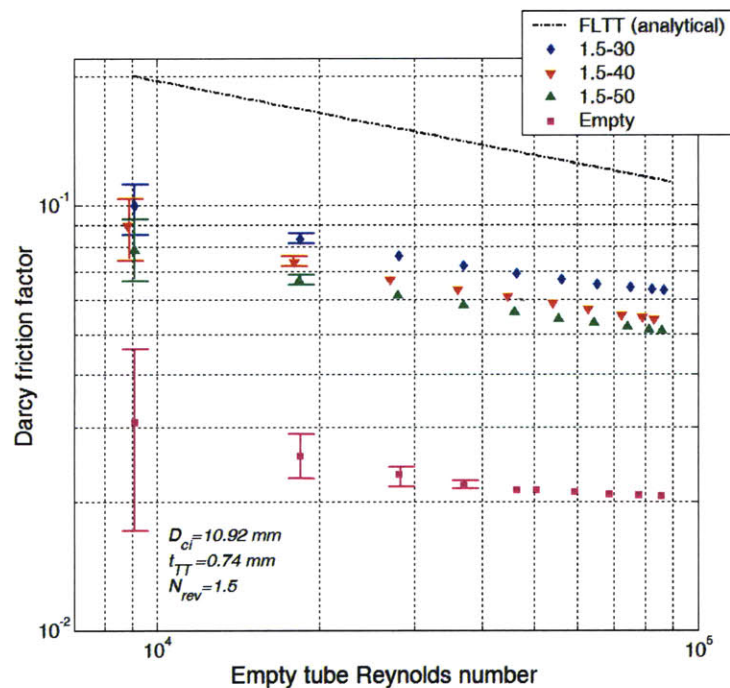


Figure 16 – SLTT module friction factor for $\gamma=1.5$ and spacing 30, 40 and 50, compared to empty tube and FLTT friction factors

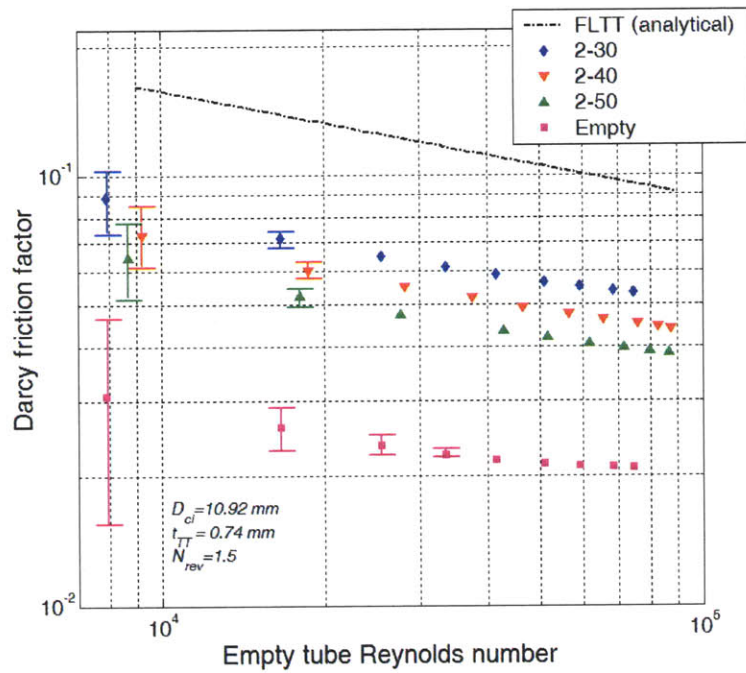


Figure 17 – SLTT module friction factor for $y=2$ and spacing 30, 40 and 50, compared to empty tube and FLTT friction factors

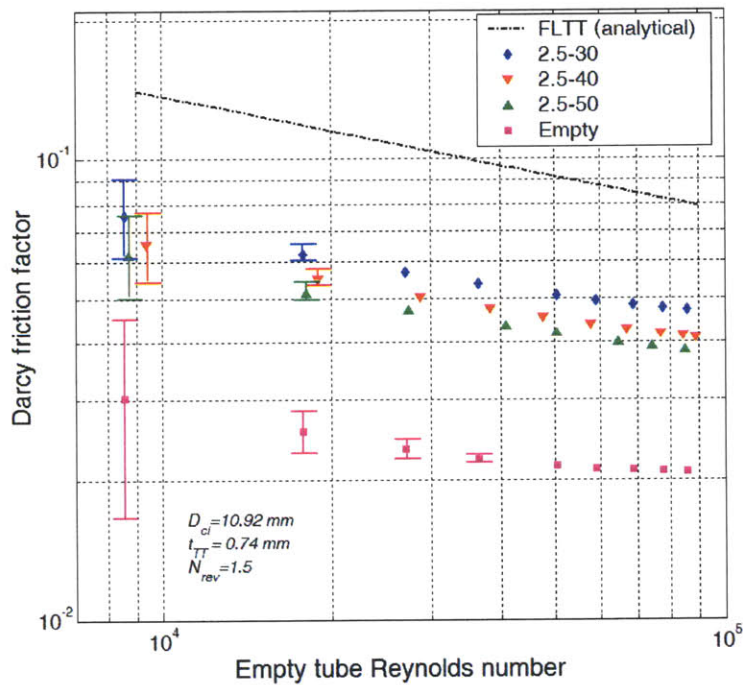


Figure 18 – SLTT module friction factor for $y=2.5$ and spacing 30, 40 and 50, compared to empty tube and FLTT friction factors

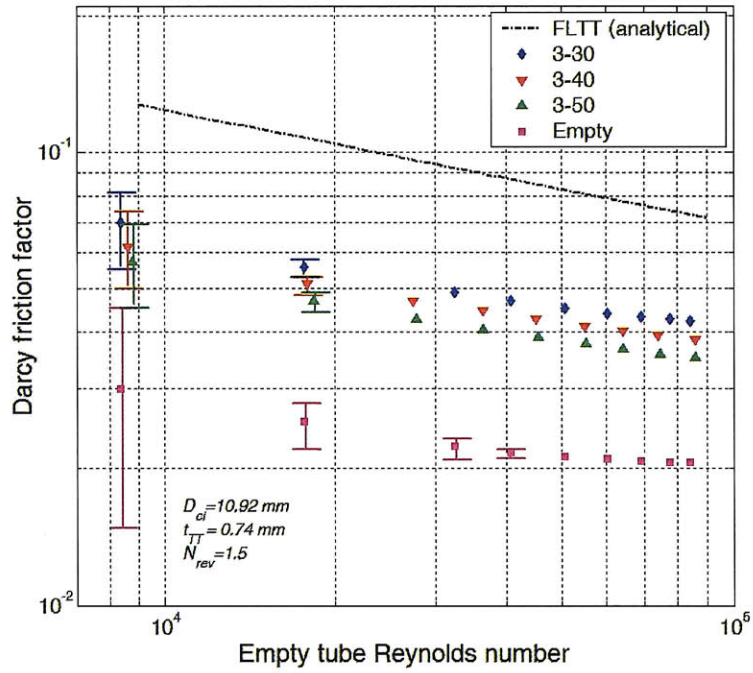


Figure 19 – SLTT module friction factor for $y=3$ and spacing 30, 40 and 50, compared to empty tube and FLTT friction factors

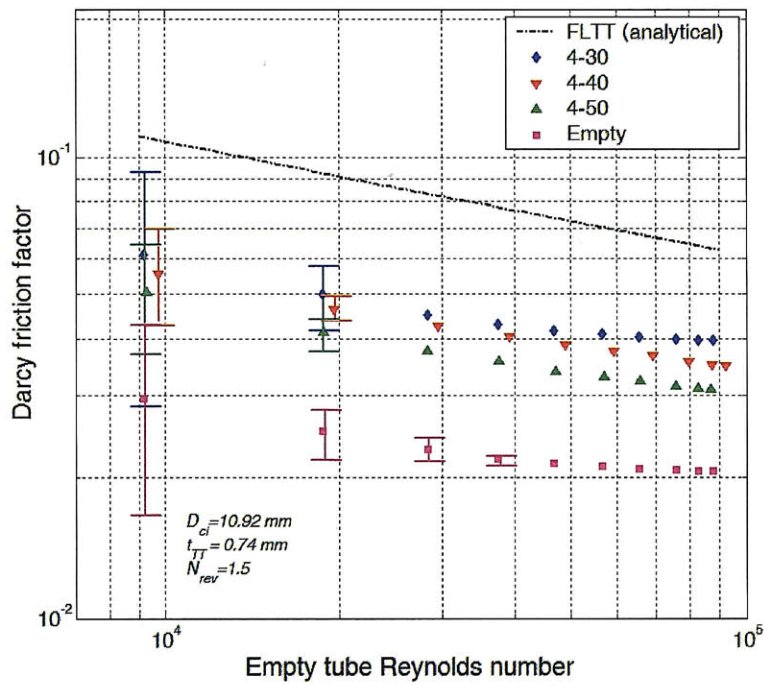


Figure 20 – SLTT module friction factor for $y=4$ and spacing 30, 40 and 50, compared to empty tube and FLTT friction factors

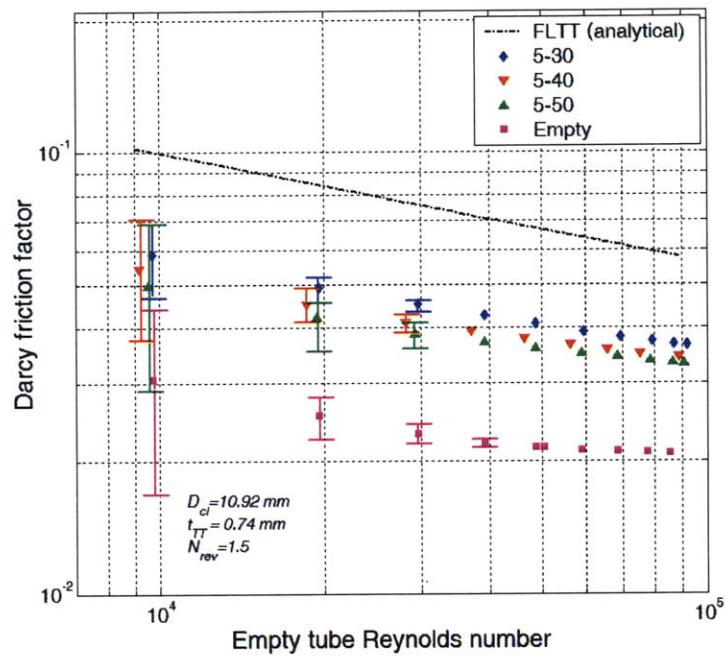


Figure 21 – SLTT module friction factor for $y=5$ and spacing 30, 40 and 50, compared to empty tube and FLTT friction factors

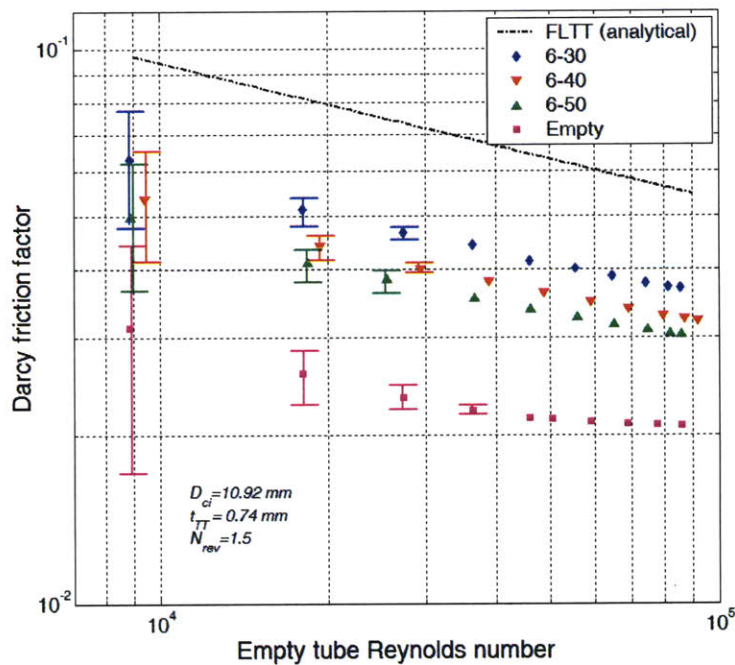


Figure 22 – SLTT module friction factor for $y=6$ and spacing 30, 40 and 50, compared to empty tube and FLTT friction factors

A non-linear least square regression analysis was performed on all the experimental data collected, and the following correlation was developed (Block et al., 2010):

$$f = f_1(\text{Re}) \times f_2(y) \times f_3(s) \quad (20)$$

where f is the Darcy friction factor of a SLTT module to be used in Eq. 19, while the terms f_1 , f_2 and f_3 have the following expressions:

$$f_1(\text{Re}) = 6.6 \text{Re}^{-0.53} + 0.047 \quad (21)$$

$$f_2(y) = 0.95y^{-1.75} + 0.54 \quad (22)$$

$$f_3(s) = 95s^{-1.67} + 0.68 \quad (23)$$

where Re is the Reynolds number of the empty tube, y is the twist ratio and s is the SLTT spacing. The correlation, which was developed using data covering the following ranges:

$$9000 \leq \text{Re} \leq 90000$$

$$y = 1.5, 2, 2.5, 3, 4, 5 \text{ and } 6$$

$$s = 30, 40 \text{ and } 50$$

predicts all the experimental data within +/- 11.6%, and 95% of the experimental data within +/-7.8%.

10.1 Result elaboration and interpretation

The results shown in Figure 16 through Figure 22 demonstrate that the friction pressure drop due to any one of the MSLTT designs examined is significantly smaller than that of a FLTT having same twist ratio. This conclusion is quantitatively presented in Figure 23 through Figure 25, which show the ratios between friction factors, evaluated near the maximum Reynolds number tested, i.e. 85000. These figures show the friction pressure drop penalty resulting from using MSLTT, relative to an empty tube, but especially the friction pressure drop benefit resulting from using MSLTTs instead of FLTTs. Each figure refers to one of the three SLTT spacings tested, i.e. 30, 40 and 50 respectively. It can be seen that:

- insertion of SLTTs causes an increase in pressure drop, relative to an empty tube, whose degree gets larger and larger as the twist ratio and the TT spacing decrease.

In particular, for $Re=85000$, such increase ranges between 3.2 and 1.9 times for $s = 30$ (see Figure 23), between 2.8 and 1.7 times for $s = 40$ (see Figure 24) and between 2.65 and 1.6 times for $s = 50$ (see Figure 25), in increasing order of twist ratio;

- MSLTT designs offer a significant pressure drop advantage relative to FLTT designs. The pressure drop reduction resulting from switching from a FLTT to a MSLTT design increases as the TT spacing increases, as expected, and as the twist ratio decreases. In particular, for $Re=85000$, such reduction ranges between 1.85 and 1.5 times for $s = 30$ (see Figure 23), between 2.1 and 1.7 times for $s = 40$ (see Figure 24) and between 2.25 and 1.8 times for $s = 50$ (see Figure 25);
- Only two data do not agree with the trends mentioned above, and they are both in Figure 25. They correspond to the MSLTT designs having $y = 2, s = 50$ and $y = 4, s = 50$. As it can be inferred from Figure 25, these designs are characterized by a lower friction factor than it should be based on the behavior of the other MSLTT designs having same spacing. Several runs were performed on these test sections, and the same results were obtained each time. An error in test section manufacture could be the cause of the inconsistent data, for example a phase angle between successive tapes very different from 0° .

Analogous data to those shown in Figure 23 through Figure 25 were obtained for all the Reynolds number tested. It was observed that, as Re decreases below 85000, the friction factor ratios either stay constant or slightly increase, with maximum values, at $Re \sim 10000$, about 15% higher than those referred to $Re=85000$. It must be mentioned, however, that while the measurement error at $Re=85000$ is negligible, at $Re \sim 10000$ is significant, as shown in Figure 16 through Figure 22.

To allow for better graphical resolution, the pressure drop increase, with respect to an empty tube, resulting from using a FLTT, is not shown in Figure 23 through Figure 25. Thus, for completeness, this increase is presented separately in Figure 26, which shows the ratio between the FLTT and the empty tube friction factors, as a function of the FLTT twist ratio. While the empty tube friction factors used to calculate this ratio were the

experimental ones, the Manglik-Berles correlation (Manglik-Bergles, 1993) discussed in Section V.3.1.2 of Volume 1 was used to predict the FLTT friction factors.

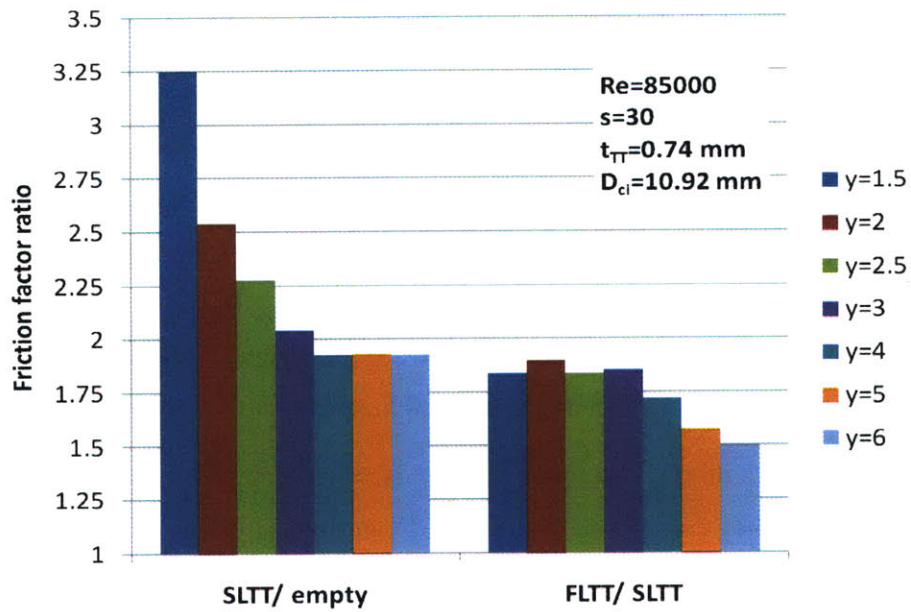


Figure 23 – Friction factor ratios for $s = 30$

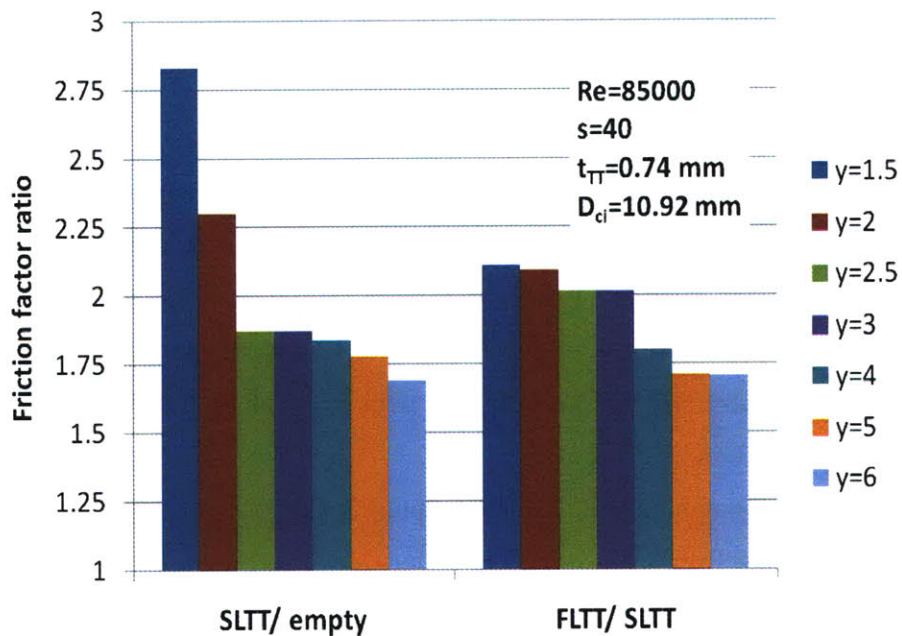


Figure 24 – Friction factor ratios for $s = 40$

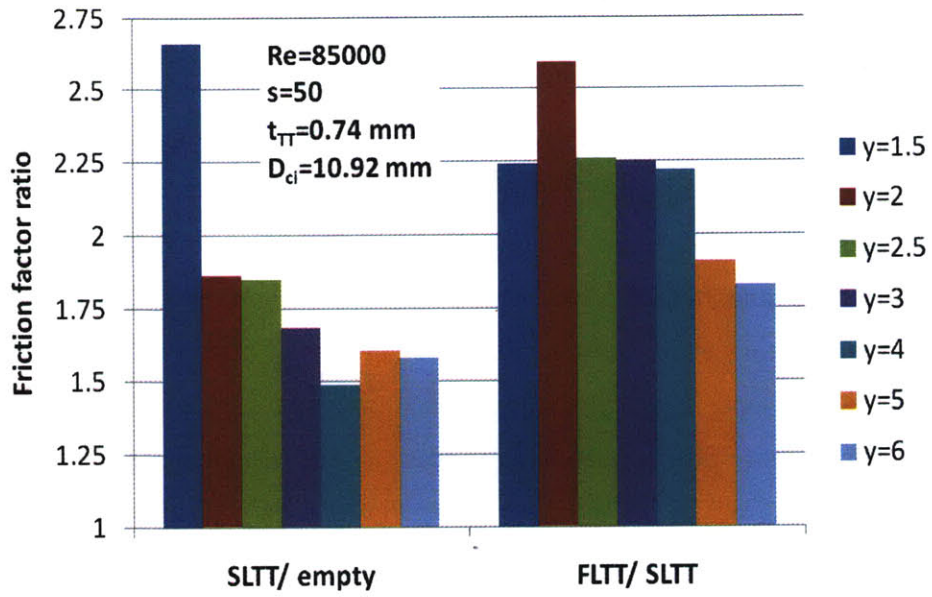


Figure 25 – Friction factor ratios for $s = 50$

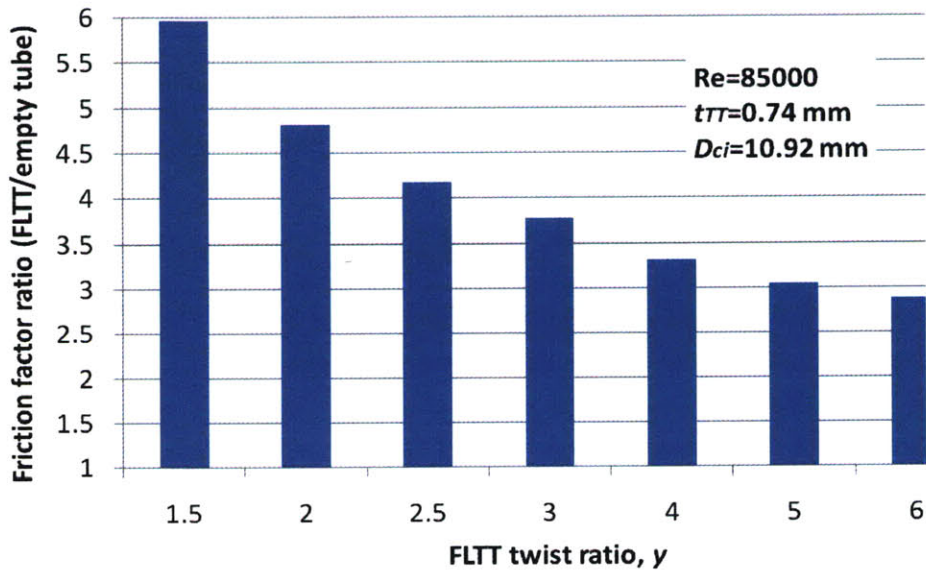


Figure 26 – FLTT/empty tube friction factor ratio. Manglik-Bergles (1993) correlation used to predict FLTT friction factor

Appendix A: Calculation of the pressure drop penalty due to the use of a FLTT

This Appendix presents a methodology to estimate the pressure drop increase, relative to an empty tube, resulting from inserting a full-length tape (straight or twisted) inside the tube, for the same mass flow rate conditions. Even though an estimate of the pressure drop penalty for a straight tape can be obtained using results from the case of a twisted tape by simply setting $y=\infty$, the case of a straight tape is discussed separately since, unlike for a twisted tape, an analytical approach is possible. Section A.1 presents such an approach. For the case of a twisted tape, instead, an entirely analytical approach is not possible and results from an interpolation of experimental data, obtained by Manglik and Bergles (2002), have to be used.

A.1 Full-length straight tape (FLST)

Analyzing a full-length straight tape has two advantages:

- it allows for an entirely analytical treatment of the problem;
- it provides the lower bound of the pressure drop increases resulting from the insertion, in a tube, of FLTTs of any twist ratio. This is because a tape with $y=\infty$ yields a pressure drop that is certainly lower than that associated with a tape having finite y .

The increase in pressure drop, relative to the empty tube, associated with a FLST can be calculated by applying simple geometrical relations to the expression for the friction pressure drop which, for a generic channel, has the following form³⁴:

$$\Delta p = \tilde{f} \frac{L_{actual}}{D_{eq}} \frac{G_{actual}^2}{2\rho} \quad (A-1)$$

³⁴ It must be stressed that this expression for the friction pressure drop is not used in the rest of the thesis, but only here due to the need of relating pressure drop to the actual characteristics of a channel. In fact, in this expression the friction factor, denoted with \tilde{f} to distinguish it from the everywhere else used f , is defined with respect to the actual geometric (D_{eq} and L_{actual}) and hydraulic (G_{actual}) characteristics of the channel: a definition that is not consistent with the convention typically used in heat transfer augmentation applications, where the empty tube parameters are instead used (Marner et al., 1983).

where \tilde{f} is the Darcy friction factor defined with respect to the actual channel parameters, L_{actual} is the length travelled by the fluid, D_{eq} is the equivalent diameter, G_{actual} is the actual mass flux and ρ is the fluid density. The friction factor can be expressed as function of the Reynolds number using the Blasius correlation (Todreas and Kazimi, 1993):

$$\tilde{f} = 0.316 \text{Re}^{-0.25} \quad (\text{A-2})$$

with: $\text{Re} = \frac{\dot{m}D_{eq}}{A_{flow}\mu}$. By introducing Eq. A-2, the expression for the Reynolds number and the definition of mass flux in Eq. A-1 we get:

$$\Delta p = 0.316 \left(\frac{\dot{m}D_{eq}}{A_{flow}\mu} \right)^{-0.25} \frac{L_{actual}}{D_{eq}} \frac{\left(\frac{\dot{m}}{A_{flow}} \right)^2}{2\rho} = 0.158 \frac{\mu^{0.25}}{\rho} \frac{\dot{m}^{1.75} L_{actual}}{D_{eq}^{1.25} A_{flow}^{1.75}} \quad (\text{A-3})$$

which, for an empty tube of diameter D_{ci} and length L , becomes:

$$\Delta p_{empty} = 0.158 \frac{\mu^{0.25}}{\rho} \dot{m}^{1.75} \left(\frac{4}{\pi} \right)^{1.75} \frac{L}{D_{ci}^{4.75}} \quad (\text{A-4})$$

Unlike in a tube provided with a twisted tape, in a tube provided with a straight tape the fluid path length is equal to the tube length, and thus $L_{actual} = L$. However, the flow area and the equivalent diameter are different than in an empty tube:

$$A_{flow} = \frac{\pi}{4} D_{ci}^2 - t_{TT} D_{ci} \quad (\text{A-5})$$

$$D_{eq} = 4 \frac{A_{flow}}{P_w} = 4 \frac{\frac{\pi}{4} D_{ci}^2 - t_{TT} D_{ci}}{\pi D_{ci} + 2D_{ci} - 2t_{TT}} = \frac{\pi D_{ci} - 4t_{TT}}{\pi + 2 - 2\frac{t_{TT}}{D_{ci}}} \quad (\text{A-6})$$

By introducing Eqs. A-5 and A-6 into Eq. A-3 we get an expression for the pressure drop of a tube provided with a full-length straight tape (FLST):

$$\Delta p_{FLST} = 0.158 \frac{\mu^{0.25}}{\rho} \dot{m}^{1.75} 4^{1.75} \frac{L}{D_{ci}^{1.75} \frac{(\pi D_{ci} - 4t_{TT})^3}{\left(\pi + 2 - 2\frac{t_{TT}}{D_{ci}} \right)^{1.25}}} \quad (\text{A-7})$$

The ratio between Eq. A-7 and Eq. A-4 gives the pressure drop increase, relative to the empty tube, resulting from the insertion of a FLST into it, for constant mass flow rate conditions:

$$\frac{\Delta p_{FLST}}{\Delta p_{empty}} = \pi^{1.75} \frac{\left(\pi + 2 - 2 \frac{t_{TT}}{D_{ci}} \right)^{1.25} D_{ci}^3}{\left(\pi D_{ci} - 4t_{TT} \right)^3} \quad (\text{A-8a})$$

which can be further simplified by taking $t_{TT} \ll D_{ci}$:

$$\frac{\Delta p_{FLST}}{\Delta p_{empty}} \approx \left(1 + \frac{2}{\pi} \right)^{1.25} = 1.85 \quad (\text{A-8b})$$

Hence, for typical geometries in which the tape thickness, t_{TT} , is much smaller than the tube inside diameter, the insertion of a full-length tape into a tube yields a pressure drop increase of about 1.85 times if the tape is straight, and larger than 1.85 times if it is twisted. The following section, referred to FLTT insertion, is aimed at quantifying the word “larger”.

A.2 Full-length twisted tape (FLTT)

Equations A-7, A-8a and A-8b cannot be used for the calculation of the pressure drop associated with a FLTT, for two reasons related to the procedure followed in Section A.1:

- the correlation used for the friction factor, i.e. the Blasius correlation, was developed for axial flow;
- the fluid path length in a FLTT-provided tube is not equal to the tube length, as adopted in the methodology presented for a FLST, but is larger because of the fluid helicoidal trajectory. According to Manglik and Bergles (2002) the actual length of the fluid path in swirl flow is:

$$L_{actual} = L \sqrt{1 + \left(\frac{\pi}{2y} \right)^2} \quad (\text{A-9})$$

While the longer fluid path length could have been easily accounted for in the methodology described in Section A.1, i.e. by simply adding the multiplicative term

$\sqrt{1 + \left(\frac{\pi}{2y}\right)^2}$ to the right hand side of Eq. A-8a, the modification of the dependence of the friction factor on the Reynolds number is not trivial and cannot be done analytically. For this reason, to estimate the ratio $\frac{\Delta p_{FLTT}}{\Delta p_{empty}}$ a different methodology from that used in Section A.1 is used here. In particular, the pressure drop increase is estimated, from the beginning, in the form of a ratio, so that the terms responsible for the pressure drop increase can be easily identified and quantified. Given a tube of length L and inside diameter D_{ci} , the pressure drop ratio between the case of a FLTT inserted in it and the case of the tube assumed to be empty is:

$$\frac{\Delta p_{FLTT}}{\Delta p_{empty}} = \frac{\left(\tilde{f} \frac{L_{actual}}{D_{eq}} \frac{G_{actual}^2}{2\rho} \right)_{FLTT}}{\left(\tilde{f} \frac{L_{actual}}{D_{eq}} \frac{G_{actual}^2}{2\rho} \right)_{empty}} = C_f \times C_L \times C_D \times C_A \quad (A-10)$$

where:

$$C_f = \frac{\tilde{f}_{FLTT}}{f_{empty}} ; \quad C_L = \frac{(L_{actual})_{FLTT}}{L} ; \quad C_D = \frac{D_{ci}}{(D_{eq})_{FLTT}} ; \quad C_A = \frac{(A_{flow}^2)_{empty}}{(A_{flow}^2)_{FLTT}}$$

It must be pointed out that C_f and C_D are treated separately even though the reduction in equivalent diameter, fully captured by C_D , is also contained in C_f . This is done since the dependence law of the friction factor \tilde{f}_{FLTT} on the Reynolds number (and therefore on D_{eq}) is not known and cannot be assumed to be of the type shown by Eq. A-2 since the flow is not axial. By using Eqs. A-9, A-5 and A-6 the last three C-factors can easily be obtained:

$$C_L = \sqrt{1 + \left(\frac{\pi}{2y}\right)^2} \quad (A-11a)$$

$$C_D = \frac{\pi + 2 - 2 \frac{t_{TT}}{D_{ci}}}{\pi - 4 \frac{t_{TT}}{D_{ci}}} \quad (\text{A-11b})$$

$$C_A = \left(1 - \frac{4t_{TT}}{\pi D_{ci}}\right)^{-2} \quad (\text{A-11c})$$

The factor C_f is not easily obtainable analytically. Manglik and Bergles (2002) developed a correlation for C_f by combining analytical methods and experimental data interpolation. This correlation, unlike what has been done in this Appendix, but consistently with the convention for heat transfer augmentation devices (Marnier et al., 1983), defines the friction factors with respect to the actual channel parameters (note the use of f_{FLTT} in place of \tilde{f}_{FLTT}):

$$\frac{f_{FLTT}}{f_{empty}} = \left(1 + \frac{2.752}{y^{1.29}}\right) \left(\frac{\pi}{\pi - \frac{4t_{TT}}{D_{ci}}}\right)^{1.75} \left(\frac{\pi + 2 - \frac{2t_{TT}}{D_{ci}}}{\pi - \frac{4t_{TT}}{D_{ci}}}\right)^{1.25} \quad (\text{A-12})$$

Eq. A-12 can be easily manipulated³⁵ to obtain an analogue expression in which \tilde{f}_{FLTT} appears in place of f :

$$C_f = \frac{\tilde{f}_{FLTT}}{f_{empty}} = \left(1 + \frac{2.752}{y^{1.29}}\right) \frac{\left(1 + \frac{2}{\pi} - \frac{2t_{TT}}{\pi D_{ci}}\right)^{0.25}}{\sqrt{1 + \left(\frac{\pi}{2y}\right)^2}} \quad (\text{A-11d})$$

³⁵ Eq. A-12 can be converted into Eq. A-11d by means of the following steps: (1) the expression for \tilde{f}_{FLTT} is obtained by equating the pressure drop evaluated using f_{FLTT} to the pressure drop evaluated using \tilde{f}_{FLTT} , i.e. $f_{FLTT} \frac{L}{D_{ci}} \frac{G_{empty}^2}{2\rho} = \tilde{f}_{FLTT} \frac{L_{actual}}{D_{eq}} \frac{G_{actual}^2}{2\rho}$ where f_{FLTT} is obtained from Eq. A-12; (2) the expression for \tilde{f}_{FLTT} is divided by the expression for f_{empty} , i.e. $f_{empty} = 0.316 \text{Re}_{empty}^{-0.25}$.

By inserting Eq. A-11a through A-11d into Eq. A-10 we get:

$$\frac{\Delta p_{FLTT}}{\Delta p_{empty}} = \left[\left(1 + \frac{2.752}{y^{1.29}} \right) \frac{\left(\pi + 2 - \frac{2t_{TT}}{D_{ci}} \right)^{0.25}}{\pi^{0.25} \sqrt{1 + \left(\frac{\pi}{2y} \right)^2}} \right] \times \left[\sqrt{1 + \left(\frac{\pi}{2y} \right)^2} \right] \times \left[\frac{\pi + 2 - 2 \frac{t_{TT}}{D_{ci}}}{\pi - 4 \frac{t_{TT}}{D_{ci}}} \right] \times \left[\left(1 - \frac{4t_{TT}}{\pi D_{ci}} \right)^{-2} \right]$$

(A-13a)

Eq. A-13a clearly shows the contributions given, to the pressure drop increase, by the various geometric parameters that differ between a FLTT-provided tube and an empty tube. Figure A- 1 shows the trend of these contributors, as a function of the FLTT twist ratio, for a typical geometry having $D_{ci} = 10$ mm and $t_{TT} = 0.74$ mm.

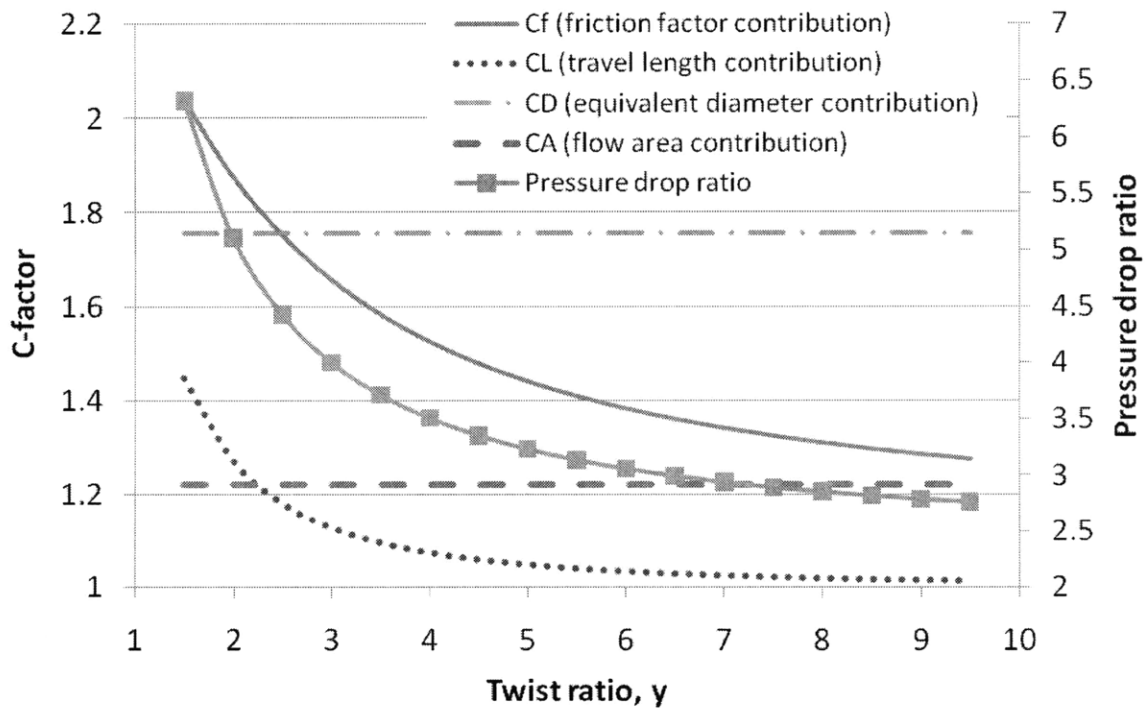


Figure A- 1 – Contributions to pressure drop increase of FLTT-provided tube relative to empty tube

It is interesting to verify that, if Eq. A-2 is used for swirl flow, analytical-derived friction factor ratios much different from the ratio, experimentally verified to be accurate, shown

in Eq. A-11d, would be obtained. This methodology, which demonstrates the impossibility to adopt the friction factor-Reynolds number dependence of Eq. A-2 for swirl flow, is presented in the next section.

A.2.1 Application of typical friction factor-Reynolds number dependence to swirl flow

The Blasius correlation, here presented as Eq. A-2, can be applied to swirl flow in three ways, depending on the velocity component chosen for the computation of the Reynolds number: the axial component, the velocity component along the tube walls or the resultant velocity. The three cases are discussed below.

Velocity axial component

If the axial component of the velocity, V_a , is used, it is straightforward to demonstrate that:

$$\left(\frac{\tilde{f}_{ELTT}}{f_{empty}} \right)_{with\ Eq.\ A-2, V_a} = \left(1 + \frac{2}{\pi} - \frac{2t_{TT}}{\pi D_{ci}} \right)^{0.25} \quad (A-14)$$

It can be noticed that, with respect to Eq. A-11D, Eq. A-14 lacks of the y -containing terms, which are responsible (except for the case of $y=\infty$ which makes the two equations identical) of the deviation of the f -Re law from the Blasius correlation of Eq. A-2.

Velocity component along the tube walls

If the component of the velocity along the tube walls, V_s , is used, knowing that (Manglik and Bergles, 2002):

$$V_s = V_a \sqrt{1 + \left(\frac{\pi}{2y} \right)^2} \quad (A-15)$$

the following relation can be obtained:

$$\left(\frac{\tilde{f}_{ELTT}}{f_{empty}} \right)_{with\ Eq.\ A-2, V_s} = \left[1 + \left(\frac{\pi}{2y} \right)^2 \right]^{0.375} \frac{\left(1 + \frac{2}{\pi} - \frac{2t_{TT}}{\pi D_{ci}} \right)^{0.25}}{\sqrt{1 + \left(\frac{\pi}{2y} \right)^2}} \quad (A-16)$$

Resultant velocity

If the resultant velocity, V_R , is used, knowing that (Kabata et al., 1996):

$$V_R = V_a \sqrt{1 + \frac{\pi^2}{2y^2}} \quad (\text{A-17})$$

the following relation can be obtained:

$$\left(\frac{\tilde{f}_{FLTT}}{f_{empty}} \right)_{\text{with Eq. A-2, } V_R} = \frac{\left(1 + \frac{2}{\pi} - \frac{2t_{TT}}{\pi D_{ci}} \right)^{0.25}}{\left(1 + \frac{\pi^2}{2y^2} \right)^{0.125}} \quad (\text{A-18})$$

Figure A- 2 shows how the values of $\frac{\tilde{f}_{FLTT}}{f_{empty}}$ obtainable with Eqs. A-14, A-16 and A-18 compare with the experimentally-derived prediction given by Eq. A-11d, for a FLTT geometry having $D_{ci} = 10$ mm and $t_{TT} = 0.74$ mm. It can be seen that, no matter what velocity component is used in the Blasius correlation, this correlation significantly underpredicts the friction factor, and cannot therefore be used in swirl flow.

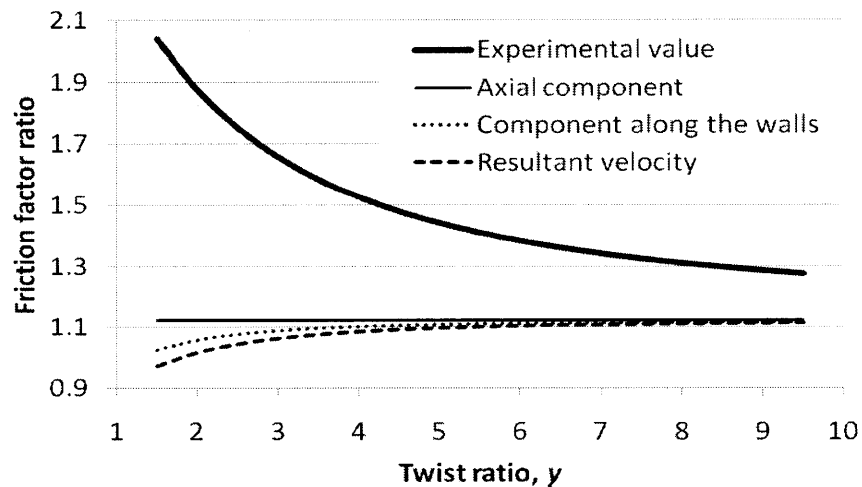


Figure A- 2 – $\tilde{f}_{FLTT} / f_{empty}$ ratio for different form of the friction factor-Reynolds number dependence

Appendix B: Criteria for the selection of N_{rev}

For a given spacing between successive SLTTs, s , the choice of the number of revolutions, N_{rev} , characterizing such tapes is based on the following principle: N_{rev} should be (1) large enough to enhance, at the maximum or close to the maximum extent, CHF throughout the whole swirl-decay region, but (2) small enough to avoid an extra-pressure drop not accompanied by a substantial increase in CHF³⁶. A value for N_{rev} that certainly satisfies the first requirement is the minimum number of revolutions required to create fully developed flow at the TT outlet, $N_{rev,FD}$. However, saying that the number of revolutions satisfying both the above requirements is $N_{rev,FD}$, and that fewer revolutions do not satisfy them, may not be true since a value smaller than $N_{rev,FD}$, eventually coupled with a reduction in s , may be sufficient to generate enough turbulence to result in a CHF augmentation close to the maximum attainable. In other words, CHF enhancement does not necessarily need a fully developed flow at the SLTT outlet, since enhanced turbulence may be sufficient. What a non-fully-developed flow does affect is the length of the region, downstream the TT, where swirl flow persists, since such region will be shorter than in the case of fully developed flow. This drawback can however be compensated by reducing the TT spacing.

B.1 Available experimental studies on $N_{rev,FD}$

No complete studies have been found on the effect that N_{rev} and s have on pressure drop and CHF, simultaneously. Three experimental works dealing predominantly either on CHF/heat transfer coefficient or on pressure drop have however been found: their main findings are summarized in the next three subsections, and a comparison of their results follows. The first work, by Hassid et al. (1966), is considered the most valuable for the inverted PWR project, since it deals with CHF enhancement using water at high pressure (5 MPa). The choice of N_{rev} equal to 1.5, for the pressure drop tests as well as for the inverted PWR design, is a direct consequence of one of the Hassid findings.

³⁶ For a fixed twist ratio, it is known that a TT making a certain number of revolutions may increase the CHF by the same extent (or only slightly less) as that due to a TT making more revolutions. This is because swirl flow does not cease at the TT outlet, but persists downstream although with progressively less intensity as the distance from the TT outlet increases.

B.1.1 Hassid et al. (1966)

Hassid et al. (1966) investigated CHF performance of uniformly-heated tubes containing single and multiple SLTTs, at pressures of 5 and 7 MPa, using subcooled but mostly two-phase water. They tested SLTTs having twist ratio³⁷ ranging between 0.6 and 3, N_{rev} ranging between 0.7 and 3.5 and length of the swirl decay region between 20 and 157 diameters. The results they obtained about the effect that N_{rev} has on CHF have been graphically manipulated to improve clarity, and are shown in Figure B- 1 through Figure B- 3. These figures refer to heated tubes, 15.1 mm in inside diameter, each containing a single SLTT followed by a long swirl decay region, tested with two-phase water at 5 MPa. Each figure shows the CHF ratio as a function of the exit steam quality, for two SLTTs geometries having same twist ratio but different number of revolutions³⁸. The CHF ratio is defined as the ratio between the CHF of the SLTT-provided tube and the CHF of the same tube assumed to be empty. It can be seen that, once the twist ratio is fixed, there is no appreciable variation of the CHF ratio with the number of revolutions³⁹.

³⁷ The fabrication of twisted tapes with such a small twist ratio was possible probably thanks to their large thickness, i.e. 2.5 mm.

³⁸ Although referred to the same twist ratio, the results showed in Figure B- 1 and Figure B- 2 cannot be combined in a single figure since the twisted tapes of Figure B- 1 have 3 threads, while those in Figure B- 2 have 2 threads. Hassid et al. (1966), in fact, also investigated the effect that this geometric parameter, typically equal to 2, has on CHF, and came to the conclusion that such an effect is small.

³⁹ The variation of the CHF ratio (and consequently of the CHF itself) with N_{rev} would not have been negligible if, instead of increasing N_{rev} above 0.7, it had been decreased below 0.7. It is intuitive to conclude that, for each twist ratio, a threshold value for N_{rev} exists, above which no appreciable variation in the CHF can be noticed.

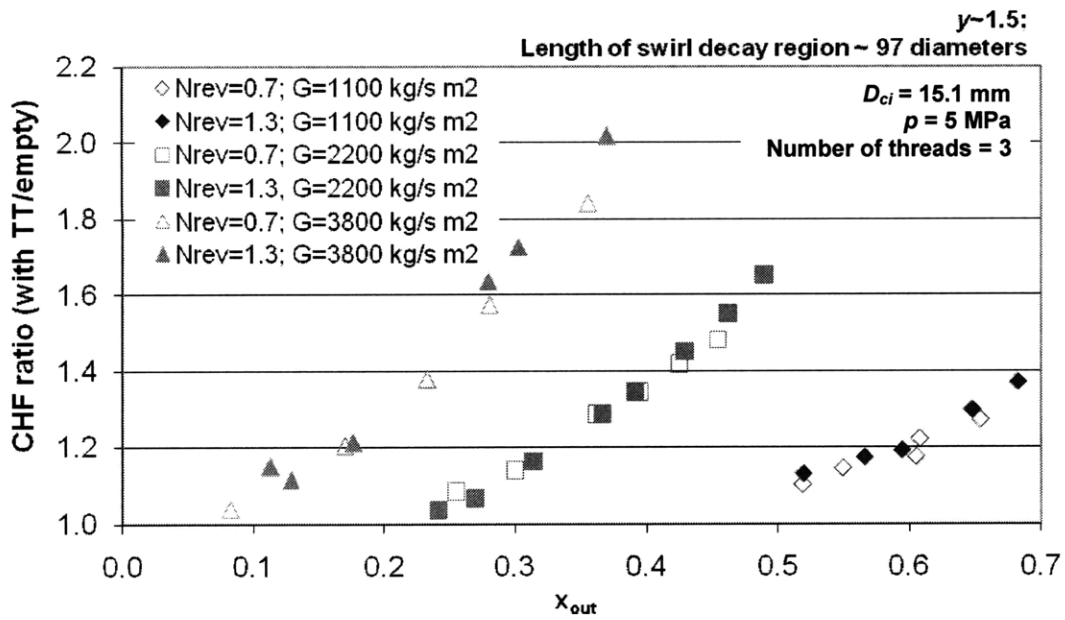


Figure B- 1– Effect of N_{rev} on CHF ratio (from Hassid et al., 1966)

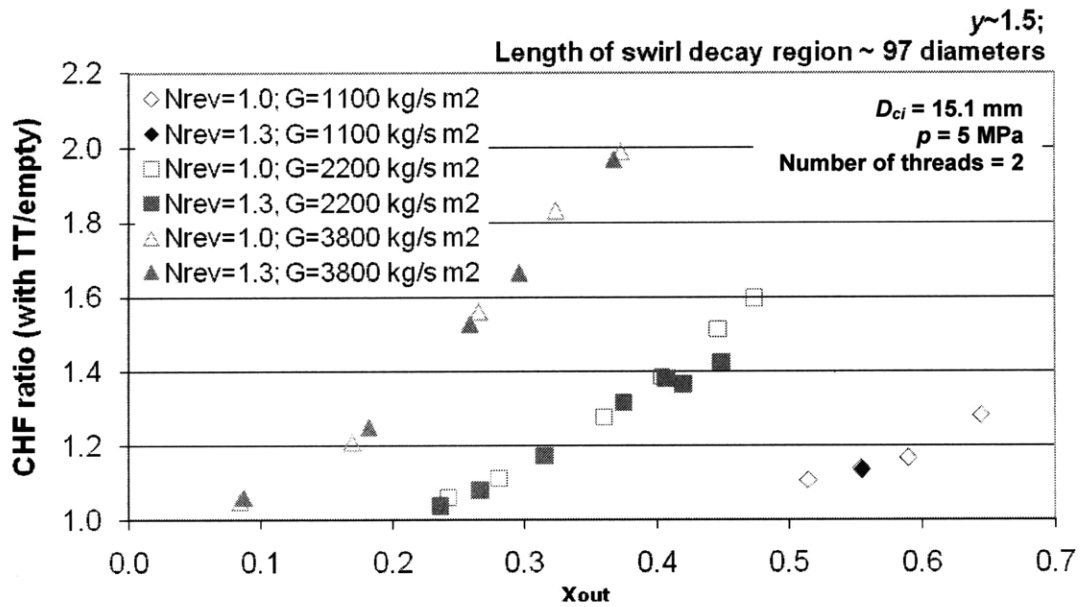


Figure B- 2– Effect of N_{rev} on CHF ratio (from Hassid et al., 1966)

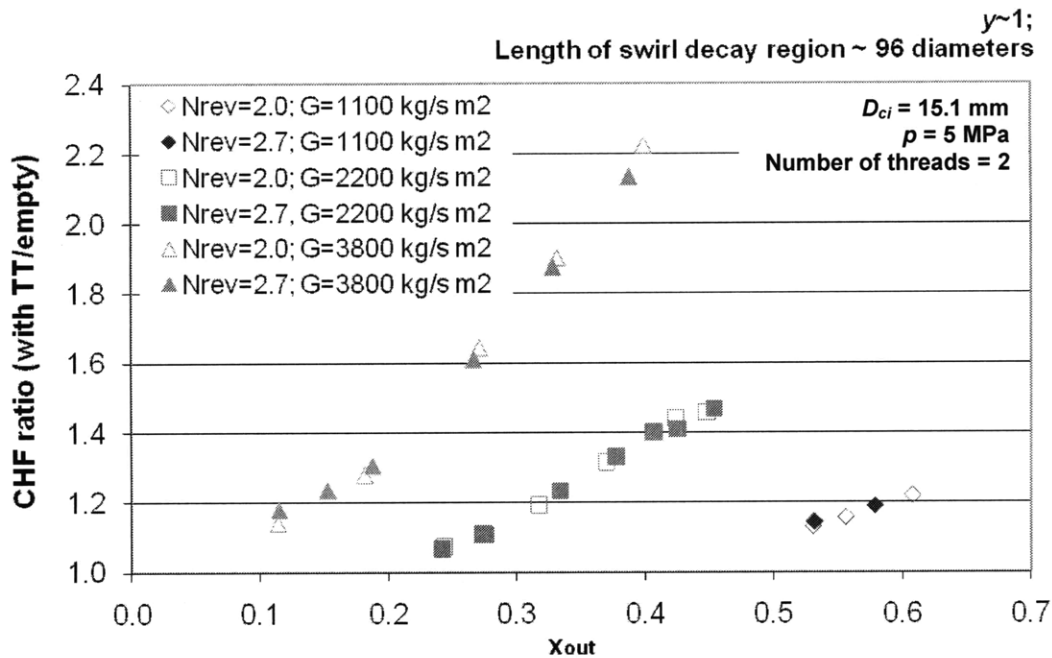


Figure B- 3– Effect of N_{rev} on CHF ratio (from Hassid et al., 1966)

Hassid et al. (1966) concluded this investigation of N_{rev} saying: “it can be inferred that from the point of view of heat transfer crisis the number of pitches can be limited to 1-1.5: any further increase should therefore be avoided since it would lead to a pressure drop increase across the promoter without any advantage”. This conclusion⁴⁰ has been adopted in the IPWR project as the basis for the choice of N_{rev} , which was therefore fixed to 1.5.

B.1.2 Seymour (1966)

Seymour (1966) investigated pressure drop performance of FLTTs of different twist ratios, using air as working fluid. In doing so, he also studied the variation of the friction factor along the whole TT, including the developing region at the inlet, and noticed that this parameter is large at the TT inlet, decreases rapidly over the first diameters, and then approaches the fully developed value in an oscillatory manner. Figure B- 4 is an example

⁴⁰ It is interesting to note that, based on the results shown in Figure B- 1, the CHF enhancement attainable with $N_{rev}=0.7$ is the same as that attainable with $N_{rev}=1.3$, but only at the mass flux values of 1100 and 2200 kg/s m². At 3800 kg/s m² reducing N_{rev} from 1.3 to 0.7 yields a slight reduction in CHF enhancement. This is probably why Hassid et al. (1966) recommended N_{rev} to be between 1 and 1.5 and not between 0.7 and 1.3.

of this trend: it shows the axial friction factor variation for an empty tube and for two tubes containing FLTTs of twist ratio equal to 5.7 and 3.8 respectively. It can be seen that the number of diameters needed to reach fully developed conditions is about 5 for the empty tube, while it is about 9 and 18 for the FLTT cases having $\gamma=3.79$ and $\gamma=5.68$ respectively. These distances are converted in number of 360° revolutions in Figure B- 5, which summarizes the values of $N_{rev,FD}$ for all the geometries considered by Seymour (1966).

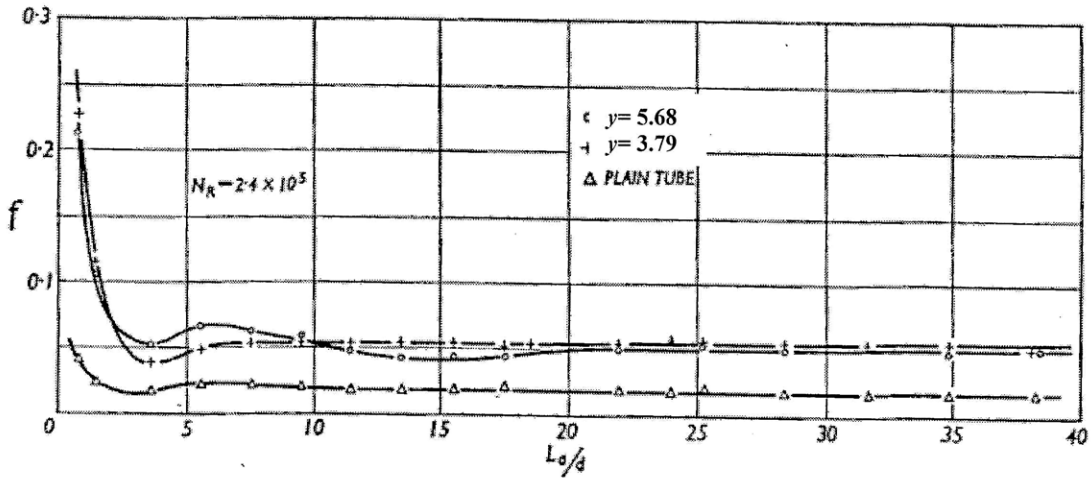


Figure B- 4– Friction factor variation with length, for an empty tube and two FLTT geometries (from Seymour, 1966)

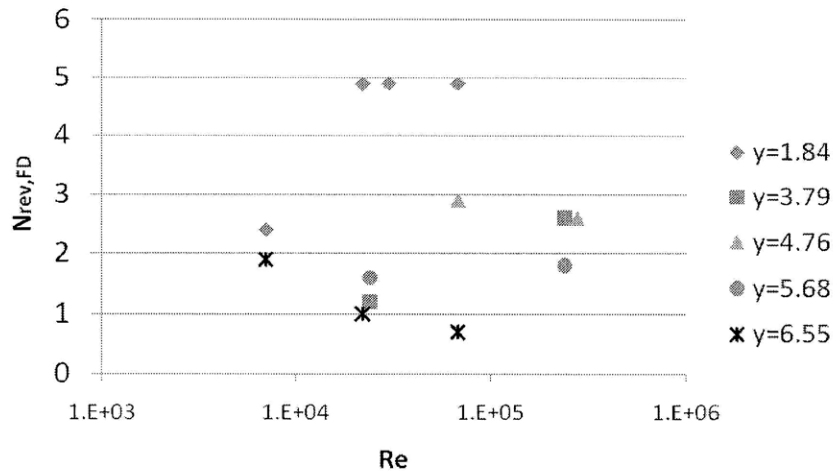


Figure B- 5– Number of 360° revolutions needed to reach fully developed conditions along the taped region, based on friction factor measurements (from Seymour, 1966)

The following observations can be made from Figure B- 5:

- the dependence of $N_{rev,FD}$ on y or Re is not the same for all TT designs. Even though data is limited, it seems however that the smaller is the twist ratio the larger is $N_{rev,FD}$: this was expectable since the significant swirl induced by tight-pitch TTs needs more revolutions to reach the asymptotic behavior;
- it is reasonable to state that $N_{rev,FD}$ ranges between 1 to 3 for $y \geq 3.5$, while for smaller values of y it is larger, and approaches 5 when $y \sim 1.8$.
- since the length of a TT is given by: $L_{TT} = N_{rev} \times P_{360} = N_{rev} \times (2P_{180}) = N_{rev} \times (2yD_{ci})$, the length needed to reach fully developed conditions is: $L_{TT,FD} = N_{rev,FD} \times (2yD_{ci})$. Using the combinations $y-N_{rev,FD}$ mentioned above, for a tube diameter of 10 mm and $1.5 \leq y \leq 6$, $L_{TT,FD}$ ranges between 0.1 and 0.3 m.

B.1.3 Klepper (1975)

Klepper (1975) investigated pressure drop and heat transfer performance of test sections consisting of a medium-length TT followed by a swirl decay region, using nitrogen as working fluid. In doing so, he also examined the reaching of fully developed swirl flow as a function of N_{rev} , through heat transfer coefficient measurements across both the taped and the untaped region. And similarly to the plot by Seymour (see Figure B- 4), the plot shown in Klepper (1975) represents the variation of the Nusselt number with the axial coordinate. This plot, shown in Figure B- 6, refers to a 1.52 m (60 in) long heated test section, containing a 0.567 m (22.33 in) long TT whose inlet was located at 0.24 m (9.5 in) from the test section inlet. The number of 360°- revolutions made by the TT was 6, and the length of the swirl decay region was about 62 diameters. To simplify the understanding of the figure, the black markers can be neglected, and only the empty triangles and the empty circles examined. The former represent the experimental Nusselt numbers for the test section, while the latter are the analytical predictions for an empty tube. It can be seen that:

- with respect to the empty tube, the TT-provided tube has a higher Nusselt number, both in the TT-provided region and in the swirl decay region;

- in the TT-provided region, the Nusselt number is low at the tape inlet, and comparable to the empty-tube value, but then increases to an asymptotic value, which is reached at about 2.8 inches from the TT inlet. The number of 360°-revolutions made by the tape in the first 2.8 inches is between 0.5 and 0.75, which is therefore $N_{rev,FD}$ for the test shown in Figure B- 6;
- the Nusselt number measured at 55 diameters downstream the TT outlet (130 diameters from test section inlet) is about 20% higher than the empty tube value: this indicates that, with the geometry investigated, swirl flow persists up to at least 55 diameters downstream the TT outlet.

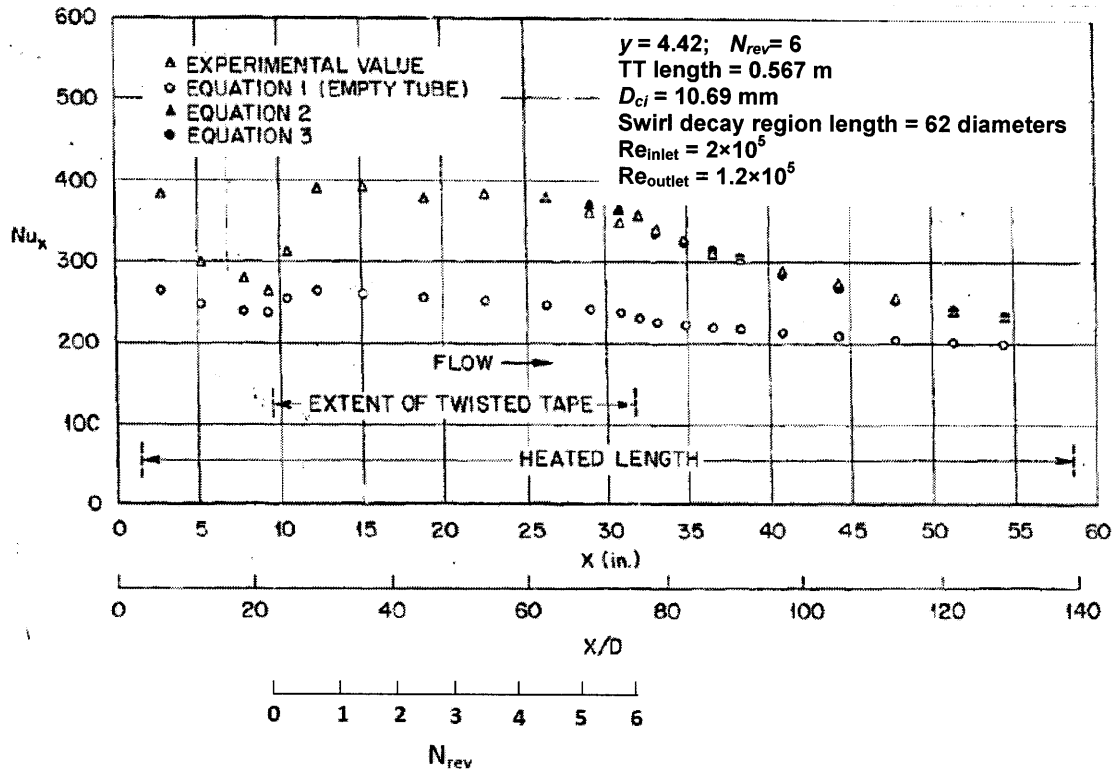


Figure B- 6– Variation of Nusselt number along TT-provided and swirl decay region (from Klepper, 1975)

The summary of the $N_{rev,FD}$ values for all the geometries examined by Klepper is shown in Figure B- 7. It can be seen that $N_{rev,FD}$ is around 0.5-0.6 for all the geometries except for the smallest twist ratio at high Re, for which it is about 5.5.

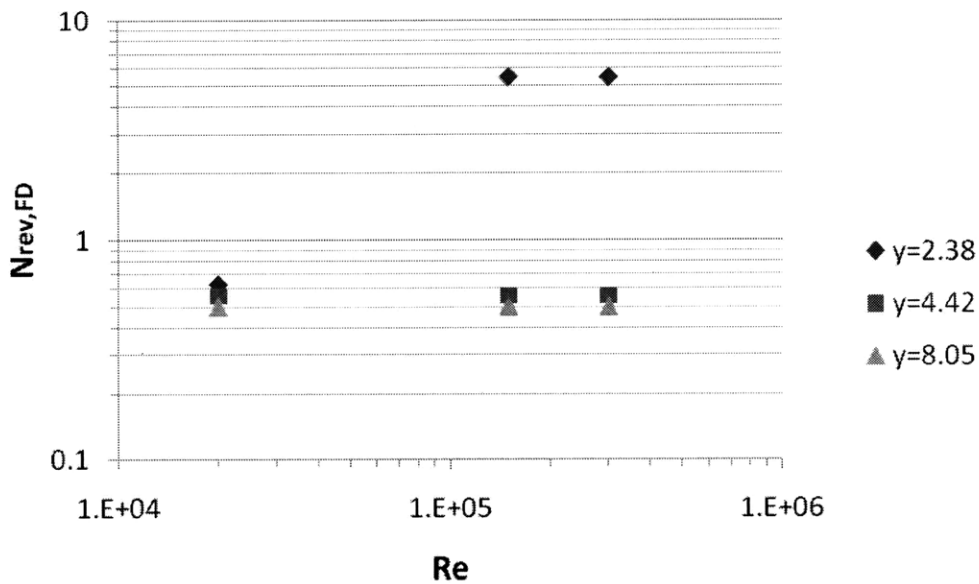


Figure B- 7– Number of 360° revolutions needed to reach fully developed swirl flow along the tape region, based on heat transfer coefficient measurements (from Klepper, 1975)

B.1.4 Comparison between Hassid, Seymour and Klepper results

Figure B- 8 summarizes the results of Seymour (1966) and Klepper (1975) on $N_{rev,FD}$, and compares them with the finding by Hassid et al. (1966). Since Hassid et al. (1966), in their investigation on N_{rev} , only tested twist ratios ≤ 1.5 , it is not possible to come to general conclusions about how $N_{rev,FD}$ compares with the minimum number of revolutions needed to reach the maximum CHF enhancement. However, for $y \leq 1.5$, it is clear that for CHF enhancement purposes it is not necessary to have SLTTs making at least $N_{rev,FD}$ revolutions, i.e. it is not necessary to have a fully-developed swirl flow at the outlet of the TT. Fewer revolutions are sufficient.

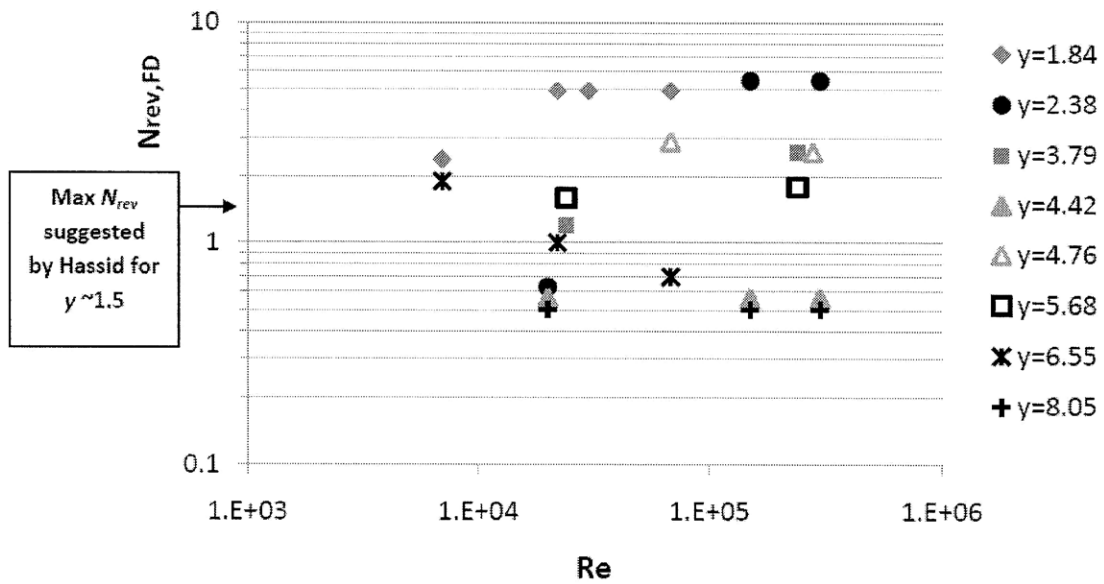


Figure B- 8– Number of 360° revolutions needed to reach fully developed swirl flow along the tape region (from Figure B- 5 and Figure B- 7), compared with Hassid finding

B.2 Implications on the IPWR design

The comparative study presented in this Appendix led to the decision, for the design of the S-IPWR, to fix the number of revolutions of the SLTTs to 1.5.

Appendix C: Investigation of swirl flow development

This Appendix presents results of the development of swirl flow, from the pressure drop viewpoint, across a series of geometrically identical SLTT modules. Such modules are shown in Figure C- 1 for a generic test section, and consist of the Entry Module plus the successive SLTT modules. However, while the pressure drop measurements for the latter modules were taken as shown in Figure C- 1, those for the Entry Module were taken with the short test sections shown in Figure 5, and presented together in this Appendix. The results obtained for the Entry Module can be consistently compared to those obtained for Module 1, 2 etc. by virtue of the pressure drop equivalence between the middle points of two consecutive swirl decay regions and the inlets of two consecutive SLTTs. Such equivalence, already discussed in Section 3, is graphically represented again here for convenience (Figure C- 2).

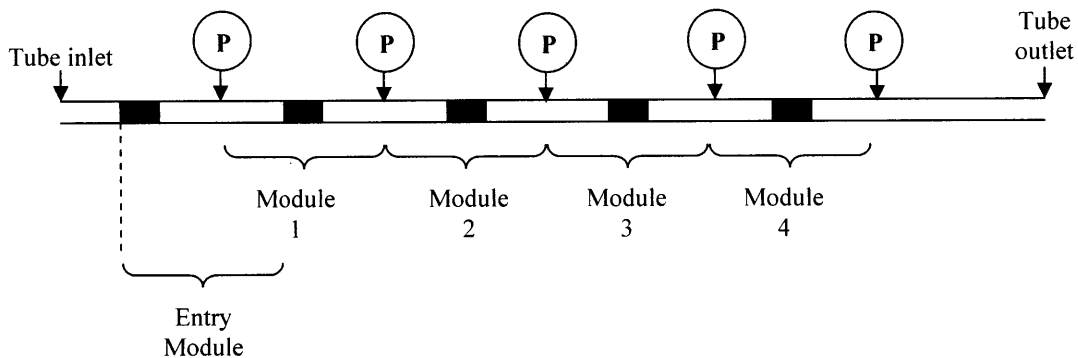


Figure C- 1– Sketch of a generic test section used to investigate the development of swirl flow across SLTT modules (black rectangles represent SLTTs, P ≡ pressure tap; not in scale)

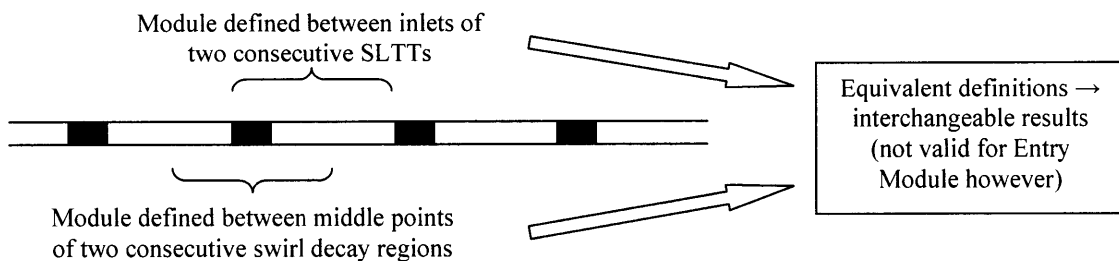


Figure C- 2– Graphical representation of Module Equivalence concept

The investigation discussed in this Appendix was performed since the key results of the pressure drop tests, i.e. the friction factors presented in Section 10, obtained by averaging the pressure drops across Module 1, Module 2 etc., are claimed to be applicable to tubes containing any number of SLTTs. In fact, unlike the test sections used for the study presented in this Appendix (see Figure C- 1), those used for the main part of the experimental work had only two pressure taps (see Figure 4), and the pressure drop claimed to be associated with any of the numbered modules (Module 1, Module 2 etc.) was calculated by dividing the pressure drop measured between the inlet of Module 1 and the outlet of the last module by the number of modules located between the two pressure taps. This calculation implicitly assumed that the swirl flow becomes fully developed soon downstream the Entry Module.

Three new⁴¹ test sections were made to carry out this investigation: 1.5-30, 3-30 and 6-30, all having the general configuration shown in Figure C- 1. The pressure drop across each SLTT module was measured and converted into the corresponding Darcy friction factor using Equation 16. The number of SLTTs in each test section was: 8 in the 1.5-30 test section, 7 in the 3-30 test section and 5 in the 6-30 test section. Figure C- 3 through Figure C- 5 show the friction factors associated with each SLTT module, in the three test sections examined, as a function of the Reynolds number. In particular:

- the markers used to identify the friction factors corresponding to different modules correspond to averaged experimental points. Each marker identifies a $Re-f$ pair, which are the average Reynolds number and the average friction factor obtained at each of the speeds at which the pump was operated. Each point is the result of averaging data pertaining to about 70 measurements, i.e. 70 friction factor and 70 Reynolds number values, close to each other, but averaged to make the plot more readable.

⁴¹ The term “new” is not used to mean that these test sections have a different geometry, in terms of twist ratio and TT spacing, than those used for the main part of the experimental work, but to highlight the fact that they were manufactured specifically for the purpose of this investigation. The test section MS 1.5-30, MS 3-30 and MS 6-30 shown in Table 2 could not be used for this investigation since pressure tap holes would have had to be drilled with the tapes already inserted, which would not have allowed the holes to be deburred. Therefore, the tubes used for the study discussed in this Appendix were first drilled and deburred, and then subjected to TT insertion and securing.

- to make the comparison between friction factors easier, average experimental points have been connected by means of interpolating lines.
- in the comparison between friction factors of different modules, at high Re , the role played by the uncertainties due to instrumentation inaccuracy is very small. Hence, the difference between the friction factors of any two modules cannot be explained by instrumentation error. This has been demonstrated for test section 6-30 only, in Figure C- 5. This figure contains vertical error bars which, in fact, can only be seen for $Re < 35000$, while at higher Reynolds numbers the marker size is sufficient to cover the error bars completely.
- Figure C- 3 also compares the friction factor of the seven modules of test section 1.5-30 with that obtained, before performing the swirl development study discussed in this Appendix, using the method mentioned above, i.e. dividing the pressure drop measured between the inlet of Module 1 and the outlet of the last module by the number of modules. This friction factor is indicated with “FD” (Fully Developed) since it derives from the assumption that the swirl flow becomes fully developed at Module 1. Because of tube type dissimilarity⁴², it was not possible to do the same for test sections 3-30 and 6-30.

⁴²The surface roughness of tube used for this new study was the same only as for test section 1.5-30, while the new test sections 3-30 and 6-30 were made with a tube having different surface roughness.

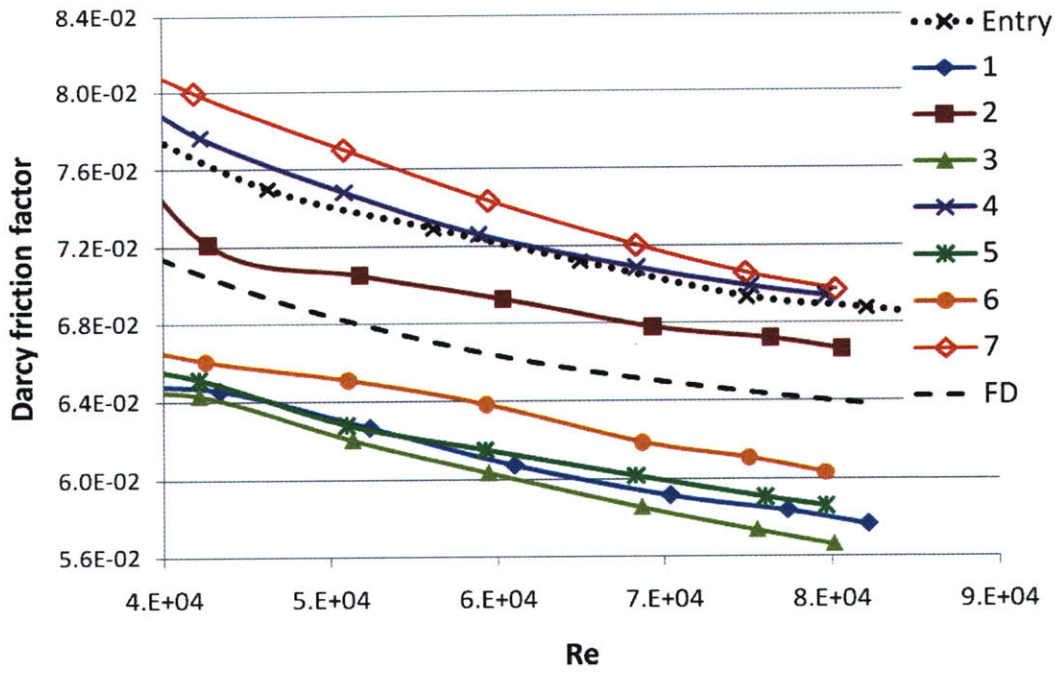


Figure C- 3 – Friction factor of the SLTT modules contained in a test section having $y=1.5$ and $s=30$

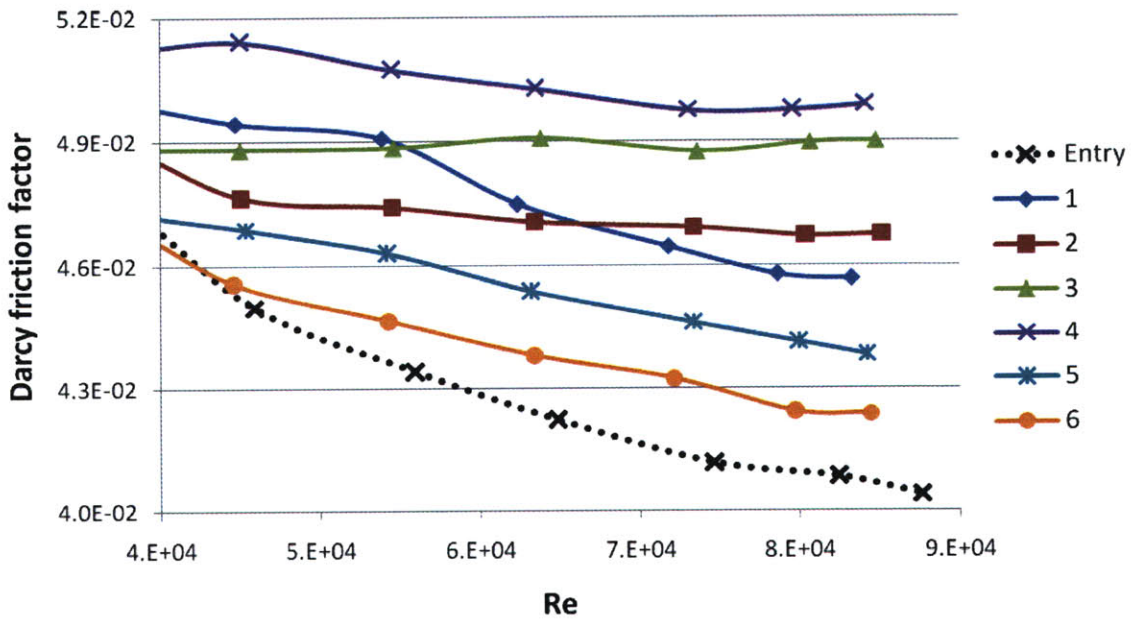


Figure C- 4– Friction factor of the SLTT modules contained in a test section having $y=3$ and $s=30$

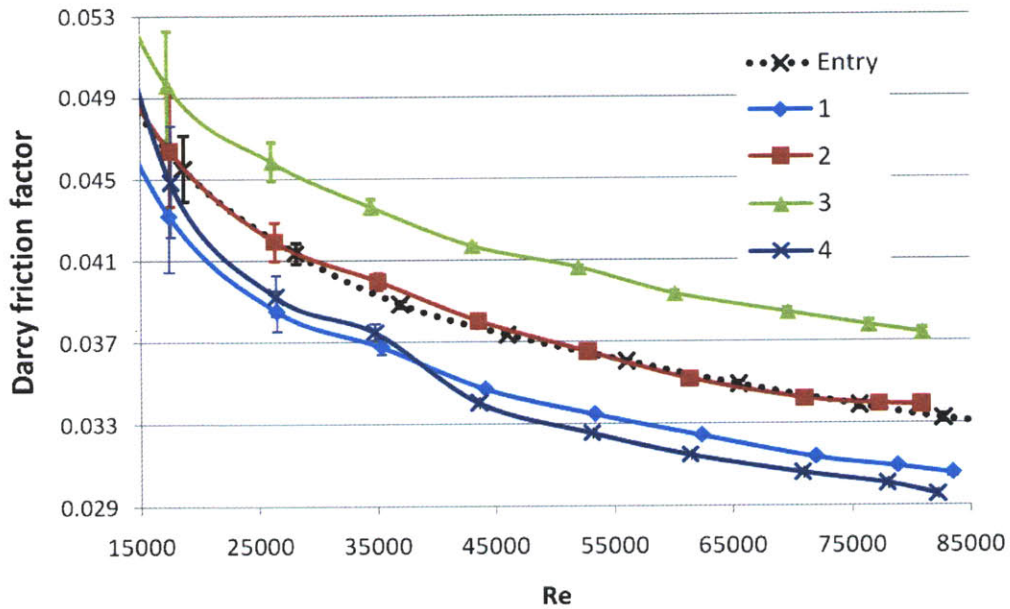


Figure C- 5– Friction factor of the SLTT modules contained in a test section having $y=6$ and $s=30$ (Note: error bands are shown but are too small to be seen for $Re>35000$)

The following observations can be made from Figure C- 3 through Figure C- 5:

- no clear trend exists when comparing the friction factor of successive SLTT modules for the same Re. This is made even more evident with Figure C- 6, which shows the friction factors of the various TT modules at a fixed Re equal to 8×10^4 . The modules, ordered based on increasing friction factor, are:
 - 3 → 1 → 5 → 6 → 2 → (4 and Entry Module) → 7 for test section 1.5-30
 - Entry Module → 6 → 5 → 1 → 2 → 3 → 4 for test section 3-30
 - 4 → 1 → (2 and Entry Module) → 3 for test section 6-30
- at the largest Re tested, the maximum difference between the friction factor of SLTT modules belonging to the same test section is about 20-25%, for all three test sections. This cannot be explained by instrument inaccuracy since, as shown in Figure C- 5, at high Re the standard deviation of the friction factor is very small. Possible reasons of this large difference were investigated, and the

attention was focused on the effects that test section manufacturing variability has on the pressure drop measurements. However, as discussed in the following section, this variability was not found to significantly affect the pressure drop measurements, and only probably half of the observed 20-25% deviations is attributable to it.

- The Entry Module does not behave differently than the other TT modules, in the sense that it was not found to have a friction factor always smaller or larger than those of the downstream SLTTs. This conclusion, which can be inferred by comparing the dotted line to the other lines in Figure C- 3 through Figure C- 5, was actually demonstrated for all the y - s combinations using the short test sections listed at the bottom of Table 2. The results of such tests, of which an example is shown in Figure C- 7, show that the friction factor associated with the Entry Module deviates from the average friction factor of the remaining SLTT modules by no more than $\pm 10\%$, which is consistent with the friction factor scatter of all the modules. Therefore, there is no reason to treat the Entry TT Module differently than the other modules.

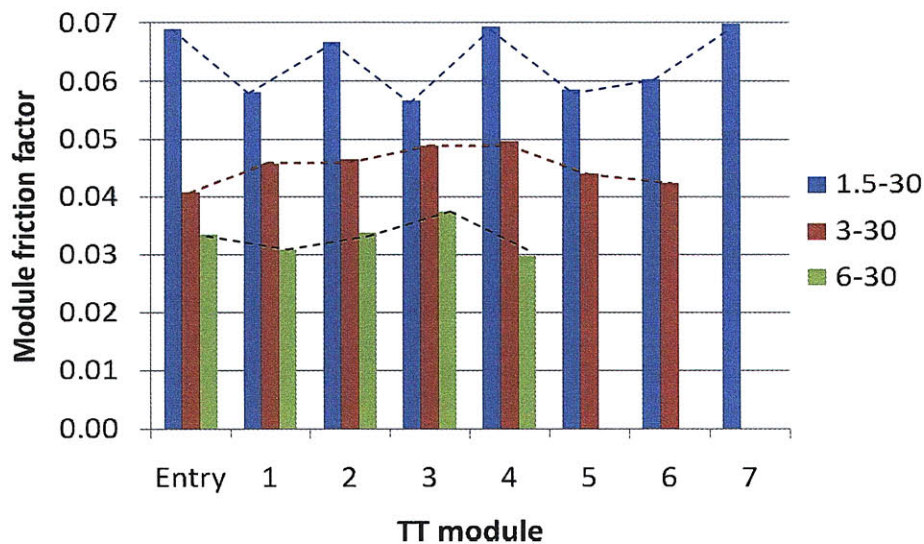


Figure C- 6– Comparison of module friction factors at $Re=8 \times 10^4$

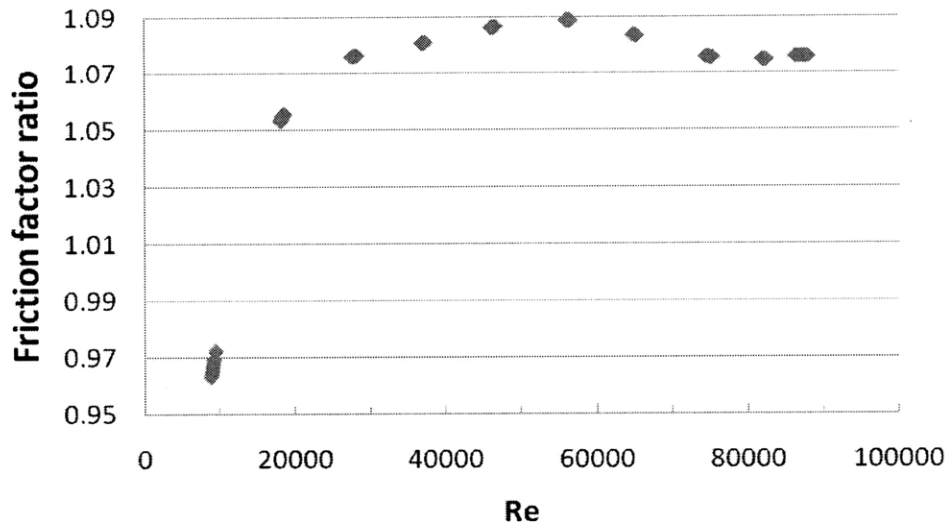


Figure C- 7– Ratio between Entry Module friction factor and average friction factor of the downstream modules ($\gamma=1.5, s=30$; NOTE: other γ - s combinations yield similar results)

C.1 Manufacturing variability effects on pressure drop measurements

The test section manufacture procedure explained in Section 5.1.2 introduces several uncertainties in some geometric characteristics that may affect the pressure drop measurements and especially their repeatability for nominally identical SLTT modules. These characteristics are:

- twisted tape phase angle: as discussed in Section 5.1.2, neither the TT insertion method nor the post-insertion phase angle checking method can guarantee that the phase angle characterizing the SLTTs contained in a test section is exactly 0° . Slight deviations from zero could occur.
- tube inside diameter at TT inlet/outlet: the TT-tube securing method consisted, as discussed in Section 5.1.2, of swaging down the tube at the inlet and outlet of the tapes, using compression fittings. This procedure allowed reduction of the tube inside diameter at those axial locations, but of a non-controllable amount between about 0.1 and 0.7 mm.

- twisted tape width: before being twisted, the tapes were sheared from a metal sheet and filed down to a width ranging between 10.6 and 10.75 mm (the general principle was to file them down to the maximum width still allowing them to be inserted into the tubes). The twisting further reduced their width, by about 0.1-0.3 depending on the twist ratio. This variability did not allow all the TTs to have the same width for the gap between the TT lateral profiles and the tube inside surface⁴³.

Since the manufacturing variability could not be controlled, it was not possible to study the effect that each of the factors mentioned above has, singularly, on pressure drop. It was therefore decided to perform two investigations. The first investigation, discussed in Section C.1.1, was mainly related to the TT phase angle, and addresses the influence that the swirl character of the flow has on the pressure drop measurements. The second investigation, discussed in Section C.1.2, examines the combined effect that the geometric parameters affected by manufacturing variability have on pressure drop measurements.

C.1.1 Effect of swirl flow

The azimuthal asymmetry of the swirl flow was investigated as possible reason for the different pressure drop associated with the SLTT modules belonging to the same test section. It was thought possible that the pressure taps located in the middle of the swirl decay regions could sense different pressures depending on how the flow is directed relative to the pressure tap. Even though the pressure taps in the test sections having general setup shown in Figure C- 1 were located in the same azimuthal position along the tube, and all in the middle of swirl decay regions, slight deviations in TT phase angle, θ_{TT} , due to unwanted TT rotation during test section manufacture (see Section 5.1.2) could have caused the impingement angle of the flow to be different for the various pressure taps. This possibility has been verified by testing two tubes, horizontally

⁴³ Seymour (1966) experimentally verified that variability in small gap widths has a negligible influence on pressure drop. For this purpose he tested FLTT designs having different twist ratios and diametral gap widths of 0.08 mm (=0.3% of the tube inside diameter) and 0.38 mm (=1.5% of the tube inside diameter), which were found to yield the same pressure drop. However, since the relative diametral gap widths of the test sections used throughout this experimental work were larger, i.e. of the order of 3-4% of the tube inner diameter, a possible influence of the gap width variability on pressure drop cannot be excluded.

- The ratio between pressure drop measurements is very close to unity, i.e. between 0.91 and 1.04, for the higher twist ratio, i.e. for $\gamma=3$.

Based on these observations it can be concluded that the existence of different impingement angles between flow and pressure taps could be responsible for a +/-10% variation in the measured pressure drops between successive SLTT modules, when the tested twist ratio is small, i.e. $\gamma < 3$. Such variation becomes negligible for twist ratios ≥ 3 .

The fact that the effect of the pressure tap azimuthal placement is larger for small twist ratio-TTs can be explained with the more vigorous swirling of the flow exiting from such tapes. This reasoning, however, needs further investigation since it cannot be used to explain why, in Figure C- 9, the ratios are closer to unity when the pressure taps are closer to the tape. By applying the same reasoning, the more vigorous swirl existing at $d=30/2$ should result in a pressure drop ratio farther from unity than for $d=40$, which is not the case.

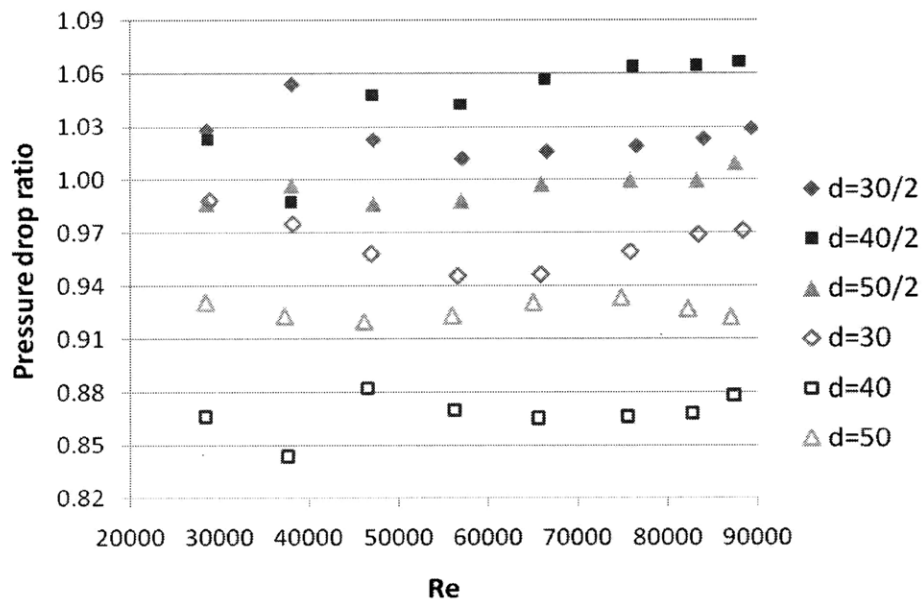


Figure C- 9– Effect of pressure tap azimuthal position on pressure drop, for $\gamma=1.5$

- The ratio between pressure drop measurements is very close to unity, i.e. between 0.91 and 1.04, for the higher twist ratio, i.e. for $y=3$.

Based on these observations it can be concluded that the existence of different impingement angles between flow and pressure taps could be responsible for a +/-10% variation in the measured pressure drops between successive SLTT modules, when the tested twist ratio is small, i.e. $y < 3$. Such variation becomes negligible for twist ratios ≥ 3 .

The fact that the effect of the pressure tap azimuthal placement is larger for small twist ratio-TTs can be explained with the more vigorous swirling of the flow exiting from such tapes. This reasoning, however, needs further investigation since it cannot be used to explain why, in Figure C- 9, the ratios are closer to unity when the pressure taps are closer to the tape. By applying the same reasoning, the more vigorous swirl existing at $d=30/2$ should result in a pressure drop ratio farther from unity than for $d=40$, which is not the case.

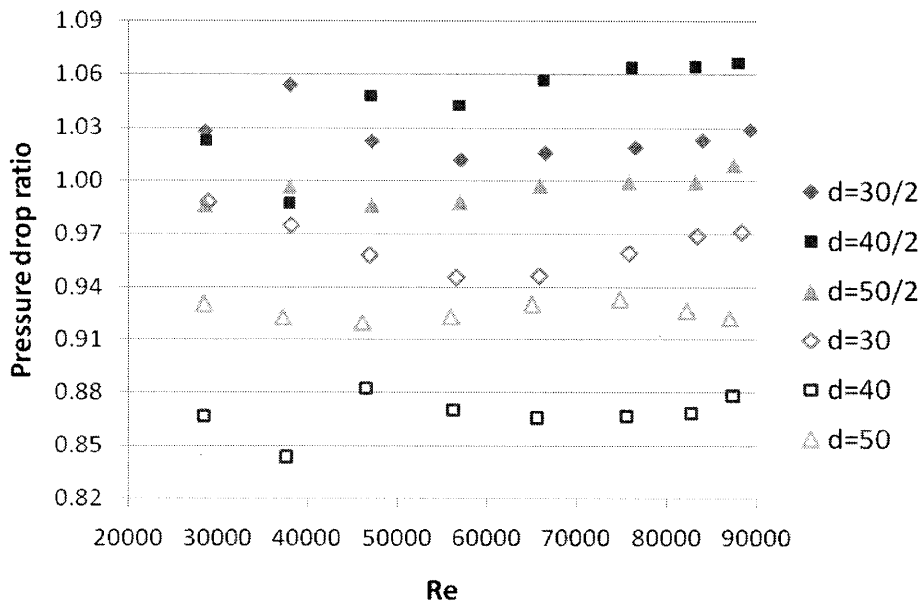


Figure C- 9– Effect of pressure tap azimuthal position on pressure drop, for $y=1.5$

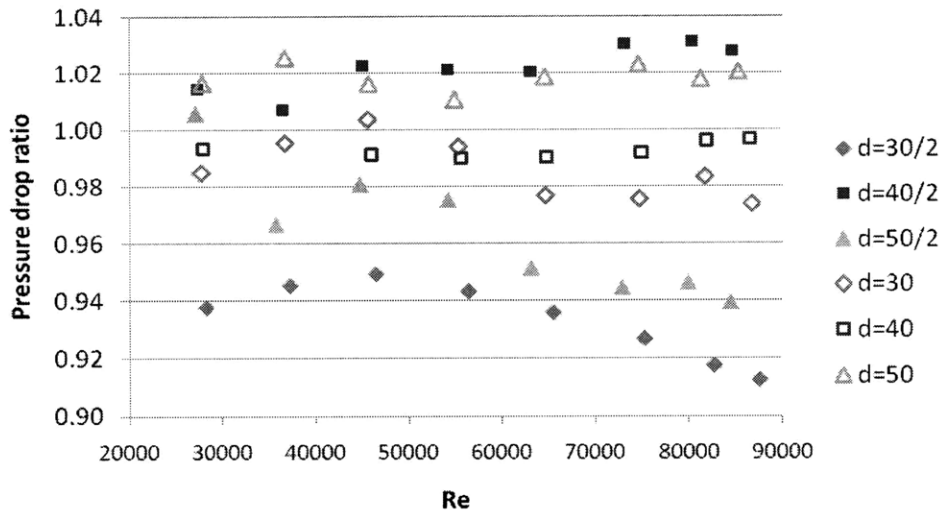


Figure C- 10– Effect of pressure tap azimuthal position on pressure drop, for $y=3$

C.1.2 Combined effect of geometric parameters affected by manufacturing variability

This investigation was performed to understand how the trend of the friction factor, across successive SLTT modules, compares between nominally identical test sections. A difference between trends was expected since manufacturing variability prevents the geometric parameters listed at the beginning of Section C.1 to be exactly the same in the two test sections. The twist ratio-TT spacing combination chosen for this investigation was 6-30. Pressure taps were mounted on the two test sections, tube 2 type, as shown in Figure C- 1, and pressure drops across the four SLTT modules were measured. For this investigation, the Entry Module was not considered. The friction factors corresponding to the modules considered were then calculated using Equation 16. Figure C- 11 shows these friction factors, as a function of the Reynolds number, for the two test sections.

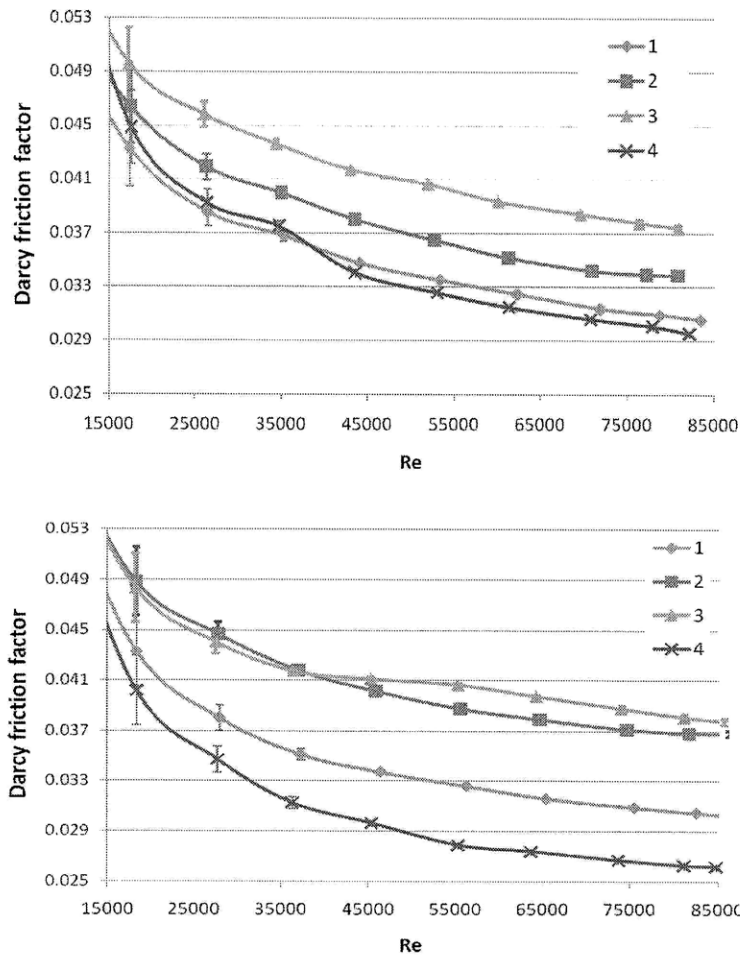


Figure C- 11– Friction factor of the four SLTT modules contained in two nominally identical test sections having $y=6$ and $s=30$ (Notes: (1) all the modules shown have swirl flow at the inlet; (2) error bands are shown but are too small to be seen for $Re>35000$)

By comparing the two plots shown in Figure C- 11, it can be seen that:

- the relative magnitude of the friction factors of the SLTT modules belonging to the two test section is the same, i.e. the order of the SLTT modules, based on friction factor, is the same, and it is: $4 \rightarrow 1 \rightarrow 2 \rightarrow 3$.
- the average friction factor of the four modules at the maximum Re tested is 0.033 for both test sections.

- the deviations between friction factors of single modules at the same Re and in the same position, e.g. the 3rd of the first test section with the 3rd of the second test section, are within 15%.

C.2 Conclusions on swirl development study and possible reason for failing to detect a flow development pattern

From the results presented in Sections C.1 it can be concluded that:

- no clear friction factor trend, typical of flow development scenarios, could be detected across a series of successive SLTT modules;
- the irregularity observed in the friction factor trend is only marginally attributable to test section manufacturing variability.

Evidently other factors, not identified in this study, are responsible for preventing observation of a flow development pattern. Two of these factors could be:

- inlet edge effect: even though, as discussed in Section 5.1.2, the inlet edge of the tapes were filed and smoothed with sandpaper to reduce flow disturbance, some burrs, too small to be noticed with naked eye, might have act as blunt bodies and therefore have induced irregular turbulence at the TT inlet;
- tradeoff between swirl development and boundary layer thinning: at the TT entry these phenomena have opposite effects on pressure drop. Near the inlet edge the swirl is still developing and therefore, relative to a developed swirl flow, the absolute fluid velocity is lower, which implies a lower pressure drop. At the same time, however, the boundary layer is thick, which increases friction at the wall thus penalizing pressure drop. It is possible that the relative importance of these effects changes from one tape to another, thus preventing observation of a regular trend in friction factor.

C.3 Implications on the IPWR design

The results of the swirl development study presented in this Appendix led to the decision, for the design of the IPWR, to not make any distinction between the way the pressure

drop is calculated across the entry TT module and the way it is calculated for all the remaining SLTT of a series.

Appendix D: Effect of water deaeration on pressure drop

This Appendix shows that the results obtained through the pressure drop tests would not have been different if, instead of using tap water, deaerated water had been used. All pressure drop tests were in fact performed with tap water which, as well known, contains air. Because of the pressure reduction experienced by water while flowing through the test section, such air could be released, in the form of bubbles, causing fluctuations in the pressure drop readings. To investigate whether this effect is real, and eventually its magnitude, the test section 1.5-30 used to study the swirl flow development was tested using tap water first, and then using deaerated water. Deaeration was performed by boiling tap water, which was then allowed to cool down to room temperature in sealed containers. Pressure drops across the seven SLTT modules⁴⁴ contained in the test section 1.5-30 were measured with the Omega PX2300-10DI differential pressure transducer. The corresponding friction factors are shown in Figure D- 1, where:

- the letter “D” identifies results obtained with deaerated water, while “ND” refers to runs performed with non-deaerated water;
- the friction factors and the Reynolds numbers obtained at each of the speeds at which the pump was operated were averaged, as to obtain a single point for each pump speed. Each point is the result of averaging data pertaining to about 40 measurements, i.e. 40 friction factor and 40 Reynolds number values.

It can be seen that, for each SLTT module, the experimental friction factor does not change when deaerated water is used in place of non deaerated water, since the friction factors in the two cases differ by less than 3%. The difference between the friction factors corresponding to different SLTT modules is instead significant, and reaches values around 25% when the 3rd module is compared to the 7th. Such difference is discussed in Appendix C.

⁴⁴ The seven SLTT modules are hydraulically identical, in the sense that all have swirl flow at the inlet. The Entry Module, i.e. the one at the tube inlet, is only used to generate swirl, is not considered as part of the test section and its friction factor is not shown in Figure D- 1. The SLTT module referred to as “1st” in Figure D- 1 is Module 1 in Figure 4.

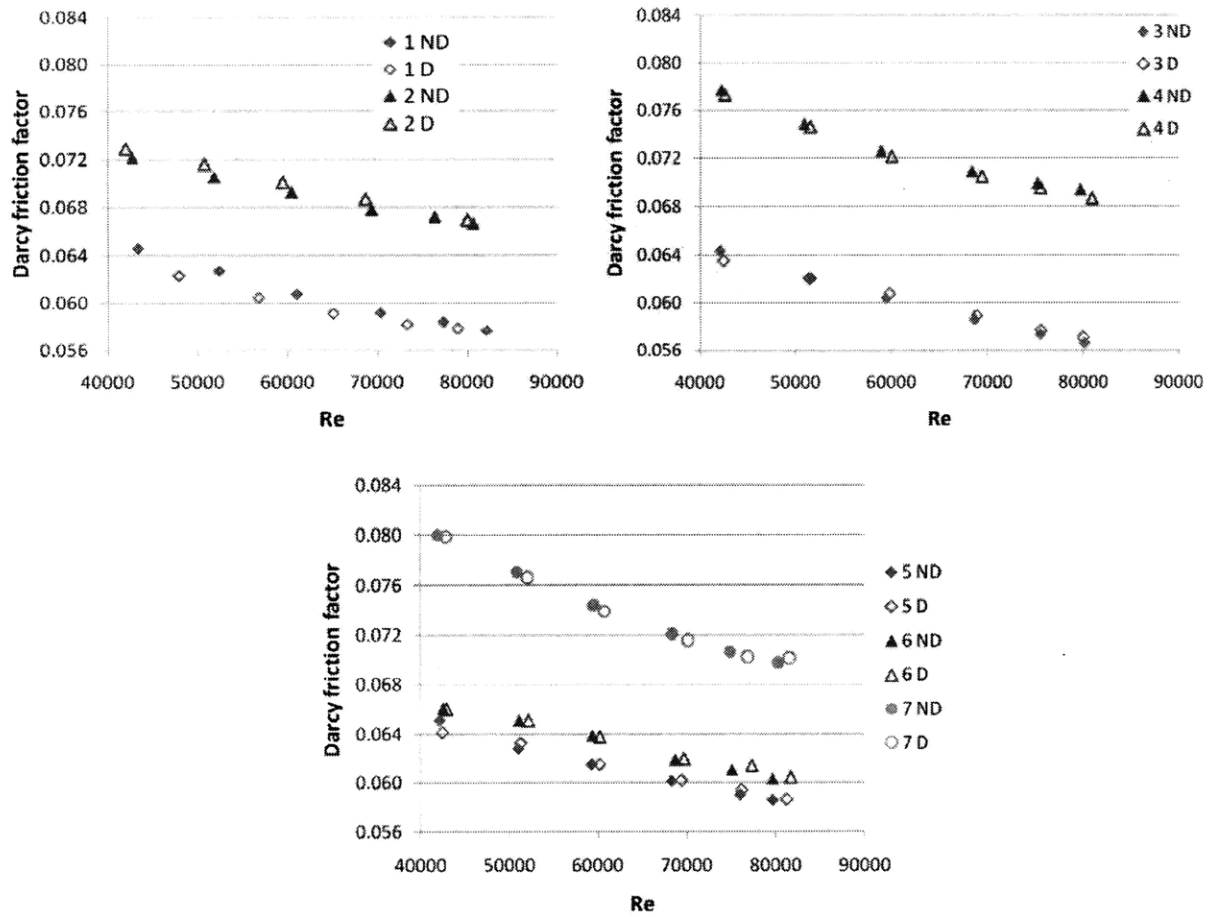


Figure D- 1 – Experimental friction factors for the 7 hydraulically equivalent SLTT modules contained in a test section having $y=1.5$ and $s=30$, for the case of deaerated (D) and non deaerated (ND) water.

References for Volume 2

Ang, A. H.-S., Tang, W.H., 1975. *Probability Concepts in Engineering Planning and Design. Volume I- Basic Concepts*. John Wiley & Sons, Inc.

Bennett, A.W., Hewitt, G.F., Kearsy, H.A., Keeys, R.K.F., 1967. Unpublished information successively reported in Whalley, P.B., The effect of swirl on critical heat flux in annular two-phase flow. Brief communication in *International Journal of Multiphase Flow*, Vol.5, 211-217, 1979.

Blackwelder, R., Kreith, F., 1970. An experimental investigation of heat transfer and pressure drop in a decaying swirl flow. In: *Augmentation of Convective Heat and Mass Transfer*, pp. 102-108. Presented at the Winter Annual Meeting of the American Society of Mechanical Engineers. New York, NY. December 2.

Block, R., Ferroni, P., Todreas, N.E., 2010. Investigation and characterization of pressure drop in evenly spaced twisted tapes. BS thesis (title is not final). Massachusetts Institute of Technology.

Blumenfeld, D., 2001. *Operations Research Calculations Handbook*. CRC Press.

Burfoot, D., Rice, P., 1983. Heat transfer and pressure drop characteristics of short lengths of swirl flow inducers interspaced along a circular duct. *Chemical Engineering Research Design*, 61 (253-258).

Date, A.W., Saha, S.K., 1990. Numerical prediction of laminar flow and heat transfer characteristics in a tube fitted with regularly spaced twisted-tape elements. *International Journal of Heat and Fluid Flow*, Vol. 11, No. 4, (346-354).

Eiamsa-ard, S., Thianpong, C., Promvongse, P., 2004. Experimental investigations of heat transfer and pressure drop characteristics of flow through circular tube fitted with regularly-spaced twisted tape. Joint International Conference on Sustainable Energy and Environment (SEE). 1-3 December, Hua Hin, Thailand.

Eiamsa-ard, S., Promvonge, P., 2005. Enhancement of heat transfer in a tube with regularly-spaced helical tape swirl generators. *Solar Energy*, Vol. 78, (483-494).

Eiamsa-ard, S., Thianpong, C., Promvonge, P., 2006. Experimental investigations of heat transfer and flow friction in a circular tube fitted with regularly spaced twisted tape elements. *International Communications in Heat and Mass Transfer*, 33 (1225-1233).

Klaczak, A., 1996. Heat transfer and pressure drop in tubes with short turbulators. *Heat and Mass Transfer*, Vol. 31, 399-401.

Klepper, O.H., 1975. Heat transfer performance of short twisted tapes. *A.I.Ch.E. Symposium Series* (Heat Transfer No. 131) Vol.8, 1975.

Harvey, A.H., Peskin, A.P., Klein, S.A., 1996. NIST/ASME Steam. Formulation for General and Scientific Use. NIST Standard Reference Database 10, Version 2.2.

Hassid, A., Manzoni, G.C., Ravetta, R., 1966. Heat transfer crisis with steam-water mixtures: an experimental study on the increase of critical power with local swirl promoters in round tubes. *Energia Nucleare*, Vol.13, No.11 (November 1966) 589-610.

Henkel, D., Mayinger, F., Schad, O., Weiss, E., 1965. Untersuchung der kritischen Heizflächenbelastung (Burnout) bei siedendem Wasser (Research into the critical heat flux (burnout) in boiling water). Quarterly Progress Report No. 09.02.07, April 1st to June 30th, 1965. Maschinenfabrik Augsburg Nurnberg AG (MAN) Report No. 057-61-RDD.

Hewitt, G.F., 2003. Boiling enhancement: response to Professor A.E. Bergles. *Rohsenow Symposium*. MIT, May 16, 2003.

ITT, Goulds Pumps: 5GB, 7GB, 10GB, 18GB, 25GB, 33GB. High Pressure Multi-Stage Booster Pump. 2008. Available at: <http://www.goulds.com/pdf/BGB5-33.pdf>.

Kabata, Y., Nakajima, R., Shioda, K., 1996. Enhancement of critical heat flux for subcooled flow boiling of water in tubes with a twisted tape and with a helically coiled wire. *International Conference on Nuclear Engineering*, Vol.1, Part B. ASME.

Lee, S., Inoue, A., 1995. Critical heat flux characteristics of R-113 boiling two-phase flow in twisted-tape-inserted tubes. *Heat Transfer – Japanese Research*, Vol.24, No. 3, 272-287.

Lokanath, M.S., 1997. Performance evaluation of full length and half length twisted tape inserts on laminar flow heat transfer in tubes. Proceedings of the 3rd ISHMT-ASME Heat and Mass Transfer Conference, and 14th National Heat and Mass Transfer Conference, December 29-31. Indian Institute of Technology. Kanpur, India.

Manglik, R.M., Bergles, A.E., 1993. Heat transfer and pressure drop correlations for twisted-tape inserts in isothermal tubes: Part II – Transition and turbulent flows. *Transactions of the ASME*. Vol. 115, 890-896.

Manglik, R.M., Bergles, A.E., 2002. Swirl flow heat transfer and pressure drop with twisted-tape inserts. *Advances in Heat Transfer*, Vol. 36, 183-266.

Marnier, W.J., Bergles, A.E., Chenoweth, J.M., 1983. On the presentation of performance data for enhanced tubes used in shell-and-tube heat exchangers. *Journal of Heat Transfer*, Vol. 105, 358-365.

Matzner, B., Moeck, E.O., Casterline, J.E., Wikhammer, G.A., 1965. Critical heat flux in long tubes at 1000 psi with and without swirl promoters. ASME paper No. 65-WA/HT-30. Presented at the Winter Annual Meeting of the ASME, Chicago, IL, November 7–11.

Marnier, W.J., Bergles, A.E., Chenoweth, J.M., 1983. On the presentation of performance data for enhanced tubes used in shell-and-tube heat exchangers. *Journal of Heat Transfer*, Vol. 105, 358-365.

OMEGA PX2300 Series data sheet, available at:
www.omega.com/Pressure/pdf/PX2300.pdf

OMEGA FTB-900 Series data sheet, available at:
www.omega.com/Green/pdf/FTB900.pdf

Peterlongo, G., Ravetta, R., Riva, B., Rubiera, L., Tacconi, F.A., 1964. Large scale experiments on heat transfer and hydrodynamics with steam-water mixtures: further critical power and pressure drop measurements in round vertical tubes with and without internal obstacles. CISE report R 122. US-Euratom Joint Research and Development Board.

Rayle, R.E., 1959. Influence of orifice geometry on static pressure measurements. *ASME paper 59-A-234*. Also available as: Rayle, R.E., 1949, An investigation on the influence of orifice geometry on static pressure measurements. MS thesis, Massachusetts Institute of Technology.

Saha, S.K., Gaitonde, U.N., Date, A.W., 1989. Heat transfer and pressure drop characteristics of laminar flow in a circular tube fitted with regularly spaced twisted-tape elements. *Experimental Thermal and Fluid Science*, 2 (310-322).

Saha, S.K., Gaitonde, U.N., Date, A.W., 1990. Heat transfer and pressure drop characteristics of turbulent flow in a circular tube fitted with regularly spaced twisted-tape elements. *Experimental Thermal and Fluid Science*, 3 (632-640).

Saha, S.K., Dutta, A., Dahl, S.K., 2001. Friction and heat transfer characteristics of laminar swirl flow through a circular tube fitted with regularly spaced twisted-tape elements. *International Journal of Heat and Mass Transfer*, 44 (4211-4223).

Saha, S.K., Dutta, A., 2001. Thermohydraulic study of laminar swirl flow through a circular tube fitted with twisted tapes. *Journal of Heat Transfer*, 123 (417-427).

Seymour, E.V., 1966. Fluid flow through tubes containing twisted tapes. *The Engineer*. Vol. 222, 634-642.

Sivashanmugam, P., Suresh, S., 2007. Experimental studies on heat transfer and friction factor characteristics of turbulent flow through a circular tube fitted with regularly spaced helical screw-tape inserts". *Applied Thermal Engineering*, Vol. 27, (1311-1319).

Smithberg, E., Landis, F., 1964. Friction and forced convection heat-transfer characteristics in tubes with twisted tape swirl generators. *Journal of Heat Transfer*, Vol. 86, No. 1, 39-49.

Todreas, N.E., Kazimi, M. S., 1993. Nuclear Systems I. Thermal Hydraulic Fundamentals. Taylor and Francis. Second printing.

Whalley, P.B., 1979. The effect of swirl on critical heat flux in annular two-phase flow. Brief communication in *International Journal of Multiphase Flow*, Vol.5, 211-217.

Zozulya, N.V., Shkuratov, I. YA., 1974. Effect of the length of a twisted-tape turbulence promoter and of its initial twisting pitch on augmenting of heat transfer inside a tube. *Heat Transfer – Soviet Research*, Vol. 6, No. 6, 98-100.